JOURNAL OF APPLIED PHYSICS

Vol. 31, No. 9 September, 1960

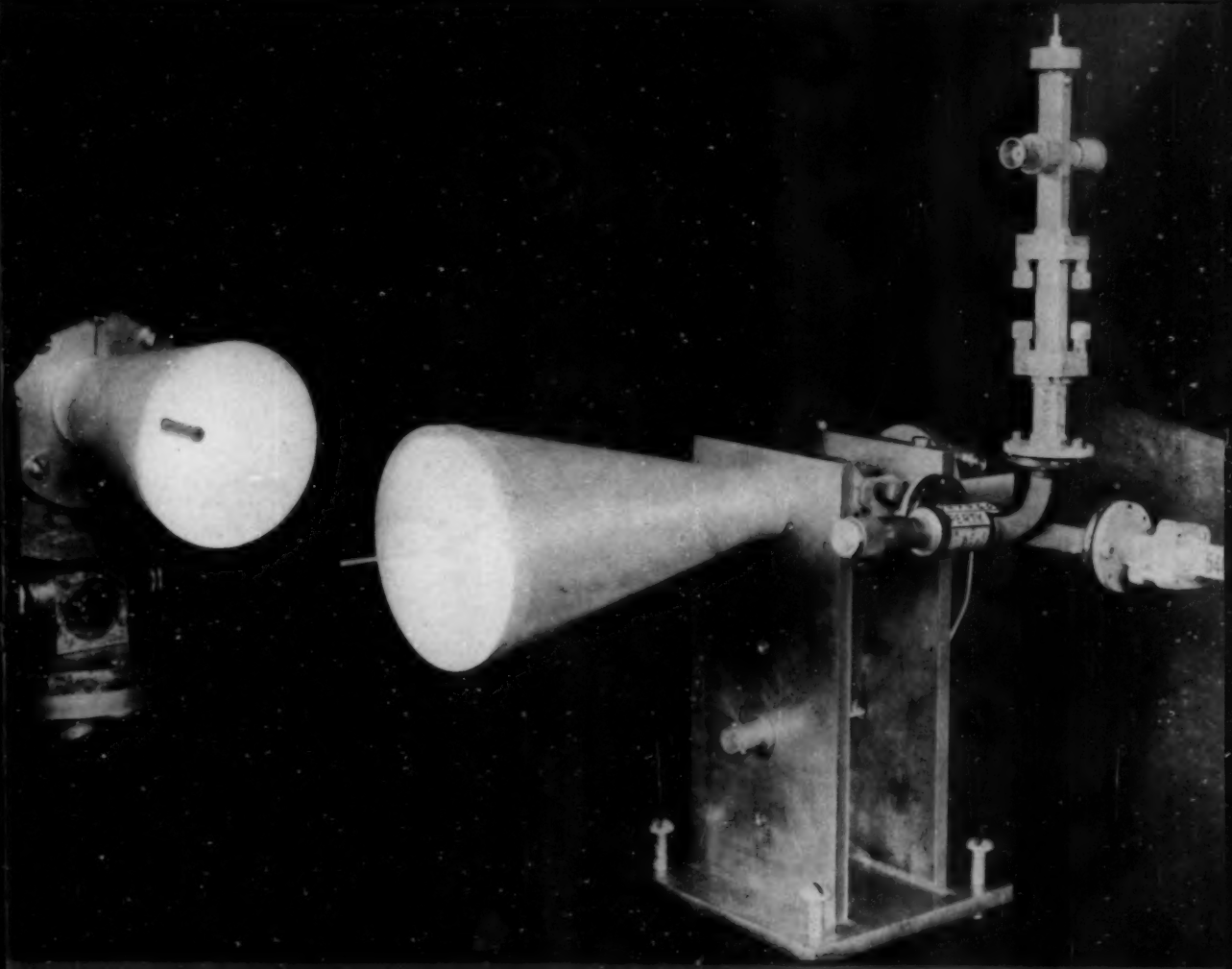

Cerenkov Production of Submillimeter Waves.
See Page 1695.

HARSHAW MANUFACTURES A COMPLETE LINE OF SCINTILLATION AND OPTICAL CRYSTALS

SCINTILLATION *Mounted* NaI(T1) *Crystals*

Crystal detectors designed for the most sophisticated counting problems. Our physics and engineering group are available to assist you in your special detector problems.

More detailed information is contained in our 32-page book, "Harshaw Scintillation Phosphors." We invite you to write for your free copy!

STANDARD LINE
(Hermetically Sealed Crystal Assemblies)

- The accepted standard of the industry
- Proven through years of service in research, medical and industrial applications
- unparalleled performance
- dependability
- consistent good quality.

INTEGRAL LINE
(Crystal photo multiplier tube combination assembly)

- Improved resolution
- Ready to use plug-in unit
- Permanently light sealed
- Capsule design facilitates decontamination
- Close dimensional tolerances
- Harshaw guaranteed

***Large Crystal* MATCHED WINDOW LINE**
(Designed primarily for crystals 4" dia. and larger)

- "Small crystal" performance achieved through improved optical design
- Low mass containers
- Available in standard aluminum or complete low background assemblies
- Convenient mounting flange
- Ready to use

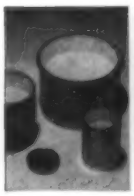

Every Harshaw crystal is a product of our experience in crystal growing technology since 1935

Other Phosphors Available from The Harshaw Chemical Company

ROUGH CUT THALLIUM ACITVATED SODIUM IODIDE CRYSTAL BLANKS • EUROPIUM ACTIVATED-LITHIUM IODIDE (NORMAL) • EUROPIUM ACTIVATED LITHIUM IODIDE (96% Li^6 ENRICHED) • THALLIUM ACTIVATED CESIUM IODIDE • THALLIUM ACTIVATED POTASSIUM IODIDE • ANTHRACENE • PLASTIC PHOSPHORS

OPTICAL *Crystals*

For Infrared and Ultra Violet Transmitting Optics

"HARSHAW QUALITY" INHERENT IN EACH HARSHAW-GROWN CRYSTAL GUARANTEES THE MOST EFFICIENT OPTICAL TRANSMISSION POSSIBLE THROUGH:

1) Negligible light scattering in crystals, permitting higher sensitivity and improved resolution
2) Freedom from absorptions caused by trace impurities in crystal optics
3) Minimum strain

"HARSHAW QUALITY" meets the demand for uniformity of optical properties such as dispersion and refractive index.

Prices, specifications, or other information will be sent in answer to your inquiry.

The following infrared and ultra violet transmitting crystals are available; others are in the process of development:

SODIUM CHLORIDE • SODIUM CHLORIDE MONOCHROMATOR PLATES POTASSIUM BROMIDE • POTASSIUM BROMIDE PELLET POWDER • (through 200 on 325 mesh) • POTASSIUM CHLORIDE • OPTICAL SILVER CHLORIDE • THALLIUM BROMIDE IODIDE • LITHIUM FLUORIDE • LITHIUM FLUORIDE MONOCHROMATOR PLATES • CALCIUM FLUORIDE • BARIUM FLUORIDE • CESIUM BROMIDE • CESIUM IODIDE

Additional information on the physical and optical properties of the above crystals is available in our 36-page booklet "Synthetic Optical Crystals". Send for your free copy.

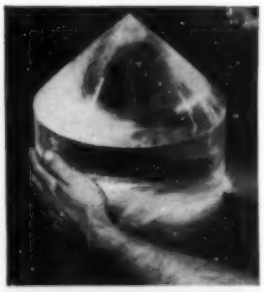

HARSHAW

THE HARSHAW CHEMICAL CO.
Crystal Division • Cleveland 6, Ohio

JOURNAL OF APPLIED PHYSICS

Vol. 31, No. 9 SEPTEMBER, 1960

In This Issue

Statistics of the Occupation of Dislocation Acceptors (One-Dimensional Interaction Statistics) . . . . . R. M. Broudy and J. W. McClure 1511

Ion-Bombardment Etching of Synthetic Fibers . . . . . Franklin R. Anderson and V. F. Holland 1516

Oscillistor—New Type of Semiconductor Oscillator . . . . . R. D. Larrabee and M. C. Steele 1519

Large Temperature Range Annealing . . . . . William Primak 1524

Elastic Constants of Bismuth . . . . . Yakov Eckstein, A. W. Lawson, and Darrell H. Reneker 1534

Dislocations in Indented Magnesium Oxide Crystals . . . . . A. S. Keh 1538

Temperature Dependence of the Velocity of Sidewise 180° Domain-Wall Motion in $BaTiO_3$ . . . . . A. Savage and R. C. Miller 1546

Circuit Dynamics of the Pinch . . . . . J. Killeen and B. A. Lippmann 1549

Irradiation Effects and Short-Range Order in Fused Silica and Quartz . . R. A. Weeks and C. M. Nelson 1555

Some Electrical Properties of Amorphous Selenium Films . . . . . Richard A. Fotland 1558

Chromium-Doped Titania as a Maser Material . . . . H. J. Gerritsen, S. E. Harrison, and H. R. Lewis 1566

Crystallography and Domain Walls in Antiferromagnetic NiO Crystals . . . . . Glen A. Slack 1571

Surface Cleaning by Cathode Sputtering . . . . . O. C. Yonts and Don E. Harrison, Jr. 1583

Apparatus for the Measurement of the Thermal Diffusivity of Solids at High Temperatures . . . . . B. Abeles, G. D. Cody, and D. S. Beers 1585

Negative Hydrogen and Deuterium Ion Beams . . . . . Sanborn F. Philp 1592

Scattering of Electromagnetic Waves from an Infinitely Long Magnetized Cylindrical Plasma . . . . . P. M. Platzman and H. T. Ozaki 1597

Effect of Orientation on Strength of a Model Solid . . . . . A. Robinson, J. E. Osborn, and C. C. Hsiao 1602

Magnetostatic Modes in Disks and Rods . . . . . J. F. Dillon, Jr. 1605

Dielectric Properties of Lead Titanate Zirconate Ceramics at Very Low Frequencies . . . Robert Gerson 1615

High-Frequency Breakdown of Air . . . . . Donald Kelly and Henry Margenau 1617

Bounds on the Nonlinear Diffusion Controlled Growth Rate of Spherical Precipitates . . . . . J. A. Morrison and H. L. Erisch 1621

Temperature Dependence of the Adiabatic Elastic Moduli of Single-Crystal Alpha Uranium . . . . . H. J. McSkimin and E. S. Fisher 1627

Photovoltaic Effect Derived from the Carnot Cycle . . . . . A. Rose 1640

Walker Modes in Large Ferrite Samples . . . . . B. A. Auld 1642

Generation of Phonons in High-Power Ferromagnetic Resonance Experiments . . . . Ernst Schlömann 1647

Etch Pits in Pyrolytic Graphite . . . . . Aram Tarpinian and George E. Gazza 1657

Crystallographic Aspects of Extra Reflections in X-Ray Spectrochemical Analysis . . . . . N. Spielberg and J. Ladell 1659

Optical Observations Concerning the Polymorphic Transition in the Potassium Halides . . . . . S. Wiederhorn and H. G. Drickamer 1665

Production of Single-Crystal Copper Films at Low Temperatures . . . Arthur Yelon and R. W. Hoffman 1672

Effect of Li-B Ion Pairing on Li^+ Ion Drift in Si . . . . . E. M. Pell 1675

Formation of Thin Polymer Films by Electron Bombardment . . . . . Robert W. Christy 1680

Influence of Crystallographic Orientation on the Charge Formation during Phase Changes in Solids . . . . . S. Mascarenhas and L. G. Freitas 1684

Letters to the Editor:

Chlorine and Iodine as Impurities in InAs and GaP . . . . . G. R. Antell 1686

Thermal Conversion in *n*-Type GaAs . . . . . Joseph J. Wysocki 1686

Direct Observation of Antiphase Domain Boundaries in the AuCu Superlattice . . . . . M. J. Marcinkowski and R. M. Fisher 1687

High-Permeability Garnets . . . . . Elmer E. Anderson and J. Richard Cunningham, Jr. 1687

Mechanism for the Production of *F* Centers in NaCl by Irradiation with Gamma Rays . . . . . J. H. Crawford, Jr., and F. W. Young, Jr. 1688

Germanium Crystals Grown from Hollow Cylindrical Seeds . . . . . R. C. Frank and J. E. Thomas, Jr. 1689

Peltier Coefficient at a Solid-Liquid Interface . . . . . J. R. O'Connor 1690

Dislocation Ribbons and Stacking Faults in Graphite . . . . . P. Delavignette and S. Amelinckx 1691

Scattering of Radiation by a Plasma . . . . . Forrest I. Boley 1692

Drift Mobility in Neutron Irradiated *n*-Type Germanium . . . . . W. H. Closser 1693

Growth Kinks in Copper Whiskers . . . . . S. Saimoto, V. Griffiths, and E. Teghtsoonian 1693

Effect of Pressure on the Dynamic Shear Behavior of Polyisobutylene . . . . . A. W. Nolle 1694

Megavolt Electronics Cerenkov Coupler for the Production of Millimeter and Submillimeter Waves . . . . . Paul D. Coleman and Charles Enderby 1695

Growth of GaAs Crystals in the (111) Polar Direction . . . . . P. L. Moody, H. C. Gatos, and M. C. Lavine 1696

Erratum: Depolarized Components of Light Scattered by Glasses. II. Influence of Nonannealable Strains on the Scattering . . . . . Martin Goldstein 1697

Books Reviewed 1697

Announcements 1698

Index to Advertisers xxxvi

JOURNAL OF APPLIED PHYSICS

A journal of general physics and its applications to other sciences and to industry

Published by the

American Institute of Physics

GOVERNING BOARD

Members

Ralph A. Sawyer, *Chairman*
James G. Baker
R. H. Bolt
W. R. Brode
Harvey Brooks
Dirk Brouwer
J. W. Buchta
Vernet E. Eaton
J. H. Elliott
Herbert A. Erf
S. A. Goudsmit
W. W. Havens, Jr.
Winston E. Kock
R. Bruce Lindsay
H. V. Neher
C. J. Overbeck
G. E. Pake
Ray Pepinsky
F. W. Sears
Frederick Seitz
John Strong
George E. Uhlenbeck
M. E. Warga
Victor F. Weisskopf
W. R. Willets

ADMINISTRATION

Elmer Hutchisson
Director

Wallace Waterfall
Secretary and Treasurer

Henry A. Barton
Administrative Consultant

W. C. Kelly
Director of Education

Eugene H. Kone
Director of Public Relations

Hugh C. Wolfe
Director of Publications

Kathryn Setze
Assistant Treasurer

Norma Frankel
Publications Editor

Sistina Greco
Circulation Manager

Edward Tober
Manager, Production and Distribution

Theodore Vorburger
Advertising Manager

Emily Wolf
Manager, Special Services

Editor
James A. Krumhansl

Assistant Editor
Ethel McMillan

Editorial Board

J. H. Crawford
Arthur Kantrowitz
A. F. Kip
J. E. Goldman
J. L. Tuck
C. A. Wert
Herman A. Haus
C. Lester Hogan
R. S. Rivlin

THE JOURNAL OF APPLIED PHYSICS is devoted to general physics and its applications to other sciences, to engineering, and to industry. Previous to 1937, this journal was called PHYSICS.

The JOURNAL OF APPLIED PHYSICS welcomes articles of two distinct kinds: (1) Descriptions of new results in experimental or theoretical physics which are of general interest to physicists. The author should explain his contribution in such a way that a physicist or engineer in another field of specialization can appreciate its objectives and essential features. (2) Critical reviews of particular areas of physics or surveys of extensive investigations at a single laboratory. Authors contemplating writing such should correspond with the Editor before they begin writing.

The JOURNAL OF APPLIED PHYSICS welcomes Letters to the Editor which are short [approximately four (4) typewritten pages] communications without abstracts. Timeliness, briefness, and degree of current importance of the subject matter will be of primary concern in the publication of Letters. Letters should not be looked upon as partial publication or announcement of more comprehensive work, but rather self-contained presentations in themselves.

Manuscripts should be submitted to the Editor, J. H. Crawford, Solid State Division, Oak Ridge National Laboratory, Oak Ridge, Tennessee. Authors should read the "Information for Contributors," facing page 1 of the January issue, before writing articles or letters. The *Style Manual* of the American Institute of Physics is also helpful to writers preparing manuscripts for journals published by the American Institute of Physics. It can be obtained for $1.00 from the American Institute of Physics, 335 East 45 Street, New York 17, New York.

Corrected proofs and all correspondence concerning papers in the process of publication should be addressed to the Publication Manager, American Institute of Physics, 335 East 45 Street, New York 17, New York.

Subscriptions, renewals, and orders for back numbers should be addressed to the American Institute of Physics, 335 East 45 Street, New York 17, New York.

Subscription Price	U.S. and Canada	Elsewhere
To members of member organizations of the American Institute of Physics and Affiliated Societies ..	$12.00	$13.00
To all others	14.00	16.00

Back Number Prices

Yearly back number rate when complete year is available: $17.00.
Single copies: $1.75 each (exception: March, 1958—$3.00 each).

Changes of address should be sent to the American Institute of Physics.

Advertising rates supplied on request. Orders, advertising copy, and cuts should be sent to the American Institute of Physics.

The Journal of Applied Physics is published monthly at Prince and Lemon Streets, Lancaster, Pennsylvania.
Second-class postage paid at Lancaster, Pa.

For the ultimate in — **RELIABILITY**
REPEATABILITY
SUPERIOR PERFORMANCE

Specify —

"MAG MOD"®

MAGNETIC MODULATORS

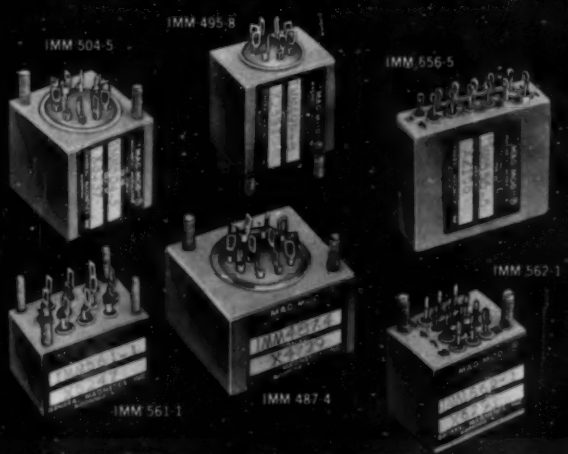

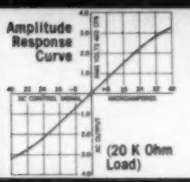

Input Magnetic Modulator
Type No. IMM 487-4

Subminiature "MAG MOD"® featuring high input signal sensitivity and high AC output impedance. Male or female mounting.

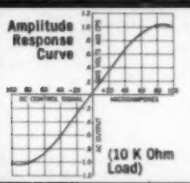

Input Magnetic Modulator
Type No. IMM 495-8

Subminiature "MAG MOD"® featuring wide band width, multiple signal input circuits, extreme zero stability from −65°C to +135°C, low null amplitude or noise level. Mounting available male or female.

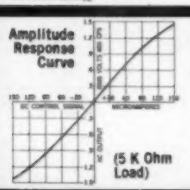

Input Magnetic Modulator
Type No. IMM 504-5

Subminiature "MAG MOD"® featuring low input and output impedance, resistance vs. temperature compensated input, extreme zero stability, repeatability and insignificant hysteresis. Supplied with male or female mounting.

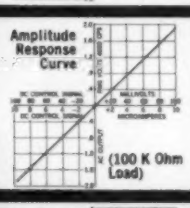

Input Magnetic Modulator
Type No. IMM 562-1

Subminiature "MAG MOD"® featuring 4 KC carrier operation, wide frequency band width, high output impedance and voltage range. Mounting male or female.

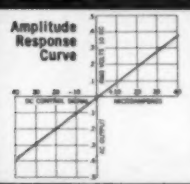

Input Magnetic Modulator
Type No. IMM 561-1

Subminiature "MAG MOD"® featuring low carrier energy level operation, very wide frequency band width, wide output operating range, minimum size and weight. Mounting male or female. May be mounted directly on printed circuit boards.

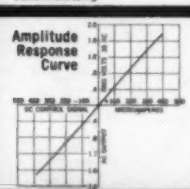

Input Magnetic Modulator
Type No. IMM 556-5

Subminiature "MAG MOD"® featuring high frequency carrier operation (35 KC), flat construction for printed circuit mounting, low output impedance and clean output fundamental frequency wave form. Mounting supplied male or female.

Designed for Subminiature
Circuit Assemblies and Printed Circuit Card Configurations

New miniature designs of these reliable "MAG MODS"® make them ideal for incorporation into transistorized printed circuit assemblies. There is no sacrifice of dynamic response. They offer the engineer/designer the solution to problems involved in a wide range of data systems where analog circuit operations are encountered. To insure complete flexibility, the mechanical mounting on any "MAG MOD" may be modified to conform to your particular packaging requirements.

- **1% repeatability throughout entire service life**
- **Negligible hysteresis**
- **Faster response time**
- **Extreme stability over a wide temperature range**
- **Infinite service life**
- **Extremely lightweight — compact design**

GENERAL MAGNETICS • INC
135 BLOOMFIELD AVENUE, BLOOMFIELD, NEW JERSEY, U. S. A.

GM INC.

See reverse side for specifications

"MAG MOD" miniaturized MAGNETIC MODULATORS

TYPE NUMBER	IMM 487-4	IMM 495-8	IMM 504-5	IMM 562-1	IMM 561-1	IMM 556-5
Excitation Carrier Voltage and Frequency	115 V @ 400 cps	115 V @ 400 cps	115 V @ 400 cps	2.5 V RMS @ 4 KC	1.0 V RMS @ 10 KC	6 to 10 V RMS @ 35 KC
Control Signal Winding DC Resistance	Winding No. 1 6200 ohms Winding No. 2 7400 ohms	Signal Winding No. 1 550 ohms Signal Winding No. 2 600 ohms	1000 ohms	Signal Winding 1300 ohms Feedback Winding 180 ohms	200 ohms	5000 ohms
Input Control Signal Range	0 to ±40 μa Each Winding	0 to ±100 μa (Both Sig. Windings in Series)	0 to ±100 μa	0 to ± 100 μa 0 to ± 1 V Bipolar	0 to ±400 μa	0 to ±400 μa
Amplitude Modulated AC Output Range	3 V RMS @ 400 cps Phase Reversing	0 to 1 V RMS @ 400 cps Phase Reversing	0 to 1.5 V RMS @ 400 cups Phase Reversing	0 to 6 V RMS @ 4000 cps Phase Reversing	0 to 3 V RMS @ 4 KC Phase Reversing	0 to 1.8 V RMS @ 35 KC Phase Reversing
Differential Gain RMS mv AC Out/μa Signal In	100 mv/μa	15 mv/μa	10 mv/μa	200 mv/μa	10 mv/μa	4.2 mv/μa
Null Amplitude (Noise Level) mv RMS	25 mv RMS Maximum	5 mv RMS Maximum	10 mv RMS Maximum	30 mv RMS Maximum	10 mv RMS Maximum	20 mv RMS Maximum
Output Impedance	Approx. 30 K ohms	1600 ohms	1000 ohms	Approx. 70 K ohms	Approx. 40 K ohms	900 ohms Each Output Wind.
External Load (Suggested)	Approx. 20 K ohms	Approx. 10 K ohms	Approx. 5 K ohms	Approx. 100 K ohms	Approx. 100 K ohms	1000 ohms Each Output Wind.
Null Drift (In terms of Input Signal) —65°C to +135°C	Less than ±0.25 μa Over Temp. Range	Less than ±0.25 μa Over Temp. Range	±1 μa Maximum Over Temp. Range	±0.5 μa Maximum Over Temp. Range	±1 μa Over Temp. Range	±2 μa Over Temp. Range
Hysteresis (% of Input Control Signal)	0.5% Maximum	0.5% Maximum	0.5% Maximum	Approx. 0.5%	0.5% Maximum	0.5% Maximum
% Harmonic Distortion in Output AC Modulated Envelope	Approx. 40% (3rd Harmonic)	Approx. 25% (3rd Harmonic)	Approx. 30% (3rd Harmonic)	Approx. 15% (3rd Harmonic)	Less Than 10% (3rd Harmonic)	Approx. 5% (3rd Harmonic)
Overall Dimensions (In Inches)	1⅛ x 1½ x ⅝	⅝ x 1 x 1	1 x 1 x 1	1 x 11/16 x ⅝	11/16 x 1 x ⅝	7/16 x 1⅛ x 1¼
Type of Mounting	4-40 Studs or Inserts	4-40 Studs or Inserts	4-40 Studs or Inserts	4-40 Studs or Inserts	2-56 Studs	4-40 Tapped Holes or Studs
Weight in Ounces	Approx. 1.25	Approx. 1	Approx. 1.1	0.75	0.6	1
Response Time (Band Width cps)	0.01 sec. for 15 K Sig. Source Imp. (12 cps Corner Frequency)	20 cps for 10 K Sig. Source Imp. 25 cps for 20 K Sig. Source Imp. (Both Sig. Windings in Series)	5 cps for 1 K Sig. Source Imp. 10 cps for 5 K Sig. Source Imp. 20 cps for 10 K Sig. Source Imp.	70 cps for 10 K Sig. Source Imp. (Time Constant Approx. 2 Milliseconds)	Corner Frequency 2 KC for Sig. Source Imp. of Approx. 6 K ohms	Corner Frequency 200 cps for 600 ohm Signal Source Imp. or 1000 cps for 5 K Source

Magnetic Multiplying Modulator Model MCM 515-1

The MAGNETIC MULTIPLIER is a miniaturized magnetic modulator specifically designed to deliver an analog output voltage which is the continuous product of two variable input voltages. One of these is an excitation voltage which varies over a pre-determined range; in this case, 0 to 1 VRMS 400 cycles per second. The other signal is a DC current which varies between 0 and ±400 μa. The output voltage is 400 cycles AC, and is always in phase or 180° out of phase with the variable excitation or fixed reference, i.e., in phase when the variable amplitude DC signal is positive, and 180° out of phase when the DC signal is negative. The general schematic is illustrated in Fig. 1. The relationship between variable alternating supply signal voltage E_S, variable direct current control signal E_C, and the alternating load voltage E_L having a sinusoidal wave shape is denoted by the equation—

$$E_L = \text{Constant} \times E_S \times E_C$$

Figure 1

This expression, which defines the fundamental principle of the four quadrant MAGNETIC MULTIPLYING MODULATOR, can be clearly illustrated by linear transfer response curve families as shown at right, in Figure 2-A and Figure 2-B.

Illustrating:

(1) **Load voltage E_L as a function of alternating supply signal voltage E_S with control DC signal voltage E_C as a parameter.**

(2) **Load voltage E_L as a function of control DC signal voltage E_C with alternating supply voltage, E_S as a parameter.**

With linearity response curves held to within approximately 1 to 2% of theoretical straight lines, the product accuracy of the fundamental equation will be within 2 to 5% of the theoretical product.

SPECIFICATIONS MODEL MCM 515-1	
Variable Excitation Carrier Voltage and Frequency	Variable AC Signal 0 to 1 V RMS 400 cps
Control Signal Winding DC Resistance	DC Signal Winding Resistance 2650 ohms
Input Control Signal Range	Variable DC Signal 0 to ±400 μa
Amplitude Modulated AC Output Range	0 to 0.9 V RMS @ 400 cps Phase Reversing
Null Amplitude (Noise Level) mv RMS at Max. AC Excitation	5 mv RMS
Output Impedance	Approx. 3500 ohms
External Load (Suggested)	Approx. 25 K ohms
Null Drift (In terms of Input Signal) —65°C to +135°C	±2 μa over Temperature Range
Hysteresis (% of Input Control Signal)	0.5% Maximum
% Harmonic Distortion in Output AC Modulated Envelope	Less than 5%
Overall Dimensions (In Inches)	27/32 x 27/32 x 1 3/16
Type of Mounting	4-40 Insert or Stud
Weight	Approx. 1 Ounce

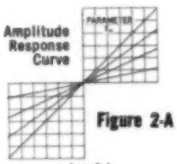

Figure 2-A

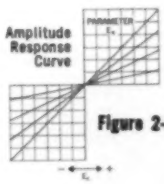

Figure 2-B

Typical "Mag Mod"® Applications—Circuit applications for MAGNETIC MODULATORS include algebraic addition, subtraction, multiplying, raising to a power, controlling amplifier gain, mechanical chopper replacement in DC to fundamental frequency conversion, filtering and low signal level amplification.

Consult General Magnetics— For magnetic amplifier components of proven reliability. These dependable instruments are widely employed in automatic flight systems, fire control, analog computers, guided missiles, nuclear equipment, antennas, gun turrets, commercial power amplifiers and complete control systems. Miniature, subminiature, standard and customized types available.

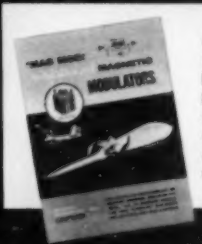

Call or write for new Brochure 102 on "MAG MOD" Miniaturized Magnetic Modulators and Magnetic Multiplying Modulators. Please address inquiries on company letterhead.

GENERAL MAGNETICS • INC
135 BLOOMFIELD AVENUE, BLOOMFIELD, NEW JERSEY, U. S. A.

15 THOUSANDTHS OF A SECOND IS A VERY LONG TIME

It's much faster than you can wink an eye, yet time enough for Bell Laboratories' new high-speed switching terminal to transfer your voice to another channel while you are talking by telephone.

The new terminal—recently introduced on the transatlantic cable—uses the idle time in the conversations of talkers on a group of channels to provide paths for other talkers. This time-sharing technique, called Time Assignment Speech Interpolation, permits the sending of 72 simultaneous phone conversations over this deep-sea system where only 36 could be sent before.

TASI takes advantage of the fact that in a normal telephone conversation you actually talk less than half the time. You do not talk when you are listening, and even when you do talk there are pauses between sentences, words, and syllables. When there are more talkers than channels, TASI puts this idle time to use.

Scanning each circuit thousands of times a second, TASI instantly notices when you aren't talking, then quickly switches in someone who *is*. TASI also notices when you resume talking, immediately finds a channel not in use that moment and switches you to it. Your voice may be switched many times during a single conversation in a time too fast —about 15 milliseconds—for your ear to perceive.

The TASI switching terminal was rendered feasible by the transistor—an invention of Bell Telephone Laboratories. More than 16,000 transistors are employed to achieve the compact, dependable, high-speed circuitry required. TASI is another example of how Bell Laboratories works to keep your telephone service the world's finest.

BELL TELEPHONE LABORATORIES

World center of communications research and development

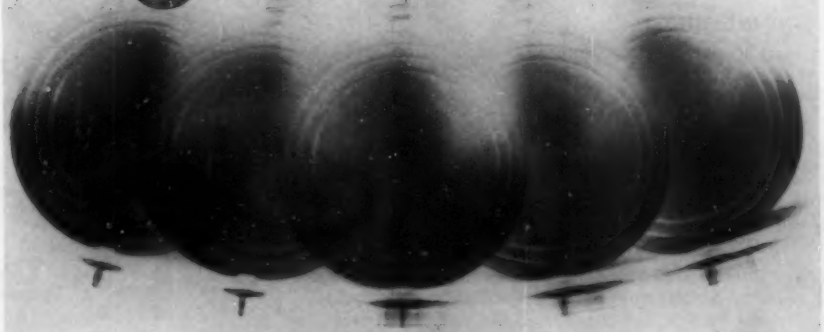

How Do You Measure Achievement?

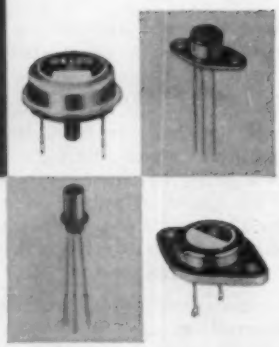

These transistors—representing the proven capability of Delco Radio to develop and mass produce the highest power transistor in the industry—are a measure of achievement.

TALENT—bold, imaginative talent stimulated by the constant challenge of new concepts—was responsible for this achievement.

However, past achievements are significant only insomuch as they indicate the path of the future. At DELCO, this path is clearly charted. We are committed—and dedicated—to uphold and maintain our position of leadership in the fields of electronics and Solid State Physics.

Fulfilling this challenge requires a constant infusion of new ideas and new talent—*aggressive new talent.* That's what we're looking for.

We are vitally interested in ambitious men with experience in the following areas:

SEMICONDUCTOR DEVICE DEVELOPMENT

—We need men with experience in the techniques of semiconductor device development including alloying and diffusion.

—We need a man with experience in the chemistry of semiconductor devices.

—We need a man with experience in semiconductor materials to lead a program on metallurgical research of new semiconductor materials.

—We need a man with experience in semiconductor device encapsulation.

PROCESS ENGINEERING

—We need several men for production set-up and trouble shooting.

EQUIPMENT DEVELOPMENT

—We need men to develop automatic and semi-automatic fabrication equipment.

The applications we see for Delco Radio capabilities in electronics and Solid State Physics are staggering. We're therefore eager to find more, experienced personnel; responsible positions are available for those who qualify.

If you're interested in becoming a member of our Delco—GM team of outstanding scientists and engineers, send your resume today to the attention of Mr. Carl Longshore, Supervisor Salaried Employment.

DELCO DEPENDABILITY RADIO RELIABILITY

Division of General Motors • Kokomo, Indiana

ARNOLD 6T CORES: PROTECTED AGAINST SHOCK, VIBRATION, MOISTURE, HEAT... AVAILABLE FROM STOCK

The hermetically-sealed aluminum casing method developed exclusively for Arnold 6T tape cores is packed full of advantages for you . . . *performance-improving and cost-saving advantages.*

It is compact: you can design for minimum space/weight requirements. It's extra-rigid to protect against strains. And it gives you maximum protection against environmental hazards. Arnold 6T tape cores are guaranteed against 1000-volt breakdown . . . guaranteed to meet military test specs for resistance to shock and vibration . . . guaranteed also to meet military specs for operating temperatures. They require no additional insulation before winding, and can be vacuum-impregnated afterward.

And now a NEW Arnold service: immediate delivery on your prototype or production requirements for Deltamax 1, 2 and 4-mil Type 6T cores in the proposed EIA standard sizes (see AIEE Publication 430). A revolving stock of approximately 20,000 Deltamax cores in these sizes is ready for you on warehouse shelves. Subject to prior sale, of course, they're available for shipment *the same day your order is received.*

Use Arnold 6T cores in *your* designs. Technical data is available; ask for Bulletin TC-101A and Supplement 2A (dated June '60). •Write *The Arnold Engineering Company, Main Office and Plant, Marengo, Ill.*

ADDRESS DEPT. J-9

ARNOLD
SPECIALISTS in MAGNETIC MATERIALS

BRANCH OFFICES and REPRESENTATIVES in PRINCIPAL CITIES • *Find them FAST in the YELLOW PAGES*

1530

OUTSTANDING LATITUDE OF PERFORMANCE

EXCEPTIONAL CHOICE OF OPTIONS

VARIAN 6-INCH

Quality that passes both high-field and wide-gap tests

The two accompanying field plots show the wide latitude of performance of the Varian 6-inch magnets: a large area of homogeneous field at moderate field strength and wide air gap; a small, but usable area of homogeneous field even at strengths as high as 17,000 gauss. In addition, an equivalent degree of time stability is provided by the matching Varian power supply. All these aspects of performance demonstrate the depth of technology behind Varian Magnet systems.

Useful differences in the choice of models

Rotation of the magnetic field about the vertical axis is a capability provided by the rotating V-4007-1. Also, for higher fields this model will accept the full 2 ampere output of a larger optional power supply, the V-2100B. Varian's other 6-inch magnet, the fixed-azimuth V-4007, is lower in cost, provides a wider selection of gap widths, and has an adjustable yoke that permits convenience and flexibility of access to the gap. Varian also offers rotating and fixed-azimuth 12-inch magnet systems.

Pole-cap options to meet varied requirements

Choice of pole caps available includes cylindrical, tapered, adjustable ring-shim and constant gradient types. Highest fields are provided by tapered pole caps. Largest homogeneous volume is available with the adjustable ring-shim type. Various gap widths on the V-4007-1 rotating magnet are provided by a choice of pole cap thicknesses. On the V-4007 the gap is varied by separating the yoke with pairs of precision ground spacer blocks.

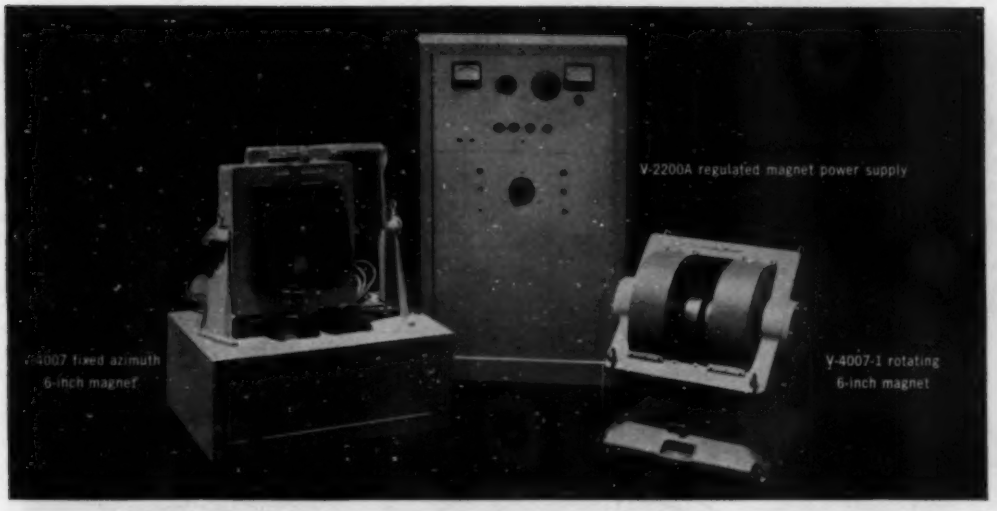

LABORATORY MAGNETS

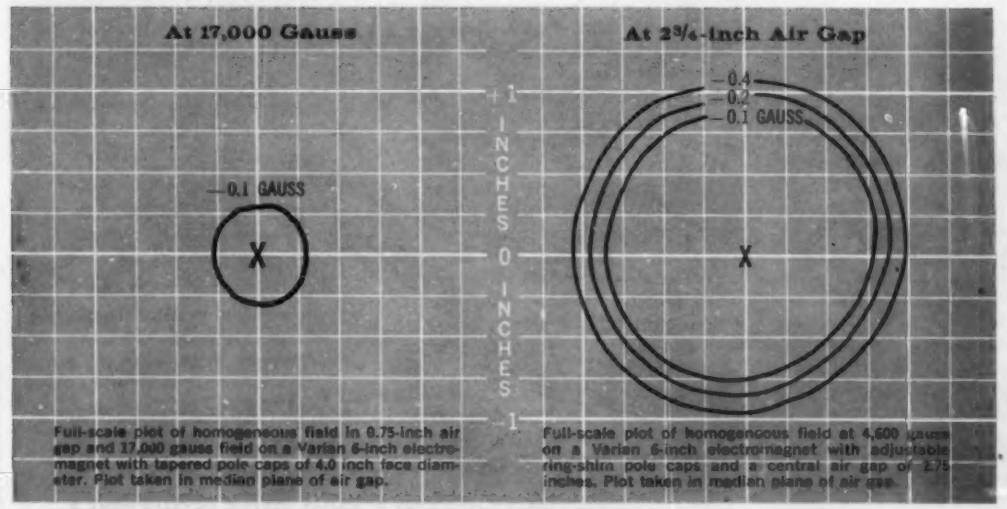

Full-scale plot of homogeneous field in 0.75-inch air gap and 17,000 gauss field on a Varian 6-inch electromagnet with tapered pole caps of 4.0 inch face diameter. Plot taken in median plane of air gap.

Full-scale plot of homogeneous field at 4,600 gauss on a Varian 6-inch electromagnet with adjustable ring-shim pole caps and a central air gap of 2.75 inches. Plot taken in median plane of air gap.

Delivery 30 to 45 days after receipt of order can be provided on most magnet systems.
For full specifications on the Varian Magnets, write the **Instrument Division.**

Varian NMR Fluxmeter provides precise measurement and/or control of magnetic fields, as an accessory to the Varian 6- and 12-inch magnet systems.

VARIAN associates
PALO ALTO 36, CALIFORNIA

NMR & EPR SPECTROMETERS, MAGNETS, FLUXMETERS, GRAPHIC RECORDERS, MAGNETOMETERS, MICROWAVE TUBES, MICROWAVE SYSTEM COMPONENTS, HIGH VACUUM EQUIPMENT, LINEAR ACCELERATORS, RESEARCH AND DEVELOPMENT SERVICES

ENGINEERS
SCIENTISTS

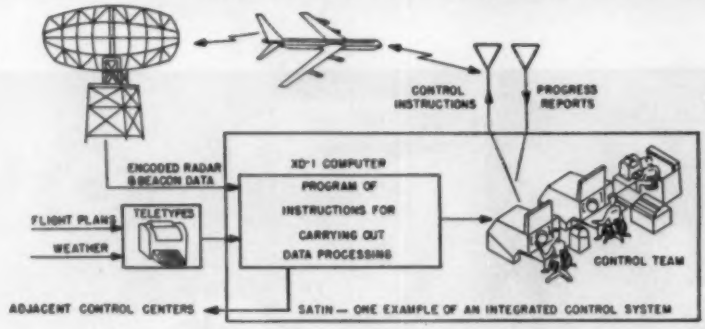

The HUMAN CATALYST

In effect, this is the role of the System Engineer at MITRE.

His technical competence and objectivity must maximize the effectiveness of complex interacting communications networks, radar systems, digital computers and countermeasures. The end result must be an integrated command and control system.

MITRE, a system engineering organization, is engaged in the design, development and evaluation of large scale command and control systems. Its convenient location in suburban Boston offers excellent opportunities for advanced study under MITRE's liberal educational assistance program.

Engineers and scientists with an interest in combining large scale system engineering with electronic development will find creative opportunities with MITRE in:

COMPUTER TECHNOLOGY • RADAR SYSTEM DEVELOPMENT • AIR TRAFFIC CONTROL SYSTEM DEVELOPMENT • HUMAN FACTORS • ADVANCED SYSTEM DESIGN • COMMUNICATION SYSTEMS • OPERATIONS RESEARCH • ELECTRONICS COUNTERMEASURES •

Inquiries may be directed in confidence to:
VICE PRESIDENT—TECHNICAL OPERATIONS

THE MITRE CORPORATION

Post Office Box 31, 1-MK — Lexington, Massachusetts

Kodak reports on:

19 pages of savvy on schlieren . . . new dimensional stability in recording film . . . little white specks that move

Kodak

Thin air can be photographed

The technique of schlieren photography has now been debased to the point where a man can send in to Kodak for a free booklet on how to do it, can carefully read all 19 pages, and can set himself up as a schlieren man. Yes, and perhaps a case can be made that it is not necessarily immoral to go at it just that way.

Though the schlieren method of photographing refractive index gradients in gases and liquids has been around for quite a while, general literature about it is scant; most of what has been published about it dwells on some particular application. You can find packaged schlieren outfits advertised, but the advertisements are low-pressure. Everybody who is doing schlieren now learned the hard way and is entitled to respect. One such savvy schlieren group works at Battelle Memorial Institute and another at Cornell Aeronautical Laboratory, Inc.

Here is an enchanting display item from Battelle's gallery—a turbulent Bunsen flame, frozen in a 13-microsecond schlieren portrait. Areas lighter than background represent decreasing index in an arbitrary direction within the plane of the picture; darker areas represent change in the opposite direction. To measure the quantitative rate of change with distance demands the very considerable elaboration of interferometric technique. A third method, called shadow photography, delineates the second derivative of refractive index with distance. Our slim volume merely hints at the existence of these other methods. Given enough encouragement to expand it some day, we might cover them in useful detail.

To start encouraging us, send for "Schlieren Photography" to Eastman Kodak Company, Special Sensitized Products Division, Rochester 4, N. Y.

He has always thought a pick was the tool with which the Erie Canal was dug.

He thinks "D Max" is the name of a guy who might have been called "Dave" but wanted a classier handle.

Dr. F. W. Spangler (left) meets R. C. Hilton, senior geophysicist in charge of geophysical data processing for Shell Oil Company, Houston. Purpose of the visit is to familiarize Dr. Spangler directly with the ideal characteristics which Shell desires in a polyester recording film for use in the Reynolds Plotter. Dr. Spangler is an assistant superintendent of Kodak's Film Emulsion Division.

With the switch to thin, rugged Estar Base that eliminates troublesome dimensional change, Fred Spangler had to decide what inherent maximum density to give the **new Kodak Linagraph Recording Film.** Dick Hilton needs more from a film than that it shouldn't be troublesome. He doesn't talk Fred's "D Max" language. He seeks a certain appearance to which his perceptual process best responds in picking a "pick" from the corrected cross-section of the deep geological formation which the Plotter puts on the film. Spangler learned plenty from him and from others with other instrumentation and other perceptual patterns of translating photographic images into technical intelligence.

Eastman Kodak Company, Photorecording Methods Division, Rochester 4, N. Y., will be glad to write you a letter answering practical questions about the new Kodak Linagraph Recording Film (Estar Base), *such as who sells it and how to handle it, but we see no purpose in spilling a lot more words about it when all you have to do is get some and see whether it suits you.*

A tip for radiographers

Little white specks have been appearing on radiographs of zirconium alloys. Since one of the principal reasons for radiographing zirconium alloys in the first place is for detection of tiny tungsten inclusions, this is not surprising. What has surprised the radiographers has been that most of the little white specks appear in different places on two successive films of the same part! Or even on two films made of the same part simultaneously!

Upon investigation* it turns out that the phenomenon does not contain enough high science to be worth the exclamation points. The moving specks are dandruff, cigarette ashes, lint, and such rubbish. So help us!

The junk gets picked up when the customer loads the film into the cardboard exposure holders. These often contain lead foils between which the film nestles. Besides serving as a filter to modify radiation quality, the lead emits electrons to intensify the image density. The junk simply casts electron shadows.

So we published a little paper in *Nondestructive Testing*. We said that in this specialized type of radiography for small inclusions it might be well to put cardboard under the front lead screen and use the lead only as a filter. We also advised surgical cleanliness, a darkroom under slight positive air pressure, and no smoking. This supplementary advice isn't really necessary if you don't try to shave exposure time by putting the lead in contact with the film, but it sounds wholesome. Furthermore, this line of thought led to the question of why make the radiographer load the film into a cardboard exposure holder in his own darkroom. Why not do it for him in our surgically clean, slight-positive-air-pressure, no-smoking factory?

We couldn't think of a good reason why not.

Kodak Industrial X-ray Film, Type M (*the maximum resolution type*) *is now available from x-ray dealers in a* Ready Pack *form, enclosed in individual, disposable, light-tight packets.*

*We needn't have investigated. We could have just dropped off the film, scooped up our money, and run, tarrying only long enough to suggest that 1) two films be routinely made of every part and then compared to distinguish moving white specks from real white specks; and 2) somebody should do a Ph.D. thesis on the effect. Sales would have doubled.

This is another advertisement where Eastman Kodak Company probes at random for mutual interests and occasionally a little revenue from those whose work has something to do with science

AVCO-EVERETT RESEARCH LABORATORY IS EXPANDING

to meet the needs of three major projects

1. **MHD POWER GENERATOR**—In cooperation with 10 leading utilities, AERL is working toward a prototype electrical power generating station using the revolutionary Magnetohydrodynamic technique.
2. **RECOVERABLE SATELLITES**—Under contract with the U.S. Air Force, AERL is developing and flight-testing recoverable satellites based on the unique Avco Drag Brake principle.
3. **ICBM DEFENSE**—AERL's superior background in laboratory and inflight studies of re-entry phenomena is being applied to the vital problem of the design of practical systems for defense against ICBM's, under several contracts with the Department of Defense.

CONTINUING RESEARCH PROGRAM—These expanding projects are results of AERL's basic research effort. To provide general support for existing projects, and to supply new fundamental knowledge for our further growth, we are seeking scientists and research-oriented engineers. In particular, we are looking for: Aerodynamicists with some background in high-temperature gas phenomena, Physicists and Physical Chemists interested in plasma and associated high-temperature gas phenomena.

Avco EVERETT RESEARCH LABORATORY

TO SPEED THESE PROJECTS, WE ARE SEEKING:

Aerodynamicists—Theoretical & Experimental
Senior Rocket Combustion Engineers
Mechanical Engineers
Engineering Physicists
Systems Engineers
Flight Test Specialists
Electronic & Electrical Engineers
Communications & Telemetry Specialists
Physicists—Theoretical & Experimental
Aeronautical Engineers
Missile and Satellite Designers
Physical Chemists
Flight Control Specialists

FOR FURTHER INFORMATION write to:
Mr. R. E. McDonald, Avco-Everett Research Laboratory, Everett, Massachusetts.

new photo-chopper-stabilized high voltage supply

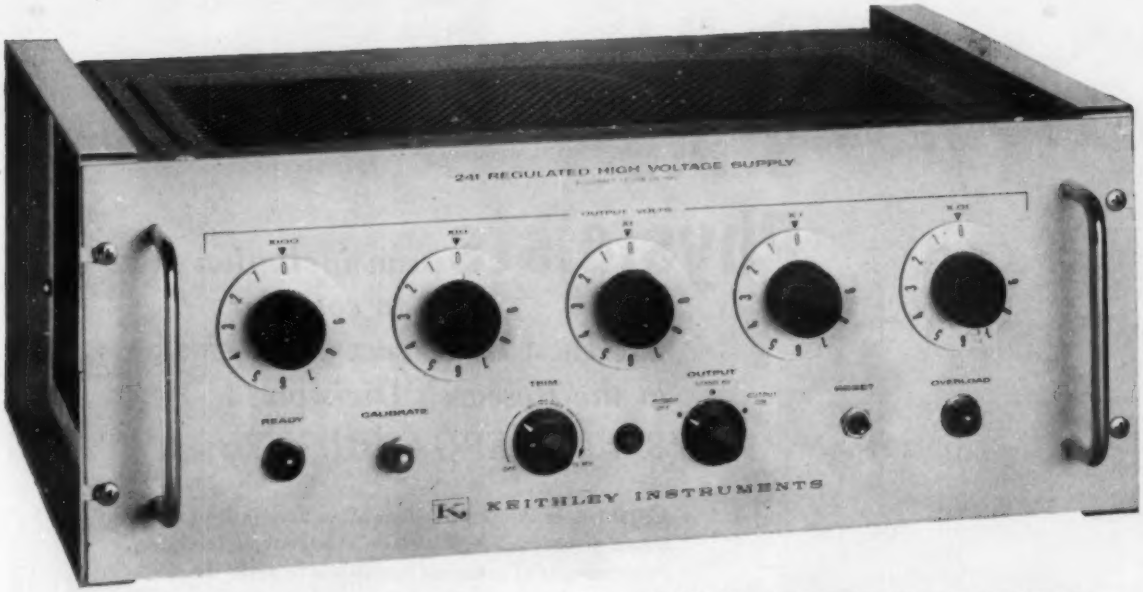

Model 241 – incorporating new photo-modulator – offers high accuracy, stability, long service life. 2411 End Frames shown adapt unit to bench use.

Model 241 offers 0.05% accuracy, five-dial resolution from 0-1000 volts.

Here is the successor to dc secondary standards that employ mechanical choppers and standard cells. The new Keithley 241 offers freedom from adjustment and calibration, long term stability to voltage or temperature variations, and immunity to shock and vibration. Complementing the popular Keithley 240 supply, it offers greater accuracy, regulation, current output and floating operation.

High output accuracy, within 0.05%, is assured through the use of encapsulated wire-wound resistors with 0.02% divider accuracy.

Extreme stability of 0.005% per hour is assured by a highly stable, shockproof zenor diode, wire-wound standards in critical positions, and a highly stable, long life photo modulator which is immune to shock and vibration.

Other features include a position which removes voltage from the output, making possible connections while the instrument is operating; bench or rack operation.

BRIEF SPECIFICATIONS

Output Voltage: 0-1000 volts, plus, minus or floating. 100, 10, 1, 0.1, 0.01 volt steps; 5 calibrated panel switches. "TRIM" potentiometer permits interpolation between steps, with a resolution of better than 100 microvolts.

Output Current: Zero to 20 milliamperes.

Output Accuracy: Within 0.05% above 2 volts, within 1 millivolt below 2 volts.

Output Impedance: Less than 0.05 ohm at d.c.

Line Regulation: 0.005% or 1 mv for 10% line change.

Load Regulation: Better than 0.005%, no load to full load.

Ripple and Noise: Less than 1 millivolt RMS.

Stability: .005% per hour with constant load, line and ambient temperature.

Recovery Time: No load to full load, less than 1 second to rated accuracy.

Overload Protection: Relay disconnects output within 50 milliseconds when output current exceeds about 24 ma.

Price: Model 241 ..... $775.00

For complete details, write:

KEITHLEY INSTRUMENTS, INC.
12415 EUCLID AVENUE CLEVELAND 6, OHIO

Solid State Physicists ... *an invitation to consider*

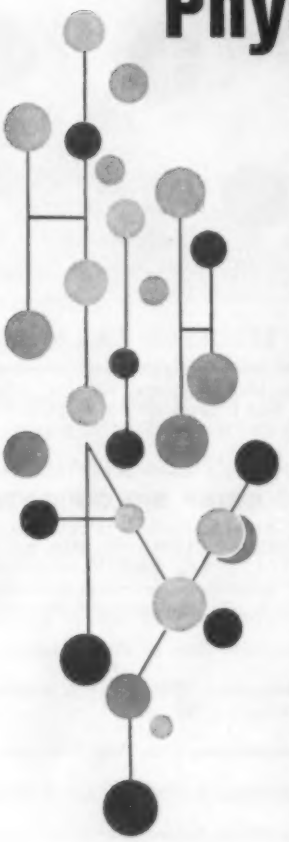

THEORETICAL AND EXPERIMENTAL INVESTIGATIONS

at the Research Division of

STROMBERG-CARLSON

Physicists enjoy the freedom of an academic environment at Stromberg-Carlson's Research Division. Programs are of sufficient breadth as to allow the investigator wide latitude in choice of research.

A sampling of the areas under exploration involves these studies:

...relation of various crystal structures to spin levels
...interaction between lattice vibrations and microwaves
...methods and techniques for preparing semiconductor materials
...electrical properties of semiconductor materials
...charge transport in semiconducting films and switching mechanism in magnetic films

Research in the commencement stage or proposed for the immediate future involves:

...theory of many-particle interaction
...defect solid state
...nucleation and growth of crystals
...cryogenics, emphasizing thermal and electrical properties of matter near absolute zero

If you would like to discuss your field of interest with the head of this research group, write informally to Mr. Maurice Downey. Background at the doctoral level or equivalent is prerequisite to a staff appointment.

STROMBERG-CARLSON

A DIVISION OF **GENERAL DYNAMICS**

1488 N. Goodman St., Rochester 3, New York

X-RAY DIFFRACTION AND SPECTROSCOPY

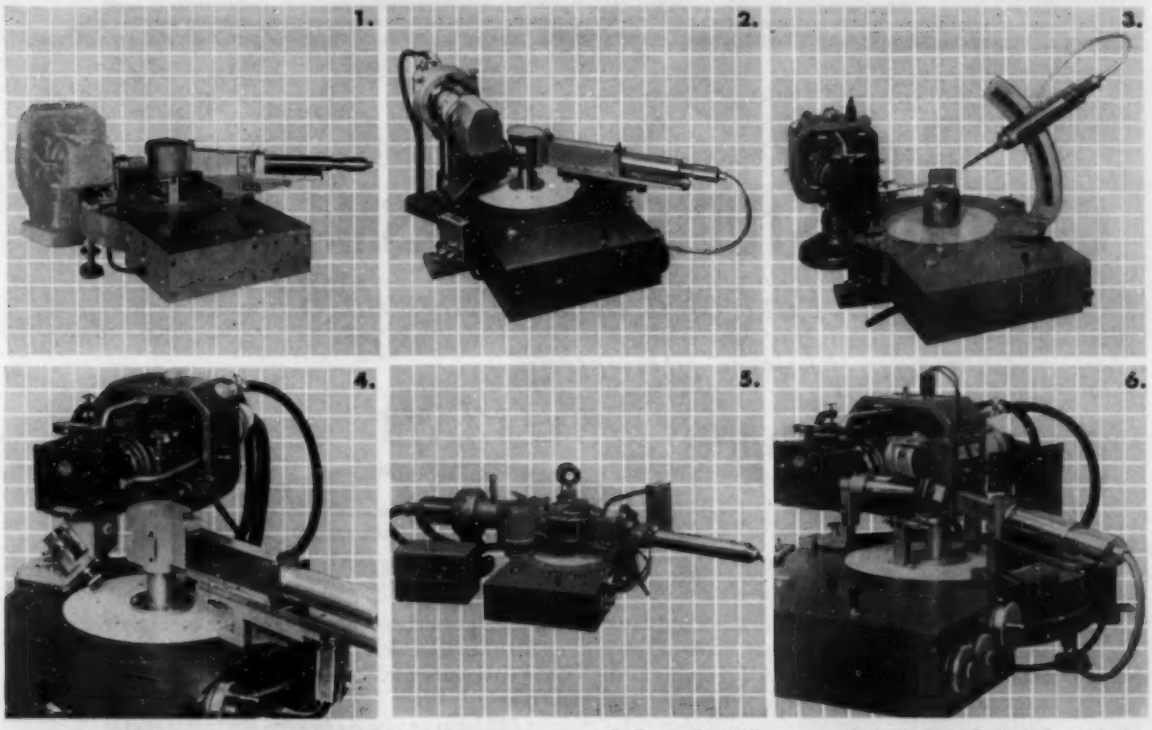

1. Counter Tube Diffractometry. 2. Spectroscopy. 3. Single Crystal Studies. 4. Spectroscopy of Small Areas. 5. Vacuum Spectroscopy of Light and Heavy Elements. 6. Studies of Orientation.

VERSATILITY!

RCA's horizontal goniometer performs 6 functions

Unusual versatility is an important distinguishing characteristic of RCA's X-Ray Diffraction and Spectroscopy Equipment. This versatility is graphically demonstrated by the horizontal goniometer which can perform six different functions merely by adding accessories, as illustrated above.

RCA X-Ray Diffraction and Spectroscopy Equipment offers many other outstanding features which make it one of today's most specified lines. For example, the DC regulated and filtered power supply; the option of mounting two tube stands on the Crystalloflex IV; a kit which permits conversion from diffraction to spectroscopy in minutes; and the new vacuum spectrometer for analysis of light and heavy elements. For those engaged in film studies of all kinds, the RCA Table Model Crystalloflex II can be bought, complete with cameras, for as little as $4000.

A NEW LEASING PLAN now makes it possible to obtain all RCA scientific instruments, including the Electron Microscope, with no down payment, low monthly terms, and a favorable option to buy.

For complete information write to RCA, Dept. L-65, Bldg. 15-1, Camden, N.J.

Crystalloflex IV and Electronic Circuit Panel with Vacuum Spectrometer and Diffractometer mounted on the generator.

RCA®

The Most Trusted Name in Electronics

RADIO CORPORATION OF AMERICA

Experimental Physicists – MS & PhD

COLLISION STUDIES IN PLASMA PHYSICS

...Part of a broad program in radio physics attracting scientists to SYLVANIA

ARL
Applied Research Laboratory

New effectiveness for communication and detection systems in natural and man-made environments may result from current Sylvania efforts in the field of plasma physics.

In the Radio Physics Department of the Applied Research Laboratory, investigators are studying a variety of wave propagation and scattering techniques in ionized gases and conducting fluids. Of particular promise are experimental developments in microwave diagnostics of ionized gas flow.

Through microwave heating, inelastic collisions are being induced between free electrons in ionized air. To measure collision frequency, the fractional energy loss G per collision must be known. New experiments will measure the temperature dependence of G in the afterglow of a DC discharge in ionized air. Small shock tube environments are also being explored.

Additional programs involve electromagnetic phenomena associated with solar flares and aurora, propagation in non-uniform media, and formulation of a new microscopic electrodynamics theory of the ionosphere.

The Applied Research Laboratory's studies in radio physics offer important opportunities to advance your professional reputation in a genuine scientific environment. Qualified physicists will be invited to meet the manager of the Radio Physics Department to discuss programs in progress and the opportunities for initiating original studies.

Please write in confidence to Dr. Leonard Sheingold, Director, Applied Research Laboratory

Waltham Laboratories / **SYLVANIA ELECTRONIC SYSTEMS**
A Division of

SYLVANIA
Subsidiary of GENERAL TELEPHONE & ELECTRONICS

100 First Avenue – Room 9-B – Waltham 54, Massachusetts

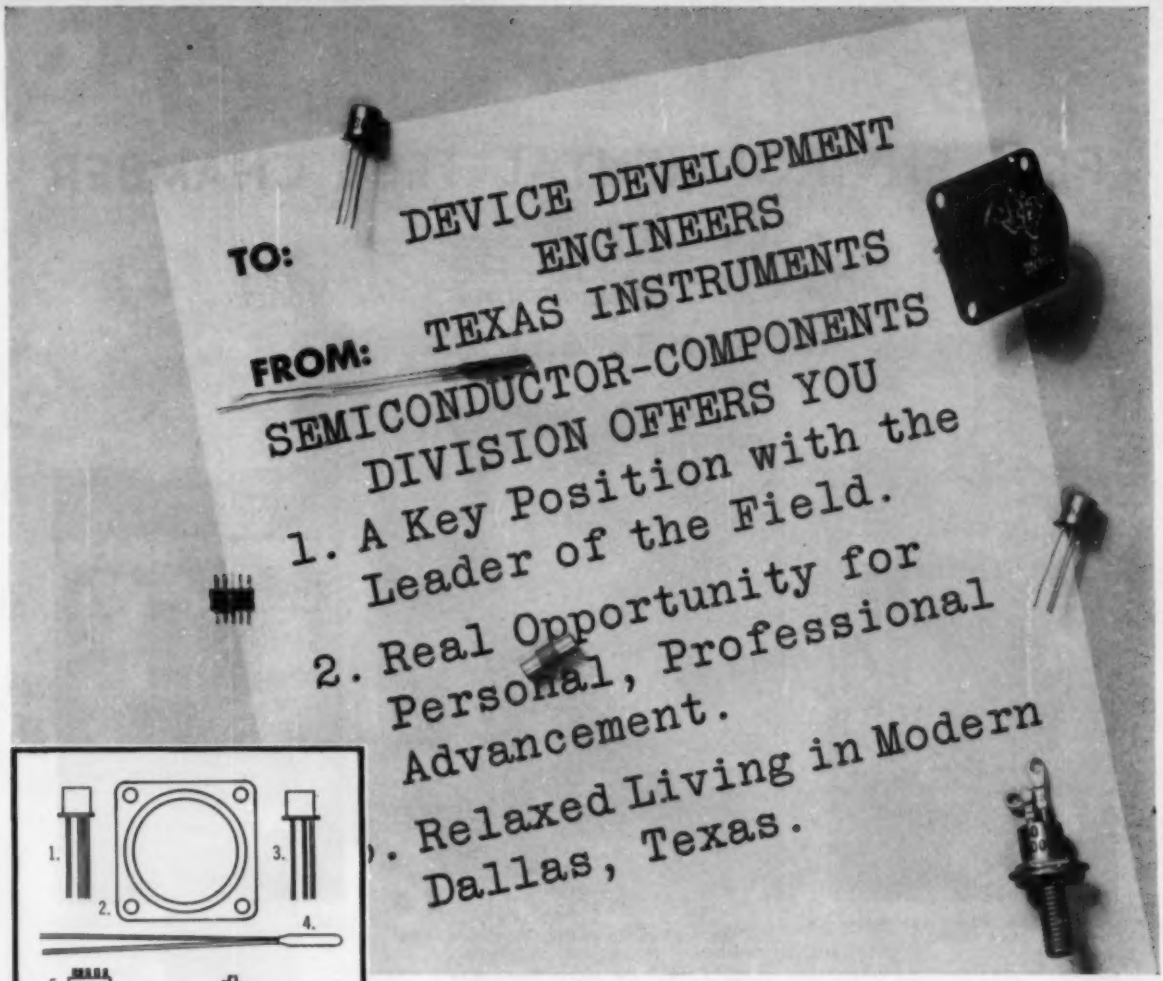
TO: DEVICE DEVELOPMENT ENGINEERS
FROM: TEXAS INSTRUMENTS SEMICONDUCTOR-COMPONENTS DIVISION OFFERS YOU
1. A Key Position with the Leader of the Field.
2. Real Opportunity for Personal, Professional Advancement.
3. Relaxed Living in Modern Dallas, Texas.

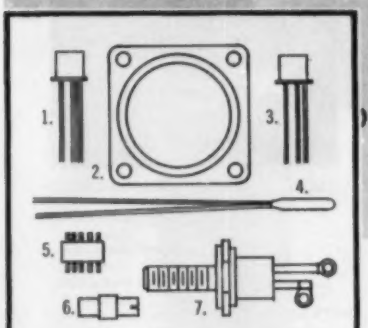

Pictured in actual size above are a few of the devices already pioneered by TI engineers: 1. P-N-P Diffused-Base Mesa Germanium Transistor, 2. N-P-N Diffused Junction Silicon Power Transistor, 3. Gallium Arsenide Tunnel Diode, 4. Diffused Photo Duodiode, 5. *Solid Circuit** Semiconductor Network, 6. Diffused Gallium Arsenide Mesa Varactor Diode, 7. Diffused Silicon Controlled Rectifier.

Texas Instruments offers solid state device development engineers the opportunity to pioneer in the application of unique phenomena in semiconductor materials to create specialized components. Studies involve high-speed, high-frequency germanium mesa transistors; tunnel diodes; computer devices; silicon transistors. *Requirements for these key posts:* degree in Electrical Engineering, Physical Chemistry or Physics and experience in semiconductor or related development areas.

INTERVIEWS are scheduled for your area. If the opportunity and challenge of device development at TI intrigues you, please send a confidential summary of your background and your interests to C. A. Besio, Dept. 135.

*Trademark of Texas Instruments Incorporated

TEXAS INSTRUMENTS INCORPORATED

SEMICONDUCTOR-COMPONENTS DIVISION
POST OFFICE BOX 312 • DALLAS, TEXAS

TEXAS INSTRUMENTS INCORPORATED
Semiconductor-Components Division
Box 312, Dept. 135, Dallas, Texas

Please send me the booklet *TIPS* containing details on career opportunities in my field at TI S-C and information on living in Dallas.

NAME_____

ADDRESS_____

CITY_____ STATE_____

My professional field is_____

My specialty is_____

FRL® ENVIRONMENTAL TEST CHAMBER

Model CS-90

For Use With Both Floor and Table Models

INSTRON TENSILE TESTERS

Chamber Entered From Rear of Instron, Door Closed

FRL Chamber Mounted On Dolly For Front Entering

Chamber Entered From Rear of Instron, Door Open

Range: −90°F to +750°F (standard); broader ranges available.

Stabilization time: To 500°F in one-half hour; To −90°F in one hour.

Size: Volume approx. 3,000 cu. in.; Maximum throw with Instron jaws is 18 in.; Special attachment permits 23½ in. throw and adapts unit for compression testing.

Accuracy: ±2°F.

Atmosphere: Air or inert gas.

Versatility: Chamber (which fits any type Instron) is self-contained on hydraulic-lift dolly, easily moved by one person, and can be used in any location independent of the Instron.

The FRL Chamber was designed in 1955 by Fabric Research Laboratories, Inc., Dedham, Mass., for use in extreme temperature studies of filamentous materials. Demand by other Instron-using laboratories for such a unit encouraged FRL to license CSI as builders of the chamber.

The new model shown above incorporates design improvements based on substantial operating experience at FRL and in other laboratories. The −90°F to 750°F unit, including dolly and Wheelco remote indicating controller, sells for $3,200.

For complete details, write

CSI **CUSTOM SCIENTIFIC INSTRUMENTS, INC.** **CSI**

541 Devon St. *Kearny, N. J.*

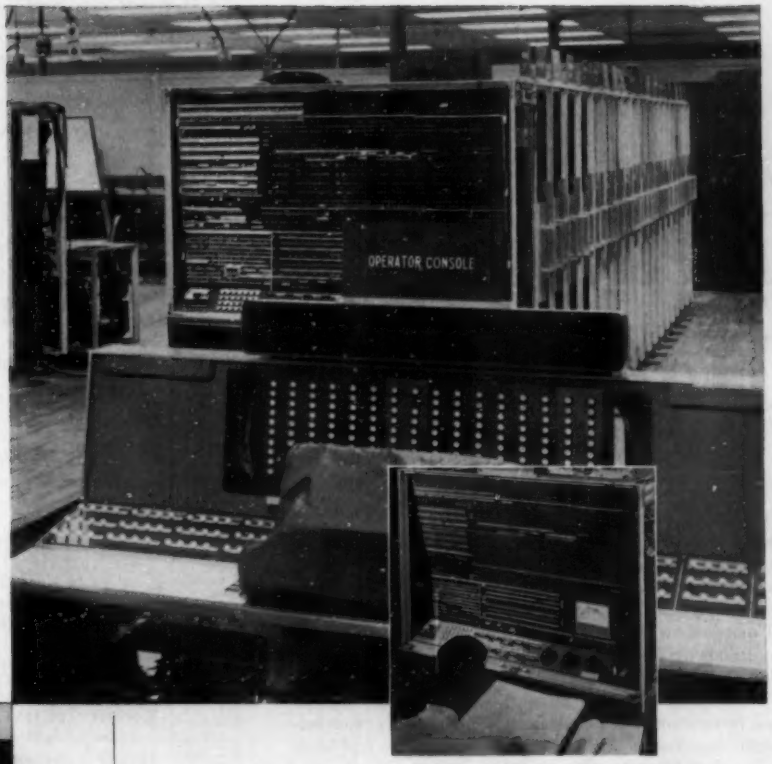

STRETCH, the world's fastest and most versatile computer, will soon be added to the array of research tools at Los Alamos Scientific Laboratory. This multi-million dollar machine, built by IBM, is 50 to 75 times faster than the IBM 704.

STRETCH can complete more than 75 billion arithmetic operations a day. The system can execute as many as 2 million instructions per second.

A "look ahead" device anticipates instructions and data requirements, thus increasing the effective memory speed to make use of the enormous speed of the arithmetic units.

For employment information write:
Personnel Director Division 60-88

los alamos
scientific laboratory
OF THE UNIVERSITY OF CALIFORNIA
LOS ALAMOS, NEW MEXICO

A thorough revision and expansion
—to four volumes and more than 3500 pages—
of the vast collection of scientific
and technical data on reactor design,
engineering and operation
first published in 1955 under AEC sponsorship

Reactor Handbook

SECOND EDITION
Revised and Enlarged
IN FOUR VOLUMES

Prepared under Contract with the
United States Atomic Energy Commission

just published—Volume I:

MATERIALS

edited by C. R. TIPTON, JR.
Batelle Memorial Institute

More than five years in preparation, some 150 reactor scientists and engineers have rewritten and entirely reorganized this first of four volumes of the new *Handbook* for a presentation along the lines of the functional usage of materials within a reactor. The coverage is extended to include liquids and gases, as well as solids, and information on irradiation behavior—all extensively referenced. Thousands of technical publications, the proceedings of two international conferences on atomic energy, and material classified at the time of the first edition and since made available have also served as source and reference material. In 53 chapters and over 1200 pages, *Materials* is today's most nearly complete, definitive source book of reactor materials information.

CONTENTS

Part A (Chapters 1–5):
GENERAL
edited by C. R. Tipton, Jr.
Part B (Chapters 6–17):
FUEL MATERIALS
edited by H. A. Saller
and C. R. Tipton, Jr.
Part C (Chapters 18–34):
CLADDING AND
STRUCTURAL MATERIALS
edited by J. R. Keeler
Part D (Chapters 35–40):
CONTROL MATERIALS
edited by S. J. Paprocki
Part E (Chapters 41–46):
MODERATOR MATERIAL
edited by E. M. Simons
Part F (Chapters 47–49):
COOLANT MATERIALS
edited by R. N. Lyon
Part G (Chapters 50–53):
SHIELDING MATERIALS
edited by V. P. Calkins
Appendix:
Constitutional Diagrams of Binary Alloy Systems
by A. A. Bauer and S. Alfant
Index

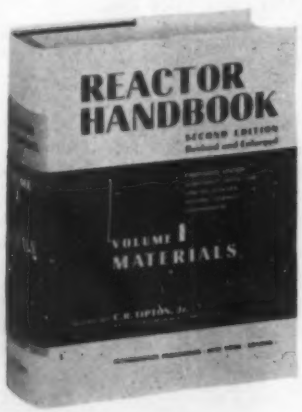

Volume 1:

MATERIALS

1223 pages 995 illustrations,
975 tables $36.50

forthcoming volumes

PHYSICS AND SHIELDING *edited by* H. SOODAK, *Nuclear Development Corporation of America, and* E. P. BLIZARD, *Oak Ridge National Laboratory*

ENGINEERING *edited by* STUART MCLAIN, *consultant to Argonne National Laboratory*

FUEL REPROCESSING *edited by* S. M. STOLLER, *consultant, formerly of Vitro Corporation of America, and* R. B. RICHARDS, *Atomic Power Equipment Department, General Electric Corporation*

Volumes may be ordered individually. For more information, write—

INTERSCIENCE PUBLISHERS, INC. *250 Fifth Avenue, New York 1, N. Y.*

A NEW STANDARD OF EXCELLENCE

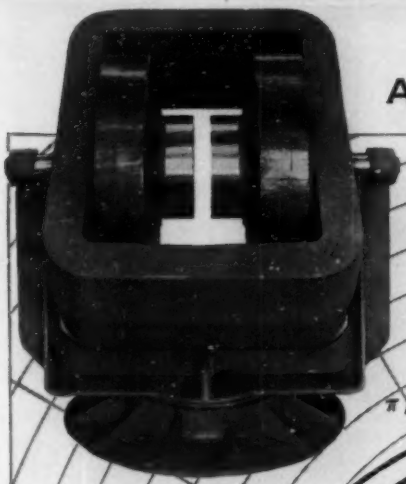

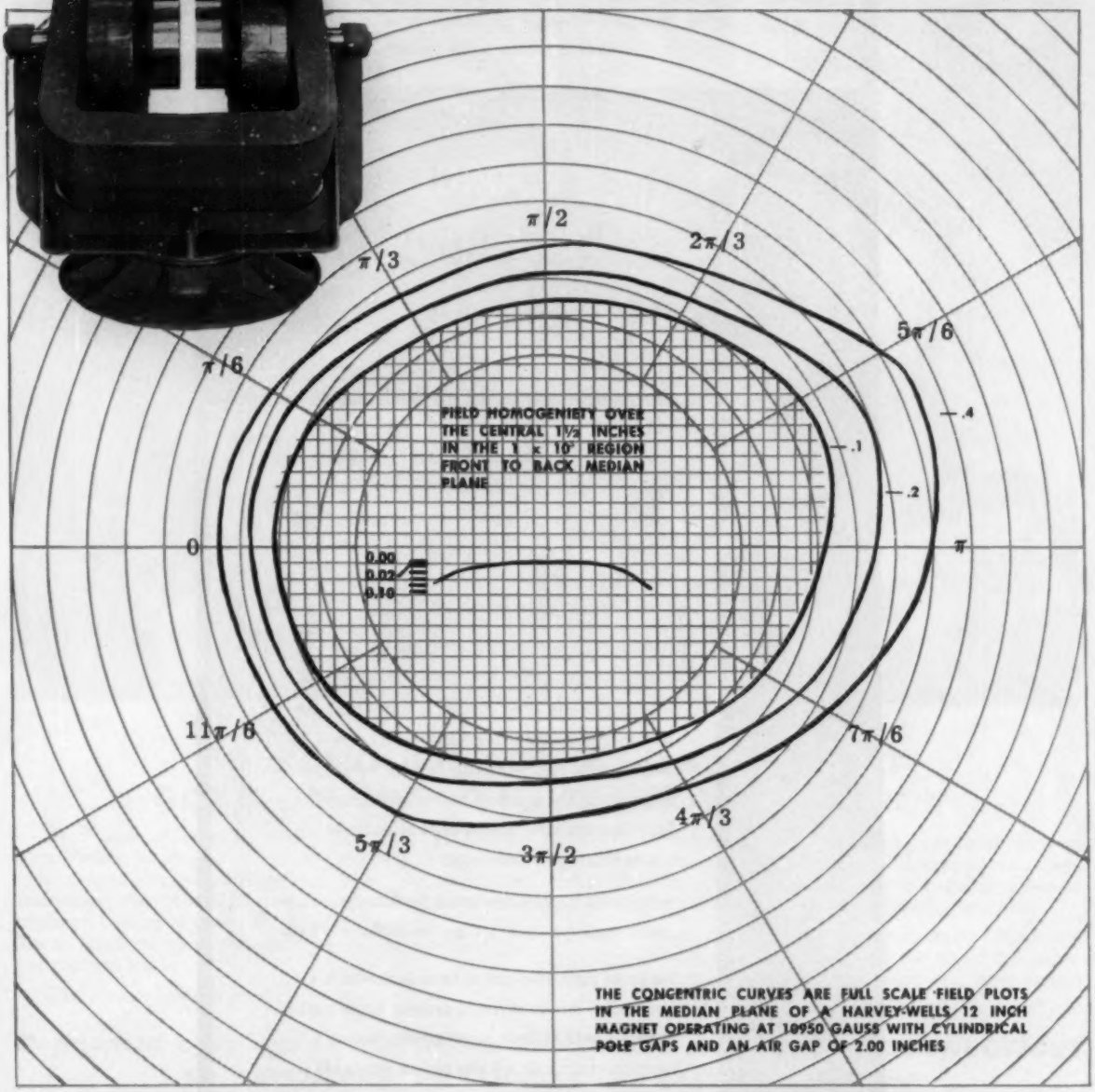

The concentric curves and specifications shown above are indicative of the performance parameters of the new Harvey-Wells Model L-128 Electromagnet. A magnet development program, staffed with specialists in metallurgy, magnet design and solid state research applications, together with consultants of recognized stature, has produced this member of a new family of electromagnets, designed with the end user in mind and which afford greater flexibility and ease of operation.

A cast yoke for increased mechanical rigidity and field homogeniety and a continuously regulated power supply are but two of the advanced features of the Model L-128. Full specifications and performance details will be sent promptly upon request.

For specifications write to

HARVEY-WELLS ELECTRONICS, INC.
14 HURON DRIVE
EAST NATICK INDUSTRIAL PARK
NATICK, MASSACHUSETTS
CE 5-7370 OL 3-7380

HW

NMR GAUSSMETER
NMR FIELD CONTROL
LABORATORY ELECTROMAGNETS AND POWER SUPPLIES
CONTRACT MAGNETS AND POWER SUPPLIES

From Varian, a completely stable high-vacuum pump, effective even when handling atmospheres with high concentrations of noble gases such as Argon.

now—Super VacIon* with argon-stable cathode!

Another significant advance from Varian's research program, solving the problem of pressure surges when requirements specify the evacuation of atmospheres containing Argon or other noble gases. Identical in all respects with Standard VacIon pumps, save for inexpensive modifications to the diode pumping element.

Super VacIon is now available in pumping speeds from 1 litre/second to 10,000 litres/second. All replacement pumping elements, either standard or Argon-stable, are interchangeable; your present VacIon pump can be modified in the field. No need for complex triode or tetrode pumps, no need for additional power supplies. Super VacIon operates from the same single power source as does the standard VacIon pump.

For complete technical data on how Super VacIon can solve your special pumping problem, address Vacuum Products Division.

The VacIon pump, developed by Varian Associates, is a revolutionary concept in vacuum pumping. VacIon employs no moving parts, no fluids, no refrigerants. VacIon's electronic construction will provide clean vacuums to one-trillionth of an atmosphere.

VARIAN associates

PALO ALTO 36, CALIFORNIA

Representatives throughout the world

KLYSTRONS, WAVE TUBES, GAS SWITCHING TUBES, MAGNETRONS, HIGH VACUUM EQUIPMENT, LINEAR ACCELERATORS, MICROWAVE SYSTEM COMPONENTS, NMR AND EPR SPECTROMETERS, MAGNETS, MAGNETOMETERS, STALOS, POWER AMPLIFIERS, GRAPHIC RECORDERS, RESEARCH AND DEVELOPMENT SERVICES.

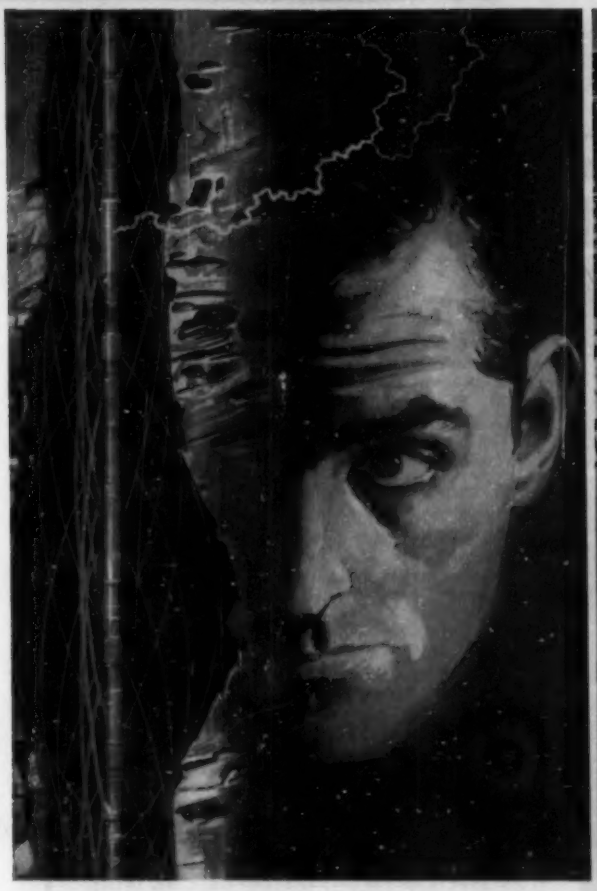

HOW WOULD YOU FIND OUT WHAT GOES ON 30,000 FEET UNDERGROUND?

Ever since the first oil well was drilled (Titusville, Pennsylvania on August 27, 1859), man has "strained his eyes" to see underground oil deposits. There had never been instruments like this in the world . . . until Schlumberger engineers developed and produced them, beginning in 1927. Today, Schlumberger is the eyes of the oil industry throughout the free world.

The pioneer Schlumberger electrical log has been refined and improved each year, along with companion services. Schlumberger now offers Electrical, Induction, Sonic, Gamma Ray, Neutron, and Gamma-Gamma Logging; Side-wall Coring, Formation Testing and Perforating services.

In Schlumberger's research and engineering laboratories (the most modern and extensive in the world for underground investigation), new approaches and new designs are under constant investigation.

Permanent openings in HOUSTON, TEXAS and RIDGEFIELD, CONNECTICUT for ENGINEERS, PHYSICISTS and MATHEMATICIANS

Positions are open in rapidly expanding Research and Development groups requiring individuals with imagination and creative ability. Outstanding facilities are provided at our international engineering laboratories in Houston, Texas and research laboratories in Ridgefield, Connecticut with high-caliber assisting personnel, exceptional benefits, and ideal working conditions.

Engineers with a minimum of three years design or allied experience and Physicists and Mathematicians with advanced degrees desired. Our work is not of a mass-production nature. Engineers and Scientists are responsible for individual Research and Development Projects and must be able to work independently with a minimum of supervision. These projects have application in petroleum technology throughout the world.

Positions open in: ELECTRONIC CIRCUIT DESIGN, UNDERWATER ACOUSTICS, MATHEMATICS, ELECTRONIC PACKAGING, FINE MECHANICS, MACHINE DESIGN.

WRITE TO: W. B. Steward

SCHLUMBERGER WELL SURVEYING CORPORATION

P. O. Box 2175, Houston 1, Texas

Triple-Tested • Performance Guaranteed • Extra Quiet

WELCH DUO-SEAL® VACUUM PUMPS

The complete line of Duo-Seal Vacuum Pumps is shown here. Descriptions and prices below.

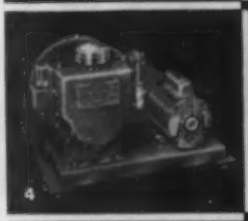

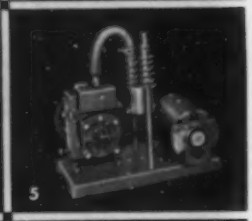

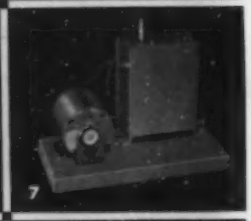

Whether it's in the laboratory, on a busy production line, in a classroom, reduced noise level means greater efficiency, higher quality work. Duo-Seal Vacuum Pumps are *quiet*. Welch engineers took noise and vibration out of the vacuum pump right on the drawing board. The result is a pump that runs as quietly as an electric motor.

Quiet operation means greater efficiency

Quiet, vibrationless operation means pumps that run smoothly year after year with virtually no maintenance beyond a periodic oil change. Duo-Seal pumps, built to close tolerances, actually improve with use, the seal and vanes become more highly polished and the fit more perfect.

There is a Duo-Seal pump available for almost every purpose, for every budget, from noncritical classroom problems to most exacting high-vacuum industrial-production and laboratory vacuum requirements.

Welch Pumps are best because:
Every pump is triple tested.
Specified performance guaranteed.
Lowest cost per year of use.
Highest vacuum of any mechanical pump.
Quietest mechanical pump made.

1. No. 1405 (2 speeds available) two-stage, No. 1405H. 0.05 micron, 33.4 liters per minute. $230.00. No. 1405B. 0.1 micron, 58 liters per minute. $255.00

2. 1400B—two-stage, 0.1 micron, 21 liters per minute. $133.00

3. 1402B—two-stage, vented exhaust, 0.1 micron, 140 liters per minute. $310.00

4. 1397B—two-stage, vented exhaust, 0.1 micron, 425 liters per minute. $645.00

5. 1392—mechanical and diffusion pump assembly, two-stage (each element) 0.001 micron, 600 liters per minute. (at 0.1 micron) $275.00

6. 1403B—single-stage, 5 microns, 100 liters per minute. $245.00

7. 1404H—Wegner Pump single-stage, 20 microns, 33.4 liters per minute. $150.00

8. 1406H—single-stage, 5 microns, 33.4 liters per minute. $150.00

9. 1410B—Wegner Pump single-stage, 20 microns, 21 liters per minute. $100.00

For complete specifications, request our pump catalog.

W. M. WELCH SCIENTIFIC COMPANY

DIVISION OF W. M. WELCH MANUFACTURING COMPANY

ESTABLISHED 1880

1515 Sedgwick Street, Dept. C-3 Chicago 10, Illinois U. S. A.

Remember A.V.S. Symposium Cleveland, Oct. 11–14

Journal
of
Applied Physics

Volume 31, Number 9 September, 1960

Statistics of the Occupation of Dislocation Acceptors (One-Dimensional Interaction Statistics)

R. M. Broudy and J. W. McClure
Union Carbide Corporation, Parma Research Laboratory, Parma, Ohio
(Received March 28, 1960)

It is known that dislocations in semiconductors can act as acceptors. This effect has been explained by noting that dislocations with edge components can have unpaired electrons at the terminating half-plane which act as acceptors; thus a dislocation contains a line of uniformly spaced acceptors only a few angstroms apart. In *n*-type materials the dislocation line becomes negatively charged and a positive space charge develops around the line. The occupation statistics are strongly modified by the electrostatic energies involved. Certain approximate solutions to this problem have already been given by W. T. Read. This paper derives improved statistics which, in addition, explicitly take into account interactions between nearest-neighbor electrons; the results are valid over the complete range of occupation. The statistics are given in terms of two functions which occur in the form of infinite series; the series have been evaluated over a considerable range of occupation and are herein tabulated. Techniques for use of the results are presented. Our theory was applied to a specific problem originally chosen by Read. The results fall between his most accurate approximations for this problem. Statistics have also been derived which take into account the proper spin degeneracy of acceptor states.

I. INTRODUCTION

THE results of several experiments on semiconductors have indicated the presence of acceptors associated with dislocations; it has been found that plastic deformation, which introduces dislocations, leads to a decrease in the number of conduction electrons.[1,2] This effect can be explained according to Shockley[3] who showed that, in certain cases, dislocations with edge components may have broken bonds terminating at the extra half-plane; this so-called "dangling bond" model of a dislocation was treated by Read[4,5] who considered specifically the 60° dislocation which can occur in the diamond structure.

According to the dangling bond model, as far as its effects on the electrical properties of semiconductors are concerned, a dislocation consists of a line of uniformly spaced acceptors only a few angstroms apart. Read[4] has derived the following expression for the spacing between dislocation acceptor sites in the diamond lattice where the dislocation and its slip vector lie in the same {111} plane

$$c=0.866b\csc\alpha,$$

where c is the spacing between acceptor sites, b is the Burgers vector, and α is the angle between the Burgers vector and the slip direction.

Since the acceptors are so closely spaced, the dislocation line becomes negatively charged and a positive space charge develops about the line. This behavior strongly modifies the treatment of the occupation statistics compared to that for the usual semiconductors in that the electrostatic energy of formation of the space charge must be considered; this energy is not negligible and in some cases actually becomes the controlling factor in determining the occupation statistics of electrons in dislocation acceptors (for more details on this see Read's paper[4]).

In his first paper[4] Read derived upper and lower limits for f, the occupation probability of electrons on dislocation acceptors, as a function of temperature.

[1] G. L. Pearson, W. T. Read, and F. J. Morin, Phys. Rev. **93**, 666 (1954).
[2] A. G. Tweet, Phys. Rev. **99**, 1245 (1955).
[3] W. Shockley, Phys. Rev. **91**, 228 (1953).
[4] W. T. Read, Phil. Mag. **45**, 775 (1954).
[5] W. T. Read, Phil. Mag. **45**, 1119 (1954).

Copyright © 1960 by the American Institute of Physics.

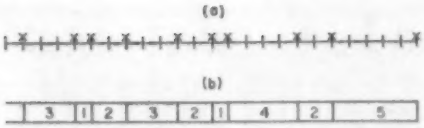

FIG. 1. (a) Typical section of a set of one-dimensional occupation sites; occupied sites are designated by ×. (b) Equivalent "block-distribution" for this problem.

The lower limit, the "minimum energy approximation," was obtained by neglecting the entropy of the distribution; the upper limit, the "Fermi approximation," was obtained by considering that the entropy of the distribution is a maximum—this will be the entropy of the Fermi-Dirac statistics. In a second paper, Read[5] derived two approximate solutions which considered the nonuniformity of the electron spacings. He called these the B (for Boltzmann) and B' approximations. As expected, these lead to results between those of the minimum energy and Fermi approximations. The B and B' results are not quite correct for relatively low and high values of f, but it is somewhat difficult to determine the limits of their validity.

In the present paper the exact statistics for electron occupation on dislocations are derived, subject only to the restriction that interactions only between nearest neighbors determine the distribution. These results are valid over the complete range of occupations.

II. ONE-DIMENSIONAL OCCUPATION PROBLEM "BLOCK-DISTRIBUTION"

For the purposes of this calculation, a dislocation is considered as a one-dimensional line of uniformly spaced acceptor sites. There are considered to be N total sites available, M of which are occupied. A typical section of this arrangement is sketched in Fig. 1(a). Figure 1(b) shows the equivalent "block-distribution" for this problem. The "block-distribution" proves particularly appropriate and helpful for this problem—the statistics for electron occupation on sites will be determined by the arrangement and nature of the blocks in the "block-distribution." The size of each block is designated by the number of unoccupied spaces between electrons in the occupation distribution. It can be seen that the block arrangement of Fig. 1(b) corresponds to the occupation arrangement of Fig. 1(a).

We wish to determine the distribution of maximum probability. This distribution can be categorized by two factors: (1) The occupation probability f. This is the parameter we wish eventually to determine. If M of N sites are occupied, then $f=M/N$. (2) The spacing distribution. In the one-dimensional occupation problem, any distribution function f will also be categorized by the distribution in spacings between occupied sites—the distribution of maximum probability will also have a unique distribution in spacings. For consideration of this point, the "block-distribution" is appropriate since the spacing distribution is the same as the equivalent distribution of blocks. That is, letting m_r equal the number of blocks of size r, the "block-distribution" can be shown as a plot of m_r vs r. At first sight, one might think that m_r would be a normal distribution with its maximum at the average block size (or the average spacing between occupied sites) $\bar{r}=N/M$; however, as will be seen later, this is not the case.

In the following, we will determine f from the "block-distribution." The free energy will be minimized first with respect to m_r and then subsequently with respect to f.

III. FREE ENERGY OF THE DISTRIBUTION (DETERMINATION OF m_r)

A. Energy

The electrostatic energy of the uniform distribution has been determined by Read.[4] His result is:

$$\mathcal{E}_{SR}=f\mathcal{E}_0\left(\frac{3}{2}\ln\frac{f}{f_c}-0.866\right), \tag{1}$$

where $\mathcal{E}_{SR}$ is the electrostatic energy per occupied site; here $\mathcal{E}_0=q^2/Kc$ is the energy of interaction of two electrons in adjacent sites, c is the spacing between nearest sites, K is the dielectric constant, and q the electronic charge. The parameter f_c is given by

$$f_c=c[\pi(N_d-N_a)]^{\frac{1}{2}}, \tag{2}$$

N_d and N_a being the donor and acceptor concentrations, respectively, in the undislocated material. The formula is valid only when $f\gg f_c$. This result includes the interaction energy between electrons, the energy of formation of the positive space charge and the interaction energy between electrons and the positive charge. At $T=0$, the distribution will be uniform, thus $m_r=0$ except at $r=\bar{r}$. As the temperature increases, electrons can move from the minimum energy position, the distribution will no longer be uniform, and an additional energy of nonuniformity will appear. Now, the derivation of (1) assumes that the radius of the positive space charge cylinder about the dislocation is much larger than the average spacing between electrons (this is the same assumption that requires $f\gg f_c$); hence, in consistency with this assumption, it can be seen that the energy of nonuniformity will affect only the electron interaction energy in (1). Thus, we write the total electrostatic energy E of the "block-distribution" in the following manner:

$$E=E_U-E_N+E_B, \tag{3}$$

where E_U = energy of the uniform distribution, E_N = the nearest-neighbor electron interaction energy of the uniform distribution, and E_B = the nearest-neighbor interaction energy of the (nonuniform) "block-distribution." The net effect is to subtract out the nearest-neighbor contribution of the uniform distribution and substitute that of the "block-distribution." E_N and

E_B are given by

$$E_N = Mq^2/\bar{r}Kc = \mathcal{E}_0 Mf; \tag{4}$$

$$E_B = \frac{q^2}{Kc}\sum_{r=1}^{\infty}\frac{m_r}{r} = \mathcal{E}_0\sum_{r=1}^{\infty}\frac{m_r}{r}. \tag{5}$$

On using (1), (4), and (5), we find

$$E = N[f\mathcal{E}_{SR} - f^2\mathcal{E}_0] + \mathcal{E}_0\sum\frac{m_r}{r}. \tag{6}$$

Or, for convenience, we write

$$E = Nf\mathcal{E}_S + \mathcal{E}_0\sum\frac{m_r}{r}, \tag{7}$$

$$\mathcal{E}_S \equiv \mathcal{E}_{SR} - f\mathcal{E}_0. \tag{8}$$

B. Entropy of the "Block-Distribution"

The entropy is given by $S = k\ln W$, where k is the Boltzmann constant and W is the number of ways of achieving the distribution. W can be obtained from the following considerations: There are M blocks available and thus $M!$ total possible perturbations, but interchanges between blocks of the same r value do not change the result, thus

$$W = \frac{M!}{m_1!m_2!m_3!\cdots m_r!\cdots}. \tag{9}$$

Using Sterling's approximation, we obtain

$$S = k\ln W = k[M\ln M - \sum_1^{\infty} m_r \ln m_r]. \tag{10}$$

C. Free Energy and "Block-Distribution"

Combining (7) and (10) and adding the energy of the dislocation acceptor level $\mathcal{E}_a$, we get for the free energy

$$F = Nf\mathcal{E}_a + Nf\mathcal{E}_S + \mathcal{E}_0\sum_{r=1}^{\infty}\frac{m_r}{r} - kT[M\ln M - \sum_{r=1}^{\infty} m_r\ln m_r]. \tag{11}$$

Now, given a particular number of occupied sites M out of a total number of sites N and thus a particular f, we wish to determine the maximum probability distribution of the m_r. Thus, the free energy must be minimized with respect to the m_r distribution subject to the restrictions

$$\sum_{r=1}^{\infty} m_r = M, \quad \sum_{r=1}^{\infty} rm_r = N. \tag{12}$$

Applying the usual Lagrangian multiplier methods, we write

$$\delta[F/N + a\sum_{r=1}^{\infty} m_r + b\sum_{r=1}^{\infty} rm_r] = 0, \tag{13}$$

where a and b are undetermined multipliers. This gives

$$\mathcal{E}_0\sum_{r=1}^{\infty}\frac{\delta m_r}{r} + kT\sum_{r=1}^{\infty}\delta[m_r\ln m_r] + a\sum_{r=1}^{\infty}\delta m_r + b\sum_{r=1}^{\infty}\delta[rm_r] = 0; \tag{14}$$

$$\sum_{r=1}^{\infty}\delta m_r\left[\frac{1}{r}\mathcal{E}_0 + a + kT + br + kT\ln m_r\right] = 0. \tag{15}$$

The bracketed term must vanish to satisfy the identity which results in the desired expression for m_r

$$m_r = Ae^{-[\beta r + s/r]}, \tag{16}$$

where A and β are constants yet to be determined and $s \equiv \mathcal{E}_0/kT$.

Note that for $s=0$ (the Fermi-Dirac case), the distribution has its maximum at $r=1$. As the electrostatic energy becomes important, the term containing s tends to move the maximum toward larger values of r. As the temperature decreases or as the electrostatic energy becomes unimportant, m_r will approach the uniform distribution, the ratio s/β increasing such that m_r becomes sharply peaked at $r = \bar{r}$.

The relation to a distribution peaked at $\bar{r}$ can be seen by rewriting (16) in the form

$$m_r = A\exp\left(-\frac{2s}{\bar{r}}\right)\exp\left(-\frac{[r-\bar{r}]^2}{\bar{r}^2/s}\frac{1}{r}\right), \tag{17}$$

where β has been eliminated by taking the maximum to be at $\bar{r}$. This has almost the form of a normal distribution with its maximum at $\bar{r}$, and in fact, if $\bar{r}^2/s = 1/f^2s < 1$ and if $\bar{r} \gg 1$, one can approximately replace the $1/r$ in the second exponential by $1/\bar{r}$, giving

$$m_r = A\exp(-2s/\bar{r})\exp(-[r-\bar{r}]^2/2\sigma^2), \tag{18}$$

which is actually a normal distribution with a standard deviation σ given by

$$\sigma^2 = \bar{r}^2/2s. \tag{19}$$

The correspondence between m_r and a normal distribution has been demonstrated mainly for didactic reasons; for most problems, the above restrictions will be satisfied only over limited ranges and thus to obtain a valid solution, the exact form of m_r must be used. However, we have demonstrated that for large enough s (low enough temperature), the distribution will approach the uniform distribution.

IV. DETERMINATION OF THE OCCUPATION STATISTICS

Equation (16) gives the form of the maximum probability distribution of m_r for a given value of $f = M/N$. Thus, the free energy in terms of the proper form for m_r can now be minimized with respect to f to determine the distribution function of maximum proba-

bility. First, we find from (16) that

$$m_r \ln m_r = m_r \ln A - \beta r m_r - (s/r) m_r. \tag{20}$$

Then, after some manipulation, we obtain for the free energy, using (11),

$$F/N = f\mathcal{E}_a + f\mathcal{E}_s - fkT\ln(M/A) - \beta kT, \tag{21}$$

where the terms in $\sum m_r/r$ in the energy and entropy have canceled out and where Eqs. (12) have been used. But

$$M/A = \sum_{r=1}^{\infty} m_r/A = \sum_{r=1}^{\infty} e^{-[\beta r + s/r]} \equiv g_0. \tag{22}$$

Thus the parameter A is eliminated.

Now, the Fermi energy $\mathcal{E}_f$ is given by the variation of the total free energy with respect to the electron occupation

$$\partial F/\partial M = \partial(F/N)\partial F = \mathcal{E}_f. \tag{23}$$

On using (20), (21), and (22) with (23), we find

$$\mathcal{E}_a + \mathcal{E}^\dagger - \mathcal{E}_f - kT\left\{\ln g_0 + \frac{f}{g_0}\frac{\partial g_0}{\partial f} + \frac{\partial \beta}{\partial f}\right\} = 0, \tag{24}$$

where

$$\mathcal{E}^\dagger \equiv \frac{\partial}{\partial f}[f\mathcal{E}_s(f)] = f\mathcal{E}_0[3\ln(f/f_c) - 2.232]. \tag{25}$$

This differs from Read's $\mathcal{E}^*$ by a factor of $2f\mathcal{E}_0$ because the nearest-neighbor electron interaction energy has been removed. But the last two terms in the bracket cancel since

$$\frac{f}{g_0}\frac{\partial g_0}{\partial f} = \frac{f}{g_0}\frac{\partial g_0}{\partial \beta}\frac{\partial \beta}{\partial f} = -1\left(\frac{\partial \beta}{\partial f}\right), \tag{26}$$

where we have used Eqs. (12) and (22) and the fact that $f = M/N$.

Thus, finally we obtain the following expression:

$$g_0(\beta) = \exp\left(\frac{\mathcal{E}_a + \mathcal{E}^\dagger - \mathcal{E}_f}{kT}\right),$$

or

$$\ln g_0 = \frac{\mathcal{E}_a + \mathcal{E}^\dagger - \mathcal{E}_f}{kT} \equiv E'[f]. \tag{27}$$

Now β is unknown, but we know that $f = M/N$. Using (22), we see that

$$f = \frac{g_0}{g_1}(\beta), \tag{28}$$

where

$$g_1 = \sum_{r=1}^{\infty} r e^{-[\beta r + s/r]} \qquad g_0 = \sum_{r=1}^{\infty} e^{-[\beta r + s/r]}. \tag{29}$$

Equations (27), (28), and (29) are sufficient to determine f. The results depend only on the knowledge of the values of $g_0(s,\beta)$ and $g_1(s,\beta)$.

V. METHODS OF APPLICATION OF RESULTS

A. Fermi-Dirac Statistics

The sums in g_0 and g_1 cannot, in general, be evaluated in closed form. However, there is one simple case which can be quickly solved and which should lead to known results; that is, if the electrostatic interaction energy is neglected (s becomes small as T becomes large), one should obtain the Fermi-Dirac statistics. Thus, we set $\mathcal{E}_0 = 0$ which makes $\mathcal{E}^\dagger = 0$ and $s = 0$. Then

$$g_0 = \sum_{r=1}^{\infty} e^{-\beta r} = \frac{e^{-\beta}}{1 - e^{-\beta}} \tag{30}$$

$$g_0/g_1 = f = 1 - e^{-\beta} \tag{31}$$

therefore

$$g_0 = \frac{1-f}{f} = \exp\left(\frac{\mathcal{E}_a - \mathcal{E}_f}{kT}\right), \tag{32}$$

which is the Fermi-Dirac statistics.

B. General Result

1. Basic Curves

The determination of the distribution function f depends on the evaluation of g_1 and g_0 vs s and β as defined in (29). Values of these sums were obtained over an extensive range using an electronic computer. The results are shown in Table I where values of $g_0/g_1 (= f)$ are shown as a function of $\ln g_0$ for various values of s; these are the basic relations needed to determine f. In the computation, values of g_0/g_1 and $\ln g_0$ were obtained for many sets of values of s and β with the values of β being chosen to provide useful results for g_0/g_1.

From the results of Table I, a family of curves can be plotted for $g_0/g_1 = f$ vs $\ln g_0$ at various values of s. This basic family can be used to determine f for all problems.

2. Determination of $E'(f)$

$E'(f)$ can be written

$$E'(f) = \frac{(\mathcal{E}_c - \mathcal{E}_f) - (\mathcal{E}_c - \mathcal{E}_a) + \mathcal{E}^\dagger}{kT}, \tag{33}$$

where $\mathcal{E}_c$ is the energy at the bottom of the conduction band. $\mathcal{E}_c - \mathcal{E}_f$ is known for the undislocated material and is a function of T, and $\mathcal{E}_c - \mathcal{E}_a$ is the energy of the dislocation acceptor level relative to $\mathcal{E}_c$. In an experimental problem $(\mathcal{E}_c - \mathcal{E}_a)$ is a parameter which will be chosen to obtain best matching between theory and experiment. $\mathcal{E}^\dagger$ contains the functional dependence of $E(f)$ on f and can be obtained from Eqs. (2) and (25) where it can be seen that f_c is determined by the properties of the specific material chosen.

3. Procedure for Determining f

For a specific problem, $\mathcal{E}_0$ is determined from the knowledge of the acceptor site spacing c. The donor

and acceptor concentrations determine f_c which, along with $\mathcal{E}_0$, determines $\mathcal{E}'(f)$ from (25)—for convenience one can graph $\mathcal{E}'$ vs f. A value of the acceptor energy level, $\mathcal{E}_c-\mathcal{E}_a$, is assumed. Then a convenient value of s is chosen, which determines the temperature for which f' will be found. The Fermi level $\mathcal{E}_f(T)$ is found by the usual methods for the undislocated material. Next, at the known value of temperature, $E'(f)$ is calculated for several arbitrarily chosen values of f; since $E'(f)=\ln g_0$, a curve of $\ln g_0$ vs g_0/g_1 can be plotted on the same graph as the basic curves—the point at which this curve intersects the basic curve for the chosen value of s gives the desired value of f from the value of g_0/g_1 at this point.

VI. APPLICATION TO READ'S PROBLEM

In his first paper, Read obtained the minimum and maximum occupation curves for a specific problem:

TABLE I. Values of the functions $\ln g_0$ vs g_0/g_1 at constant β for various values of the parameter s, where

$$g_0=\sum_{r=1}^{\infty}\epsilon^{-[\beta r+\alpha/r]};\quad g_1=\sum_{r=1}^{\infty}r\epsilon^{-[\beta r+\alpha/r]}.$$

s	$\ln g_0$	g_0/g_1	s	$\ln g_0$	g_0/g_1
1	3.833	0.0189	20	0.334	0.0452
	3.084	0.0364		−1.388	0.0718
	2.631	0.0530		−3.588	0.1110
	2.300	0.0688		−5.173	0.1417
	2.036	0.0839		−6.467	0.1678
	0.630	0.2156		−7.583	0.1909
3	2.916	0.0329	25	1.167	0.0296
	2.409	0.0468		0.045	0.0421
	2.032	0.0598		−1.812	0.0662
	1.727	0.0719		−4.205	0.1016
	0.013	0.1705		−5.940	0.1292
	−2.510	0.4050		−7.360	0.1527
				−8.587	0.1735
5	3.646	0.0168			
	2.783	0.0308	35	−0.465	0.0376
	2.238	0.0432		−2.558	0.0584
	1.826	0.0546		−5.288	0.0887
	1.491	0.0652		−7.282	0.1122
	0.335	0.1104		−8.921	0.1321
	−0.443	0.1480		−10.341	0.1498
8	2.618	0.0284	50	−1.119	0.0331
	2.024	0.0394		−5.247	0.0646
	1.571	0.0493		−7.894	0.0867
	1.199	0.0584		−10.452	0.1089
	−0.105	0.0967		−12.566	0.1277
	−1.706	0.1551		−14.749	0.1474
	−2.829	0.2017		−16.670	0.1649
	−3.733	0.2415		−18.951	0.1859
	−4.505	0.2768		−23.754	0.2308
				−31.256	0.3017
10	2.520	0.0273		−44.826	0.4630
	1.898	0.0375			
	1.422	0.0467	100	−8.295	0.0481
	1.027	0.0552		−11.873	0.0639
	−1.322	0.1196		−15.360	0.0796
	−5.134	0.2589		−18.258	0.0930
				−21.26	0.1069
15	0.656	0.0493		−23.91	0.1194
	−0.912	0.0793		−27.07	0.1343
	−2.893	0.1239		−33.73	0.1660
	−4.310	0.1590		−44.19	0.2165
	−5.461	0.1889		−63.16	0.3165
	−6.451	0.2155			

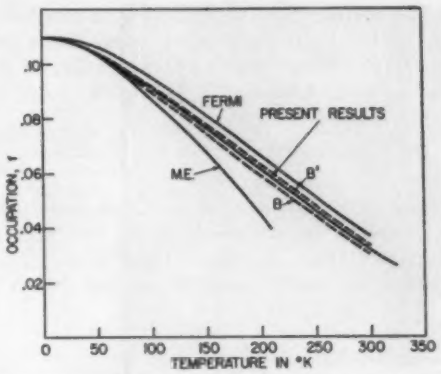

FIG. 2. The results of the application of our statistics to a problem originally specified by Read. The Fermi (maximum occupation), M.E. (minimum occupation), B and B' curves are Read's results for the various approximations.

germanium, n type with $N_D-N_A=10^{15}$ cm^{-3} and a donor ionization energy of 0.01 ev—thus $f_c=0.00586$ and $\mathcal{E}_c-\mathcal{E}_f$ can be found; $c=4$ A—thus $\mathcal{E}_0=0.225$ ev; $\mathcal{E}_c-\mathcal{E}_a=0.225$ ev. The results for $\mathcal{E}_c-\mathcal{E}_f$ and $\mathcal{E}^*$ are given in Figs. 4 and 3 of Read's paper, respectively. We have applied our statistics to Read's problem in the manner described above. The results are shown in Fig. 2 along with the Fermi, Minimum Energy, B, and B' solutions taken from Read's second paper. It can be seen that our results fall between Read's B and B' solutions.

VII. "A" STATISTICS

The present statistics, and in fact the Fermi-Dirac statistics, are derived on the assumption that each occupation level can contain only one electron; spin degeneracy is taken account of by multiplying by two in the proper place. Actually, however, neither situation quite applies for the usual acceptors and donors in semiconductors which are due to the presence of substitutional impurities. In the acceptor case, each acceptor state has a degeneracy of two since electrons of both spin directions can be accepted; but yet, only one electron can be accommodated and hence the degeneracy of occupied sites reduces to one.[8] It seems reasonable to expect that this situation would also apply for the dislocation acceptors. In fact, if the simple dangling bond picture applies, then statistics taking this effect into account are very likely the correct ones.

This effect can readily be taken into account in the present case. The only difference is that (9) for W is now written as

$$W=\frac{M!}{m_1!m_2!m_3!\cdots}\times 2^{(N-M)},\qquad(34)$$

since the degeneracy of the $N-M$ unoccupied sites $=2$.

[8] For consideration of this point, see, e.g., Eberhard Spenke in *Electronic Semiconductors* (McGraw-Hill Book Company, Inc., New York, 1958), pp. 387ff.

Then it turns out that the succeeding calculations are almost identical with the previous except that a factor $=\ln 2$ carries through and we obtain, finally, for these statistics which we call the "A" statistics

$$\ln g_0 - \ln 2 = \frac{\mathcal{E}_0 + \mathcal{E}^\dagger - \mathcal{E}_f}{kT} \equiv E'(f). \tag{35}$$

Thus, the calculation method described above follows through exactly the same way in the "A" statistics, but in the final plot, one adds $\ln 2$ to $E'(f)$.

To check the results for $\mathcal{E}_0=0$, we find that in this case (35) becomes

$$\frac{1-f}{f} = 2\exp\left(\frac{\mathcal{E}_0 - \mathcal{E}^\dagger}{kT}\right), \tag{36}$$

which is the proper result for noninteracting acceptors.[6]

VIII. CONCLUSIONS

The occupation statistics for electrons on dislocation acceptors (or the one-dimensional occupation problem) have been derived subject only to the restrictions that only nearest-neighbor interactions are considered. As required, the results approach the Fermi-Dirac statistics at high enough temperature and a uniform distribution as $T \to 0$. The neglect of higher-order ($2d$ and higher nearest-neighbor) interaction terms will probably not greatly affect the result, since not only are they small compared to the first-order effects but they have not been completely excluded because their effects have been approximated by those of a uniform distribution as can be seen from (3). The general tendency of the higher-order terms will be to change the distribution towards a slightly more uniform one.

For the specific problem chosen by Read, over the temperature range considered, our results fall between Read's B and B' curves. One cannot say whether the agreement will be similar in general; particularly, in the case of very low values of f Read points out that the B and B' occupation numbers will be somewhat too large, possibly even falling above the Fermi curve; this cannot be the case for our statistics since the results approach the Fermi case at low f.

For most applications, the "A" statistics should probably be used since they more accurately consider the effects of spin degeneracy as applied to acceptors. These statistics were not used in computing Read's problem since we wanted to make a proper comparison with his results which do not take spin degeneracy into account. Although the results are not shown here, we find that for Read's problem the "A" statistics give results significantly, although not qualitatively, different from those shown on Fig. 2. Below 50°K, f has almost the same value as that computed for the case which does not consider acceptor spin degeneracy, and it is about 30% lower at 300°K.

IX. ACKNOWLEDGMENT

We wish to acknowledge the assistance of Mr. Lyle B. Smith who set up the computer program and obtained the values for g_0 and g_1.

JOURNAL OF APPLIED PHYSICS VOLUME 31, NUMBER 9 SEPTEMBER, 1960

Ion-Bombardment Etching of Synthetic Fibers

FRANKLIN R. ANDERSON AND V. F. HOLLAND
*The Chemstrand Corporation Research Center, Decatur, Alabama**

(Recieved April 15, 1960)

An ion-bombardment etching method was used to prepare synthetic fiber samples for study in the electron microscope. Reproductible results were obtained by bombardment in a constantly changing argon atmosphere at a pressure of 1–2 cm Hg for 2–5 min. The etch patterns produced by this method were characteristic of the orientation of the fiber samples which were investigated.

INTRODUCTION

RECENT developments have revealed the presence of periodicities in synthetic fibers larger than those defined by the polymer unit cell. Hess *et al.*[1] have shown by staining techniques the presence of repeat distances of 100 A and larger in fibrils of drawn polymides. Keller[2] used shadowing techniques to reveal a periodicity of 120 A in fibrils of nylon 610. The presence of a periodicity of 120 A in single crystals of polyethylene was confirmed by low-angle x-ray scattering.[3] This periodicity was related to the regularity of chain folding. The most recent results of low-angle x-ray scattering studies of polyethylene have revealed periodicities of the order of 400 A in drawn fibers.[4] The existence of a polymer structural unit, which is larger than the unit cell as defined by minimum repeat distances, seems quite possible. The presence of such a unit could prove to be helpful in explaining fiber properties.

* Contribution No. 69.

[1] K. Hess, E. Gutter, and H. Mahl, Naturwiss. 46, 70 (1959).

[2] A. Keller, J. Polymer Sci. 36, 361 (1959).

[3] A. Keller and A. O'Conner, Nature 180, 1298 (1957).

[4] A. S. Posner, L. Mandelkern, C. R. Worthington, and A. F. Diorio, J. Appl. Phys. 31, 536 (1960).

By using the electron microscope, we observe a periodicity of the same order of magnitude as that seen by other investigators in drawn and undrawn fibers. This was made possible through the use of an etching technique for specimen preparation.

Solution and ion-bombardment etching have been used for many years to prepare metal samples for internal structural studies. Recently, Khoury[5] used solvent etching and light microscopy to reveal the crystalline-amorphous nature of spherulites in films of nylon 66. Also Kassenbeck[6] exposed the internal structure of cotton, for study in the electron microscope, by ion-bombardment etching. In the present study, ion-bombardment etching was applied to synthetic fibers in an attempt to elucidate internal structural arrangements.

APPARATUS

Bombardment of samples was carried out in an SC-3 high-vacuum evaporator which was equipped with a glow discharge attachment. This attachment furnished 4000 v ac at a current of 30 ma.

Two brass electrodes were connected to the glow discharge terminals. The electrodes were 5 cm long with a diameter of 9 mm. The electrode which held the sample was bored in the center to a depth of 3.5 cm and a diameter of 5 mm. The other electrode was solid. The faces of both electrodes were polished to a mirror finish.

TECHNIQUES

A. Sample Preparation

Several different techniques were used to prepare the samples for bombardment. Fiber samples were embedded in polymethyl methacrylate to facilitate handling. Bristles which were large enough were handled directly. Some of the samples were cut cross-sectionally and polished using, respectively, 600 A carborundum paper, 4/0 emery polishing paper, and type B Linde fine abrasive on a lapping cloth. Other samples were fractured cross-sectionally in liquid nitrogen; however, difficulty arose in handling drawn nylon 66 samples. They fractured longitudinally instead of cross-sectionally; consequently, the longitudinally fractured faces of several drawn nylon 66 samples were bombarded.

FIG. 1. Outside surface of undrawn, nonspherulitic nylon 66 fiber. Etched 5 min at 2-cm pressure in argon. All electron-micrographs are of direct Pt-C replicas.

FIG. 2. Outside surface of undrawn, relaxed, highly spherulitic nylon 66 ribbon. Etched 5 min at 1 cm pressure in argon.

The outside surfaces of many fibers were bombarded by mounting a bundle of the fibers across the face of one of the electrodes. Direct platinum-carbon replicas were then prepared without removing the fibers from the electrode. This ensured that the surfaces which were bombarded would be replicated and not turned under during handling.

B. Bombardment

An atmosphere of air was initially used during ion-bombardment of samples. This produced a carbonaceous material on the surfaces of most of the samples. This material was apparently due to some type of degradative oxidation which resulted from localized heating during the bombardment. At high pressures (3–6 cm Hg) the ion beam was quite concentrated and the heating effect was much greater than at lower pressures. Pressures of 0.5–2.5 cm Hg were therefore used and much of the carbonaceous material was eliminated.

An argon atmosphere was used in an attempt to eliminate all this material. A much cleaner etch was thereby obtained; however, a dynamic or constantly changing argon atmosphere produced the cleanest etch of all. Argon pressures of from 1–6 cm Hg were tried. The most reproducible results were obtained at pressures from 1–2 cm Hg.

Bombardment time was not too critical except at very low pressures (10–350 mm Hg). Nylon 66 was surface cross linked at this pressure, if bombardment times in excess of 1 min were used.

Several different electrode distances were tried. A distance of 2.5 cm proved to be the most suitable.

C. Replication

The outside surfaces of all the fibers which were bombarded were replicated directly with platinum and carbon. This was accomplished by using low angles for evaporation, i.e., platinum was evaporated at 15° and carbon at 45°. The use of the low evaporation angles resulted in the replication of a small portion of the fiber

[5] F. Khoury, J. Polymer Sci. **26**, 375 (1957).
[6] P. Kassenbeck, Melliand Textilber. **39**, 55 (1958).

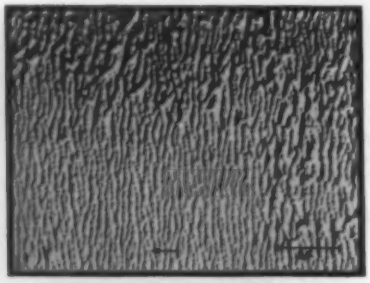

FIG. 3. Outside surface of drawn nylon 66 fiber. Etched 5 min at 1 cm pressure in argon. Arrow denotes direction of draw.

surface and thus prevented folding of the replicas. When fibers were shadowed parallel to their long axis there was no need for using small evaporation angles.

Longitudinal and cross-sectional surfaces of fibers and bristles were replicated directly except when the samples were to be reused. In this case two-stage polyvinyl alcohol-platinum-carbon replicas were prepared.

DISCUSSION

Characteristic etch patterns were produced by ion-bombardment on drawn, undrawn, and spherulitic fiber samples. These etch patterns were composed of small elongated units of variable lengths. The spacings defined by two parallel units varied from 300–700 A. On the outside surface of undrawn, nonspherulitic nylon 66 fibers the units were oriented randomly. This is shown by Fig. 1. Etched cross sections of these fibers were also covered with randomly oriented units.

The etch pattern produced by ion bombardment of the outside surface of undrawn, relaxed, highly spherulitic nylon ribbon is exemplified by Fig. 2. Here, the units have spacings of approximately 300–400 A. They are oriented in the direction of the radiating fibrils of the spherulites. A boundary between two spherulites is also shown in this micrograph.

Figure 3 shows the etch pattern which is characteristic of drawn nylon 66. The arrow denotes the fiber axis, i.e., the direction of draw; thus, the units are oriented at approximately 90° to the axis of draw. They vary in width from 300–600 A. This same perpendicular orientation was observed when drawn nylon was fractured longitudinally and bombarded.

Other drawn polymer samples were examined to determine if this unexpected result was peculiar to nylon 66. Figure 4 is the etch pattern produced by ion-bombardment of the outside surface of a drawn polyethylene terephthalate fiber. Again the arrow denotes the fiber axis. It was bombarded under the same conditions as the sample in Fig. 3. The spacings of the units in Fig. 4 are 400–700 A.

A sample of nylon 66 fiber, which was drawn through a hot tube at 175°C with equal feed roll and draw roll speeds, was etched using the same conditions as for the samples in Figs. 3 and 4. The units which were thereby exposed were also oriented perpendicularly to the axis of draw. This result was surprising since very little stretch was exerted on the fiber; however, the orientation of the units may take place during the first small changes in the orientation of the fiber.

At the present, our knowledge of the true etching mechanism is such that no definite conclusion can be made as to why these rod-shaped units, which comprise the etch patterns on synthetic polymers, are exposed. Neither is their structural significance or origin known; however, Keller[7] has suggested that the chain folding proposed for polymer single crystals is also present in drawn fibers. These etch units may have some relation to the folding of the chains in fibers. The fold period in single crystals is, however, on the order of 100 A

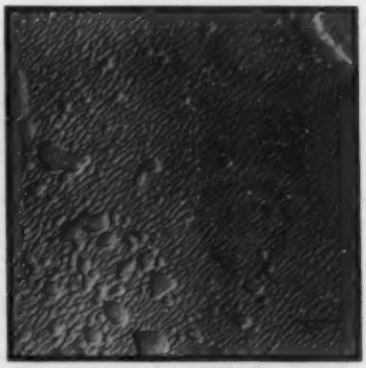

FIG. 4. Outside surface of drawn polyethtlene terephthalate fiber. Etched 5 min at 1 cm pressure in argon. Arrow denotes direction of draw.

and is considerably less than the width of the units exposed in fibers by ion-bombardment etching, It was also reported that the fold period is dependent on temperature[8]; therefore, the greater width of the units in fibers could be a temperature effect if they are related to chain folding.

CONCLUSION

The ion-bombardment etching method described should be of great value in extending the usefulness of the electron microscope in synthetic polymer research. Although a completely satisfactory interpretation of the etch patterns produced by this method has not yet been made, they are characteristic of the orientation of the samples used.

[7] A. Keller, Makromol. Chem. **1** (Special), 1 (1959).
[8] A. Keller and A. O'Conner, Discussions Faraday Soc. **25**, 114 (1958).

The Oscillistor—New Type of Semiconductor Oscillator

R. D. Larrabee and M. C. Steele
RCA Laboratories, Princeton, New Jersey

(Received February 23, 1960)

A new magneto-oscillatory effect has been observed in the electron-hole plasma within a semiconductor. The plasma can be produced by such agents as contact injection and optical or thermal excitation of minority carriers. When the semiconductor specimen is subjected to an electric field (through suitable contacts) and a magnetic field, current oscillations can be detected across a series load resistance. This device has been termed the oscillistor to suggest a semiconductor oscillator. The experiments suggest that the oscillistor mechanism involves a magnetically induced interaction of the bulk plasma of electrons and holes with the exposed free surface areas of the specimen.

INTRODUCTION

It has been observed[1] that current oscillations occur in an N-type germanium sample placed in parallel electric and magnetic fields. Oscillations, which are probably of a similar nature, have also been observed[2] in P-type indium antimonide at 77°K. These oscillations have been confirmed by the present experiments, in which this effect has been observed in N- and P-type germanium (at 300°K); N- and P-type germanium, P-type silicon, and N- and P-type indium antimonide (at 78°K); and in N-type germanium (at 4.2°K). This device will be referred to as the oscillistor since its one outstanding property is that it produces oscillations.

In this paper some basic properties of the oscillistor will be described and specific experiments that yield important clues regarding the mechanisms of oscillation will be discussed.

BASIC OSCILLISTOR

Basically an oscillistor consists of a semiconductor sample and a load resistance connected in series across a dc or pulsed power supply, as shown in Fig. 1. In its simplest form, a rectangular sample is equipped with one contact that is "ohmic" for majority carriers and one contact which is capable of injecting minority carriers, e.g., a forward biased P-N junction. The specimen may be immersed in a coolant if necessary. A magnetic field is oriented so that it is approximately parallel to the electric field produced by the contacts (within approximately $\pm 10°$). If the conditions of the experiment are satisfactory,[3] current oscillations will be observed as an oscillating voltage across the load resistance. The fundamental properties of this basic oscillistor will be discussed in the following section.

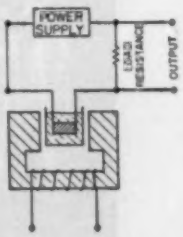

Fig. 1. Schematic illustration of basic oscillistor.

OSCILLISTOR PROPERTIES

The basic oscillistor has many interesting properties. A few of the more fundamental ones, determined experimentally, are discussed as follows.

(a) *Frequencies* of oscillation from a few kilocycles to about ten megacycles have been observed in different crystals. The frequency depends mainly on the magnitude and relative orientation of the applied electric and magnetic fields as well as the condition of the surface of the semiconductor specimen. The frequency is virtually independent of the magnitude of the load resistance and other parameters of the external circuit, provided, of course, that the voltage applied to the specimen is held constant as the circuit parameters are varied.

(b) *Waveforms* of all descriptions have been observed. A typical example is shown in Fig. 2 in which a germanium oscillistor is operated in a pulsed manner at room temperature to avoid excessive heating. The pulse length is 700 μsec, 2 pulses/sec, and time progresses from left to right. The oscillograms represent the voltage across a small load resistor for different experimental conditions and for the same sample. The oscillations are coherent from pulse to pulse. Notice the variety of frequencies and waveforms that are observable in a single specimen. Although complicated waveforms seem to be the most common, waveforms approaching sinusoidal are also observed, as illustrated in Fig. 3, which represents an oscillogram of a 1-Mc germanium oscillistor operating continuously in a liquid nitrogen bath.

(c) *Percentages of modulation* up to about 70% of the dc component of current have been observed. This indicates that the oscillistor mechanism is a first-order effect. The percentages of modulation shown in Fig. 2 are typical of what one generally observes in germanium oscillistors operating at room temperature.

[1] I. L. Ivanov and S. W. Ryvkin, Soviet Phys.-Tech. Physics 3, 722 (1958).
[2] J. Bok and R. Veilex, C. R. 248, 2300 (1959).
[3] Typical operating conditions are sample size: 1 sq mm cross section by 1 cm long; material: relatively pure (intrinsic) germanium; load res: 10 to 100 ohms; power supply: 100 v (pulsed); magnetic field: 10 000 gauss (for room temperature operation).

FIG. 2. Typical characteristics of basic germanium oscillistor operating in a pulsed manner at room temperature.

(d) *Noise* is sometimes observed when comparatively high electric and/or magnetic fields are applied to the sample. It would seem as though the oscillistor was simultaneously operating at many frequencies incoherently. The appearance of this mode of oscillation on the oscilloscope and its characteristics as observed with a radio receiver are suggestive of white noise.

(e) *A magnetic field* is always required for oscillistor action. The minimal magnetic field required is given by the empirical condition that the ambipolar mobility of the plasma of electrons and holes times the minimal magnetic field be approximately 0.1 dimensionless mks units.

(f) *Synchronization* of the free-running oscillistor frequency to that of a synchronizing signal is only possible if these two frequencies are within approximately $\pm 1\%$ of each other. If the frequencies are more than about 1% removed from each other, the oscillistor will synchronize so as to maintain an arbitrary integer ratio with the synchronizing frequency.

(g) *The stability* of the oscillistor is limited by the constancy of the parameters that effect the characteristics of the oscillations. In the course of the present experiments it was observed that the frequency, waveform, and amplitude of the oscillations remained virtually constant over a period of 8 hr (after which the test was terminated).

(h) *The current-voltage characteristic* of the oscillistor does not display a negative resistance. This fact, coupled with its relative insensitivity to outside influences (in the external circuit or to synchronization), suggest that the semiconductor specimen is the complete oscillator. Consequently, the oscillistor can be looked upon as a complete functional semiconductor oscillator.

EXPERIMENTS RELATING TO BASIC PHYSICAL MECHANISM

Some specific experiments, designed to yield important clues regarding the oscillistor mechanism, will now be discussed. Although many experiments have been performed, only a few stand out as critical regarding the fundamental oscillation mechanism.

Experiment No. 1—Minority Carriers

A specimen of 18 ohm-cm *P*-type germanium was equipped with one majority carrier "ohmic" contact (In+½% Ga) and one contact similar to the collector of the Thyristor.[4] This Thyristor contact is "ohmic" to majority carriers and in addition has the property of injecting minority carriers (electrons) when biased negatively. Therefore, since the voltage drop across the contacts was negligible in comparison with the voltage across the semiconductor specimen, it was possible to turn the minority carrier injection on and off by simply reversing the polarity of the voltage applied to the sample.

It was found that oscillations were easily observed when the polarity of the applied voltage was adjusted so as to have minority carrier injection. However, when biased so that both contacts behaved as simple majority

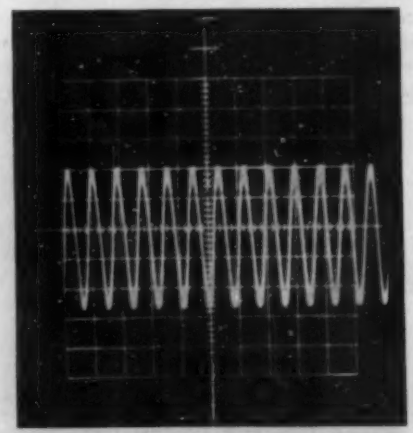

FIG. 3. Illustration of near sinusoidal oscillistor oscillations.

[4] C. W. Mueller and J. Hilibrand, IRE Trans. Electron Devices Ed-5, 2 (1958).

carrier "ohmic" contacts (no injection of minority carriers), the oscillations were completely absent. No oscillations could be found for this polarity even when the electric field was adjusted so that the actual current was the same or greater than in the former case.

This experiment indicates that there must be a large number of minority carriers (approximately equal to or greater than the extrinsic majority carrier density) present in order to observe oscillistor action. There is a striking analogy between a distribution of majority and minority carriers in a semiconductor and the electrons and ions in a gas discharge plasma. Aside from differences in the magnitude of the physical parameters involved (mobilities, mean free path, etc.) the analogy is very good, and hence the combination of minority and majority carriers will be referred to as a plasma. It is interesting to note that unexplained oscillations have been observed in gas discharges subjected to a magnetic field.[5]

Experiment No. 2—Contacts

In order to evaluate the importance of the contacts, a sample was constructed that effectively prevented the plasma from touching either contact. A crystal of 16 ohm-cm *P*-type germanium was abruptly doped to 0.01 ohm-cm *P*-type during the crystal growing process. A thin wafer section of this crystal was cut to the "*S*" shape shown in Fig. 4. The thin middle region of this "*S*" sample should be considered as the active region of the sample and the remaining large portions of the sample (top and bottom in Fig. 4) should be considered as part of the contact assembly.

The minority carrier injection mechanism (top section) consists of a majority carrier "ohmic" contact (labeled *A*) biased negatively and strong illumination of the large area between this contact and the thin middle section. The purpose of the illumination is to produce, optically and/or thermally, majority and minority carrier pairs. The majority carriers thus created are collected by the "ohmic" contact and the minority carriers

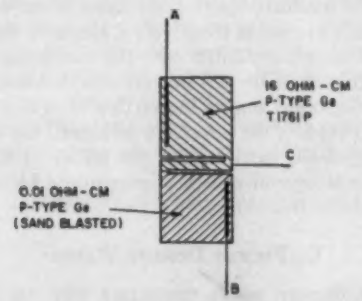

FIG. 4. Schematic illustration of the "*S*" sample.

are swept into the thin middle section by the applied electric field. Only the large top section of the sample adjacent to the contact labeled *A* was illuminated. All contacts and other portions of the sample were shielded from the light.

Since the resistivity of the large region below the thin middle section (adjacent to the "ohmic" contact labeled *B*) is so very much lower than the resistivity of the rest of the sample, the electric field in this region will be proportionately lower. Therefore, the minority carriers will drift very slowly toward the contact *B*. Consequently, by sand blasting the surface of this low resistivity region to assure very low minority carrier lifetime, one can make the transit time across this region (milliseconds) large compared to the lifetime (microseconds). Hence the minority carriers will never survive the journey to contact *B*.

Such an "*S*" sample comes as near as possible to an oscillistor without any contacts, since the plasma never touches either majority carrier "ohmic" contact.

A small minority carrier injecting contact (labeled *C* in Fig. 4) was included to enable one to test the sample for oscillations in the absence of illumination. By utilizing this injecting contact and the contact *B*, oscillations were readily observed at room temperature.

An experiment to observe oscillations between the two contacts *A* and *B*, in the *absence of light*, gave negative results. This was expected (see experiment No. 1 in the foregoing), since both contacts were majority carrier "ohmic" contacts and no minority carrier injection was taking place. However, when the large region near contact *A* was illuminated, oscillations were observed between contacts *A* and *B*.

It can be concluded, therefore, that the plasma need not touch (and thus interact with) the contacts in order to have oscillistor action. Consequently, it is felt that the contacts play the passive role of supplying minority and majority carriers to the sample as required by the applied voltage, but *do not directly* enter into the fundamental oscillation mechanism.

Experiment No. 3—Magnetic Field

Experiments were performed to ascertain the relative importance of the components of magnetic field parallel and transverse to the applied electric field. The following conclusions were drawn from such experiments:

(a) Both components of magnetic field are generally required to obtain coherent repetitive oscillations. A strictly longitudinal field parallel to the electric field (to within $\pm\frac{1}{2}°$) generally results in the white noise mode of operation.

(b) The parallel component of magnetic field is approximately an order of magnitude larger than the transverse component when coherent oscillations are observed. Because of this it is conjectured that there is a first-order interaction in the transverse component and a higher-order interaction in the parallel component.

[5] See, for example, R. Bohm, E. H. S. Burhop, H. S. W. Massey, and R. W. Williams in *Characteristics of Electrical Discharges in Magnetic Fields*, edited by Guthrie and Wakerling (McGraw-Hill Book Company, Inc., New York 1949), Chap. 9.

(c) The oscillations are very much more sensitive to a perturbation in the transverse component than to a similar percentage perturbation in the parallel component of magnetic field.

Because of the importance of the comparatively small transverse component of magnetic field, some light might be shed on the oscillistor mechanism by studying its effects. Since the electrons and holes move in opposite directions under the influence of the applied electric field there exists a first-order Lorentz force (due to the transverse component of magnetic field) tending to push both electrons and holes in the same direction. This will cause the plasma to "pile up" against a surface of the specimen until ambipolar diffusion counter-balances the Lorentz force.[6] This increased density of plasma on the surface can increase the relative importance of all surface parameters. For example, a very large magnetoresistance is always observed in oscillistors. This is due to the enhanced surface recombination brought about by the large plasma density at the surface (Suhl effect). Hence, it is therefore, believed that the main purpose of the transverse component of magnetic field is to enhance the surface effects and thus allow the surface to participate in the oscillation mechanism.

Experiment No. 4—Surface

A comparatively large sample of germanium (about 8 cm^3) of approximately cylindrical shape was provided with two small closely spaced contacts in the middle of one end. In this way, the plasma could only be influenced by the surface at the end upon which the contacts were made since all other surfaces of this large sample were so far removed from the contacts that bulk recombination would occur before the plasma could reach them. When the transverse component of magnetic field was aligned so as to "push" the plasma to the surface upon which the contacts were made, oscillistor oscillations and a large magnetoresistance (Suhl effect) were observed. Upon reversal of the transverse component of magnetic field, the plasma was "pushed" into the (infinite) bulk so that there was no surface upon which to concentrate the plasma. This caused the oscillations to vanish and the magnetoresistance to become very much smaller. This experiment clearly points out the importance of the surface in the oscillistor mechanism. This experiment does not specify what property of the surface is of prime importance, but only that a surface is required.

EXPERIMENTAL DEDUCTIONS AND SPECULATIONS

On the basis of the experiments outlined, it may be concluded that the oscillistor mechanism involves a magnetically induced interaction of a plasma of electrons and holes within a semiconductor with the exposed free surface areas of the specimen. The foregoing experiments do not specify the function of the parallel component of magnetic field or suggest exactly what property of the surface is involved in the oscillation mechanism. Since the density of plasma at the surface may be sufficiently high to reduce the surface potential to a very small value, it is quite likely that the surface potential is not an important parameter in the oscillistor mechanism. The surface recombination velocity can give rise to unusual effects if it is a strong function of the plasma density at the surface. The storage and subsequent release of charge from the surface states are equivalent to a capacitance. On the other hand, the time required for the bulk plasma to adjust to changing surface conditions produces an inductive effect. Combinations of these effects can give rise to oscillations.

TENTATIVE MODELS

Several models of the oscillation mechanism are suggested by the foregoing experiments. A few comments about each model are appropriate at this point.

A. Self-Pinch Effect

Stable or unstable pinch effects can be eliminated immediately since the currents in oscillistors are generally several orders of magnitude less than the minimum current necessary to initiate or maintain a pinch.[7] The importance of nonuniform injection at the contacts seems improbable in view of the results of the experiment (No. 2) in which a uniform injection of minority carriers was obtained optically. Since the pinch effect could not maintain a "streamer" produced by nonuniform injection, it seems likely that within a short distance from the contact, the conditions would be substantially uniform.

B. Other Magneto-Hydrodynamic Effects

Magneto-hydrodynamic effects (e.g., Alfven waves) seem improbable because of the following condsiderations. The conductivity of the plasma in an oscillistor is too small to confine effectively a magnetic field for a period of time compatible with the oscillation period. The magnitude of the self-magnetic fields are too small to give rise to any known interaction of sufficient magnitude to explain the effect. In addition, the collision frequency of the carriers with the lattice of the semiconductor is several orders of magnitude higher than the oscillation frequency.

C. Plasma Density Waves

Plasma density waves resonating with the sample length is not a probable situation in view of experiment No. 2 in which the sample had no abrupt dis-

[6] See, for example, W. Shockley in *Electrons and Holes in Semiconductors* (D. Van Nostrand Company, Inc., Princeton, New Jersey, 1950), pp. 325–328.

[7] M. Glicksman and M. C. Steele, Phys. Rev. Letters **2**, 461 (1959).

continuous ends as far as the plasma was concerned. It is difficult to see how plasma density waves can be reflected into a standing wave pattern in this experiment.

D. Variable Surface Recombination Velocity

The surface recombination velocity S is in general a function of the plasma density N at the surface. That is $S=f(N)$. If dS/dN is negative, one can picture an unstable equilibrium between the Lorentz force tending to push plasma to the surface, diffusion tending to counteract the Lorentz force, and the density dependent surface recombination velocity acting as a boundary condition. This unstable equilibrium can give rise to oscillations in the plasma density which would be reflected as current oscillations.

E. Variable Surface Plasma Density

The storage of charge on the surface states will vary with the plasma density at the surface. This will give rise to a component of current to the surface which depends upon the rate of change of surface plasma density rather than upon the surface recombination velocity. This is a capacitive effect which, for sinusoidal oscillations, can be described by a complex surface recombination velocity $S=S_0+J\omega C/\epsilon$, where S_0 is the ordinary, well known, surface recombination velocity, $J=(-1)^{\frac{1}{2}}$, $\omega=2\pi$(frequency,) $\epsilon=$permittivity of the semiconductor, and $C=$the effective capacitance of the surface. It is felt that this capacitance can resonate with the inductive delay effect of the transport of plasma within the bulk of the specimen.

F. Cyclotron and Plasma Resonance

From the empirical condition that the minimal magnetic field times the ambipolar mobility is equal to 0.1 dimensionless mks units, it is clear that $\omega_c\tau\geq 0.1$, where $\omega_c=(2\pi)$ (cyclotron resonance frequency) and $\tau=$scattering time. Certainly at the lower magnetic fields where $\omega_c\tau=0.1$ it is difficult to see how cyclotron resonance can be an effective mechanism. There may be an interaction between the cyclotron and plasma resonances since the densities in certain portions of the sample give rise to plasma resonance frequencies approximately equal to the cyclotron resonance frequency. However, it is difficult to see how any such interaction can result in the observed oscillation frequencies which are orders of magnitude below the cyclotron resonance frequency.

Of all the models listed, only D and E are consistant with the experimental observations. However, it is realized that further experiments are needed to distinguish between these models or to suggest other models for the oscillation mechanism.

OSCILLISTOR AS A DEVICE

When considered as a controllable oscillator, the oscillistor should be classed as a useful device. Aside from the complications imposed by the necessity of an externally applied magnetic field, the basic circuitry required is extremely simple (Fig. 1). The oscillations can have a reasonable amplitude, frequency, and power. The characteristics of the oscillations are easily controlled by such parameters as magnitude and relative orientation of applied electric and magnetic fields, condition of the surface of the specimen, application of light, chemically active ambient, or potentials through additional electrodes (to alter the plasma density of potential distribution in the specimen). When considered as a detector or transducer, the oscillistor should again be classed as a practical device. Perturbations in the characteristics of the oscillations (e.g., frequency) can be used to detect changes in any parameter that will effect the oscillations.

With increased understanding of the exact nature of the mechanism of oscillation, the oscillistor should find use as a tool for measuring semiconductor properties. Perhaps the possibility of measuring surface parameters is the most promising prospect. A correlation between the frequencies of oscillation and the speed of response of the surface states has been suggested by our experiments.

CONCLUSION

A new type of magneto-oscillatory plasma effect in semiconductors has been described. Experiments have been discussed which suggest the basic ingredients for a model of the pertinent mechanisms. The experiments indicate a wide range of diverse device possibilities for the oscillistor.

ACKNOWLEDGMENTS

The authors are indebted to Murray Lampert and I. Adawi for their stimulating suggestions regarding both theory and experiment; to Richard O. Wance for his valuable efforts in the preparation of samples and in the actual collection of experimental data; and to Karl Zaininger for many discussions regarding the interpretation of the experiments.

Large Temperature Range Annealing*

WILLIAM PRIMAK
Argonne National Laboratory, Argonne, Illinois
(Received February 4, 1960; and in final form June 2, 1960)

Vand's analysis of distributions in activation energy is reexamined through a new derivation which leads to a better approximation to the activation energy spectrum and which permits a treatment of step annealing data. The cases of distributions in frequency factor and the twofold distributions in activation energy and frequency factor are also treated.

INTRODUCTION

THERE are several classes of disordered solids whose properties alter gradually when they are heated and continue to alter as the temperature is raised over a range of temperatures several times the absolute temperature at which the property change is first noted. The alteration of the properties (as well as the heating program which the specimen has been subjected to) is usually termed annealing, and the particular behavior noted here will be referred to as extended annealing. It is not possible to explain extended annealing with any reasonable assumptions involving one kind of kinetic process. To explain the extended annealing of the electrical resistivity of metals condensed from the vapor phase at low temperatures, Vand[1] assumed kinetic processes of first order, independent of each other, possessing one frequency factor, and distributed quasi-continuously in activation energy. He derived two methods for determining the original distribution from annealing data: the first from the rate of annealing in specimens heated at constant temperature, a method which he called *isothermal annealing*; and the second, from the rate of annealing in specimens whose temperature was raised at a uniform rate, a method which he called *tempering*. Following a lengthy controversy (mostly unpublished) concerning the propriety of assuming first order processes, it was shown[2] that Vand's method is equally applicable to other orders of reaction. Thus, although the kinetic data are used to determine the original distribution, this determination yields no information about the kinetics, the original distribution having been present before the annealing was begun. Some peculiarities of such systems and some rudimentary methods for investigating the kinetics have also been given.[2]

Kinetic systems involving distributions of processes could be set up in all the states of matter, but usually would not be studied in the cases of gases and liquids because the environment could generally be made uniform by stirring and because the individual types of processes could generally be distinguished by chemical analysis. In the case of solids, the atomic environment is apt to be quite variable because of crystalline defects and the normal anisotropy of the solid, and the physical measurements employed can rarely distinguish unique processes, hence the kinetics naturally is that of quasi-continuous distributions. Magnusson, Palmer, and Koehler[3] have recently pointed out that in these circumstances the concentration of like processes occurring at any instant of time is so low compared to kinetically distinguishable ones with which interaction could occur that the order of reaction observed even when processes interact would still be unity. The true original distribution then cannot be determined by a kinetic investigation of any ordinary kind and may involve further complications which can affect the kinetics. The case of successive reactions has been mentioned elsewhere.[2] However, such detailed considerations are hardly justifiable as yet in most cases, because the nature of the processes which are involved are not understood. In the cases of gases and liquids the processes which are observed are almost invariably those of reaction, but in the case of solids freeing an entity from a site at which it is located (trapped) may involve a higher potential barrier than approaching the site at which reaction occurs. This would lead to first-order reactions. Thus it would seem, in summary, that first-order reactions should be the most important. The theory will be developed here for first-order reactions, but it can be easily extended to all orders of reaction. However, if the order is not unity, it is necessary to be cautious about the limits of integration which are employed.

Other applications of the theory would be to the analysis of the decay data of a complex mixture of radioactive species not subjected to energy analysis, and to the expansion of a function in terms of exponential functions or in terms of the related functions which arise in the theory of other orders of reaction.

ISOTHERMAL ANNEALING

The differential equation obeyed at constant temperature by a suitable property p whose value is proportional to the number of processes which can yet occur is

$$-dp/dt=Ae^{-\epsilon/\tau}p,$$

* Based on work performed under the auspices of the U. S. Atomic Energy Commission.
[1] V. Vand, Proc. Phys. Soc. (London) **A55**, 222 (1943).
[2] W. Primak, Phys. Rev. **100**, 1677 (1955).
[3] G. D. Magnusson, W. Palmer, and J. S. Koehler, Phys. Rev. **109**, 1990 (1958).

where t is the time, A is a constant with the units reciprocal time called the frequency factor, ϵ is the activation energy, and τ is the product of Boltzmann's constant and temperature with the same units as ϵ. In the following, electron volts/atom will be used as the unit of activation energy, and seconds as the unit of time. The solution for the differential equation is

$$p = p_0 \exp(-e^{-\epsilon/\tau}) \equiv p_0\Theta, \tag{1}$$

where p_0 is the value of p at $t=0$. This equation also holds when the processes are distributed in activation energy, but now p and p_0 are distribution function of ϵ and possess the units (units of property)/ev and cannot be measured directly; only P the total value of the property can be measured and is

$$P(t) = \int_0^\infty p_0(\epsilon)\Theta(\epsilon,t)d\epsilon. \tag{2}$$

The function Θ is for most of its range of ϵ nearly zero (at small values of ϵ) or nearly one (at large values of ϵ) and varies from zero to one over only a small range of ϵ, several times τ. As time proceeds it remains unaltered in shape and is translated along ϵ at a rate proportional to $\ln t$ and may be thought of as sweeping out the original distribution. There are two derivatives of Θ which are of interest, $\dot{\Theta} = d\Theta/dt$ and $\Theta' = d\Theta/d\epsilon$, and are related as $\Theta' = -(t/\tau)\dot{\Theta}$. For the simple case treated here, the point of inflection of Θ and the maxima in Θ' and $\dot{\Theta}$ all occur at the point $\epsilon_0 = \tau \ln At$. If $p_0(\epsilon)$ is broad compared to several times τ, then ϵ_0 is (at least) very nearly the value of ϵ for which $dP/dt \equiv \dot{P}$ is a maximum. For this case Vand showed that an approximate set of values for the function $p_0(\epsilon)$ could be obtained from the kinetic data. He replaced Θ with a Heaviside function having its step located at ϵ_0. Then

$$-P \cong \int_{\epsilon_0}^\infty p_0(\epsilon)d\epsilon,$$

and on differentiating the definite integral with respect to t there is obtained,

$$p_0(\epsilon_0) \cong -(t/\tau)\dot{P}. \tag{3}$$

The following alternative derivation is now proposed. Equation (2) is differentiated with respect to t, whence

$$\dot{P}(t) = -\int_0^\infty p_0(\epsilon)\dot{\Theta}(\epsilon,t)d\epsilon, \tag{4}$$

and

$$\dot{P}(t) = -\frac{\tau}{t}\int_0^\infty p_0(\epsilon)\Theta'(\epsilon,t)d\epsilon. \tag{5}$$

The processes undergoing active annealing at any time are

$$\dot{p} = p_0\dot{\Theta}$$

which is proportional to the integrand of Eq. (5). The function Θ' has an appreciable value over only a small range of ϵ, several times τ; and if the original distribution is much broader, $p_0(\epsilon)$ may, for the zeroth approximation p_{00}, be considered sensibly constant and taken out of the integral. The average activation energy $\bar{\epsilon}$ at which annealing is occurring is

$$\bar{\epsilon} = \int_0^\infty p_0\dot{\Theta}\epsilon d\epsilon \Big/ \int_0^\infty p_0\dot{\Theta}d\epsilon;$$

for this approximation (when $At \gg 1$),

$$\cong \int_0^\infty \dot{\Theta}\epsilon d\epsilon \Big/ \int_0^\infty \dot{\Theta}d\epsilon$$

$$= \int_0^\infty \Theta'\epsilon d\epsilon \Big/ \int_0^\infty \Theta' d\epsilon$$

$$= \epsilon_0 + \tau\gamma,$$

where $\gamma = 0.577\cdots$, Euler's constant. Thus it is seen that

$$\dot{P} \cong -\frac{\tau}{t}p_{00}(\bar{\epsilon})\int_0^\infty \Theta' d\epsilon$$

$$p_{00}(\bar{\epsilon}) \cong -(t/\tau)\dot{P}, \tag{6}$$

since the integral is unity.

The result, Eq. (6), is nearly identical with Vand's result except for the minor correction that the distribution has been evaluated not at ϵ_0 but more properly at $\bar{\epsilon}$ which occurs at a value slightly greater than ϵ_0. This is a trivial point since it may be inferred intuitively that the step in the Heaviside function should have been located by Vand not at the value of ϵ at which the maximum rate of annealing of processes occurs, but rather at the average activation energy for annealing. This derivation does show in a very simple way that the essential physical assumption of the result obtained by Vand is that the distribution is constant over the range of activation energies at which active annealing is occurring, but this too is trivial because it is readily proven in other ways that Vand's result is an exact one only in the case that $p_0(\epsilon)$ is constant over the region of activation energies undergoing active annealing. The major advantage of the present derivation is that with it, it is no longer necessary to assume that the distribution is constant. Two applications are given: the first leads to a method for determining the distribution to a slightly better degree of approximation; the second, to a treatment of step annealing.

If, instead of assuming p_0 constant over the range of activation energies at which appreciable annealing is occurring, it is assumed that p_0 has a slope b, then

$$p_0 = a + b\epsilon \tag{7}$$

and

$$\dot{P}=-\int_0^{\infty}(a+b\epsilon)\dot{\Theta}d\epsilon.$$

Since At at the earliest possible measurement is so large (an infinite limit for all practical purposes), the substitution $z=At\epsilon^{-\epsilon/\tau}$ and integration of the elementary terms leads to

$$\dot{P}=-\frac{\tau}{t}(a+b\tau\ln At)+\frac{b\tau^2}{t}\int_0^{\infty}\epsilon^{-z}\ln z dz$$

$$=-(\tau/t)(a+b\epsilon_0+b\tau\gamma).$$

Now from Eq. (7) $p_0(\epsilon_0)=a+b\epsilon_0$. Therefore, the equation

$$-\dot{P}t/\tau=p_0(\epsilon_0)+b\tau\gamma,$$

leads to the result

$$p_0(\epsilon_0)=p_{00}(\bar{\epsilon})-b\tau\gamma. \tag{8}$$

For an arbitrary distribution, $p_0(\epsilon_0)$ may be thought of as a first-order approximation, and its value at ϵ_0 is, therefore, our zeroth order approximation at $\bar{\epsilon}$ less $b\tau\gamma$.

A practical method of applying Eq. (8) is to plot $p_{00}(\bar{\epsilon})$ and determine an approximate b by measuring its slope. This approximate value of b is substituted in Eq. (8) to obtain a new approximate distribution function. Its slope is measured, and the process is repeated until the slopes no longer alter on successive iteration. Thus,

$$p_{00}(\bar{\epsilon})=-(t/\tau)\dot{P}$$

has the slope $dp_{00}(\bar{\epsilon})/d\bar{\epsilon}$. Hence,

$$p_{01}(\epsilon_0)=p_{00}(\bar{\epsilon})-\tau\gamma dp_{00}(\bar{\epsilon})/d\bar{\epsilon}$$

has the slope

$$\frac{dp_{01}(\epsilon_0)}{d\epsilon_0}=\frac{dp_{00}(\bar{\epsilon})}{d\bar{\epsilon}}\frac{d\bar{\epsilon}}{d\epsilon_0}-\tau\gamma\frac{d^2p_{00}(\bar{\epsilon})}{d\bar{\epsilon}^2}\frac{d\bar{\epsilon}}{d\epsilon_0}.$$

[This slope can be evaluated from $\bar{\epsilon}=(1+\alpha)\epsilon_0=(1+\alpha)\tau\ln At$, where α is a small number to be evaluated separately.] Therefore,

$$p_{02}(\epsilon_0)=p_{00}(\bar{\epsilon})-\tau\gamma\frac{d\bar{\epsilon}}{d\epsilon_0}\left[\frac{dp_{00}(\bar{\epsilon})}{d\bar{\epsilon}}-\tau\gamma\frac{d^2p_{00}(\bar{\epsilon})}{d\bar{\epsilon}^2}\right],\quad\text{etc.}$$

It is immediately seen that if the graph of P plotted against $\ln t\equiv\xi$ is a straight line, no iterations are possible in accordance with Vand's formula being an exact result for this case. If P is expanded further as a polynomial in ξ, then, to second-order terms

$$P=a_0-a_1\xi-a_2\xi^2. \tag{9}$$

The number of iterations possible are 2 when $\bar{\epsilon}$ and ϵ_0 are distinguished. Thus the following result is obtained:

$$p_{02}(\epsilon_0)=[(a_1+2a_2\xi)-2a^2\gamma]/\tau. \tag{10}$$

This is an exact result. For further iteration it would be necessary to take into account higher-order terms in the expansion of p_0. This can easily be done in terms of the Laplace transforms of the powers of the logarithm. It must be appreciated that although Eq. (10) derives the original distribution p_0 from the kinetic data which involves t, p_0 is not a function of t or ξ, but of ϵ only. It is the image function of the Laplace transform of which the time derivative of Eq. (9) is the original function. The method evaluates the image function at ϵ_0, a discrete value of ϵ in terms of the parameter t (or ξ). The Laplace transform of the original distribution,[4] Eq. (4), can be written

$$\dot{P}=-\tau\int_0^{\infty}p_0(\epsilon)\epsilon^{-tz}dz, \tag{11}$$

where $z=A\epsilon^{-\epsilon/\tau}$ since A (the exact upper limit) is a very large number. In extended annealing, the kinetic data plotted against ξ is always nearly a straight line. Consequently, the interest here is in small deviations from this behavior, and accordingly, in a polynomial expansion in ξ,

$$P=a_0-a_1\xi-a_2\xi^2-a_3\xi^3-\cdots \tag{12}$$

and

$$\dot{P}=-\frac{1}{t}(a_1+2a_2\xi+3a_3\xi^2+\cdots). \tag{13}$$

From the derivatives of the Γ function[5]

$$\left[\frac{d^n\Gamma(x)}{dx^n}\right]_{x=1}=t\int_0^{\infty}\epsilon^{-tz}(\ln t+\ln z)^n dz,$$

the following expressions are obtained for

$$\int_0^{\infty}\epsilon^{-tz}\ln^n z dz:$$

$$n=1\quad-(1/t)(\gamma+\ln t)$$

$$n=2\quad+(1/t)[(\gamma+\ln t)^2+\tfrac{1}{6}\pi^2]$$

$$n=3\quad-(1/t)[(\gamma+\ln t)^3+\tfrac{1}{2}\pi^2(\gamma+\ln t)+2\zeta(3)],$$

etc. from which it is readily shown that the Laplace transform of

$$p_0=-b_0+b_1(\gamma+\ln z)-b_2(\ln^2 z+2\gamma\ln z+\gamma^2-\tfrac{1}{6}\pi^2)+b_3[\ln^3 z+3\gamma\ln^2 z+(3\gamma^2-\tfrac{1}{2}\pi^2)\ln z+\gamma^3-\tfrac{1}{2}\pi^2\gamma+2\zeta(3)]+\cdots \tag{14}$$

is

$$\dot{P}=-(\tau/t)(b_0+b_1\ln t+b_2\ln^2 t+\cdots). \tag{15}$$

Now $\ln z=-(\epsilon/\tau)+\ln A$, and if the image function is evaluated at the discrete points ϵ_0, then $\ln z_0=-\xi$, and

[4] I am indebted to O. C. Simpson for suggesting the use of the Laplace transform at this point.

[5] J. LeCaine, National Research Council of Canada Rept. NRC No. 1553.

the original distribution corresponding to Eq. (13) can be obtained by substituting $-\xi$, an experimental quantity, for $\ln s$ in Eq. (14) and comparing the terms of Eq. (15) with Eq. (13).

STEP ANNEALING

The ordinary isothermal-annealing data obtained by heating a specimen which has not yet undergone annealing at any temperature approaching the one at which the data are being obtained usually show only small deviations from linearity when plotted as a function of $\ln t$ for the cases of extended annealing. This is no longer the case when a series of isothermal annealings are conducted at successively increased temperatures ($\Delta\tau\sim 0.1\tau$). What is studied under these conditions is no longer the original distribution, but the original distribution as modified by the previous annealing; and this new distribution is a very steep one, the slope being of the order of magnitude of $p/\tau e$ where e is the base of Naperian logarithms. This new distribution is much too steep to be considered constant or expandable into a polynomial in ϵ over the range of ϵ in which Θ has an appreciable value. The theory of this case is so different from ordinary isothermal annealing that it is given a special name—step-annealing.

After an annealing at τ_1 for a time t_1, the original distribution has been modified to

$$p_1(\epsilon)=p_0(\epsilon)\Theta(t_1,\tau_1)\equiv p_0\Theta_1.$$

After the nth annealing, it is

$$p_n=p_0\prod_{i=1}^{n}\Theta_i.$$

During the nth annealing, the observed rate of property change is

$$\dot{P}=\int_0^\infty p_0\left[\prod_{i=1}^{n-1}\Theta_i\right]\dot{\Theta}_n d\epsilon. \tag{16}$$

While it is not permissible to consider the actual distribution

$$p_0\prod_{i=1}^{n-1}\Theta_i$$

as constant over the range of ϵ for which $\dot{\Theta}_n$ is appreciable, it is equally as permissible as before to consider p_0 to be constant; then

$$\dot{P}\cong p_{00}(\bar{\epsilon})\frac{\tau}{t}\int_0^\infty\left[\prod_{i=1}^{n-1}\Theta_i\right]\Theta_n' d\epsilon=-\frac{\tau}{t}p_0 I,$$

and

$$p_{00}(\bar{\epsilon})\cong-(t/\tau)(\dot{P}/I), \tag{17}$$

the integral I being less than unity. If $n=2$, an approximation for I expressed in gamma functions can be derived for $t=0$. For other values of t it seems best to evaluate I numerically or graphically.

Although isothermal annealings have been conducted over decades of time δt much longer, it is customary in systematic work to cover about three decades. The segment of the original distribution which can be investigated is then[6] $\tau\ln\Delta t$ which is but a small portion of the several electron-volt-wide distributions which are associated with extended annealing. To obtain more of the original distribution it is necessary to conduct other isothermal annealings at other temperatures. As long as annealing is conducted at a single temperature, the value of A is undetermined. But if annealings have been conducted at several temperatures, two segments of the distribution calculated from these data will be translated from each other $\Delta\tau\ln\lambda$ along ϵ, where $\Delta\tau=\tau_2-\tau_1$ is the difference in τ for the two annealings, and λ is the factor by which the assumed value of A differs from its correct one. The sensitivity of this method of determining the correct value of A depends on the slope of the distribution. If the vertical displacement which can be detected for the segments is μp_0, and the slope of the distribution function is σ, the translation along ϵ is $\mu/\sigma=\Delta\tau\ln\lambda$. In a favorable circumstance, when the distribution is broad enough to be determined by the methods given here and reasonably steep, rising to its maximum height over about a 1-ev range, A is thus determined to about an order of magnitude. For less steep distributions the precision of the determination is proportionately less.

The method of step annealing permits another determination of A based upon similar requirements. The distributions investigated after the successive step annealings are very steep. A small translation along ϵ therefore causes a large change in the value calculated for the (very) approximate result for the modified distribution p_{n-1} obtained from Vand's formula, and hence in the value of the factor I^{-1} which gives p_0. If a value of A is chosen too large, the segments will start at high values and fall toward the correct values of p_0 after the annealing has been conducted for a long enough time for ϵ_0 to have been displaced several times τ. If too small a value is chosen for A, the segments will start at a low value and then rise toward p_0. The slope of p_{n-1} is about $p_0/\tau_{n-1}e$. If a vertical displacement μp_0 can be detected, the translation along ϵ is $\mu\tau_{n-1}e=\Delta\tau\ln\lambda$. In typical step annealings, τ is increased by the order of magnitude 0.1τ; hence, if μ is about 0.02, λ is about $1\frac{1}{2}$. Thus A is determined by this method to 50%, a very precise determination since *a priori* A is not known to orders of magnitude. The method is equally valid for other orders of reaction, and the value of A obtained will be nearly the same. The precision $(\lambda-1)$ is reduced in proportion to the

[6] At 800°C, τ is about 0.1; at liquid-nitrogen temperatures, it is 0.01.

order, and there is a slight difference obtained for the value of A because $\bar{\epsilon}$ is somewhat different for other orders of reaction. However A is still determined to better than an order of magnitude, and within this precision the value obtained is the same when any reasonable order of reaction is assumed for the data. Thus, in the same manner that Vand's method gives the correct approximate original distribution,[2] this method gives the correct approximate value for A no matter what the order of reaction is.

TEMPERING

In cases where (a) the property can be measured while the substance is being heated, (b) the thermal coefficient of the property can be handled, and (c) the temperature of the specimen can be increased at a constant rate, the method of tempering is a very rapid method of investigating the distribution. The mathematical difficulties are increased, however, because τ is now a function of t

$$t=c\tau,$$

where c is a constant. Then

$$p(\epsilon,\tau)=p_0(\epsilon)\exp[-Ac\tau E_2(y)]. \tag{18}$$

Here $y=\epsilon/\tau$ and E_n as defined by Placzek[7] is

$$E_n(x)=x^{n-1}\int_x^\infty u^{-n}e^{-u}du. \tag{19}$$

Note that

$$dE_n(x)/dx=-E_{n-1}(x). \tag{20}$$

For the values of x of interest here, the functions are easily manipulated by the approximations

$$E_n(x)\cong(x+n)^{-1}e^{-x}, \tag{21}$$

and

$$\left.\begin{aligned}(x+n_a)(x+n_b)&\cong(x+n_c)(x+n_d),\\ \text{where}\qquad n_a+n_b&=n_c+n_d.\end{aligned}\right\} \tag{22}$$

The result Eq. (21) is from Blanch. The measured value of the property when the thermal coefficient has been taken into account is

$$P(\tau)=\int_0^\infty p_0(\epsilon)\exp[-Ac\tau E_2(y)]d\epsilon \equiv\int p_0(\epsilon)\phi(\epsilon,\tau)d\epsilon, \tag{23}$$

and

$$\frac{d[P(\tau)]}{d\tau}=-\int_0^\infty p_0(\epsilon)\exp[-Ac\tau E_2(y)]\times\left[Ac\tau E_2(y)+Ac\tau\frac{\epsilon}{\tau^2}yE_1(y)\right]d\epsilon. \tag{24}$$

[7] G. Placzek, National Research Council of Canada Rept. NRC-1547 (1946), (available from the National Research Council of Canada).

The tempering functions ϕ and $d\phi/d\tau$ are similar in form to the isothermal annealing functions Θ and $d\Theta/dt$ except that these functions alter in shape as the annealing progresses. The last equation shows that the processes occurring simultaneously involve only a very small range of activation energies. The maximum rate of annealing occurs at the maximum of $d\phi/d\tau$ and is located at the point of inflection of ϕ at $\epsilon_0=\tau y_0$ and

$$y_0+\ln(y_0+2)=\ln Ac\tau\cong a+by_0, \tag{25}$$

where

$$\left.\begin{aligned}b&=(y+3)/(y+2)\\ \text{and}\qquad a&=[\ln(y+2)]-y/(y+2)\end{aligned}\right\}. \tag{26}$$

The approximation is a very good one because a very small range of y is involved. However it must be remembered that a and b vary mildly with τ, and when differentiating with respect to τ, the exact form should be used. The substitution $z=Ac\tau E_2(y)$ is made in Eq. (24), and Eq. (22) is used to reduce the polynomial in y to give the result

$$\frac{dP}{d\tau}=-\int_0^\infty p_0(\epsilon)\cdot(1+y)e^{-z}dz,$$

since terms in $1/y$ are to be neglected in the approximation of Eq. (22). As before, p_0 is assumed constant over the range of ϵ in which processes are annealing actively. Then

$$\frac{dP}{d\tau}\cong-p_0(\bar{\epsilon})\int_0^\infty[1+(1/b)(\ln Ac\tau-a-\ln z)]e^{-z}dz$$
$$=-p_0(\bar{\epsilon})[1+(1/b)(\ln Ac\tau-a+\gamma)] \tag{27}$$
$$p_0(\bar{\epsilon})=-\frac{dP}{d\tau}\frac{1}{1+(\epsilon_0/\tau)+\gamma}.$$

The value of $\bar{\epsilon}$ can be obtained by similar techniques:

$$\bar{\epsilon}=\int_0^\infty(d\phi/d\tau)\epsilon d\epsilon\Big/\int_0^\infty(d\phi/d\tau)d\epsilon,$$

and it is found that

$$\bar{y}=\bar{\epsilon}/\tau$$
$$=\frac{y_0^2+y_0+(2\gamma/b)y_0-1+(\gamma/b)+(\gamma/b)^2+(\pi^2/6b^2)}{y_0+(\gamma/b)+1} \tag{28}$$
$$\equiv y_0+\alpha,$$

where α is just a few percent more than γ. Thus

$$\bar{\epsilon}\cong\epsilon_0+\tau\gamma \quad\text{and}\quad p_0(\bar{\epsilon})\cong-(dP/d\tau)[1/1+(\bar{\epsilon}/\tau)]. \tag{29}$$

Vand's original derivation was based on a Heaviside function approximation with the step located at ϵ_0. His solution was given in parametric equations, and

its relation to the preceding result is difficult to see. An explicit solution by his method is the following:

$$P=\int_0^\infty p_0\phi d\epsilon \cong \int_{\epsilon_0}^\infty p_0 d\epsilon,$$

$$dP/d\tau = -p_0 d\epsilon_0/d\tau.$$

Implicit differentiation of Eq. (25) is used to obtain $d\epsilon_0/d\tau$ and since this is reduced by Eq. (22), terms in τ/ϵ_0 are neglected. Then $p_0=-(dP/d\tau)[1/1+(\epsilon_0/\tau)]$. Since ϵ_0/τ is apt to be between 20 and 40, the difference between this result and Eq. (29) is less than a few percent, and the error introduced by the approximation Eq. (22) is of the same order of magnitude. For a more precise result it is best to return to Eq. (24), take out p_0, and then integrate numerically. It is not necessary to assume p_0 constant; it may be assumed to have a slope, and the method used for isothermal annealing can be applied here. In a similar way, isothermally annealed specimens can be analyzed by tempering to obtain a value for A.

DISTRIBUTIONS IN FREQUENCY FACTOR

The distribution remaining when first-order independent processes are undergoing isothermal annealing is in this case:

$$p(t)=p_0(A)\exp(-At e^{-\epsilon/\tau}) \equiv p_0(A)\Psi(A,t).$$

The function Ψ is formally similar to Θ except that A is the variable in Ψ while ϵ is the variable in Θ. The property observed is

$$P(t)=\int_{A_1}^{A_2} p_0(A)\Psi(A,t)dA.$$

From the behavior of the function Ψ it is obvious that A_2/A_1 is at least several orders of magnitude for extended annealing. The distribution $p_0(A)$ is swept out by $\Psi(A,t)$ receding in time in a manner similar to the one in which $p_0(\epsilon)$ is swept out by advancing $\Theta(\epsilon,t)$. The recession of Ψ may be marked by $A_0 t=e^{\epsilon/\tau}$ for $A_0<A_2$ and hence the order of magnitude of $P(t)$ is

$$P(t)\sim p_0(A)\cdot(A_0-A_1).$$

At the beginning of the annealing $A_0=A_2$, and for much of the annealing $A_0 \gg A_1$, hence $P(t)=A_0 p_0(A)$. Most properties used to measure the annealing would be considered insignificant when their value had declined by 2 orders of magnitude, and hence long before A_1 were approached, the experiment would be concluded. Thus distributions of the class considered, without steep variations in A, would be considered to be described by a frequency factor in the upper part of the distribution and would not show extended annealing behavior.

Extended annealing is shown by other kinds of frequency factor distributions, and the one which leads to the simplest behavior is one which does not show steep variations in intervals of $\ln A$. Let $\ln A=\zeta$; then

$$p=p_0\exp[-te^{\zeta-(\epsilon/\tau)}]=p_0(A)\Psi(\zeta,t). \qquad (30)$$

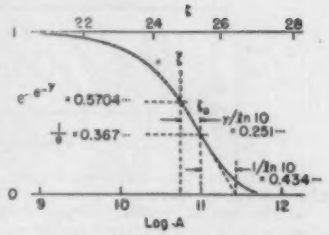

FIG. 1. A graph of the function $\Psi=\exp(-Ate^{-\epsilon/\tau})$ plotted against the variable A when the fixed quantities $e^{-\epsilon/\tau}$ and t are 10^{-11} and 10^9, respectively. The tangent at the point of inflection is also shown.

The function $\Psi(\zeta,t)$ is plotted in Fig. 1 as a function of $\log A$ for $te^{-\epsilon/\tau}=10^{-11}$. It is seen that Ψ varies from unity to zero. It possesses a point of inflection at a value of ζ

$$\zeta_0=(\epsilon/\tau)-\ln t \qquad (31)$$

where Ψ has the value $1/e \cong 0.368$. This is where the maximum values of both $d\Psi/dt \equiv \dot{\Psi}$ and $d\Psi/d\zeta \equiv \Psi'$ occur, hence the value of ζ at which processes are annealing most rapidly. The slope of Ψ at ζ_0 is $-1/e$, hence when plotted against $\log A$ it is $-2.303/e$. The average value of ζ is

$$\bar{\zeta}=\int_{-\infty}^{+\infty}\Psi'\zeta d\zeta \Big/ \int_{-\infty}^{+\infty}\Psi' d\zeta = \zeta_0-\gamma, \qquad (32)$$

where γ is Euler's constant $0.577\cdots$. At $\bar{\zeta}$ the value of Ψ is $\exp(-e^{-\gamma}) \cong 0.5704\cdots$. In Fig. 1 where $\log A$ is the variable, the difference between the point of inflection and the average value of $\log A$ is about 0.434γ or 0.251. As time proceeds, the function moves unchanged in shape from higher values of the frequency factor to lower ones according to Eq. (31). Except for this difference in sign (hence direction of proceeding) it is similar to the behavior of a Θ for an extremely high temperature; i.e., when τ is unity. Thus it may be considered that during the annealing, the original distribution $p_0(\zeta)$ is swept from larger values of ζ to smaller ones as Ψ proceeds in this manner. The processes which are simultaneously undergoing rapid annealing range over a decade of frequency factors. Hence, a solution for $p_0(\zeta)$ by the methods given above requires that $p_0(\zeta)$ should not be steep over many decades of A. For such a case

$$-\dot{P}=\int_{-\infty}^{+\infty} p_0\Psi d\zeta = \frac{1}{t}\int_{-\infty}^{+\infty} p_0\Psi' d\zeta$$

$$\cong \frac{1}{t}p_0(\bar{\zeta})\int_{-\infty}^{+\infty}\Psi' d\zeta,$$

and

$$p_0(\bar{\zeta})=-t\dot{P}. \qquad (33)$$

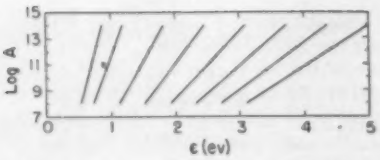

FIG. 2. Intersections (from left to right) of the planes $\epsilon_0=\tau\ln At$ with the $\log A$-ϵ coordinate plane for the respective values of τ: 0.0236, 0.0322, 0.04945, 0.0666, 0.0839, 0.1011, 0.01358 ev (corresponding approximately to the temperatures 0, 100, 200, 300, 500, 700, 900, 1100, and 1300°C) and for the time 100 sec.

The problem of determining ϵ is now similar to the problem of determining A when the distribution is one of activation energy. As long as annealing is performed at only one temperature, no decision on the assignment of ϵ can be made on the basis of the kinetic data alone. But if data at several temperatures are available, ϵ becomes fixed by the requirement of a continuity of the distribution provided that $p_0(\tilde{\zeta})$ has a sufficient slope.

The range of frequency factors which can be covered in annealings of reasonable duration is about three to four decades of A, the same number of decades as the annealing periods given in decades of time. Thus, two or three steps of step annealing would cover the reasonable range of frequency factors. Since many of the cases of disordered solids which have been investigated are only partially annealed in several steps of step annealing (τ increased the order of magnitude 10% per step), it must be concluded that the processes do possess a distribution in activation energy. They may yet be distributed in frequency factor, however.

TWOFOLD DISTRIBUTIONS IN ACTIVATION ENERGY AND FREQUENCY FACTOR

The equations considered previously may be used to describe a twofold distribution in which both A and ϵ are variable. Again ϵ_0 is a prominent parameter in describing the system, and is equal to $\tau\ln At$ as before, however, A is now variable also, and it proves more satisfactory to state the results in terms of ζ. Thus,

$$\epsilon_0(\zeta,t)=\tau\ln t+\tau\zeta. \tag{34}$$

In a manner similar to those in the foregoing, the isothermal annealing of independent first-order processes can be described by the modification of the original distribution $p_0(\zeta,\epsilon)$ by the exponential function $\Theta(\zeta,\epsilon,t)$. The behavior can be represented by the diagram of Fig. 2. The vertical axis is ζ, the horizontal axis is ϵ, and the distribution is plotted perpendicular to the paper. Then ϵ_0 is a plane whose intersection with the coordinate plane shown is a line of slope τ. The surface $\Theta(\zeta,\epsilon,t)$ varies from 0 to 1. Its intersections with the planes ζ constant are the familiar curves considered for the onefold distribution, and corresponding to the fact that altering ζ translates those curves along ϵ without changing their shapes, the surface $\Theta(\zeta,\epsilon,t)$ consists of parallel elements; i.e., it is an oblique-Θ cylinder,[8] obliqueness $\frac{1}{2}\pi-\tau$. Similarly, $\Theta'(\zeta,\epsilon,t)$ is an oblique-Θ' cylinder. The area of any section formed by intersection of the Θ' cylinder with planes ζ constant is unity, and thus the volume lying between the planes ζ_1 and ζ_2 is simply $\zeta_2-\zeta_1$. For a broad distribution which does not contain steep changes, we may neglect the shape of the distribution in computing the average value of the activation energy of the processes annealing simultaneously. The average activation energy is then

$$\bar{\epsilon}(\zeta,t)=\epsilon_0(\zeta,t)+\tau\gamma, \tag{35}$$

a plane parallel to $\epsilon_0(\zeta,t)$ separated from it by $\tau\gamma$ measured along ϵ. The observed value of the property is

$$P(t)=\int_{-\infty}^{+\infty}d\zeta\int_0^{\infty}p_0(\zeta,\epsilon)\Theta(\zeta,\epsilon,t)d\epsilon.$$

As for a onefold distribution in ϵ, the original distribution may here be thought of as being swept out by the function Θ being translated as t increases. When the procedure developed for the onefold distribution is applied here, there is obtained

$$-\dot{P}(t)=\int_{-\infty}^{+\infty}d\zeta\int_0^{\infty}p_0(\zeta,\epsilon)\dot{\Theta}(\zeta,\epsilon,t)d\epsilon$$

$$\cong\frac{\tau}{t}\int_{-\infty}^{+\infty}p_0(\zeta,\bar{\epsilon})d\zeta\int_0^{\infty}\Theta'(\zeta,\epsilon,t)d\epsilon.$$

The integral along ϵ is an ordinary integral, and is unity as shown. The integral along ζ is the area under the curve formed by projecting the intersection of the $p_0(\zeta,\epsilon)$ surface with the $\bar{\epsilon}$ plane upon an ϵ constant plane. Thus the information obtained from the isothermal annealing alone is

$$\int_{\zeta=-\infty}^{\zeta=+\infty}p_0(\zeta,\bar{\epsilon})d\zeta=-\frac{t}{\tau}\dot{P}(t), \tag{36}$$

and is the volume per unit activation energy (or specific volume) of the distribution function taken along the plane $\bar{\epsilon}$. At another temperature the slope of the intersection of $\bar{\epsilon}$ with the coordinate plane of ζ and ϵ is different, and hence a different section of the distribution is observed.

The analysis of the isothermal-annealing system is greatly simplified because the mathematical surfaces are cylindrical. For step annealing this simplification is lost because the multipliers $\Theta(\epsilon,\zeta,t_{i<n})$ truncate the cylindrical surface $\Theta'(\epsilon,\zeta,t_n)$ obliquely. In general, it is necessary to resort to a twofold numerical integration over ϵ and ζ to obtain a solution. However, at the beginning of a second step of annealing, an analytical solution can be given for particular cases. Consider

[8] Nomenclature in analogy with, e.g., *oblique elliptical cylinder*.

as an example, a uniform distribution in ζ extending over the range $\Delta\zeta=\zeta_2-\zeta_1$ corresponding to $\Delta A=A_2-A_1$. From isothermal annealing the twofold distribution p_0'' (from Eq. (36)) is

$$p_0''=-(t/\tau)\dot{P}(t)/\Delta\zeta.$$

This may be compared with the apparent onefold distribution p_0', $\Delta\zeta$ times greater, obtained by inserting the annealing rate into Eq. (3). If there had been a previous step of annealing, the annealing rate would have been

$$-\dot{P}(t_2)=\int_{A_1}^{A_2}p_0''\frac{dA}{A}\int_0^\infty\frac{\tau_2}{t_2}\exp[-At_1\exp(-\epsilon/\tau_1)-At_2\exp(-\epsilon/\tau_2)]At_2\exp(-\epsilon/\tau_2)\frac{d\epsilon}{\tau_2}. \quad (37)$$

At the beginning of the second annealing $t_2=0$. Let $\sigma=\tau_1/\tau_2$ and $z=\Delta t_1\exp(-\epsilon/\tau_1)$. Then, since At_1 is very large,

$$-\dot{P}(t_2=0)=\int_{A_1}^{A_2}\frac{\tau_1}{t_1}(At_1)^{1-\sigma}p_0''\frac{dA}{A}\int_0^\infty e^{-z}z^{\sigma-1}dz$$

$$=\int_{A_1}^{A_2}\frac{\tau_1}{t_1}(At_1)^{1-\sigma}p_0''\Gamma(\sigma)\frac{dA}{A}$$

$$=p_0''\frac{\tau_1}{t_1}\frac{\Gamma(\sigma)}{1-\sigma}t_1^{1-\sigma}(A_2^{1-\sigma}-A_1^{1-\sigma}).$$

If a onefold distribution had been assumed, the result

$$-\dot{P}(t)=\frac{\tau_1}{t_1}(A't_1)^{1-\sigma}\Gamma(\sigma)p_0'$$

would have been obtained and its solution for A' is

$$A'=(-t_1\dot{P}/\tau_1\Gamma(\sigma)t_1^{1-\sigma}p_0')^{1/(1-\sigma)}.$$

When the annealing rate given in terms of the twofold distribution constants is introduced, the result

$$A'=[(A_2^{1-\sigma}-A_1^{1-\sigma})/\Delta\zeta(1-\sigma)]^{1/(1-\sigma)}$$

is obtained for A', which gives nearly a mean value for ζ'. Thus if $\sigma=0.9$, $\log A_1=8$, and $\log A_2=13$, the value of $\log A'$ is about 10.6.

TABLE I. Rates of property change with a unit twofold distribution of indefinite extension in ϵ and extension in $\log A$ for $\dot{P}_1$:8–10, for $\dot{P}_2$:8–13; heated first at $\tau_1=0.0791$ for 18 000 sec, then at $\tau_2=0.0874$ for the time stated.

t_2 (sec)	$10^5\dot{P}_1$ Property/sec	$10^5\dot{P}_2$ Property/sec
[a]	2.024	5.059
0	39.41	142.54
60	37.37	131.40
180	33.86	113.74
600	25.41	77.55
1800	14.71	40.68
18 000	21.44	54.20

[a] At the end of the first heating.

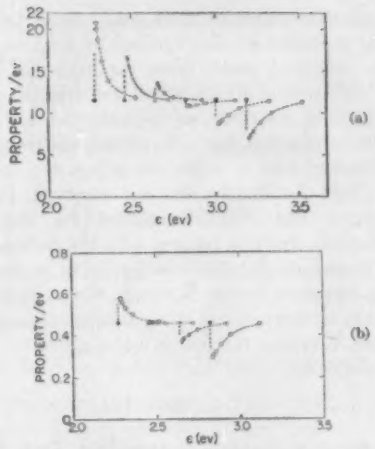

FIG. 3. Upper set of curves: The apparent onefold distribution obtained from Eq. (17) assuming $\log A$ to be the respective values 8, 9, 10, 11, 12, and 13 for a unit twofold distribution in activation energy and $\ln A$ (ζ) extending over the range 8–13 for $\log A$ and over an indefinite range of ϵ. The respective calculated points in each set are for 18 000 sec with $\tau=0.0791$, and then 0, 60, 180, 600, 1800, and 18 000 secs at $\tau=0.0874$. The lower set of curves: A distribution extending over the range 8–10 for $\log A$ and otherwise the same as before. The curves are given for the apparent onefold distributions obtained assuming values 8, 9, 10, an 11 for $\log A$.

For the uniform distribution in ζ, when particular values of τ are chosen, the calculation can be extended to further times by means of a onefold numerical integration, because the integration over A can be carried forward analytically. Thus for the twofold distribution Eq. (37) can be written

$$-\dot{P}(t_2)=\int_0^\infty p_0''\frac{\tau_2}{t_2}t_2\exp(\epsilon/\tau_2)\frac{d\epsilon}{\tau_2}\int_{A_1}^{A_2}\times\exp A[-t_1\exp(-\epsilon/\tau_1)-t_2\exp(-\epsilon/\tau_2)]dA$$

$$=\int_0^\infty p_0''\frac{\tau_2}{t_2}\frac{\beta_2}{\beta_1+\beta_2}\{\exp[-A_1(\beta_1+\beta_2)]-\exp[-A_2(\beta_1+\beta_2)]\}\frac{d\epsilon}{\tau_2},$$

where $\beta_1=t_1\exp(-\epsilon/\tau_1)$ and $\beta_2=t_2\exp(-\epsilon/\tau_2)$. The function within the brackets has an appreciable value over a small range of ϵ, and the numerical integration is thus quite feasible. The values of $-\dot{P}(t)$ for two particular cases are given in Table I. The integrals I required by Eq. (17) were calculated, by numerical integration, for integral values of $\log A$ from 8–13, and $p_0'(\epsilon)$ corresponding to them are plotted in Fig. 3. It is seen that throughout the whole range of times the system exhibits closely the behavior of a onefold distribution in ϵ having a mean value of ζ.

It may be expected that some small peculiarities such as inconsistent distributions or frequency factors will be obtained under some conditions of annealing when the twofold distributions are treated as if they were onefold distributions because the $\epsilon_0(\zeta,t)$ planes cut the distribution $p_0(\zeta,\epsilon)$ in slightly different sections. It was noted that in single annealings the existence of the twofold distribution was not observed. For double annealings, the results obtained for the twofold distributions could be treated with the techniques used for the onefold distributions by using a mean value for the frequency factor. However, the twofold distributions may be amenable to study through triple annealing methods. Consider the planes $\epsilon_0(\zeta,t)$ given by Eq. (34). Their slopes are

$$1/(\partial\epsilon_0/\partial\zeta)=1/\tau,$$

independent of the time of annealing. Thus the differences of the results obtained for the analysis of two specimens, the first of which had previously been subjected to annealing for one time t_1 at τ_1, and the second for another time t_2 at τ_1 are the results for a cylindrical region out from the distribution. The success of such an analysis depends upon a method like step annealing in which the elements of the Θ_n'-cylindrical surface are at an angle to the elements of the Θ_{n-1}-cylindrical surface of the previous step of annealing. When the thermal coefficient of the property which is used in the investigation can be handled, the method of linear tempering should be a more effective method of determining the twofold distribution. The maximum rate of linear tempering occurs at ϵ_{0T} given by

$$(\epsilon_{0T}/\tau)+\ln[(\epsilon_{0T}/\tau)+2]=\ln Ac\tau=\zeta+\ln c\tau, \quad (38)$$

where c is the inverse of the heating rate (sec/deg). The surface ϵ_0 in ζ,ϵ,Θ coordinates is very nearly a plane, and its intersection on the $\zeta-\epsilon$ coordinate plane

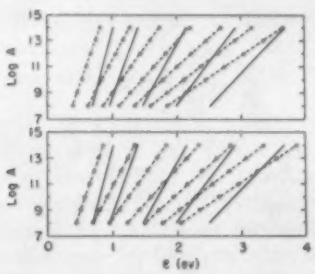

FIG. 4. The lines are intersections of the $\epsilon_0=\tau\ln At$ planes with the $\log A$-ϵ coordinate plane for the first five values of τ used in Fig. 2 when the time is 10^3 sec. The points on the upper curves are at integral values of $\log A$ between 8 and 14 of the intersections of the $\log A$-ϵ coordinate plane and the surfaces which contain the points of inflection ϵ_{0T} of the tempering function φ obtained with a heating rate 1 deg/sec for the last 7 values of τ used in Fig. 2. The points on the lower curves are for a tempering function obtained with a heating rate 1/5 deg/sec, and otherwise the same.

has the slope

$$1/(d\epsilon_{0T}/d\zeta)=(\epsilon_0+3\tau)/\tau(\epsilon_0+2\tau).$$

It is a function of τ, and hence also of t; since it is a function of ϵ_0, it is also a function of c. Since the relations are not readily visualized, the functions are plotted in Fig. 4 for two reasonable values of c. It is seen that the surfaces of constant ϵ_{0T} are at a considerable angle to the planes of constant ϵ_0.

The analysis of these systems would properly require a double numerical integration. It would be desirable in a particular case to have some indication that such an analysis was in order. An approximation can be derived by a method analogous to Vand's. The first case considered is one in which two specimens annealed for times t_1 and t_2 at τ_1 were each subjected to annealing at τ_2. Then the differences in the values of the property at the particular times t are

$$\delta P=\int_{-\infty}^{+\infty}d\zeta\int_0^{\infty}p_0(\epsilon,\zeta)\Xi \times\exp[-At\exp(-\epsilon/\tau_2)]d\epsilon, \quad (39)$$

where

$$\Xi\equiv\exp[-At_1\exp(-\epsilon/\tau_1)]-\exp[-At_2\exp(-\epsilon/\tau_1)]$$

and $\zeta=\ln A$ as before. The function Ξ is cylindrical with a maximum at

$$\epsilon_m=\tau_1\ln[A(t_2-t_1)/\ln(t_2/t_1)].$$

It has an appreciable value over only a very small range of ϵ in which $p_0(\epsilon,\zeta)$ can be considered constant for a particular value of ζ. The amount of property associated with unit length of this cylinder along ζ is just

$$\int_0^{\infty}p_0(\epsilon,\zeta)\Xi d\epsilon\cong p_0(\epsilon,\zeta)\tau_1\ln(t_2/t_1).$$

This may be plotted in the plane of the maximum in Ξ, or alternatively, in the plane ϵ_Δ midway between

$$\epsilon_{01}=\tau_1\ln At_1 \quad\text{and}\quad \epsilon_{02}=\tau_1\ln At_2,$$

since the true mean $\bar{\epsilon}$ is difficult to calculate. This midplane will be designated $\epsilon_0=\tau_1\ln At_f$. Thus the double integral Eq. (39) is reduced to the integral

$$\delta P=\int_{-\infty}^{+\infty}p_0(\epsilon_0,\zeta)\tau_1[\ln(t_2/t_1)] \times\exp[-At\exp(-\epsilon_0/\tau_2)]d\zeta. \quad (40)$$

It is not necessary to introduce a projection factor because the projection was accounted for when the previous integration was performed, not normal to the plane ϵ_0, but rather, normal to ζ. However, it is necessary that all values of A which are used be those in the plane. Then Vand's Heaviside function approxi-

mation becomes

$$\delta P \cong \int_0^{\bar{\xi}} p_0(\epsilon_0,\xi)\tau_1[\ln(t_2/t_1)]d\xi,$$

and following his procedure, it may be differentiated with respect to t,

$$\delta\dot{P} = p_0(\epsilon_0,\bar{\xi})\tau_1[\ln(t_2/t_1)]d\bar{\xi}/dt. \tag{41}$$

The quantity $\bar{\xi}$ given by Eq. (32) is equal to $\ln\bar{A}$. Hence,

$$\bar{A} = t^{-1}\exp(\epsilon/\tau_2)e^{-\gamma} = A_0 e^{-\gamma} \cong 0.5615A_0,$$

where γ is the Euler constant, and A_0 is obtained from $\epsilon = \tau_2 \ln A_0 t$. Then, when these values are inserted into Eq. (41), the result is

$$\delta\dot{P} = p_0(\epsilon_0,\bar{\xi})\tau_1[\ln(t_2/t_1)](0.5615/A_0)dA_0/dt.$$

The point A_0 is on the plane ϵ_0. Thus

$$\tau_2 \ln A_0 t = \tau_1 \ln A_0 t_f$$

and

$$\tau_2(1/A_0)dA_0/dt + (\tau_2/t) = (\tau_1/A_0)dA_0/dt.$$

Accordingly, the equation

$$(1/A_0)dA_0/dt = -[\tau_2/(\tau_2-\tau_1)](1/t),$$

leads to the result

$$p_0(\epsilon_0,\bar{\xi}) = -\frac{t}{\tau_2}\delta\dot{P}\frac{(\tau_2/\tau_1)-1}{\ln(t_2/t_1)}. \tag{42}$$

The choice of the plane ϵ_0 does not affect the result provided it is a parallel plane. However, it does affect the location at which the result is plotted.

The same procedure may be used if tempering is used to analyze the distribution. Then Eq. (40) becomes

$$\delta P = \int_{-\infty}^{+\infty} p_0(\epsilon_0,\xi)\tau_1[\ln(t_2/t_1)]\exp[-Ac\tau_2 E_2(\epsilon/\tau)]d\xi$$

and Vand's Heaviside function approximation becomes

$$\delta P = \int_0^{\bar{\xi}} p_0(\epsilon_0,\bar{\xi})\tau_1[\ln(t_2/t_1)]d\xi.$$

For this case $\bar{\xi}$ is (as for the preceding case) $\xi_0-\gamma$, and ξ_0 is the value of ξ given by Eq. (38). Differentiation performed with respect to τ_2, gives,

$$d(\delta P)/d\tau_2 = p_0(\epsilon_0,\bar{\xi})\tau_1[\ln(t_2/t_1)]d\bar{\xi}/d\tau_2.$$

It is now necessary to evaluate the derivative $d\bar{\xi}/d\tau_2$ on the ϵ_0 plane. This is done by differentiating Eq. (38) implicitly with respect to τ_2, remembering that ϵ_0 depends on $\bar{\xi}$ through

$$\epsilon_0 = \tau_1 \ln t_f + \tau_1\xi. \tag{43}$$

With the approximation Eq. (22), the result can be cast into the form

$$p_0(\epsilon_0,\bar{\xi}) = -\frac{d(\delta P)}{d\tau_2}\frac{\tau_2[(\epsilon_0/\tau_2)-1]-\tau_1}{\tau_1[\ln(t_2/t_1)][(\epsilon_0/\tau_2)+1]}, \tag{44}$$

where the values of ϵ_0 and $\bar{\xi}$ are obtained by solving Eqs. (38) and (23) as simultaneous equations.

ACKNOWLEDGMENT

This investigation was performed in order to understand the annealing of irradiated vitreous silica as investigated by H. Szymanski and D. Keiffer at Canisius College, Buffalo, New York.

Elastic Constants of Bismuth

YAKOV ECKSTEIN,* A. W. LAWSON, AND DARRELL H. RENEKER†
Department of Physics and Institute for the Study of Metals, University of Chicago, Chicago, Illinois
(Received May 26, 1960)

The six adiabatic elastic stiffness constants of bismuth have been determined at 301°K by an ultrasonic pulse echo technique. The results are: $c_{11}=63.5$, $c_{33}=38.1$, $c_{44}=11.30$, $c_{66}=19.4$, $c_{14}=+7.23$, and $c_{13}=24.5$, all in units of 10^{10} d/cm². These values were redundantly determined by the measurement of 14 different velocities in four different single crystals of zone-purified bismuth. The velocities are believed accurate to better than 1%, the principal error arising from the uncertainty of the transducer transit time correction. The moduli are in poor agreement with the previously determined static elastic compliance constants reported by Bridgman. Some data on the velocity of sound in bismuth at 98° and at 4.2°K are also presented.

INTRODUCTION

THE acoustic determination of the adiabatic elastic constants of bismuth reported here was instigated in conjunction with measurements of the magneto acoustic-resistance of bismuth.[1] These initial observations were not in agreement with static values reported by Bridgman,[2] and, indeed, suggested that the latter were in error. However, the initial values were not redundant, nor even unambiguously determined. Because knowledge of the elastic constants is helpful in the theoretical investigation of the electronic band structure, the study was extended to provide more definitive results.

The primitive cell of bismuth is a rhombohedron ($\alpha=57°\,41'$) containing two atoms. The body diagonal of the rhombohedron has threefold symmetry and this trigonal axis is commonly designated as the z axis of the crystal. The plane perpendicular to the trigonal axis, containing the center of inversion, contains also three twofold axes and three bisectrices. To specify the other axes, we use the convention described by Cady,[3] according to which, a positive y axis is chosen to be along the projection of one edge of the primitive cell on the plane perpendicular to the [111] direction, and the positive x axis is then chosen along the binary axis which completes a right-handed orthogonal system. Such a detailed specification of axes is required in order to determine the sign of c_{14} unambiguously.

The six Voigt elastic constants for this class of crystal ($3m$) may be represented schematically by the matrix,

$$c_{ij}=\begin{vmatrix} c_{11} & c_{12} & c_{13} & c_{14} & 0 & 0 \\ c_{12} & c_{11} & c_{13} & -c_{14} & 0 & 0 \\ c_{13} & c_{13} & c_{33} & 0 & 0 & 0 \\ c_{14} & -c_{14} & 0 & c_{44} & 0 & 0 \\ 0 & 0 & 0 & 0 & c_{44} & c_{14} \\ 0 & 0 & 0 & 0 & c_{14} & \dfrac{c_{11}-c_{12}}{2} \end{vmatrix}. \quad (1)$$

We note in passing that according to the Laval-Raman[4] formalism, as modified by Joel and Wooster,[5] a more extended representation is required owing to their use of an unsymmetrical stress tensor. Previous tests[6–9] of this theory have been confined to piezoelectric materials in which the issue is confused by complications and experimental difficulties arising from electromechanical interactions. The symmetry in bismuth is such that a direct test of the Laval-Raman theory may be carried out in a simple manner, the test being limited only by the accuracy of the velocity of sound measurements used to determine the elastic constants.

EXPERIMENTAL PROCEDURE

The velocity of sound in the variously oriented crystals was determined by the pulse echo technique at 12 Mc using an apparatus previously described by Lazarus.[10] The delay line of a Dumond 256D oscilloscope was used to measure the difference in arrival time of successive echoes. The delay line was calibrated frequently during the course of the measurements by use of 10-μsec markers.

The principal source of error in this type of measurement arises from uncertainty about the correction time to be applied for the effective transit time in the transducer. This correction varies in magnitude depending on the relative velocities and lengths of the crystal and transducer. The acoustic mismatch at the crystal-transducer interface, which in turn is also a function of the type and thickness of adhesive used, also produces[11] a progressive distortion in the pulse shape of successive echoes. The distortion depends on the phase of the sound wave at the time of its incidence on the interface and thus depends on the frequency and length of the crystal for a given orientation. McSkimin[12] has de-

* Bell Telephone Laboratories Predoctoral Fellow.
† National Science Foundation Predoctoral Fellow. Now at Polychemicals Department, E. I. du Pont de Nemours and Company, Wilmington, Delaware.
[1] D. H. Reneker, Phys. Rev. **115**, 303 (1959).
[2] P. W. Bridgman, Proc. Acad. Arts and Sci. **60**, 305 (1925).
[3] W. G. Cady, *Piezoelectricity* (McGraw-Hill Book Company, Inc., New York, 1946), p. 23.
[4] J. Laval, Compt. rend. **242**, 2502 (1956); C. V. Raman and K. S. Viswanathan, Proc. Ind. Acad. Sci. **42**, 1 (1955); **42**, 51 (1955).
[5] N. Joel and W. A. Wooster, Nature **182**, 1078 (1958).
[6] Y. LeCorre, Bull. soc. franç. minéral et crist. **78**, 1363 (1954).
[7] V. G. Zubov and M. M. Firsova, Kristallografiya **1**, 546 (1956).
[8] N. Joel and W. A. Wooster, Acta Cryst. **11**, 575 (1958).
[9] H. Jaffe, Bull. Am. Phys. Soc. **4**, 427 (1959).
[10] D. Lazarus, Phys. Rev. **76**, 545 (1949).
[11] S. Eros and J. R. Reitz, J. Appl. Phys. **29**, 683 (1958).
[12] H. J. McSkimin, IRE Trans. on Ultrasonics Eng. PGUE-**5**, 25 (1957).

veloped an ingenious resonant scheme for avoiding this inherent difficulty of the pulse echo technique. In our case, the errors were reduced to a minimum by the empirical procedure of determining the time interval between echoes with and without a dummy transducer attached to the reflecting end of the sample. The change in time interval produced by addition of the dummy was used to estimate the effective transit time correction for the identical driving transducer. The transit time correction so determined varied between 0.02 and 0.06 μsec. Most of the samples employed in these measurements were somewhat over 1 cm in length. Hence, the correction at most is of the order of 1% in velocity.

The bismuth single crystals were cut from a zone refined bar whose impurity concentration is estimated to be about 1 ppm. The crystal blocks approximately $1\times\frac{3}{4}$ in. in cross section were ground so their ends were flat and parallel to within 0.0001 in.

Most of the measurements of sound velocity were made at room temperature, actually 301°K. No effort was made to control the temperature accurately because of the small temperature coefficients of the elastic constants. Measurements made at helium and liquid nitrogen temperatures were made using the cryostat previously described by Reneker.[1]

The orientation of the crystals was determined to within ±1° by the standard Laue back reflection x-ray technique. The problem of ascertaining the directions of the positive x and positive y axes in the crystal was resolved as follows. One notes that on a stereographic projection, such as that given by Vickers[12] for the larger rhombohedral unit cell containing eight atoms per unit cell, the three positive x axes point in the $[01\bar{1}]$, $[\bar{1}01]$, and $[1\bar{1}0]$ directions and the three positive y axes point in the $[\bar{2}11]$, $[1\bar{2}1]$, and $[11\bar{2}]$ directions. For crystals not oriented along principal axes, we specify the orientation by polar angles θ and φ, where θ is the angle between the direction of propagation and the z axis and φ is the angle between the xz plane and the plane containing the z axes and the propagation direction. In our case, we are concerned only with $\theta=45°$, and $\varphi=\pm 90°$. The differentiation between $=+90°$ and $=-90°$ is based on the fact that for $\varphi=-90°$ a very strong reflection corresponding to the (100) planes in Vicker's diagram occurs 11.5° from the center of the Laue picture. No such strong reflection occurs for $\varphi=+90°$. In addition, the identification may be checked by the occurrence of a relatively strong spot on the $\varphi=+90°$ picture corresponding to the $(11\bar{1})$ planes at an angular distance of about 26.5° from the center.

RESULTS

Fourteen independent velocities were measured at room temperature on an X-cut, a Y-cut, a $\theta=45°$, $\varphi=+90°$, and a $\theta=45°$, $\varphi=-90°$ crystal. The velocities are given in Table I. Using the method described

[12] W. Vickers, J. Metals **9**, 827 (1957).

TABLE I. Observed velocities of sound on bismuth at 301°K.

Symbol	Direction of propagation	Velocity in 10^5 cm/sec	Mode
v_1	x axis	2.540±0.022	Longitudinal
v_2	x axis	1.550±0.009	Fast shear
v_3	x axis	0.850±0.004	Slow shear
v_4	y axis	2.571±0.018	Longitudinal
v_5	y axis	1.407±0.009	Shear polarized along x
v_6	y axis	1.022±0.006	Shear polarized along y
v_7	z axis	1.972±0.015	Longitudinal
v_8	z axis	1.074±0.011	Degenerate shear[a]
v_9	$\theta=45°$, $=+90°$	2.082±0.019	Longitudinal
v_{10}	$\theta=45°$, $=+90°$	1.522±0.017	Shear polarized along x
v_{11}	$\theta=45°$, $=+90°$	1.150±0.006	Shear polarized along $\theta=95°$
v_{12}	$\theta=45°$, $=-90°$	2.441±0.041	Longitudinal
v_{13}	$\theta=45°$, $=-90°$	0.910±0.003	Shear polarized along x
v_{14}	$\theta=45°$, $=-90°$	1.055±0.006	Shear polarized along 135°

[a] Owing to the degeneracy of the shear modes of propagation along the trigonal axis, internal conical refraction occurs and the transmitting crystal must be laterally displaced with respect to the receiving crystal in order to detect the pulses.

by Mason,[14] we may relate these velocities to the elastic constants by the equations[15–17]:

$$\rho v_1^2=c_{11} \tag{2}$$

$$\rho v_8^2=c_{66}=\tfrac{1}{2}(c_{11}-c_{12}) \tag{3}$$

$$\rho v_6^2=c_{44} \tag{4}$$

$$\rho v_7^2=c_{33} \tag{5}$$

$$\rho v_{13}^2=\tfrac{1}{2}(c_{66}+c_{44})-c_{14} \tag{6}$$

$$\rho v_{10}^2=\tfrac{1}{2}(c_{66}+c_{44})+c_{14} \tag{7}$$

$$\rho v_2^2=\tfrac{1}{2}[(c_{66}+c_{44})+\{(c_{44}-c_{66})^2+4c_{14}^2\}^{\frac{1}{2}}] \tag{8}$$

$$\rho v_3^2=\tfrac{1}{2}[(c_{66}+c_{44})-\{(c_{44}-c_{66})^2+4c_{14}^2\}^{\frac{1}{2}}] \tag{9}$$

$$\rho v_4^2=\tfrac{1}{2}[(c_{11}+c_{44})+\{(c_{44}-c_{11})^2+4c_{14}^2\}^{\frac{1}{2}}] \tag{10}$$

$$\rho v_5^2=\tfrac{1}{2}[(c_{11}+c_{44})-\{(c_{44}-c_{11})^2+4c_{14}^2\}^{\frac{1}{2}}]. \tag{11}$$

These are the equations which we have used to determine all the constants, except c_{13}. In addition, we have four additional relations

$$2\rho v_{12}^2=\tfrac{1}{2}(c_{11}+c_{33})+c_{44}+c_{14}+\{(\tfrac{1}{2}c_{11}-\tfrac{1}{2}c_{33}+c_{14})^2+(c_{13}+c_{44}+c_{14})^2\}^{\frac{1}{2}} \tag{12}$$

$$2\rho v_{14}^2=\tfrac{1}{2}(c_{11}+c_{33})+c_{44}+c_{14}-\{(\tfrac{1}{2}c_{11}-\tfrac{1}{2}c_{33}+c_{14})^2+(c_{13}+c_{44}+c_{14})^2\}^{\frac{1}{2}} \tag{13}$$

[14] W. P. Mason, *Physical Acoustics and the Properties of Solids* (D. van Nostrand Company, Inc., Princeton, New Jersey, 1958), p. 368.

[15] These formulas have also been given by Bhimasenacker but are repeated here because there are some typographical errors in his paper. Some formulas derived in the manner described by Mayer and Hiedemann are slightly different, apparently because they neglect certain nonzero off diagonal matrix elements of Eq. (1) in deriving their Eq. (7).

[16] J. Bhimasenacker, Proc. Ind. Acad. Sci. **A29**, 200 (1949).

[17] W. G. Mayer and E. A. Hiedemann, Acta Cryst. **12**, 1 (1959).

TABLE II. Comparison of adiabatic elastic stiffness and compliance constants with isothermal values measured by Bridgman. The values in parentheses are calculated adiabatic values.

	Elastic constants of Bi	
	Echo method d/cm²	Bridgman d/cm²
C_{11}	63.5 $\times 10^{10}$	62.9 $\times 10^{10}$ (63.3)
C_{12}	24.7 $\times 10^{10}$	35.0 $\times 10^{10}$ (35.56)
C_{13}	24.5 $\times 10^{10}$	21.1 $\times 10^{10}$ (21.6)
C_{33}	38.1 $\times 10^{10}$	44.0 $\times 10^{10}$ (44.35)
C_{44}	11.30$\times 10^{10}$	10.84$\times 10^{10}$
C_{14}	+7.23$\times 10^{10}$	−4.23$\times 10^{10}$
C_{66}	19.40$\times 10^{10}$	13.87$\times 10^{10}$
S_{11}	27.8 $\times 10^{-12}$	26.9 $\times 10^{-12}$
S_{12}	−10.2 $\times 10^{-12}$	−14.0 $\times 10^{-12}$
S_{13}	−11.3 $\times 10^{-12}$	−6.2 $\times 10^{-12}$
S_{33}	40.8 $\times 10^{-12}$	28.7 $\times 10^{-12}$
S_{44}	130.7 $\times 10^{-12}$	104.8 $\times 10^{-12}$
S_{14}	−24.4 $\times 10^{-12}$	16.0 $\times 10^{-12}$
S_{66}	76.0 $\times 10^{-12}$	81.2 $\times 10^{-12}$

$$2\rho v_2^2 = \tfrac{1}{2}(c_{11}+c_{33})+c_{44}-c_{14}+\{(\tfrac{1}{2}c_{11}-\tfrac{1}{2}c_{33}-c_{14})^2 + (c_{13}+c_{44}-c_{14})^2\}^{\frac{1}{2}} \quad (14)$$

$$2\rho v_{11}^2 = \tfrac{1}{2}(\tfrac{1}{2}c_{11}+\tfrac{1}{2}c_{33}+c_{44}-c_{14})-\{(\tfrac{1}{2}c_{11}-\tfrac{1}{2}c_{33}-c_{14})^2 + (c_{13}+c_{44}-c_{14})^2\}^{\frac{1}{2}}, \quad (15)$$

which have been used to determine c_{13}. The error in the latter is larger than for the other five constants since the error in constants derived solely from crystals not oriented along principal axes is inherently larger, being proportional to the error in misorientation rather than to the square as for a crystal oriented along principal axes.

If one proceeds to insert the measured velocities in Eq. (2) to Eq. (15) to determine the elastic constants, one should have eight redundant checks because there are only six unknowns and 14 equations. In particular, the trace of the Christofel determinant for the X-cut crystal (i.e., $v_1^2+v_2^2+v_3^2$) should equal that for the Y-cut crystal $v_4^2+v_5^2+v_6^2$. The two observed traces are 9.580×10^{10} cm²/sec² and 9.654×10^{10} cm²/sec², respectively. Similarly, the traces of $\varphi=+90°$ and $\varphi=-90°$ crystals should be equal. In this case, the observed values are 7.974×10^{10} cm²/sec² and 7.899×10^{10} cm²/sec², respectively. Further checks of similar nature are easily made by considering sums and differences of pairs of equations such as Eq. (6) and Eq. (7).

Our actual procedure was somewhat different. The values of c_{11}, c_{33}, c_{66}, c_{44}, and c_{14} were calculated from from Eq. (2)–Eq. (11). The value of c_{11} was then slightly readjusted within the experimental error to improve the over-all agreement with all the equations. No effort was made to use a least-square procedure in view of the labor involved. The values of these constants so determined are given in Table II. The value of c_{13} is determined by solution of Eq. (12) – Eq. (15). One obtains two solutions for each pair of the four equations. The two pairs of equations have only one common root, however, and only this root will yield a positive volume compressibility. This value is also given in Table II.

It should be noted that the sign of c_{14} is positive because of the convention adopted in defining our axes. For problems involving only the propagation of sound, this convention is of no importance. However, when one desires to investigate the interaction of these sound waves with electrons, it is imperative that the sign convention adopted for designating the elastic properties be the same as that for describing the Fermi surface of the carriers. We have adopted Cady's convention because of its widespread use in the description of quartz crystals.

The values of the elastic constants reported in Table II satisfy all the stability requirements on the lattice. These conditions are easily derived by requiring the determinant of the elastic constants, corresponding to the matrix of Eq. (1), and all its principal minors, be positive in the manner described by Alers and Neighbors.[18] In calculating the elastic constants, the density of bismuth was taken to be 9.80 g/cm³ in accordance with the latest precision determination of the lattice parameters by Barrett.[19]

In addition to the measurements at room temperature, all the elastic constants except c_{13} were determined also at the boiling point of liquid N_2 and of liquid He. These values are given in Table III. Corrections for the change in length of the bismuth with temperature were made with the thermal expansion data of Erfling.[20] The determination of c_{13} as a function of temperature was not carried out owing to the high uncertainty.

DISCUSSION

In Table II, for purposes of comparison with our values, we have recorded the static values of the elastic

TABLE III. Temperature dependence of the elastic constants in units of 10^{10} d/cm².

	300°K	80°K	4.2°K
c_{11}	63.5	68.6	68.7
c_{33}	38.1	40.6	40.6
c_{44}	11.3	12.7	12.9
c_{66}	19.4	22.4	22.5
c_{14}	7.23	8.05	8.44
c_{12}	24.5	...	...

TABLE IV. Comparison of adiabatic linear and volume compressibilities.

	Echo technique cm²/d	Bridgman[a] cm²/d
K_a	18.16×10^{-12}	16.13×10^{-12}
K_c	6.28	6.59
K_v	30.7	29.31

[a] Calculated from adiabatic values.

[18] G. P. Alers and J. R. Neighbors, J. Appl. Phys. **28**, 1514 (1957)
[19] C. S. Barrett, Australian J. Phys. (to be published).
[20] H. D. Erfling, Ann. Physik **34**, 136 (1939).

compliance constants s_{ij} determined many years ago by Bridgman.[2] The s_{ij} determined by Bridgman are isothermal values; the c_{ij} values reported here are adiabatic. We have, therefore, converted Bridgman's values of s_{ij} to isothermal c_{ij} by inverting the matrix of Eq. (1), and thence to adiabatic c_{ij}, by use of thermodynamic formulas of the standard type.[21] These values are also given in Table II. Finally, we have inverted our c_{ij} matrix to obtain adiabatic s_{ij} which within experimental error are the same as the isothermal values. It is to be noted that our values of the c_{ij} obtained by inverting Bridgman's s_{ij} are materially different from those reported by Betts *et al.*[22]

We focus attention on the comparison of our adiabatic measured values of c_{ij} with the adiabatic values of the c_{ij} computed from Bridgman's static s_{ij}. Several large discrepancies, far larger than the combined estimated experimental errors, are apparent for c_{33} and c_{12}. The origin of these discrepancies is difficult to ascertain. However, we note that Bridgman's values are only partially redundant, that several of his samples were reported as polycrystalline, and that the purity of his samples was dubious. We suspect a gross orientational error[23] (perhaps concealed as an occluded grain or an unnoticed twin) in one or more of his crystals. The discrepancy in the sign of c_{14} is only apparent and arises presumably because of a difference between Bridgman's unspecified axis convention and that used here.

A more rewarding comparison (see Table IV) is afforded by the agreement between Bridgman's directly observed adiabatic volume compressibility and that calculated from our data: the former is 29.3×10^{-13} cm²/d and the latter, 30.7×10^{-13} cm²/d. The difference between these two values is well within the combined experimental error.

We turn now to the question of whether the Voigt theory provides an adequate description of the elastic properties of bismuth. In view of the numerous redundant checks, the answer must certainly be affirmative to within the accuracy of our experiments. However, in view of the existing uncertainty over the applicability of the Laval-Raman theory to various crystals, it might be worthwhile to set some quantitative limits on the permitted deviations from the Voigt framework, at least, as applied to bismuth.

Briefly, the difference between the Voigt and the Laval-Raman theory may be stated as follows. The Voigt theory considers the case of a static (or homogeneous) strain in which the strain tensor may be separated into symmetric and antisymmetric components. The latter correspond to rigid body rotations which invoke no stress. The stress tensor may then be proved symmetric. In a dynamic and, consequently, inhomogeneous strain, the rotational part of the displacement has a spatial variation and hence requires torques to sustain the changes in angular momentum. It is therefore impossible to demonstrate that the stress tensor is symmetric. In the most general case, one requires 45 constants to relate the stress to the strain, after imposing exactness conditions, rather than 21 constants as in the Voigt theory. Wooster has shown that this number is further reduced by compatibility requirements to 39 constants. This number of constants is further reduced by the requirements of crystal symmetry so that for the simplest crystal classes (e.g., isotropic materials), there is no difference between the two theories.

Particularizing to the case of Bi, one finds that eight constants are required to specify the relation between stress components X_{ij} and strain components x_{ij}. In fact,[24,25]

$$X_{ij}=\begin{vmatrix} d_{11} & d_{12} & d_{13} & d_{14} & d_{15} & 0 & 0 & 0 \\ & d_{11} & -d_{13} & -d_{14} & -d_{15} & 0 & 0 & 0 \\ & & d_{33} & 0 & 0 & 0 & 0 & 0 \\ & & & d_{44} & \frac{d_{44}+d_{55}}{2} & 0 & 0 & 0 \\ & & & & d_{55} & \frac{d_{44}+d_{55}}{2} & d_{15} & d_{15} \\ & & & & & d_{66} & d_{14} & d_{14} \\ & & & & & & d_{66} & d_{66} \\ & & & & & & & d_{66} \end{vmatrix} x_{ij}. \tag{16}$$

[21] See J. F. Nye, *Physical Properties of Crystals* (Oxford University Press, Oxford, England, 1957), p. 283.
[22] D. D. Betts, A. B. Bhation, and G. K. Horton, Phys. Rev. **104**, 43 (1956).
[23] The discrepancy between the value for V_{12} previously reported by one of us and that in Table II was owing to a "false" trigonal axis being mislabeled in a Laue pattern.
[24] Note that this matrix differs slightly from that given by Raman and Viswanathan owing to a misprint in their article. We have used their notation which differs from that of LeCorre.
[25] Y. LeCorre, Bull. Soc. franc. Mines. Crist. **70**, 80 (1957).

The Christofel determinantal equation for the velocities of propagation along the x axis of bismuth is

$$\begin{vmatrix} d_{11}-\rho v^2 & 0 & 0 \\ 0 & d_{66}-\rho v^2 & d_{15} \\ 0 & d_{15} & d_{55}-\rho v^2 \end{vmatrix} = 0, \quad (17)$$

and that for propagation along the y axis of bismuth is

$$\begin{vmatrix} d_{66}-\rho v^2 & 0 & 0 \\ 0 & d_{11}-\rho v^2 & -d_{15} \\ 0 & -d_{15} & d_{55}-\rho v^2 \end{vmatrix} = 0. \quad (18)$$

These particular cases are quite simple and differ from the corresponding equations for the Voigt theory in that d_{55} replaces c_{44} and d_{15} replaces c_{14}.

From Eq. (17), we have

$$d_{55}+d_{66}=\rho v_2^2+\rho v_3^2 \quad (19)$$

and, from Eq. (18)

$$d_{11}+d_{55}=\rho v_4^2+\rho v_6^2. \quad (20)$$

Furthermore, $d_{11}=c_{11}$ and $d_{66}=c_{66}$.

The sum, $v_2^2+v_3^2-v_6^2$, is $1.145\pm0.034\times10^{10}$ cm^2/sec^2, which is to be compared with the directly observed v_6^2, $1.153\pm0.017\times10^{10}$ cm^2/sec^2. It is clear that d_{44} and d_{55} cannot differ by more than 4%. Equation (20) does not yield as small an estimate for the possible difference between d_{44} and d_{55} owing to the large error introduced by the uncertainty in c_{11}.

ACKNOWLEDGMENTS

It is a pleasure to acknowledge partial support of this work from the Office of Naval Research and the National Science Foundation.

JOURNAL OF APPLIED PHYSICS VOLUME 31, NUMBER 9 SEPTEMBER, 1960

Dislocations in Indented Magnesium Oxide Crystals

A. S. Keh
Edgar C. Bain Laboratory for Fundamental Research, United States Steel Corporation Research Center, Monroeville, Pennsylvania

(Received April 14, 1960; and in final form May 26, 1960)

Dislocation rosette patterns produced by spherical and pyramidal indentors on the cleaved surfaces of magnesium oxide crystals were studied in detail. The three-dimensional arrangement of dislocation loops as deduced from the two-dimensional etching patterns is discussed. Cracks formed on $\{110\}_{90}$ planes around pyramidal indentations are believed to be due to the interaction of dislocations on $\{110\}_{45}$ planes. The temperature dependence of hardness was found to be related to the widening of dislocation bands, rather than to the distance of travel of leading dislocations. Some observations were also made on the pinning of dislocations and recovery at elevated temperatures, and on the interaction of dislocations with grown-in subboundaries.

INTRODUCTION

THE indentation hardness test is probably the simplest method of measuring the strength of materials. However, it is also the least understood test in terms of stress and strain distribution. Some progress has been made in analyzing the stress and strain distributions of several types of indentations using the continuum theory of plasticity.[1] However, the results cannot be applied directly to crystalline solids having well-defined slip systems.

In the last decade, a few attempts have been made to study the deformation mechanism associated with indentation. Tolansky and Nickols[2] studied several matrials by means of multiple-beam interference microscopy. Churchman, Geach, and Winston[3] investigated materials with a diamond structure. Smakula and Klein[4] used a prismatic punching method to study glide in ionic crystals. Votava, Amelinckx, and Dekeyser[5] employed an interferometric method to study indentation figures on cleavage faces of mica and NaCl.

With the advancement of dislocation theory and techniques of revealing dislocations in crystals in the past few years, it was thought possible to attain a better understanding of the deformation caused by indentation of a material with a simple crystalline structure. In this investigation, dislocation etching technique[6,7] was used to study the dislocation structures associated with various types of indentations at various temperatures in magnesium oxide crystals. This type of study may

[1] R. Hill, *The Mathematical Theory of Plasticity* (Oxford University Press, New York, 1950).
[2] S. Tolansky and D. G. Nickols, Nature, **164**, 113 (1949); Phil. Mag. **43**, 410 (1952); Nature **164**, 840 (1949).
[3] A. T. Churchman, G. A. Geach, and J. Winston, Proc. Roy. Soc. (London) **A238**, 194 (1956).
[4] A. Smakula and M. W. Klein, Phys. Rev. **84**, 1043 (1951).
[5] E. Votava, S. Amelinckx, and W. Dekeyser, Acta Met. **3**, 89 (1935).
[6] J. Washburn, A. E. Gorman, and E. R. Parker, Trans. A. I. M. E. **215**, 230 (1959).
[7] R. J. Stokes, T. L. Johnston, and C. H. Li, Trans. A. I. M. E. **215**, 437 (1959).

lead not only to an understanding of the hardness test, but also may serve to explain the observation of one type of surface dislocation source (rosettes), which have a dislocation structure similar to that of a hardness indentation and which are believed to play an important role in plastic deformation of bulk materials.[7,8]

EXPERIMENTAL PROCEDURE

Magnesium oxide crystals obtained from Norton Company, Worcester, Massachusetts were first annealed at 1000°C, then cleaved to convenient sizes. The cleaved crystals were then polished in orthophosphoric acid. For room temperature hardness tests, either a Vickers machine with a 2-mm ball indentor and a 10-kg load, or a microhardness tester with a diamond pyramid indentor and loads varying from 5–500 g was used. Hot-hardness tests were performed between 300 and 1000°C, using a diamond pyramid indentor. In this case, loads varying from 2 to 10 kg were used, and the total loading time was 2 min. After indenting, the specimens were etched in a mixture of 5-parts saturated ammonium chloride, 1-part sulfuric acid, and 1-part distilled water. Dislocations due to room-temperature deformation gave sharply defined conical pits whereas grown-in dislocations or dislocations aged at high temperatures gave flat-bottomed pits. A Zeiss interference microscope was used to study the deformed regions produced by indentation at elevated temperatures.

RESULTS

Dislocation Structure from a Spherical Indentation

Dislocation Arrangement in a Rosette Pattern

The dislocation pattern associated with a spherical indentation on a cleaved and polished MgO crystal was revealed by etching, and is shown in Fig. 1. This rosette pattern is very similar to those observed in NaCl, LiF,[9,10,11] and MgO[7] when the cleavage surface was brought in contact with some hard material. Each etch pit corresponds to the intersection of a segment of a dislocation loop with the surface.[12] The pattern consists of eight wings with lines of etch pits either in the ⟨100⟩ direction or in the ⟨110⟩ direction. The glide distance decreases gradually from the outside to the center of each wing. Pits in the ⟨100⟩ direction form continuous lines through the indented area. In the ⟨110⟩ directions, the lines of etch pits are interrupted at the indented

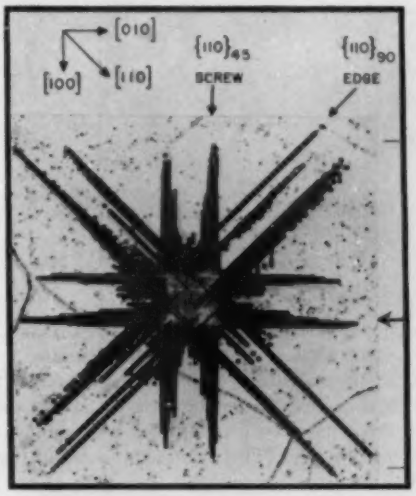

FIG. 1. Dislocation pattern for a spherical indentation on the (001) surface. 50×.

region. Closer examination revealed that pits in the ⟨110⟩ directions are symmetric and those in the ⟨100⟩ directions are asymmetric as Gilman[8] first observed in LiF. Symmetric pits suggest that dislocation lines are perpendicular to the etching surface; while asymmetric pits are associated with dislocation lines inclined to the etching surface. Some low-angle subboundaries were also delineated by etch pits (Fig. 1).

In order to study the three-dimensional dislocation structure some crystals were chemically polished to different levels from the indented surface; others were cleaved through the indentation. Figure 2 shows the etch pattern on a plane cleaved perpendicular to the indented plane of Fig. 1. The cleavage plane is indicated by the arrow in Fig. 1. One can easily deduce from these two-dimensional figures that all the dislocation lines lie in the {110} planes, which are the known slip planes for MgO crystals. Two of them are perpendicular to

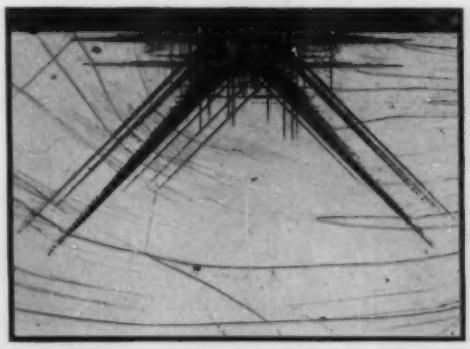

FIG. 2. Dislocation pattern of (100) surface, cleaved after indentation (arrow in Fig. 1 designates plane of cleavage). 50×.

[8] J. J. Gilman and W. G. Johnston, *Dislocations and mechanical properties of crystals* (John Wiley & Sons, Inc., New York, 1957), p. 116.

[9] E. Aerts, S. Amelinckx, and W. Dekeyser, Acta Met. **7**, 29 (1959).

[10] W. H. Vaughan and J. W. Davisson, Acta Met. **6**, 554 (1958).

[11] A. D. Whapham, Phil. Mag. **3**, 103 (1958).

[12] Recently Johnston and Gilman[13] have shown that some etch pits on glide planes in LiF correspond to imperfections other than dislocations.

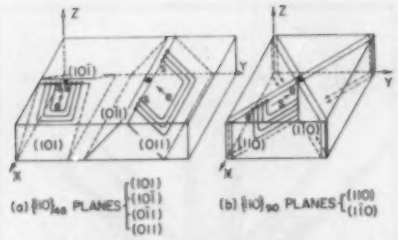

FIG. 3. Slip planes and dislocation half-loops in indented MgO crystals.

the indented surface and will be referred to as $\{110\}_{90}$ planes (after Stokes *et al.*[7]). Four of them are inclined at 45° to the indented surface and will be referred to as $\{110\}_{45}$ planes. From the etch-pit study, one can sketch the dislocation loops formed by the indentation on the two types of {110} planes, as shown in Fig. 3(a) and (b). It becomes obvious that pits in the ⟨110⟩ directions in Figs. 1 and 2 correspond to edge components of dislocations, because the segments are perpendicular to the Burgers vector. Those in the ⟨100⟩ direction are screw components because the segments are parallel to the Burgers vector.

The distances of travel of leading dislocations of the edge (e) and screw (s) dislocations on the $\{110\}_{45}$ and $\{110\}_{90}$ planes were measured for several indentations. It was found that

$d_{s\{110\}_{45}} \cong 1.4 d_{e\{110\}_{90}}$ [Measured on the indented surface (Fig. 1).]

$d_{s\{110\}_{45}} \cong d_{e\{110\}_{45}}$
$d_{e\{110\}_{90}} \cong 2 d_{s\{110\}_{90}}$ [Measured from both the indented and cleaved surfaces (Figs. 1 and 2).]

Motion of Dislocations of the Rosette Structure by External Stress

When a stress is applied externally to the indented crystal, some of the dislocations associated with the indention will move depending on the direction of the resolved shear stress. A crystal was first etched after indentation, stressed under tension, and then re-etched to show the new positions of dislocations, as shown in Fig. 4. For the edge dislocations only four of the eight branches have moved. For the screw dislocations only some of those in planes with horizontal traces have moved, because there is no component of shear stress in the planes with vertical traces.

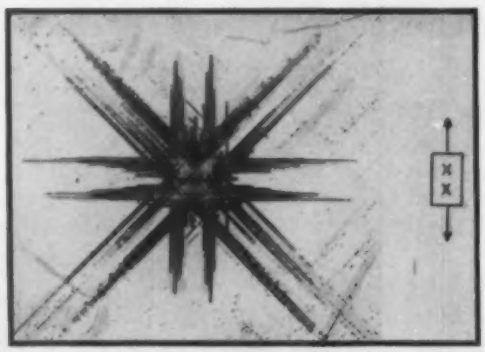

FIG. 4. Double-etching pattern of dislocations of a crystal stressed after indentation. 50×.

Pinning of Dislocations at an Elevated Temperature

When the same crystal was further stressed, glide bands grew from those dislocations in the rosette pattern which were expanded. However, these dislocations can be pinned if the crystal is annealed at some elevated temperature between 750° and 1000°C. A crystal was indented with several indentations on one surface and then annealed at 1000°C for ½ hr. Then several more indentations were put on the opposite surface. The crystal was then etched to show the fresh and aged dislocations. After that, it was stressed in compression until macroscopic yielding occurred. It was re-etched for a short time to show new dislocations in the glide bands. As shown in Fig. 5(a), most glide bands were initiated

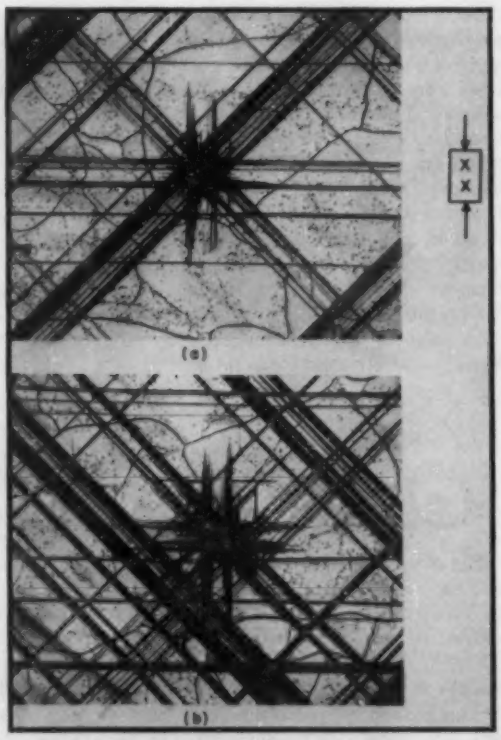

FIG. 5. (a) Glide bands originated from fresh dislocation rosette. (b) Glide bands not originated from aged dislocation rosette. 25×.

from the unaged dislocation rosette, while none was initiated from the aged one as shown in Fig. 5(b). This pinning of dislocations is probably an impurity effect. Similar observations were made in LiF[13] and Si-Fe[14]. Although the aged dislocations did not move under the yield stress, they may move at a higher stress.

Rearrangement of Dislocations during Recovery

When the indented crystals were annealed at temperatures above 1000°C recovery effects were observed. The motion of dislocations during annealing can be detected by etching before and after annealing. The early stage of recovery consists of (1) extension of edge dislocations to the unstressed region and (2) noncrystallographic dispersion of screw dislocations. As annealing temperature increases, the dispersed area of screw dislocations increases and the density of dislocations decreases. Figure 6 shows the position of both edge and screw

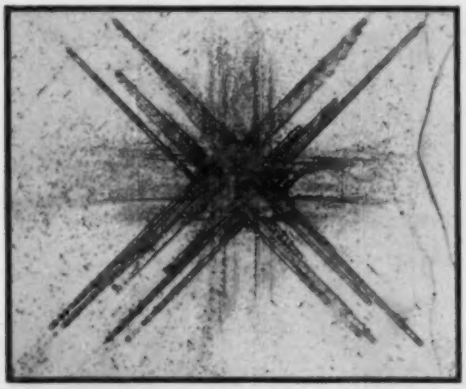

FIG. 6. Double-etching pattern of dislocation rosette of a spherical indentation before and after annealing at 1500 C. 50×.

dislocations before and after the crystal was heated to 1500°C.

Interaction of Dislocations with Grown-in Subboundaries

It is of interest to note that dislocations resulting from indentation pass through most grown-in subboundaries with little apparent difficulty. Occasionally a pile-up against a subboundary was observed. Figures 7 and 8 show some features of the interaction of dislocations with a grown-in twist boundary. This boundary is shown at the left of Fig. 7(a). The misorientation across the boundary was determined by the x-ray Laue back reflection method and was found to have a 3°-twist component and a small tilt component (<1°). Some piled-up groups of edge dislocations can be seen

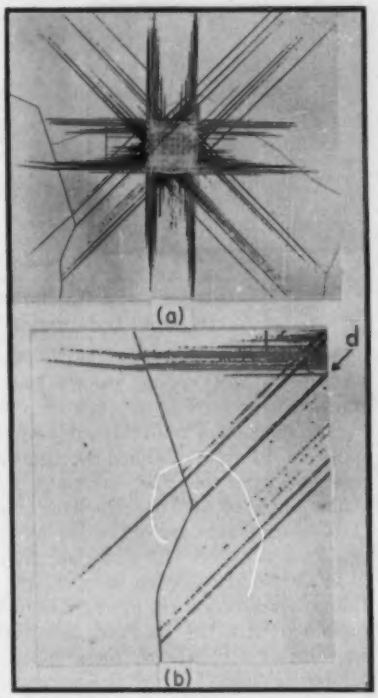

FIG. 7. Interaction of dislocations with 3°-twist boundary. (a) 40×, (b) 100×.

at the lower left corner of Fig. 7(a). Figure 8 shows etching patterns on two parallel surfaces lying beneath the indented surface. Some pileup of screw dislocations can be seen. The row of edge dislocations marked d, in Fig. 7(b) which piled-up against the boundary on the indented surface broke through this barrier inside the crystal. After passing through the boundary, the lines of edge pits bent about 2° and the lines of screw pits bent 1° and 4°, respectively [Fig. 8(a)], to comply with the misorientation between the adjacent subgrains. This checks quite well with the x-ray determinations.

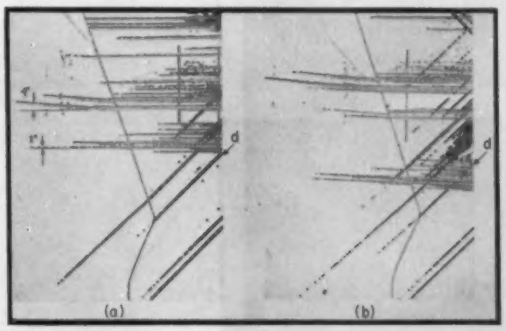

FIG. 8. Interaction of dislocations with a 3°-twist boundary. 57×. (a) 50 μ from the indented surface. (b) 150 μ from the indented surface.

[13] W. G. Johnston and J. J. Gilman, J. Appl. Phys. 30, 129 (1959).
[14] D. F. Stein and J. R. Low, Jr., Gen. Elect. Rept. No. 59-RL-2262M (1959).

FIG. 9. Dislocations and cracks around a microhardness indentation. ~333×.

Dislocations and Cracks from a Pyramid Indentation

When a pyramid indentation is made on a cleaved surface of a MgO crystal, using a load of a few grams, cracks usually form in the ⟨110⟩ directions as shown in Fig. 9. With loads above about ½ kg, irregular cracks appeared. It was established by chemical polishing that those cracks in the ⟨110⟩ directions lay in the $\{110\}_{90}$ planes, but they were not slip plane cracks. When these $\{110\}_{90}$ slip planes are delineated by lines of edge dislocation pits in the ⟨110⟩ direction, the cracks generally lie in the middle of each wing of etch pits where the dislocation density is the lowest. The dislocation pattern associated with the pyramid indentation is again in the form of a rosette, as for a spherical indentation. In addition, there is a high density of screw dislocations forming a square block around the indentation, as shown in Fig. 9. The cracks generally terminate at the corners of the square block.

Indentation at High Temperatures

The lightest load that can be applied to the specimen with the hot-hardness tester used in this investigation is 2.12 kg. With this load, the specimen developed cracks around the impression at 500°C and below. Most of the results shown here are from tests between 550° and 900°C. Figures 10 (a) and (b) show the slip lines and interference pattern around an impression, respectively, made at 650°C with a 5-kg load. The slip lines form a square block in ⟨100⟩ directions. Regardless of the orientation of the indentor, slip concentrates at the four corners of the square block. Interferograms of the indentations as shown in Fig. 10(b) indicate that four hills were built up near the impression at these four corners. The contour of the hill in the ⟨110⟩ direction is shown in Fig. 11. The height of the hill is about 2.3 μ and the deformed region extended to about 170 μ from the indentation.

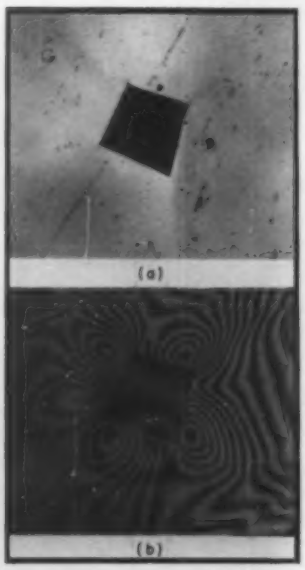

FIG. 10. Slip lines (a) and interference pattern, (b) around a pyramid indentation at 650° C. 70×.

In order to determine what slip planes are responsible for the ⟨100⟩ slip traces observed on the indented surface,

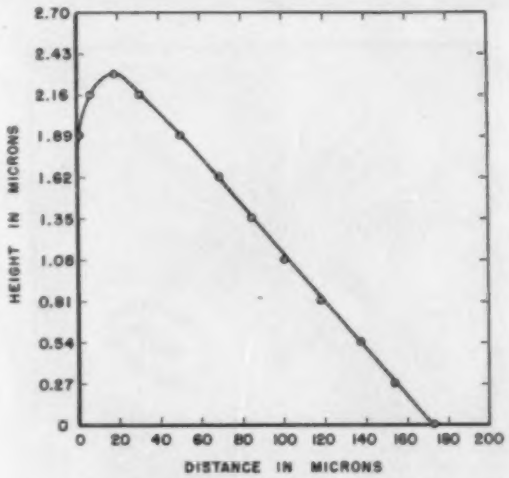

FIG. 11. Profile of an indentation in the ⟨110⟩ direction (650° C, 5 kg).

a crystal was cleaved through the indentation and etched for dislocations. They were found to be on $\{110\}_{45}$ planes. Slip also takes place on the $\{110\}_{90}$ planes but the slip traces can only be revealed by transmission light microscopy. The dislocation configuration associated with indentation at four different temperatures is shown in Figs. 12(a)–(d). Two features can be seen in these figures: (1) As the temperature of indentation increases, the etch pits become less sharp; (2) the widths of the edge and screw bands increase with increasing temperature. Figure 13 shows the temperature dependence of hardness, impression size, width of glide bands, and distance of travel of leading edge dislocations for the same load. The width of the glide bands increases with the impression size, while the distance of travel of the leading edge dislocation remains constant with temperature. Several crystals were studied and similar results were obtained.

The average height of the four hills around the indentation were measured from the interferograms and found to increase with increasing temperature.

In another set of experiments, indentations were made on each crystal with four different loads (3, 5, 7, and 10 kg) at four temperatures (550°, 650°, 700°, and 750°C). Figure 14 shows the plot of maximum width of screw band vs the impression size for one of these crystals. Within the limits of experiment accuracy, all the 16 points fell on the same straight line going through the origin.

DISCUSSION

Dislocation Structure from a Spherical Indentation

When the indentor first contacted the crystal, there was a resolved shear stress on the $\{110\}_{45}$ planes but

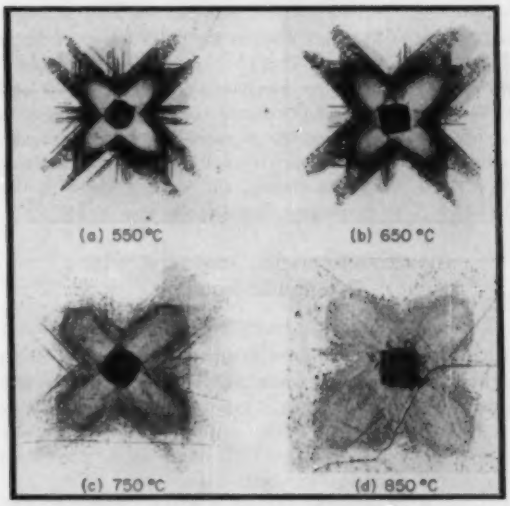

FIG. 12. Dislocation pattern from hot-hardness indentations on (001) surface of MgO crystal. 33×.

not on the $\{110\}_{90}$ planes. This stress on the $\{110\}_{45}$ planes either opens existing sources or nucleates new dislocations. In the latter case, the local stress concentration should be close to the theoretical strength of the material. On using the Hertz theory of elastic contact as a first approximation, the maximum stress under the indentation is approximately $G/25$ where G is the shear modulus of the crystal. Therefore, one would expect homogenous nucleation of dislocations, as recently pointed out by Gilman.[15] The dislocation loops so generated on these slip planes are shown schematically in Fig. 3. After the indentor penetrated into the crystal, there was a small component of shear stress on the $\{110\}_{90}$ planes. The dislocation loops formed on these planes are shown schematically in the same figure.

[15] J. J. Gilman, J. Appl. Phys. **30**, 1584 (1959).

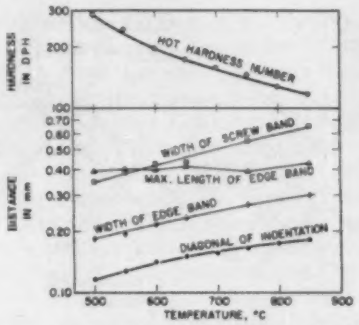

FIG. 13. Temperature dependence of hardness indentation of MgO crystal.

Moreover, during the process of indentation the material in the region inside each wing of dislocations in Figs. 1 and 2 was pushed away from the indentor. Therefore, the dislocations formed on the two sides of each wing are of opposite sign as shown in Fig. 15. This was demonstrated by the motion of dislocation so created under applied stress as shown in Fig. 4. As one would expect, dislocations with the same sign as the applied shear stress moved out along their glide planes.

Johnston[16] has found in MgO that the linear velocity of the edge component of a dislocation half-loop is approximately 200 times that of the screw component of another loop under the same applied shear stress in a homogeneous stress field. However, in the present investigation, it was found that in a glide band, the distance of travel of the edge component of the leading dislocation is approximately the same as that of the screw component. This may indicate that the stress field around an indentation is not homogeneous and Johnston's result cannot be applied directly.

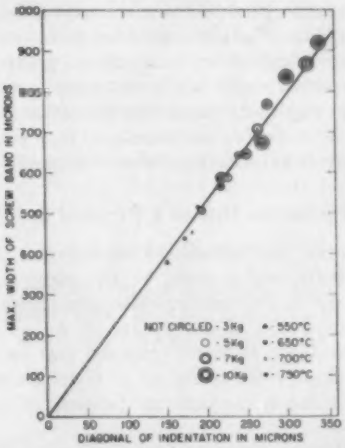

FIG. 14. Linear dependence of slip bandwidth on size of indentation.

[16] W. G. Johnston, private communications.

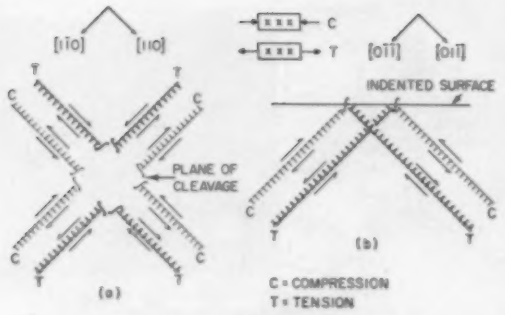

FIG. 15. Arrangement of edge dislocations on (a) indented and (b) cleaved surfaces.

Rearrangement of Dislocations during Recovery

The motion of dislocations as shown in Fig. 6 represents the first stage of recovery. Internal stress is probably the driving force for the motion of dislocations. The screw dislocations tend to cross-slip to other planes, and the edge dislocations, which cannot cross-slip, tend to glide a little further along their original slip planes into the elastic region. This has been observed in other crystals when subjected to simple deformations before annealing.[17,18] The density decrease of dislocations during annealing is due to the collapse of some small loops and cancellation of dislocations of opposite signs. Some dislocation climb and local polygonization must also occur at very high temperature. However, they were not observed.

Interaction of Dislocations with a Subboundary

The fact that dislocations from indentation went through most subboundaries ($\sim<1°$) indicates that they are not very effective barriers for dislocations. The 3°-twist boundary studied here seems to be a moderate barrier for dislocations because some went through and others were stopped to form pileup groups. In the present experiment, the local strain setup by an indentation is very high and it is possible that at an early stage of plastic deformation, subboundaries may play a more important role in hindering dislocation motion.

Crack Formation Due to a Pyramid Indentation

The cracks formed around an indentation lie on $\{110\}_{90}$ planes, which could be the planes on which slip took place. Previously, several mechanisms have been proposed to explain slip plane cracks in Zn, NaCl, and also in MgO. Gilman[19] proposed that such cracks in Zn are due to the piling up of dislocations on the slip plane which is the same as the plane of crack formation. Stroh[20] explains this type of crack as due to the displacement of a subboundary intersected by the slip plane. Smakula and Klein[21] found the same type of cracks in NaCl after punching, and these were explained on the basis of shear on slip planes. Stokes *et al.*[22] found cracks on {110} slip planes in MgO in in bending, tension, and compression tests. They showed that these cracks formed in the region where dislocations pile up against heavy slip bands and so concluded they were of the Stroh type. However, the cracks observed here cannot be the same as the type formed in Zn because the $\{110\}_{90}$ planes on which the cracks formed are generally in the center of the dislocation wings, where the dislocations are absent. Also they cannot be the type of cracks which Stokes *et al.* observed because the geometry of slip planes does not allow the formation of that type of crack. As was pointed out before, the cracks all terminate at the corners of the square blocks of screw dislocations on $\{110\}_{45}$ planes. This strongly suggests that they are due to the interaction of these dislocations on neighboring $\{110\}_{45}$ planes, making 120° with each other. The mechanism was proposed and analyzed in detail in a previous publication.[23] In essence, it involves the piling up of dislocations on two slip planes making 120° angles to each other to form a crack on a third slip plane making the same angle with the first two. This is shown schematically in Fig. 16.

Plastic Deformation Associated with a Pyramid Indentation

The plastic deformation associated with a pyramid indentation is shown by the slip traces in Fig. 10(a) and by the interferogram in Fig. 10(b).[24] Votava *et al.*[5] observed in NaCl the same type of deformation as was

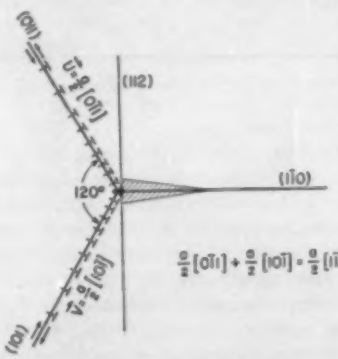

FIG. 16. Crack formation on (1$\bar{1}$0) plane in MgO crystals.

[17] W. J. Hibbard, *Creep and Recovery* (American Society for Metals, Cleveland, 1957), p. 52.
[18] J. J. Gilman, *Creep and Recovery* (American Society for Metals, Cleveland, 1957), p. 79.
[19] J. J. Gilman, Trans. A. I. M. E. 212, 783 (1959).
[20] A. N. Stroh, Phil. Mag. 3, 597 (1958).
[21] A. Smakula and M. W. Klein, Phys. Rev. 84, 1043 (1951).
[22] R. J. Stokes, T. L. Johnston, and C. H. Li, Phil. Mag. 3, 718 (1958); Phil. Mag. 4, 920 (1959).
[23] A. S. Keh, J. C. M. Li, and Y. T. Chou, Acta Met. 7, 694 (1959).
[24] The asymmetry of the indentations may indicate that the indented surface is slightly tilted from the normal position.

observed in this investigation. They suggested that the traces are probably due to slip on {100} planes. This was not found to be true for MgO in the present case. Instead, these traces are on the {110} planes as pointed out previously. However, if one uses the Schmidt-Boas relationship of critical resolved shear stress, assuming that the radical stresses due to applied load are the same everywhere, slip should be most pronounced near the middle of the four sides instead of the corners of the square blocks. This is the opposite of what was observed. As pointed out before,[21] dislocations on neighboring $\{110\}_{45}$ planes tend to form a barrier for pileup. At low temperatures these piled-up groups build up stress to cause local fracture. When the temperature is sufficiently high, some segments of the piled-up dislocations will cross-glide and form new dislocation sources on parallel glide planes. This multiplication mechanism was first suggested by Koehler[25] and Orowan[26] and was recently adopted by Low and Guard[27] and modified by Johnston and Gilman.[28] The four hills detected by interferometry in Fig. 10(b) are probably due to a high concentration of dislocations as a result of pileup, and the heavy slip lines near the corner of square blocks in Fig. 10(a) are thus caused by cross-slip as a result of pileup.

Temperature Dependence of Hardness

The observation that, while hardness decreases with increasing temperature, the distance which the leading dislocation travels remains unchanged was unexpected. As Johnston and Gilman[13] found in LiF, the softer the crystal, the higher the dislocation velocity for the same applied stress. Aerts *et al.*[9] used this distance of travel due to indentation as a measure of hardness change due to radiation damage. The fact that this distance does not change much with changing temperature may indicate that the temperature dependence of hardness is not controlled by the linear velocity of dislocation motion. Alternatively, this may indicate that the stress distribution around the indentation changes with changing temperature.[29] As shown in Fig. 13, for the same load, the width of both edge and screw bands increases with increasing temperature. This widening of glide bands is probably due to more nucleation or multiplication of dislocations at high temperatures. On the other hand, Fig. 14 shows that when the width of glide band was plotted against the impression size, all points taken at different temperatures with various loads fell on the same straight line. This means that for the same impression size the width of glide band is independent of the testing temperature. Johnston and Gilman[13] have found that in LiF the dislocation density inside the glide bands increases with decreasing temperature for the same amount of strain. Similar change of dislocation density with temperature should be expected in indented MgO crystals when the impression size is kept constant. However, this type of measurement was not made in the present work because the dislocation density changes continuously as the distance from the indentation increases.

[25] J. S. Koehler, Phys. Rev. **86**, 52 (1952).
[26] E. Orowan, *Dislocation in Metals* (A.I.M.E., New York, 1954), p. 103.
[27] J. R. Low and R. W. Guard, Acta Met. **7**, 171 (1959).
[28] W. G. Johnston and J. J. Gilman, Gen. Elec. Rept. No. 59-RL-2313M, November, 1959.
[29] The author is indebted to W. G. Johnston for pointing out this possibility.

SUMMARY AND CONCLUSIONS

The mechanism of plastic deformation by indentation of cleavage surfaces of MgO crystals was studied by observing the dislocations and slip traces. It was found that in accordance with known behavior slip always took place on {110} planes. When a large spherical indentation was used, slip on both $\{110\}_{90}$ and $\{110\}_{45}$ planes was almost equally pronounced and the dislocation structure consisted of a rosette with eight wings. When a pyramid indentor was used, there was a high concentration of dislocation on the $\{110\}_{45}$ near the impression, forming a square block, and the region of slip increased with increasing temperature. Cracks formed on the $\{110\}_{90}$ planes at low temperature are believed to be caused by interaction of dislocations in the adjacent $\{110\}_{45}$ planes. As the temperature increases, the hardness of the material decreases; the distance of travel of leading-edge dislocation remained constant while the width of glide band increases.

After annealing between 750° and 1000°C, dislocations introduced by indentation are pinned and fail to move at the yield stress of the crystal. Above 1000°C, dislocation rearrangement in the rosette structure was observed.

Low-angle subboundaries in the crystals are not very strong barriers for dislocations introduced by indentation.

ACKNOWLEDGMENTS

The author is indebted to Y. T. Chou and J. C. M. Li for discussions and to R. S. Cline and R. R. Keck for assistance in some of the experimental work.

Temperature Dependence of the Velocity of Sidewise 180° Domain-Wall Motion in $BaTiO_3$

A. SAVAGE AND R. C. MILLER
Bell Telephone Laboratories, Inc., Murray Hill, New Jersey
(Received April 19, 1960)

The velocity of the sidewise 180° domain-wall motion in single-crystal $BaTiO_3$ has been measured over a temperature range from 25° to 100°C as a function of the applied electric field. The velocity, described by $v=v_\infty \exp(-\delta/E)$, where δ is the activation field, E the applied electric field, and v_∞ the extrapolated wall velocity for $E=\infty$, increases by about four orders of magnitude with this increase in temperature. It was found that the temperature dependence of v lies primarily in δ and not in v_∞. The magnitude of δ decreases with increasing temperature and is also dependent on the impurity concentration in the crystal as well as the crystal thickness. The effects of impurities are most pronounced at room temperature, where $(1/\delta)(d\delta/dT)$ is 1% °C^{-1} for undoped samples and 2% °C^{-1} for Fe doped samples. Though δ itself is very sensitive to the sample thickness, $(1/\delta)(d\delta/dT)$ does not appear to depend on the crystal thickness. Additional data are required before a critical comparison can be made between experiment and theory.

INTRODUCTION

IN several recent investigations, the velocity of the sidewise 180° domain-wall motion in single-crystal BaTiO has been measured. These studies involved electrical [1,2] and optical measurements[3] of the growth rate of single domains as a function of the applied electric field for both liquid and metal electroded crystals. The sidewise wall velocity v is given by $v=v_\infty \exp(-\delta/E)$, where E is the applied electrical field, and δ and v_∞ are constants over a range of several decades of velocity. The temperature dependence of δ for a nucleation controlled wall motion mechanism is calculated[4] to be through $P_s^2 T^{-1} \epsilon_a^{-\frac{1}{2}}$. The quantity ϵ_a is the small signal dielectric constant measured perpendicular to the direction of the spontaneous polarization P_s. The predicted temperature dependence of δ was found to be in fair agreement with the limited published data.[2] The published data[2] on the temperature dependence of the wall velocity cover the temperature range of 20° to 30°C and give a change in δ of about 1%°C^{-1}. These previous measurements of wall velocity with temperature as a parameter were made with liquid electroded samples and were restricted to a small temperature range due to the inherent temperature instability of the aqueous liquid electrodes.

The electric field dependence of the wall velocity has been shown to be different for liquid electroded samples than for metal electroded samples.[2] It was suggested that this result may arise from differences in the nonferroelectric surface layers in the two cases, the layer being less effective in the liquid electroded samples than in those samples electroded with metal. Since the characteristics of the wall motion depend on the type of electrode, the temperature dependence of the wall velocity may also be different for these two types of electrodes.

This paper presents quantitative wall velocity measurements of metal electroded crystals over a temperature range from 25° to about 100°C. The effects on $(1/\delta)(d\delta/dT)$ due to variations in sample thickness and impurity dopings are described. A brief discussion comparing some of these results with theory is also given.

METHOD

Single-crystal $BaTiO_3$ plates were prepared in the usual manner.[5] Semitransparent Au electrodes 200 A thick, and 2.4 mm in diam, were evaporated on to opposite crystal plate faces and aluminum foil electrical leads were attached to the electrodes with air drying silver paste. The crystal was placed in a small heating oven adapted for transmitted light and the optical technique[6] of continuous direct observation of the domains during polarization reversal was employed.

An automatic voltage cycle was used to reverse the polarization. Each cycle consisted of a positive pulse 50 sec long of variable amplitude, followed by a 22 v, 50 sec long negative pulse and then a 50-sec interval with no voltage applied. Generally, reproducible domain configurations could be obtained in this manner. The wall velocities were calculated from measurements of the time for a domain wall to move through a known distance. A stop watch was used to measure the time interval of the domain wall movement so that an upper limit of about 10^{-2} cm/sec was imposed by this method on the measured values of the wall velocity.

Not every sample could be measured at elevated temperatures even though measurements of the wall velocity were possible at room temperature. Occasionally rough and irregular domain walls resulted when the temperature of the sample was increased. This phenomenon might be related to changes in the relative humidity. Changes in the relative humidity with constant temperature have had marked effects on the wall velo-

[1] R. C. Miller and A. Savage, Phys. Rev. **112**, 755 (1958).
[2] R. C. Miller and A. Savage, Phys. Rev. **115**, 1176 (1959).
[3] R. C. Miller and A. Savage, J. Appl. Phys. **31**, 662 (1960).
[4] R. C. Miller and G. Weinreich, Phys. Rev. **117**, 1460 (1960).
[5] R. C. Miller and A. Savage, J. Appl. Phys. **30**, 808 (1959).
[6] R. C. Miller and A. Savage, Phys. Rev. Letters **2**, 294 (1959).

city[5] and in some cases rough walls have resulted.[7] Some of the effects due to variations in the relative humidity are illustrated in Fig. 1, which shows data for a sample measured under two different conditions of relative humidity. The data for the lower and upper curve were taken at 25°C with 17 and 30% relative humidity, respectively. In the present experiments, the wall velocity measurements were made under conditions of approximately equal room relative humidity to avoid any effects that may result from differences in the room relative humidity.

Because the small oven used to heat the samples was not an isothermal enclosure, the sample temperature was obtained in the following way. The temperature, indicated by a thermocouple placed near the sample, was recorded at each point where the wall velocity was measured. In addition, P_s was measured by means of a 60-cps hysteresis loop as a function of the temperature indicated by the same thermocouple. These data are shown in Fig. 2 as the dashed curve. Then, part of the small oven jig, with the sample and thermocouple at-

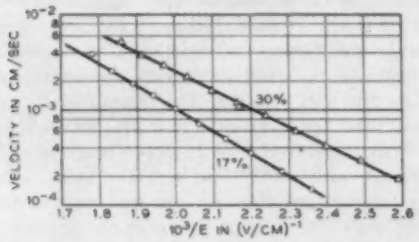

FIG. 1. Logarithm of the sidewise 180° domain-wall velocity vs the reciprocal of the applied electric field for a sample 1.2×10^{-2} cm thick measured under different relative humidity conditions. The data indicated by triangles were taken at 30% relative humidity while the circular points were taken at 17% relative humidity.

tached, was immersed in silicone oil and placed in a large oven. The 60-cps hysteresis loop was measured again as the temperature was increased. These data of $P_s(T)$ are the solid curve shown in Fig. 2. From the two curves in Fig. 2 and similar plots for other samples, an accurate temperature could be determined for each set of wall velocity data. At temperatures near the Curie point, the fields used were the minimum fields necessary for saturation of the hysteresis loop to avoid any alteration of the Curie point due to the applied field.[8] Curie point determinations from these measurements of $P_s(T)$ are in excellent agreement with the Curie points reported in other researches.[8,9]

RESULTS AND DISCUSSION

Increases in the domain-wall velocity as great as four orders of magnitude were observed for a temperature increase of about 75°C. Figure 3 shows wall velocity

[7] R. C. Miller and A. Savage (unpublished data).
[8] W. J. Merz, Phys. Rev. 91, 513 (1953).
[9] A. Nishioka, K. Sekikawa, and M. Owaki, J. Phys. Soc. Japan 11, 180 (1956).

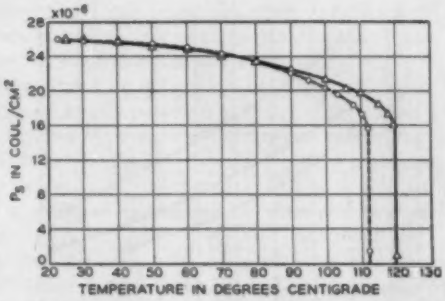

FIG. 2. P_s plotted as a function of T for a pure sample. The curve drawn through the circular points was obtained under the same conditions as the wall velocity measurements were taken. The curve through the triangular points was measured with the sample and thermocouple immersed in silicone oil.

data over a temperature range from about 25° to 100°C for two samples, each 1.2×10^{-2} cm thick. Curves 1 through 5 are for a "pure" sample (no impurities added to the growth melt) while curves 6 through 9 are for a sample whose growth melt contained 0.2 at. % Fe (hereinafter referred to as Fe-doped samples). The data for both samples, when plotted as in Fig. 3 could, in general, be fitted with straight lines. Extrapolation of the data to infinite field shows that the temperature dependence of v lies primarily in δ and not in v_∞. Some features of the room temperature data presented in Fig. 3 are not in agreement with data presented in an earlier paper.[5] In particular, δ for a pure sample de-

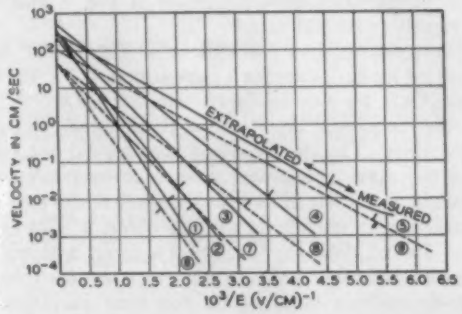

FIG. 3. Logarithm of the wall velocity vs E^{-1} for two samples, each 1.2×10^{-2} cm thick but with different impurity concentrations. The measured temperature range is from about 25° to 100°C. Curves 1 through 5 are wall velocities for a "pure" sample and curves 6 through 9 are wall velocity measurements for a sample whose growth melt contained 0.2 at. % Fe. The portions of the plots which extend to velocities higher than the short lines drawn normal to the curves are extrapolations. The sample temperatures are given below.

Curve	Temperature °C	Curve	Temperature °C
1	25	6	25
2	44	7	44
3	64	8	64
4	84	9	84
5	98		

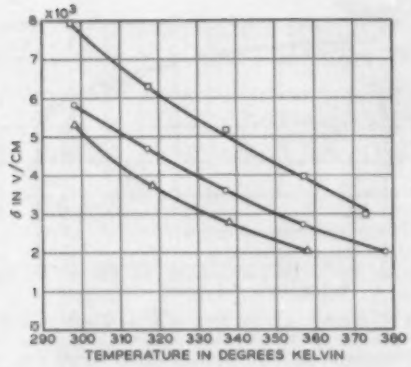

FIG. 4. Plots of the activation field δ vs T. The triangular and square points are for samples which had 0.2 at. % Fe added to the growth melt and which were 1.2×10^{-2} and 7.7×10^{-3} cm thick, respectively. The data indicated by circles are for a pure sample 1.2×10^{-2} cm thick.

scribed in the previous paper was smaller than the δ for an Fe-doped sample, whereas in the present research, the δ for a pure sample is higher than that for the Fe-doped sample. However, changes in relative humidity affect the wall velocity, and in addition, "identical" crystal lots, and in some cases crystals from the same lot, do not necessarily behave in the same manner.[3] Since the present data were taken under different relative humidity conditions than the earlier data, and the present crystals were also from different crystal batches, a meaningful discrepancy may not exist between the room temperature data presented in Fig. 3 and the previously published data.[3]

Three plots of δ vs T are shown in Fig. 4. The data indicated by circles are for a pure sample, 1.2×10^{-2} cm thick. Data for two Fe-doped samples, 1.2×10^{-2} and 7.7×10^{-3} cm thick, are shown as triangles and squares, respectively. The two Fe-doped samples did not come from the same crystal lot; in fact, the crystals were grown in somewhat different ways so that the two Fe-doped samples may be inherently different. However, these limited data for the two Fe doped samples of different thicknesses indicate that the pronounced thickness dependence of δ, which has been investigated previously at room temperature,[3] might still be present at elevated temperatures.

The data in Fig. 4 show that at room temperature, $(1/\delta)(d\delta/dT)$ is about 2%°C^{-1} for the Fe-doped samples and 1%°C^{-1} for the pure sample. Earlier work[3] with Fe-doped liquid electroded crystals gave a value of 1%°C^{-1} for the change of δ with temperature in the room temperature region. It is suggested that the variation of $(1/\delta)(d\delta/dT)$ with the impurity content of the crystal and the electrode material may arise from effects which originate in nonferroelectric surface layers.[3]

It has been proposed[4] that the temperature dependence of δ should be through $P_s^{\frac{2}{3}}T^{-1}\epsilon_a^{-\frac{1}{3}}$. Plots of δ vs $P_s^{\frac{2}{3}}T^{-1}\epsilon_a^{-\frac{1}{3}}$ are shown in Fig. 5. The ϵ_a used in the calculations of the data are the clamped crystal values measured by Benedict and Durand.[10] The data in Fig. 5 show that plots of δ vs $P_s^{\frac{2}{3}}T^{-1}\epsilon_a^{-\frac{1}{3}}$ are not straight lines as predicted. It should be pointed out that if one uses the more or less constant value of ϵ_a as calculated from the Devonshire theory,[10,11] the plots of δ vs $P_s^{\frac{2}{3}}T^{-1}\epsilon_a^{-\frac{1}{3}}$ are nearly straight lines; however, we have no reason to doubt the experimental data on ϵ_a.

One difficulty encountered in this comparison between theory and experiment is the effect of nonferroelectric surface layers which were not considered in the theoretical calculation of δ.[4] The wall velocity data given in Fig. 3 show that for a given v, e.g., 10^{-3} cm sec^{-1}, δ/E is practically constant independent of temperature. One implication of this is that, as stated earlier, v_∞ is not a function of temperature. Therefore, the field E_1 required for $v=10^{-3}$ cm/sec, and δ must have the same temperature dependence. It has been shown[3,12] that E_1 can be written

$$V_1/d \equiv E_1 = E_b(1+d_0/d), \qquad (1)$$

in which V_1 is the applied voltage required for $v=10^{-3}$ cm/sec, d is the crystal thickness, E_b is the average field in the bulk ferroelectric portion of the crystal, and d_0 characterizes the effects of the nonferroelectric surface layers on the wall velocity. The quantities E_b and d_0 are constants[3] for a given v and are 400 v/cm and 5×10^{-3} cm, respectively, for Fe-doped material at room temperature with $v=10^{-3}$ cm/sec. The field E_b is the driving force responsible for the wall motion and is reduced below the average value of the applied field E_1 as a result of nonferroelectric surface layers. Therefore, E_b, and not E_1, should vary with temperature as $P_s^{\frac{2}{3}}T^{-1}\epsilon_a^{-\frac{1}{3}}$. Experimental data on the temperature dependence of E_b and d_0 have not been obtained. The

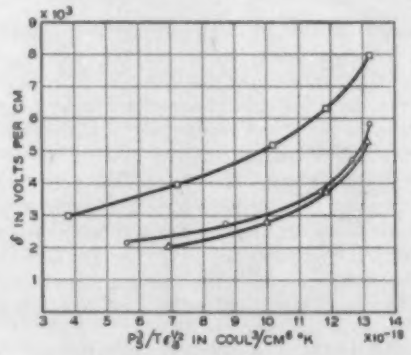

FIG. 5. The activation field δ plotted against $P_s^{\frac{2}{3}}T^{-1}\epsilon_a^{-\frac{1}{3}}$. The points indicated by triangles and squares are for samples which had 0.2 at. % Fe added to the growth melt, and which were 1.2×10^{-2} and 7.7×10^{-3} cm thick, respectively. The circular points are for a pure sample which was 1.2×10^{-2} cm thick.

[10] T. S. Benedict and J. L. Durand, Phys. Rev. **109**, 1091 (1958).
[11] A. F. Devonshire, Phil. Mag. **42**, 1065 (1951).
[12] M. E. Drougard and R. Landauer, J. Appl. Phys. **30**, 1663 (1959).

most recent surface layer model[3,12] assumes that a charge of $2P_s$ per unit area is deposited on the interface between the bulk ferroelectric material and the surface layer behind the advancing 180° domain wall and that this charge distribution results in a lowering of the average field in the bulk from E_1 to E_b. In time, the charge on the interface is assumed to be neutralized through some unspecified mechanism. With this model, for $d \gg l$

$$d_0 = 16\pi\gamma P_s l/\epsilon_l E_b, \tag{2}$$

where $2l$ is the total surface layer thickness (a layer of thickness l on each side of the specimen), ϵ_l is the dielectric constant of the layer, and γ is the effective fraction of unneutralized charge on the interface. It does not appear possible to estimate the temperature dependence of d_0 because, e.g., the process by which the charge neutralization takes place is not even known. Therefore, a critical test of the theory (i.e., the temperature dependence of E_b) cannot be made at this time. It should be remarked that on the basis of past experience, we do not believe that a calculation of the temperature dependence of d_0, and hence E_b, from the present data for the two Fe-doped samples would lead to a meaningful result. As already noted, the two samples were not grown in the same manner; however, even if they had come from the same crystal batch, the normal sort of scatter of these data[3] would require that more than two samples be considered.

Comparison of data given by Merz[13] with the data presented in this paper show that the activation field α determined from switching transient studies by Merz and the activation field δ do not have the same temperature dependent characteristics. In Fig. 4, the plot $\delta(T)$ has a different general shape than the plot of $\alpha(T)$ given by Merz. Also, if $\delta(T)\times T$ is plotted vs T, the resulting curve does not look similar to the spontaneous polarization P_s[13] vs T curve found by Merz for $\alpha(T)\times T$ vs T. It has been shown that under certain conditions α and δ should be similar.[1] However, in general, α and δ are presumably different in that α not only contains a contribution due to wall motion (i.e., δ), but also a contribution from the nucleation rate of new domains. Therefore, it is not surprising that α and δ do not exhibit the same temperature dependent characteristics.

ACKNOWLEDGMENTS

The authors would like to express their appreciation to R. C. Linares and J. P. Remeika for the crystals used in this research.

[13] W. J. Merz, Phys. Rev. **95**, 690 (1954).

JOURNAL OF APPLIED PHYSICS VOLUME 31, NUMBER 9 SEPTEMBER, 1960

Circuit Dynamics of the Pinch*

J. Killeen and B. A. Lippmann
Lawrence Radiation Laboratory, University of California, Livermore, California
(Received May 3, 1960)

Instead of analyzing a portion of an hydromagnetic pinch apparatus in detail, and replacing the remainder by a boundary condition, the entire pinch apparatus is treated here as a single dynamical system. A circuit equation and a mechanical equation, coupled together, result. These equations describe the dynamical development of the pinch and exhibit explicity its dependence on the physical parameters (electrical and mechanical) of the system. As examples, the equations have been used to analyze the snow-plow model and the adiabatic pinch, yielding curves that show the geometrical development of the pinch in time, as well as the distribution of mechanical and magnetic energies at any stage. Analogous analyses may be made for other physical quantities of interest, and can be used to adjust the parameters of the system so as to optimize specific pinch characteristics.

I. INTRODUCTION

IN this paper, we wish to analyze the dynamics of a pinch tube, including the reaction back on the energy source. That is, in contrast to the usual procedure, which considers the pinch tube in detail and replaces the remainder of the apparatus by a boundary condition,[1] we propose to treat the pinch tube and the auxiliary equipment that is coupled to it as a single dynamical system.

The main reason for including the external circuitry in the dynamical description is that we thereby include reaction effects in the analysis. The analysis then furnishes quantitative information concerning the geometrical development of the pinch in time, the amount of energy delivered to the pinch tube, the division of this energy between the magnetic field and mechanical motion, the voltages and currents at arbitrary times, etc. In short, the analysis is capable of providing detailed descriptions of the time variation of all the physical quantities that are of interest for design or diagnostic purposes, and, indeed, the equations to be discussed here have been used for these purposes at Livermore for some time.

* This work was performed under the auspices of the U. S. Atomic Energy Commission.
[1] R. Garwin, A. Rosenbluth, and M. Rosenbluth, Los Alamos Rept. 1850 (1954).

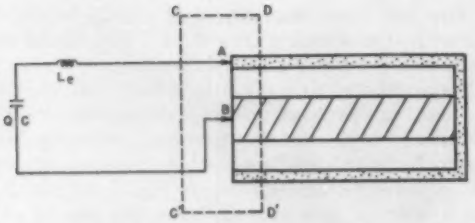

FIG. 1. The pinch tube and its associated circuitry. The plasma region is shaded with lines, the tube walls with dots.

In Sec. 2 we present a detailed discussion of the dynamical equations. Although we consider the simplest case only, where the fields in the pinch tube correspond to the dominant mode in coax, we also discuss how the analysis may be extended to cover more complicated situations. The dynamical equations are specialized, in Sec. 3, to apply to the snow-plow model and to the adiabatic pinch. Numerical analyses appropriate to both cases are presented in Sec. 4.

2. DYNAMICAL EQUATIONS

Our analysis is based on a model which regards the plasma as a perfectly conducting fluid and the outer wall of the pinch tube as a perfect conductor. We also assume that no external magnetic fields are present, i.e., we analyze a simple unstabilized pinch. The extension to a stabilized pinch (external H_z field) seems to offer complications in detail but not in principle.

We start with the arrangement shown in Fig. 1. Here, the pinch tube is formed by two coaxial cylinders. The plasma, shown shaded, forms the inner cylinder while the conducting wall of the pinch tube constitutes the outer cylinder. The plasma is assumed to move radially only; it always retains its cylindrical shape. As drawn, the geometry of Fig. 1 seems to apply only to a specialized form of pinch tube. However, this is not really so, and Fig. 1 may be applied to toroidal or similar geometries if the minor radius of the torus is very much less than its major radius.

The apparatus external to the pinch tube has been shown in circuit-symbolic form in Fig. 1. L_e is the external inductance, C is the capacity of the condenser bank, and Q is the charge stored in the bank. The dissipation of the external circuit has been assumed to be negligible; if it is not, its influence may be included by adding a resistance, of the proper value, in series with the other circuit elements..

The symbolic representation of the apparatus to the left of the dotted line CC' by a circuit diagram implicitly assumes that the electromagnetic field problem has been solved and that the fields to the left of CC' can be described by a single mode, with C and L_e being defined in the usual way in terms of the stored electric and magnetic energies in this mode. More generally, the electromagnetic field to the left of CC' would require several modes for its description; in that case, the circuit to the left of CC' would no longer be a simple series combination of L_e and C (and, perhaps, R), but would require one such circuit for each mode, with all the modes coupled both to one another and to the structure on the right of CC'. Since the theory of guided waves shows in detail how such mutually coupled modes, whether existing on waveguides, wires, or other structures, can be represented by means of equivalent circuits, we feel that a more elaborate discussion of these matters is unnecessary here.

Similar remarks hold for the region to the right of DD'. Although in the general case several modes, all coupled to one another and to the region to the left of DD' are required, in the present instance we assume that the electromagnetic field to the right of DD' can be adequately described by a single mode, namely, the principal mode in coax. Moreover, in our case this principal mode is short-circuited at the right-hand end of the pinch tube. Since the pinch tube, and indeed the entire apparatus, is assumed to be small compared with the distance characteristic of the spatial variation of the electromagnetic fields (wavelength), we conclude that the entire structure to the right of DD' is electrically equivalent to a single inductance L defined, as customary, in terms of the magnetic energy stored in the pinch tube.

We now come to the consideration of the region $CC'DD'$, which couples L to the C, L_e circuit. On the left of this region the electromagnetic field consists of a single mode; on the right, too, only a single mode is present. However, the geometries of these modes are quite different from one another, so the field in the transition region can become quite complicated. The nature of the field in $CC'DD'$ determines the character of the equivalent circuit used to represent the coupling between the regions on each side, i.e., the circuit that couples L to C and L_e. The assumption that only a single mode exists on each side of $CC'DD'$ means that the coupling circuit can be represented by a four-terminal network, the reactive elements of which account for the stored electromagnetic energy present in $CC'DD'$, while the resistive elements account for the energy dissipated in this region, either by radiation or Joulean heating

Fortunately in the cases of interest to us, the stored energy and the Joulean heating in the region $CC'DD'$ are negligible; furthermore, since all dimensions are small compared with a wavelength, the electromagnetic radiation from $CC'DD'$ may also be ignored. As a consequence, the equivalent circuit for $CC'DD'$ contains neither resistive nor reactive elements; in fact, the coupling network reduces to an ideal transformer. If we now choose the usual definitions of current and voltage, the transformer ratio turns out to be 1:1, and we have, as the final result, that L is simply connected in series with L_e and C at the points A and B.

According to this discussion, the electromagnetic fields on the structures in Fig. 1 can be completely described by considering a simple circuit in which C, L_e, and L are connected in series. This justifies us in replacing the field problem by the circuit equation

$$(Q/C)+(d/dt)(L_e+L)I=0. \tag{1}$$

We emphasize that Eq. (1) describes only the simplest possible situation—namely, only one mode to the left of CC', one mode to the right of DD', and the coupling between the two modes being equivalent to a simple series connection of the circuits representing the fields in each of the two regions. In contrast, the most general case would require a set of modes to describe the fields to the left of CC' and another set for the fields to the right of DD'. Each mode would have its own equivalent circuit and interactions among the modes of each set would be represented by elements coupling the equivalent circuits to one another. In this more general situation, then, the region to the left of $CC'DD'$ would be represented by a complex group of networks, mutually coupled together; similarly, for the region to the right of $CC'DD'$. The two complexes are coupled by a network representing the region $CC'DD'$, including the radiation and Joulean heating in this region.

With these qualifications, we return to Eq. (1). We note that the L that appears in Eq. (1) is a function of the radius R_p of the plasma cylinder. This gives us two variables R_p and Q [$I=dQ/dt$]. We therefore need another equation to fix the dynamics of the problem completely.

The additional equation is obtained from the following considerations. First, we apply Poynting's theorem to the volume of the pinch tube to the right of DD'. The resulting relation confirms the conservation of energy in the pinch-tube region, for it states that the rate at which energy enters the tube through the surface DD' [which rate is given by $Id/dt(LI)$, since we have assumed the field to the right of DD' corresponds to the principal mode only] is equal to the rate of increase of the magnetic energy within the tube plus the rate of doing mechanical work on the plasma. Or, if W is the rate at which mechanical work is done on the plasma, we have

$$I(d/dt)(LI)=W+(d/dt)(\tfrac{1}{2}LI^2). \tag{2}$$

From this, we find the additional equation we have been seeking

$$\begin{aligned} W&=\tfrac{1}{2}I^2(d/dt)(L)\\ &=[(d/dt)(\tfrac{1}{2}LI^2)]_{I=\text{const}}. \end{aligned} \tag{3}$$

Equations (2) and (3) express a familiar theorem: If external sources are used to maintain the currents constant during a displacement, the sources supply energy in the form of mechanical work and in the form of magnetic field energy at equal rates.

The quantity W is simply related to the magnetic stress-tensor $\mathbf{T}$ and the surface velocity of the plasma $\mathbf{v}$ by

$$W=-\int_{\substack{\text{plasma}\\ \text{surface}}} \mathbf{dS}\cdot\mathbf{T}\cdot\mathbf{v}. \tag{4}$$

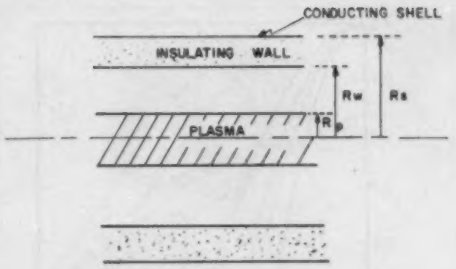

FIG. 2. Cross sections through the pinch tube showing the coordinates used.

In dyadic form, $\mathbf{T}$ is given by

$$4\pi\mathbf{T}=\mu\mathbf{HH}-\tfrac{1}{2}\mu\mathbf{H}^2\mathbf{I}, \tag{5}$$

where, μ is the permeability and $\mathbf{I}$ is the unit dyadic.

The combination of Eqs. (3) and (4) furnishes an alternative statement of the mechanical equation

$$\tfrac{1}{2}I^2(d/dt)(L)=-\int_{\substack{\text{plasma}\\ \text{surface}}} \mathbf{dS}\cdot\mathbf{T}\cdot\mathbf{v}. \tag{6}$$

The dynamical behavior of the pinch is completely described by the circuit Eq. (1) and the mechanical equation in the form of (3) or (6). In these equations, C and L_e are prescribed constants, I is $\dot{Q}$ and $\mathbf{v}$ is $\dot{R}_p$. For the coaxial geometry we have been considering, L is a known function of R_p, and H is a known function of R_p and I. Hence, if R_p, $\mathbf{v}$, Q, and I are given at $t=0$, the pair of coupled equations, (1) and (6), permits us to determine the subsequent behavior of all the mechanical and electrical variables that enter into the description of the pinch.

3. MECHANICAL MODELS

In order to carry the analysis further, we must commit ourselves to a definite model of the plasma. That is, L may be computed, since the geometry has already been settled upon, but in order to compute the rate at which work is done on the plasma, we require some assumption concerning its mechanical properties. Two models in current use are both simple and solvable, the snow-plow model and the adiabatic model, we shall consider each of them in turn, taking the geometry of the plasma and the pinch tube to be coaxial in both cases. The coordinates that describe the pinch tube are exhibited in Fig. 2. R_p is the plasma radius, R_w is the radial distance to the insulating wall, and R_s is the corresponding distance to the outer, conducting shell.

With the field conforming to the dominant mode in

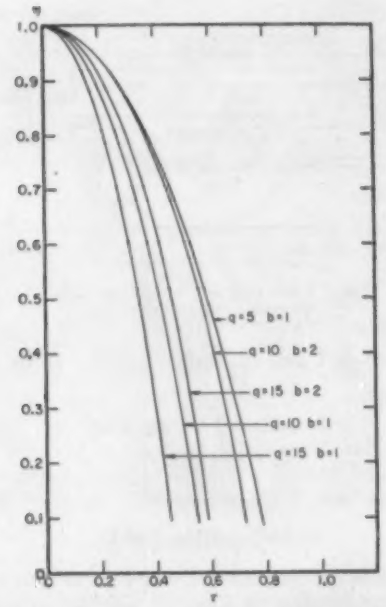

FIG. 3. Radius of the plasma layer as a function of time.

coax, the total inductance (in henries) is

$$L_c+L=2\times10^{-9}l_p\{b+\ln(R_w/R_p)\}, \qquad (7)$$

where

$$b=(L_c/2\times10^{-9}l_p)+\ln(R_a/R_w),$$

and l_p is the length of the pinch tube (in cm). Note that

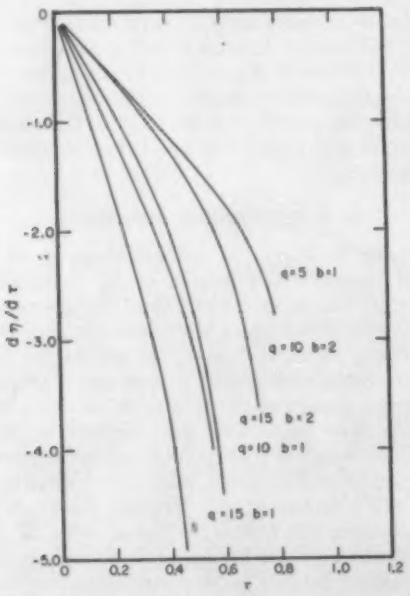

FIG. 4. Velocity of the plasma layer as a function of time.

we are using cgs practical units; i.e., electrical quantities are expressed in practical units, mechanical quantities in cgs units.

The snow-plow model assumes that the pinch develops as follows: Originally, the plasma fills the pinch tube to the radius of the insulating wall R_w. At some later time, the radius of the plasma is R_p, and all the plasma that initially was present between R_w and R_p has been scooped up into a thin layer lying on the surface of the plasma and moving with the velocity of the plasma surface $\dot{R}_p$. If ρ_0 is the original plasma density, according to this model the mechanical equation becomes

$$d/dt\{(R_w^2-R_p^2)dR_p/dt\}=-(I^2/100\pi\rho_0R_p).$$

In dimensionless form, this equation becomes

$$d/d\tau\{(1-\eta^2)d\eta/d\tau\}=-(1/\eta)(dq/d\tau)^2, \qquad (8)$$

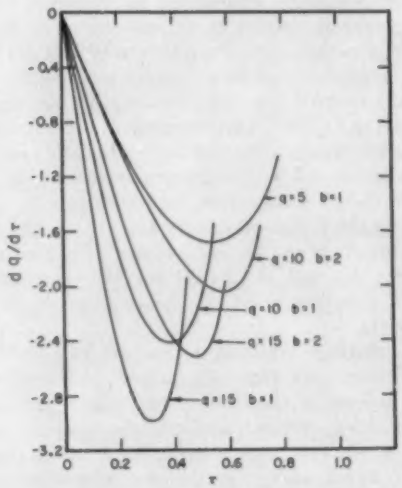

FIG. 5. Current as a function of time.

where τ is defined by Eq. (11) below and we have put $I=\dot{Q}$, and

$$q=Q/10R_w^2(\pi\rho_0)^{\frac{1}{2}}; \quad \eta=R_p/R_w. \qquad (9)$$

On turning to the circuit equation, (1) becomes, indimensionless form,

$$q+d/d\tau\{(b-\ln\eta)dq/d\tau\}=0, \qquad (10)$$

where q and η are given by (9) and

$$\tau=t(2\times10^{-9}l_pC)^{-\frac{1}{2}}. \qquad (11)$$

Equations (8) and (10) describe the dynamics of the pinch according to the snow-plow model. Typical solutions of these equations are discussed in the next section.

For the adiabatic model, the circuit equation is unaltered; that is, Eq. (10) is again applicable, but the mechanical equation must be derived anew. This is done by noting that the mechanical behavior of the

model is completely specified by the adiabatic condition

$$p v^{\gamma} = \text{const.} \tag{12}$$

In effect, (12) is equivalent to integrating (3).

The only pressure that acts, in the adiabatic model, is that due to the field. Thus $p \sim (I/R_p)^2$. The volume of the plasma varies as R_p^2; hence (12) can be written, in dimensionless form, as

$$(dq/d\tau)\eta^{\gamma-1} = (dq/d\tau)_0, \tag{13}$$

where $(dq/d\tau)_0$ is the value of $(dq/d\tau)$ at $t=0$.

We now introduce another dimensionless variable

$$\bar{q} = q/(dq/d\tau)_0 = (Q/I_0)(2\times 10^{-9} l_p C)^{-\frac{1}{2}}, \tag{14}$$

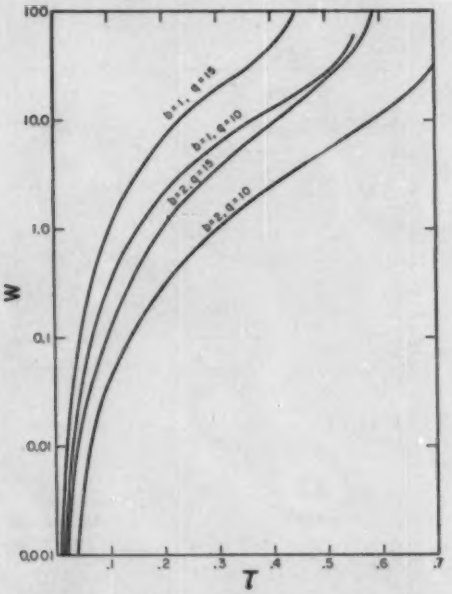

FIG. 6. Rate of doing mechanical work in the snow-plow model as a function of time.

and we note that

$$I = I_0 d\bar{q}/d\tau. \tag{15}$$

In terms of these variables

$$\bar{q} + (d/d\tau)\{(b - \ln\eta) d\bar{q}/d\tau\} = 0, \tag{16}$$

and

$$(d\bar{q}/d\tau)\eta^{\gamma-1} = 1. \tag{17}$$

These are the appropriate equations for discussing the dynamics of the adiabatic pinch. Solutions of (16) and (17) are presented in the next section.

Finally, we consider the energy relations in the system. If we write U_m for the magnetic energy, $U_m = \frac{1}{2}LI^2$, we find that

$$W = (A/2)(dq/d\tau)^2 d/d\tau(b - \ln\eta), \tag{18}$$

and

$$dU_m/dt = (A/2) d/d\tau\{(b - \ln\eta)(dq/d\tau)^2\}, \tag{19}$$

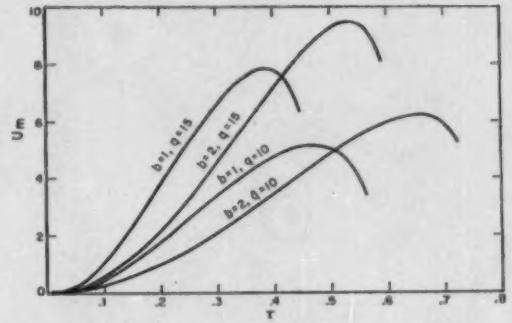

FIG. 7. Magnetic energy in the snow-plow model as a function of time.

where

$$A = 100\pi\rho_0 R_m^4/(2\times 10^{-9} l_p C^2)^{\frac{1}{2}}. \tag{20}$$

Another useful quantity is ψ, the rate at which energy leaves the pinch tube through the surface DD'. From (2)

$$\psi + W + dU_m/dt = 0, \tag{21}$$

while, from (18), (19), and (10),

$$\psi = A d/d\tau(\tfrac{1}{2}q^2). \tag{22}$$

The expressions given in Eqs. (18), (19), and (22) are useful for determining, on the basis of energy flow, just how efficient a given pinch apparatus may be.

4. NUMERICAL ANALYSIS

We now present some results obtained by solving the equations presented in specific cases.

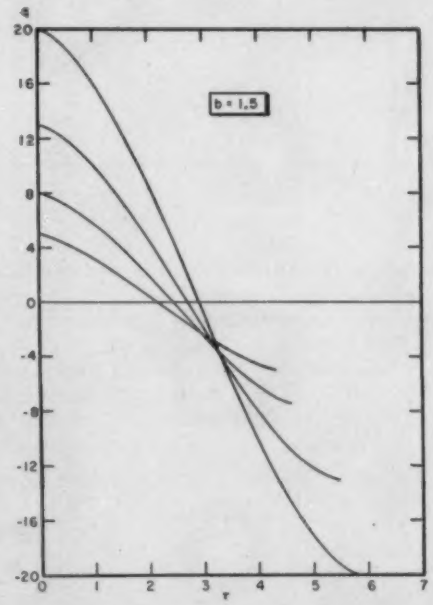

FIG. 8. Charge as a function of time, for $b=1.5$.

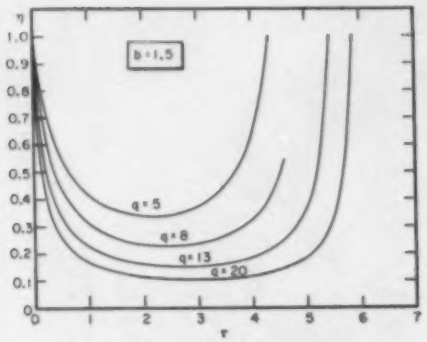

FIG. 9. Radius of the plasma layer as a function of time, for $b=1.5$.

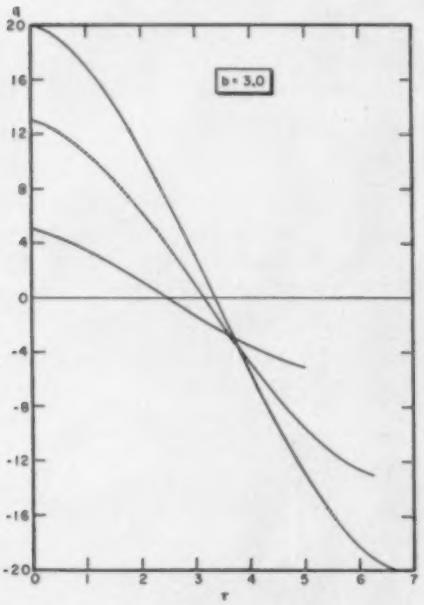

FIG. 10. Charge as a function of time, for $b=3.0$.

As an example of a solution of the equation that are applicable to the snow-plow model, we consider a device studied at Livermore.[2] It is of linear pinch with the following parameters: $l_p=30$ cm; $R_w=15$ cm; $R_s=16.5$ cm. The parameters of the external circuit are $L_0=10^{-7}$ h; $Q=5.61$ coul; $C=18.7\times10^{-6}$ farads. These characteristics yield the values $q(0)=10.6$; $b=1.86$.

The curves shown in Figs. 3–7 are those for $q(0)=5$, 10, 15, and $b=1$, 2. In Fig. 3 we show $\eta(\tau)$, which gives the position of the imploding current sheath as a function of time. In Fig. 4 $d\eta/d\tau$ is plotted, which gives the velocity of the sheath, while in Fig. 5 the current is shown.

The energy balance is exhibited in Figs. 6 and 7, where W and U_m are plotted for the cases enumerated.

The parameters chosen as a typical example of the adiabatic model were adapted from the published[3] values for the large pinch device Zeta as follows: $R_s=50$ cm; $R_w=53.5$ cm; $L_0=3.3\times10^{-6}$ h; $l_p=1160$ cm; $C=0.13$ farad; $Q=360$ coul (25 kv); $I_0=50\times10^3$ amp. With these values, $b=1.5$ and $q(0)=13$, γ was taken to be 2.

Figures 8–11 show the results obtained using the equations of the adiabatic model for $b=1.5$, 3.0 and

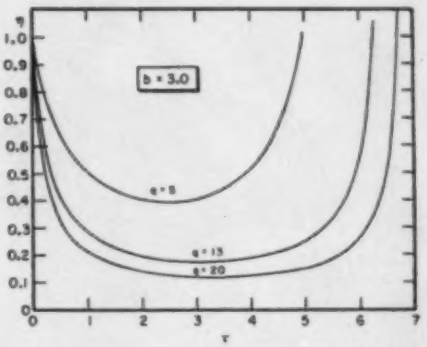

FIG. 11. Radius of the plasma layer as a function of time, for $b=3.0$.

$q(0)=5$, 8, 13, 20. As noted in the foregoing, $q(0)=13$ corresponds to a voltage of 25 kv on the bank. Also, we note that the current is obtained from $1/\eta$ by using the relations (15) and (17) (with $\gamma=2$):

$$I=I_0 dQ/d\tau=-I_0/\eta.$$

For $q(0)=13$ and $b=1.5$, the peak current is about 300 kamp. One notes that the shape of the waveform exhibited in Fig. 9 seems to correspond to the oscilloscope traces shown in the published report on Zeta.

ACKNOWLEDGMENTS

The analytical part of this work was performed in the summer of 1957, when one of the authors (B. A. Lippmann) was a consultant to UCRL; it was stimulated by conversations with Dr. Stirling Colgate.

[2] S. A. Colgate, University of California Radiation Laboratory Rept. UCRL-5010-T (1957).

[3] P. C. Thoneman *et al.*, Proc. 2nd Conf. Peaceful Uses Atomic Energy **32**, 42 (1958).

JOURNAL OF APPLIED PHYSICS VOLUME 31, NUMBER 9 SEPTEMBER, 1960

Irradiation Effects and Short-Range Order in Fused Silica and Quartz*

R. A. WEEKS AND C. M. NELSON
Solid State Division, Oak Ridge National Laboratory,† Oak Ridge, Tennessee
(Received January 21, 1960; and in final form May 23, 1960)

The eigenvalues of the g tensor of an irradiation produced defect of the quartz structure have been found to be $g_1=2.0003$, $g_2=2.0006$, $g_3=2.0018$. The data on the center are consistent with the assignment of $S=\frac{1}{2}$. Assuming that the hyperfine interaction with Si^{29} ($I=\frac{1}{2}$ and 4.7% abundant) is negligible, the envelope of the line is calculated for 4 widths of the line. Good agreement is found between the calculated envelope for a width of 0.2 oe and the envelope observed in γ-ray and in neutron-irradiated ($\leq 10^{18}$ fast neutrons/cm^2) silica. The observed envelope deviates from the calculated envelope for increasing neutron irradiation. It is suggested that a correlation of the Si-O tetrahedra, similar to α-quartz, exists around any point in the more common forms of silicas and has a diameter of ≥ 5 A.

INTRODUCTION

A NUMBER of paramagnetic defects of the quartz structure produced by neutron irradiation have been observed by electron-spin-resonance techniques (ESR) at room temperature[1–3] in silica and quartz single crystals. For neutron irradiations $>4\times10^{19}$ fast neutrons/cm^2, the ESR spectra in silica is the same as that observed in a single crystal.[4] For neutron irradiations $<4\times10^{19}$ fast neutrons/cm^2, many lines are observed in a single crystal,[1] and the relation of the individual lines to their envelope which is observed in silica is not obvious. In the case of one group of lines observed in a single crystal, the envelope observed when the crystal was crushed, was compared with the spectra of silica, and a reasonable correspondence of the envelopes was found.[1]

This particular defect has been labeled E_1'.[5] A tentative model for this defect is that it is due to an electron trapped at an oxygen vacancy.[5] The eigenvalues of the g tensor have been found.[6] Knowing these values it is possible to calculate the envelope of the lines in the single crystal when they are summed over random orientations. A calculation of this kind has been made for a paramagnetic impurity found in some silicas.[7] A similar calculation for the E_1' center is described below. The calculated envelope is compared with the envelope observed in various silica specimens which have been given a variety of irradiation treatments. Close agreement is found for γ-ray irradiation and for neutron doses $\leq 10^{18}$ fast neutrons/cm^2. In heavily neutron-irradiated ($>4\times10^{19}$ fast neutrons/cm^2) single crystals and silicas, the envelopes are the same but differ from the initial envelope observed in the silica.

EXPERIMENTAL APPARATUS

The ESR measurements were made with a superheterodyne bridge spectrometer. In this spectrometer the frequency of the signal oscillator is controlled by the specimen cavity. The signal-oscillator frequency is, therefore, always the same as the specimen cavity. This arrangement means that the detected signal is pure absorption; there is no admixture of the dispersion signal. Such a spectrometer is particularly useful for the observation of the ESR line shapes at high concentrations of magnetic centers. The measurements were all made at room temperature.

EXPERIMENTAL RESULTS

(a) Specimens

Two varieties of silica were used in the experiments and measurements described below. These were Amersil O.G.1 and Corning 7940. The single-crystal specimens were Brazilian quartz obtained from the Cambridge Thermionic Corporation and synthetic quartz grown by General Electric Company, Ltd. In the succeeding discussion, no distinction between the natural and synthetic crystals is necessary.

(b) Single Crystals

In the single crystal the E_1' center was found to have the following eigenvalues[7a] for the spectroscopic splitting factor:

$$g_1=2.0003, \quad g_2=2.0006, \quad g_3=2.0018,$$

where subscripts refer to the coordinate system of the g tensor. The relative accuracy of these values was ±0.0001, the absolute accuracy ±0.0005. There are 6

* A preliminary report of this paper was presented at the American Physical Society Meeting, Cambridge, Massachusetts, March, 1959. Bull. Am. Phys. Soc. 4, 159 (1959).

† Oak Ridge National Laboratory is operated by Union Carbide Corporation for the U. S. Atomic Energy Commission.

[1] R. A. Weeks, J. Appl. Phys. 27, 1376 (1956).

[2] C. M. Nelson and R. A. Weeks, Bull. Am. Phys. Soc. 3, 136 (1958).

[3] R. A. Weeks and C. M. Nelson, see footnote reference 5.

[4] R. A. Weeks, *Proceedings of the 13th Annual Symposium on Frequency Control*, (U. S. Army Signal Research and Development Laboratory, Fort Monmouth, New Jersey), p. 37.

[5] R. A. Weeks and C. M. Nelson, J. Am. Ceram. Soc. (to be published).

[6] Unpublished data of R. H. Silsbee and R. A. Weeks, Solid State Division, Ann. Progr. Rept. for period ending August 30, 1956, ORNL-2188.

[7] R. H. Sands, Phys. Rev. 99, 1222–25 (1955); J. W. Searl, R. C. Smith, and S. J. Wiard, Proc. Phy. Soc. (London) 74, 491 (1959).

[7a] See appendix for orientation of eigenvalues with respect to the crystalline lattice.

possible orientations of the g tensor in the unit cell. These orientations, with respect to the crystalline axis, were also determined for this g tensor.[8]

It is assumed that the defects are randomly located in the lattice, and that their concentration is such that there are no cooperative effects. The only possible hyperfine interactions are with Si^{29} whose nuclear spin $I=\frac{1}{2}$. Since this isotope of silicon has natural abundance of 4.7%, such interactions are assumed to be negligible. The experimental evidence is consistent with the assumption that the defect has a spin of $S=\frac{1}{2}$. The spin Hamiltonian $\mathcal{H}$ can then be written as

$$\mathcal{H}=\beta H\cdot g\cdot S \quad (1)$$

$$=\beta(H_1g_1S_1+H_2g_2S_2+H_3g_3S_3), \quad (2)$$

where β is the Bohr magneton and H is the applied magnetic field at some arbitrary orientation relative to g. The energy of the transition induced by an applied oscillating-magnetic field at right angles to H is

$$h\nu=\beta H(g_3^2\cos^2\Theta+g_1^2\sin^2\Theta\cos^2\Phi+g_2^2\sin^2\Theta\sin^2\Phi)^{\frac{1}{2}}, \quad (3)$$

where the angle Θ is with respect to the direction of g_3, and Φ is with respect to g_1.

(c) Comparison of Calculated Envelope Shape with Observed Envelope Shape

In the silica, all orientations of the crystalline field are equally probable, and a summation over all orientations is required. By using Eq. (3), the fraction of centers $f(H_0)$, contributing to the envelope at a field between H_0 and (H_0+dH), can be calculated for values of $h\nu/g_1\beta\leq H_0\leq h\nu/g_3\beta$. Up to this point, the line in the single crystal has been assumed to have no width. The calculation can thus be extended by introducing a finite linewidth. With the introduction of the finite linewidth, an amplitude $A(H)$ at any field H can be found. In calculating the envelope shape expected for the silica, it has been assumed that the line shape is of Lorentzian form. The contribution of each fraction of centers $f(H_0)$ from $h\nu/g_1\beta\leq H_0\leq h\nu/g_3\beta$, at some field H, can be found by multiplying the equation for a Lorentzian line and the appropriate expression for $f(H_0)$ determined from Eq. (3) and then integrating from

$$H_1=h\nu/g_1\beta \text{ to } H_2=h\nu/g_2\beta.$$

The amplitude $A(H)$ is, therefore,

$$A(H)=\int_{H_1}^{H_2}\frac{T_2/\pi}{1+C^2T_2^2(H_0-H)^2}f(H_0)dH_0, \quad (4)$$

where T_2 has been chosen such that the maximum amplitude of the line is T_2/π as is customary.[8] This form does not include cutoff terms.[9] Since the line is observed to saturate at low-power levels ($\sim 100\,\mu$w input to the cavity), it has been assumed that T_1, the spin-lattice relaxation, is quite long. It, therefore, has not been included in the expression for the line shape. C^2 is a constant. The function $f(H_0)$ is evaluated from

$$h\nu/g_1\beta\leq H_0<h\nu/g_2\beta \text{ and } h\nu/g_3\beta<H_0\leq h\nu/g_3\beta. \quad (5)$$

The term $f(H_0)$ has a singularity at $H_0=h\nu/g_3\beta$. In the region of $H_0=h\nu/g_3\beta$, the finite linewidth eliminates the singularity. Because of the difficulty of obtaining an analytic solution of Eq. (4), a numerical integration was performed using 9 values of H_0 and 12 values of H.

In order to assess the effect of linewidth in the single crystals on the shape of the envelope observed in the silicas, calculations were made for four different widths assuming the Lorentzian line shape. The results of the calculations are shown in Fig. 1. As can be seen, a factor of 4 change in linewidth alters the envelope only slightly. The linewidth in single crystals has been observed to vary from 0.06 to 0.5 oe from specimen to specimen. As Fig. 1 indicates, the envelope shape is not very sensitive to a change in the linewidth over the range that has been experimentally observed.

The envelopes observed for this center in various silicas given different irradiation treatments are compared with the envelope calculated for a linewidth of 0.2 oe in Fig. 2. The silicas and single crystal were given a heat treatment of 300°C for 30 min prior to recording the envelope shape. This heat treatment eliminates the E_2' center.[5] Good agreement is found between the observed envelope for the gamma-ray irradiated silica (Fig. 2, curves 1, 2) and the calculated envelope. The silica irradiated with $\sim 10^{18}$ fast neutrons/cm^2 (Fig. 2, curve 3) also is in reasonable agreement with the calculated envelope. The heavily irradiated silica (Fig. 2, curve 4) shows a much greater departure

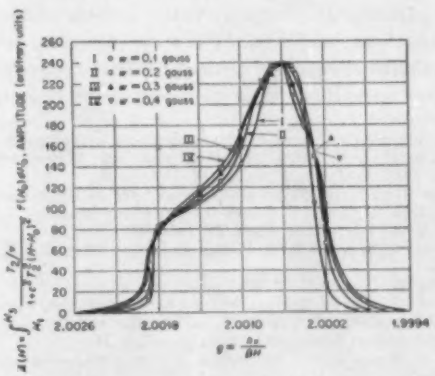

FIG. 1. The effect of linewidth on the envelope shape is shown assuming the shape of the line for the four different widths is Lorentzian. Since $w\ll H_0$, an approximation to the Lorentzian was used.

[8] D. J. Ingram, *Free Radicals as Studied by Electron Spin Resonance* (Butterworth Publications, Ltd., London, 1958), p. 128.

[9] C. Kittel and E. Abagams, Phys. Rev. **90**, 238 (1953).

from the calculated envelopes. The concentration of paramagnetic centers contributing to this line in these specimens ranges from approximately 10^{17} cm^{-3} for the gamma-ray irradiated silicas to $\sim 3\times 10^{19}$ cm^{-3}. In the latter case the concentration of centers is quite high, $\sim$0.1 at. %, and magnetic interactions between the different ESR centers give rise to a dipole-dipole broadening.[10] The broadening of the line (Fig. 2, curve 4) in the heavily irradiated silica is evident, and there is an apparent alteration in the shape of the envelope. There are three factors which will determine the envelope in the silicas: (1) magnetic interactions between centers, (2) alteration of the crystalline field which determines the eigenvalues of the g tensor, and (3) the generation of a different center at high neutron dose. For the silica which had been given a dose of $<10^{15}$ fast neutrons/cm^2 (Fig. 2, curve 3), the broadening in the wings of the envelope suggests that (1) is probably the primary factor. In the heavily irradiated material (Fig. 2, curve 4), all three of these factors probably determine the envelope shape.

DISCUSSION

The comparison of the envelope calculated from the eigenvalues of the g tensor of the E_1' center with the envelope observed in silica has borne out the association of a defect in a single crystal with one found in silica.[1] The agreement between the observed envelope and calculated envelope makes the identification of the defect in the two different materials quite certain.

There is an additional implication in this agreement. The anisotropy of the g tensor is determined by the crystalline-field interaction of the surrounding atoms on the orbital state of the paramagnetic center. The dominant interaction is then with the nearest neighbor atoms. The agreement of the observed envelope shape and that calculated from single-crystal parameters suggests that the crystalline-field interactions are the same in both cases; however, the present model for silica is one in which the Si-O tetrahedra are randomly oriented with respect to each other.[11] The foregoing results suggest that there may be a short-range correlation of the Si-O tetrahedra.

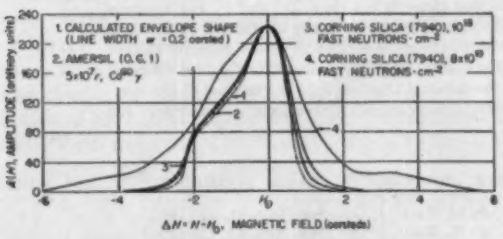
1. CALCULATED ENVELOPE SHAPE (LINE WIDTH w = 0.2 oersted)
2. AMERSIL (O. G. 1)
3. CORNING SILICA (7940), 10^18 FAST NEUTRONS · cm^-2
4. CORNING SILICA (7940), 8×10^19 FAST NEUTRONS · cm^-2
A(H), AMPLITUDE (arbitrary units)
ΔH = H − H0, MAGNETIC FIELD (oersteds)

FIG. 2. The shape of the envelope calculated for $w=0.2$ oe is compared with the envelope shape observed in various silicas given different irradiation treatments. The linewidth w is defined as the halfwidth at half-maximum amplitude.

For the purpose of estimating the range of this apparent correlation, the model for this defect that has been suggested will be accepted. The g tensor would then be determined primarily by the way in which these Si atoms were affected by the vacancy and the three remaining O atoms on each Si. The approximate distance from the vacancy to the nearest O atoms is $\sim$2.6 A, and the next-nearest shell of O atoms is $\sim$3.2 A.[12] From these atom spacings, it seems reasonable to conclude that in the silicas the orientation of the Si-O tetrahedra with respect to each other varies slowly with respect to a distance between 5 and 10 A. Thus, around any point in the silica there is a high degree of correlation in the positions of the atoms. The correlation extends over a distance $\geq$5 A. Neutron-diffraction studies have shown the existence of diffraction peaks.[13] The results of Breen *et al.*[14] apparently support the model in which the Si-O tetrahedra are randomly oriented with respect to the surrounding tetrahedra about the Si-O-Si bond[11]; however, small-angle x-ray scattering has given evidence of scattering regions of $\sim$30 A diam.[15] Other objections to the random structure proposed on the basis of earlier x-ray data have been made.[16–18] In view of these objections to the completely random model and the ESR envelope-shape data presented above, it is reasonable to conclude that in those silicas which we have studied there exists a correlation of the Si-O tetrahedra around any point, similar to the α quartz. This correlation probably extends over a region $\geq$5 A. This condition is required by the ESR data on the gamma-ray irradiated silica since the defects produced are assumed to be of random distribution. The order may extend to a greater distance. Tilton[19] has suggested that such an ordering may be produced by a form of crystallization that is self-limiting.

Neutron irradiation ($\sim 10^{18}$) of silica (Corning 7940 or Amersil) produces the same center as gamma irradiation. The envelope shape, however, is slightly different. From the data it cannot be determined whether the change in envelope shape is due to magnetic interactions of the centers or to alterations in the crystalline field. There is an indication that it may be due to a broadening of the lines which comprise the envelope (Fig. 2, curve 3). With prolonged neutron irradiation, the envelope shape in the silicas and single crystals alters.

[10] J. H. Van Vleck, Phys. Rev. **74**, 1168 (1948).
[11] G. W. Morey, *The Properties of Glass* (Reinhold Publishing Corporation, New York, 1954), p. 564.
[12] R. W. G. Wychoff, *The Structure of Crystals* (The Chemical Catalog Company, Inc., New York, 1931).
[13] I. W. Ruderman, Phys. Rev. **78**, 317 (1950).
[14] R. J. Breen, R. M. Delaney, P. J. Persiani, and A. H. Weber, Phys. Rev. **105**, 517 (1957).
[15] E. R. Lippincott, J. Research Natl. Bur. Standards **61**, 65 (1958).
[16] T. C. Hoffman and W. O. Stratton, Nature **176**, 561 (1955).
[17] W. A. Weyl, J. Soc. Glass Technol. **35**, 421 (1951).
[18] C. L. Babcock, S. W. Barber, and K. Fajans, Ind. Eng. Chem. **46**, 161 (1954).
[19] L. W. Tilton, J. Research Natl. Bur. Standards **59**, 139 (1957).

After such treatment, the envelope shape is the same in both materials.

CONCLUSIONS

(a) The agreement of the envelope shape calculated from single-crystal parameters and the envelope observed in the silicas for the E_1' center is a reasonable proof that the resonance observed in the two materials arises from the same defect.

(b) An implication of the envelope-shape data is that a short-range correlation of the Si-O tetrahedra exists in certain silicas, e.g., Corning 7940 and Amersil. This correlation probably extends over the Si-O tetrahedra surrounding any point in the material and may be characterized as similar to the α phase in crystalline quartz.

(c) Heavy neutron irradiation apparently alters this order in silicas as it does in a single crystal.

ACKNOWLEDGMENTS

The contributions of H. C. Schweinler through many discussions are gratefully acknowledged. Our appreciation of the many useful suggestions of J. H. Crawford, Jr., and R. H. Silsbee is also to be noted. Rod Lide and Warren Pegram have assisted in many of the measurements. C. S. Brown, General Electric Company, Ltd. Wembley, England, very generously supplied specimens of synthetic quartz.

APPENDIX

Orientation of g Tensors with Respect to Crystal Axes

Axis	g_1	g_2	g_3
$\Delta g \times 10^4$	12.2±0.3	−0.5±0.3	−3.1±0.2
θ, deg	67.0±1.5	57.5±7	48±11
ϕ, deg	12.1±1.3	−93.5±3.3	127±17

The principal values of the g tensor are given as departures from the g measured with the applied field along the c axis ($g_{c\ axis}=2.0006\pm0.0003$). The appropriate directions for the other 5 lines may be obtained by setting $\theta'=\theta$ and $\phi'=\phi\pm120°$ and also $\theta'=(180°-\theta)$ and $\phi'=-\phi\pm120°$ or $-\phi$, where the angle θ is with respect to the c axis ([00.1]) and the angle ϕ is with respect to a principal axis ([10.0]) in the basal plane. The errors are based on the scatter in the results for the 6 lines, and no estimate of the magnitude of systematic errors has been made.

JOURNAL OF APPLIED PHYSICS VOLUME 31, NUMBER 9 SEPTEMBER, 1960

Some Electrical Properties of Amorphous Selenium Films*

RICHARD A. FOTLAND
Horizons, Inc., Cleveland, Ohio

(Received March 25, 1960; and in final form May 16, 1960)

The dark current and photocurrent characteristics of amorphous selenium and arsenic-selenium alloy films have been investigated. One millisecond after the application of an electric field, the dark current (neglecting capacitance charging) is several orders of magnitude higher than the steady-state dark current. A hysteresis effect is observed in the dark volt-ampere curves with the descending voltage branch exhibiting an exponential volt-ampere relationship. The voltage of a charged Se plate in the dark discharges logarithmically with time as anticipated from the exponential volt-ampere relationship. Upon admitting air to a freshly evaporated Se plate, a negative surface potential of 150 mv is observed. The phenomenon of "fatigue" (i.e., the temporary increase in dark current following an exposure to illumination) obtained with highly absorbed radiation indicates surface barrier effects exert a large measure of control over dark currents. Photogenerated holes and electrons in Se films are trapped with trapping parameters such that the hole range/unit field is on the order of 10^{-6} cm²/v, and the electron range is less than 10^{-9} cm²/v. The addition of As to the Se greatly increases the electron effective lifetime. Trapped holes are eliminated in the dark exponentially with time through a process having an activation energy of 0.77 ev. A 40-mv negative surface photovoltage is observed in Se films upon illumination. This voltage may be accounted for by hole diffusion away from the surface. The addition of As to Se extends the spectral response into the red end of the spectrum, results in the initiation of secondary photocurrent effects, intensifies fatigue effects, and increases the softening temperature of the film.

THE occurrence of photoconductivity in the amorphous form of selenium appears to have been first noted in 1948.[1,2] Since that time several papers have appeared concerning the photoconductivity,[3–10] dark currents,[10–16] optical absorption,[17–22] and struc-

* This work was supported by Haloid Xerox, Inc.

[1] R. M. Schaffert and C. D. Oughton, J. Opt. Soc. Am. **38**, 991 (1948).
[2] P. K. Weimer, Phys. Rev. **97**, 171 (1950).
[3] M. A. Gilleo, J. Chem. Phys. **19**, 1291 (1951).
[4] M. A. Gilleo, Bull. Am. Phys. Soc. **26**, 43 (1951).
[5] P. K. Weimer and A. Danforth Cope; R C A Rev. **12**, 312 (1951).
[6] P. H. Keck, J. Opt. Soc. Am. **41**, 53 (1951).
[7] P. H. Keck, J. Opt. Soc. Am. **42**, 221 (1952).
[8] Von Manfred Keller and Martin Ploke, Z. angew. Physik, **7**, 562 (1955).
[9] F. I. Kolomoitsev and F. F. Kodzhespirov, Zhur. Tekh. Fiz. **27**, 899 (1957).
[10] V. M. Fridhin, Doklady Akad. Nauk. U.S.S.R. **118**, 273 (1958).
[11] M. K. Shidlovskii, Zhur. Tekh. Fiz. **24**, 837 (1954).
[12] F. Echart, Ann. Physik **17**, 84 (1956).
[13] R. A. Hyman, Proc. Phys. Soc. (London) **B69**, 743 (1956).
[14] W. E. Spear, Proc. Phys. Soc. (London) **B69**, 1141 (1956).

ture[23–25] of this material. This form of selenium is used in photoconductive-type television camera tubes although its largest use at present is in xerography.

The investigation described here was undertaken in order to obtain some general ideas concerning certain mechanisms associated with the behavior of the insulating form of selenium used in xerography. In this form of photography a vacuum vapor deposited amorphous Se film, perhaps 50 μ thick, is electrostatically charged to a potential of several hundred volts with respect to a conducting substrate. While in the dark, the magnitude of this potential suffers a small dark decay. Upon exposure, the light-struck areas discharge to some low potential. The remaining charge on the dark areas may be thought of as a latent image which is developable by virtue of the electrostatic attraction between this image and small particles. These small particles, usually some form of carbon, adhere to the selenium plate in the unexposed areas to form a positive image. The "fatigue effect" referred to later involves the phenomenon whereby a previous exposure to illumination in an uncharged condition changes the properties of a Se film in some manner for a certain period of time. In severe cases this effect may last several days.

INSTRUMENTATION AND SAMPLE PREPARATION

The majority of the cell measurements were obtained with the aid of a Bausch and Lomb 150-mm grating spectrophotometer fitted with a mechanical shutter and a series of neutral density filters, a Keithley model 303-dc indicating amplifier, and a long-persistence oscilloscope.

Mobilities and trapping times were determined using a cathode-ray tube as a pulsed light source which would generate an intense spot of blue light (P16 phosphor) on the sample for a period of 2×10^{-7} sec at repetition rates of 30 to several hundred pulses/sec. The sample was connected in series with a biasing dc voltage source and an amplifier whose input resistance is R. Shunting this resistance is C, the sum of the input, wiring, and sample capacities. The time constant RC was adjusted to be equal to several times the transit time so that, for times on the order of (or shorter than) the transit time for charge carriers in the film, the potential developed across R is proportional to the charge on C which is proportional to the charge displacement due to the motion of the carriers within the film. The transport of only 10^5 electrons (1.6×10^{-14} coul) across a Se film may be observed with this equipment.

[16] W. E. Spear, Proc. Phys. Soc. (London) **B70**, 669 (1957).
[17] R. Eppe, Z. angew. Physik, **9**, 261 (1957).
[18] M. A. Gilleo, J. Chem. Phys. **19**, 1291 (1951).
[19] P. D. Fochs, Proc. Phys. Soc. (London) **B69**, 70 (1956).
[20] C. Hilsun, Proc. Phys. Soc. (London) **B69**, 506 (1956).
[21] J. J. Dowd, Proc. Phys. Soc. (London) **B64**, 783 (1957).
[22] W. J. Choyke and Lyle Patrick, Phys. Rev. **108**, 25 (1957).
[23] R. S. Caldwell and H. Y. Fan, Phys. Rev. **114**, 664 (1959).
[24] M. P. Givens, C. J. Keoster, and W. L. Goffe, Phys. Rev. **100**, 1112 (1955).
[25] H. Stegman, Naturwissenschaften, **44**, 108 (1957).
[26] H. Krebs and Schultze-Gebhardt, Acta Cryst. **8**, 412 (1955).

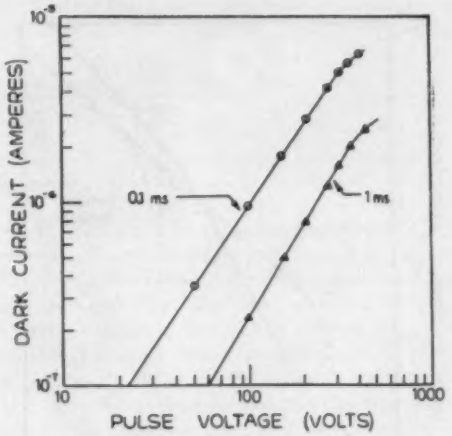

FIG. 1. Initial dark current in selenium films.

Measurements of the surface potential on Se films were made using a modification of the Kelvin technique. This method has been described elsewhere in some detail.[26]

The dark-decay measurements were obtained with the aid of a transparent conducting glass probe spaced a few millimeters above the photoconductor plate. This probe fed a Keithley model 210 electrometer. The output of the electrometer was recorded as a function of time on an Esterline-Angus strip-chart recorder. The ratio of the probe-plate capacity to the electrometer input capacity is 1:50.

The Se cells were prepared by the vacuum vapor deposition of Se upon either brass or conducting glass substrates. The starting material consisted of xerographic-grade selenium obtained from Haloid Xerox, Inc. Spectrographic analysis indicated the following impurities to be present:

Element	Cu	Fe	Te	Hg	S	Cl
ppm	0.5	2	4	1	nil	5

The material to be vaporized was heated in an Alundum crucible with a resistance heater. The crucible-substrate distance was 12 in., and the power input to the heater was regulated so that a 40-g charge of Se would be completely evaporated during a period of approximately 1 hr. In order to satisfy this requirement, the temperature of the molten Se was kept near 240°C. The thickness of the deposited films was determined with a measuring microscope to be near 50 μ.

The front electrodes were formed by the vacuum deposition of gold through a $\frac{1}{4}$-in. diam mask.

DARK CURRENTS

Several films were examined in order to determine (1) the transient dark current obtained by applying a

[26] *Semiconductor Surface Physics* (University of Pennsylvania Press, 1957), p. 297.

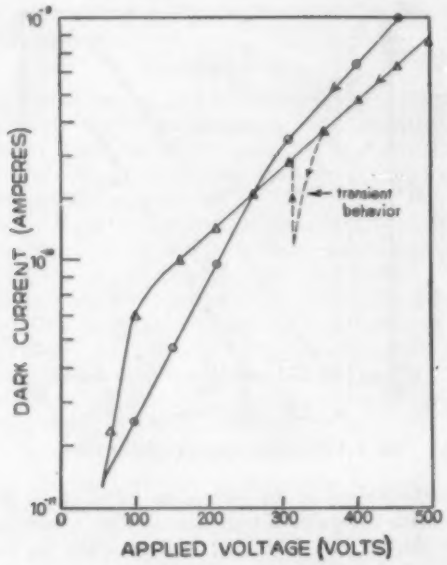

FIG. 2. Steady-state dark currents in selenium films.

voltage step to a sample, (2) the steady-state dark current, and (3) the dark decay of an electrostatically charged photoconductive film.

A graph indicating the relationship between the applied voltage and the magnitude of the dark current, 0.1 msec and 1.0 msec after the application of the voltage step, is shown in Fig. 1. Since 0.1 msec corresponds to 100 time constants (the time constant being the RC product for the test apparatus), the displacement current is only 10^{-80} the initial current or approximately 10^{-88} amp.

Figure 2 shows a typical steady-state dark current curve. The transient nature of the current changes is indicated on this graph. Attempts were made to fit the data to a Schottky plot since certain information in the literature[11,27] indicates the resistance of Se is controlled by Schottky barriers. Such attempts were unsuccessful. These steady-state currents are over three orders of magnitude smaller than the transient dark currents.

Recordings were made of the dark-discharge characteristics of several Se plates. Figure 3 shows typical voltage-discharge plots of a Se plate and discharge curves for an area of the plate covered with a gold electrode. In all cases the unfatigued curves were obtained after the plates had rested in the dark overnight, while the fatigued-plate measurements were obtained immediately after exposing the uncharged plate to tungsten illumination. Assigning a decay constant α equal to the voltage decay/natural logarithmic decade, we obtain an α of 100 v/decade for the unfatigued plate and 190 v/decade for the same plate in the fatigued condition.

The surface potential of Se was measured as the selenium was deposited on a brass plate and as air was subsequently admitted to the evaporating chamber.

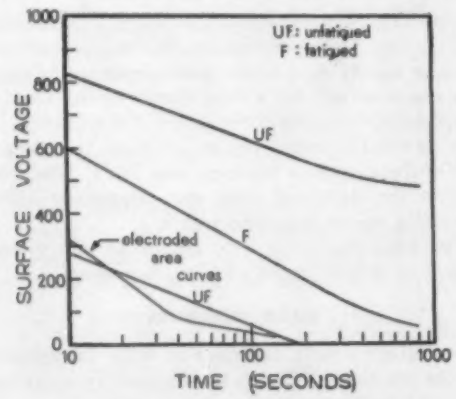

FIG. 3. Voltage-decay curve for an unelectroded and an electroded selenium film.

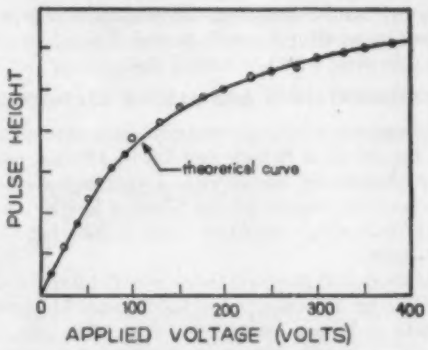

FIG. 4. Hecht curve for a selenium film.

Upon evaporating the film, the surface potential change was -0.04 v. After a 5-μ film was formed the vacuum was broken and the surface potential rose to -0.15 v.

PHOTOEFFECTS

Charge Transport

The transport of charge liberated by illumination absorbed in selenium is easily studied by the techniques originally developed by Gudden, Pohl, and Hecht in the 1920's. Recently, Spear[15] has determined carrier mobilities in amorphous selenium.

The measurement is performed by connecting a film, biased with a voltage V_0, in series with a resistor R (the amplifier input resistance). C is the sum of the sample capacity and all shunting capacities as mentioned previously. At time $t=0$, a short burst of highly absorbed illumination is applied to the surface of the Se. The photoelectrons are immediately neutralized at the

[27] M. Kuwagata, E. Otsuka, and M. Tomura, J. Phys. Soc. (Japan) 9, 300 (1954).

anode while the photogenerated holes travel across the film as a sheet of charge moving at a velocity

$$v=\mu E_0=\mu V_0/d,$$

where d is the film thickness. If the transit time for the holes is smaller than $RC/10$ sec, then the effect of R during the transit time is negligible. As the charge moves across the film, a charge

$$q=n_0 ex/d$$

is induced on C; n_0 is the number of holes in the moving sheet and x is the distance from the plate front surface to the charge. This leads to a voltage

$$V=n_0 et/CT_r \quad \text{for} \quad O<t<T_r$$

appearing across C. Here T_r is the transit time. For

$$T_r<t<RD/10, \quad V=n_0 e/C.$$

Then

$$\mu=d^2/T_r V_0.$$

By measuring T_r and d, μ is readily determined.

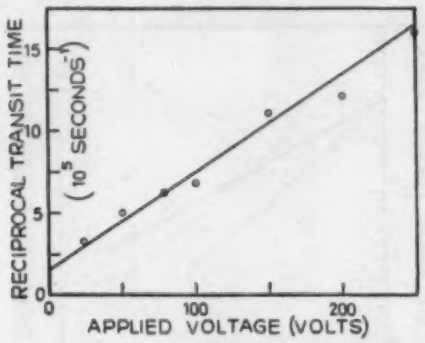

FIG. 5. Reciprocal transit time vs applied voltage for a selenium film.

This simple analysis is complicated since some of the excited carriers are trapped (held immobile) during the transit. It is logical to assume that the rate of trapping is proportional to the number of carriers at any time. Then the number trapped will vary exponentially with time or

$$n_t=n_0(-e^{-t/T}),$$

where T is a parameter characterizing the rate of trapping. After traveling a distance x there will therefore remain

$$n=n_0 e^{-t/T}=n_0 e^{-x/\mu E_0 T}=n_0 e^{-x/W},$$

where W is the carrier range which is equal to the distance a carrier will travel in a time T. By integrating the contributions to the input capacity charge provided by the trapped carriers and adding to this the number of charges crossing the film, we obtain

$$q/n_0 e=\mu E_0 T/d(1-e^{-d/\mu E_0 T})$$

for the pulse height. Now, if a plot of the pulse height vs applied voltage is made, the foregoing equation may be fitted to these data by choosing the proper μT. This parameter $\mu T=r$, the range/unit field, is an important parameter in describing the effectiveness of an insulating photoconductor. For the condition $W \gg d$, the pulse rise is equal to the transit time of the carriers; the mobility is easily determined by obtaining the slope of a $1/T_r$ vs V_0. At low fields where $W<d$, a majority of the carriers are trapped and the rise time is determined by the trapping time. In Fig. 4 it may be seen that a good fit to the theoretical curve is obtained. Figure 5 shows the corresponding mobility determination plot.

TABLE I. Charge transport properties of selenium.

Plate description	μ_+ cm²/v-sec	μ_- cm²/v-sec	T_+ μsec	T_- μsec	r_+ cm²/v	r_- cm²/v
Se	0.72	0.003[a]	0.13	<0.5	9.3×10^{-3}	$<0.2\times10^{-3}$
Se plus 0.5 mole % As	0.067	0.001	0.47	18	3.1	1.8

[a] See footnote reference 15.

Table I summarizes the calculated parameters for a Se film and for an As-Se alloy film. In the case of selenium, the μ_+ value is about five times greater than that obtained by Spear. Since electron pulses were unobservable in our apparatus, the value of μ_- from Spear is quoted together with an upper bound for T_-.

The effective field, i.e., the internal field may be reduced from V_0/d by the trapping of photoexcited carriers. For this reason, the transit-time measurements were performed so that a picture of the crt trace was obtained very shortly after the voltage was applied to a cell. The repetition rates of the applied illumination pulses are reduced as much as practical.

An experiment was performed in order to examine the field reduction due to trapping. A plate made of Se+0.5 As whose carrier range was previously determined was used for this experiment. With 124-v applied voltage, it was calculated that 75% of the photoexcited

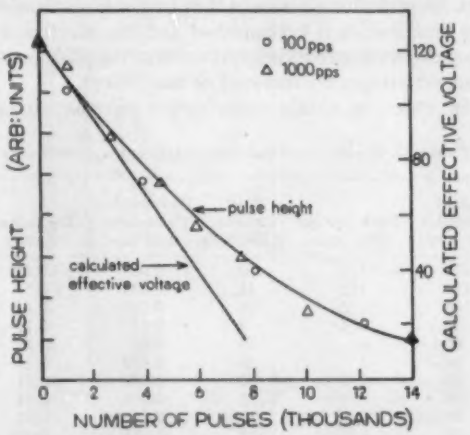

FIG. 6. Pulse height vs number of illuminating pulses.

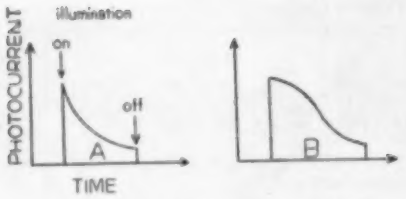

FIG. 7. Typical photocurrent transients.

holes would be trapped before crossing the film. From both the pulse height vs applied voltage curves and the output pulse height from a calibrated photomultiplier it was determined that each illumination pulse produced 10^{-12} coul of charge. Since the cell capacity was 5×10^{-11} farads, each illumination pulse would then reduce the internal field by 0.015 v. At voltages below 200 v, the transit-time current pulse is proportional to the effective field. Therefore, the pulse height and the effective field should decrease linearly and at the same rate with the number of applied pulses.

Figure 6 shows that this does occur until an effective voltage of approximately 60 v is reached. Furthermore, this effect is independent of the pulse repetition rate and hence independent of time over the interval examined.

Photocurrent Transients

Because of the trapping effects present in selenium, large steady photocurrents are not observed. The presence of blocking-type contacts prevents the internally trapped charge from being immediately neutralized. Upon application of the illumination, a photocurrent is observed which decays with time (Fig. 7) as a fraction of the photoexcited carriers are trapped thereby reducing the internal field. The photocurrent decay time τ_d is arbitrarily defined as the time required for the photocurrent to decay to $1/e$ of its initial value although the transient decay is not, in general, exponential. After the termination of the photocurrent transient, the illumination is extinguished and the effective field starts increasing to its original value as the photoexcited trapped charges are removed or neutralized.

In order to obtain quantitative information concerning these processes, a selenium plate was investigated to determine (1) the effect of illumination upon the photocurrent transient and (2) the effect of storing a previously illuminated plate in the dark for varying lengths of time. The illumination was monochromatic having a wavelength of 4000 A and the applied voltage was 200 v; the illuminated transparent gold electrode being held positive with respect to the base.

TABLE II. Results of photocurrent transient measurements.

Light intensity (μw/cm^2)	Dark storage time (min)	Peak current $\times10^{-7}$ amp	Photocurrent pulse decay time (sec)	Total charge (μcoul)
200	1/2	60	0.033	0.11
140	1/2	41	0.033	0.1
80	1/2	30	0.040	0.14
20	1/2	8	0.15	0.11
80	3	36	0.07	0.25
80	1	36	0.054	0.19
80	1/2	30	0.037	0.11
80	1/4	22	0.018	0.04
80	1/12	10	0.018	0.02
80	1/60	2	0.018	0.004

Table II summarizes the results and experimental conditions. During the second part of the experiment, the plate was first subjected to one second illumination and the plate was allowed to rest in the dark, with the voltage still applied, a length of time known as the dark-storage time. At the end of this time the photocurrent transient was obtained.

It can be seen from the data that the total charge passed is fairly independent of the illumination and that the peak current varies approximately linearly with the illumination. The results of the second part of the experiment are shown graphically in Fig. 8 where it

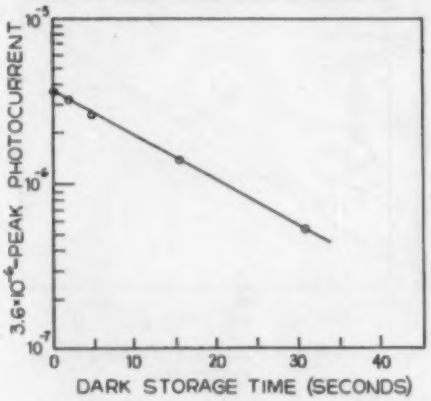

FIG. 8. Photocurrent transient recovery.

appears that the peak photocurrent i_p is related to the dark-storage time τ_s by the relationship,

$$i_p=3.6\times10^{-6}(1-e^{-\tau_s/16}) \text{ amp.}$$

In Fig. 8, the difference between the largest photocurrent and the photocurrent of time t is plotted vs t. Figure 7(a) illustrates the form of the transient obtained after a fraction of a minute dark-storage time. The transient of Fig. 7(b) was observed after dark-storage times greater than 1 min. When the illuminated electrode of this plate is made negative, the photocurrent transients are reduced over two orders of magnitude indicating that the electron range is less than the hole range.

A depolarizing activation energy U_p may be assigned to the process responsible for reducing the trapped polarization charge during dark storage. Figure 9 indicates an activation energy U_p of 0.75 to 0.80 ev for this process. These experiments were performed with the

positive electrode illuminated so that the trapped carriers possessed a positive charge.

Measurements of the photocurrent transients provide a rapid means of evaluating carrier ranges. Some photocurrent transient effects were investigated in four selenium plates prepared under different conditions. These plates were prepared from a different selenium supplier. Plates prepared from this material possessed a lower fatigue and a larger electron range. Table III lists the coating parameters and some observations concerning the photocurrent transients.

It appears that low-coating temperatures greatly reduce the electron range while medium-coating temperatures and long-coating times increase the range. The hole range is not appreciably effected by these variables.

TABLE III. Effects of some coating variables on the photocurrent transients.

Sample No.	Coating time (min)	Substrate coating temp. (°C)	Hole transient decay (sec)	Electron transient decay (sec)	Photocurrent ratio (i_+/i_-)	Photovoltage (mv)
A	60	61	0.04	0.04	7.5	−9
B	20	76	0.04	0.10[a]	0.87	0.6
C	60	66	2	2	2.3	−3.6
D	20	66	0.04	0.25	1.0	0.8

[a] Secondary effects observed at high voltages.

TABLE IV. Results of transient photovoltage experiments.

Light intensity ($\mu w/cm^2$)	Rise time to 90% of peak (sec)	Peak photovoltage (mv)	Initial rise of photovoltage (mv/sec)
120	...	41	...
12	0.02	39	3000
6	0.033	34	1600
3	0.058	28	1100
0.6	0.23	18	170

Photovoltaic Effects

The photovoltage of a typical high-fatigue Se film was found to be of such a polarity that the illuminated electrode was negative. The magnitude of the photovoltage was found to be independent of the voltmeter input resistance as long as the input time constant was larger than the photovoltage rise time. Table IV summarizes the results obtained by varying the illumination. A 30-sec dark-storage time was utilized in this experiment. The illumination was monochromatic having a wavelength of 4000 A.

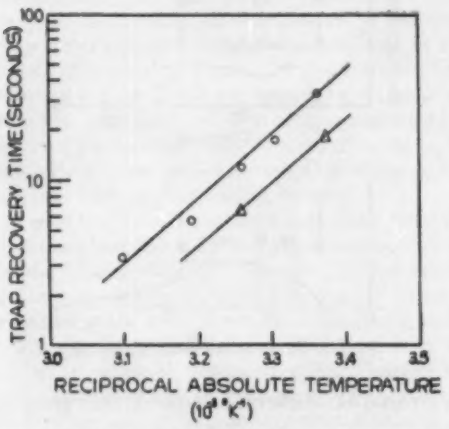

FIG. 9. Photocurrent transient recovery time constant vs reciprocal temperature.

Figure 10 illustrates the effect of dark-storage time upon the magnitude of the photovoltage. For short times, the recovery is exponential with a time constant of 17 sec. An illumination of 2 $\mu W/cm^2$ was used in this experiment.

In general, plates possessing nearly equal positive and negative photocurrent transient amplitudes were observed to possess saturated photovoltage generally n the range of +1 to +5 mv. Plates possessing a larger r_+/r_- exhibited a negative photovoltage on the order of 20–50 mv.

Spectral Response

Figure 11 illustrates the effect of the applied voltage upon the spectral response of an amorphous selenium plate. In this figure, the photocurrent peaks are normalized at 4000 A. At 6000 A the normalized transient photocurrent was almost doubled as the applied voltage was increased from 100 to 600 v.

One effect of adding As to Se (the As being alloyed with the Se in a sealed Pyrex tube before evaporation) is to extend the spectral response of an Se-25% As plate as shown in Fig. 12.

Secondary Effects

Photoconductors having secondary effects are generally recognized as possessing quantum yields greater than unity and relatively long decay times. Effects such

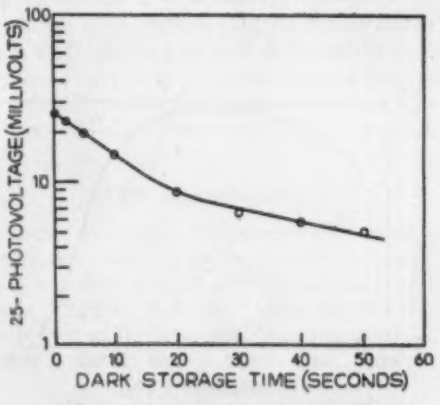

FIG. 10. Photovoltaic transient recovery.

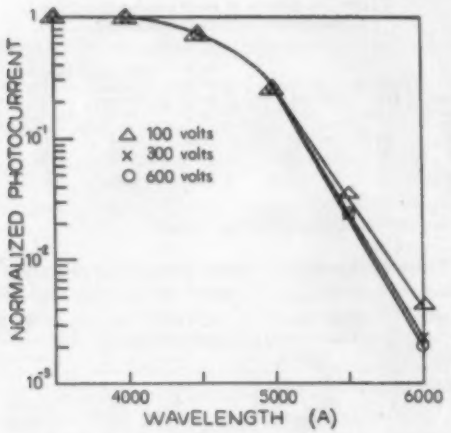

FIG. 11. Spectral response of selenium film for different applied voltages.

as these have been observed in a selenium cell prepared at a substrate temperature of 76°C (Sample B, Table III) and measured under high field conditions, and Se 25% As plates.

In the case of the selenium cell, the secondary current was observed only when the illuminated electrode was negative and at applied fields greater than 60 kv/cm. At the onset of the secondary effect, the peak photocurrent jumped by a factor of ten and the waveform changed from the conventional transient to that shown in Fig. 13. The quantum yield was approximately five under these conditions.

With an Se-25% As plate the situation is somewhat reversed. The secondary effects were exhibited only when the positive electrode is illuminated. Hole currents exhibiting quantum yields of three to four were obtained. A typical hole current transient waveform is also shown in Fig. 13. The transients obtained with the negative electrode illuminated appeared normal except for wavelengths longer than 5500 A. Beyond this point, the decay time of the photocurrent, after the illumination was extinguished, increased rapidly. This effect is undoubtedly due to hole effects arising as the penetration depth of illumination increases.

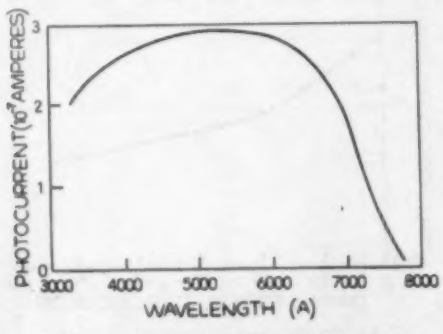

FIG. 12. Spectral response of selenium-25% arsenic film.

CONCLUSIONS

Any mechanism involving the dark current in amorphous selenium must account for the exponential steady-state V-A curve and the high transient dark currents. The exponential V-A curve immediately suggests the presence of a surface barrier while the transient dark current as well as some photocurrent effects suggest that trapping and the buildup of a space charge are important processes to be considered.

The logarithmic xerographic dark decay is easily explained by the exponential nature of the dark V-A curve obtained by gradually decreasing the applied voltage. This curve, Fig. 2, follows the relationship

$$i_d = Ae^{KV}.$$

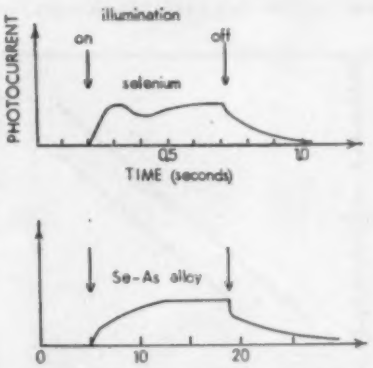

FIG. 13. Secondary current waveforms.

The xerographic discharge equation is then given by

$$C\,dV/dt = Ae^{KV}.$$

On integrating between the limits V_0 at $t=0$ and V_1 at t_1, and assuming $V_1 < V_0$, we have

$$V_1 = (\ln C - \ln A - \ln K - \ln t_1)/K,$$

and therefore $1/K = \alpha$, where α corresponds to the xerographic decay constant.

From Fig. 2 we have the measured fatigued-cell decay curve of

$$V_1 = V_0 - 190 \ln t \quad \text{for} \quad T > 10 \text{ sec.}$$

From the previous analysis and the V-A curve of this same cell, the calculated decay curve is

$$V_1 = 800 - 184 \ln t_1 \quad \text{for} \quad V_1 < V_0,$$

which is in good agreement with the measured curve.

The exponential nature of the V-A curve indicates the presence of an energy barrier impeding the flow of the dark current since the probability of charge crossing a barrier is generally given by the Boltzmann factor

$e^{-\phi/KT}$, where ϕ is the barrier height. That this barrier exists on the surface is indicated by the fatigue effect. The fatigue effect (temporary increase in α due to illumination applied previously to charging) is observed for wavelengths of illumination such that the incident photons are absorbed within 10^{-5} cm of the surface. Without an applied voltage it is doubtful if any activity due to this illumination is present near the center of an Se film.

The absence of electrode effects or the lack of secondary effects is indicated by (1) the fast rise time of the photocurrents, (2) the near unity quantum efficiency, (3) the close agreement of the photocurrent-voltage curve to the theoretical curve, and (4) the direct proportionality between illumination intensity and photocurrent.

Under conditions of constant applied voltage, a fraction of the photoexcited carriers is trapped before crossing the insulating film. The equations for this phenomenon have been discussed earlier. Figure 6 illustrates how these trapped charges serve to reduce the internal field. The total amount of trapped charge that may be contained in the film is equal to CV since at this point the surface charge is neutralized. As the internal field is reduced because of the trapping, the photocurrent is reduced and the photocurrent transients shown in Fig. 7 are observed. It is easily calculated that the observed photocurrent decay times are on the order of magnitude of times predicted from a knowledge of the carrier range and the illuminating intensity.

Most photoconductors exhibit a peak sensitivity for wavelengths where the reciprocal absorption coefficient equals the photoconductor thickness. Longer wavelengths are not as highly absorbed resulting in a decrease of the photocurrent while shorter wavelengths increase the carrier density near the surface. The sensitivity for shorter wavelengths is decreased either through bimolecular recombination or through a decrease in the carrier lifetime due to high surface trap densities. In hexagonal selenium the spectral response is of the type previously described.

Amorphous selenium, as well as iodine and tellurium, exhibit an unusual spectral response in that the photocurrents do not reach a maximum until the excitation is in the peak absorption range (Fig. 14). The extremely low photoresponse at photon energies on the order of 1.8 ev may be caused either by a high recombination rate for free carriers generated from these photons or by the presence of an absorption mechanism that does not produce free hole-electron pairs or by a combination of both methods.

While small amounts of impurities as well as variations in the preparational procedures both appear to effect all of the charge transport parameters, the electron range undergoes the most pronounced variation.

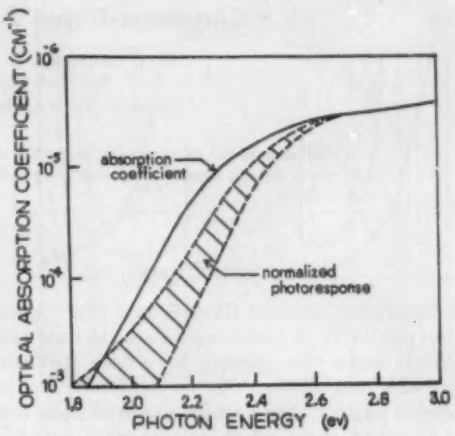

FIG. 14. Absorption coefficient of selenium.

High-coating (crucible) temperatures or the addition of small percentages of As to the Se serve to increase r_{-}. The temperature required to maintain a given vapor pressure of Se increases as As is added to the Se. Small amounts of As also inhibit the crystallization of Se at slightly elevated temperatures. The indications are that As serves to crosslink Se chains. Each As atom might then terminate a chain end and possibly remove a deep electron trap. This would occur since each chain end possesses an unfilled p orbital in the neutral state.

A correlation may be made between the observed and predicted rate of rise of photovoltage. The system may be thought to consist of a current generator charging the series combination of the sample bulk capacity and the instrument input capacity. The current generator represents the hole-diffusion current and is equal to FeL_{+} where F is the rate of generation of carriers given by $F=\lambda L/hC$. At an illumination of 12 μw/cm^2, F is equal to 2.4×10^{13}/sec/cm^2. The current is then 19×10^{-11} amp. dV/dt initially is given by i/C, where C is the series sum of the capacitors. We then obtain

$$(dV/dt)(19\times10^{-11}/2.5\times10^{-11})=7.6 \text{ v/sec.}$$

The measured rise is 3.2 v/sec which is within the limits of experimental error. A rough proportionality between rate of rise and light intensity may also be observed in the data.

ACKNOWLEDGMENTS

The author gratefully acknowledges the advice and encouragement furnished by Dr. Fred A. Schwertz of Haloid Xerox, Inc. The aid and assistance of Edward F. Mayer, Virgil E. Straughan, Virgil McIntosh, and Gunars Rankis of Horizons, Inc., is also appreciated.

Chromium-Doped Titania as a Maser Material*†

H. J. GERRITSEN, S. E. HARRISON, AND H. R. LEWIS
RCA Laboratories, Princeton, New Jersey

(Received March 4, 1960; and in final form May 16, 1960)

A discussion of the paramagnetic properties of Cr^{3+} in TiO_2 is given with particular reference to its use in solid-state masers. Energy level diagrams are included for magnetic fields in the (110), (1$\bar{1}$0), (001), and (100) planes.

I. INTRODUCTION

IN the short time since Bloembergen[1] first suggested the possibility of producing a cw solid-state maser, amplifiers using this principle have been operated at frequencies ranging from 300[2] to 39 000 Mc.[3] A large variety of circuits have been employed in these amplifiers including those which use resonant cavities to strengthen the coupling of the radiation to the paramagnetic ions and those which use slow wave structures for the same purpose. However, the most important element in a device of this kind is the paramagnetic material and to date little choice has been available for this component. By far the largest number of masers have employed chromium as the paramagnetic ion in a host lattice of either $K_3Co(CN)_6$ or Al_2O_3. Gadolinium ethyl sulphate[4] has also been used in a maser, but has relatively poor properties for this application. Iron-doped alumina has been used in at least one amplifier and is principally of interest because it can be used in a zero-field device.[5] This article describes in detail the properties of a new maser material, chromium-doped titania,[6] which has already been used to extend the frequency range of masers and which should in addition lead to improved amplifiers at the lower frequencies.

II. HOST LATTICE (TiO_2)

Titania is a very hard crystal (7–7½ mohs) with a Debye temperature of 758°K at 4°K.[7] It withstands large temperature changes with no apparent damage. Its crystal structure[8] (Fig. 1) is tetrahedral (D_{4h}), and the c axis can be found conveniently by using polarized light. The dielectric constant of titania is rather large and varies slowly with frequency. At 9 kMc[9] it is 91 perpendicular to the c axis. Measurements of dielectric constant have recently been made at 23 kMc by Magid and Sabisky, at RCA Laboratories: the result is 88 perpendicular to the axis at room temperature, increasing to 121 at 77°K. Large changes in the dielectric constant of titania may be made by adding small amounts of certain metal ions to the lattice.[10a] However, the addition of about 1% chromium or iron does not radically alter its dielectric properties. Large single crystals of "pure" titania can be obtained from Linde Air Products and the National Lead Company. These samples normally contain about 0.005% iron, an amount easily detectable by paramagnetic resonance. This can lead to some confusion in analyzing the spectrum of samples intentionally doped with other paramagnetic ions.

III. CHROMIUM IN TITANIA

While pure titania is fairly translucent and slightly yellow, titania containing 0.075% chromium by weight is black. Even slabs 0.030 in. thick are quite opaque and the crystal axis must be found by x-ray analysis. The paramagnetic spectrum of this material is easily observed at room temperature; the absorption lines are strong and relatively narrow (~60 Mc) so that the hyperfine structure due to the 9% of isotope Cr^{53}, with nuclear spin of ⅔, is easily detected in unenriched samples. A minor practical difficulty in observing the spectrum is caused by the large dielectric constant of

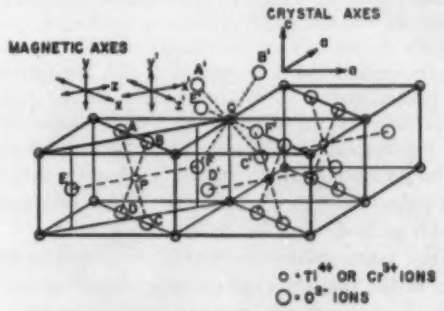

FIG. 1. Crystal structure of TiO_2 and its magnetic axes.

* Partially supported by U. S. Army (Signal Corps).

† Energy levels at 10^5 intervals in these planes as well as transition-probabilities along the axes can be obtained from the authors.

[1] N. Bloembergen, Phys. Rev. **104**, 324 (1956).

[2] R. H. Kingston, Proc. I.R.E. **46**, 916 (1958).

[3] S. Foner and L. R. Momo, Lincoln Laboratory Rept. M82-16 (December 11, 1959).

[4] H. E. D. Scovil, G. Feher, and H. Seidel, Phys. Rev. **105**, 762 (1957).

[5] R. W. Terhune and I. E. King, Information Note 2, Project Michigan (1959).

[6] H. J. Gerritsen, S. E. Harrison, H. R. Lewis, and J. P. Wittke, Phys. Rev. Letters **2**, 153 (1959). J. Sierro, K. A. Müller, and R. Lacroix, Arch. sci. (Geneva) **12**, 122 (1959).

[7] P. M. Keesom and N. Pearlman, Phys. Rev. **98**, 1539(A) (1955).

[8] R. W. C. Wyckoff, *Crystal Structures Handbook* (Interscience Publishers, Inc., New York, 1958).

[9] J. G. Powles and W. Jackson, Proc. Inst. Elec. Engrs. (London) **96**, 383 (1949).

[10] (a) Ia. M. Ksendzov, Acad. Sci. U.S.S.R. **22**, 3 (1958); (b) B. Marinden and A. Magneli, Acta Chem. Scand. **11**, 1635 (1957).

titania, which has the effect of making even very small samples significantly perturb cavity fields. One way of avoiding this difficulty is to mount samples in waveguide without using a cavity. The material itself acts as a resonant structure and a movable plunger behind the sample can be used to adjust the coupling. The theory of this kind of resonant structure has been studied by O. Okaya[11] at Columbia University.

An analysis[6] of the paramagnetic resonance spectrum (Figs. 2–4) of titania containing 0.075% by weight of chromium shows that trivalent chromium ions substitutionally replace titanium ions in the lattice. The local crystal field at the chromium ions is orthorhombic and has the symmetry D_{2h}. The appropriate Hamiltonian[12] is then

$$H=\beta H\cdot g\cdot S+DS_z^2+E(S_x^2-S_y^2)+AI\cdot S.$$

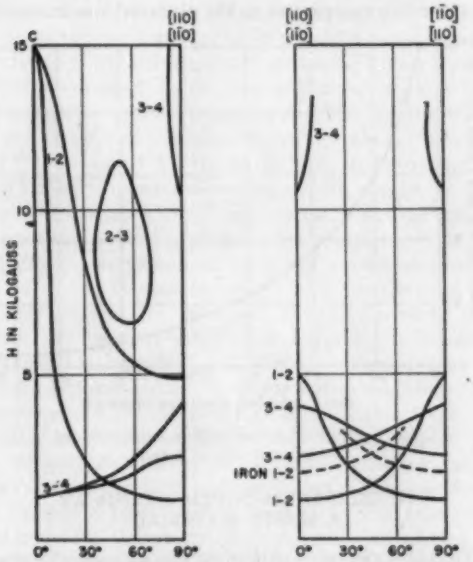

FIG. 2. Observed spectrum of chromium in titania at 9.52 kMc.

The crystal-field parameters D and E and the value of g (assumed isotropic) have already been given in a brief note[6] on the paramagnetic spectrum of this material. In the present article a change has been made in the magnetic coordinate system to agree with the convention of choosing the z axis to minimize the ratio of E/D. To make footnote reference 6 confirm with the present choice, the y and z axes must be interchanged and the value of D and E must be transformed to refer to the new coodinate system. In order to make reading easier, reference will also be made to the crystal axes wherever it seems important. The direction cosines of the new coodinate system with respect to the crystal axes, and the appropriate values of D, E, and g are

[11] O. Okaya (private communication).
[12] K. D. Bowers and J. Owen, Repts. Progr. Phys. 18, 304 (1955).

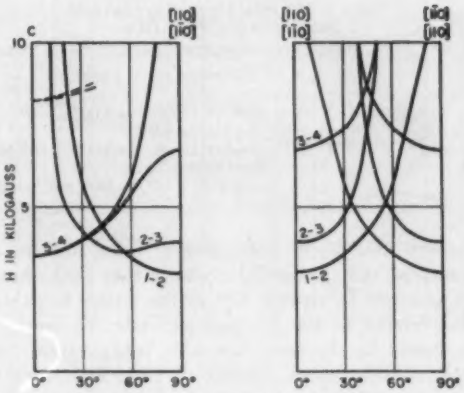

FIG. 3. Observed spectrum of chromium in titania at 23.8 kMc.

given in Table I. The crystal field parameters are quite insensitive to temperature change. There are two titanium (or chromium ions) per unit cell and these are related by a 90° rotation about the y axis. The sign of D was determined by observing absorption intensity ratios at 4.2° and 1.4°K. As is well known, a change in the sign of D inverts the energy levels but leaves them otherwise unchanged. Generally speaking, this is of little importance for materials like ruby where the zero-field splitting is small, but may be quite significant in chromium-doped titania where even at low fields some levels are separated by energies of the order of kT at 4.2°K. In choosing the sign of E, the convention of labeling the axes as xyz according to increasing ratio of $|D/E|$ was followed. Because of the particular arrangement of the two systems of magnetic axes, the absolute sign of E could not be determined.

According to susceptibility measurements on powdered rutile with iron and chromium concentrations of 1% and higher[13] it seems that those ions are mainly in the 4^+ state when replacing titania in the lattice.

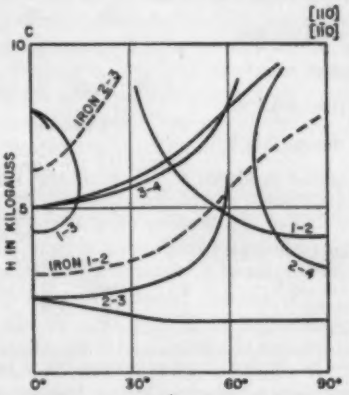

FIG. 4. Observed spectrum of chromium in titania at 34.0 kMc.

[13] P. W. Selwood and Lorraine Lyon, Discussions Faraday Soc. 8, 227 (1950).

TABLE I. Magnetic axes and crystal field parameters of Cr^{3+} in TiO_2.

	a	a	c	$D=-0.68\ cm^{-1}(\pm0.005)$
x	$-\sqrt{2}/2$	$\pm\sqrt{2}/2$	0	$E=-0.14\ cm^{-1}(\pm0.005)$
y	0	0	1	$g=1.97(\pm0.01)$
z	$\pm\sqrt{2}/2$	$+\sqrt{2}/2$	0	$A=0.0015\ cm^{-1}(\pm0.0002)=45$ Mc
				Zero field splitting $=2(D^2+3E^2)^{\frac{1}{2}}=43.3(\pm0.2)$ kMc

However, two recent publications[10] bring forward experimental and theoretical evidence that both chromium and iron do replace Ti^{4+} in the lattice but themselves remain in the 3+ valence state. Theoretically this should be the most favorable configuration from energy considerations, because all three ionic radii involved are rather closely the same, while Cr^{4+} and Fe^{4+} with their much smaller radii would introduce large strains in the lattice.

In order to determine how much chromium is in a valence state different from 3+, two sets of experiments were carried out. One was to see whether any extra lines which would be due to chromium in a valence state other than 3+ could be detected. The experiments were done at 4.2°K, because Cr^{4+}, if present, would have short spin lattice relaxation times and thus broad lines, except at low temperature. The search was made at frequencies ranging from 9 to 57 kMc and indeed extra lines were observed, but all of them were 1% or less the intensity of the main Cr^{3+} spectrum. Part of those lines could be identified as iron 3+ and part tentatively as Cr^{3+} in a different lattice position, perhaps with an oxygen vacancy nearby. The zero field splitting for the latter ions is 36.5 (+0.1) kMc at 77°K as compared to 43.3 kMc for the abundant Cr^{3+}. More work is needed, however, to determine the symmetry and constants in the Hamiltonian for this small fraction. All those weak lines were also observed at 77°K. Because it is quite well possible that all the lines due to Cr^{4+} fall outside our frequency magnetic field range, a second method was applied. Careful measurements were done of the magnetic Q at liquid air for five resonances along the three magnetic axes. These values agreed within 10% with Q values computed for those resonances, assuming all the chemically determined Cr to be in the 3+ valence state. Ten different dielectric resonances were used and the mode pattern in each of them could be fairly well determined by comparing calculated transition probabilities with the intensities of the five resonance lines. The spread in the results was about 10%, so that practically all of the chromium in the rutile contributes to the observed spectrum.

TABLE II. Characteristics of maser crystals doped with chromium.

	$K_3Co(CN)_6$	Al_2O_3	TiO_2
Zero field splitting (kMc)	5.1	11.4	43.3
Maximum signal frequency[a] (kMc)	9	20	72
Maximum operating field[a] (kgauss)	3	7.5	28
Pump frequency range[b] (kMc)	4.5–20	10–45	30–180
Relaxation time at 4.2°K[c] (m-sec)	50	10–50	40
Relaxation time at 78°K[c]	very short	0.2–1.0	0.5
Dielectric constant at 300°K	5	8–10	85 160 (and about 50% higher at 4°K)
Concentration in wt % of paramagnetic ions for a 20-gauss linewidth	0.5	0.05	0.1
Ions per unit cell	2	1	2

[a] This is an approximate number based on the field at which the transition probability for the pump decreases to about 10% of its maximum value.
[b] In the case of titania, a more practical limit may be imposed by magnetic field requirements. If the magnetic field is limited to 10 kgauss, the maximum signal frequency for TiO_2 is 30 kMc and the pump range is 30–120 kMc.
[c] The relaxation times of titania were measured using the cw method and are subject to appreciable error because of the difficulty in calculating H_{rf} within a high dielectric sample in a resonant cavity.

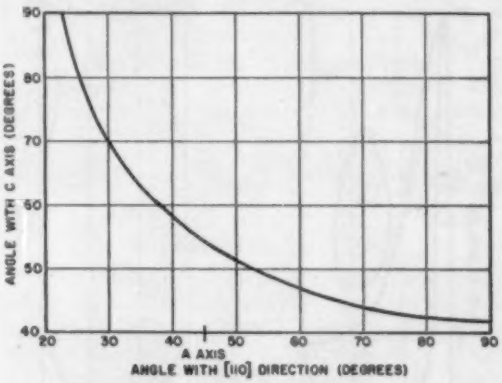

FIG. 5. Orientations for push-pull operation of chromium in titania masers.

IV. CHROMIUM-DOPED TITANIA AS A MASER MATERIAL

Titania doped with chromium has a number of properties which make it important as a maser material (Table II). Because of its large zero field splitting, 43.3 kMc, it can be used in amplifiers operating at frequencies up to 50 kMc with magnetic fields under 10 kgauss. If this field limitation is lifted, higher signal frequencies can be obtained. A maser has been operated at a signal frequency of 23 kMc[14] using a pump at 50 kMc and it should not be difficult to construct an amplifier at the first atmospheric "window" (approx 35 kMc). Moreover, the zero-field splitting is not so large that pump power becomes a problem. For example, a 9 kMc maser[14] was pumped with a Philips DX-184 klystron operating at 34 kMc. This device had a gain-bandwidth product of 25 Mc at 4.2°K and performance was limited by oscillation. Klystrons providing sufficient pump power are also available at higher frequencies

[14] H. J. Gerritsen and H. R. Lewis, Quantum Electronics Conference, Bloomingsburg, New York, September, 1959.

to exploit fully the high-signal-frequency possibilities of this material.

The relaxation times of titania are much like those of ruby in both absolute value and temperature dependence. Thus operation at temperatures above 4.2°K should be possible for titania. The very high dielectric constant of titania has some interesting device implications. In the 9-kMc maser reported above a sample 0.25×0.75×0.1 in. was used. Because of the high dielectric constant, this sample formed a resonant cavity operating in a very high mode. Thus cavity resonances at the signal frequency were spaced at intervals of about 10 Mc and it was possible to make several of these resonances simultaneously emissive. This suggests that by using a somewhat larger sample, cavity resonances can be made to overlap at the signal frequency to produce an electronically tuneable cavity maser.

Alternatively, the high dielectric constant can be used to advantage in a traveling wave maser. If a waveguide is entirely filled with dielectric, a slowing factor equal to $(\epsilon)^{\frac{1}{2}}$ is obtained. In the case of titania this may be sufficient slowing for a practical amplifier. In addition the less tangent of chromium-doped rutile is only about 5.10^{-5} at 77° and 4°K. The advantages of this arrangement are very broad tuneable bandwidth and an exceptionally simple structure. Experiments to test the feasibility of this kind of application are planned.

A direct comparison of ruby and chromium-doped titania at low frequencies where both can be used is of some interest. To date only the titania maser reported has been operated at 9 kMc. The measured gain-bandwidth product of 25 Mc was obtained using a rather primitive circuit in which the cavity coupling was not adjustable. A new device with variable coupling is under construction and should give a better idea of the ultimate capabilities of the amplifier. Many ruby masers have been built and the design of these devices has reached a fairly sophisticated state. For example, workers at the University of Michigan have reported a gain-bandwidth product of 500 Mc in a 9-kMc device operated at 4.2°K.[15]

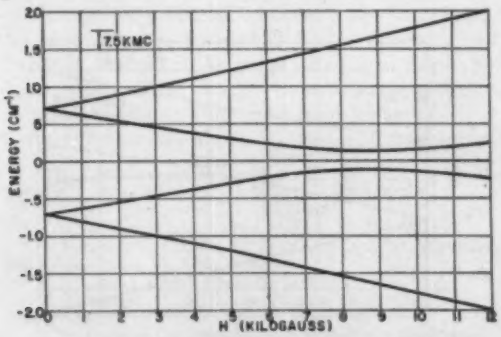

FIG. 6. Push-pull energy levels for magnetic field at minimum angle with c axis.

[15] R. W. Terhune, University of Michigan (private communication).

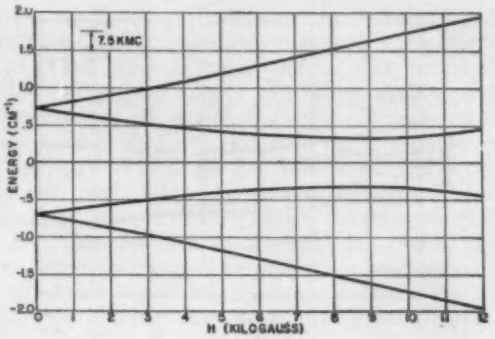

FIG. 7. Push-pull energy levels along a axis.

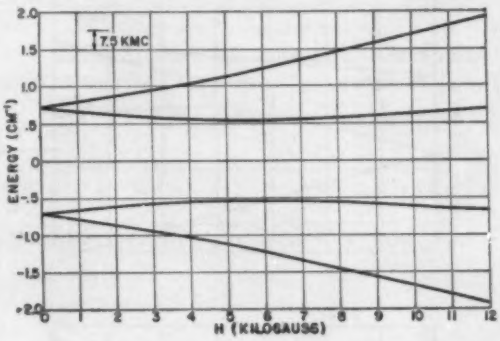

FIG. 8. Push-pull energy levels for magnetic field at maximum angle with c axis.

The possibility that chromium-doped titania can equal and even surpass this figure is suggested by the following argument. The density of chromium ions in rutile is twice the density of chromium ions in ruby in crystals with equal line width (50 Mc). This advantage of rutile just compensates for its disadvantage of two ions per unit cell. Consequently one expects the magnetic Q of chromium-doped rutile to be lower than that of ruby because it can be pumped at a higher frequency. Moreover, rutile can be operated in orientations where the two ions per unit cell are identical. In this case its magnetic Q is further reduced by 50% and consequently its bandwidth can be increased.

Both ruby and chromium-doped titania can be operated in either the push-push or the push-pull mode[16,17] to increase inversion. Because titania is orthorhombic, a variety of energy levels suitable for push-pull operation can be found while in ruby only one energy level diagram is available for this purpose. On the other hand, it should be easier to orient ruby than titania to obtain push-pull operation. The crystal orientations for push-pull operation of chromium-doped titania are given by

[16] Lincoln Lab., Quarterly Progr. Rept. July, 1959 (unpublished).

[17] C. Kikuchi, J. Lambe, G. Makhov, and R. W. Terhune, J. Appl. Phys. **30**, 106 (1959).

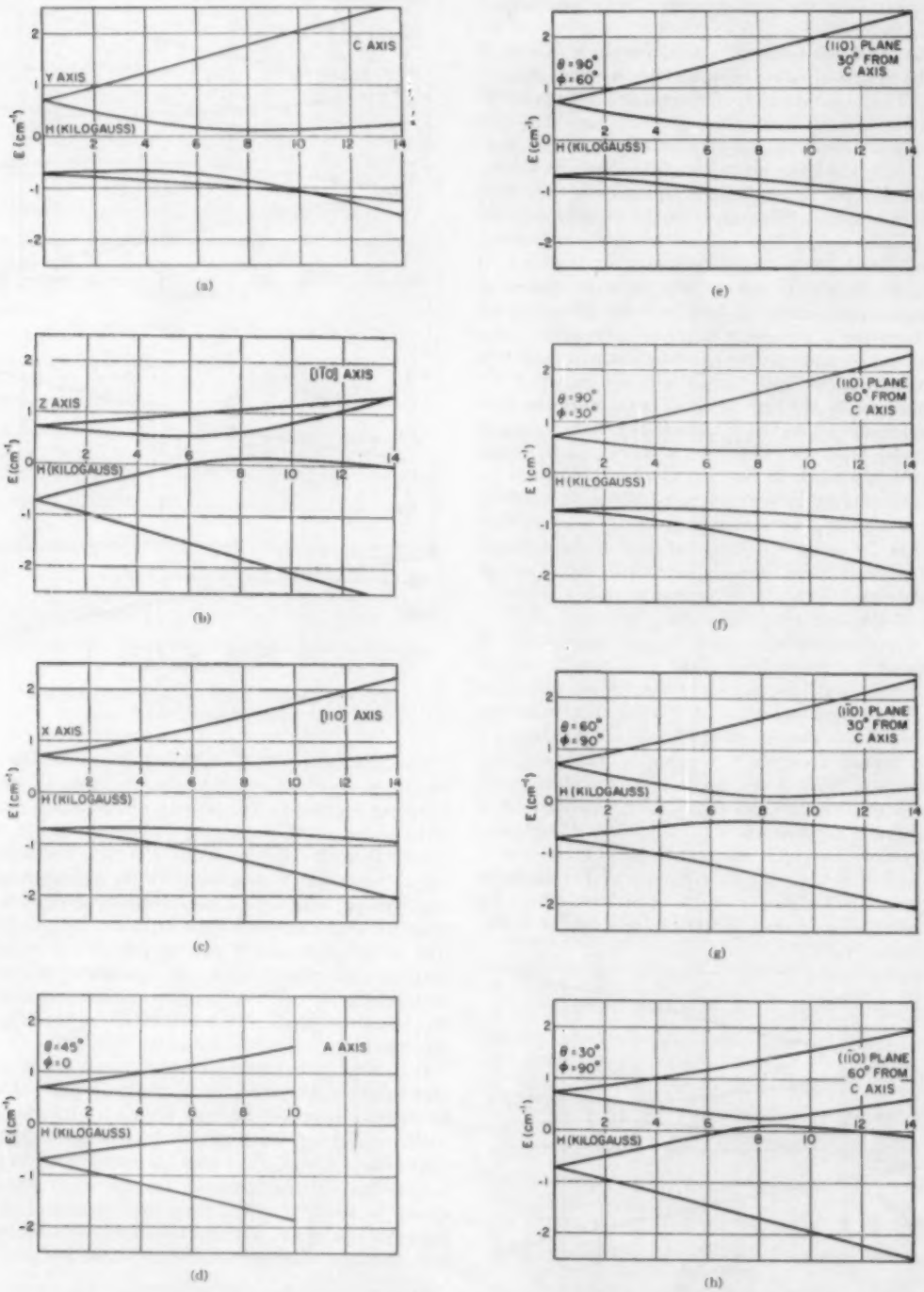

FIG. 9. Energy levels of Cr^{3+} in TiO_2.

the relation[17]

$$\cos 2\phi = (D/E)[1-(2/3\sin^2\theta)],$$

where θ and ϕ are the polar coodinates. Figure 5 is a plot of this relation relative to the c axis of the crystal.

Figures 6–8 show representative push-pull energy level diagrams of titania. Figure 7 may be of special interest since it combines push-pull operation with an orientation in which all ions are identical.

ACKNOWLEDGMENTS

The authors express their thanks to I. Bernal for his assistance in the study of the paramagnetic resonance spectra and to Macy Heller for his help in the construction of equipment and data taking. We have also profited from discussions with A. Okaya of Columbia University.

APPENDIX

Energy Levels of Cr^{3+} in TiO_2

The energy levels which follow are given in two distinct notations. On the left side of each graph the appropriate spherical coordinates of the magnetic field relative to the magnetic axes are stated. Although these axes have been chosen to conform with convention, they are not particularly well suited to this crystal. For example, the two ions per unit cell are related to one another by a rotation about the y magnetic axis. Therefore, the plane in which the two ions are identical is not simply stated in spherical coordinates in the magnetic system. For this reason, the energy level diagrams have also been labeled with orientations relative to the crystal axes. This designation appears on the right-hand side of each graph. For example, the plane in which the two ions are identical is the ac plane in this notation.

In using these diagrams one should remember that a single graph applies to one of the two nonequivalent ions. The energy levels for the second ion are found by looking at the graph appropriate for a magnetic field rotated 90° about the y (or c) axis from the actual field. [See Figs. 9(a)–9(h).]

JOURNAL OF APPLIED PHYSICS VOLUME 31, NUMBER 9 SEPTEMBER, 1960

Crystallography and Domain Walls in Antiferromagnetic NiO Crystals

GLEN A. SLACK
General Electric Research Laboratory, Schenectady, New York
(Received May 24, 1960)

Twin-domain walls in large crystals of antiferromagnetic NiO have been observed by specular reflection in optically polished and annealed crystals. These walls can be moved in annealed crystals by small mechanical stresses ($<10^6$ d/cm^2) or by moderate magnetic fields ($<25\,000$ oe) to yield completely untwinned crystals. The ease with which a twin wall moves appears to be limited by a spin-rotation energy loss. Crystallographic measurements of the rhombohedral distortion agree with the x-ray data, and verify the [111] antiferromagnetic contraction. The anisotropy in the magnetic susceptibility vs field has been measured for untwinned crystals, and is compared with earlier work.

INTRODUCTION

NICKELOUS oxide NiO is antiferromagnetic at room temperature, and paramagnetic above its Néel temperature T_N of 523°K.[1–4] Large single crystals of NiO can be prepared by at least two techniques.[5–7] All of the crystals reported on here were grown by the Verneuil process[8] in an oxygen-hydrogen flame. Some were grown at the General Electric Research Laboratory,[9] and some were obtained from Japan.[6,10]

At temperatures above T_N the crystal structure of NiO is cubic, whereas below T_N the crystals become slightly distorted from this cubic structure to a rhombohedral one.[11] The amount of this distortion increases as the temperature decreases. This distortion accompanies the antiferromagnetic ordering,[12,13] and consists of contraction of the original cubic unit cell along any one of the four ⟨111⟩ axes. The rhombohedral structure in the antiferromagnetic state can be based on a monomolecular unit cell in which the rhombohedral angle α' is slightly larger than 60°. This scheme was used by Rooksby.[11] However for the present purposes it is more convenient to use a rhombohedral unit cell containing 4-NiO molecules. Its rhombohedral angle α is slightly larger than 90°, and, as can be seen from Fig. 1, this unit cell is a slightly distorted cube. In the present case where this distortion is small, the angles α' and α are related by

$$(\alpha-90°)=\sqrt{3}(\alpha'-60°)/2. \quad (1)$$

[1] J. R. Tomlinson, L. Domash, R. G. Hay, and C. W. Montgomery, J. Am. Chem. Soc. **77**, 909 (1955).
[2] G. Foëx, Compt. rend. **227**, 193 (1948).
[3] C. H. LaBlanchetais, J. phys. radium, **12**, 765 (1951).
[4] H. Kondoh, E. Uchida, Y. Nakazumi, and T. Nagamiya, J. Phys. Soc. Japan, **13**, 579 (1958).
[5] E. J. Scott, J. Chem. Phys. **23**, 2459 (1955).
[6] Y. Nakazumi, J. Chem. Soc. Japan (Ind. Chem. Sec.) **59**, 1304 (1956).
[7] R. E. Cech and E. Alessandrini, Trans. Am. Soc. Metals **51**, 150 (1949).
[8] A. Verneuil, Compt. rend. **135**, 791 (1902).
[9] These crystals were grown by R. Newman.
[10] Tochigi Chem. Ind. Co. Ltd., Osaka, Japan.
[11] H. P. Rooksby, Acta Cryst. **1**, 226 (1948).
[12] S. Greenwald and J. S. Smart, Nature, **166**, 523 (1950).
[13] J. Kanamori, Progr. Theoret. Phys. (Japan) **17**, 197 (1957).

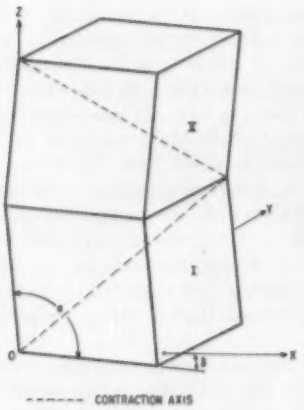

FIG. 1. An exaggerated model of the rhombohedral distortion in NiO below T_N. The Oxyz axes are orthogonal. The rhombohedral angle α is greater than 90°, and each of the rhombohedral axes makes an angle δ with the Oxyz axes. A twin wall on a (001) plane between regions of types I and II is shown.

The maximum value of α occurs at 0°K and present measurements give a value of 90°6′. Here we are concerned only with the chemical unit cell, the magnetic unit cell contains eight chemical unit cells, and its lattice constant is twice as large.[14,15]

This small distortion may cause a macroscopic crystal of NiO to be twinned below T_N, and to be composed of many small regions each characterized by one of the four ⟨111⟩ contraction axes, and each twinned to other such regions on {100} or {110} planes. These twinning planes form one kind of antiferromagnetic domain wall.

In the antiferromagnetic state the magnetic moments of NiO are arranged into ferromagnetic sheets. In a region where the rhombohedral contraction occurs along a [111] axis, these sheets are (111) planes. The orientation of the magnetic moments with respect to these (111) planes had been uncertain,[15–17] but recent neutron-diffraction work[18] on untwinned crystals has shown that the moments all lie within the (111) planes. This is in agreement with the calculations of the minimum magnetic-dipolar energy.[19,20] However the direction within the plane is still uncertain, and appears to be variable. A further complication arises in NiO from the cubic crystal structure and the nature of the superexchange interaction. In the antiferromagnetic state below T_N the magnetic moments of the Ni ions are spin-only values with $S=\frac{1}{2}$, as shown by the neutron diffraction results.[15,17] The magnetic susceptibility measurements[21–23] in the paramagnetic state above T_N appear to indicate a magnetic moment larger than the spin-only value. The present concern is with the antiferromagnetic state, and thus the spin-only moment is used. The superexchange interaction[14] between nickel ions on opposite sides of an oxygen ion causes the spins of the nickel ions to be antiparallel. If this superexchange is the only coupling between the spins, then only next-nearest nickel ions are coupled, and no nearest-neighbor coupling of nickel ions exists. Consequently there are four independent submotifs[14,15] in the nickel lattice on NiO. Each submotif is a simple cubic lattice of nickel ions with a lattice constant twice that of the chemical unit cell. Figure 2 shows the magnetic unit cell of nickel ions with the submotifs 1, 2, 3, 4. The spin on 1′ is antiparallel with that on 1. The spins on 1 and on 2 etc. are not necessarily parallel. Within each submotif there is a long-range antiparallel coupling of the spins. Any abrupt change in this long-range antiparallel order of a given submotif is an antiferromagnetic-domain wall. The very short-range misalignment of spins which may exist between nearest-neighbor nickel ions, which are on different submotifs, cannot be called a domain wall. However there appears to be[20] a nearest-neighbor exchange interaction between the nickel ions which keeps all four submotifs with a (111) sheet aligned in both sense and direction. This interaction is also responsible for the rhombohedral deformation.[13,20] Therefore in the succeeding discussion it is assumed that in a single-domain crystal there are alternate (111) sheets of positive and negative spin all pointing in a given direction. This is the single spin-axis[15] model.

The purpose of the present paper is to show how the ambiguity of the spin direction in the {111} planes leads to the formation of domain walls, and how these walls affect the crystallographic and magnetic properties of NiO. In the companion paper Roth[24] treats the effects of the domain walls on the optical transmission and neutron scattering.

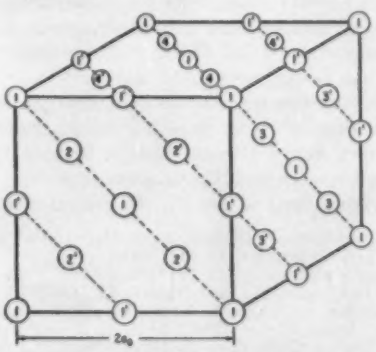

FIG. 2. The Ni^{+2} ions in the magnetic unit cell of antiferromagnetic NiO. The magnetic cell dimension is twice the chemical unit cell parameter a_0. The Ni^{+2}-ion lattice is shown divided into 4 submotifs where in a given submotif the primed ions have spins antiparallel to the unprimed ions. Even though all of the spins lie in the dotted (111) planes, the superexchange alone provides no correlation of spin directions among the 4 submotifs.

[14] P. W. Anderson, Phys. Rev. **79**, 350 (1950).
[15] W. L. Roth, Phys. Rev. **111**, 772 (1958).
[16] W. L. Roth, Phys. Rev. **110**, 1333 (1958).
[17] C. G. Shull, W. A. Strauser, and E. O. Wollan, Phys. Rev. **83**, 333 (1951).
[18] W. L. Roth and G. A. Slack, J. Appl. Phys. **31**, 325S (1960).
[19] J. I. Kaplan, J. Chem. Phys. **22**, 1709 (1954).
[20] F. Keffer and W. O'Sullivan, Phys. Rev. **108**, 637 (1957).
[21] J. R. Singer, Phys. Rev. **104**, 929 (1956).
[22] J. R. Singer, U. S. Naval Ordnance Laboratory Rept. No. 4314, (September, 1956).
[23] N. Perakis, J. Wucher, A. Serres, and G. Parravano, Colloque National de Magnètisme, C.N.R.S., Paris (1958), p. 159.

DOMAIN WALLS

As a consequence of the ambiguity in the contraction axis and in the spin orientation in a single crystal of NiO, several varieties of antiferromagnetic-domain walls can exist. One variety is a twin wall, i.e., a twinning plane, across which a change in the contraction axis occurs. This is called a T (twin)-variety domain wall. A second variety of domain wall can occur within a region which possesses a given contraction axis but where, for a given submotif, there is a rather abrupt (say in about 100 lattice constants) change in the spin orientation within the (111) plane. This is called an S (spin rotation) variety of domain wall. Only T-walls have been seen either by x rays[11] or by the present crystallographic measurements. Walls of variety S apparently produce an extremely small crystallographic distortion, and cannot be observed by the above two techniques. The occurrence of S-walls does affect the magnetic susceptibility and the neutron scattering, as explained by Roth.[24]

Figure 3 shows in a schematic fashion the spin arrangement in a NiO crystal which contains two S-domain walls and one T-domain wall. The S_{11} and $S_{\perp}$ are for spin rotations[24] parallel or perpendicular to [111]. The numbering system is explained later. A crystal which is free of domain walls of variety T, i.e., is untwinned, may still possess many walls of variety S.

Observing and Removing Domain Walls

A specular reflection technique has been developed which will reveal, by observation of small facial tilt angles, whether or not any T-walls are present in a crystal. The details are explained later. Furthermore a method has been developed for the production of almost completely untwinned crystals. The steps of this method are first to anneal the crystal at a temperature of 1400°±100°C in an argon atmosphere containing about 10^{-4} parts of oxygen. The trace of oxygen prevents the reduction of the NiO to Ni. Then when it is slowly cooled to room temperature only a small number of T-walls are left in the crystal. These walls are quite mobile,[4,24,25] as will be shown quantitatively. Thus they can be swept from the crystal by applying a small momentary stress at room temperature along [111].

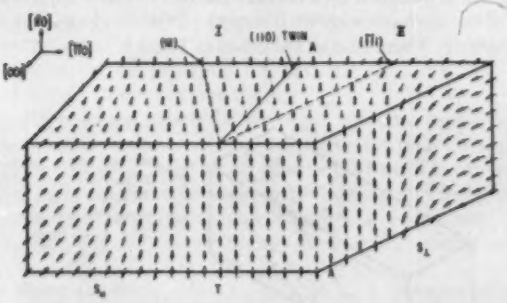

FIG. 3. A representation of the spin orientations at a twin domain wall, T, and at spin-rotation domain walls S. Regions of type I and II are shown twinned on a (110) plane. At this T-wall the spin direction, $[1\bar{1}0]$, is necessarily perpendicular to both $[111]$ and $[\bar{1}11]$.

About a dozen completely untwinned crystals have been made by this annealing and stressing technique. The absence of twins has been verified by the observation of the specular reflection, and by measurement of the anisotropy of the magnetic susceptibility. These conclusions have been positively confirmed on one crystal (7–9B) by observation[18,24] of the neutron diffraction. Over 98% of the volume of the crystal was a single type I region.

Previous authors such as Singer[21] and Kondoh *et al.*[4] have used a stress-anneal technique to produce partially-untwinned crystals. The scheme used by them was to anneal the crystals, and to cool them from a high temperature of about 1000°K under a constant stress of from $1\text{–}40\times10^7$ d/cm² applied during the entire cooling process. An alternative scheme of ultrasonic treatment at a pressure of 3×10^7 d/cm² at room temperature was also used.[4] These previous results demonstrated that an external stress can actually change the number of T-walls in a given volume of crystal. These authors also concluded from their measurements of the magnetic susceptibility that their crystals still possessed a multidomain structure with many T-walls. The present procedure of annealing, slow cooling, and then stressing at room temperature has produced almost completely untwinned crystals.

CRYSTALLOGRAPHY OF TWINS

It is worthwhile to consider just what a twinned crystal of antiferromagnetic NiO looks like crystallographically. The four differently oriented rhombohedral regions that a cube can distort into will be designated as regions of crystal of types I, II, III, and IV. The corresponding contraction axes of the original cubic structure at high temperatures are I—[111], II—$[\bar{1}11]$, III—$[1\bar{1}1]$, and IV—$[11\bar{1}]$. Figure 1 shows a type I region whose contraction axis is chosen to be exactly along the [111] direction of the Oxyz coordinate system. The rhombohedral axes of the unit cell of I all make a small angle δ with the nearest orthogonal axis. Since α is nearly 90°, then $\delta=(\alpha-90°)/\sqrt{2}$ to a good approximation. If this type I region is thus fixed with respect to the Oxyz coordinates, the exact orientation of regions of types II, III, and IV with respect to these coordinates will depend on how they are twinned to the type I region. Figure I shows types I and II twinned through a (001) T-wall.

The possible twinning planes between regions of type I and II can be calculated. At a temperature above T_N a NiO crystal has a true cubic crystal struc-

[24] W. L. Roth, J. Appl. Phys. (to be published).

[25] R. Street and B. Lewis, Nature **169**, 1036 (1951).

TABLE I. Twinning planes and facial tilt angles for 6 crystal faces, and for the 12 possible twin walls in NiO.

Region pair	Twinning plane	Crystal face[a] (100)	(010)	(001)	(111)	(1$\bar{1}$0)	(11$\bar{2}$)
I–II	(001)	0°	90°	···	0°	54°44′	90°
		(2.000)	(2.000)	···	(1.886)	(0.000)	(0.943)
I–III	(010)	90°	···	0°	60°	−35°16′	39°14′
		(2.000)	···	(2.000)	(1.886)	(1.000)	(0.745)
I–IV	(100)	···	0°	90°	−60°	−35°16′	−39°14′
		···	(2.000)	(2.000)	(1.886)	(1.000)	(0.745)
II–III	(100)	···	0°	90°	−60°	−35°16′	−39°14′
		···	(2.000)	(2.000)	(0.000)	(1.000)	(2.236)
II–IV	(010)	90°	···	0°	60°	−35°16′	39°14′
		(2.000)	···	(2.000)	(0.000)	(1.000)	(2.236)
III–IV	(001)	0°	90°	···	0°	54°44′	90°
		(2.000)	(2.000)	···	(0.000)	(2.828)	(0.000)
I–II	(110)	90°	0°	−45°	0°	−35°16′	90°
		(0.000)	(0.000)	(2.828)	(0.943)	(0.000)	(1.886)
I–III	(101)	0°	−45°	90°	60°	19°28′	−38°31′
		(0.000)	(2.828)	(0.000)	(0.943)	(1.732)	(1.106)
I–IV	(011)	−45°	90°	0°	−60°	19°28′	38°31′
		(2.828)	(0.000)	(0.000)	(0.443)	(1.732)	(1.106)
II–III	(01$\bar{1}$)	45°	90°	0°	30°	90°	0°
		(2.828)	(0.000)	(0.000)	(1.633)	(1.732)	(0.577)
II–IV	(10$\bar{1}$)	0°	45°	90°	−30°	90°	0°
		(0.000)	(2.828)	(0.000)	(1.633)	(1.732)	(0.577)
III–IV	(1$\bar{1}$0)	90°	0°	45°	90°	···	0°
		(0.000)	(0.000)	(2.828)	(1.633)	···	(2.309)
Reference line for ψ		[010]	[001]	[100]	[1$\bar{1}$0]	[11$\bar{2}$]	[111]

[a] The crystal faces are designated by their outward normals. The angle ψ is so defined that a positive angle is measured counterclockwise from the reference line which lies in the crystal face. The facial tilt angle η is given as a fraction of $(\alpha-90°)$. The entries in the table are first ψ and beneath it (η).

ture. Consider such a crystal above T_N which is free of twins of the cubic-on-cubic variety that might occur, for example, on (111) faces. No such twins have been reported for synthetic NiO. Then at all temperatures below T_N the antiferromagnetic contraction must take place along one of the four diagonals of the original cubic lattice. Now a twinning plane is a reflection plane in which the crystal on one side of it is a mirror image of that on the other. The only planes which satisfy this condition are those which bisect the angles between the cube diagonals. These are the {100} and {110} planes, and these only. For a twin between regions of types I and II these planes are the (001) and (110) planes. For other pairs, the other planes of the {100} and {110} forms are twinning planes. The various combinations are shown in Table I.

Figure 4 shows schematically the T-walls found by the specular reflection technique on a crystal of NiO designated as J832A-1. This was cut from boule 832 obtained from Japan.[10] The growth and characteristics of crystals from this source have been reported in the literature.[4,6,26–28] Notice that in Fig. 4 all four types of regions are found. For this particular crystal these are twinned on the following planes: types I and II on (001), types I and III on (101), types II and IV on (10$\bar{1}$), and types III and IV on (001). These twinning plane designations are referred back to the original high-temperature cubic lattice. The solid lines in Fig. 4 indicate visible T-walls where the facial tilt angle is greater than zero. The dotted lines represent T-walls where the tilt angle happens to be zero. For example, the wall between domain types III and IV is visible on (1$\bar{1}$0) and (111) faces, but not on a (11$\bar{2}$) face. In Table I are shown the various possible twin walls which can occur on six different faces of NiO crystals. The entries in the table are first the angle ψ that the edge of the twin wall makes with a particular direction in the chosen crystal face, and secondly the facial tilt angle η as a fractional multiple of $(\alpha-90°)$. The actual experimental values of ψ usually agree with those in the table to within at least $\pm5°$. Some of the disagreement is caused by misorientation in the cutting of the crystal face, and some is caused when the T-walls tilt and distort under small residual stresses.

There are two sets of faces (100), (010), (001); and (111), (1$\bar{1}$0), (11$\bar{2}$) in Table I. Each is a right-handed set of three mutually (nearly) perpendicular faces. With a crystal cut according to the first of these sets it is difficult to tell whether a particular domain wall might, for example, be one between regions of types I and II or between types III and IV. When cut according to the second set, it is quite easily to tell. For this reason, and the fact that a pressure applied to a (111) face aids the contraction along the [111] axis, most of the crystals were cut with the second set of faces.

SPECULAR REFLECTION TECHNIQUE

The basis of this technique is illustrated in Fig. 1 where regions of types I and II are twinned on a (001) T-wall. The contraction axis of the type I region is chosen to be along the [111] direction of the Oxyz coordinate system. Hence the axis of the type II region is nearly but not exactly along the [$\bar{1}$11] direction of Oxyz. Furthermore the unit vectors of the rhombohedral cell of type II neither coincide with those of type I, nor with the Oxyz axes. This small mismatch gives rise to a small tilt angle between the (100) and (010) faces of these two twinned regions, as can be seen in Fig. 1. The amount of this tilt η can be calculated from the angle α by a careful analysis of the orientations of the various twins with respect to the Oxyz coordinate system. These results are given in Table I.

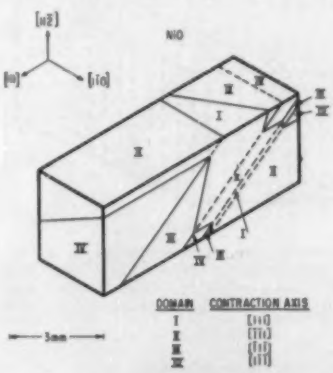

FIG. 4. The twinning pattern observed by specular reflection in crystal J832A-1 after a high-temperature anneal. The solid lines indicate visible T-walls, the dotted ones are walls with zero-facial tilt angles. This is an example of a complex 4-wall pattern where regions of all 4 types are present.

[26] Y. Shimomura, Bull. Naniwa Univ. **A3**, 175 (1955).
[27] Y. Shimomura and S. Saito, Bull. Univ. Osaka Prefect. **A4**, 111 (1956).
[28] E. Yamaka and K. Sawamoto, Phys. Rev. **112**, 1861 (1958).

The occurrence of these small facial tilt angles is a direct consequence of the antiferromagnetic distortion, hence they will disappear if the crystal is warmed above T_N. These facial tilt angles are used to show up the presence of twinning on the surface of bulk crystals of NiO where other methods fail. Some twin walls can be seen in thin sections of NiO by using polarized light transmitted through the sample.[15,24,29] Bulk crystals of NiO thicker than about $\frac{1}{2}$ mm are not sufficiently transparent[30] either in the visible or accessible[31] infrared for this technique to be useful. A colloidal suspension of Fe_3O_4 [32] was also tried on a crystal where a twin wall was visible by the reflection technique. No concentration of colloidal magnetite was observed. There are no stray magnetic fields at a T-wall, as can be seen from the spin arrangement in Fig. 3.

The procedure for making these facial tilt angles visible is to polish the faces of a crystal of NiO to an optical smoothness so that specular reflection of light can be observed. For a rectangular parallelpiped all six faces should be polished. During the polishing process the surface and the interior of the crystal usually become very highly twinned from the stress concentrations produced during the polishing operation. As will be shown later, very small stresses of less than 10^6 d/cm^2 will move twin boundaries in NiO. Such stresses are easily produced during polishing. Thus an optically polished surface consists of many twinned regions whose individual areas on the polished face may be 10^{-4} cm^2 or less. When such a polished crystal of NiO is annealed at high temperatures most of these T-walls will disappear, leaving only a small number of residual T-walls in the crystal. An untwinned area of the face of such an annealed crystal possesses a slightly pebbly appearance as contrasted to its original optical polish. But it still exhibits considerable specular reflection. This pebbly appearance arises from the disappearance of the many T-walls present at the surface of the crystal after polishing but before annealing. The few T-walls that remain after annealing are now visible as a tilt angle in the optically polished surface, as shown much exaggerated in Fig. 1. The pebbly surface could probably be avoided by polishing the crystals at temperatures above T_N. This was not tried.

By carefully observing the light reflected from such polished and annealed crystals all of the T-walls that come to the surface can be observed. Most of them can be seen with the unaided eye. For some which are spaced closely together a low-power microscope is needed. Figure 4 shows T-walls found by this technique. The magnitude of the tilt angles η is shown in Table I.

The nonzero values of η vary from 0.577 to 2.8828. At room temperature this means that the tilt angles for the six crystal faces listed vary from 2.5′ to 12′ of arc. Angles of this size can be and have been seen in the present work on NiO crystals from differences in specular reflection. When a T-wall produces no tilt in the crystal faces at the surface, then its presence and position must be determined from the emergence of the T-wall on a different surface.

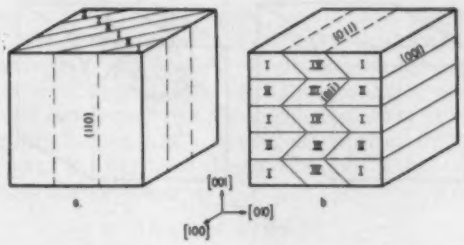

FIG. 5. Possible multiple twinning structures in unstrained crystals. (a) Parallel, nonintersecting T-walls with only two types of regions. (b) 4-wall structure in which all 4 T-walls intersect along a [100] line.

Multiple Wall Patterns

Several crystallographic features of multiple wall patterns are important in interpreting the observations of the specular reflection technique. First, it is impossible to produce a twinned region of any single type or mixture of types completely enclosed by a crystal of a given region type. This can be demonstrated by attempting to construct a completely enclosed twin volume from the twinning planes in Table I. This means that if a crystal possesses any twins at all, then some T-walls must terminate at the crystal surface. Thus if no T-walls occur at the surface, the crystal is completely untwinned.

In Table I are listed all of the twelve possible T-walls that can occur as single twins in an otherwise perfect crystal. In general a crystal may possess many T-walls, and the various combinations of T-walls can be studied. For example, Fig. 5(a) shows a crystal which contains a lamellar structure of alternate regions of types I and II twinned on (110) planes. The solid lines indicate T-walls with visible facial tilt angles, and the dotted ones T-walls with zero tilt angles. Such a multiply twinned crystal is almost free of strain, and this type of pattern has been found in well-annealed crystals. There is probably a small free energy/unit area associated with a T-wall, and a crystal would have a lower free energy if no T-walls were present. The free energy/unit area is quite small, and small imperfections in a crystal or at its surface can easily stabilize a domain pattern such as that in Fig. 5a.

Note that in Fig. 5(a) all of the T-walls terminate at the surface. More complicated multiple wall patterns of very low energy/unit volume can exist in which T-walls intersect. From Table I it is possible to construct patterns in which 2, 3, 4, 5, 6, 7, or 8 different

[29] P. W. Anderson, *Proceedings of the International Conference of Theoretical Physics*, (Tokyo and Kyoto 1953), p. 713.
[30] R. Newman and R. M. Chrenko, Phys. Rev. **114**, 1507 (1959).
[31] W. C. Dash, J. Appl. Phys. **23**, 1193 (1956).
[32] W. C. Elmore, Phys. Rev. **54**, 309 (1938).

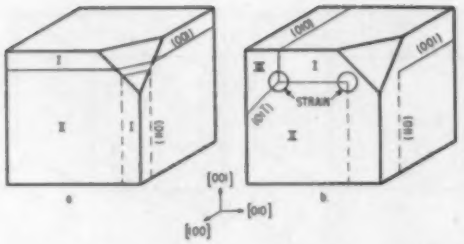

FIG. 6. Other possible multiple twinning patterns. (a) Type II region with 2 type I regions of different orientation. There is no strain. (b) 2-wall and a 3-wall twin pattern in which large strains are involved. These latter patterns are rare in well-annealed crystals.

T-walls can intersect along a common line. Of these only the 4-wall pattern has a low strain energy per unit volume. All the others have high strain energies associated with them. A multiple-wall crystal of this 4-wall pattern is shown in Fig. 5(b). Here all 4 types of regions intersect along a common [100] line. The pattern actually observed in Fig. 4 is just such a 4-wall pattern, but there the common line is [010].

Figure 6(a) shows another low-energy wall configuration where a crystal of type II has two type I regions near its surface. The spatial orientations of the rhombohedral axes in the two-type I regions are nearly but not exactly the same. Thus if the 2 T-walls in Fig. 6(a) could be moved together so that they join as in Fig. 6(b), then the crystal would be very highly strained. A junction of 3 T-walls with regions of types I, II, and III is also shown in Fig. 6(b). This configuration again produces a very high strain. The patterns illustrated in Fig. 6(b) do not occur frequently in a well-annealed crystal, but a few 3-wall patterns have been seen experimentally in annealed samples.

The strain energy of the 2-wall pattern can be computed by reference to Fig. 7. Here the 2-wall pattern shown in Fig. 6(b) is drawn schematically in its relaxed state where the strain energy is zero. In this state the I and II type regions fail to meet along the (001) plane by an angle of $2\sqrt{2}(\alpha-90°)$, or 12′ of arc at room temperature. If these regions were forced to meet, a tensile (but no shear) strain energy/unit volume would be uniformly distributed throughout the crystal volume. This energy can be estimated from the x-ray value of α and the measured value[28] of Young's Modulus Y above T_N. It is

$$U_v = 2Y[(\alpha/\pi)-\tfrac{1}{2}]^2, \qquad (2)$$

which is about 3×10^5 erg/cm³. The strain energy/unit volume for the 3-wall pattern is compressive and is about half as large. The strain energy associated with a 4-wall pattern is of the order of $[(\alpha/\pi)-\frac{1}{2})]^2$ less than the above, or about 10^{-2} erg/cm³.

Since the various T-wall patterns that are possible in annealed and nearly strain-free NiO crystals are quite simple, and since the T-wall separation is generally of the order of millimeters or larger, the specular reflection technique will reveal the presence of all such walls. In a badly twinned crystal where the distance between T-walls is 0.1 mm or less the specular reflection technique begins to fail. The limitations are the pebbly nature of the surface, and the limited magnification of a microscope.

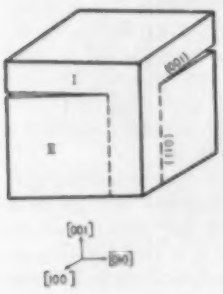

FIG. 7. A 2-wall multiple twinning pattern in which the strain has been removed by separating the type I and II regions along (001). The angular mismatch between the two (001) faces is about 12′ of arc.

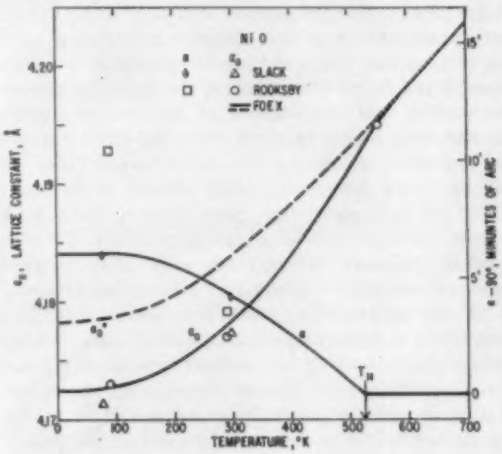

FIG. 8. The lattice constant a_0 and rhombohedral angle α in the 4-molecule unit cell of NiO as a function of temperature. The distortion at temperatures below T_N is evident. The curve a_0'' represents the nonmagnetic portion of the thermal contraction.

X-RAY MEASUREMENTS OF RHOMBOHEDRAL DISTORTION

The lattice constant and the rhombohedral angle in NiO at temperatures above and below T_N have been measured by Rooksby[11] using a back reflection x-ray technique on a powdered sample. These data are shown in Fig. 8. From the plotted temperature dependence his value for α at 297°K would be 90° 3.5′. Measurements by Shimomura *et al.*[29] give 90° 3.8′ at about this temperature. The present x-ray measurements on well-annealed NiO powder give $\alpha = 90°\ 4.2' \pm 0.3'$ at 297°K,

[29] Y. Shimomura, I. Tsubokawa, and M. Kojima, J. Phys. Soc. Japan, 9, 521 (1954).

and 90° 6′ at 78°K. These values of α are used in all the present calculations. The observed variation in α at 297°K may be caused by impurities in the NiO,[34] or by excess oxygen.[35,35] It is felt that Rooksby's value at 90°K is too high, since the temperature variation of α should approximate that of the sublattice magnetization. The powder sample for the x-ray work in the present experiment was prepared from $NiCO_3$ by decomposing it to NiO and then by annealing at 1500°C in argon containing about 0.01% by volume of oxygen at a total pressure of one atmosphere. This small amount of oxygen in the argon prevents reduction of the NiO, and should produce a NiO product not far from stoichiometric.[35,36] A careful annealing treatment is required in order to obtain the sharp x-ray lines necessary for measuring such a small distortion. One test was made in which a well-annealed single crystal of NiO was ground to a fine powder with a mortar and pestle. The grain size of the powder was about 100 μ as measured with a microscope. The (420) x-ray reflection lines from this powder were quite broad compared to their width as measured with the annealed powder. This smearing out of the x-ray lines is probably caused by the very small size of the twin regions in the freshly ground powder. From the x-ray line broadening it is estimated that the size of these regions is about 0.1 μ, which is much smaller than the grain size. In view of the small pressures required to move T-walls in NiO, it is not surprising that the grinding procedure produces a highly twinned crystal. Such a small size smears out the rhombohedral distortion as seen by x rays, and makes the crystal structure appear to be a simple cubic. This is probably the origin of the pure, cubic NiO reported by several recent authors[26,37] for temperatures well below T_N.

The x-ray measurements yield, simultaneously with α, the lattice constant a_0. The value measured in the present experiments at 297°K is $a_0=4.177$ A using the Cu $K\alpha_1$ wavelength of 1.54050 A. This agrees well with many of the recent determinations[6,11,26,27,30,33,35,37] when the conversion from X units ($a_0=4.167$) to A is made. The temperature dependence of a_0 is also shown in Fig. 8. The three points measured by Rooksby agree quite well with the solid curve obtained from the temperature dependence of thermal-expansion coefficient as measured by Foëx.[2,38] The integral of the linear thermal-expansion coefficient over a temperature interval gives the fractional change in a_0. A small correction to this integral is caused by the temperature dependence of α, but this is negligible. The solid curve of a_0 vs T obtained from the data of Foëx was fitted to Rooksby's data at 548°K. The agreement is quite good. The curve a_0'' is an estimate of the behavior that would be observed if only thermal contraction occurred. The difference between a_0 and a_0'' is a magnetic contraction, in the same sense[39] that the specific heat capacity of an antiferromagnet has a lattice and a magnetic component. The fractional change in a_0 at 0°K due to the magnetic contraction[13] is

$$\Delta a_0/a_0=-1.5\times10^{-3} \qquad (3)$$

from Fig. 8. The relationship between $\Delta a_0/a_0$ and α at 0°K is rather complicated, and appears[13] to involve the spatial derivatives of both the direct exchange and superexchange integrals. A crude order-of-magnitude argument, however, can be constructed as follows. Consider a cubic unit cell of NiO at 0°K which has not been distorted by a magnetic contraction. Then let a magnetic contraction occur along [111], and in no other direction. The consequent dilation in the (111) plane is assumed to be governed by Poisson's ratio μ. This model states that

$$\Delta a_0/a_0=-[(1-2\mu)/(2+2\mu)][\alpha-(\pi/2)]. \qquad (4)$$

On using $\mu=0.22$ at 0°K from data[40] on MgO, and $\alpha=90°\ 6'$, the result is $\Delta a_0/a_0=-0.4\times10^{-3}$. This is of the same order of magnitude as that given in Eq. (3).

CRYSTALLOGRAPHIC MEASUREMENT OF RHOMBOHEDRAL DISTORTION

Figure 9 shows schematically the facial tilt angle η produced at a T-wall between regions of types I and II in an otherwise untwinned crystal. This facial tilt angle is directly proportional to the rhombohedral distortion ($\alpha-90°$). A measurement of this tilt angle can readily be made in a crystal goniometer. Crystal J832A-1 was optically polished on its $(1\bar{1}0)$ and $(11\bar{2})$ faces, and then annealed. It was stressed at room temperature along [111] and converted to a single, untwinned crystal of type I. Then a small stress was applied to one end of the crystal along $[11\bar{2}]$ in order to convert that end to type II as in Fig. 9. The type I and II regions are twinned on a (110) plane. The tilt angle η was measured as $11'\pm1'$. From Table I the calculated value of η is

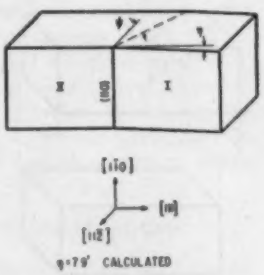

FIG. 9. A single (110) T-wall between regions of types I and II. The facial tilt angle η is exaggerated. The angle ψ between the $[11\bar{2}]$ direction and the invisible T-wall is nearly 35°.

[34] Y. Shimomura and I. Tsubokawa, J. Phys. Soc. Japan, **9**, 19 (1954).
[35] D. P. Bogatskii, Zhur. Obshchei Khim. **21**, 3 (1951).
[36] F. D. Richardson and J. H. E. Jeffes, J. Iron Steel Inst. (London) **160**, 261 (1948).
[37] H. E. Swanson and E. Tatge, Natl. Bur. Standards (U.S.) Circ. 539, Vol. I (1953).
[38] G. Foëx, Bull. Soc. Chem., France **19**, 373 (1952).
[39] J. W. Stout and E. Catalano, J. Chem. Phys. **23**, 2013 (1955).
[40] M. A. Durand, Phys. Rev. **50**, 449 (1936).

TABLE II. Values of facial tilt angle and length change in NiO at 300°K. Regions are types I and II twinned on (110).

Quantity	Crystal	Measured value	Calculated value
Facial tilt angle on $(11\bar{2})$	J832A-1	$11' \pm 1'$	$7.9'$
Fractional length change along $[111]$	J832A-1	1.1×10^{-6}	1.6×10^{-6}
	7–9A	1.3×10^{-6}	1.6×10^{-6}
	7–9A[a]	1.9×10^{-6}	1.6×10^{-6}

[a] Reannealed at 1500°C.

1.886 ($\alpha-90°$), or 7.9′ using the present α value of 90°4.2′. See Table II.

Notice that the $[11\bar{2}]$ direction makes an angle of only 19°28′ with the $[\bar{1}\bar{1}1]$ direction. This latter direction is the contraction axis for type II regions. The angle between $[11\bar{2}]$ and $[\bar{1}1\bar{1}]$ or $[1\bar{1}\bar{1}]$ is 61°52′, while the angle between $[11\bar{2}]$ and $[111]$ is 90°. Thus a stress along $[11\bar{2}]$ will favor a type II region over those of any of the other three types. As long as some critical stress is exceeded a well-annealed NiO crystal stressed along $[11\bar{2}]$ will become a single region of type II. From the angles between the contraction axes and the possible twinning planes in Table I, it can be shown that as long as the angle between the direction of the stress and the particular contraction axis in question is less than 35°16′, then the type of region with that contraction axis will be the favored one.

Another check that can be made on the x-ray value of α is to measure the change in length of a macroscopic crystal when it is switched from, say, a type II region to a type I. Consider a crystal of NiO cut with the set of faces (111), $(1\bar{1}0)$, $(11\bar{2})$ as shown in Fig. 10. After annealing, this crystal can be converted to type II by stressing along the $[11\bar{2}]$ axis. Then by a stress applied along $[111]$ it can be completely converted to type I. The length of the $[111]$ dimension of the crystal will decrease as the crystal changes from type II to type I. It follows that the crystal dimension in the $[\bar{1}\bar{1}1]$ direction will therefore increase. The density and hence the overall volume of the crystal remain unchanged during this switching process. It should be remembered that the crystallographic directions used here are based on the high-temperature cubic unit cell. The dimensions of the true rhombohedral unit cell do not change during this switching process, but the orientation of this cell in space does change. The fractional change in length of the $[111]$ dimension can be calculated for this switching process, and at 300°K is given by

$$\Delta l/l = (2/\sqrt{3})[\alpha-(\pi/2)] = 1.6\times10^{-6}, \qquad (5)$$

where α is in radians.

For a crystal 0.5-cm long, this length change amounts to 8 μ. The two crystals that were measured were 0.54-cm (7–9 A) and 0.85-cm (J832A-1) long. Thus the length change was readily observed with an optical microscope using a filar eyepiece and a linear magnification of about 60 times. The results of these measurements are given in Table II.

From this table it is clear that at present the x-ray measurements are more precise and reproducible than either the measurements of facial tilt angle or length change. The measurement of the tilt angle is limited in accuracy because of the pebbly nature of the crystal surface, and because the tilt angle will differ from the calculated value if the crystal face is not exactly a $(11\bar{2})$ face. The scatter in the data for $\Delta l/l$ in part represents the uncertainty in the particular measuring technique where the change in overall length was measured. However, if the entire volume of the crystal does not change region type during the switching process, the measured $\Delta l/l$ will be less than the calculated one. This may account for the low value for J832A-1. From Table II and from several other kinds of measurements it appears that crystal 7–9 A changed completely. At present the results of the facial tilt angle and length change measurements are in substantial agreement with the x-ray work. They all indicate a rhombohedral distortion in NiO at 300°K.

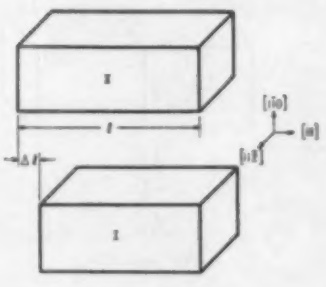

FIG. 10. A single crystal changes dimensions when it is converted from one type of region to another. A region of type I is shorter in a $[111]$ direction than a type II by an amount Δl.

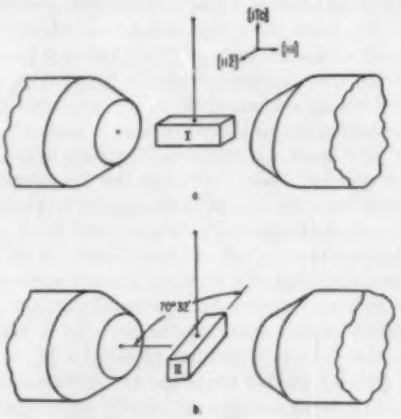

FIG. 11. A single crystal of NiO suspended about a $[1\bar{1}0]$ axis in a magnetic field. When the crystal is type I the long dimension, $[111]$, is parallel to **H**. After "pinching" along $[11\bar{2}]$ the crystal is type II, and makes an angle of 70° 32′ with respect to **H**.

MAGNETIC SUSCEPTIBILITY OF UNTWINNED CRYSTALS

Once it is known that a particular crystal of NiO is untwinned, then meaningful measurements of its magnetic susceptibility χ can be made. Consider a crystal cut with the set of faces (111), $(1\bar{1}0)$, $(11\bar{2})$ and suspended about a $[1\bar{1}0]$ rotation axis in a magnetic field **H**. The **H** field is directed perpendicular to $[1\bar{1}0]$ as shown in Fig. 11(a). The anisotropy in χ can be measured by using a sensitive torque magnetometer. Consider a crystal of type I which has no domain walls of either *T* or *S* variety, and in which all four of the submotifs are aligned parallel (or antiparallel). Such a crystal will have three different principal susceptibilities χ_{11}, χ_{12}, and χ_{11}, see Fig. 12. Here χ_{11} and χ_{12} are both measured in a direction perpendicular to the preferred spin direction, and χ_{11} is along the preferred spin direction. Both χ_{12} and χ_{11} are measured in the (111) plane, but have no necessarily preferred crystallographic directions. However χ_{11} is measured perpendicular to the plane along the crystallographic [111] direction. Torque measurements were made on crystal 7–9A in an untwinned type I state, but without any effort made to remove the *S*-walls, i.e., to align the spins within (111). These measurements yield susceptibility differences only, but allow a comparison of the present results with those of previous studies. The susceptibility in the (111) plane when checked at low **H** fields ($H=1000$ oe) was found to be nearly isotropic. The spin orientation within the (111) planes is completely random. Similar isotropies have been seen by Singer[21] and by Kohdoh *et al.*[4] Thus the susceptibility in the (111) plane has a value of $\frac{1}{2}(\chi_{12}+\chi_{11})$. In such a case the torque measurements in the $(1\bar{1}0)$ plane at low fields ($H<1000$ oe) give the value of $\chi_{11}-\frac{1}{2}(\chi_{12}+\chi_{11})$. The torque vs angular position is given very nearly by $\tau \sin 2\theta$, as expected for an antiferromagnet. The measured value of τ is plotted vs H in Fig. 13. For $H\leq 1000$ oe τ is accurately proportional to H^2, as expected from simple theory.[41] For $H>1000$ oe τ does not increase quite as rapidly as H^2. For $H\leq 1000$ oe the value of $\chi_{11}-\frac{1}{2}(\chi_{12}+\chi_{11})=3.3\times10^{-6}$ emu/gm ($\rho=6.80$ gm/cc) from Fig. 13. At higher fields the anisotropy in χ continues to decrease as **H** increases, because the spins in the (111) planes tend to rotate to become perpendicular to **H** in magnetic fields greater than about 2400 oe.[18] At fields of above 10 000 oe the susceptibility in $(1\bar{1}0)$ is tending toward $\chi_{11}-\chi_{12}$ due to this spin rotation. In Fig. 13 are shown some data for crystal J832A-1. At low **H** fields the results on this crystal agree with those on crystal 7–9A. However, before the high H field measurements were made, crystal J832A-1 became twinned, and consequently the torque was considerably less than for an untwinned crystal. By using the curve in Fig. 13, it is possible to compare the present results with those of Singer,[21,22] and of Kondoh *et al.*[4] At 295°K and 6000 oe Singer[22] found a susceptibility anisotropy of 2.4×10^{-6} emu/gm for NiO. This corresponds to approximately $\chi_{11}-\frac{1}{2}(\chi_{12}+\chi_{11})$, and gives an equivalent torque of 290 d-cm/cc. Kondoh *et al.*, found a torque value of 352 d-cm/cc at $H=6720$ oe for their best crystal. These two points are plotted in Fig. 13. Since these points fall very nearly on the curve for an untwinned crystal, the conclusion is that their stressing techniques produced crystals nearly free of twins. Unfortunately they had no direct method of checking for the presence of twins. Their estimated values (50% Singer, 75% Kondoh *et al.*) for the fractional volume that was untwinned were based on various theoretical assumptions concerning χ which may be invalid.

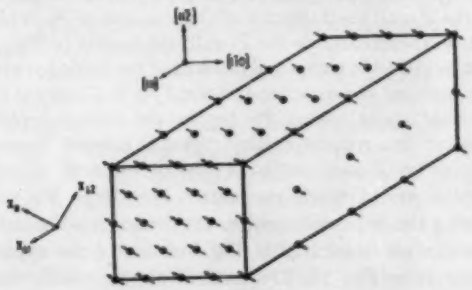

FIG. 12. A crystal in which no domain walls exist has 3 principal magnetic susceptibilities. They are χ_{11} measured along [111]. χ_{12} measured in the (111) plane perpendicular to the spins, and χ_{11} measured in the (111) plane parallel to the spins.

[41] L. F. Bates, *Modern Magnetism* (Cambridge University Press, Cambridge, 1951), 3rd ed., p. 161.

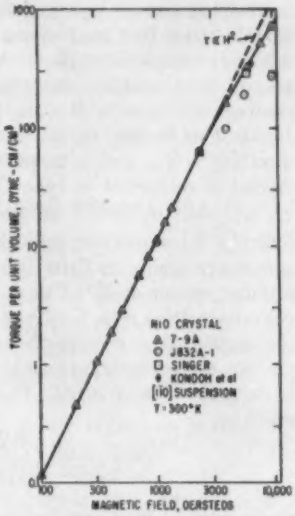

FIG. 13. The torque/unit volume exerted on single crystals of NiO in a magnetic field. A constant anisotropy in χ produces a torque proportional to H^2. The deviations from H^2 are caused by spin rotation (7–9A), and twinning (J832A-1). Representative data of other authors are shown.

TWIN WALL MOTION UNDER STRESS

The technique for producing untwinned crystals involves the removal of twin walls by a small stress applied to the crystal at room temperature after a

suitable anneal at high temperatures. The magnitude of this stress has been measured. Consider a crystal which is completely type I. When such a crystal is placed in a uniform magnetic field its equilibrium position will be with H along [111], as shown in Fig. 11(a). This is due to the fact that χ in the [111] direction is χ_{11}, and is larger than $\frac{1}{2}(\chi_{12}+\chi_{11})$. If the crystal is converted to type II, then the direction of χ_{11} will shift by 70°32′ lie along the $[\bar{1}\bar{1}1]$ direction. Since $[\bar{1}\bar{1}1]$ is also perpendicular to $[1\bar{1}0]$, the crystal will rotate about its $[1\bar{1}0]$ suspension to a new equilibrium position at 70°32′ as shown in Fig. 11(b). If the conversion from type I to type II is not complete, i.e., the applied stress was insufficient, then the equilibrium position ϕ of a crystal suspended in a magnetic field will be between 0° and 70°32′. The equilibrium angle ϕ is given by

$$\phi=\tfrac{1}{2}\arctan\left[\frac{4\sqrt{2}(1-g)}{16g-7}\right], \tag{6}$$

where g is the fractional volume of the crystal that is type I. Hence a measurement of ϕ yields a value of g. The g values as a function of applied stress were obtained in this way. The sequence of the experiment was as follows. The value of ϕ was determined in an H field of 2370 oe. The crystal was then removed from the H field and the stress, uniformly distributed over the crystal face, was slowly (in 10 sec) increased to the chosen value. After slowly removing the stress the crystal was replaced in the H field, and ϕ was remeasured. For the I to II conversion, the stress was applied to the $(11\bar{2})$ face, for the II to I conversion it was applied to the (111) face. The data for several crystals are shown in Fig. 14. In the case of crystal

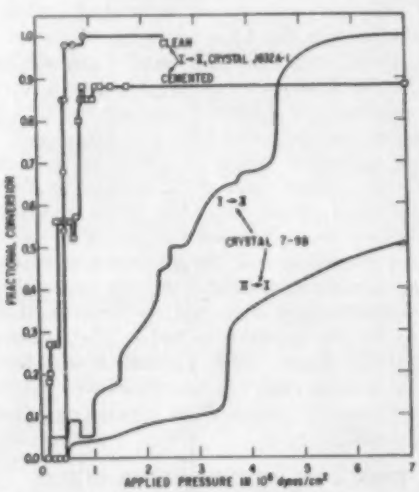

FIG. 14. The fractional conversion between 2 types of regions in crystals of NiO. The amount of conversion is a function of the condition of the crystal and the applied unidirectional pressure. The conversion is abrupt in a nearly perfect crystal.

J832A-1 (clean surface) the conversion was caused by a single T-wall (110) moving along the crystal. The value of g computed from the position of the wall observed by reflection was in good agreement with the value computed from ϕ.

The four curves in Fig. 14 show that the stress required depends on the past history of the crystal. The two curves for crystal J832A-1 were taken on a well-annealed crystal with optically polished surfaces. In the first run a small amount of organic cement (G. E. glyptal #1286) had been applied to the crystal surface near the center. This was removed with acetone before the second run, but otherwise the crystal was the same as in the first run. Note the very abrupt conversion in the second run compared to the erratic conversion in the first. The twin boundary was followed visually in both runs. In the first it was arrested at the thin layer of cement near the center of the crystal (i.e., near $g=0.5$). In the second run no such arrest is seen. Thus defects on the crystal surface can hinder the motion of a twin wall. The other two curves are for crystal 7–9B taken after an annealing treatment, but not before the crystal had been handled quite a bit and many type I-type II conversions had been performed. Furthermore this crystal had a coarsely ground (#380 mesh SiC) surface. For this crystal the stresses required are much larger, and the conversion is not abrupt but gradual. Many different twin walls are probably moving instead of just one. This crystal was polished, reannealed, and stressed before the neutron results[24] were obtained. The low applied stresses (10^6–10^7 d/cm²) in Fig. 13 can be compared with those used by Kohdoh *et al.*, (1.2×10^6 d/cm²) and the somewhat larger values of Singer ($\geq1.4\times10^7$ d/cm²). The observation that the conversion to an untwinned state can be performed at room temperature by small stresses that can easily be applied by the thumb and index finger has led to the name "pinch-effect" for this conversion process.

The external stress that is applied to a crystal face can be converted to an equivalent wall pressure $\mathbf{P}_w$ acting inside the crystal and uniformly over the surface of the T-wall itself. By use of this concept of $\mathbf{P}_w$, which acts perpendicular to the T-wall, the results in Fig. 14 can be stated in terms independent of the angle between the external stress vector and the T-wall. Clearly if the external stress vector $\mathbf{P}_A$ lies in the twinning plane between two regions, neither region is favored. In such a case no T-wall motion would occur, and no conversion would result no matter how large $\mathbf{P}_A$ was. During the conversion process the crystal must actually contract an amount Δl in the direction of the applied stress as in Fig. 10. The amount of this contraction, $\Delta l/l$, is a function of the angle between the stress vector and the twinning plane. For a given value of $\mathbf{P}_A$ the magnitude of the equivalent wall pressure is given by

$$P_W=P_A\Delta l/l. \tag{7}$$

For a [111], [$\bar{1}$11], or a [11$\bar{2}$] stress direction $\Delta l/l$ is given by Eq. (5). A pressure of 5×10^5 d/cm² applied along [111] or [11$\bar{2}$] as shown in Fig. 14 thus corresponds to $P_W=800$ d/cm², or about $\frac{1}{2}$ mm Hg. With this pressure a T-wall was found to move through the crystal J832A-1. As this T-wall moves through the crystal there is an energy dissipation of 800 erg/cm², which is lost as heat. The minimum wall pressure for any T-wall motion in Fig. 14 is 240 d/cm² corresponding to a $\mathbf{P}_A$ value of 1.5×10^6 d/cm².

One dissipative mechanism that is present when a T-wall moves is the spin rotation in the (111) plane. At a T-wall two different {111} planes intersect, as shown in Fig. 3. When this occurs the only way a spin can lie simultaneously in both planes is to be parallel to their line of intersection. So in Fig. 3 at a T-wall between regions of type I and II the spins are forced to lie parallel or antiparallel to the [1$\bar{1}$0] direction in the vicinity of the wall. Consider the (111) plane A–A which cuts across the T-wall from region I to region II. This plane in region I has, by definition, all of its spins directed in the same sense along [1$\bar{1}$0]. In region II only half of the spins are in the [1$\bar{1}$0] direction, the other half are [$\bar{1}$10] direction. The 1 and 2 submotifs in region I suffer no change in spin sense across the T-wall, but the 3 and 4 motifs suffer a spin rotation of 180°. Thus a T-wall has a built in partial S-wall. This means that as the T-wall advances into the type II region this partial S-wall must also advance, and spin rotation occurs. Torque magnetometer measurements have shown[18] that the spin rotation in the (111) planes in untwinned NiO crystals is accompanied by a rotational energy loss of 375 erg/cm³-cycle. Measurements made on J832A-1 gave 400 erg/cm³-cycle for $\mathbf{H}$ fields above 4500 oe. As a T-wall advances one half of the spins in a unit volume must rotate through one-half cycle (180°). Hence the dissipation/unit volume as the T-wall moves would be $\frac{1}{4}$ of 400 erg/cm³. This corresponds to a $\mathbf{P}_W$ of 100 d/cm², which is close to the minimum value observed in Fig. 13. Thus spin rotation appears to be the factor which limits the ease with which a T-wall will move, and the present measurements are approaching this limit.

In view of the small values of $\mathbf{P}_W$ and the small energy dissipations of the order of 10^2 erg/cm³ during T-wall motion, it becomes apparent why badly twinned crystals exhibit no "pinch-effect" at small applied stresses. A badly twinned crystal will probably possess many 2, 3, 5, etc. T-wall patterns where there is a large strain energy of the order of 10^5 erg/cm³. In order to move one such multiple wall pattern through the strain field of a neighboring multiple wall pattern wall pressures of the order of 10^5 d/cm² would be required. This corresponds to external pressures $\mathbf{P}_A$ of the order of 10^8 d/cm². Such pressures are well above the range where just two fingers can be used, and the T-walls are effectively locked in place. Figure 6 illustrates the manner in which a crystal can become locked so that small pressures cannot produce an untwinned crystal. In Fig. 6(a) both of the I–II walls are mobile, but further motion will join them in a highly strained region such as shown in Fig. 6(b). The only way to conveniently unlock such a multiply twinned crystal is to reanneal it.

Other "Pinch-Effects"

It has been observed that NiO crystals will also exhibit the "pinch-effect" when they are cooled to 78°K in liquid nitrogen. Furthermore an annealed crystal of MnO cut with the set of faces (111), (1$\bar{1}$0), (11$\bar{2}$) exhibited a "pinch-effect" in liquid nitrogen. The type I to type II conversion and the reverse was performed at 78°K, and was verified by noting the equilibrium orientation of the crystal in a magnetic field of 1700 oe. On this particular crystal J432[10] the stress required for conversion was about 10^8 to 10^9 d/cm², and thus much higher than for NiO. The crystallographic and magnetic structures of MnO[16,17] are very similar to those of NiO, hence the ability to remove twins by an applied stress is not surprising.

The production and motion of twin walls under small applied stresses has been observed in ferroelectrics such as $BaTiO_3$,[42] and in ferrimagnetics such as Fe_3O_4.[43] These materials also undergo a small distortion from a high-temperature cubic crystal structure to one of lower symmetry. These transition temperatures are 390°K for $BaTiO_3$ and 118°K for Fe_3O_4.

Another interesting comparison can be made between NiO crystals and metal crystals. Stresses of the order of 10^8 to 10^9 d/cm² are customarily required to produce and move twins in metal crystals.[44] These stresses are considerably larger than those measured above for NiO. One similarity between NiO and metals is that the twinning "cry" heard in metals[45] can also be heard in NiO when the twins walls move.

TWIN WALL MOTION IN MAGNETIC FIELDS

In a well-annealed crystal in which a few T-walls already exist it has been found possible to move these walls with moderate magnetic fields from 5000 to 20 000 oe. For example, crystal 7–9A was freely suspended on a fine nylon thread with a [1$\bar{1}$0] rotation axis as in Fig. 11. The crystal had been previously stressed so that only type I and II regions were present, and so that at the start of the experiment, g the fraction of the crystal that is type I was about $\frac{1}{2}$. As the $\mathbf{H}$ field was slowly increased both g and ϕ changed slowly and somewhat irregularly. After each increment of $\mathbf{H}$ the angle ϕ was measured and g was computed. The data

[42] P. W. Forsbergh, Jr., Phys. Rev. **76**, 1187 (1949).
[43] L. R. Bickford, Jr., Revs. Modern Phys. **25**, 75 (1953).
[44] R. Clark and G. B. Craig, Progr. in Metal Phys. **3**, 115 (1952).
[45] B. Chalmers, Nature, **129**, 650 (1932).

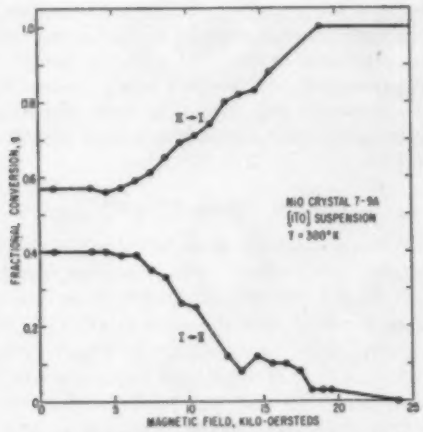

FIG. 15. The fractional conversion between 2 types of regions in NiO in a magnetic field. The fraction g was set close to 0.5 at $H=0$, and then g was monitored as $\mathbf{H}$ increased. At $H>20\,000$ oe the conversion is almost complete, and an untwinned crystal results.

are shown in Fig. 15. When the crystal is hanging freely, the average susceptibility measured along $\mathbf{H}$ is

$$\bar{\chi}(g)=\tfrac{1}{2}[\chi_{11}+\tfrac{1}{2}(\chi_{12}+\chi_{11})]+\tfrac{1}{6}[\chi_{11}-\tfrac{1}{2}(\chi_{12}+\chi_{11})][9-32g(1-g)]^{\frac{1}{2}}. \quad (8)$$

This is based on the assumption that the spins in all the (111) planes are random, and only type I and II regions are present. This $\chi(g)$ has a minimum at $g=\frac{1}{2}$. Hence if $|g-\frac{1}{2}|$ increases in an applied magnetic field, there is a decrease in potential energy of the system. This energy is dissipated in moving the T-walls. An equivalent wall pressure can be calculated as a function of g and H from

$$P_W=\frac{H^2}{2}\rho\frac{\partial\bar{\chi}(g)}{\partial g}, \quad (9)$$

where ρ is the density of NiO. From Fig. 15 it can be seen that the twin wall starts moving at about $H=5000$ oe, or a P_W of about 100 d/cm². The whole crystal becomes a single type at about 4000 d/cm². The average wall pressure for the conversion is about 600 d/cm² which is close to the 800 d/cm² found mechanically. The T-walls start moving at 100 d/cm², again close to the value for the spin rotation resistance. Some recent results[46] on the magnetostriction of polycrystalline NiO may be interpreted as T-wall motion for $H>5000$ oe, i.e., comparable to the present values.

The transition from type I to II (or the reverse) in the magnetic field is not very sharp. This gradual transition may be caused by the roughness of the crystal surface, and some damage caused by previous switching. It should be mentioned that at the highest fields employed it is not necessarily true that the spins in the (111) planes will be random. They will tend to become aligned perpendicular to $\mathbf{H}$. A complete spin alignment perpendicular to $\mathbf{H}$ will change the anisotropy in χ at $g=1$ from $\chi_{11}-\frac{1}{2}(\chi_{12}+\chi_{11})$ to $(\chi_{11}-\chi_{12})$. This latter anisotropy may be quite small, and hence account for the large $\mathbf{H}$ fields necessary to make g approach 0 or 1.

CONCLUSIONS

The crystal structure of NiO in the antiferromagnetic state is a slightly distorted cubic. This distortion may lead to the occurrence of multiple twinning and to the presence of many antiferromagnetic domains. These domains may be separated either by twin walls or by spin-rotation walls. The twin domain walls in crystals of NiO may be readily observed by a specular reflection technique. It is possible to remove these walls in a suitably annealed crystal by small mechanical stressed applied to room temperature, or by moderate magnetic fields. The resistance to twin wall motion may be caused by other twin walls, surface imperfections, crystal impurities, and finally spin-rotational hysteresis. Crystallographic measurements of the fractional length change during the conversion of a crystal from a type I to a type II region, and of the facial tilt angle between these two regions confirm the x-ray measurement of the rhombohedral distortion below T_N. Untwinned crystals possess an anisotropic susceptibility which has been measured and compared with earlier results.

ACKNOWLEDGMENTS

The author wishes to thank W. L. Roth for many valuable discussions, J. S. Kouvel for some of the torque magnetometer measurements, L. M. Osika for the x-ray measurements, and C. D. Graham for the use of a torque magnetometer. Furthermore, he wishes to especially thank J. H. McTaggart for preparing the specimens and assisting with the measurements.

[46] K. P. Belov and P. E. Levitin, Zhur. Eksp. i Teoret. Fiz. **37**, 565 (1959).

Surface Cleaning by Cathode Sputtering

O. C. YONTS
*Oak Ridge National Laboratory, Oak Ridge, Tennessee**

AND

DON E. HARRISON, JR.
Permanent Address: Engineering Physics Department, University of Toledo, Toledo, Ohio

(Received April 7, 1960; and in final form May 11, 1960)

Evidence is presented to indicate that surface recontamination from background gases may be a significant factor in quantitative sputtering measurements, even for beam current densities of 0.1 ma/cm² and operating pressures of 5×10^{-5} mm of Hg. An oversimplified mechanism is discussed which leads to criteria for a clean-surface sputtering experiment.

THE problem of cathode sputtering has plagued workers in gaseous electronics for generations. Proper understanding of the phenomena has been severely hampered by a gross lack of reliable experimental data, and the failure of many authors to report parameters which are now known to be highly significant. One aspect of our program has been the accumulation of a large mass of data applying to the same experimental system, but subject to the usual vagaries of a "repeated" experiment. While analyzing these experiments, the authors found confirmation of an effect which has been largely overlooked in previous sputtering studies at higher energies, but had been observed by Wehner at low energies.[1]

Results of the bombardment of copper by singly charged argon ions, using a calutron-type mass spectrometer, have been reported,[2] and the advantages of this system discussed in some detail. The factors influencing this experiment were relatively well known, and the anticipated reproducibility was somewhat less than 5%. As usual, the apparatus did not cooperate, and the actual spread was considerably greater, often approaching 20%. Figure 1 shows a plot of raw data for annealed copper targets. When enough data were accumulated we found that the dispersion could be explained as a dependence of the sputtering ratio upon the vacuum-system operating pressure. This is shown in Fig. 2 where sputtering ratios obtained at 30 kev are plotted against tank pressure.

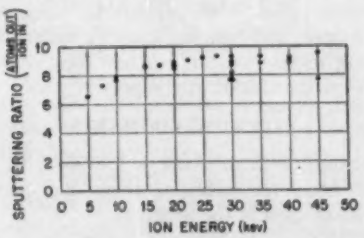

FIG. 1. Sputtering of annealed copper by argon ions uncorrected for pressure.

This effect was particularly surprising as back diffusion of sputtered material to the target had been the only pressure-sensitive mechanism considered, and it should cease to be significant at pressures below 10^{-3} mm of Hg, where particle mean free paths approach the tank dimensions. The new pressure dependence is unmistakable.

The oversimplified analysis described in the following has led us to ascribe the pressure dependence to a surface layer effect. Clearly, any surface layer left by the preparatory cleaning process cannot significantly affect the experiment, as it is destroyed during the first few minutes of bombardment. This is a well-known method of final cleaning in ultravacuum systems. Furthermore, we would expect a bombardment-cleaned surface to remain clean for the duration of the sputtering experiment. In ultravacuum systems this is true; the surface layer has no opportunity to rebuild, but in the usual dynamic vacuum system we deal with a steady-state balance between the destructive properties of the beam and regeneration from the system residual gas. Suppose we consider a naive analysis of this steady state.

In the following, we assume that the surface layer is always less than half a monolayer, so that the gas sticking probability may be assumed a constant. The sticking process is governed by the equation

$$\partial n/\partial t = n_s - n_e, \tag{1}$$

where n is the surface layer density (atoms/area), n_s is

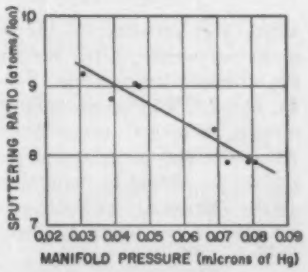

FIG. 2. Sputtering of copper by 30-kev argon ions as a function of manifold pressure.

* Operated by Union Carbide Corporation for the U. S. Atomic Energy Commission.

[1] Gottfried K. Wehner, Phys. Rev. **108**, 35 (1957).

[2] O. C. Yonts, D. E. Harrison, Jr., and C. E. Normand, J. Appl. Phys. **31**, 447 (1960).

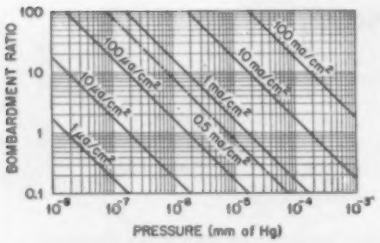

FIG. 3. Bombardment ratio (n_i/n_g) as a function of pressure for different current densities.

the number of atoms striking a unit area per second, and n_e is the number of atoms emitted per second from a unit area. It is convenient to write

$$n_e = An_g,$$

where n_g is the number of reactive gas atoms striking a unit surface per second, and A is the sticking probability for a single atom. Similarly,

$$n_e = Bn_i,$$

where n_i is the beam particle current density, and B is the emission ratio, defined by this equation. We shall assume that n_i is constant, the usual experimental arrangement, so that the variation of B need not affect our work.

We further assume that the emission ratio is proportional to the surface density, $B=Cn$, so that

$$n_e = (Cn_i)n = Dn.$$

The integration is trivial, giving

$$n = n_0 e^{-Dt} + (A/D)n_g(1-e^{-Dt}), \tag{2}$$

which demonstrates that the initial layer n_0 will be destroyed, and that the equilibrium layer is

$$n_\infty = (A/D)n_g = (A/C)(n_g/n_i). \tag{3}$$

Now A is certainly less than unity, but we have no information about C. Still it is possible to keep n_∞ small if $n_i \gg n_g$. *Thus for a good sputtering experiment, i.e., on a clean surface, it is imperative that the beam particle-current density be very much greater than the gas particle-current density.* Kinetic theory gives

$$n_g = p[8N_0/3\pi MkT]^{\frac{1}{2}},$$

where p is pressure, N_0 Avogadro's number, M the molecular weight, k the Boltzmann's constant, and T the absolute temperature. For a molecular weight of 40, $n_g = 3.50\times10^{20}p$, where p is in mm of Hg. Graphs of n_i/n_g for several current densities are shown in Fig. 3. As a concrete example, the pressure of *reactive* background gas should be maintained around 10^{-8} mm Hg *during operation*, when current densities of 100 μa/cm² are used in the beam, to ensure that surface buildup is not affecting the sputtering ratio. Our experiments, done with beam densities of 0.2 ma/cm² and tank pressures around 5×10^{-6} mm Hg clearly did not meet this criteria.

As mentioned earlier, Wehner has been cognizant of this problem, and has taken pains to be certain that his experiments were carried out on clean surfaces. Recent work by Hagstrum and D'Amico[3] provides excellent confirmation of his procedures. The data of Grønland and Moore[4] were taken in a borderline region, but probably are free from surface effects. Data from other sources which do not present beam current densities and background pressures are immediately suspect, *even at high energies*. The results reported by McKeown[5] are anomolous. This experiment apparently was conducted in a "dirty" system, but the results agree with Wehner's[6] low-energy work. Either McKeown's neutral beam was keeping the surface clean, or there are other effects which we do not understand in the low-energy region.

If we assume that the emission probability

$$C = n_e/nn_i$$

is independent of n, and therefore also independent of the contamination pressure, Fig. 2 allows us to calculate sticking probabilities, for the contamination, which are about 0.5. Alternatively, we can view this emission as a sputtering process which is limited by the quantity of material available to sputter, rather than the usual parameters of sputtering. This "surface sputtering" process will compete with the bulk process, appearing as the reduction in the bulk-sputtering ratio indicated in Fig. 2.

It is also interesting to calculate a "zero-pressure sputtering ratio" from the linear pressure dependence. Thus the "true" sputtering ratio for argon on copper at 30 kev appears to be about 10.3, which may be compared with the experimental value of 9.2. At the present time we do not have enough data to make similar extrapolations for other energies, but we anticipate corrections of the same order of magnitude.

Further experiments determined that oxygen was *not* the reactive agent in our apparatus when Ar^+ bombarded copper, and cast suspicion on water vapor, but removal of the equipment to a new location precluded further experimentation at the present time.

ACKNOWLEDGMENTS

The authors wish to thank J. P. Wood, H. L. Huff, and D. F. Leach for operation, design, and construction of equipment used in the program.

[3] H. D. Hagstrum and C. D'Amico, J. Appl. Phys. **31**, 715 (1960).
[4] F. Grønland and W. J. Moore, J. Chem. Phys. (to be published).
[5] D. McKeown, Bul. Am. Phys. Soc. Ser. II, **5**, 286 (1960).
[6] R. V. Stuart and G. K. Wehner, Phys. Rev. Letters **4**, 409 (1960).

Apparatus for the Measurement of the Thermal Diffusivity of Solids at High Temperatures*

B. Abeles, G. D. Cody, and D. S. Beers
RCA Laboratories, Princeton, New Jersey
(Received May 19, 1960)

An apparatus is described for measuring the thermal diffusivity of solids in the temperature range 30°–1000°C. It employs a method in which the dispersion and the attenuation of a thermal wave, propagated through the solid, are measured. The theory underlying this method is presented, and results are given of measurements on Armco iron and germanium.

I. INTRODUCTION

A MAJOR difficulty in measuring the thermal conductivity κ of a solid at high temperatures is the elimination of radiation losses. Sidles and Danielson,[1] using a modification of Ångstrom's method,[2] have shown that in measuring the thermal diffusivity D (thermal conductivity divided by specific heat), radiation effects can be taken into account and a high degree of accuracy is attainable at temperatures as high as 600°C. In this method a thermal wave is propagated through the solid, and the thermal diffusivity is determined from the dispersion and attenuation of that wave. In order to determine κ from measurements of D, it is necessary to know the specific heat c. This is not a serious complication since specific heats can be measured to an accuracy better than 1% even at high temperatures. Moreover, in the vicinity of the Debye temperature and above it, the specific heats of most solids do not vary appreciably with temperature and can be estimated from Dulong-Petit's law. Sidles and Danielson[1] described an apparatus for measuring thermal diffusivities of metal wires about 20 in. in length. Samples of this length are, however, unobtainable for many materials. Kanai and Nii[3] measured thermal diffusivities of semiconductors at temperatures which did not exceed 380°C.

In this paper an apparatus is described for measuring thermal diffusitivies of solids from room temperature up to about 1000°C with an accuracy of about 2%. The samples employed can vary in length from about ½ to 2 in. The method can be extended readily to yet higher temperatures. The technique used here differs from that of Sidles and Danielson's[1] in the use of higher frequencies and a more accurate method of phase measurement. The use of higher frequencies affords the following advantages: Radiation effects are reduced, it is possible to use shorter samples, the measuring time is reduced, and a better signal-to-noise ratio is obtained. A wide range of diffusivities have been measured with this apparatus, ranging from the very high values for metals in which the thermal conductivity $\kappa=4$ w deg^{-1}cm^{-1}, to the very low ones for poor thermal conductors in which $\kappa=0.005$ w deg^{-1} cm^{-1}. Results of measurements of thermal diffusivities are reported for Armco iron from 30°–1025°C and for germanium from 30°–800°C.

II. THEORY OF THE METHOD

Consider a rod of arbitrary, yet constant, cross section; it is bounded by the surfaces $z=0$, $z=L$, and $F(x,y)=0$. A small heat input, which varies sinusoidally, is applied to the rod at the $z=0$ boundary. The temperature T at time t and at any point x, y, z of the rod is given by

$$T(x,y,z,t)=T_0+\theta(x,y,z,t), \tag{1}$$

where T_0 is the mean absolute temperature of the rod and θ satisfies the differential equation

$$\Delta\theta=D^{-1}\partial\theta/\partial t, \tag{2}$$

subject to the boundary conditions

$$\kappa(\partial\theta/\partial n)=-4\epsilon\sigma T_0^3\theta, \tag{3}$$

and

$$\theta(x,y,0,t)=\theta_0 e^{-i\omega t}. \tag{4}$$

$D\equiv\kappa/c$ is the diffusivity, c is the specific heat per unit volume at constant pressure, κ is the thermal conductivity, n is the normal to the surface of the rod, ϵ is the total emissivity of the surface, σ is the Stefan-Boltzmann constant, θ_0 is the amplitude of the applied temperature variation, and ω is its angular frequency. The boundary condition given by Eq. (3) applies to the case where heat radiates from the surface of the rod into a blackbody environment at temperature T_0 and $T_0\gg\theta_0$. The solution of the differential equation is given by a superposition of damped sine waves with complex wave numbers[4] k_n [see Appendix, Eq. (32)]. Far enough away from the boundaries $z=0$ and $z=L$, the temperature modulation θ can be approximated by the expression[5]

$$\theta=f(x,y)e^{-i\omega t}(e^{ikz}+\gamma e^{-ikz})/(1+\gamma), \tag{5}$$

* This research has been sponsored in part by the U. S. Air Force, Wright Air Development Center, under contract; and in part by the U. S. Navy Bureau of Ships under contract.

[1] P. H. Sidles and G. C. Danielson, J. Appl. Phys. **25**, 58 (1954).

[2] A. J. Ångstrom, Ann. Physik **114**, 513 (1861); Phil. Mag. **25**, 130 (1863); **26**, 161 (1863).

[3] Y. Kanai and R. Nii, J. Phys. Chem. Solids **8**, 338 (1958).

[4] H. S. Carslaw and J. C. Jaeger, *Conduction of Heat in Solids* (Clarendon Press, Oxford, England, 1959), 2nd ed., p. 219, Eq. (13).

[5] In the absence of radiation, Eq. (5) represents an exact solution of the differential equation in the whole range of z.

where all waves other than wave k_1 were neglected and the index 1 was dropped. The error introduced in this approximation is quite small; an estimate of it, for the case of the cylindrical rod, is given in the Appendix. The form of the function $f(x,y)$ depends on the shape of the rod's cross section. The quantities k and γ are given by

$$k=a+ib \tag{6}$$

and

$$\gamma(k)=e^{2ikL}(ik+\tfrac{1}{2}\alpha^2R)/(ik-\tfrac{1}{2}\alpha^2R). \tag{7}$$

Here,

$$a=(1/\sqrt{2})\{[\alpha^4+(\omega/D)^2]^{\frac{1}{2}}-\alpha^2\}^{\frac{1}{2}}, \tag{8}$$

$$b=(1/\sqrt{2})\{[\alpha^4+(\omega/D)^2]^{\frac{1}{2}}+\alpha^2\}^{\frac{1}{2}}, \tag{9}$$

and α, which is determined by surface radiation, is given to a good approximation by [see Appendix, Eq. (39)]

$$\alpha=(8\sigma\epsilon T_0^3/DcR)^{\frac{1}{2}}, \tag{10}$$

wherein R is a length parameter which depends on $F(x,y)$. For a circular cross section, f is the zeroth-order Bessel function and R is the radius of the rod, whereas for a square cross section f is the sine function and $2R$ is a side of the cross section. The quantities a and b are the phase shift and the logarithmic attenuation, per unit length, of the thermal wave. The coefficient γ characterizes the reflection from the boundary $z=L$; $\gamma=0$ corresponds to the case of a semi-infinite rod.

In the absence of radiation $\alpha=0$, and

$$a=b=(\omega/2D)^{\frac{1}{2}}. \tag{11}$$

Surface radiation causes a to decrease, b to increase, and

$$\alpha=(b^2-a^2)^{\frac{1}{2}}. \tag{12}$$

The product ab, however, depends solely upon the thermal diffusivity and the frequency of the applied heat wave

$$D=\omega/2ab. \tag{13}$$

So long as radiation from the surface of the rod can be represented by Eq. (3) and ϵ is constant, D can be determined in accordance with Eq. (13) from knowledge of a and b. However, inhomogeneities of the surface which give rise to variation in ϵ, or any departure from the boundary condition specified in Eq. (3), will introduce errors in the value of D calculated from Eq. (13). To minimize this source of uncertainty, it is desirable to reduce the effects of the surface on the quantities a and b; i.e., α^2 should be small compared to ω/D [Eqs. (8) and (9)] and $|\gamma|$ should be much less than unity. These conditions set lower limits on the values of ω, R, and L to be used

$$\omega R\gg 8\sigma\epsilon T^3/c \tag{14}$$

and

$$e^{-2bL}\ll 1. \tag{15}$$

Since the attenuation increases roughly exponentially with $(\omega)^{\frac{1}{2}}$, the upper limit of ω that can be used is fixed by the sensitivity of the apparatus.

The quantities a and b can be determined by measuring the phases and amplitudes of the temperatures $\theta_1(x,y,z_1,t)$ and $\theta_2(x,y,z_2,t)$ at two points on the rod, and taking their ratio

$$\theta_2/\theta_1\equiv\exp(i\tilde{K})=[e^{ikz_2}+e^{-ikz_2}\gamma(k)]/[e^{ikz_1}+e^{-ikz_1}\gamma(k)]. \tag{16}$$

$\tilde{K}$ is defined by Eq. (16). A solution of the foregoing transcendental equation, approximate to first order in γe^{-2ikz_1}, is

$$kl=\tilde{K}+i[\exp(-2i\tilde{K}z_2)/L-\exp(-2i\tilde{K}z_1/L)]\gamma(\tilde{K}/L), \tag{17}$$

where $l=z_2-z_1$.

With semiconductors, there is usually some difficulty in attaching thermocouples to the surface so that they follow the temperatures θ_1 and θ_2 without lag. Furthermore, most metallic thermocouples form eutectics with semiconductors well below the melting point of the semiconductor. These difficulties are eliminated by utilizing the thermal emf of the semiconductor itself for measuring relative temperature differences along the sample. The thermal emf's can be measured between three probes of tungsten, or other nonreactive metals, welded along the sample. This method will be referred to as the "differential method." There are several additional advantages to this method. Temperature differences rather than absolute temperatures are measured, and therefore effects due to slow drifts are eliminated. Since only electrical contacts are necessary between the sample and the tungsten probes, the problem of thermal lag, present in the case of thermocouples, is eliminated. The large thermoelectric power of semiconductors affords greater sensitivity than that obtainable from metal thermocouples.

To determine a and b by the "differential method," thermal emf's V_{21} and V_{32} are measured between three probes, P_1, P_2 and P_2, P_3, respectively. The ratio of the two measured emf's is a complex quantity which can be written as

$$V_{32}/V_{21}\equiv e^{iK}. \tag{18}$$

The emf's V_{mn} are related to the temperature distribution on the sample

$$V_{mn}=\int_{\theta_n}^{\theta_m} Q\,d\theta, \tag{19}$$

where Q is the thermoelectric power of the sample with respect to the probes. When Q is constant between the probes, it can be taken out of the integration sign, and consequently

$$e^{iK}=(\theta_3-\theta_2)/(\theta_2-\theta_1). \tag{20}$$

If we substitute for θ_m from Eq. (5), we obtain

$$kl=K+i[e^{-iK(z_2+z_1)/l}-e^{-iK(z_2+z_1)/l}]\gamma(K/l), \tag{21}$$

where only terms which are first order in $\gamma\epsilon^{-i(z_m+z_n)}$ have been retained. The probes are assumed equally spaced, and l is their separation.

If the probes are not equally spaced, a correction term K' must be added to the right side of Eq. (21):

$$K'=(K\Delta l/l_{21})e^{iK}/(1-e^{iK}). \tag{22}$$

l_{21} and l_{32} are the spacings between the probes, $\Delta l=l_{32}-l_{21}$ is the difference between the spacings, and it is assumed that $b\Delta l\ll 1$. In Eq. (21), l is to be replaced by l_{21}.

When Q varies due to inhomogeneities in doping or a steady temperature gradient along the sample, its variation must be taken into account in Eq. (19). The integral is first transformed to

$$V_{mn}=\int_{z_n}^{z_m} Q(d\theta/dz)dz. \tag{23}$$

On substituting Eq. (5) in Eq. (23) and integrating repeatedly by parts, one obtains, for the case of the semi-infinite rod,

$$V_{mn}=\theta_m g_m-\theta_n g_n, \tag{24}$$

where

$$g_m=\sum_{s=0}^{\infty}[(-ik)^{-s}(d^sQ/dz^s)_m]. \tag{25}$$

Equation (18) now becomes

$$e^{iK}=e^{ikl}(g_2e^{ikl}-g_2)/(g_2e^{ikl}-g_1). \tag{26}$$

As can be seen from this equation, the larger bl the smaller will be the effect of a variation of Q on K. For the case where Q varies linearly with z, and $(1/bQ)dQ/dz\ll 1$ and $(l/Q)dQ/dz\ll 1$, Eq. (26) simplifies and one obtains

$$a=\mathrm{Re}(K/l), \tag{27}$$

$$b=\mathrm{Im}(K/l)+(dQ/dz)/Q(z_2). \tag{28}$$

Thus in this approximation, only the imaginary part of K will be affected by a variation in Q; however, in the case where higher derivatives of Q cannot be neglected, both the real and imaginary part of K will be affected.

From the thermal diffusivity measurements, it is also possible to determine the thermoelectric power of the sample:

$$|Q|=|V_{mn}|/|\theta_m-\theta_n|, \tag{29}$$

where $|V_{mn}|$ is the amplitude of the thermal emf measured between the probes, or similar arms of thermocouples m and n.

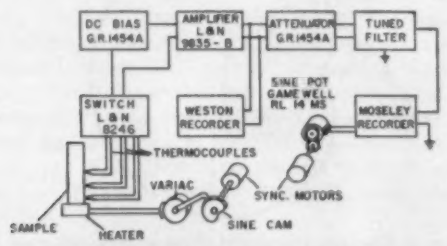

FIG. 1. Block diagram of measuring setup.

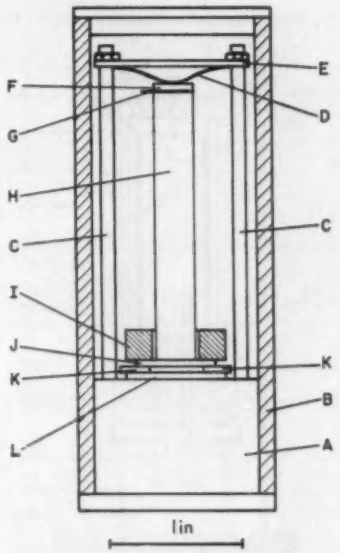

FIG. 2. Sample holder: A, molybdenum sink; B, molybdenum shielding tube; C, stainless steel screws; D, tungsten spring; E, molybdenum clamp; F, ceramic insulating plate; G, tungsten current lead to the sample; H, sample; I, lava shield; J, ceramic heating element; K, nickel current tabs of the heating element; L, ceramic insulating plate.

To illustrate the preceding considerations, the diffusivity parameters are computed for a typical example: The thermal diffusivity is to be measured at 1000°K on a cylindrical rod where $L=\frac{3}{4}$ in., $R=\frac{1}{8}$ in., $\kappa=0.05$ w deg^{-1}cm^{-1}, $c=1.5$ joule cm^{-3} deg^{-1}, and $\epsilon=0.5$. Thermocouples are welded to the sample at $z_1=\frac{1}{4}$ in. and $z_2=\frac{1}{2}$ in., so that their separation is large enough to permit an accurate determination of l. By using a frequency of 3 cycles/min, we compute $\alpha=1.2$ cm^{-1}; $a=2.0$ cm^{-1}; $b=2.3$ cm^{-1}; $|\gamma\epsilon^{-2ikz_2}|=0.056$; $\mu(z_1)=2\times 10^{-5}$ [Appendix, Eq. (40)]; $al=73°$; $|\theta_2/\theta_1|=0.23$. The foregoing values of phase shift al and attenuation $|\theta_2/\theta_1|$ can be measured very accurately (see Sec. III). Effects due to the boundaries $z=0$ and $z=L$ are small since $\mu\ll 1$ and $|\gamma\epsilon^{-2ikz_2}|\ll 1$. Effects due to radiation from the sides of the sample are also small since $a\approx b$. Thus Eqs. (17) and (13) are applicable to a high degree of accuracy. With shorter samples, l must be decreased and ω increased.

III. APPARATUS

The block diagram of the experimental arrangement employed in the present work is depicted in Fig. 1. The sample holder with a mounted sample is shown in

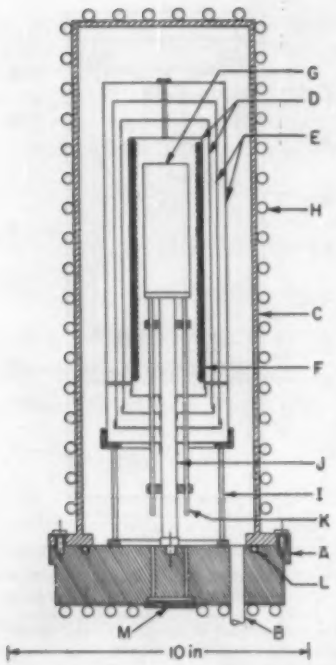

FIG. 3. Furnace: *A*, brass base; *B*, vacuum outlet; *C*, brass bell jar; *D*, tantalum radiation shields; *E*, nickel radiation shields; *F*, Kanthal heater coil with ceramic beads; *G*, sample holder; *H*, copper water cooling coil; *I*, steel stand for heater-shield assembly; *J*, stainless steel tube; *K*, ceramic tubes for electrical leads; *L*, vacuum O-ring; *M*, vacuum seal for electrical leads.

Fig. 2. The sinusoidal heat input to the sample was provided by a small electrical heater, flat in shape and in thermal contact with the sample. The heating element *J* (see Fig. 2) was a 40-mil thick Alundum[6] platelet, metallized on both sides with 1-mil layers of molybdenum. Grooves were inscribed on one side of the metallized ceramic to increase the electrical resistance of the molybdenum film to 2 ohms at room temperature. The heating element with its grooved side facing down, the nickel tabs *K*, the insulating Alundum plate *L*, and the molybdenum sink *A* were all brazed together with silver or with copper. The nickel tabs served as current leads to the heating element and the ceramic plate *L* insulated it electrically from the molybdenum sink. The sample was brazed to the heating element and held in position by a tungsten spring *D* and a ceramic plate *F*. A tungsten foil *G* between the sample and plate *F*, and a nickel tab brazed on the upper side of the heating element, served as current leads to the sample for electrical conductivity measurements. Over the molybdenum sink fit a molybdenum shield *B*, coated on the inside with Sauereisen No. 8 cement, to prevent reflection of radiant heat. A lava shield *I* screened the sample from radiation off the heater. Thermocouples and electrical leads, contained in ceramic insulating tubing, passed through holes in the molybdenum sink.

Temperatures were measured by three chromel-alumel thermocouples, 3 mils in diameter, welded to the sample. Two thermocouples would have sufficed to determine the phase shift a and attenuation b of the thermal wave; the third thermocouple was used for an additional check. Whenever the "differential method" was employed, use was made of three tungsten probes, 1.5 mils in diameter, welded to the sample. These thin chromel, alumel, and tungsten wires were welded to heavier wires of the corresponding kinds, brought out of the vacuum furnace and soldered to copper wires leading to a selector switch and amplifier. The junctions were immersed in oil in a thermally insulated heavy copper container, thus reducing the temperature variations to less than 0.5°C in the course of a day.

The sample holder was mounted in the vacuum furnace shown in Fig. 3. The furnace could be evacuated to a pressure of about 10^{-6} mm Hg, and its temperature was regulated by a West saturable reactor controller. Measurements could be made in the temperature range from 2°C above room temperature to the brazing temperature of the sample holder assembly. Effects of slow temperature variations on the signal were eliminated by the use of a filter (see Fig. 1), and data could be taken while the furnace temperature was drifting. This reduced considerably the time required for measurements.

The sinusoidal power in the heater was produced by modulating a 60-cps current at an angular frequency $\omega=2\pi f$, where f was chosen to be 1, 3, 5, 12, or 30 cycles/min. The modulation was obtained by driving a Variac with a sine cam, illustrated in Fig. 4. A lever of length p, rigidly connected to the axis of the Variac, was constrained to move on the cam, which was driven by a synchronous motor at the angular frequency ω. The shape of the cam, in polar coordinates (r,ζ), is prescribed by

$$r=2p\sin\tfrac{1}{2}[\beta_1(1+\cos\zeta)^{\frac{1}{2}}+\beta_0], \tag{30}$$

wherein β_0 is the zero position and $\sqrt{2}\beta_1$ is the maximum

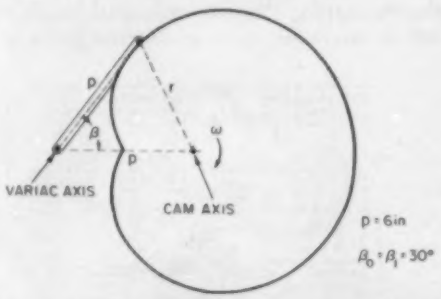

FIG. 4. Sine cam: The numerical values of the parameters appearing in Eq. (30) are listed in the figure.

[6] Ceramic No. 4462, supplied by Frenchtown Porcelain Company.

swing of the Variac, respectively. The time variation of the angle β is given by

$$\beta=\beta_1(1+\cos\omega t)^{\frac{1}{2}}+\beta_0. \tag{31}$$

The voltage output is proportional to $\beta-\beta_0$, and consequently the power output is proportional to $\beta_1^2(1+\cos\omega t)$. The dc component in the power gave rise to a small steady temperature gradient on the sample (less than 1°C/cm) which had negligible effect on the measurements. The sinusoidal term in the power produced the desired modulation at frequency ω; the 60-cps carrier was averaged out due to the thermal inertia of the heater. Ordinarily, the heater was supplied with about 3 w of power (peak to peak), which produced a modulation of about 3°C in temperature at the base of the sample and 1°, 0.3°, and 0.1°C modulations at the first, second, and third thermocouple, respectively.

Any one of the three thermocouples or pairs of probes could be selected by a switch and fed into a dc preamplifier (see Fig. 1). The dc part of the thermal emf was bucked out with a dc voltage obtained from a voltage divider. The output of the dc preamplifier was passed through an attenuator and a filter, tuned to the signal frequency ω, and recorded on the X of an X-Y recorder. For monitoring purposes the output of the dc preamplifier was recorded on a Weston recorder. For each measurement the attenuator was adjusted so as to maintain nearly the same signal input level to the X-Y recorder. The filter consisted of two low-pass and two high-pass resistance capacitance sections, which were coupled to one another by cathode followers. Normally the measurements were made with the crystal insulated electrically from ground, and the dc amplifier grounded. At the very high temperatures a substantial electrical leakage often developed between the crystal and ground; in those cases the crystal was grounded and the amplifier floated off ground. Since the sample's resistance at these temperatures was always quite low, the voltage developed across it due to 60-cps leakage currents from the amplifier's power supply to ground was small enough to have negligible effects.

The amplitude of the signal was determined from the deflection on the X-Y recorder. The phase was measured as follows: to the Y input of the XY recorder was applied a sinusoidal reference voltage obtained from a sine potentiometer driven by a synchronous motor having the same rpm as the cam motor. The phase of the reference voltage was adjusted by means of a graduated differential gearing mechanism until it coincided with that of the signal. The in-phase condition corresponded to a straight line Lisajou figure. The lowest sine temperature variation that could be detected was about 0.001°C. Below this level, the signal was lost in "furnace noise" and noise from the dc amplifier.

The quantities al and bl are determined from differences of two sets of measurements; al from the difference of two phase angles and bl from the difference of the logarithms of two amplitudes. Hence, the effects of absolute measuring errors in phase and amplitude are reduced in importance the larger al and bl are. On the other hand, large values of al and bl are associated with large signal attenuation and hence low signal-to-noise ratio. Thus, there exists an optimum value of al and bl for which maximum accuracy is attained. With the present apparatus, the maximum accuracy attained in al and bl was about $\pm 0.5\%$ with $al\approx bl\approx 1$. Thus with an 1% accuracy in $ab\bar{l}^2$ and 1% accuracy in $\bar{l}^2$ the accuracy in D was about 2%. Other sources of error were perturbations introduced in the temperature wave due to the boundaries $z=0$ and $z=L$; both these effects were negligible for the sample geometry used.

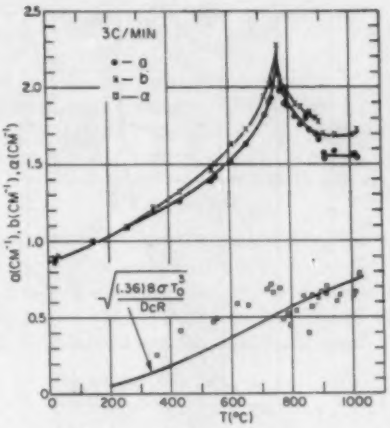

FIG. 5. Phase shift a, attentuation b, and radiation factor $\alpha=(b^2-a^2)^{\frac{1}{2}}$ as functions of temperature for Armco iron. The curve for α was computed from Eq. (10) using the measured values of D, published values[8] of c and assuming $\epsilon=0.36$.

IV. ARMCO IRON

The sample, 2 in. in length and $\frac{3}{16}$ in. in diameter, was machined from rod stock Armco iron purchased from Mapes and Sprowl. The sample was brazed on the heater with copper in a hydrogen atmosphere at 1100°C. A frequency of 3 cycles/min was used for the sinusoidal heat input to the sample. The phase shift a and attenuation b of the thermal wave were measured with thermocouples welded to the sample at distances $\frac{1}{4}$, $\frac{1}{2}$, and $\frac{3}{4}$ in. from its base.

Electrical conductivity measurements at room temperature were made on the sample before brazing and after the completion of the experiment. The conductivity measured before brazing agreed with that of the Armco iron used by Powell[7] for his thermal conductivity measurements. A 3% lower value of electrical conductivity, obtained for the sample after brazing, was

[7] R. W. Powell, Proc. Phys. Soc. (London) **46**, 659 (1934); *ibid.* **51**, 407 (1939).

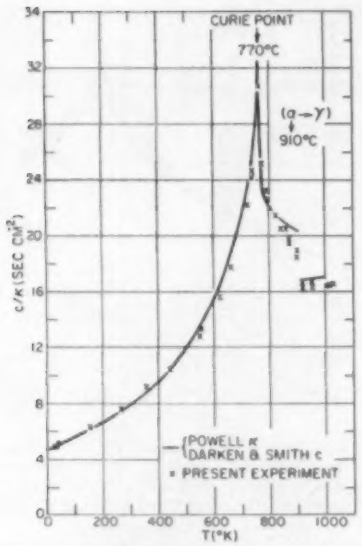

FIG. 6. The reciprocal of the measured thermal diffusivity of Armco iron as a function of temperature. The full curve was computed from the literature values of the specific heat[8] and thermal conductivity.[7]

ascribed to contamination of the sample by copper during the brazing.

The experimental results for a, b, and $\alpha=(b^2-a^2)^{\frac{1}{2}}$ in the temperature range 30°–1025°C are plotted in Fig. 5. The theoretical curve for the radiation factor α was computed from Eq. (10), using the measured values of D, published values of specific heat[8] c and assuming $\epsilon=0.36$. The value used for ϵ is considerably larger than that of $\epsilon=0.05$ for electrolytic iron[9]; this is probably due to an oxide layer on the sample. It should be noted that $\alpha^2=b^2-a^2$ is the difference between two nearly equal quantities, and thus has a large relative error. Moreover, variations in emissivity or heat losses from the sample, due to changing vacuum condition with temperature, will affect α strongly. However, the product ab from which the diffusivity is computed, is not affected by these variations.

The reciprocal of the thermal diffusivity $1/D\equiv c/\kappa$, determined according to Eq. (13) from the measured values of a and b, is plotted in Fig. 6. The solid curve in Fig. 6 was computed from published values of the specific heat[8] c and thermal conductivity[7] κ. Corrections were made for the effects of thermal expansion,[10] and volume change[10] at the $\alpha\rightarrow\gamma$ phase transition on the density of the sample and on the separation between the thermocouples.

The results of the present investigation agree well with the values of D computed from previous measurements of c and κ, except near the Curie point (770°C) and the $\alpha\rightarrow\gamma$ transition (910°C). In comparing our results with those computed from previous measurements, it should be borne in mind that the properties of Armco iron depend on the crystalline perfection and chemical purity of the sample. Thus the observed departures might be due to differences in the samples used by the various workers. On the other hand, the measurements of c and/or κ might be in error. This question is discussed in greater detail elsewhere.[11]

V. GERMANIUM

The thermal diffusivity was measured on a single crystal of germanium cut to the shape of a rod 2 in. in length with a (111) axis along the rod axis. The cross section of the rod was square with 0.3-in. sides. The crystal was arsenic doped n type, with a room temperature resistivity of 0.3 ohm cm. The heating element J (see Fig. 2) was silver plated on the top side and the germanium sample brazed to it at 651°C in vacuum. The Ag-Ge eutectic, which forms at 651°C, provided a solid bond from room temperature to the eutectic point; above this temperature the contact became liquid and the sample was held in position by the tungsten spring D (see Fig. 2). Three chromel-alumel thermocouples, 3 mils in diameter and three tungsten probes 1.5 mils in diameter were welded along two opposite faces of the sample. The welds were spaced $\frac{1}{4}$ in. along the center line of the long face of the rod. The lowest thermocouple and probe were welded $\frac{1}{4}$ in. from the base of the rod. The thermocouples were prepared by butt-welding the chromel and alumel wires end to end. The thermocouple junction was then spot-welded to the germanium sample at 400°C in a helium atmosphere.

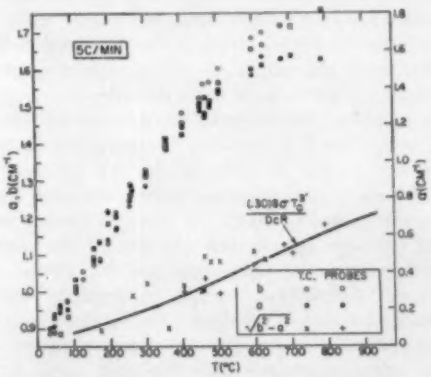

FIG. 7. Phase shift a, attenuation b, and radiation factor $\alpha=(b^2-a^2)^{\frac{1}{2}}$ as a function of temperature for germanium. The curve for α was computed from Eq. (10) using the measured values of D and assuming $c=1.83$ joule cm^{-3} deg^{-1} and $\epsilon=0.3$.

[8] L. S. Darken and R. P. Smith, Ind. Eng. Chem. **43**, 1815 (1951).

[9] *American Institute of Physics Handbook* (McGraw-Hill Book Company, Inc., New York, 1957), pp. 6–69.

[10] R. M. Bozorth, *Ferromagnetism* (D. Van Nostrand Company, Inc., Princeton, New Jersey, 1951), p. 54.

[11] G. D. Cody, B. Abeles, and D. S. Beers (unpublished).

The thermal diffusivity was measured in the temperature range 30°-800°C at frequencies of 3, 5, and 12 cycles/min. Since the results obtained at the different frequencies agreed with one another within experimental error, and most of the measurements were made at 5 cycles/min, only results at this frequency will be given. The maximum correction of D, for the effect of thermal expansion,[12] amounted to only 0.5%. Measurements taken with thermocouples above 680°C were erratic, because of reaction of the thermocouples with germanium, and are therefore omitted; above this temperature only the probes were used.

The measured values of a and b, plotted in Fig. 7 follow the same pattern as those for Armco iron. At low temperatures $a=b$ within experimental error, at high temperatures $a<b$ due to radiation. The theoretical curve for a was computed using Eq. (10), the Dulong-Petit value of the specific heat $c=1.83$ joule cm^{-3} deg^{-1} and the total emissivity of germanium[13] $\epsilon=0.3$. This value of ϵ gives the best fit of the computed curve to the measured values of a. The values of c/κ in Fig. 8, obtained for the probes and thermocouples, respectively, are in good agreement above 300°C. The slight discrepancy between the two measuring methods below this temperature is probably due to a small inhomogeneity along the sample, as evidenced by a variation of thermoelectric power and electrical conductivity along the sample below 300°C.

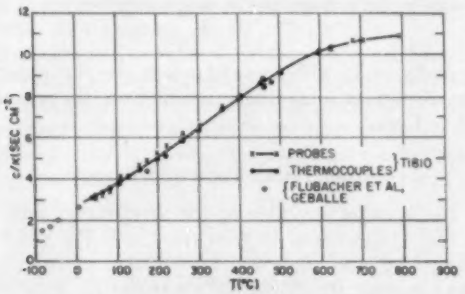

FIG. 8. Reciprocal of the measured thermal diffusivity of germanium as a function of temperature. The points represented by the open circles were computed from published values of specific heat[14] and thermal conductivity.[15]

The room temperature results of the present investigation are consistent with the values of c/κ (circles in Fig. 8) calculated from published values of specific heat[14] and thermal conductivity[15] below room temperature. No similar comparison could be made above room temperature for lack of specific heat data. The values of the thermoelectric power, computed from Eq. (29), and the measured electrical conductivity were found to be in good agreement with previously published results. The physical significance of the results on germanium will be discussed elsewhere.

[12] D. F. Gibbons (private communication); and Phys. Rev. **112**, 136 (1958).
[13] F. G. Allen, J. Appl. Phys. **28**, 1510 (1957), reports the value of 0.55 for the spectral emissivity of germanium at 0.65μ.
[14] P. Flubacher, A. L. Leadbetter, and J. A. Morrison, Phil. Mag. **4**, 273 (1959).
[15] J. Carruthers, T. H. Geballe, H. M. Rosenberg, and J. M. Ziman, Proc. Roy. Soc. (London) **A238**, 502 (1957).

APPENDIX

The error, introduced in approximating the solution to Eqs. (1)–(4), is estimated for the case of a rod of length L with a circular cross section of radius R. The time dependent solution to Eqs. (1)–(4) is obtained from the time-indepenent solution[4] in the usual manner,

$$\theta=e^{-i\omega t}\sum_n [2\theta_0 hJ_0(r\alpha_n)/J_0(R\alpha_n)R(h^2+\alpha_n^2)] \times[(e^{ik_n z}+\gamma_n e^{-ik_n z})/(1+\gamma_n)], \quad (32)$$

where

$$k_n=a_n+ib_n, \quad (33)$$

$$a_n=(1/\sqrt{2})\{[\alpha_n^4+(\omega/D)^2]^{\frac{1}{2}}-\alpha_n^2\}^{\frac{1}{2}}, \quad (34)$$

$$b_n=(1/\sqrt{2})\{[\alpha_n^4+(\omega/D)^2]^{\frac{1}{2}}+\alpha_n^2\}^{\frac{1}{2}}, \quad (35)$$

$$\gamma_n=e^{2ik_nL}(ik_n+h)/(ik_n-h), \quad (36)$$

and

$$h=4\sigma\epsilon T_0^3/\kappa. \quad (37)$$

α_n are the roots of the transcendental equation

$$\alpha J_0'(R\alpha)+hJ_0(R\alpha)=0, \quad (38)$$

J_0 is the zero-order Bessel function, and the other quantities are as defined in Sec. II.

Carslaw and Jaeger list the six lowest roots of Eq. (38): the dependence of the lowest two roots α_1 and α_2 on the parameter $(2hR)^{\frac{1}{2}}$ is plotted in Fig. 9. In the case where $(2hR)^{\frac{1}{2}}<1$ the root α_1 can be approximated by

$$\alpha_1=(2h/R)^{\frac{1}{2}}=(8\sigma\epsilon T_0^3/DcR)^{\frac{1}{2}}. \quad (39)$$

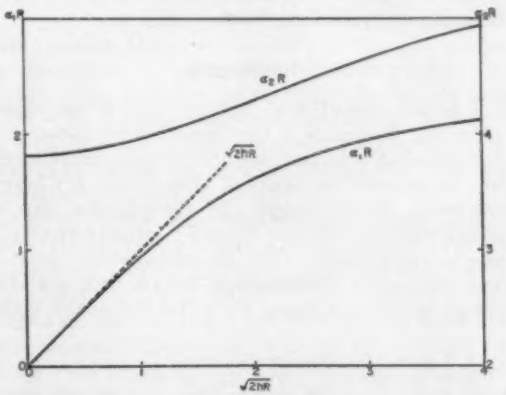

FIG. 9. The dependence of the first two roots α_1 and α_2 of Eq. (38) on the parameter $(2hR)^{\frac{1}{2}}$.

θ, given by Eq. (32), is a superposition of damped sine waves with complex wave numbers k_n. As z increases, wave k_1 dominates over all the other waves and Eq. (32) can be approximated by Eq. (5), where all waves other than k_1 have been neglected. The error introduced by this approximation is of the order of the ratio $\mu(z)$ of the amplitudes of waves k_2 and k_1; higher-order waves are of negligible importance, and

$$\mu = e^{z(b_2-b_1)}(h^2+\alpha_1^2)|1+\gamma_1|/(h^2+\alpha_2^2)|1+\gamma_2|. \quad (40)$$

JOURNAL OF APPLIED PHYSICS VOLUME 31, NUMBER 9 SEPTEMBER, 1960

Negative Hydrogen and Deuterium Ion Beams

SANBORN F. PHILP
High Voltage Research Laboratory, Electrical Engineering Department, Massachusetts Institute of Technology, Cambridge, Massachusetts

(Received March 28, 1960; and in final form May 16, 1960)

The charge state of a monoenergetic beam of hydrogen atomic and molecular ions traversing a hydrogen gas target has been measured as a function of the energy of the beam and the thickness of the gas target. The yield of negative ions from protons has a maximum of 1.5% at 13 kev. From diatomic and triatomic molecular ions the maximum yields were 3.0% and 4.5% at 26 and 39 kev, respectively. The experiments have also been performed with deuterium ions traversing the hydrogen gas target. The deuterium results are almost identical with those of hydrogen if the energy scale for the hydrogen data is multiplied by two.

INTRODUCTION

THE transfer of electrons to a fast ion as it traverses matter is a well-established phenomenon which has been the subject of many investigations, particularly for the case of hydrogen and helium ions traversing various gases. One may mention in particular the work of Keene,[1] Whittier,[2] and Stier and Barnett.[3] A large part of the existing information on such transfer experiments has been summarized recently by Allison.[4]

DESCRIPTION OF THE APPARATUS

The experiments were performed by passing a beam of positive ions of a certain energy (in the range 5–60 kev) through a gas target. The particle beam emerging from the gas target contains, in general, positive, neutral, and negative components, which are identified by magnetic analysis of the beam.

Ion Source

Ions are created in a capillary type of ion source (S in Fig. 1) similar to that described by Lamar and Buechner.[5] A principal objective of these experiments was to examine the behavior of molecular ion beams traversing the gas target, and the capillary type of source was used because it readily supplies molecular ions as well as protons. The ion source usually operated at a pressure of approximately 200 μ with a total discharge current of 4 amp at 100 v. The ion output would typically be 75–85% molecular ions (see, for example, Fig. 3) with a total beam current from the source of 0.5 to 1 ma.

Acceleration Tube and Target

The vacuum envelope of the acceleration tube (A in Fig. 1) consists of 12 glass rings, 6-in. i.d. and 1 in. thick. The glass rings and the aluminum diaphragms which support the cylindrical electrodes E_1, E_2, and E_3 are cemented together using a vinyl acetate polymer. The cylindrical electrodes, separated by small gaps for focusing action, effectively shield the beam from spurious charges which form on the inside wall of the acceleration tube.

The total target thickness required to reach equilibrium in the charge state of the beam (even at the highest energy used) was of the order of 5×10^{15} molecules/cm^2 and therefore a windowless gas target must be used. The gas target T is a tube 0.5 cm in diam and 20 cm long. Gas enters T at its center and flows out of both ends. D_1 and D_2 are differential pumping constrictions (tubes 0.5 cm. in diam and 7 cm. long). During operation the pressure in the volume between D_1 and D_2 was approximately 10^{-3} mm and the pressure in the acceleration tube A and the analyzing chamber C was approximately 5×10^{-6} mm.

Analyzer and Beam Measuring Device

The analyzing chamber C is of welded aluminum construction. The cylindrical poles of the analyzing magnet M protrude through the upper and lower walls of C. The magnet is excited by an Alnico permanent magnet in a part of the magnetic circuit external to C and the

[1] J. P. Keene, Phil. Mag. **40**, 369 (1949).
[2] A. C. Whittier, Can. J. Phys. **32**, 275 (1954).
[3] P. M. Stier and C. F. Barnett, Phys. Rev. **103**, 896 (1956).
[4] S. K. Allison, Revs. Modern Phys. **30**, 1137 (1958).
[5] E. S. Lamar and W. W. Buechner, J. Appl. Phys. **18**, 22 (1947).

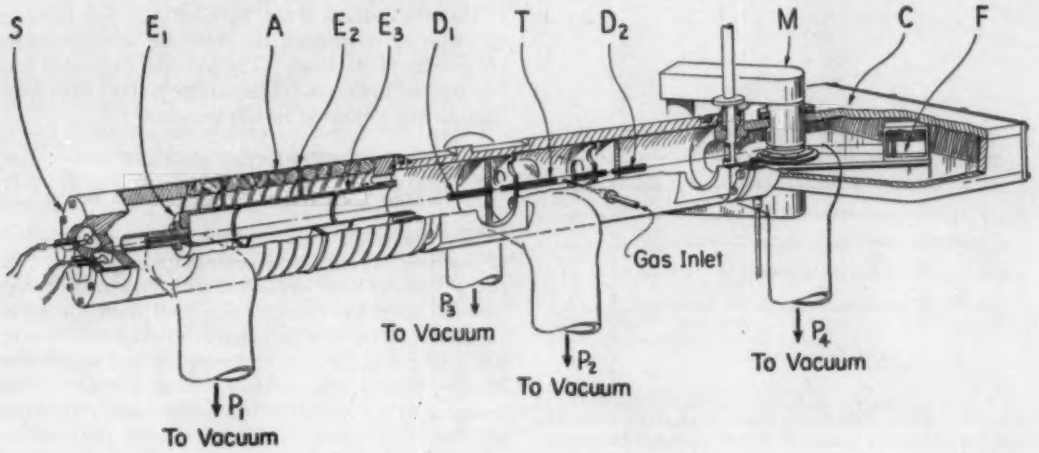

FIG. 1. Charge transfer apparatus.

magnetic field is changed by changing the air gap of an adjustable magnetic shunt.

The beam measuring device F is a cylindrical Faraday cage formed by the cylindrical wall C_2 and the ends C_3 and D (Fig. 2). The Faraday cage must be shielded from stray charged particles in the analyzing chamber so it is enclosed in another Faraday cage C_1. An initial defining slit S_1 prevents the direct beam from striking the edges of slits S_2 and C_3, which are slightly wider than S_1. The assembly shown in Fig. 2 is mounted on an arm inside the analyzing chamber and swings in an arc about the magnet pole as an axis.

EXPERIMENTAL PROCEDURE

The ion source is at ground potential and the ion accelerating voltage applied to the cylindrical tube which contains T, D_1, and D_2, and to the analyzing chamber M. The pumps P_1, P_2, P_3, and P_4 are at ground potential and are connected to the high-voltage parts by Pyrex pipe elbows.

A potential of approximately -8 kv is required on E_1 for optimum ion extraction and beam formation. To obtain a well-focused beam at low total accelerating voltages it is necessary to maintain E_2 at a positive potential with respect to E_1.

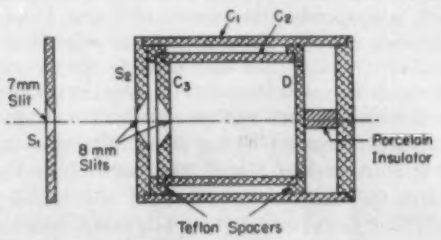

FIG. 2. Cylindrical beam measuring device.

Measurement of Gas Target Thickness

The gas target thickness (average pressure multiplied by effective length) is varied by changing the flow of gas into the center of T. A thermocouple gauge is connected into T near its center and this was routinely used as an index of the gas target thickness, that is, a given pressure read by the thermocouple corresponds to a given target thickness which was determined as follows:

A wire stretched centrally through the target tube was heated by passage of electric current. The hot wire in turn is cooled by the gas—the Pirani gauge principle—and the heat loss through the gas from any place on the wire is proportional to the gas pressure at that place and to the temperature difference between the wire and the surrounding surfaces.

The wire was calibrated by filling the whole apparatus with hydrogen gas at various pressures measured with a McLeod gauge.

For a wire of sufficiently large diameter the temperature variation along the length will be negligible and so the power supplied to the wire is directly proportional to gas target thickness (neglecting radiation and lead loss). A $\frac{1}{32}$-in. diam copper wire was used. For a current of 0.66 amp and a hydrogen pressure of 0.2 mm, the wire temperature was calculated to be 27°C over the central 42-cm length of the wire.

Computing the target thickness by assuming a linear drop from the center to zero pressure at the ends of the 20-cm tube, one obtains values which are within 20% of those obtained from the hot-wire measurements. This simple calculation gives lower values, which is reasonable since the effective target length will certainly include the differential pumping tubes D_1 and D_2 as well as T. The Pirani wire traverses this entire region and well into the high vacuum in A and C, so it should properly measure the thickness.

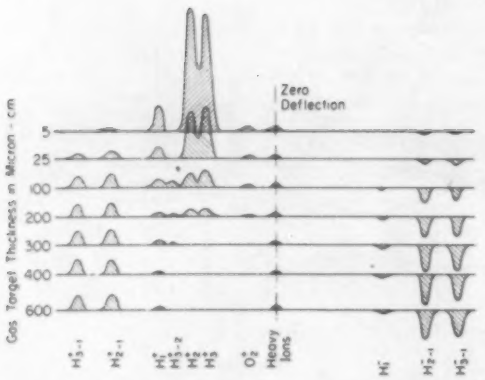

FIG. 3. Magnetic analysis of 20-kev beam after it has traversed a hydrogen target of various thicknesses. (Negative ion currents have been multiplied by a factor of 10 with respect to the positive currents.)

Measurement of Analyzed Beam

In measuring the analyzed beam, the current to the Faraday cage F (Fig. 1) is amplified and fed to a recorder. F swings at a constant angular velocity while the recorder paper moves and a spectrogram such as those in Fig. 3 is produced.

The slits in the beam measuring device must be wide enough to include an entire current peak of the analyzed beam. Various slit widths were tried and it was found that a 7-mm slit width was adequate.

Wherever the ion beam strikes a metal surface, secondary electrons are produced and this may create measurement difficulties. The initial 7-mm slit (S_1 in Fig. 2) protects the 8-mm slits S_2 and C_2 from the direct beam. The slits are made in a knife-edge form to minimize the surface exposed at tangential incidence for secondary electron production. In addition, slit S_2 is maintained at -30 v with respect to S_1, C_2, and the inner Faraday cage. This tends to prevent electrons produced in the inner Faraday cage from escaping, and electrons produced outside from entering.

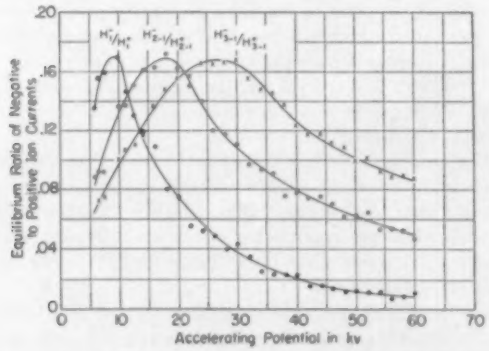

FIG. 4. Equilibrium ratio of negative to positive ions in a hydrogen ion beam traversing hydrogen gas.

The effectiveness of the Faraday cage may be tested by swinging it through the relatively intense neutral component of the beam. (The secondary emission from fast neutral hydrogen is comparable to that from ions). The current measured should be zero.

EXPERIMENTAL RESULTS

Charge Transfer in Hydrogen Ion Beam

After traversing the gas target, the ion beam consists of positive, negative and neutral hydrogen ions. The charge transfer is accomplished with very small energy loss and very few particles scattered from the beam. Experiments are now in progress to examine the scattering of the beam as it traverses the gas target. Preliminary results indicate that even at a relatively low energy of 10 kev (and after traversing a target, thickness sufficient to produce equilibrium among the positive, negative and neutral charge states) practically the entire beam is contained within a cone angle about the

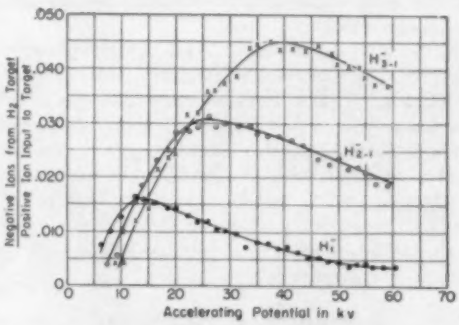

FIG. 5. Yield of negative hydrogen ions from protons and hydrogen molecular ions traversing an equilibrium thickness of hydrogen gas.

forward direction which is less than 0.01 rad, and probably only a few thousandths of a radian. The scattering decreases with decreasing target thickness and increasing energy.

It was found that hydrogen molecular ions dissociate in the gas target, again with very small energy loss and very little scattering. In dissociation the momentum of the molecular ion is divided equally among the constituent atoms (or ions). This is verified by the occurrence of sharp peaks in the magnetically analyzed beam current corresponding to protons of $\frac{1}{2}$ and $\frac{1}{3}$ the full accelerating energy. These apparently arise from the dissociation of H_2^+ and H_3^+ ions. As the gas target thickness is increased from zero one sees the disappearance of molecular ions and the appearance of protons and hydrogen negative ions of three different energies. This is illustrated in Fig. 3. The notation in Fig. 3 indicates the dissociation process, if any, which has taken place. For example, H_{3-1}^+ is a proton which was accelerated as an H_3^+ molecular ion. For thin gas targets,

a small amount of partially dissociated H_3^+ (labeled H_{3-2}^+ in Fig. 3) is found.

The experimental results are presented in terms of two quantities: (1) the equilibrium ratio of negative to positive ions (Fig. 4); (2) The yield of negative ions, which is the number of negative ions in the beam after equilibrium has been reached in traversing the gas target, divided by the number of positive ions which entered the target (Fig. 5).

By analyzing the beam with no gas in the target, the input ion currents are obtained. Then, with gas in the target, those ions which are dissociation fragments of molecular ions may be identified as discussed before and as illustrated in Fig. 3. Thus one may separate the charge transfer processes for protons and for diatomic and triatomic molecular ions. This is how the data shown in Figs. 4 and 5 were obtained.

In Fig. 4 one sees that the mass 1 (proton), mass 2, and mass 3 curves reach their maximum values at 9, 18, and 27 kv accelerating potential. This is another

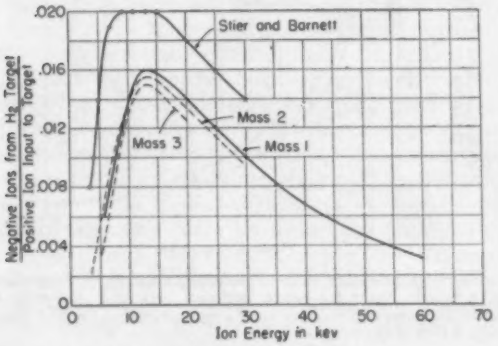

FIG. 6. Yield of negative ions from protons traversing an equilibrium thickness of hydrogen gas.

indication that in dissociation of the molecular ion there is only very little energy loss and the energy is divided equally among the dissociation fragments. Thus an H_2^+ molecular ion of energy ev contributes on dissociation two-mass 1 particles of energy, $\frac{1}{2}$ ev, etc.

In the yield curves of Fig. 5, once again the maxima occur at accelerating potentials which are integral multiples of the mass 1 maximum, namely, 13, 26, and 39 kv. In addition, the yields of negative ions from diatomic and triatomic positive ions are, respectively, 2 and 3 times those from monatomic ions at 2 and 3 times the accelerating potential.

Neither the charge state nor the excitation state of the dissociation fragments is known in these experiments, but the results in Figs. 4 and 5 seem to indicate that, provided the target thickness is sufficient, the negative ion production from a dissociation fragment is exactly what would be produced by a proton introduced into the target at the same velocity as the dissociation fragment.

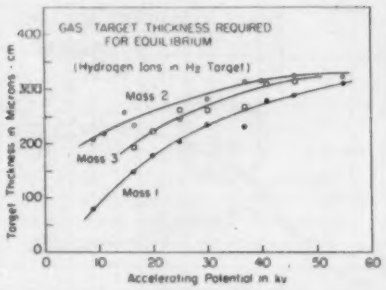

FIG. 7. Gas target thickness required for equilibrium in the charge transfer processes which occur when a hydrogen ion beam traverses hydrogen gas.

One might expect therefore that if Fig. 4 were replotted with the abscissae for the mass 2 and mass 3 curves divided by 2 and 3, respectively, all three curves would coincide. Likewise, replotting Fig. 5 with both ordinate and abscissa of the mass 2 and mass 3 data divided by 2 and by 3, the three curves would coincide. With such replotting the curves do in fact very nearly coincide. Figure 6 shows the data of Fig. 5 replotted in this way, together with a comparison with the data of Stier and Barnett.[3]

In this connection it may be remarked that the apparatus used by Whittier[2] did not produce a stable, focused beam of protons at energies below 12.6 kev. To obtain data at lower energies Whittier accelerated H_2^+ and H_3^+ at 2 and 3 times the desired single particle energy. The results so obtained joined smoothly with the proton data taken at higher energies.

Figure 7 shows the gas target thickness required for equilibrium. Since the charge transfer cross sections decrease with increasing energy above 10 kev, it would be expected that the target thickness required for equilibrium would increase.

Charge Transfer in Deuterium Ion Beam

The experiments were also performed with deuterons and deuterium molecular ions incident on the gas target.

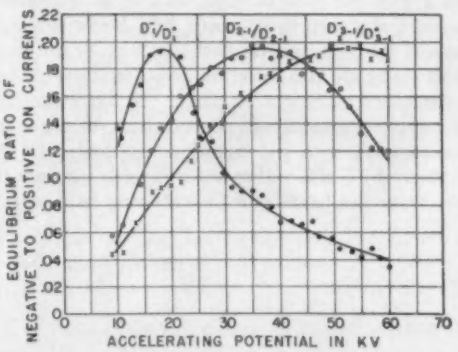

FIG. 8. Equilibrium ratio of negative to positive deuterium ions in a deuterium ion beam traversing hydrogen gas.

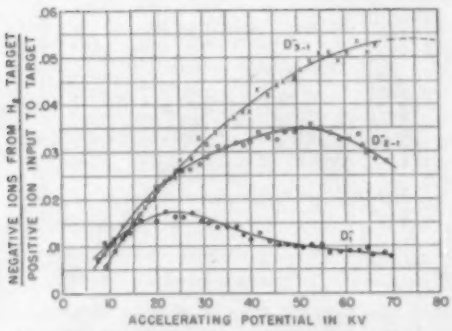

FIG. 9. Yield of negative deuterium ions from deuterons and deuterium molecular ions traversing hydrogen gas.

The equilibrium ratio of negative to positive deuterium ions (Fig. 8) and the yield of deuterium ions (Fig. 9) are to be compared with the hydrogen data of Figs. 4 and 5, respectively. This comparison leads to the conclusion that the deuterium data would coincide almost exactly with the hydrogen data if the energy scale of the deuterium data were multiplied by $\frac{1}{2}$. In other words, if the deuterium and hydrogen data were both plotted as a function of velocity, instead of accelerating potential, the results would be identical. It should be pointed out, however, that the deuterium curves lie in all cases about 10% above the corresponding hydrogen curves.

DISCUSSION OF RESULTS

From these results it is seen that negative ion production from molecular hydrogen ions traversing a hydrogen gas target (in which they experience both dissociation and charge transfer) is almost identical with the negative ion production from protons having the same velocity as the dissociation fragments of the molecular ions.

Also it is seen that negative ion production from deuterium ions traversing a hydrogen target is almost identical with that from hydrogen ions of the same velocity.

In Fig. 6 the yield of negative ions as measured in this work is shown to lie about 20% below the values obtained by Stier and Barnett.[3] In Fig. 10 the results of this study are also shown to lie below those obtained by the other investigators cited. The agreement with other results improves somewhat with increasing energy. This, together with the fact that the deuterium data lies about 10% above that for hydrogen suggests that losses from the beam due to scattering have affected the results. The scattering is now under investigation, but the preliminary measurements (as mentioned previously under Experimental Results) indicate that scattering should have considerably less than a 20% effect on the yield data.

The low values in the equilibrium ratio (Fig. 10) could not be explained by scattering unless the scattering of the negative beam is greater than that of the positive beam (which may in fact be true). However, in this connection it should be noted that the charge transfer chamber used by Whittier[2] had entrance and exit apertures 1 mm in diameter spaced nearly 25 cm apart, so the effects of scatter should be more prominent in his results than in the results presented here.

In Fig. 6 the results obtained from H_2^+ and H_3^+ molecular ions lie below the proton results. This could

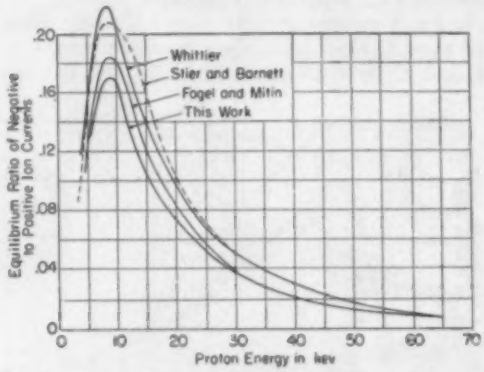

FIG. 10. Equilibrium ratio of negative to positive hydrogen ions in a proton beam traversing hydrogen gas from the work of Whittier,[2] Stier and Barnett,[3] and Fogel and Mitin [Soviet Phys. —JETP 3, 334 (1956)].

be explained by scattering of the fragments as the molecular ion dissociates. Since the mass 1, 2, and 3 curves in Fig. 6 are in reasonably good agreement, such a scattering effect is apparently not large.

ACKNOWLEDGMENTS

This research problem was suggested by Professor John G. Trump and Professor Robert J. Van de Graaff. The author has enjoyed the privelege of their guidance throughout the work and is pleased to acknowledge with graditude their interest and support. The work was made possible by generous financial support from the National Science Foundation and the Godfrey M. Hyams Trust.

JOURNAL OF APPLIED PHYSICS VOLUME 31, NUMBER 9 SEPTEMBER, 1960

Scattering of Electromagnetic Waves from an Infinitely Long Magnetized Cylindrical Plasma

P. M. PLATZMAN* AND H. T. OZAKI
Hughes Research Laboratories, A Division of Hughes Aircraft Company, Malibu, California
(Received January 25, 1960; and in final form June 2, 1960)

The magnetically contained plasma is characterized, in an average way, in terms of its macroscopic dielectric tensor. The problem of the scattering of plane electromagnetic waves from a uniform cylindrically symmetric plasma configuration is solved analytically. Numerical results for the uniform case are obtained and graphed for interesting ranges of the parameters involved. Possible applications of the results for use in investigating the plasma's properties are discussed.

INTRODUCTION

THE infinitely long, cylindrically symmetric plasma confined in an axial static magnetic field is an extremely interesting and particularly simple configuration. Its properties under the action of an applied, time varying electromagnetic field are approximately described by a linear macroscopic dielectric tensor. As a result, it is susceptible to analysis. That is to say, in certain cases Maxwell's equations for this configuration may be solved exactly.

The externally applied field will act as an indirect probe of the microscopic processes taking place inside the configuration. The scattered fields bring with them information pertaining to the density, and the average collision frequency inside the plasma. If, in addition, the plasma is in thermal equilibrium, the principle of detailed balancing, aided by the general principles of thermodynamics, allow us to relate the scattered radiation from the plasma to the emitted radiation. From these many points of view then, a consideration of the interaction of high-frequency waves with the plasma is interesting.

A number of people[1-3] have looked at the general characteristics of the normal modes of oscillation of cylindrically symmetric, magnetically confined, plasma configurations. However, in cases where interaction with an external plane wave was considered, two simplifying assumptions were put into the computation. The magnetic field was taken to be infinite, thus restricting the motion of the electrons to a line in the direction of the magnetic field. Secondly, collisions of the electrons were neglected entirely. Here the problem without these restrictions is considered. In addition, actual numerical scattering cross sections are computed for a wide range of plasma parameters. It is this second feature which gives this article its real value. The analytic expressions for the scattering cross sections, although interesting, are in general too complicated to extract much quantitative information. This is particularly true in cases where the radius of the cylinder is large compared to the wavelength of the incident radiation.

ELECTROMAGNETIC PROPERTIES OF THE PLASMA

Throughout, we will make the assumption that the plasma may be adequately described in terms of an average macroscopic dielectric tensor. This amounts to neglecting higher-order correlation effects among the electrons. Many of the simple particle aspects of the plasma are, as a result, thrown out. However, the collective aspects of its behavior, more precisely its average interaction with an externally applied field, are correctly given by this so-called "continuous fluid" approximation. In this approximation the dynamics of all the heavy particles are neglected. Their interaction with the electrons are included, only by assuming a constant (independent of energy) inelastic scattering cross section. The net result of these approximations is a Boltzman-like equation involving only the single-particle-electron-distribution function. The resulting transport equation may then be suitably averaged to arrive at an equation of motion for a single "average electron"

$$m d\mathbf{v}/dt = q[\mathbf{E}+\mathbf{v}\times(\mathbf{B}+\mathbf{B}_0)]-m\nu_c\mathbf{v}, \qquad (1)$$

where ν_c is the collision frequency and $\mathbf{v}$ the average velocity of the charged particle under consideration. $\mathbf{B}$ is the time-varying, self-consistent field and $\mathbf{B}_0$ an externally applied static field. If we now neglect the time-varying magnetic field, it is possible to find the total current in the medium. That is to say,

$$\mathbf{J}=-i\omega\epsilon_0\mathbf{E}+Nq\mathbf{v}. \qquad (2)$$

The solution for τ has been carried out in a number of papers.[4,5] If we assume that $\mathbf{B}$ is along the z axis, then the results of these computations indicate that it is

* Present address: Bell Telephone Laboratories, Murray Hill, New Jersey.

[1] H. Wilhelmsson, Trans. Chalmers Univ. Technol., Gothenberg No. 168 (1955).

[2] J. Dawson and C. Oberman, Phys. Fluids 2, 103 (1959).

[3] Akhiezer *et al.*, *Proceedings of the Second United Nations International Conference on the Peaceful Uses of Atomic Energy* (United Nations, New York, 1958), Vol. 31, p. 99, p/2300.

[4] C. H. Pappas, California Institute of Technology, ONR No. 4 (May, 1954).

[5] H. T. Ozaki, Hughes Aircraft Company, Tech. Mem. No. 477 (June, 1957).

possible to write J as

$$\mathbf{J}=-i\omega((\epsilon))\mathbf{E}, \tag{3}$$

where

$$((\epsilon))=\begin{vmatrix} \dfrac{1-Q(1+i\nu)}{(1+i\nu)^2-s^2} & \dfrac{-iQs}{(1+i\nu)^2-s^2} & 0 \\ \dfrac{iQs}{(1+i\nu)^2-s^2} & \dfrac{1-Q(1+i\nu)}{(1+i\nu)^2-s^2} & 0 \\ 0 & 0 & 1-Q/(1+i\nu) \end{vmatrix} \tag{4}$$

with

$$Q=(\omega_p/\omega)^2, \quad s=\omega_c/\omega, \quad \nu_c/\omega=\nu,$$

and where

$$\omega_p=Ne^2/m\epsilon_0, \quad \omega_c=eB_0/m.$$

$((\epsilon))$ is defined for convenience as

$$((\epsilon))=\begin{vmatrix} \epsilon_1 & i\epsilon' & 0 \\ -i\epsilon' & \epsilon_1 & 0 \\ 0 & 0 & \epsilon_3 \end{vmatrix}. \tag{5}$$

The quantities M, K, M_3 which will be used subsequently are defined by the following relations: $M=\epsilon_1/d$, $K=-\epsilon'/d$, $M_3=1/\epsilon_3$, $d=\epsilon_1^2-\epsilon'^2$.

The solutions of Maxwell's equations in such a medium have been extensively studied by a number of authors.[6] Since we shall be concerned with the problem of normal incidence, we may consider the most general field as a superposition of two independent modes. The first of these being the so-called transverse mode with $H_z=0$. H_x, H_y, can be derived from a Hertzian function ϕ by the operation

$$H_x=\partial\phi/\partial y, \quad H_y=-\partial\phi/\partial x, \tag{6}$$

where the function ϕ satisfies the equation

$$(M_3\partial^2/\partial x^2+M_3\partial^2/\partial y^2+\mu_0k_0^2)\phi=0. \tag{7}$$

The electric field is longitudinal and is equal to

$$E_z=-ik_0\mu_0\phi. \tag{8}$$

This situation is as to be expected. Since the E field points along the z axis, the motion of the electrons driven by the time-dependent electric field is not affected by the magnetic field and the medium behaves like an isotropic medium with dielectric constant $1/M_3$.

The other z independent mode is more interesting since in this case $H_x=H_y=0$, $H_z\neq0$, and the E vector is transverse. In this case the medium does behave as an anisotropic medium. H_z can be shown to satisfy a one-dimensional wave equation of the form

$$[M\partial^2/\partial x^2+M\partial^2/\partial y^2+\mu_0k_0^2]H_z=0. \tag{9}$$

E in this case is related to H by the operator

$$\mathbf{E}=-i/k_0\begin{pmatrix} iK & -M \\ M & iK \end{pmatrix}\begin{pmatrix} \partial H_z/\partial x \\ \partial H_z/\partial y \end{pmatrix}. \tag{10}$$

[6] Paul S. Epstein, Revs. Modern Phys. **28**, 3 (1956).

SCATTERING FROM A PLASMA CYLINDER

We consider in this section the problem of the scattering of an incident plane wave off an infinitely long cylinder whose principal axis lies along the z direction and whose radius is a. The plane wave is incident with its direction of propagation perpendicular to the z axis (see Fig. 1). The polarization may take an arbitrary direction. We consider first the case of H parallel to z and E perpendicular to z.

The incident H field may be written as the real part of the following expression:

$$H_{\text{inc}}=H_{z0}\mathbf{u}_ze^{i(k_0r\cos\theta-\omega t)}, \tag{11}$$

where $\mathbf{u}_z$ is a unit vector in the z direction.

The total external H field, incident plus scattered, may then be simply written as

$$H_{\text{total}}=H_{\text{inc}}+H_{\text{scatt}}=H_{z0}\mathbf{u}_z\sum_{m=-\infty}^{+\infty}(i^mJ_m(k_0r)+a_mH_m^{(1)}(k_0r))e^{i(m\theta-\omega t)}. \tag{12}$$

By using the solution of Eqs. (9) and (10) in a cylindrical coordinate system, we find in a straightforward manner that

$$a_m=\frac{i^m\{-J_m(k_0r)\Delta_1^m(k_ar)-(M/\epsilon_0)^{\frac{1}{2}}J_m'(k_0r)J_m(k_ar)\}}{\{H_m^{(1)}(k_0r)\Delta_1^m(k_ar)-(M/\epsilon_0)^{-\frac{1}{2}}H_m^{(1)\prime}(k_0r)J_m(k_ar)\}}, \tag{13}$$

where

$$\Delta_1^m=\{J_m'(k_ar)-(K/M)mJ_m(k_ar)/k_ar\}$$

and

$$k_a^2=\mu_0/Mc^2k_0^2.$$

In general, k_a is complex and the Bessel function becomes a linear combination of the J_m and I_m, the Bessel functions of the first and second kind, respec-

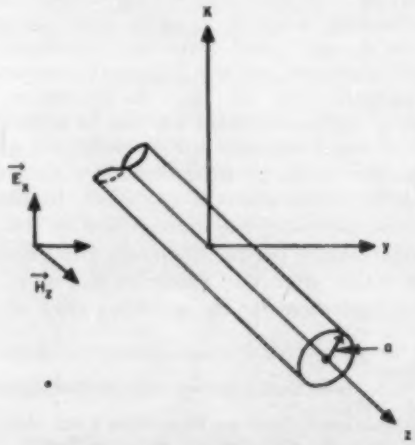

FIG. 1. Plane wave incident on a permanently magnetized plasma cylinder.

tively. For the case where the gyroelectric medium becomes isotropic, k_s becomes real K goes to zero, and $M^{-\frac{1}{2}}$ becomes equal to the square root of the relative dielectric constant (ϵ_3/ϵ_0). In this case, our answer agrees precisely with the well known solution for the dielectric rod.[7]

If E is parallel to z and H lies in the xy plane, then the equations of Sec. II indicate that the solution of the problem is identical with the solution of the problem of the scattering off a dielectric rod with relative dielectric constant (ϵ_3/ϵ_0). The solution of this problem is well known and

$$a_m=\frac{i^m\{-J_m(k_0r)J_m'(k_sr)+(\epsilon_3/\epsilon_0)^{\frac{1}{2}}J_m'(k_0r)J_m(k_sr)\}}{H_m^{(1)}(k_0r)J_m'(k_sr)+(\epsilon_3/\epsilon_0)^{\frac{1}{2}}J_m(k_sr)H_m^{(1)\prime}(k_0r)}, \tag{14}$$

where $k_s=(\epsilon_3)^{\frac{1}{2}}k_0$, and a_m is the coefficient in the expansion of the outgoing part of the total electric field

$$E_z=E_{z0}\sum_{m=-\infty}^{m=+\infty}\{i^mJ_m(k_0r)+a_mH_m^{(1)}(k_0r)\}e^{i(m\theta-\omega t)}. \tag{15}$$

It is to be pointed out that for the plasma, in general, ϵ_3 will be complex, so that in this respect the scattering will deviate from that of a lossless dielectric rod.

The scattering cross section is conventionally the convenient quantity to define and all results will be written in terms of it. The flux incident per unit area is equal to

$$N_0=\tfrac{1}{2}(\mu_0/\epsilon_0)^{\frac{1}{2}}|H_{z0}|^2. \tag{16}$$

Since the scattered fields asymptotically approach

$$H_z=H_{z0}\mathbf{u}_z(2/\pi k_0r)^{\frac{1}{2}}e^{i(k_sr-\omega t)}\sum_{m=-\infty}^{+\infty}a_me^{i[m\theta-(2m+1)\pi/4]}, \tag{17}$$

the flux, per unit length of cylinder, which is scattered

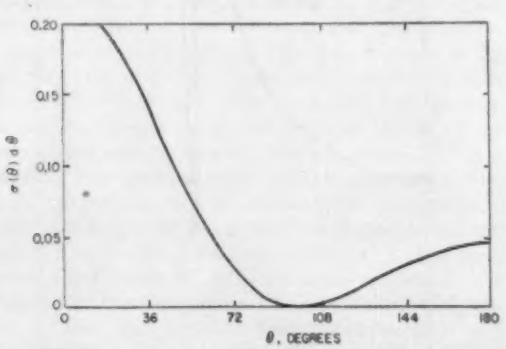

FIG. 2. Differential scattering cross section for a dielectric rod of dielectric constant two.

[7] W. R. Smythe, *Static and Dynamic Electricity* (McGraw-Hill Book Company, Inc., 1950).

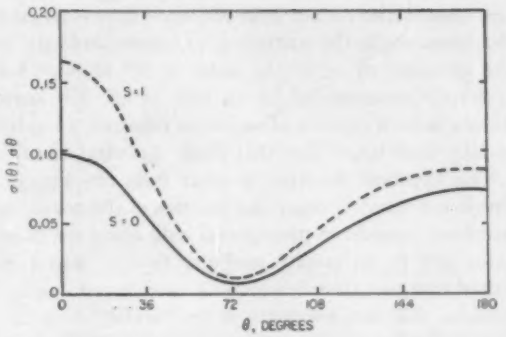

FIG. 3. Differential scattering cross section for a uniform plasma without a magnetic field and with a magnetic field at the cyclotron resonance value. $Q=10$, $\nu=0.1$, $z=1.0$.

into a two dimensional element of solid angle is

$$\bar{N}_r(\phi)=\tfrac{1}{2}(\mu_0/\epsilon_0)^{\frac{1}{2}}|H_z|^2. \tag{18}$$

The differential cross section is then defined as

$$\sigma(\phi)d\phi=\frac{\bar{N}_rd\phi}{N_0}=\frac{2}{\pi k_0}\left|\sum_{m=-\infty}^{+\infty}a_me^{im(\theta-\pi/2)}\right|^2. \tag{19}$$

RESULTS OF MACHINE COMPUTATION

In a compilation of results one must consider the four parameters involved in a calculation of the scattering. These are $k_0a=z$, s, Q, ν. Experimentally interesting values of these parameters cover a wide range of values depending upon the particular physical setup in the laboratory. We present here only a few selected cross sections which we feel are of some general interest. Those interested in additional data will be furnished with a deck of IBM cards for computation with arbitrary values of the parameters. In all cases in this section we plot the results for H in the z direction. The other orthogonal case is relatively uninteresting, since as we have pointed out, the plasma behaves like a dielectric rod. All cross sections are plotted per unit height per unit radius.

We include for the reference purpose a plot of the entire differential cross section for a lossless dielectric rod (Fig. 2). The general character of the angular distribution is quite similar in all cases where $k_0a=z\approx1$. The only terms in the expansion of the outgoing field which are of any magnitude are the zeroth or isotropic term and the first term which multiplies $\cos\theta$ in the scattering amplitude. Thus, all cross sections for $k_0a\approx1$ have a single characteristic minimum, with the relatively large diffraction peak in the forward direction.

In Fig. 3 we plot a rather interesting set of cross sections. We consider the same physical plasma with no magnetic field and then with a magnetic field strong enough to achieve so-called cyclotron resonance. The result is rather surprising. The difference between the

two cross sections is not large. Others[8,9] have estimated the resonance in the scattering, or, correspondingly in the emission, to be of the order of 10^4 as large for cyclotron resonance as for no field at all. The cross section in both cases is, as was to be expected, an order of magnitude larger than that of the dielectric, rod.

This apparent discrepancy arises from two sources. Previous estimates concerning emission at the cyclotron frequency considered propagation only along the magnetic field in an infinite medium. In this case it is indeed true that there is a resonance in the propagation constant due to a resonance in the "scalar" dielectric constant which may be used to characterize the plasma in these two modes.

The present treatment is quite different. In the first place, the medium is not infinite and the wave properties of electromagnetic disturbances in the plasma are of utmost importance. In the second place, the normal modes in the medium represent cylindrical wave propagating perpendicular to the magnetic field. For plane wave propagation in an infinite medium, and at right angles to the magnetic field, two propagation constants characterize the plasma.

The effective propagation constants for these two modes are

$$k_+^2=\omega^2\mu_0\epsilon_0\left\{1-\frac{Q\left[1-\frac{s^2(1-Q)}{(1-Q)^2+\nu^2}\right]-iQ\nu\left[1+\frac{s^2}{(1-Q)^2+\nu^2}\right]}{\left[1-\frac{s^2(1-Q)}{(1-Q)^2+\nu^2}\right]^2+\nu^2\left[1+\frac{s^2}{(1-Q)^2+\nu^2}\right]^2}\right\}, \tag{20}$$

$$k_-^2=\omega^2\mu_0\epsilon_0\{1-[Q(1-i\nu)/(1+\nu^2)]\}. \tag{21}$$

The "plus wave" corresponding to a wave with an H_z and a transverse $\mathbf{E}$ exhibits a resonance as it does for parallel propagation. The existence of this resonance has been pointed out by various authors.[1,2] Interestingly, the resonant field for small ν is not the cyclotron frequency but is given as

$$s=(1-Q)^{\frac{1}{2}}.$$

For large values of Q the propagation constant is relatively insensitive to changes in the magnetic field. If we believe our cylindrical waves to be of a similar nature, this would account for the lack of a scattering resonance at $s=1$, for perpendicular incidence resonance.

However, as Figs. 4 and 5 indicate, there is apparently a strong resonance in the scattering at $\pi/2$ centered about the value indicated by (4.3). We consider the scattering near $\pi/2$ because apparently the scattering in the "$\cos\theta$" mode increases steadily with increasing Q. Qualitatively, we might expect this. If we neglect the effect of the magnetic field, the electric field would drive the electrons in a line giving rise to a dipole field in the cross sectional plane. At $\pi/2$ this dipole field vanishes and the resonance is clearly visible. Formulas (20) and (21) indicate that if the collision frequency is small, the propagation constant for the "plus mode" approaches that of free space at a value of s close to its "resonant" value. The result is the tremendous minimum in the cross section (Fig. 4). The resonance in Fig. 5 is less pronounced and not as simple since the cosine dependence from higher modes contributes quite strongly in this case. In contrast, a similar plot (Fig. 6) for s near 1 at $\pi/2$ indicates no corresponding resonance.

The existence of this resonance which depends on both

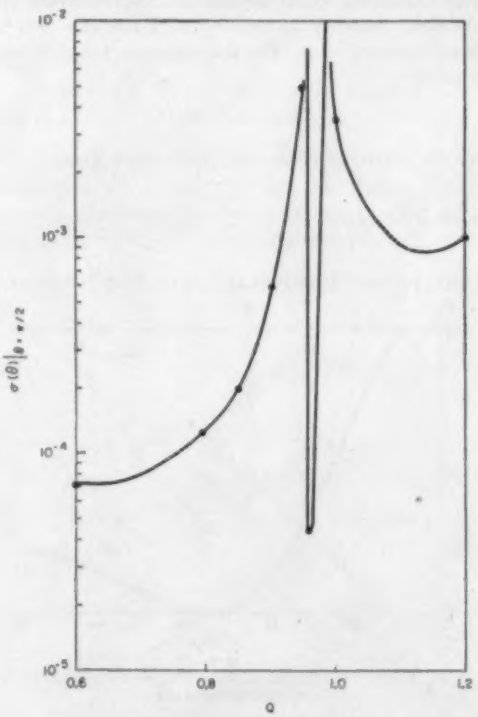

FIG. 4. Differential scattering cross section near 90° through "perpendicular resonance." $s=0.2$, $\nu=0.01$, $z=1.0$.

[8] Lockheed Aircraft Company, Tech. Rep. LMSD-48394 (February 27, 1959).

[9] Trubnikov and Kudiyavtsev, *Proceedings of the Second United Nations International Conference on the Peaceful Uses of Atomic Energy* (United Nations, New York, 1958), p. 2213.

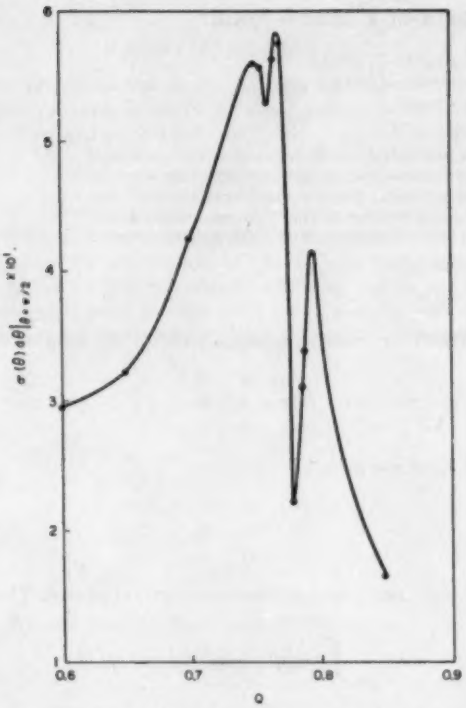

FIG. 5. Differential scattering cross section near 90° through "perpendicular resonance." $s=0.5$, $\nu=0.01$, $z=5.0$.

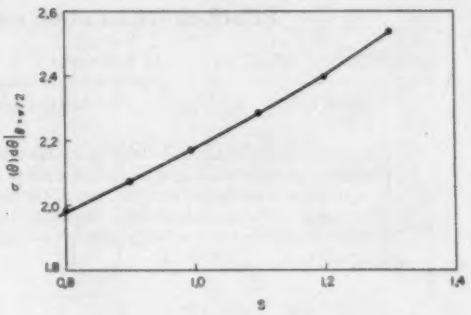

FIG. 6. Differential scattering cross section near 90° through cyclotron resonance. $Q=10.0$, $\nu=0.1$, $z=1.0$.

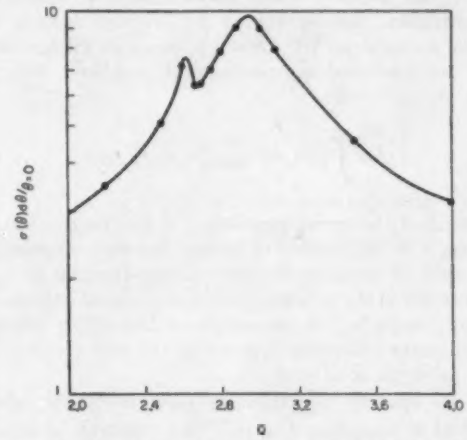

FIG. 7. Differential scattering cross section at 0° through plasma resonance. $s=0.2$, $\nu=0.01$, $z=1.0$.

H and Q opens up the possibility of using it to determine the density of the plasma. Since the shape must be influenced by changes in the collision frequency, a detailed study of these shapes experimentally may allow the experimenter to determine the collision frequency quite accurately. The problem investigated here is highly idealized. The "perpendicular resonance," as we call it, is extremely sensitive to the parameters involved in the problem. Owing to extremely tricky cancellations of the coefficients which come about because of their phase relationships with one another, the cross sections in the neighborhood of the resonance are relatively small in magnitude. Observed at different angles, the "perpendicular resonance" occurs for different values of the parameters and has quite different shapes. Since a physical measurement must subtend some finite solid angle and too wide an angle will wash out the resonance, subtended angles of the order of a degree or less are required in this idealized case to observe a clear resonance. Modifications due to nonuniformities in the plasma, the effect of container walls, the finite length of the cylinder, and deviation from "cylindricality" will also prove to be extremely important effects in the "perpendicular resonance" region. The calculation is of value insofar as it indicates the existence of this extremely sensitive resonance for an idealized system.

Figure 7 is a plot of the scattering in the forward direction through so-called plasma resonance. It is well known that, for the case of a homogeneous plasma rod devoid of magnetic field, the scattering goes through a resonance where the real part of the dielectric constant becomes -1. For zero collision frequency, the scattering is presumably infinite. Shapiro[10] has actually measured the existence of this resonance in a series of experiments. In our case this resonance, at $\theta=0°$ and in the total cross section, is also present. This analysis would then seem to indicate that at least for perpendicular propagation the principle emission lines for the plasma occur not at the cyclotron frequency but at approximately twice the plasma frequency.

[10] H. Shapiro, California Institute of Technology, Antenna Laboratory Tech. Rept. No. 11 (May 31, 1957).

Effect of Orientation on Strength of a Model Solid*

A. Robinson, J. E. Osborn, and C. C. Hsiao
University of Minnesota, Minneapolis, Minnesota

(Received March 30, 1960)

A mathematical analysis is given to describe the effect of orientation on the variation of the mechanical strength of a model solid. For the simple state of uniaxial orientation the fracture strength in the direction of orientation is evaluated as a function of the degree of orientation in terms of the orientation strain and the strength of the unoriented solid. Assuming the fracture strain remains constant, the maximum fracture strength obtainable for a perfectly oriented solid is found to be six times that of the solid without preferred orientation.

IN his paper on mechanical breakdown and molecular orientation, Hsiao[1] has presented a quasi-static theory for a model linear polymer solid in terms of deformation. By considering an oriented system of linear spring elements, the stress tensor in the vicinity of a point referred to an orthogonal coordinate system may be expressed as

$$\sigma_{ij}^* = \int E l^2 \lambda \rho^* f^* \epsilon_{mn}^* s_m^* s_n^* s_i^* s_j^* d\omega^*,$$

where E is the spring modulus, l is the length of any spring, λ is the number of springs per unit volume in the solid, ρ^* is the probability density function of the orientation of the springs, f^* is the fraction of unbroken springs, $\epsilon_{mn}^* s_m^* s_n^*$ is the strain of the spring whose instantaneous direction is given by the unit vector s_i^*, and $d\omega^*$ is the solid angle.

If the fracture mechanism is considered to be independent of time, then $f = f_0$ will be a constant. In other words, the model is a static one and all the unbroken spring elements taken into account do not break and reform during loading. However, the fracture strength is still time dependent.[2] Only the strengths obtained at one constant rate of straining are considered and compared. If we let $C = El^2\lambda f_0$, then the stress tensor may be written as follows:

$$\sigma_{ij}^* = C \int \rho^* \epsilon_{mn}^* s_m^* s_n^* s_i^* s_j^* d\omega^*.$$

First a calculation of the strength for the random case, i.e., when $\rho^* = \rho$ is independent of θ and ϕ, the spherical coordinates, and all the stars in the foregoing expression may be dropped for the system without orientation. Now $\int \rho d\omega = 1$ and $d\omega = \sin\theta d\theta d\phi$. Thus

$$\int \rho d\omega = \rho \int_0^{2\pi} \int_0^{\pi} \sin\theta d\theta d\phi = 4\pi\rho,$$

and $\rho = 1/4\pi$. Now assume ϵ_{mn} to be of the form

$$\begin{pmatrix} \epsilon_{11} & 0 & 0 \\ 0 & \epsilon_{22} & 0 \\ 0 & 0 & \epsilon_{33} \end{pmatrix}$$

and σ_{ij} of the form

$$\begin{pmatrix} \sigma_{11} & 0 & 0 \\ 0 & \sigma_{22} & 0 \\ 0 & 0 & \sigma_{33} \end{pmatrix}$$

and that their principal directions are coincident. Thus

$$\sigma_{11} = \frac{C}{4\pi} \int (\epsilon_{11} s_1^4 + \epsilon_{22} s_1^2 s_2^2 + \epsilon_{33} s_1^2 s_2^2) d\omega$$

with similar expressions for σ_{22} and σ_{33}. It is easily seen that nine integrals will arise in these expressions. Denoting the first one by $\int_1$, the second by $\int_2$, etc., then

for σ_{11}:

$$\int_1 = \int s_1^4 d\omega, \quad \int_2 = \int s_1^2 s_2^2 d\omega, \quad \int_3 = \int s_1^2 s_3^2 d\omega,$$

for σ_{22}:

$$\int_4 = \int s_1^2 s_2^2 d\omega, \quad \int_5 = \int s_2^4 d\omega, \quad \int_6 = \int s_2^2 s_3^2 d\omega,$$

for σ_{33}:

$$\int_7 = \int s_1^2 s_3^2 d\omega, \quad \int_8 = \int s_2^2 s_3^2 d\omega, \quad \int_9 = \int s_3^4 d\omega.$$

Here $s_1 = \sin\theta\cos\phi$, $s_2 = \sin\theta\sin\phi$, and $s_3 = \cos\theta$. The values for the nine integrals are as follows:

$$\int_1 = \int_6 = \int_8 = \frac{4\pi}{5},$$

$$\int_2 = \int_3 = \int_4 = \int_5 = \int_7 = \int_9 = \frac{4\pi}{15}.$$

Therefore

$$\sigma_{11} = (C/5)[\epsilon_{11} + \tfrac{1}{3}(\epsilon_{22} + \epsilon_{33})],$$

$$\sigma_{22} = (C/5)[\epsilon_{22} + \tfrac{1}{3}(\epsilon_{33} + \epsilon_{11})],$$

* Supported in part by the U. S. Atomic Energy Commission.

[1] C. C. Hsiao, J. Appl. Phys. **30**, 1492 (1959); J. Polymer Sci. 44, 71 (1960).

[2] C. C. Hsiao, Nature **186**, 535 (1960).

and

$$\sigma_{33}=(C/5)[\epsilon_{33}+\tfrac{1}{3}(\epsilon_{11}+\epsilon_{22})].$$

For simple tension in the 33 direction, $\epsilon_{11}=\epsilon_{22}$. For a fixed value of ϵ_{33} we desire ϵ_{11} and ϵ_{22} to be such that both σ_{11} and σ_{22} are zero. Setting $\sigma_{11}=\sigma_{22}=0$, we find

$$\epsilon_{11}=\epsilon_{22}=-\tfrac{1}{4}\epsilon_{33}.$$

Thus $\sigma_{33}=(C/6)\epsilon_{33}$.

Next a calculation is made for the stress in the case of complete orientation in the 33 direction. In this case the probability will be "lumped" in or divided into equal parts at $\theta=0$ and $\theta=\pi$. Thus $\rho d\omega=\frac{1}{2}$ at $\theta=0$ and $\rho d\omega=\frac{1}{2}$ at $\theta=\pi$ and is zero elsewhere. Therefore

$$\begin{aligned}\sigma_{33}&=C\int\rho(\epsilon_{11}s_1^2s_3^2+\epsilon_{22}s_2^2s_3^2+\epsilon_{33}s_3^4)d\omega\\&=C\epsilon_{33}\int\rho d\omega\\&=C\epsilon_{33}(\tfrac{1}{2}+\tfrac{1}{2})\\&=C\epsilon_{33}.\end{aligned}$$

We now see that for a given strain ϵ_{33},

$$\frac{\sigma_{33}\text{ (complete orientation)}}{\sigma_{33}\text{ (complete random)}}=6.$$

In the general case, as mentioned before, the stress tensor for an oriented system is given by

$$\sigma_{ij}^*=C\int\rho^*\epsilon_{mn}s_m^*s_n^*s_i^*s_j^*d\omega^*.$$

Again there will be nine integrals to evaluate. In the evaluation of these use will be made of the equality, $\rho^*d\omega^*=\rho d\omega$, i.e., the number of linear spring elements in a small solid angle is the same before and after orientation. Thus

$$\sigma_{ij}^*=C\int\rho\epsilon_{mn}s_m^*s_n^*s_i^*s_j^*d\omega.$$

For uniaxial orientation if we let a finite strain ϵ indicate the degree of orientation of the system, then the new coordinates of a point will be

$$z'=(1+\epsilon)z,\quad x'=x/(1+\epsilon)^{\frac{1}{2}},\quad y'=y/(1+\epsilon)^{\frac{1}{2}}$$

after orientation on the basis of assuming the incompressibility of the solid. Transforming the above integral by use of these relations, we obtain

$$\begin{aligned}\int_1&=\int_{\phi=0}^{2\pi}\int_{\theta=0}^{\pi}\frac{\sin^5\theta\cos^4\phi d\theta d\phi}{(1+b^2\cos^2\theta)^2}\\&=\frac{3\pi}{4}\left[\frac{3+b^2}{b^4}+\frac{-3-2b^2+b^4}{b^5}\tan^{-1}b\right],\end{aligned}$$

where $b^2=(1+\epsilon)^3-1$.

$$\begin{aligned}\int_2=\int_4&=\int_{\phi=0}^{2\pi}\int_{\theta=0}^{\pi}\frac{\sin^5\theta\cos^2\phi\sin^2\phi d\theta d\phi}{(1+b^2\cos^2\theta)^2}\\&=\frac{\pi}{4}\left[\frac{3+b^2}{b^4}+\frac{-3-2b^2+b^4}{b^5}\tan^{-1}b\right].\end{aligned}$$

$$\begin{aligned}\int_3=\int_7&=\int_{\phi=0}^{2\pi}\int_{\theta=0}^{\pi}\frac{\cos^2\theta\sin^3\theta\cos^2\phi d\theta d\phi}{a^2(1+b^2\cos^2\theta)^2}\\&=\pi\left[\frac{-3}{a^2b^4}+\frac{3+b^2}{a^2b^5}\tan^{-1}b\right],\end{aligned}$$

where $a=1/(1+\epsilon)^{\frac{1}{3}}$.

$$\begin{aligned}\int_5&=\int_{\phi=0}^{2\pi}\int_{\theta=0}^{\pi}\frac{\sin^5\theta\sin^4\phi d\theta d\phi}{(1+b^2\cos^2\theta)^2}\\&=\frac{3\pi}{4}\left[\frac{3+b^2}{b^4}+\frac{-3-2b^2+b^4}{b^5}\tan^{-1}b\right].\end{aligned}$$

$$\begin{aligned}\int_6=\int_8&=\int_{\phi=0}^{2\pi}\int_{\theta=0}^{\pi}\frac{\sin^3\theta\cos^2\theta\sin^2\phi d\theta d\phi}{a^2(1+b^2\cos^2\theta)^2}\\&=\pi\left[\frac{-3}{a^2b^4}+\frac{3+b^2}{a^2b^5}\tan^{-1}b\right].\end{aligned}$$

and

$$\begin{aligned}\int_9&=\int_{\phi=0}^{2\pi}\int_{\theta=0}^{\pi}\frac{\sin\theta\cos^4\theta d\theta d\phi}{a^4(1+b^2\cos^2\theta)^2}\\&=2\pi\left[\frac{3+2b^2}{a^4b^4(1+b^2)}-\frac{3}{a^4b^5}\tan^{-1}b\right].\end{aligned}$$

Thus

$$\begin{aligned}\sigma_{11}=\sigma_{22}=\frac{C}{4\pi}\Bigg[&\frac{3\pi}{4}\left(\frac{3+b^2}{b^4}+\frac{-3-2b^2+b^4}{b^5}\tan^{-1}b\right)\epsilon_{11}\\&+\frac{\pi}{4}\left(\frac{3+b^2}{b^4}+\frac{-3-2b^2+b^4}{b^5}\tan^{-1}b\right)\epsilon_{22}\\&+\pi\left(\frac{-3}{a^2b^4}+\frac{3+b^2}{a^2b^5}\tan^{-1}b\right)\epsilon_{33}\Bigg],\end{aligned}$$

and

$$\begin{aligned}\sigma_{33}=\frac{C}{4\pi}\Bigg[&\pi\left(\frac{-3}{a^2b^4}+\frac{3+b^2}{b^5a^2}\tan^{-1}b\right)\epsilon_{11}\\&+\pi\left(\frac{-3}{a^2b^4}+\frac{3+b^2}{a^2b^5}\tan^{-1}b\right)\epsilon_{22}\\&+2\pi\left(\frac{3+2b^2}{a^4b^4(1+b^2)}-\frac{3}{a^4b^5}\tan^{-1}b\right)\epsilon_{33}\Bigg].\end{aligned}$$

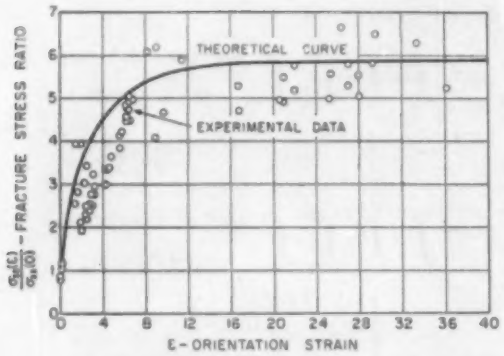

FIG. 1. Effect of uniaxial orientation on the fracture stress ratio of polyethylene.

As before, for a simple tension test in the 33 direction, $\epsilon_{11}=\epsilon_{22}$. For a fixed value of ϵ_{33} we desire ϵ_{11} and ϵ_{22} to be such that $\sigma_{11}=\sigma_{22}=0$. Proceeding as before we find

$$\sigma_{33}=\frac{C\epsilon_{33}}{2}\left\{\left(\frac{3+2b^2}{a^4b^4(1+b^2)}-\frac{3}{a^4b^5}\tan^{-1}b\right)-\frac{\left(\frac{-3}{a^4b^4}+\frac{3+b^2}{a^4b^5}\tan^{-1}b\right)^2}{\left(\frac{3+b^2}{b^4}+\frac{-3-2b^2+b^4}{b^5}\tan^{-1}b\right)}\right\}.$$

It can be shown that

$$\lim_{\epsilon\to 0}\sigma_{33}=C\epsilon_{33}/6,$$

and

$$\lim_{\epsilon\to\infty}\sigma_{33}=C\epsilon_{33},$$

which check with the direct method used for finding the limiting cases. On dividing the formula for the stress at some arbitrary ϵ by the one for $\epsilon=0$, we obtain

$$\frac{\sigma_{33}(\epsilon)}{\sigma_{33}(0)}=\left\{3\left\{\left(\frac{3+2b^2}{a^4b^4(1+b^2)}-\frac{3}{a^4b^5}\tan^{-1}b\right)-\frac{\left(\frac{-3}{a^4b^4}+\frac{3+b^2}{a^4b^5}\tan^{-1}b\right)^2}{\left(\frac{3+b^2}{b^4}+\frac{-3-2b^2+b^4}{b^5}\tan^{-1}b\right)}\right\}\frac{\epsilon_{33}(\epsilon)}{\epsilon_{33}(0)}\right\}.$$

In order to obtain a failure stress theory some assumption must be made about the ratio $\epsilon_{33}(\epsilon)/\epsilon_{33}(0)$, where $\epsilon_{33}(\epsilon)$ is the small strain at failure when unoriented.

TABLE I.

ϵ	$\sigma_{33}(\epsilon)$
0	1.00 $\sigma_{33}(0)$
$\frac{1}{2}$	1.97 $\sigma_{33}(0)$
1	2.65 $\sigma_{33}(0)$
2	3.65 $\sigma_{33}(0)$
4	4.65 $\sigma_{33}(0)$
8	5.36 $\sigma_{33}(0)$
16	5.80 $\sigma_{33}(0)$
∞	6.00 $\sigma_{33}(0)$

If this ratio is assumed to be constant, i.e., the small breaking strain $\epsilon_{33}(\epsilon)$ is not affected by orientation, we obtain a failure theory which predicts a failure stress at complete orientation of six times that for random orientation. The variation of failure stress, in this case, as a function of ϵ is shown in Table I and Fig. 1. Data of failure stress for polyethylene are also given for comparison.

JOURNAL OF APPLIED PHYSICS VOLUME 31, NUMBER 9 SEPTEMBER, 1960

Magnetostatic Modes in Disks and Rods*

J. F. DILLON, JR.
Bell Telephone Laboratories, Incorporated, Murray Hill, New Jersey
(Received April 19, 1960)

Ferrimagnetic-resonance experiments have been performed using disk- and rod-shaped samples cut from single crystals of a manganese ferrite and of yttrium iron garnet. A multiplicity of absorption maxima were observed which can be identified as magnetostatic modes. The excitation of different sets of modes by rf magnetic field configurations of varying symmetries aids in assigning indices to the modes observed. By far the narrowest lines were observed in thin disks with the steady field normal to the plane of the disk.

INTRODUCTION

FERRIMAGNETIC-RESONANCE (FMR) experiments represent one of our most potent means of obtaining information on the behavior of exchange-coupled spin systems. Such experiments may be thought of as a study of the splitting of the ground state of these crystals. In spin-wave language they have in the past been regarded as the simple excitation of the infinite-wavelength spin wave. The observation of a multiplicity of absorption maxima under certain conditions in this and other work showed that it was necessary to consider other long-wavelength modes. The subsequent theoretical understanding of the magnetostatic modes has considerably broadened our knowledge of the spectrum of disturbances to the magnetic-spin system.

Spherical specimens have been usual in recent FMR experiments since the resonance condition is greatly simplified in that case, and the excursions of the field for resonance when the crystallographic direction of the steady field is varied can be attributed to the magnetocrystalline anisotropy. Some sort of ellipsoid was considered necessary in order to have the internal field uniform within the sample. Only in such cases is there validity to the concept of the spatially uniform internal steady field, and the shape demagnetizing factors. White, Solt, and Mercereau[1] observed multiple resonances in spheres when placed in nonuniform rf magnetic fields. The bulk of the experiments reported in this paper were performed with other than spherical samples. The disks and rods are only approximately ellipsoids, and it will be seen that the deviations from ellipticity are significant in the excitation of many of the more complicated modes. Some of the results given here have been quoted in the papers by Walker.[2]

The theory of magnetostatic modes given by Walker deals with long-wavelength disturbances of the spin system of a ferromagnetic spheroid. The characteristic distances involved are assumed to be so great that exchange effects may be neglected, and they are assumed to be short enough so that propagation effects may also be ignored. The theory is thus truly magnetostatic in scope. It includes the shape of the sample, but not its size. Within this framework it is found that a large number of precessional modes are possible in the motion of the magnetization. These are identified by three index numbers, n, m, and r, written $(n,m,r,)$ for a given mode.

Let us attempt to visualize the magnetostatic modes. Walker's theory in its present form applies to the motion of magnetization in ellipsoids of revolution with the steady field along the axis. The simplest physical description of the motion of the transverse magnetization in a single mode may be found by writing down its radial and tangential components. It is known that any mode may be characterized by a complex magnetic potential which may be written $f_{n,m,r,}(z,\rho)\exp[j(m\varphi+\omega t)]$, where $\rho^2=x^2+y^2$, φ is the azimuth, and the z axis is along the steady field. The radial component m_ρ and the tangential component m_φ of the magnetization may then be written

$$m_\rho=\frac{M_0}{H_i^2-\omega^2/\gamma^2}\left[H_i\frac{\partial f}{\partial\rho}+\frac{\omega}{\gamma}\frac{m}{\rho}f\right]\cos(m\varphi+\omega t),$$

and

$$m_\varphi=-\frac{M_0}{H_i^2-\omega^2/\gamma^2}\left[\frac{\omega}{\gamma}\frac{\partial f}{\partial\rho}+H_i\frac{m}{\rho}f\right]\sin(m\varphi+\omega t).$$

These equations show that the transverse magnetization is, in general, elliptically polarized with the principal axes radial and tangential. The ellipticity is independent of azimuth, but the phase varies as $m\varphi$. The circularly polarized components rotate with an angular velocity $-(\omega/m)$. In a coordinate system rotating with angular velocity $-(\omega/m)$, the pattern will appear to be stationary. Nodal planes on which the magnetization is at rest can occur for general m only when f and $\partial f/\partial\rho$ are zero together. This condition is met in the plane $z=0$ for modes with $n-m$ odd. If $m=0$, a nodal plane may also occur where $\partial f/\partial\rho=0$.

Questions arise as to whether a particular mode will be excited by a given rf magnetic field distribution. These may be answered by regarding the rf magnetic field as a driving term, and seeking its projection on the transverse magnetization of the mode in question.

* A preliminary report of this work was presented at the American Physical Society Meeting, Pittsburgh, March 16, 1956. See J. F. Dillon, Jr., Bull. Am. Phys. Soc. Ser. II, 1, 125 (1956); Ser. II, 2, 128 (1957).

[1] R. L. White, I. H. Solt, and J. E. Mercereau, Bull. Am. Phys. Soc. Ser. II, 1, 12 (1956); R. L. White and I. H. Solt, Phys. Rev. 104, 56 (1956).

[2] L. R. Walker, (a) Bull. Am. Phys. Soc. Ser. II, 1, 125 (1956); (b) Phys. Rev. 105, 390 (1957); (c) J. Appl. Phys. 29, 318 (1958).

SPECIMENS

All of our experiments have been performed using the best single crystals of ferrimagnetic crystals available at the time. In the earlier phase of the work this meant a manganese-ferrite single crystal. Later, single crystals of yttrium iron garnet (YIG) were available, and they were used. The manganese-ferrite samples were all cut from a single boule which was grown by the Verneuil (flame fusion) process at the Linde Air Products Company under the direction of Dr. G. W. Clark and Dr. R. W. Kebler. It was not the same boule from which samples were cut for other FMR experiments which the author has reported. The YIG crystals were grown from lead-oxide flux by J. W. Nielsen.[5]

The disks we have used had their major plane parallel to one of the principal crystallographic planes. The surfaces were polished very carefully. In all cases the final surfaces were approached by polishing through several thousandths of an inch with Linde A polishing powder.

The plano-convex and double-convex disks were made by the very careful application of standard lens polishing techniques.

The rods were made by rolling rectangular bars of appropriate size between two flat abrasive surfaces. This operation was done by hand. The rods were not polished.

EXPERIMENTAL PROCEDURE

The complexity of the absorption vs field curves was such that semiautomatic data taking was essential. Let us describe briefly the technique used. Microwave absorption is measured by placing the sample at the desired point in a transmission cavity. The cavity is located between the pole pieces of an electromagnet. The microwave source, a klystron, is frequency modulated by applying a sawtooth voltage to its repeller. This is sufficient in amplitude to sweep through an entire klystron mode. The center frequency of this mode is that of our cavity.

In the case of the YIG disks where the Q of the ferrimagnetic resonance is considerably greater than that of the cavity an amplitude-modulated constant-frequency source is used. It is set at the center frequency of the cavity. A detector on the far side of the cavity from the klystron enables us to display the maximum transmission of the cavity. A peak-detecting network gives us a voltage proportional to the height of this transmission, and this is recorded on the x axis of an x-time recorder. The relation between the voltage output of this circuit and the relative absorption may be calibrated by means of markers introduced with a precision rotating-vane attenuator between the cavity and the detector. The procedure used is to drive the magnetic field slowly across the field region of interest. Changes in the voltage at the recorder represent changes in the loss term of the permeability of the sample.

An indication of the magnetic field was introduced with a nuclear resonance magnetometer.[6] This instrument was modified slightly in that the condenser in the oscillator circuit was replaced by a bank of ten variable condensers, any one of which could be switched into the circuit. Each of these was pretuned to a frequency appropriate to a desired field. For instance, in the recording from which Fig. 2(a) was made, condensers were set so that they tuned the tank circuit to frequencies corresponding to fields of 5700, 5800, 5900, . . . up to 6700 oe. Each time the NMR resonance passed across the face of an oscilloscope, a marker was introduced onto our absorption recording. The operator then turned to the next condenser, waited till its resonance crossed the center of the screen, and continued the process. When the linewidth of a single-absorption peak was to be determined, more closely spaced markers were used as appropriate. In general when it was desired to know the positions of the lines most accurately, the fields of the absorption maxima were measured directly using the NMR magnetometer.

The experimental arrangement just described is well suited to such an investigation as this. Direct detection is feasible because there is no intensity problem whatsoever. The samples are very large by ordinary ferromagnetic-resonance standards, the linewidths are relatively narrow, and the spin systems are all aligned. The simple nonlinear presentation of the absorption which results is appropriate since it allows the same plot to show both large and small absorptions. It is sufficiently automatic to make possible the recording of the complex absorptions encountered.

Figure 1 is taken from another paper on "Modes in

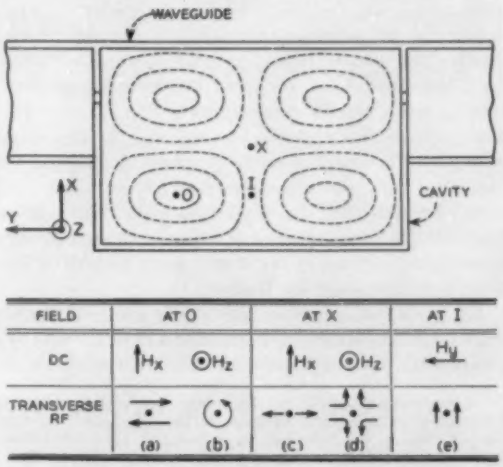

FIG. 1. Schematic drawing of a microwave cavity showing the various transverse rf magnetic-field configurations which are available at special positions.

[5] J. W. Nielsen and E. F. Dearborn, J. Phys. Chem. Solids 5, 202 (1958).

[6] H. E. Earl (to be published).

spheres." [5] It is intended to show the various nonuniform distributions of rf magnetic field available in a simple rectangular cavity. The field situation (e) is that usual in a magnetic-resonance experiment. However, at the point O two quite different rf field configurations are available depending on whether the steady field is along the z axis or in the xy plane. At the point X, again there are two quite different field configurations available. We have been able to excite modes in disks with the field configurations (a), (c), and (e). Reference to the paper on "Modes in spheres" will show that we were then able to associate particular modes with (b) and (d); however, these have not been thoroughly explored in the case of disks and rods.

If a specimen of reasonable size is placed in the fields of Fig. 1(e), the absorption is so large that the cavity resonance is completely blotted out for a considerable field range on either side of the resonance. It is found to be convenient to reduce the magnitude of this absorption by making the steady field almost parallel to the rf field. The wavelength connections to the cavity are made with flexible waveguide. The cavity itself is mounted on a rocking mechanism which allows it to be rotated about both a vertical and a horizontal axis. Angular settings to closer than 1 min of arc are possible. In addition to the necessity of adjusting the height of the absorption due to the uniform component of the field, it is desirable to make the symmetry axis of the sample accurately parallel or perpendicular to the magnetic field. This also is achieved by use of the rocking mechanism. The field for resonance is either a maximum or a minimum at this setting, and the angular position can be easily found by rocking the cavity and measuring the field for resonance.

DISKS—FIELD NORMAL

The three absorption curves of Figs. 2(a)–2(c) show modes observed using a circular disk of manganese ferrite with the steady field normal to the major faces. This disk was 0.100 in. in diameter and 0.005 in. thick. Figure 2(a) was taken with the disk at the position of uniform transverse rf magnetic field [Fig. 1(e)]. If FMR represented only the uniform precession of the entire spin system, we would expect in this case a single-absorption peak. Its location would be given by the Kittel condition which for the ellipsoid of revolution is $\omega_0=\gamma[H_z+(H_T-H_z)M]$. Since this specimen is not perfectly elliptical we cannot assign meaningful rf and dc demagnetizing factors to it. The uniform precession corresponds to the largest of the absorption maxima which is that at the highest field.

In Fig. 2(b) the rf field has opposite phase on opposite semicircular halves as in Fig. 1(c). Finally the curve of Fig. 2(c) was taken with an rf field which was odd along the steady field, the configuration of Fig. 1(a). Note that the modes of the first curve, Fig. 2(a), mesh perfectly with those of (b). We will see later that these are the odd and even members of the same series of modes. From the field which excites it, it seems quite clear that the series of Fig. 2(c) arises from modes in which the magnetization has opposite phase above and below a plane perpendicular to the z axis.

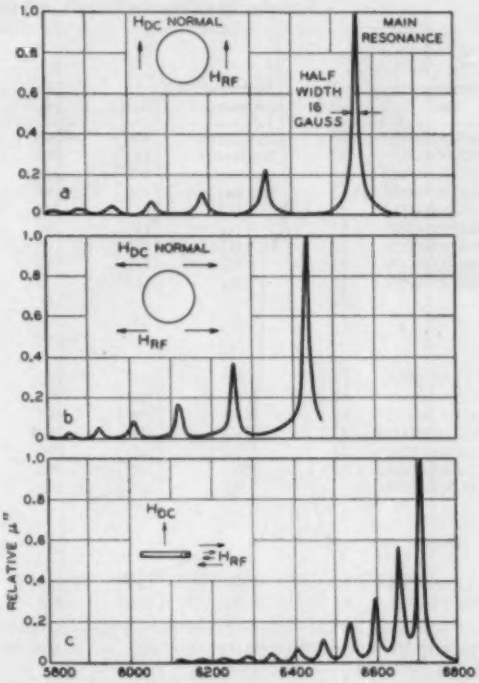

FIG. 2. Absorption curves obtained with a 0.100- ×0.005-in. disk of manganese ferrite with three different transverse rf magnetic-field configurations. Frequencies were close to 9226 Mc.

Though the experimental equipment for the 9000-Mc work was not intended for use at any but room temperature, absorption traces were made at about 195°K by packing dry ice around the cavity. The field for resonance increased considerably, and the spacing between adjacent modes increases on going to a lower temperature. If we consider the spacing of the first two modes excited in Fig. 2(a), we find it is 288 oe at 300°K and 347 oe at 195°K. The magnetization of another supposedly similar crystal of magnanese ferrite was measured, and the ratio $M_{195}/M_{300}=1.25$. This corresponds fairly closely to the ratio of the mode spacings just quoted $(H_1-H_3)_{195}/(H_1-H_3)_{300}=1.21$. These first experiments implied that the mode spacing varies at least roughly with the magnetization.

Some of the experimentally determined quantities are set down in Table I. It will be noted from the first two lines of this table that two disks of magnanese ferrite of identical dimensions, but different in orientation showed the same spacing between the first two modes

[5] J. F. Dillon, Jr., Phys. Rev. 112, 59 (1958).

TABLE I. Summary of measurements with disk shape samples, steady field normal to the plane of the disk.

(a)

Sample dimensions (in.)	D/t	Nominal composition	[hkl]	T °K	H_1[a]	ΔH_1	M_s	f	H_1-H_3
0.100×0.005	20	Mn ferrite	[100]	~295	6425	16	351	9226	207
0.100×0.005	20	Mn ferrite	[111]	295	6223	31	351	9228	207
0.030×0.0020	15	Mn ferrite	[100]	295	6238	21	351	~9200	288
0.030×0.0020	15	Mn ferrite	[100]	~195	6792	···	438	~9200	347
0.050×0.0029	17	YIG	[111]	528	···	···	···	8946	71.7
0.050×0.0029	17	YIG	[111]	295	4815	1.1	143	9257	105.2
0.050×0.0029	17	YIG	[111]	295	10 132	3.6	143	~24 000	123
0.050×0.0029	17	YIG	[111]	77	···	14.0	192	23 941	157
0.050×0.0029	17	YIG	[111]	4.2	···	···	197	24 036	157

(b)

					H_1-H_2[a]	H_1-H_3	H_1-H_4	H_1-H_5	H_1-H_6	H_1-H_7	H_1-H_8	H_1-H_9
0.122×0.0064	19.1	YIG	[100]	~295	60	127	174	217	···	···	···	···
0.100×0.0058	17.2	YIG	[100]	295	···	135	···	228	···	301	···	405
0.061×0.0032	19.1	YIG	[100]	295	···	123	···	224	···	285	···	···
0.0415×0.0015	27.7	YIG	[100]	295	···	88	···	160	···	···	···	···
0.024×0.0010	24	YIG	[100]	295	···	102	···	184	···	250	···	···
0.102×0.0033	34	YIG	[100]	295	···	79	···	143	···	197	···	244
0.099×0.0070	···	YIG	[100]	295	···	124	···	219	···	292	Double convex	

(c)

					$H_1'-H_1$[b]	$H_2'-H_1$	$H_3'-H_1$	$H_4'-H_1$	$H_5'-H_1$	$H_6'-H_1$
0.122×0.0064	19	YIG	[100]	295	85	69	52	36	16	···
0.061×0.0032	19	YIG	[100]	295	90	···	57	···	20	···

[a] H_m is the field at which the mode $(m,m,0)$ occurs.
[b] H_m' is the field at which the mode $(m+1, m, 0)$ occurs.

in the series which starts off with the uniform precession. A disk with a less extreme diameter to thickness or aspect ratio shows a larger spacing.

When single crystals of yttrium iron garnet (YIG) became available it was soon obvious that they were the preferred samples for experiments on ferrimagnetic resonance. The results of some measurements of a disk of YIG are also given in Table I. These include measurements of the mode spacing at two frequencies and at a number of temperatures. The ratio of the mode spacings at two temperatures again approximates the ratio of the magnetizations. However, the mode spacing at the same temperature does not appear to be identical for the two different frequencies used, 9.2 and 24.0 kMc. In these YIG disks the linewidths were so much narrower than the mode spacings that the individual modes stood completely isolated from each other. Reference to Fig. 8(a) below will give some idea of the scale.

The deepest absorption observed in uniform transverse rf magnetic field is taken to be the spatially uniform precession of the entire spin system of the sample. This is often spoken of as the Kittel mode; and in the present notation is indexed (1,1,0). The following modes in that series are taken to be $(m,m,0)$ with m an odd integer. The most prominent member of the series of Fig. 2(b) is presumably (2,2,0), and the whole series consists of the modes $(m,m,0)$ with m even.

In Fig. 2(c) the series excited is presumably odd in z and even in x since this is the symmetry of exciting field. We believe these to be the modes (2,1,0), (4,3,0), (6,5,0), etc. The demonstration that this is correct and the modes odd in x are not included is contained in a comparison of Fig. 8(a) with the corresponding curve for a disk of almost exactly the same aspect ratio, the 0.061-×0.0032-in. disk. The 0.122-in. disk is flawed as described later, and an rf field even in x excites modes which are odd in x. This we attribute to the lowered symmetry of the sample. On comparing the positions of the higher field series for this disk with the 0.061-in. sample we see that the smaller disk is only excited in modes which are even in x. The pertinent numbers are given in Table I(c).

A series of samples were cut from YIG crystals all grown in the same run. The major plane of each sample was a (100) plane. We have measured the mode spacings for these disks, which have a range of aspect ratio. Some of these spacings are given in Table I(b). Figure 3 shows mode spacing plotted against aspect ratio. The important point is that, aside from an experimental spread, the points for each mode fall on a smooth curve. Near an aspect ratio of 20 there are disks ranging in size from 0.122×0.0064 in. down to 0.024×0.0010 in. points for all of which fall on the curve. We have demonstrated experimentally that the mode spacing is a function of sample shape and not of sample size.

Samples of other shapes than a disk were also made from this same lot of oriented YIG. In particular we made measurements on a plano-convex and a double-convex sample. Curves for these are actually given in connection with the discussion of the excitation of

modes; see Figs. 8(b)–8(d). In the case of the double-convex sample we can measure the positions of several members of the series excited by a uniform transverse rf magnetic field. If we do this, and taking these spacings, enter the diagram of Fig. 3 we find that the lenticular sample has mode spacings in this series which correspond to a circular disk with an aspect ratio of 18.5. The dimensions of the double-convex sample are given in Fig. 7(c). Its aspect ratio is 14. This shape is a much closer approximation to an ellipsoid than the right circular disk, but it is still significantly different from an ellipsoid. It is however, clear that the mode spacings of this principal series for a disk approximate those of an ellipsoid of the same diameter which is considerably thicker.

Let us compare the observed mode spacings with those obtained from Walker's theory. In addition to the experimental points mentioned, Fig. 3 shows the theoretical spacings for (3,3,0), (5,5,0), and (7,7,0) from (1,1,0). The expressions from which these were obtained are given in the Appendix. The modes of a disk at any aspect ratio correspond roughly with those of an ellipsoid of considerably smaller aspect ratio. The points designated (b) in Fig. 3 are the mode spacings of the double-convex sample. It will be seen that they are closer to the theoretical curve than are the disk points. These particular modes are supposed to be frequency independent, yet we see in Table I(a) data on a YIG disk taken at two different frequencies which show the mode spacings have changed significantly. In terms of Fig. 3, it might be said that the disk is deviating more and more from the behavior of an ellipsoid of the same aspect ratio as the frequency and thus the applied field go up. As the field increases the magnetization within the disk, particularly near the edges, comes to lie more nearly parallel to the applied field. At high fields the contrast with an ellipsoid is greatest.

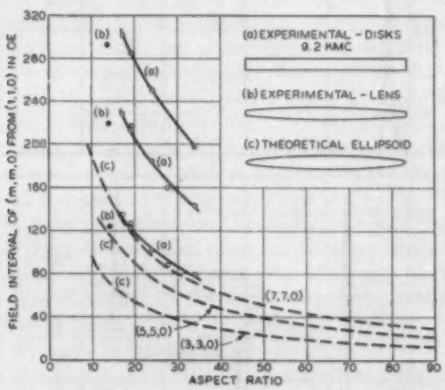

FIG. 3. The solid curves (a) are drawn through the measured mode spacings in circular disks with the steady field normal. These are the spacings of modes (3,3,0), (5,5,0), and (7,7,0) from (1,1,0) in oe. The material was YIG, and the field was along [100]. The dashed curves (c) are the theoretical spacings computed from the relations given in the Appendix. $4\pi M_s$ was taken to be 1796 gauss. The points (b) were taken with the double-convex sample. In all cases the diameter to thickness ratio of the shape determines the horizontal coordinate. Frequencies were near 9200 Mc.

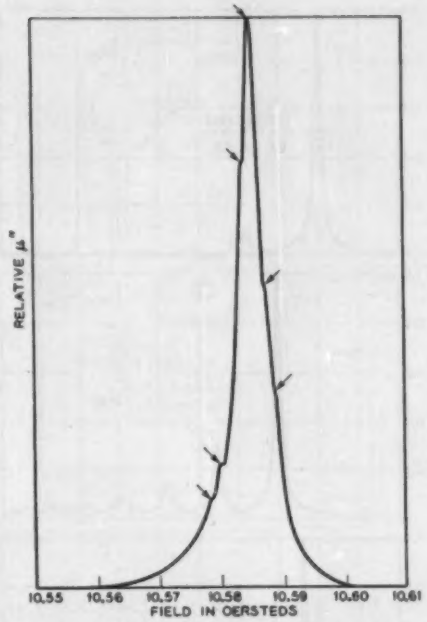

FIG. 4. Tracing of the uniform mode absorption of a 0.050-×0.0029-in. YIG disk; H_{dc}, normal to disk and parallel to [111]. This trace was taken at 2.85°K. The frequency was 24 036 Mc. The arrows call attention to the structure in the absorption curve.

The liquid helium temperature measurements on thin disks of YIG revealed another curious phenomenon. The (1,1,0) mode shows considerable structure. In Fig. 4, which is a tracing of the experimental recording we see that at least six components clustered within about 10 oe. The effect is slightly more prominent at 2.85° than at 4.2°K. The corresponding plots at 300° and 77°K show smooth symmetric absorption lines with the disk identically positioned in the same cavity; that at 300°K is about the same over-all width. If the structure in Fig. 4 consisted of other modes than (1,1,0) one would certainly expect them to be evident in the room-temperature plot where sample shape, position, and field configuration are the same. We would like to suggest tentatively that this structure represents the interaction of magnetostatic and acoustic modes. The magnetostrictive coupling which is effective only at very low temperatures is associated with the presence of rare earth impurities in the YIG.[6]

DISKS—FIELD IN THE PLANE

The resonance conditions for a thin disk with the steady field in the plane are very different from those

[6] J. F. Dillon, Jr., and J. W. Nielsen, Phys. Rev. Letters 3, 30 (1959); J. Appl. Phys. 31, 43S (1960).

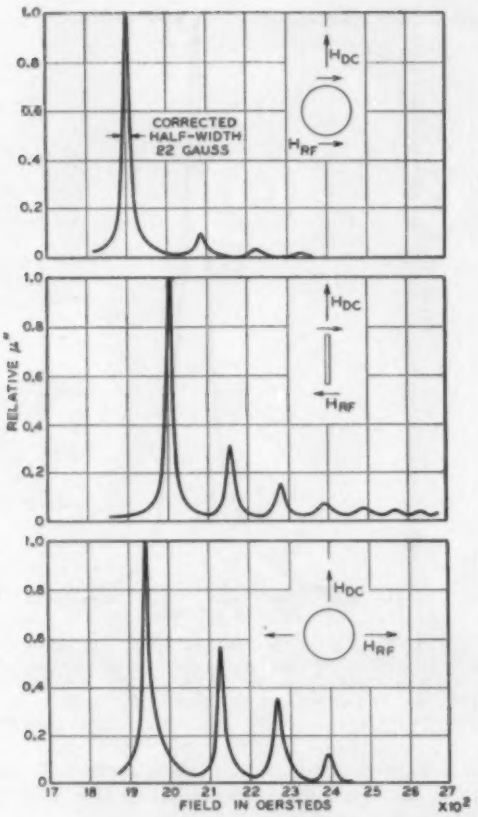

FIG. 5. Mode structures observed in various transverse field configurations for a disk of manganese ferrite with the steady field in the plane. The frequencies were close to 9226 Mc.

for a disk with the field normal. The transverse demagnetizing factors are important and the field for resonance is approximately given by $\omega=\gamma(BH)^{\frac{1}{2}}$. The mode structure observed in our experiments is also very different. The most important members of the series observed are now at the low field end of their series. Figures 5(a)–5(c) show the modes observed in three different transverse rf magnetic field configurations. The identification of the mode representing uniform precession is made by assuming it to be the deepest absorption excited in a uniform transverse rf field. In this case it is the lowest field mode we have observed.

Walker's theoretical work followed closely the initial experiments showing modes in disks with steady field either in or normal to the plane of the disk. However that theory has only been worked out for ellipsoids of revolution whose axis lies along the applied H_{dc}. The most interesting features are obviously contained in the present theory. Therefore we have not continued the measurements of modes in disks on edge further than these initial correlations of the three series with the field patterns.

CYLINDRICAL RODS—FIELD ALONG AXIS

Resonance experiments to determine the magnetostatic mode structure of cylindrical rods were carried on with a few samples. Figures 6(a) and (b) show the results in the case of a rod 0.130 in. long ×0.013 in. in diameter. As in the case of the disk on edge the most prominent mode of a series is the lowest lying. Above the lowest field mode observed are a number of odd and even numbers of what is apparently the same series. Merely from the symmetry of the exciting field it is fairly clear that the lowest lying mode in Fig. 6(b) has a nodal plane at the center perpendicular to the axis of symmetry. It would seem that the major series in Fig. 6(a) represents the modes with even symmetry along the z axis, and that the series of Fig. 6(b) is odd along z. The prominent series of modes in Fig. 6(a) are apparently (1,1,0), (3,1,0), (5,1,0), (7,1,0), etc., whereas these in Fig. 5(b) are (2,1,0), (4,1,0), (6,1,0),etc. In addition to these series there are several other modes in each trace. No attempt has been made to identify these.

EXCITATION

The question naturally arises as to why such a large number of modes as we observe are excited in nearly uniform or in very simple rf field configurations. There

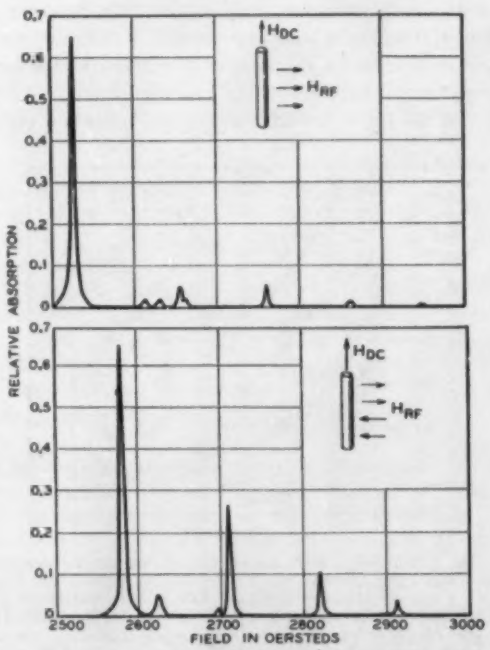

FIG. 6. Modes observed in a YIG rod 0.130×0.013 in. with two transverse field configurations. The [100] axis was parallel to the axis of the rod, and the frequencies were 9175 Mc.

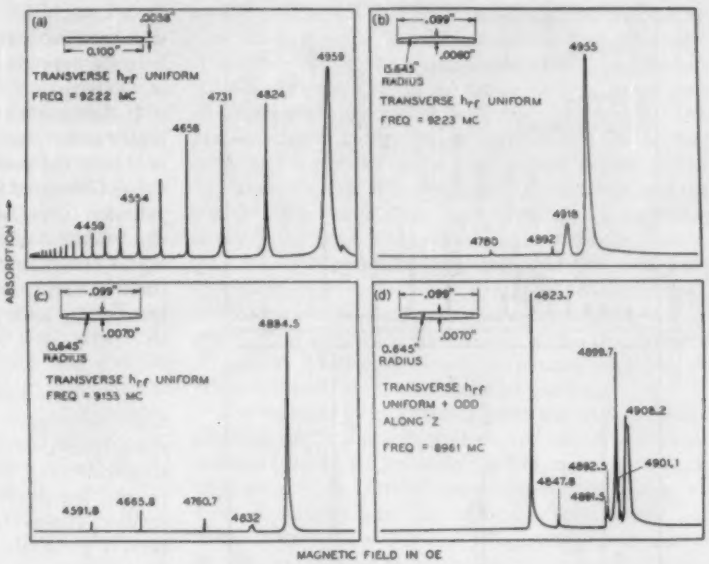

FIG. 7. Absorption structure observed in circular samples with steady field along the axis. In (a)–(c) transverse field is uniform, whereas in (d) it contains a component odd along z. In the plano-plano sample (a) a long series of modes are excited, but in the plano-convex (b) and the double-convex (c) samples many fewer modes are observed. In (d) there are a large number of peaks in the region where we might expect the modes $(m, m-1, 0)$.

are several factors to be mentioned here. The magnetostatic mode theory[2] has very carefully excluded propagation effects. Yet the size of our specimen is so large (many of the disks were 0.100 in. diameter) that the actual modes of the spin system must contain propagation effects. Probably more important, however, is the fact that the samples are not true ellipsoids. The rectangular cross section of the disks gives them a great deal more material near the outer edges than ellipsoids with the same major and minor axial dimensions. The dc and rf magnetic fields within the disks cannot be uniform as they could be in a true ellipsoid. We have experimental data which demonstrate this point clearly.

Figure 7(a) shows the absorption observed with the steady field normal to a circular disk 0.100×0.0058 in. which was in a uniform transverse magnetic field. With only very minor exceptions all the modes are separate from each other, they fall off slowly in amplitude. These are the modes $(m,m,0)$ with m odd, and in the original trace all the modes are distinguishable out to (55,55,0). In Fig. 7(b) is a corresponding plot of the modes in a plano-convex disk. Such a shape is a considerably better approximation to an ellipsoid than the right circular disk. The difference in the mode structure is striking. In place of the long series of modes we now have only two, the more prominent of which is the spatially uniform precession. The identity of the other peak is in doubt, but it might well be associated with the fact that the shape is odd along z. In Fig. 7(c) is the mode pattern for a double-convex sample. Here even more clearly the uniform mode stands by itself. Traces of other modes are however, visible, and their positions are indicated in the figure.

In Fig. 7(d) we show the mode pattern obtained when the disk is subjected to a transverse rf field which is at least in part odd along z. A number of other modes are seen near the position where we would expect the series of Fig. 2(c) to start. We might have expected that these modes $(m, m-1, 0)$ would be particularly sensitive to the shape of the disk along the z axis. No attempt has been made to assign indices to these modes. We have seen in our consideration of the curves in Fig. 7 that deviations of the sample from ellipticity are associated with the excitation of many of the modes we have seen.

It also occasionally happens that our samples have flaws in them, a void which occurred during the growth process, or a large chip lost during the very delicate preparative procedures. The results of such a void are shown in Fig. 8(a). The sample was a circular disk 0.122 in. in diameter by 0.0064 in. thick. From the edge a small void perhaps 0.001 in. wide extended about 0.010 in. toward the center of the disk. Otherwise the disk was circular and very well polished, effort having even been spent on polishing its outer edge. The mode pattern shown in Fig. 8(a) was observed with a predominantly uniform transverse rf field, however, some components of the field were odd in z. The uniform mode stands clear of any others. But at the position at which we might expect the higher modes $(m,m,0)$ there are several peaks. Notice that the lower symmetry of the disk leads to the observation of both the odd and even members of the series. The modes near (2,2,0), (3,3,0), and (4,4,0) are shown in Fig. 8(b) on an expanded field scale. One curious fact is discernible here, namely that near (2,2,0), there are two peaks, near (3,3,0) there are three peaks, and near (4,4,0) there are four peaks. This continues very clearly up to the

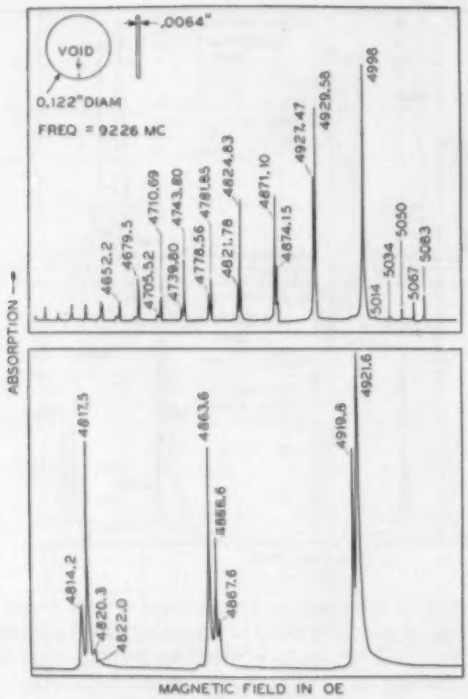

FIG. 8. Modes observed in a disk which contained a small flaw. Transverse field was predominantly uniform, but contained a component odd along the z axis. In (b) the second, third, and fourth members of the principal series are shown on an expanded field scale.

fifth member of the series, beyond which point it becomes difficult to resolve and thus count the various separate peaks.

The modes $(m+1, m, 0)$ were referred to in the discussion of their identity. We might note in passing that they are all single peaked.

We have direct evidence that other perturbations of the shape very strongly affect the excitation of modes. A manganese ferrite disk similar to that used for the traces of Figs. 2(a)–2(c) was modified by drilling a 0.012-in. hole through the center along the axis. Figure 9 shows the pattern observed with the disk in a uniform transverse h_{rt}. It seems that the excitation of the modes other than the (1,1,0) has been greatly reduced by the introduction of the hole. The expression for the magnetic potential of these $(m,m,0)$ modes is $\psi \sim r^m \exp[j(m\varphi+\omega t)]$. From this it may be seen that the variation with position of a component of the transverse magnetization $m_z \sim r^{m-1} \cos[(m-1)\varphi+\omega t]$. Aside from their azimuthal variation they vary from each other in their r dependence. It is not implausible to suppose that by drastically changing the boundary conditions near $r=0$ we can effect the excitation of the higher order $(m,m,0)$ modes more than that of (1,1,0). It is conceivable that some radial perturbation of the disk less drastic than the hole all the way through might enhance the excitation of some particular higher member of the series.

It does not seem out of place here to mention that higher-order modes can be excited by distorting the rf field near the sample. In Fig. 6 of footnote reference 5 this is illustrated for a sphere in contact with a dielectric cylinder. A conducting surface on or close to the sample distorts the rf field and increases the excitation of many higher-order modes. This too, if done very carefully could probably be made to enhance selectively the absorption by some particular modes.

LINEWIDTH

It has been realized for some time that it is very difficult to compare ferrimagnetic resonance linewidths measured on different samples. With the preparation of chemically and mechanically better crystals, the narrowest linewidths measured have gradually become smaller. However, the variation between samples has been so great that the only valid comparisons were between the same sample at different temperatures and frequencies. In the course of these experiments we have accumulated measurements of the linewidth on specimens of various shapes.[1]

The ferrimagnetic-resonance linewidth theory set forth by Clogston, Suhl, Walker, and Anderson[7] suggests that at least a part of the observed width arises in the scattering from a low-order mode, in particular (1,1,0) to modes in the spin-wave manifold of the same frequency. The density of available spin-wave modes would be very much less for a thin disk with the steady field normal than for a sphere or rod.

Thus there is an obvious temptation to compare linewidths of different shaped samples from the same crystal. As a matter of interest Table II includes some of these data for samples cut from a single batch of YIG.

The small sphere was ground in an improved version of a Bond-type[8] sphere grinder, then polished by running

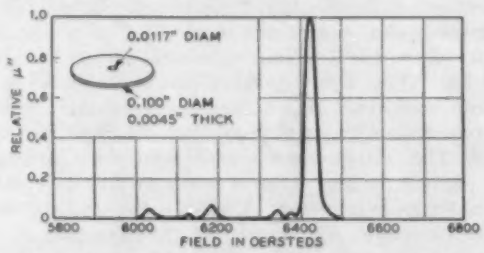

FIG. 9. The absorption structure observed in a disk which has been modified by drilling a hole through the center. The sample was of manganese ferrite, the frequency was 9220 Mc. Transverse rf field was uniform.

[7] A. M. Clogston, H. Suhl, L. R. Walker, and P. W. Anderson, Phys. Rev. **101**, 903 (1956), and J. Phys. Chem. Solids **1**, 129 (1956).

[8] W. L. Bond, Rev. Sci. Inst. **22**, 344 (1951).

it for a long period of time against 0000 French Emery paper. Its surface was polished though not nearly so well as the surfaces of the spheres used in studies of modes in spheres.[8] The surface of the large sphere was left rough ground; that of the rod was also rough. The thin disk was very carefully polished on its major faces as described earlier. The edges were rough ground.

In the case of the small polished sphere, measurements of the line at 9.1 and 23.7 kMc gave essentially the same width at room temperature. This value of about 10 oe was the largest line width observed with any of the samples. Even the roughly ground large sphere showed a narrower line by a factor of 2. It is perhaps significant that the linewidths of the rod and the large sphere are nearly the same. They are of comparable size, and the surfaces are of similar texture. The linewidths for the disks are by far the narrowest. Here the line measured at 24.0 kMc is several times wider than that taken at 9.3 kMc. The 300°K, 9-kMc linewidths are available for all these samples, and that for the thin disk with the field normal is by far the narrowest. The same disk with the field in the plane gives a linewidth two and a half times greater.

There is very direct evidence in the domain structures observed in these thin disks[9,10] that the state of strain introduced by the mechanical polishing has a very considerable effect on the magnetization. Although these crystals have ⟨111⟩ directions in or near the plane, the observed domain structures show only regions in which the magnetization is normal to the major plane. If the strained surface is removed by etching, the magnetization takes up some distribution among easy directions. Thus the state of strain apparently leads to an effective easy-direction normal to the major surface. In the case of experiments on a disk with the field normal, this strain induced easy-direction is parallel to the applied field; but is normal to the applied field if that field is in the plane of the disk. Presumably this strain and the variations in its intensity are operative in scattering energy from the $k=0$ mode to higher-order spin waves. The two configurations are quite different, and from this discussion it does not seem that one can draw valid conclusions about the shape dependence of linewidth from them. Experiments on strain-free polished ellipsoidal samples of various shapes are necessary to fill in this part of the experimental picture.

TABLE II. Summary of linewidth measurements on specimens of various shapes cut from YIG crystals of the same batch.

SAMPLE	T IN °K	f IN KMC	ΔH	Δf/f
0.008" [100] → H_{DC}	295	9.1	11.0	0.0034
	295	23.7	10.2	0.0012
	70	23.7	25	0.0030
	4.2	23.7	11.2	0.0013
0.056" H_{DC} IN (110)	295	9.2	5.7	0.0017
0.013" [100] → H_{DC}, 0.130"	295	9.2	5.5	0.0017
0.050" [111] → H_{DC}, 0.0029"	295	9.3	1.1	0.0003
	400	8.9	0.8	0.00025
	295	24.0	3.5	0.00024
	77	23.9	14.0	0.0016
	4.2	23.0	5.2	0.00062
→ H_{DC}	295	9.1	2.8	0.00089

The data given in Table II must not be interpreted as giving us the shape dependence of linewidth. They do illustrate the fact that linewidth has a great deal to do with sample preparation, and also, that of the shapes we have chosen here, we can achieve a very narrow line most easily with a thin flat disk—steady field normal to the plane. This is not at all surprising when one considers the two procedures used: wet polishing through a considerable thickness of material as contrasted with the dry tumbling in the Bond sphere grinder. From optical observations of the domain structure in some of these disks we conclude that there is associated with the mechanical polishing procedure a surface layer which is somehow strained, perhaps the surface is compressed. In the best cases the strain may be very uniform, that is, there will be no lines or regions exhibiting a different degree of strain as is associated with the surface just after the polishing has passed the bottom of the pits. The presence of this strain is not related to the size of the abrasive particles in the polishing powder, though it may be associated with their hardness. Apparently no matter how small the particles of the polishing powder, there will be an inhomogeneity in spin-lattice coupling associated with a mechanically polished surface. This might be circumvented by adopting a different polishing procedure, but probably the only suitable method would be to polish very carefully and then remove the strained layer by etching.

Perhaps it should also be pointed out that surface damage such as we are discussing here would almost certainly be anisotropic. This effect probably accounts for a part of the anisotropy of linewidth measured in ferromagnetic resonance experiments.

In many cases the linewidths of the second and third members of the series observed in disks with the field normal were measured. In all cases they were found to be essentially the same as that of the (1,1,0) mode.

In the case of the manganese-ferrite disks linewidths of 16 oe were observed in the 0.100-×0.005-in. disk with the field normal to the disk and parallel to [100]. The corresponding linewidth in a small sphere cut from

[9] J. F. Dillon, Jr., J. Appl. Phys. **29**, 539 (1958).
[10] J. F. Dillon, Jr., J. Appl. Phys. **29**, 1286 (1958).

the same boule was 32 oe. These widths are a great deal broader than for YIG. In the case of a ferrite crystal grown by the flame fusion method there is probably a built-in inhomogeneity which contributes to the linewidth in some degree. These crystals grow near the tip of a flame through which falls a fine powder of the appropriate oxide mixture. In most cases, and in particular in Linde's procedure,[11] these powders were introduced discontinuously into the flame by mechanical tapping of a hopper. In the case of Al_2O_3 crystals which are impurity colored (sapphire and ruby), it is found that there is a periodic variation along the growth direction in the color of the crystal. This periodicity is found to be correlated with the growth rate and the rate of tapping of the powder hopper. It arises as a result of the differing volatilities of the various oxides. In this case the crystal is grown from an oxide mixture and it seems certain that there will be a fine scale variation of the composition, and thus, of the magnetization and anisotropy. A period of perhaps a thousandth of an inch might be expected for this variation. The spinel structure with its tolerance of several valences of each of the anions in a close-packed oxygen lattice could easily support such inhomogeneities. The garnet structure on the other hand only seems to tolerate trivalent iron ions under the circumstances of Nielsen's growth procedure. This discussion suggests in quite general terms an explanation for the broad FMR lines observed with Verneuille grown manganese ferrite as contrasted with those seen with PbO flux-grown YIG.

CONCLUSION

In this paper we have reported the observation of a number of modes in the motion of the magnetization of a ferrimagnetic sample. The simplest of these, the spatially uniform precession of the entire spin system is the ordinary Kittel mode of ferrimagnetic resonance. The observation of the others has provided the experimental background for Walker's theory of magnetostatic modes. In the case of the samples described here the modes fall into well-defined series. A consideration of the spatial distribution of the transverse rf magnetic field in which a given series of modes is excited, aids greatly in its identification. The relative ease of excitation of higher modes is considered to reflect the deviation of the samples from exact ellipticity, and possibly the warping of the magnetostatic modes by propagation effects. A considerable variation in linewidth has been observed in different shaped samples cut from the same crystal or same batch of crystals. It seems that conclusions regarding the shape dependence of linewidth cannot be drawn from these differences because of variations in the mechanical handling of the different shapes. However, our experience does seem to indicate that the thin disks can be made more uniform and more nearly strain free than any other shape sample; and attempts to achieve the narrowest possible linewidth might well use in this shape.

[11] The author wishes to thank Dr. G. W. Clark for several discussions of this subject.

ACKNOWLEDGMENTS

The author wishes to express his thanks to A. M. Clogston and to L. R. Walker for many discussions. He is happy to acknowledge the able technical assistance of H. E. Earl.

APPENDIX

L. R. Walker[12] has given relatively simple expressions for the resonant fields associated with certain modes. Equation (25) of footnote reference 2(b), applied to the modes $(m,m,0)$ and $(m\pm1, m, 0)$, is

$$\Omega-\Omega_N=m/G_{mm}.$$

In this $\Omega_N=(H_0-4\pi M_0N_z)/4\pi M_0=H_i/4\pi M_0$ and $\Omega=\omega/4\pi M_0$; H_0 is the applied field and H_i, the internal field. The ratio of minor axis to major axis is α, the reciprocal of the aspect ratio used throughout this paper. For the modes $n=m$,

$$G_{nn}=A\alpha+A^2 +A(A^2-m-\tfrac{1}{2})\alpha+A^2[A^2-(4m+1)/3]\alpha^2 +A[A^4+A^2(10m+1)/6+(4m^2-1)/8]\alpha^3.$$

For the modes $n=m+1$,

$$G_{nm}=1/\alpha^2+A/\alpha +(A^2-2m-2)+A(A^2-3m-\tfrac{5}{2})\alpha +[A^4-(4m+3)A^2+4(m+1)(2m+1)/3]\alpha^2.$$

The appropriate values for A are given in Table III.

TABLE III.

n	m	A	n	m	A
1	1	$4/\pi$	1	0	$\pi/2$
2	2	$16/3\pi$	2	1	$3\pi/4$
3	3	$32/5\pi$	3	2	$15\pi/16$
4	4	$256/35\pi$	4	3	$35\pi/32$
5	5	$512/63\pi$	5	4	$315\pi/256$
6	6	$2048/231\pi$	6	5	$693\pi/512$
7	7	$4096/429\pi$	...	...	...

[12] L. R. Walker (private communication). The author is indebted to Dr. Walker for permission to quote these results.

Dielectric Properties of Lead Titanate Zirconate Ceramics at Very Low Frequencies*

ROBERT GERSON
Electronic Research Division, Clevite Corporation, Cleveland 8, Ohio
(Received May 16, 1960; and in final form June 2, 1960)

Dielectric properties of lead titanate zirconate were determined between room temperature and 140°C at frequencies between 0.1 and 10 cps. A measured increase in dielectric constant and dissipation factor at low frequency and high temperature was interpreted as an anomalous conduction phenomenon, rather than as an effect due to ferroelectric polarization. Over the frequency and temperature range studied the relationship between the real and the imaginary components of the dielectric constant was found to be linear. The data for unpoled ceramic and for material which had been poled to a maximum in piezoelectric activity were quite similar.

INTRODUCTION

THE electric coercive field required to cause domain realignment in ferroelectric perovskites has been found to be a function of the time of field application as well as of temperature and the magnitude of the field applied.[1] In general it is found that low fields applied for a short time will not cause domain reorientation, but the same fields, applied for much longer periods of time, do have some effect. It may then be expected that the dielectric constant of ferroelectrics will increase at very low frequencies because ferroelectric switching will contribute to the dielectric polarization. In this article it will be shown that the dielectric constant and loss of some ferroelectric ceramics at low frequencies (10 to 0.1 cps) did not display any effects connected with time-dependent ferroelectric switching.

Two types of ceramics were used. The first was lead titanate zirconate ($PbZr_{0.53}Ti_{0.47}O_3$), and the second was the same material modified with a one percent addition of niobia by weight.[2] The niobia addition lowers the coercive field of the ceramic appreciably and raises its resistivity by several orders of magnitude.[3,4] Thus in the second material it was to be expected that effects due to switching would be emphasized, while effects which were purely due to conductivity or interfacial polarization would be minimized.

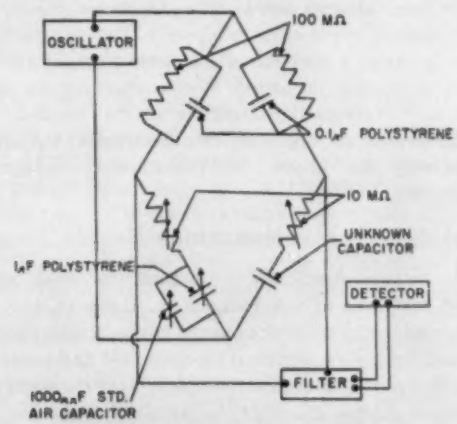

FIG. 1. Diagram of the apparatus used in these measurements.

EXPERIMENTAL PROCEDURE

The apparatus used for the measurement is shown in Fig. 1. In order to obtain reasonable sensitivity, the unknown capacitors in the bridge circuit were about 0.01 mfarad, corresponding to an impedance of about 10^6 ohms at 0.1 cps. Polystyrene capacitors were found to be sufficiently free of dielectric absorption effects to serve as standards in these measurements. In constructing the bridge, care was exercised to avoid leakage currents from tie points which would lead to spurious readings. The measured capacitance and resistance are series values, and must, as in the case of the Schering bridge, be converted to parallel values for the determination of the dielectric constant. The oscillator used was a Krohn-Hite ultralow-frequency oscillator, and a Ballantine low-frequency voltmeter was used as a detector between 10 and 1 cps. At lower frequencies a sensitive dc vacuum-tube voltmeter served as a detector. The measuring field was 200 v/cm.

Low-frequency measurements of this type are time

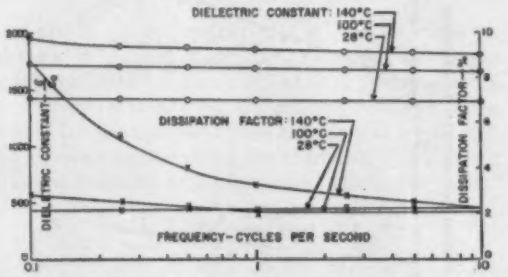

FIG. 2. Dielectric constant and dissipation factor of unpoled lead titanate zirconate containing niobia at low frequencies.

* Supported by the Office of Naval Research.
[1] J. W. Merz, Phys. Rev. **95**, 690 (1954).
[2] F. Kulcsar, J. Am. Ceram. Soc. **42**, 343 (1959).
[3] D. Berlincourt and H. H. A. Krueger, J. Appl. Phys. **30**, 1804 (1959).
[4] R. Gerson, J. Appl. Phys. **31**, 188 (1960).

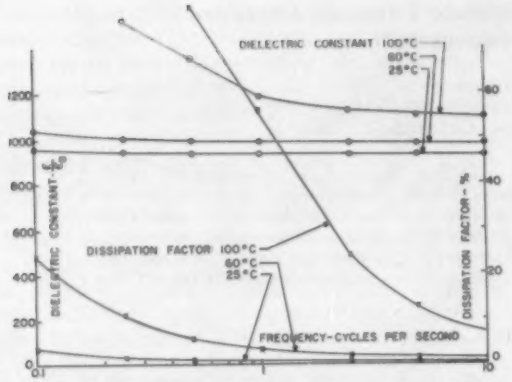

FIG. 3. Dielectric constant and dissipation factor of unmodifed lead titanate zirconate at low frequencies.

consuming, but can be made reproducibly. Capacitance measurements reported here are accurate to about 2%. The dissipation factor was subject to an absolute error of ±0.2% for values of this quantity below 3%. Where the dissipation factor exceeds 3%, the error was about ±10% of its value.

RESULTS

Figure 2 shows the results of the measurements on the high-resistivity lead titanate zirconate material containing niobia. It is seen that there is little variation with frequency at 28° or 100°C. At 140°C, however, the dissipation factor and dielectric constant both increase with decreasing frequency. When the material has been poled, or subjected to an electrical alignment process, the variation in dielectric properties with frequency is not changed.

In the unmodified, or low-resistivity ceramic, the results are quite different (Fig. 3). Here the change in

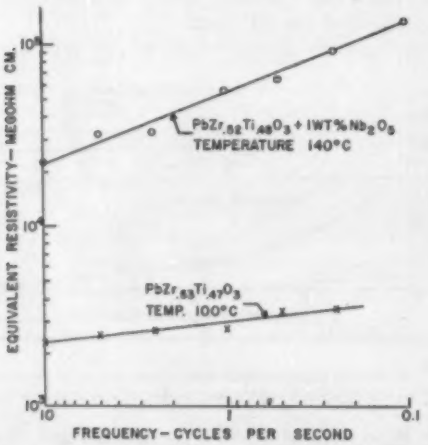

FIG. 4. Equivalent resistivity of lead titanate zirconate ceramics as a function of frequency.

properties at low frequencies was detectable at room temperature and was very pronounced at 100°C.

The data presented can be put into a somewhat different form. The increased dissipation factor at low frequencies can be used to calculate an equivalent resistivity, such that if the ceramic had this resistivity it would have the observed dissipation factor (Fig. 4). This equivalent resistivity varies inversely with a power of the frequency lying between zero and one. This is in agreement with the common observation that the observed resistance of the dielectric increases with the time of application of the measuring voltage.

In a Debye-type relaxation the curve relating dielectric loss factor and dielectric constant is a semicircle with its center denoting a characteristic relaxation frequency.[5] Cole and Cole[6] have modified the Debye approach to try to fit it to other types of relaxations. In their presentation the loss factor vs dielectric constant curve becomes an arc of a circle. Figure 5 shows the

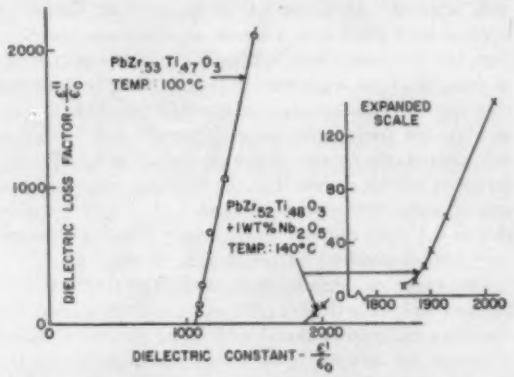

FIG. 5. Dielectric loss factor vs dielectric constant for lead titanate zirconate ceramics at low frequencies.

loss factor as a function of dielectric constant for the data previously presented. Within experimental error the curve is completely linear. Either the Cole and Cole analysis does not apply or the measurement frequency was very far above the characteristic relaxation frequency.

CONCLUSIONS

An increase was found in the dielectric constants of these materials at low frequencies. However, this increase was much more pronounced in the ceramic characterized by higher electrical coercive field and lower dc resistivity. It thus seems more likely that the dielectric constant change was due to interfacial polarization (related to conductivity) than to ferroelectric switching

[5] P. Debye, *Polar Molecules* (Dover Publications, Inc., New York, 1947), Chap. V.
[6] K. S. Cole and R. H. Cole, J. Chem. Phys. **9**, 341 (1941).

These results have a practical value in that the ceramics tested are now in use as piezoelectric detectors. It is indicated that the time constant is well in excess of 10 sec at room temperature for both ceramics. The time constant is well over 10 sec at 100°C for the modified ceramic.

ACKNOWLEDGMENTS

I wish to thank Dr. Hans Jaffe and Don Berlincourt for many helpful discussions. Delmar Kopp is also thanked for his patient assistance with the measurements. The financial support of the Office of Naval Research is gratefully acknowledged.

JOURNAL OF APPLIED PHYSICS VOLUME 31, NUMBER 9 SEPTEMBER, 1960

High-Frequency Breakdown of Air*

DONALD KELLY AND HENRY MARGENAU
Laboratory of Marine Physics, Yale University, New Haven, Connecticut
(Received March 21, 1960; and in final form May 4, 1960)

Kinetic theory is applied to the problem of ionization breakdown of the air surrounding a high-speed vehicle. It is found that electrons are removed primarily by being swept out of the field of the moving antenna, and that in the interesting cases this action predominates over diffusion losses. Breakdown voltages are plotted against altitude for frequencies of 225 Mc, 1 kMc, and 10 kMc. The theory may offer an explanation of some types of signal loss during missile flights.

DISCUSSION

THE theory of microwave breakdown in air under controlled laboratory conditions has been developed by Herlin and Brown[1–3] and others.[4–6] More recently, MacDonald[7] has carefully treated the special problem of high-frequency breakdown in air at high altitudes. We here consider the situation of an electromagnetic radiator moving with high velocity through an atmosphere containing free electrons. The electrons are "heated" by absorbing the radiated microwave power. If the electric field is of sufficient strength the electrons can gain enough energy to cause breakdown of the surrounding air. Two types of propagation may be distinguished: cw and pulsed transmission. The two modes differ with respect to characteristic times. For cw transmission the electron atmosphere is subjected to the heating microwaves for a time

$$\tau = L(\text{length of radiator})/V(\text{velocity of radiator}).$$

With $V \approx 10^5$(cm/sec) (2500 miles/hr) and L roughly 1–10 cm we have $\tau \sim 10^{-5}-10^{-4}$ sec (cw transmission). For pulsed transmission the characteristic time τ is usually equal to the pulse duration (i.e., τ pulse $< V/L_1$ generally). Breakdown can occur only if the electron concentration becomes large enough to attenuate the microwave in a time τ, since the radiator encounters a cool electron atmosphere every τ sec.

Attenuation of the microwave becomes appreciable when the plasma frequency ω_p equals or exceeds the microwave radian frequency ω, and

$$\omega_p^2 = (4\pi e^2/m)n(t);$$
$$n(t) = \text{electrons/cc at time } t \text{ after applying fields.}$$

The maximum time available for $n(t)$ to build up is τ. The breakdown condition is therefore

$$n(\tau)_{\text{breakdown}} = m\omega^2/4\pi e^2,$$

or

$$n_B(\tau) = 1.24\times 10^{-8} f^2; \quad f = \omega/2\pi. \tag{1}$$

The electron concentration $n(t)$ is given by

$$n(t) = 4\pi \int_0^\infty f(v,t)v^2 dv, \tag{2}$$

$f(v,t)$ being the isotropic part of the distribution function for electrons which satisfies

$$(\partial f/\partial t) + \mathcal{E}f = \{q(v) - \nu_a(v) - \nu_x(v) - \nu_i(v)\}. \tag{3}$$

Here $q(v)$ is the appearance rate of slow electrons resulting from exciting and ionizing collisions. $\nu_a(v)$ is the attachment rate (oxygen only) while $\nu_x(v)$ and $\nu_i(v)$ are the frequencies of exciting and ionizing collisions which remove fast electrons and yield slow ones at a rate $q(v)$. $\mathcal{E}$ is an operator describing the change in f as a result of elastic collisions and the applied microwave fields.[8]

$$\mathcal{E}f = -\frac{1}{v^2}\frac{\partial}{\partial v}\left\{\frac{mv^4}{Ml}f + \left(\frac{kT}{Ml}+\frac{A}{6l}\right)v^2\frac{\partial f}{\partial v}\right\}$$

$$A = (\gamma l)^2/[(\omega l)^2+v^2]; \quad \gamma = eE/m. \tag{4}$$

* Supported by the Office of Naval Research.
[1] M. A. Herlin and S. C. Brown, Phys. Rev. **74**, 291 (1948).
[2] M. A. Herlin and S. C. Brown, Phys. Rev. **74**, 910 (1948).
[3] M. A. Herlin and S. C. Brown, Phys. Rev. **74**, 1650 (1948).
[4] A. D. MacDonald and S. C. Brown, Phys. Rev. **75**, 411 (1949).
[5] A. D MacDonald and S. C. Brown, Phys. Rev. **76**, 1634 (1949).
[6] A. D. MacDonald, Phys. Rev. **88**, 420 (1952).
[7] A. D. MacDonald, Proc. I. R. E. **47**, 436 (1959).

[8] For a rigorous derivation of this expression, see E. A. Desloge and S. Matthysse, Am. J. Phys. **28**, 1 (1960); see also W. P. Allis, *Handbuch der Physik* (Springer-Verlag, Berlin, Germany, 1956), Vol. 21.

The free path l for electrons in air is assumed to be independent of electron speed and equal to that for nitrogen. From the data of Brode,[9]

$$l=T/8000p \quad T=\text{air temperature, °K};\quad p=\text{air pressure, mm Hg.} \tag{5}$$

M is the mean mass of an "air molecule." Let

$$f(v,t)=e^{\nu t}\varphi(v). \tag{6}$$

Then from (2),

$$n(t)=e^{\nu t}4\pi\int_0^\infty \varphi(v)v^2dv=e^{\nu t}n(0).$$

By using (1), the breakdown condition may be written

$$\nu_T=4.6\log_{10}f-26.0. \tag{7}$$

In arriving at this result we have followed MacDonald[7] by taking $n(0)=3\times10^3$/cc as the ambient electron concentration. The substitution of (6) in (3) gives

$$\delta\varphi(v)=[q-\nu_a-\nu_s-\nu_i-\nu]\varphi(v).$$

If we multiply through by $4\pi v^2dv$ and integrate, we obtain

$$-4\pi\left[\frac{mv^4}{Ml}\varphi(v)+\left(\frac{kT}{Ml}+\frac{A}{6l}\right)v^3\frac{\partial\varphi}{\partial v}\right]_0^\infty = n(0)[\bar{q}-\bar{\nu}_a-\bar{\nu}_s-\bar{\nu}_i-\nu], \tag{8}$$

where a bar indicates that the quantity has been averaged over $\varphi(v)$, i.e.,

$$n(0)\bar{X}=4\pi\int_0^\infty \varphi(v)X(v)v^2dv, \tag{9}$$

but

$$\bar{q}=\bar{\nu}_s+2\bar{\nu}_i,$$

since each exciting collision gives one slow electron and each ionizing collision gives two slow electrons. For all physically reasonable forms of $\varphi(v)$ the left side of (8) vanishes, hence

$$\nu=\bar{\nu}_i-\bar{\nu}_a. \tag{10}$$

To determine $\varphi(v)$ over the full velocity range is extremely difficult because of the many collision processes. It is possible to circumvent this difficulty by using the experimental results of Herlin and Brown[8] who measured

$$\zeta=\nu/DE^2, \tag{11}$$

D is the free-diffusion coefficient given by

$$D=\int_0^\infty \frac{v^4}{3}\left(\frac{l}{v}\right)\varphi(v)dv\Big/\int_0^\infty \varphi(v)v^2dv. \tag{12}$$

On using (5)

$$D=l\bar{v}/3=l\bar{v}/24{,}000p. \tag{13}$$

[9] R. B. Brode, Revs. Modern Phys. **5**, 257 (1933).

It is far simpler to compute $\bar{v}$ than $\bar{\nu}_i-\bar{\nu}_a$ for two reasons: (i) The functional dependence of $\nu_i-\nu_a$ on v may be very complicated. More important is the fact that (ii) $\bar{\nu}_i$ and $\bar{\nu}_a$ depend very strongly on the form of $\varphi(v)$ in the ranges where ionization (high velocities) and attachment (low velocities) are important—and these portions of the velocity spectrum are just those where it is most difficult to determine $\varphi(v)$. On the other hand, $\bar{v}$ depends primarily on the form of $\varphi(v)$ over the range of velocities occupied by the majority of electrons. If we assume that only elastic collisions are important over this range, then $\varphi(v)$ takes on a particularly simple form. Margenau[10] has shown that for electrons undergoing elastic collisions with a mean free path l,

$$\varphi(v)=C\exp(-Bx^2-Fx^4),$$

with the abbreviations

$$B\equiv\frac{m(\omega l)^2}{2kT}\Big/\frac{M}{12m}\left(\frac{eEl}{kT}\right)^2,$$

$$F\equiv\frac{6m}{M}\left(\frac{kT}{eEl}\right)^2 \tag{14}$$

$$x^2\equiv mv^2/2kT.$$

By substituting the appropiate value for l and taking $T=250°$ as representative of the atmospheric temperature,

$$\varphi(v)=C\exp\left[-\frac{50x^2}{(E\lambda)^2}-\frac{x^4}{1.95\times10^4(E/p)^2}\right]. \tag{15}$$

$\lambda=2\pi c/\omega=$ free space wavelength.

Because an electron with ionizing energy quickly loses it by excitation or ionization, we assume the presence of a negligible number of electrons with velocities above v_i, where $\frac{1}{2}mv_i^2\equiv u_i=$ ionization potential of $O_2=12.57$ ev (or possibly NO, $u_i=9.28$ ev). If we take $u_i=10$ ev, $kT\approx1/50$ ev we find $x_i^2\approx500$; however, for the values of $E\lambda$ and E/p of interest in the breakdown problem, we expect

$$\exp\left[-\frac{50x_i^2}{(E\lambda)^2}-\frac{x_i^4}{1.95\times10^4(E/p)^2}\right]\approx1. \tag{16}$$

It is found *a posteriori* that this approximation is always valid, typical results giving

$$\left.\begin{aligned}E_B\lambda&\gtrsim1000\\E_B/p&\gtrsim10\end{aligned}\right\}\text{long wavelengths}$$

$$\left.\begin{aligned}E_B\lambda&\gtrsim3000\\E_B/p&\gtrsim40\end{aligned}\right\}\text{short wavelengths}$$

$E_B=$ rms breakdown field.

[10] H. Margenau, Phys. Rev. **69**, 508 (1946).

Hence it is clear that $\varphi(v)$ is practically a step function

$$\varphi(v)=C \qquad v\leqq v_i \tag{17}$$
$$\varphi(v)=0 \qquad v>v_i,$$

and

$$\bar{v}=\tfrac{3}{4}v_i. \tag{18}$$

By taking $\frac{1}{2}mv_i^2=12.5$ ev and using this value of $\bar{v}$ to determine D from (13), we find

$$Dp=1.63\times10^6(\text{cm})^2/\text{sec}(\text{mm Hg}). \tag{19}$$

By writing

$$\nu\lambda=\zeta Dp\cdot p\lambda\cdot(E/p)^2;\quad \zeta=\nu/DE^2, \tag{20}$$

we can use the data of Herlin and Brown[3] to calculate $\nu\lambda$ and thus ν. A choice of λ fixes the frequency (f) and the pressure (p) to which the Herlin and Brown values of ζ refer, so that upon choosing an appropriate τ the breakdown field strength E_B may be determined. The

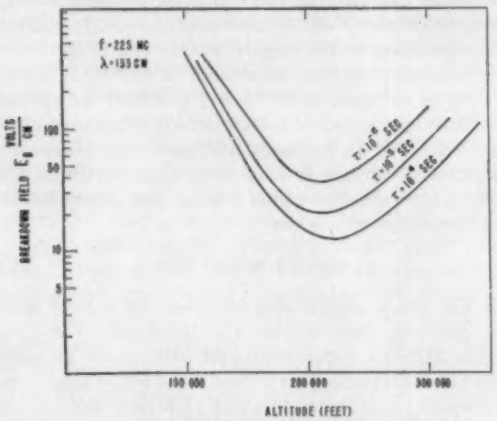

FIG. 1. Root-mean-square breakdown voltage E_B vs altitude for a frequency of 225 Mc.

breakdown field strength is plotted as a function of altitude for frequencies of 225 Mc, 1 kMc, and 10 kMc in Figs. 1–3. Comparison with the results of MacDonald for $f=10$ kMc in Fig. 3 reveals rather minor differences over the pressure range where reliable data are available. Dashed lines in the figures indicate extrapolation. To facilitate comparison the pressure-altitude curve given by MacDonald was used in all calculations.

The present analysis neglects diffusion losses completely. We now give thought to this mechanism of electron removal. To include it one replaces ν by $\nu-D/\Lambda^2$, D being the *appropriate* diffusion coefficient. For free diffusion, to which Eq. (19) refers

$$D_{\text{free}}=1.63\times10^6/p(\text{cm})^2/\text{sec}.$$

For ambipolar diffusion, the speed of diffusion is governed by the slower ions and

$$D_{\text{amb}}\sim(m/M)^{\frac{1}{2}}\quad D_{\text{free}}\sim10^{-2}D_{\text{free}}.$$

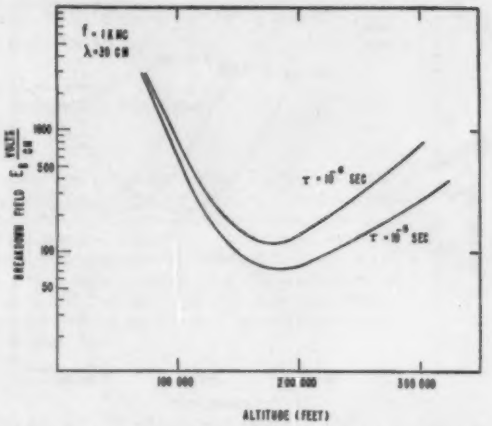

FIG. 2. Root-mean-square breakdown voltage E_B vs altitude for a frequency of 1 kMc.

Λ is the characteristic diffusion length—a quantity which is undefined for diffusion into an infinite medium. MacDonald takes $\Lambda=\lambda/2$ since the breakdown theory assumes a uniform electric field. This is reasonable if the electrons have a chance of diffusing a distance $\lambda/2$ in the time during which they can be accelerated, a condition envisioned by MacDonald. But if diffusion does not carry them that far, another consideration is appropriate. If we approximate the surface housing the antenna by a plane surface, then diffusion leads to an electron distribution varying as

$$n(x,t)\sim(Dt)^{-\frac{1}{2}}\exp[-(x^2/4Dt)],$$

where, $x=$distance from antenna and $t=$time diffusion has proceeded, so that if

$$4D\tau<(\lambda/2)^2,$$

one should choose

$$\Lambda^2=4D\tau \quad\text{or}\quad D/\Lambda^2=1/4\tau,$$

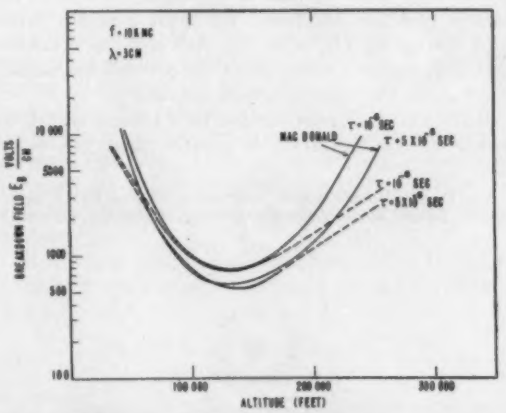

FIG. 3. Root-mean-square breakdown voltage E_B vs altitude for a frequency of 10 kMc.

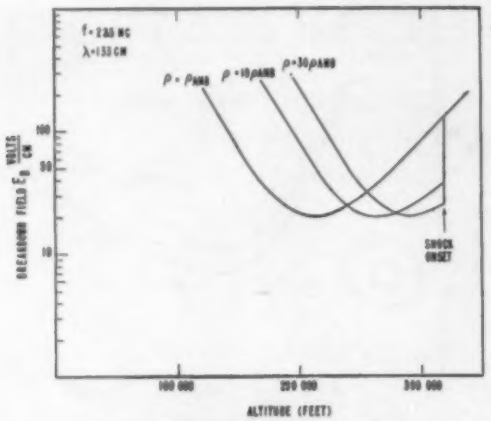

FIG. 4. Effect of shock on breakdown voltage for a frequency of 225 Mc.

since there are essentially no electrons in the region where $x^2 > 4D\tau$. Hence in this case $\nu\tau$ should be replaced by $\nu\tau - \frac{1}{4}$ in the breakdown condition. The required values of $\nu\tau$ are always $\gtrsim 10$ so that we can safely neglect the diffusion term.

When

$$(\lambda/2)^2 < 4D\tau \tag{21}$$

one should again, following MacDonald, replace $\nu\tau$ by

$$\nu\tau - (4D\tau/\lambda^2),$$

and use the ambipolar value for D. We take

$$D_{amb} = (1/40)D_{free},$$

a value suggested by MacDonald.[11] Then

$$4D\tau/\lambda^2 = [1.63\times 10^5/(p\lambda)^2]p\tau.$$

A typical value of ν is 10^6/sec. The minimum value of $p\lambda$ for which the results of Herlin and Brown apply is 2(mm Hg) (cm) so that if $\nu \gg 4\times 10^4 p$ we can still neglect the diffusion term. We must generally have $p \leqslant 1$ mm for Eq. (21) to be true. As a result we conclude that diffusion is a minor factor in determining breakdown under the conditions here considered.

If the antenna is surrounded by a plasma sheath in which the concentration is greater than the value $n(0) = 3\times 10^9$/cc used in deriving Eq. (7), one must make the necessary change.

The discrepancy between the present curves and those of MacDonald in Fig. 3 seems to arise from a difference in emphasis on diffusion. He takes the diffusion coefficient to be proportional to the mean energy, whereas in our calculation, which is based on a constant mean free path, D is proportional to the mean speed of the electrons and thus increases less rapidly. In the region covered by experimental data the curves agree.

One last point should be noted. We have assumed that the air density to be used in the calculations is that ambient in the atmosphere. For high-speed vehicles capable of producing shock waves the density is increased because of the compression. In such cases it is necessary to determine the pressure and temperature in the plasma sheath from a study of the type of flow occurring near the antenna. A shock can develop when the mean free path of the molecules becomes smaller than the characteristic dimension of the vehicle. Taking this dimension to be roughly 100 cm one finds that a shock can develop near an altitude of 300 000 ft (Cross section of molecule $\approx 10^{-16}$(cm)^2) provided the vehicle has sufficient speed. A shock affects transmission in two ways: (i) It increases $n(0)$ and thus lowers the breakdown voltage. It may in fact raise $n(0)$ to the point where effective signal attenuation occurs for all field strengths, viz., when

$$n(0) \gtrsim 1.24\times 10^{-8} f^2. \tag{1'}$$

(ii) The shock compression increases the density near the antenna, thus shifting the breakdown curve to higher altitudes. Figure 4 illustrates this point. To make possible a comparison with conditions which might approximate those encountered by reentrant missiles, we have plotted a series of breakdown curves for $\rho = 1$, 10, and 30 times the ambient density. The shock is assumed to begin at 320 000 ft, where the mean-free path is comparable to the size of a vehicle, and f has not been taken to be 225 Mc. Our curves may not, of course, be directly comparable with flight data because the shock ionization itself can cause attenuation.

ACKNOWLEDGMENTS

The authors wish to acknowledge the very helpful comments and correction of a numerical error by Professor A. D. MacDonald.

[11] A. D. MacDonald, paper delivered at Plasma Sheath Symposium, Boston, Massachusetts, December, 1959 (to be published).

JOURNAL OF APPLIED PHYSICS VOLUME 31, NUMBER 9 SEPTEMBER, 1960

Bounds on the Nonlinear Diffusion Controlled Growth Rate of Spherical Precipitates

J. A. Morrison and H. L. Frisch
Bell Telephone Laboratories, Inc., Murray Hill, New Jersey
(Received May 4, 1960)

This paper considers a nonlinear diffusion problem in which there is a change of phase. The physical situation is e.g., the diffusion of solute in a crystal towards a growing precipitate. The nonlinear-diffusion coefficient is a function of the local concentration of solute. A radially symmetric precipitate which grows at a rate proportional to the square root of the time is considered in n dimensions ($n=1, 2, 3$); thus $\rho=s(D_0t)^{\frac{1}{2}}$, where ρ is the radius, D_0 is a constant having dimensions of area/time and s is a number, the quantity of particular interest. A comparison theorem is established which, in part, states that s increases with increasing diffusion coefficient. A consequence of the theorem is that a unique value of s is associated with a prescribed diffusion coefficient. The comparison theorem also leads to bounds on s. Some other bounds, involving functionals of the diffusion coefficient, are also obtained for s.

1. INTRODUCTION AND SUMMARY

MIRANKER and Frisch[1] and Miranker and Keller[2] have recently discussed a nonlinear mathematical model of a diffusion process during which a change of phase occurs. The physical situation in mind was, for example, the diffusion of various solutes to and precipitation at imperfections of a host crystal. The imperfection in the crystal acts as a nucleus about which precipitation of the solute can occur. Incorporation of the solute into the precipitated phase is often instantaneous (and will be considered as such in this paper) and the process becomes one of diffusion of the solute to a growing precipitate particle. In general one must distinguish two aspects of this problem, the first dealing with the diffusion controlled growth of a single (essentially isolated) precipitate particle and the second dealing with the competition for the diffusing solute by the presence of a multiplicity of precipitate particles in the crystal sample. Only the first of these aspects is considered in this paper. The theory of these processes has been the subject of a number of investigations[3–8] and the results and their interpretation have recently been summarized in two review articles.[9,10] The new feature which leads to the nonlinear diffusion is the explicit recognition that the diffusion coefficient changes with variations in the local chemical equilibria, ensuing in the combined diffusion and precipitation process, and thus depends on the concentration of the solute.

A radially symmetric precipitate is considered. Restricting ourselves to the interpretation of essentially the initial kinetic data only, in a way more fully discussed by Ham[5] among others,[9] one can say: The 3-dimensional case corresponds to the formation of a spherical particle, as in the case of precipitation onto a vacancy, and this may occur in the precipitation studies by Morin and Reiss[11] of Li in Ge. The 2-dimensional case corresponds to the cylindrical growth of a long dislocation line which appears to be the case with In in ZnO studied by Thomas.[12] The 1-dimensional case corresponds to planar growth, which may be of interest in connection with diffusion and precipitation in gel systems which have been studied by Hermans.[13] Miranker and Frisch[1] and Miranker and Keller[2] confined their attention to the 1-dimensional case and their main result was the establishment of the existence, under suitable conditions, of a solution to the nonlinear equation in which the phase boundary moved at a rate proportional to the square root of the time.

In this paper we do not restrict ourselves to the 1-dimensional case but do assume the existence of a solution in which the precipitate grows at a rate proportional to the square root of the time. We then proceed to establish a comparison theorem. Let c_0 be the initial value of the concentration of solute and $D=D_0g(c/c_0)$ be the diffusion coefficient, where c is the concentration of the solute at a subsequent time at a point outside the precipitate and D_0 is a constant, having dimensions of area/time, so that g is a dimensionless function of c/c_0. Also, let $s(D_0t)^{\frac{1}{2}}$ be the radius of the precipitate at time t (s being the growth parameter), and let $\lambda=kc_0$ where k^{-1} is the density of the precipitate. It is supposed that $g(v)>0$, $(0\leq v\leq 1)$, and that $0<\lambda<1$. The comparison theorem is as follows:

If s_1 is a growth parameter corresponding to λ_1 and $g_1(v)$, and s_2 is a growth parameter corresponding to λ_2 and $g_2(v)$, then

$$\lambda_1\geq\lambda_2 \quad \text{and} \quad g_1(v)\geq g_2(v), \quad (0\leq v\leq 1), \quad \text{implies that } s_1\geq s_2. \tag{1}$$

[1] W. L. Miranker and H. L. Frisch (unpublished).
[2] W. L. Miranker and J. B. Keller, J. Math. and Mech. **9**, 67 (1960).
[3] C. Zener, J. Appl. Phys. **20**, 950 (1949).
[4] H. Reiss and V. K. LaMer, J. Chem. Phys. **18**, 1 (1950); H. Reiss, ibid. **19**, 482 (1951).
[5] F. C. Frank, Proc. Roy. Soc. (London) **A201**, 586 (1950).
[6] H. L. Frisch, Z. Elektrochem. **56**, 324 (1952).
[7] H. L. Frisch and F. C. Collins, J. Chem. Phys. **20**, 1797 (1952); ibid. **21**, 1116, 2158 (1953).
[8] F. S. Ham, J. Phys. Chem. Solids **6**, 335 (1958).
[9] A. G. Tweet, J. Appl. Phys. **30**, 1244 (1959).
[10] H. Reiss, J. Appl. Phys. **20**, 1141 (1959).
[11] F. J. Morin and H. Reiss, J. Phys. Chem. Solids **3**, 196 (1957).
[12] D. G. Thomas, J. Phys. Chem. Solids **9**, 31 (1958).
[13] J. J. Hermans, J. Colloid Sci. **2**, 387 (1947).

An immediate consequence of (1) is that there is a unique s corresponding to a given λ, $(0<\lambda<1)$, and a given $g(v)>0$, $(0\leq v\leq 1)$. The comparison theorem provides bounds for the growth parameter s, since s may be obtained when $g(v)=\text{const}$, say $1(0\leq v\leq 1)$. A more general class for which the solution may be obtained is $g(v)=\text{const}\ (1-\alpha v)^{-1}$, where $\alpha<1$, this being demonstrated in the Appendix.

This theorem is basically used without proof in the analysis of the precipitation kinetics obtained by Thomas,[12] since in the In in ZnO systems studied the variation of the diffusion coefficient with the diffusing In concentration may well be as large as a factor of 10. Further analysis of these data along the lines suggested below is not warranted at this time since the behavior of the diffusion coefficient is not known experimentally in sufficient precision.

In the final section other bounds are obtained for the growth parameter and these involve functionals of $g(v)$. Thus, for instance, it is shown that in n dimensions

$$\lambda\int_0^1 \frac{(1-v)}{(1-\lambda v)}g(v)dv\leq\frac{s^2(1-\lambda)}{2n\lambda}\leq\int_0^1 g(v)dv. \quad (2)$$

Note that as $\lambda\to 1-0$ the ratio of the upper to lower bound tends to unity, but as $\lambda\to 0+$ this ratio is unbounded. In the 1-dimensional and 3-dimensional cases the bounds have been improved so that the ratio of the upper to lower bound remains bounded in the whole range of λ, $0<\lambda<1$. Thus, it is shown that

$$\int_0^1 \frac{(1-v)}{(1-\lambda v)}g(v)dv\leq\frac{s^2(1-\lambda)}{2\lambda^2}$$

$$\leq\min\left[2\int_0^1 \frac{(1-v)}{(1-\lambda v)}g(v)dv,\ \int_0^1 g(v)dv\right],\quad (n=1), \quad (3)$$

and

$$\int_0^1 g(v)dv+2\lambda\int_0^1 \frac{(1-v)}{(1-\lambda v)}g(v)dv\leq\frac{s^2(1-\lambda)}{2\lambda}$$

$$\leq 3\int_0^1 g(v)dv,\quad (n=3). \quad (4)$$

2. THE MATHEMATICAL EQUATIONS AND THEIR TRANSFORMATION

We are concerned with the growth of a radially symmetric precipitate in n dimensions $(n=1,2,3)$. Let $r=\rho(t)$ be the equation of the radius of the precipitate at time t. The concentration of the solute $c(r,t)$ is governed by the diffusion equation

$$\frac{\partial c}{\partial t}=(1/r^{n-1})\partial/\partial r\left[D_0 g(c/c_0)r^{n-1}(\partial c/\partial r)\right],\quad r>\rho(t), \quad (5)$$

where c_0 is the initial value of the concentration and the nonlinear diffusion coefficient is $D=D_0 g(c/c_0)$, where D_0 is a constant. The boundary condition at the edge of the precipitate is

$$c(\rho(t),t)=0. \quad (6)$$

There is a further equation which describes the motion of the moving boundary and this is obtained by combining Fick's first law of diffusion and the law of conservation of mass. The condition is

$$d\rho/dt=kD_0 g(0)(\partial c/\partial r)|_{r=\rho(t)}, \quad (7)$$

where k^{-1} is the density of the precipitate. It is assumed, if $n=2$ or 3, that the precipitation occurs about an infinitesimally small imperfection and therefore that

$$\rho(0)=0. \quad (8)$$

Following Miranker and Frisch[1] we now suppose that the problem possesses a $t^{\frac{1}{2}}$ time dependent solution with

$$\rho(t)=s(D_0 t)^{\frac{1}{2}}, \quad (9)$$

s being the growth parameter. We assume that the concentration has the functional form

$$c(r,t)/c_0=v(y), \quad (10)$$

where

$$(y+s)=r(D_0 t)^{-\frac{1}{2}}. \quad (11)$$

Note that Eq. (9) satisfies the condition in Eq. (8). Under the transformation defined by Eqs. (10) and (11), the diffusion equation (5) is reduced to an ordinary differential equation,

$$\frac{d}{dy}\left[g(v)(y+s)^{n-1}\frac{dv}{dy}\right]+\tfrac{1}{2}(y+s)^n\frac{dv}{dy}=0,\quad y>0; \quad (12)$$

equations (6) and (7) yield the boundary conditions

$$v(0)=0;\quad s=2\lambda\left[g(v)(dv/dy)\right]_{y=0}, \quad (13)$$

where $\lambda=kc_0$. The condition on the initial value of the concentration, namely $c(r,0)=c_0$ for $r>0$, gives

$$v(\infty)=1. \quad (14)$$

In what follows it will be supposed that

$$g(v)>0,\quad (0\leq v\leq 1)\quad \text{and}\quad 0<\lambda<1. \quad (15)$$

From Eq. (12) and the second boundary condition in Eq. (13) we derive, by a single integration,

$$g(v)(y+s)^{n-1}\frac{dv}{dy}=\frac{s^n}{2\lambda}\exp\left\{-\int_0^v\frac{(z+s)}{2g[v(z)]}dz\right\}. \quad (16)$$

At this point we will depart from the approaches of Miranker and Frisch[1] and Miranker and Keller[8] who restricted themselves to the 1-dimensional problem and established existence of a solution s and $v(y)$ for suitably behaved $g(v)$ and $0<\lambda<(g/\hat{g})$, where $0<g\leq g(v)\leq\hat{g}$ for $0\leq v\leq 1$. The proof given by Miranker and Keller in-

cludes uniqueness and they have also shown that no solution exists if $\lambda \geq (\bar{g}/g)$, but no conclusion is reached for $(g/\bar{g}) \leq \lambda < (\bar{g}/g)$. They also quote W. T. Kyner, in unpublished work, as extending these results to the 2-dimensional and 3-dimensional cases.

In this paper we will assume the existence (for $n=1,2,3$) of a solution with $s>0$, for $0<\lambda<1$, and establish a comparison theorem, of which an immediate consequence is the uniqueness of the solution. It is clear that, once s is determined, Eq. (12), together with the boundary conditions in Eq. (13), forms an initial value problem and there is only one solution $v(y)$ corresponding to a given s, so that it is sufficient to establish the uniqueness of s.

We first observe that since $g(v)>0$ and $s>0$, Eq. (16) implies that $dv/dy>0$, $0\leq y<\infty$. Thus, instead of regarding v as a function of y we will now consider y as a function of v. Since $v(0)=0$ and $v(\infty)=1$ the range of v to be considered is $0\leq v\leq 1$. Now Eq. (12) may be written in the form

$$(y+s)^n+2d/dv[g(v)(y+s)^{n-1}(dv/dy)]=0. \quad (17)$$

Let us therefore define,

$$(y+s)^n=s^nF'=s^n(dF/dv). \quad (18)$$

Equation (17) may then be integrated to give

$$s^nF(v)+2g(v)(y+s)^{n-1}(dv/dy)=0,$$

with

$$F(0)=-1/\lambda, \quad (19)$$

on using Eq. (13). But on differentiating Eq. (18),

$$s^nF''=n(y+s)^{n-1}(dy/dv). \quad (20)$$

Hence, from Eqs. (18)–(20),

$$s^2FF''+2ng(v)(F')^{2(1-1/n)}=0, \quad (0<v<1). \quad (21)$$

The boundary conditions are

$$F(0)=-1/\lambda; \quad F'(0)=1; \quad F'(1)=+\infty. \quad (22)$$

We remark that the nonlinearity in the differential equation is now an algebraic one, but that a singularity has been introduced at the end point $v=1$. We show that the condition $F'(1)=+\infty$ implies that $F(1)=0$. Observe that, from the definitions in Eqs. (18) and (19), $F'(v)>0$, $0\leq v\leq 1$ and $F(0)<0$. On writing Eq. (21) in the form

$$s^2(2/n)F''(F')^{(2/n)-1}=-4g(v)F'/F$$

and integrating,

$$s^2(F')^{2/n}=s^2-4\int_0^v g(\tau)[F'(\tau)/F(\tau)]d\tau,$$

$$=s^2-4g(v)\ln[-\lambda F(v)]$$

$$+4\int_0^v g'(\tau)\ln[-\lambda F(\tau)]d\tau, \quad (23)$$

where use has been made of Eq. (22). Since $F'(1)=+\infty$, $\ln[-\lambda F(v)]$ must diverge to $-\infty$ as $v\to 1-0$ and so

$$F(1)=0; \quad F(v)<0, \quad 0\leq v<1. \quad (24)$$

We also have

$$F'(v)\geq 1; \quad F''(v)>0 \quad \text{for} \quad 0\leq v\leq 1, \quad (25)$$

the second condition following from Eqs. (15), (21), and (24)

3. THE COMPARISON THEOREM AND SOME APPLICATIONS

We will show that if s_1 is a growth parameter corresponding to λ_1 and $g_1(v)$, and s_2 is one corresponding to λ_2 and $g_2(v)$, then $\lambda_1\geq\lambda_2$ and $g_1(v)\geq g_2(v)(0\leq v\leq 1)$ $\to s_1\geq s_2$. For let us suppose to the contrary that $s_1<s_2$. Equation (21) may be written in the form

$$F_i''=-2n(s_i)^{-2}g_i(v)(F_i')^{2(1-1/n)}/F_i, \quad (i=1,2), \quad (26)$$

where, from Eqs. (22) and (24),

$$F_i(0)=-1/\lambda_i; \quad F_i'(0)=1; \quad F_i(1)=0; \quad (i=1,2). \quad (27)$$

Since $\lambda_1\geq\lambda_2$ and $(s_1)^{-2}g_1(v)>(s_2)^{-2}g_2(v)$ [under the contrary supposition] and $F_i(v)<0$ and $F_i'(v)>0$, $0\leq v<1$ [from Eqs. (24) and (25)], it follows by geometrical considerations, from Eq. (26) and the first two boundary conditions of Eq. (27), that $F_1(v)>F_2(v)$, $0<v\leq 1$ and, in particular, that $F_1(1)>F_2(1)$. This conclusion is a contradiction since $F_1(1)=0=F_2(1)$. We proceed to give an analytical proof of the contradiction.

Let

$$H_i(v)=F_i''(v), \quad (i=1,2). \quad (28)$$

Then, by integration of Eq. (28) and use of the boundary conditions in Eq. (27),

$$F_i'(v)=1+\int_0^v H_i(w)dw, \quad (29)$$

$$F_i(v)=(v-1/\lambda_i)+\int_0^v (v-w)H_i(w)dw, \quad (30)$$

and since $F_i(1)=0$,

$$(1/\lambda_i-1)=\int_0^1 (1-w)H_i(w)dw. \quad (31)$$

On substituting for F_i and its derivatives from Eq. (28)–(30), Eq. (26) becomes

$$2n(s_i)^{-2}g_i(v)$$

$$=\frac{H_i(v)\left[(1/\lambda_i-v)-\int_0^v (v-w)H_i(w)dw\right]}{\left[1+\int_0^v H_i(w)dw\right]^{2(1-1/n)}}. \quad (32)$$

Note that, from Eqs. (25) and (28), $H_i(v)>0$, $0\leq v\leq 1$.

Now, from Eq. (32), $H_i(0)=2n\lambda_i(s_i)^{-2}g_i(0)$, so that under the contrary supposition $H_1(0)>H_2(0)$. Suppose that for some $V(0<V<1)$ we have $H_1(V)=H_2(V)$ and $H_1(v)>H_2(v)$, $0\leq v<V$. Then from Eq. (32), under the contrary supposition,

$$\frac{\left[(1/\lambda_1-V)-\int_0^V (V-w)H_1(w)dw\right]}{\left[1+\int_0^V H_1(w)dw\right]^{2(1-1/n)}} > \frac{\left[(1/\lambda_2-V)-\int_0^V (V-w)H_2(w)dw\right]}{\left[1+\int_0^V H_2(w)dw\right]^{2(1-1/n)}}. \quad (33)$$

Since

$$\int_0^V H_1(w)dw > \int_0^V H_2(w)dw > 0,$$

the inequality (33) holds for the numerators such that

$$\int_0^V (V-w)[H_2(w)-H_1(w)]dw > (1/\lambda_2-1/\lambda_1)\geq 0. \quad (34)$$

This is a contradiction since $H_1(w)>H_2(w)$, $0\leq w<V$. Hence $H_1(v)>H_2(v)$, $0\leq v<1$. But, from Eq. (31),

$$\int_0^1 (1-w)[H_2(w)-H_1(w)]dw=(1/\lambda_2-1/\lambda_1)\geq 0. \quad (35)$$

Accordingly, we are led to another contradiction and so the supposition that $s_1<s_2$ is false. Thus, we have the comparison theorem,

$$\lambda_1\geq\lambda_2 \text{ and } g_1(v)\geq g_2(v), \quad (0\leq v\leq 1), \quad \rightarrow s_1\geq s_2. \quad (36)$$

An immediate corollary is that there is a unique s corresponding to a given $0<\lambda<1$ and $g(v)>0 (0\leq v\leq 1)$. Let this be denoted by $s[\lambda,g(v)]$. It also follows from the comparison theorem (36) that $s[\lambda,g(v)]$ is a nondecreasing function of λ, $0<\lambda<1$, for a given $g(v)$. The comparison theorem may be stated in two parts:

$$s[\lambda,f(v)]\leq s[\lambda,g(v)]\leq s[\lambda,h(v)], \quad (37)$$

if

$$0<f(v)\leq g(v)\leq h(v), \quad (0\leq v\leq 1),$$

and

$$s[\kappa,g(v)]\leq s[\lambda,g(v)]\leq s[\mu,g(v)], \quad (38)$$

if

$$0<\kappa\leq\lambda\leq\mu<1.$$

Now it is readily seen from Eq. (21) that

$$s[\lambda,\gamma g(v)]=\gamma^{\frac{1}{2}}s[\lambda,g(v)], \quad \gamma>0, \quad (39)$$

since then the differential equation for $F(v)$ is unaltered and the boundary conditions (22) do not involve s. In particular, from Eqs. (37) and (39),

$$g^{\frac{1}{2}}\leq\frac{s[\lambda,g(v)]}{s[\lambda,1]}\leq\bar{g}^{\frac{1}{2}},$$

where

$$0<\underline{g}\leq g(v)\leq\bar{g}, \quad (0\leq v\leq 1). \quad (40)$$

But when $g(v)\equiv 1$, $0\leq v\leq 1$, we can obtain an equation for $s=s[\lambda,1]$. Thus Eq. (23) gives

$$s^nF'(v)=[s^3-4\ln(-\lambda F)]^{n/2}. \quad (41)$$

Since $F(0)=-1/\lambda$ and $F(1)=0$, Eq. (41) leads to

$$1=s^n\int_{-1/\lambda}^0 [s^3-4\ln(-\lambda F)]^{-n/2}dF$$

$$=\frac{s^n}{2\lambda}\exp(s^2/4)\int_s^\infty x^{-(n-1)}\exp(-x^2/4)dx. \quad (42)$$

Thus Eq. (40) leads to crude bounds on the growth parameter $s[\lambda,g(v)]$. It is shown in the Appendix that an equation for s may be obtained when $g(v)=(1-\alpha v)^{-1}$, $\alpha<1$, the case $n=3$ requiring the solution of a cubic equation prior to the quadrature. Fujita[14] has given the solution for this form of $g(v)$ in 1 dimension,[15] but the generalization to n dimensions appears to be new. In view of Eq. (39) this means that s may be computed for the two-parameter family $g(v)=\gamma(1-\alpha v)^{-1}$.

There is a different approach which may be adopted in order to obtain good comparison functions close to a given function $g(v)$. This is to generate functions $F(v)$ satisfying the boundary conditions $F(1)=0$, $F'(0)=1$ in such a way that $F(v)<0$, $F'(v)>0$ and $F''(v)>0$, $0\leq v<1$, and $1/\lambda=-F(0)>1$. In this connection we examine the nature of the singularity of $F(v)$ at $v=1$. From Eq. (23), in the neighborhood of $v=1$,

$$s^nF'\sim[-4g(1)\ln(-F)]^{n/2}. \quad (43)$$

Hence,

$$[4g(1)s^{-2}]^{n/2}(1-v)\sim\int_p^0 [-\ln(-G)]^{-n/2}dG$$

$$=\int_{-\ln(-F)}^\infty x^{-n/2}e^{-x}dx\sim(-F)[-\ln(-F)]^{-n/2}. \quad (44)$$

Thus,

$$F(v)\sim-(1-v)[-4g(1)s^{-2}\ln(1-v)]^{n/2}, \quad (45)$$

at $v=1-0$.

4. OTHER BOUNDS ON THE GROWTH PARAMETER

We now proceed to derive some bounds on s from Eq. (21) and the boundary conditions (22), and from

[14] H. Fujita, Textile Research J. 22, 757 (1952).

[15] Fujita's solution is actually for the problem with a fixed boundary but his method is readily extended to the moving boundary case.

the monotonic properties of F and its derivatives in Eqs. (24) and (25). By starting with Eq. (25), we first derive bounds on $F(v)$. Upon integration, $F'(v)\geq 1$, $0\leq v\leq 1$, leads to the inequality $F(v)\geq(v-1/\lambda)$. Also, $vF''(v)\geq 0$ implies that $[vF'(v)-F(v)]\geq 1/\lambda$, so that $(F/v)'\geq 1/(\lambda v^2)$, $v>0$ and hence $-F/v\geq(1/v-1)/\lambda$. By combining these two results we have the bounds

$$(1-v)/\lambda\leq -F(v)\leq(1-\lambda v)/\lambda. \tag{46}$$

From Eqs. (21), (25), and (46) we find that $(1-v)F''(v)\geq 2n\lambda s^{-2}g(v)(1-v)/(1-\lambda v)$. Integration of this inequality gives

$$-[(1-v)F'(v)+F(v)]\geq 2n\lambda s^{-2}\int_v^1 \frac{(1-w)g(w)}{(1-\lambda w)}dw. \tag{47}$$

On setting $v=0$ and using the boundary conditions of Eq. (22), we obtain

$$s^2(1-\lambda)/\lambda^2\geq 2n\int_0^1 \frac{(1-v)g(v)}{(1-\lambda v)}dv. \tag{48}$$

Also from Eqs. (21), (25), and (46), we deduce that $-FF''/(F')^2\leq 2ns^{-2}g(v)$. Integration yields the inequality

$$-F(v)/F'(v)\leq(1-v)+2ns^{-2}\int_v^1 g(w)dw. \tag{49}$$

On setting $v=0$, we obtain

$$s^2(1-\lambda)/\lambda\leq 2n\int_0^1 g(v)dv. \tag{50}$$

It is seen that the lower and upper bounds for s^2 in (48) and (50) coalesce as $\lambda\to 1-0$, so that

$$s^2\sim 2n(1-\lambda)^{-1}\int_0^1 g(v)dv, \quad (\lambda\to 1-0). \tag{51}$$

As $\lambda\to 0+$ the ratio of the upper to lower bound increases indefinitely, however. We proceed to rectify this situation, first for $n=1$ and then for $n=3$.

From Eqs. (21) and (46), $-F/F'\leq(1-\lambda v)/\lambda$. This inequality may be written in the form

$$-(1-\lambda)F\geq -[F+(1-v)F'](1-\lambda v).$$

But, for $n=1$, $2s^{-2}g(v)=-FF''$. Hence,

$$4s^{-2}g(v)(1-\lambda)(1-v)/(1-\lambda v)\geq -2[F+(1-v)F'](1-v)F''. \tag{52}$$

On integrating from 0 to 1 we obtain

$$4(1-\lambda)s^{-2}\int_0^1 \frac{(1-v)g(v)}{(1-\lambda v)}dv \geq[-[F+(1-v)F']^2]_0^1=[(1-\lambda)/\lambda]^2. \tag{53}$$

By combining (48) and (53), with $n=1$,

$$1\leq s^2(1-\lambda)\left[2\lambda^2\int_0^1 \frac{(1-v)g(v)}{(1-\lambda v)}dv\right]^{-1}\leq 2, \quad (n=1). \tag{54}$$

A consequence of the inequalities (54) is that $s=0(\lambda)$ for small λ. This fact can also be deduced from Eq. (40) and Eq. (42) for $s[\lambda,1]$. It is interesting to note, however, that the ratio of the upper to lower bound for s^2 given by Eq. (40) is $\bar{g}/g$, which may be greater than 2.

We may also improve the upper bound (50), for $n=1$, in another way. Thus we have

$$(1-v)F''=-2s^{-2}g(v)(1-v)/F\leq 2\lambda s^{-2}g(v),$$

using (4.1). On integrating, we have

$$-[F(v)+(1-v)F'(v)]\leq 2\lambda s^{-2}\int_v^1 g(w)dw. \tag{55}$$

On setting $v=0$ and using the boundary conditions of Eq. (22) we obtain

$$s^2(1-\lambda)/\lambda^2\leq 2\int_0^1 g(v)dv, \quad (n=1). \tag{56}$$

As $\lambda\to 1-0$ this is the best possible bound [see Eq. (51)]. For $\lambda\to 0+$ it may, or may not, be better than the upper bound in (54), according as

$$\int_0^1 (1-2v)g(v)dv\gtrless 0.$$

We now consider $n>2$, the case of interest here being $n=3$. By making use of Eq. (21),

$$\begin{aligned}[F(F')^{-(1-2/n)}]'&=-(1-2/n)FF''(F')^{-2(1-1/n)}+(F')^{2/n}\\&=2n(1-2/n)s^{-2}g(v)+(F')^{2/n}.\end{aligned} \tag{57}$$

Since $F'\geq 1$, Eq. (57) gives

$$[F(F')^{-(1-2/n)}]'\geq 1+2n(1-2/n)s^{-2}g(v). \tag{58}$$

Integrating from 0 to 1 and using the boundary conditions,

$$s^2(1-\lambda)/\lambda\geq 2n(1-2/n)\int_0^1 g(v)dv, \quad (n>2). \tag{59}$$

On combining (50) and (59),

$$(1-2/n)\leq s^2(1-\lambda)\left[2n\lambda\int_0^1 g(v)dv\right]^{-1}\leq 1, \quad (n>2). \tag{60}$$

For $n=3$, the lower bound in (60) is $\frac{1}{3}$. A consequence of the inequalities (60) is that $s=0(\lambda^{\frac{1}{3}})$ for small λ. This may also be obtained from Eq. (40) and Eq. (42) for $s[\lambda,1]$ and it is interesting to note that $(s[\lambda,1])^2/\lambda \to 2(n-2)$ as $\lambda\to 0+$, so that the lower bound in (59) is attained for this case. But as $\lambda\to 1-0$ the lower bound in (48) is attained, and this is better than that

in (59). We proceed to find a lower bound which is an improvement on both of these.

We find from Eqs. (21), (25), and (46) that

$$(2/n)F''(F')^{(2/n-1)} = -4s^{-2}g(v)F'/F \geq 4\lambda s^{-2}g(v)/(1-\lambda v). \quad (61)$$

Integration gives

$$(F')^{2/n} \geq 1+4\lambda s^{-2}\int_0^v \frac{g(w)}{(1-\lambda w)}dw. \quad (62)$$

By using (62) in Eq. (57) and integrating from 0 to 1,

$$s^2(1-\lambda)/\lambda \geq 2n(1-2/n)\int_0^1 g(v)dv + 4\lambda\int_0^1 \frac{(1-v)g(v)}{(1-\lambda v)}dv, \quad (n>2). \quad (63)$$

On combining this with the inequality in (50), we have

$$\int_0^1 g(v)dv \geq s^2(1-\lambda)/(2n\lambda) \geq \left[(1-2/n)\int_0^1 g(v)dv + (2/n)\lambda\int_0^1 \frac{(1-v)g(v)}{(1-\lambda v)}dv\right] = \left[\int_0^1 g(v)dv - (2/n)(1-\lambda)\int_0^1 \frac{g(v)}{(1-\lambda v)}dv\right], \quad (n>2). \quad (64)$$

Note that

$$\left\{\left[\int_0^1 g(v)dv - (2/n)(1-\lambda)\int_0^1 \frac{g(v)}{(1-\lambda v)}dv\right] - \lambda\int_0^1 \frac{(1-v)g(v)}{(1-\lambda v)}dv\right\} = (1-2/n)(1-\lambda)\int_0^1 \frac{g(v)}{(1-\lambda v)}dv > 0,$$

for $n>2$ and $0<\lambda<1$.

This, consequently, is an improvement on the lower bound in (48).

APPENDIX

We consider here the specific case $g(v)=(1-\alpha v)^{-1}$, $\alpha<1$. At first it will be supposed that $\alpha\neq 0$. (The case $g(v)\equiv 1$ has already been considered, anyway.) Now, Eq. (21) may be written, with $g(v)=(1-\alpha v)^{-1}$, in the form

$$\frac{2n}{s^2(1-\alpha v)} = -\frac{FF''}{(F')^2}\cdot(F')^{2/n} = (F')^{2/n}\left[\frac{F}{F'}+\frac{(1-\alpha v)}{\alpha}\right]'. \quad (A1)$$

Hence,

$$\frac{2n}{\alpha s^2}\ln\left[\frac{1}{(1-\alpha v)}\right] = (F')^{2/n}\left[\frac{F}{F'}+\frac{(1-\alpha v)}{\alpha}\right] - \frac{2}{n}\int\left[\frac{F}{F'}+\frac{(1-\alpha v)}{\alpha}\right](F')^{(2/n-1)}F''dv = (F')^{2/n}\left[\frac{F}{F'}+\frac{(1-\alpha v)}{\alpha}\right] + \frac{4}{s^2}\int\frac{F'}{F(1-\alpha v)}\left[\frac{F}{F'}+\frac{(1-\alpha v)}{\alpha}\right]dv = (F')^{2/n}\left[\frac{F}{F'}+\frac{(1-\alpha v)}{\alpha}\right]+\frac{4}{\alpha s^2}\ln\left[\frac{1}{(1-\alpha v)}\right] + \frac{4}{\alpha s^2}\ln(-F)+\text{const.} \quad (A2)$$

By using the first-two boundary conditions in (22),

$$\frac{2(n-2)}{\alpha s^2}\ln\left[\frac{1}{(1-\alpha v)}\right] = (F')^{2/n}\left[\frac{F}{F'}+\frac{(1-\alpha v)}{\alpha}\right] + \frac{4}{\alpha s^2}\ln(-\lambda F)+\left(\frac{1}{\lambda}-\frac{1}{\alpha}\right). \quad (A3)$$

Now let

$$F=(1-\alpha v)^{(1-n/2)}G. \quad (A4)$$

Then

$$F'=(1-\alpha v)^{-n/2}[(1-\alpha v)G'-\alpha(1-n/2)G]. \quad (A5)$$

On substituting into (A3) from (A4) and (A5),

$$[(1-\alpha v)G'-\alpha(1-n/2)G]^{2/n}\times\left\{\frac{\alpha G}{[(1-\alpha v)G'-\alpha(1-n/2)G]}+1\right\} = (1-\alpha/\lambda)-4s^{-2}\ln(-\lambda G). \quad (A6)$$

Note that (A6) holds for $\alpha=0$, as may be seen from Eqs. (41) and (A4).

The solution of an algebraic equation (quadratic for $n=1$, linear for $n=2$ and cubic for $n=3$) leads to

$$(1-\alpha v)G'=W[\alpha G,\ (1-\alpha/\lambda)-4s^{-2}\ln(-\lambda G)], \quad (A7)$$

which may be integrated by quadrature. Now, from equations (22) and (24), $F(0)=-1/\lambda$ and $F(1)=0$. Hence, from (A4),

$$G(0)=-1/\lambda;\quad G(1)=0. \quad (A8)$$

Now, $F\leq 0$ and $F'>0$. Hence, from (A4), $G\leq 0$ and from (A5) we may assert that $G'>0$ if $\alpha(1-n/2)\leq 0$. Provided that $G'>0$, Eq. (A7) may be integrated from $v=0$ to $v=1$, and on using (A8) we obtain

$$\ln\left(\frac{1}{1-\alpha}\right) = \alpha\int_{-1/\lambda}^{0} \frac{dG}{W[\alpha G,\ (1-\alpha/\lambda)-4s^{-2}\ln(-\lambda G)]} = (\alpha/\lambda)\int_{0}^{1} \frac{dx}{W[-(\alpha/\lambda)x,\ (1-\alpha/\lambda)-4s^{-2}\ln x]} = Z(\alpha/\lambda, s^{-2}). \quad \text{(A9)}$$

A possible procedure is to choose values for (α/λ) and s^{-2}, to compute $Z(\alpha/\lambda, s^{-2})$ and hence determine α from (A9), which then gives the value of λ. If this value of λ lies between 0 and 1 then we know s for these particular values of α and λ, provided $G'>0$, and $G(v)$ can then be found by inverting the quadrature of (A7). The reduced concentration $v=v(y)$ can then be obtained as the solution of the equation arising from the substitution of (A4) into (18).

JOURNAL OF APPLIED PHYSICS VOLUME 31, NUMBER 9 SEPTEMBER, 1960

Temperature Dependence of the Adiabatic Elastic Moduli of Single-Crystal Alpha Uranium

H. J. McSkimin* and E. S. Fisher†

(Received February 19, 1960)

The ultrasonic-wave velocities in small alpha-uranium single crystals have been measured at various temperatures using the phase-comparison technique. Details in the experimental procedure, direct computation of the stiffness moduli, and cross-checking by indirect methods are given. The temperature dependence of the moduli are reported for the range −195° to +300°C for c_{11}, c_{12}, and c_{23} and −195° to +35°C for the remaining 6 principal moduli. The results show a very marked abnormal temperature dependence of the elasticity in the [100] direction; c_{11} decreases with temperature below −17.2°C and the linear compressibility in [100] increases from +35° to −195°C. The bulk modulus passes through a maximum at −100°C. These abnormalities indicate a strong temperature dependence of the electron interactions involved in the second nearest-neighbor bond.

1. INTRODUCTION

THE adiabatic single-crystal elastic moduli for the orthorhombic phase of uranium metal were reported previously by the present authors from measurements of high-frequency acoustic-wave velocities at 25°C.[1] The mode of variation of the elastic moduli with crystal direction showed a strong direct relationship to the directions between nearest and next nearest-neighbor atoms in the α-uranium structure. A study of the temperature dependence of the elastic moduli should then provide at least a qualitative approach to the temperature dependence of the forces in the different interatomic bonds in the crystal and perhaps assist in explaining the pronounced anisotropy in the temperature dependence of the thermal expansion.[2]

The present paper gives the results for all 9 principal moduli in the range 35° to −195°C and for the dilational moduli c_{11}, c_{22}, and c_{33} over the range 300° to −195°C. Implications of the anomalies in the results are discussed.

2. SPECIMENS

The specimens were the small single-crystal plates which were used for the 25°C measurements.[1] The apparatus and procedure for preparing 2 faces on each specimen which were flat and parallel to a preselected crystal plane are given in footnote reference 1. Six of these specimens were used in the present study, in 3 of which the faces were parallel to the principal planes. For the remaining three specimens the face normals were aligned 90° to one principal axis and close to 45° to the remaining axes. The measured orientation of each crystal at 25°C is given in Table I.

TABLE I. Thickness dimension and orientation of uranium crystals at 25°C.

Crystal	Thickness (mm)	Inclination of wave propagation direction of principal axes [100]	[010]	[001]
A	2.9108	0°	...	...
B	3.9185	...	0°	...
C	2.7923	...	...	0°
D	2.5400	...	90°	$45°32'^{a}=(\theta_0)_D$
E	2.8116	90°	...	$35°20'^{a}=(\theta_0)_E$
E'	1.6388	90°	...	$37°55'^{a}=(\theta_0)_{E'}$
F	1.7730	$44°29'^{a}=(\theta_0)_F$	...	...

[a] Estimated probable error of ±4'.

* Bell Telephone Laboratories, Murray Hill, New Jersey.
† Argonne National Laboratory, Argonne, Illinois.

[1] E. S. Fisher and H. J. McSkimin, J. Appl. Phys. **29**, 1473 (1958).

[2] J. R. Bridge, C. M. Schwartz and D. A. Vaughan, Trans. A.I.M.E. **206**, 1282 (1956).

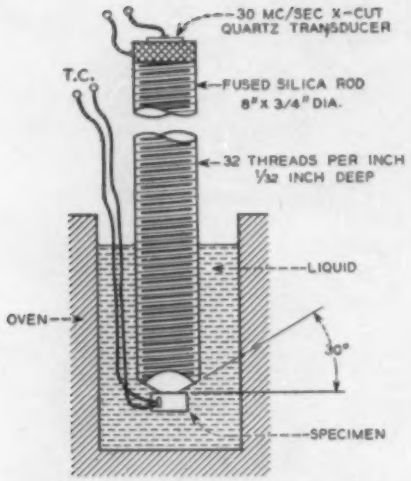

FIG. 1. Assembly of buffer unit for high-temperature measurements.

The specimen thicknesses ranged from about 1.5–4 mm and the lateral dimensions were 4–5 mm. After the 25°C measurements most of the crystal faces were resurfaced with 1-μ diamond paste to remove blemishes caused primarily by surface oxidation. The measured thicknesses, at room temperature, after this resurfacing are given in Table I. The procedure for computing the effects of thermal expansion on thickness and orientation are discussed in Sec. 4.

Because of difficulties in maintaining coupling seals at low temperatures for shear-wave propagation, crystals D, E, and F were resurfaced after longitudinal wave measurements so as to provide one face with a rougher finish (14-μ diamond). Although this treatment apparently solved the problem for crystals D and F, crystal E gave inadequate pulse patterns and a specimen of essentially duplicate orientation was then prepared, designated E' in Table I.

3. MEASURING TECHNIQUES

3.1 Phase Comparison Method

The general problem of determining elastic moduli by means of ultrasound involves the measurement of wave velocities in arbitrary directions of the crystal specimens.[3] When the path length is quite small (as for the specimens used in the present study) phase comparison of waves reflecting back and forth within the specimen can be used to good advantage as described previously for the 25°C measurements on uranium.[1]

If one considers two successive wave trains actuating the transducer, whatever the means of coupling may be, the generated voltages may be represented by E_t, the first received signal, and E_t', the second. Then

$$E_t' = E_t \cdot Ae^{i\gamma} \cdot e^{-i2t\omega/V}. \tag{1}$$

In Eq. (1) above t is the specimen thickness, V is the velocity, $\omega = 2\pi$ times the frequency (f_n), and $Ae^{i\gamma}$ is the product of the complex reflection coefficients for waves reflected back into the specimen at either end. The phase angle γ will therefore depend in general on the coupling arrangement, and is considered in greater detail in Sec. 3.4.

If the echoes are now kept exactly in phase by adjusting the frequency as the temperature is varied, the expression for phase angles may be written as

$$\gamma - 2t\omega_n/V = -2\pi n, \tag{2}$$

in which n is an integer. From this

$$V = \frac{2tf_n}{n+\gamma/2\pi}. \tag{3}$$

If successive echoes are maintained out of phase, as for the shear-wave measurements to be described, n is simply replaced by $(n+\frac{1}{2})$ in Eqs. (2) and (3).

Since the 25°C valves of velocity (V_0) had already been measured, it was only necessary for the present study to determine variations in V with temperature holding n constant. From Eq. (3)

$$\frac{V}{V_0} = \frac{t}{t_0} \cdot \frac{f_n}{(f_n)_0} \cdot \frac{n+\gamma_0/2\pi}{n+\gamma/2\pi} = \frac{t}{t_0} \cdot r. \tag{4}$$

In Eq. (4) t/t_0 can be determined from thermal expansion data, and $f_n/(f_n)_0$ can be measured directly. In many cases, the factor involving γ can be replaced by unity; however, further discussion of this factor is given in Sec. 3.4.

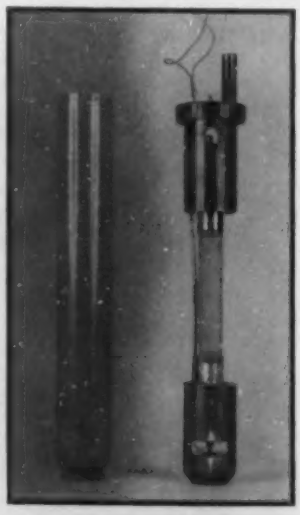

FIG. 2. Photograph of assembled high-temperature unit and container.

[3] See for example: W. P. Mason, *Physical Acoustics and Properties of Materials* (Van Nostrand Company, Inc., New York, 1958).

3.2 Apparatus for Longitudinal Waves

For longitudinal waves, coupling into the specimen was obtained through use of a fused-silica buffer rod as shown in Figs. 1 and 2. The system was designed so that the specimen could be heated in an inert surrounding to minimize oxidation.

After the specimen was set in place and the unit was placed into the glass tube, the system was evacuated and degassed Dow Corning DC-703 silicone oil was introduced. The oil acted as both seal and heat-transfer media. Argon gas was introduced for measurements in the 200°–300°C range, with pressure restored to one atmosphere. For temperatures over 300°C the silicone oil ceased to provide satisfactory coupling.

Although uranium is highly reactive chemically, especially with oxygen, the specimen surfaces remained relatively free of contamination during heating. A blue interference film was noted after immersion at 200°C which turned quickly to light brown upon admission of the gas. No surface roughening or other possibly harmful effects were noted.

At temperatures between +25° and −195°C, normal propanol was used instead of the silicone oil. It was found unnecessary to employ degassing techniques since oxidation took place very slowly at the lower temperatures. Although the alcohol froze at about −125°C the seal was generally maintained to temperatures near −180°C. Spot measurements at −195.8°C were also made using a bath of liquid nitrogen to provide the coupling.

Temperatures were measured with a copper-constantan thermocouple directly on the specimen and a high-sensitivity potentiometer, providing precision to ±0.5° at −195°C and ±0.2° at +300°C. The intermediate low temperatures were obtained by a temperature gradient between a bath of liquid nitrogen around the lower part of the system and an exposed top section.

A description of the electronic circuit used and the pulse-overlap technique for following f_n as the temperature was varied is described in some detail in footnote reference 4.

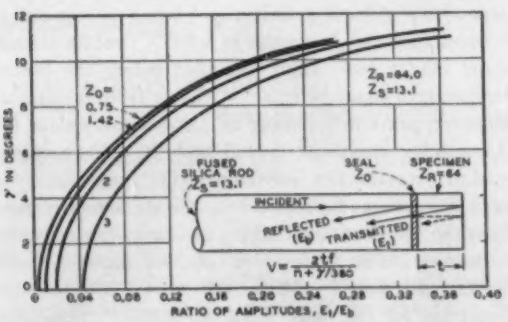

FIG. 3. Curves for estimating reflection phase-angle correction γ from amplitudes of received signals, for longitudinal waves in alpha uranium, fused-silica buffer, and coupling fluid with acoustic impedances Z_R, Z_S, and Z_0 ($\times 10^5$ mech ohms/cm^2), respectively.

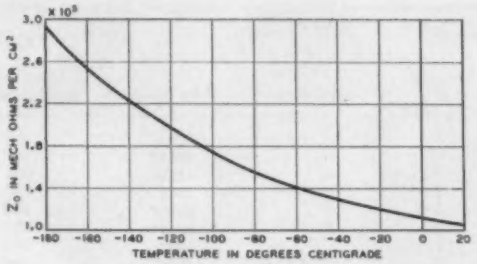

FIG. 4. Acoustic impedance for *n*-propanol, for longitudinal waves at 54 Mcps.

3.3 Apparatus for Shear Waves

Because of the low viscosity of coupling fluids at elevated temperatures, shear wave measurements above 50°C await further development in techniques suitable for the small specimens available.

At low temperatures the anomalously high attenuation in fused silica made the only available shear-wave buffer unsuitable. All of the results listed in this paper were obtained with 20-Mcps Y-cut quartz transducers (3×3 mm) affixed directly to the specimen with Nonaq stopcock grease (Fisher Scientific Company). Operation near the 60-Mcps 3rd harmonic frequency was used, with f_n being determined by overlapping adjacent pulses (wave trains) and phase-opposing them. A few check measurements were later made with a quartz buffer rod oriented with length in the "*AC*" direction, which were in good agreement with the given data.

The specimens were placed on a copper plate within a brass housing which could be cooled slowly by means of liquid nitrogen. Temperatures were measured with a thermocouple directly on the specimen, as noted previously for the longitudinal wave measurements.

3.4 Evaluation of γ

For the longitudinal-wave measurements using the buffer rod technique, γ can be evaluated from a measurement of reflected and transmitted components as shown by Fig. 3. The pulse duration is made short enough so that time separation of the wave trains can be obtained. The method of calculating γ in terms of the ratio of amplitudes is explained in Appendix B of footnote reference 4.

A typical value of 64×10^5 mech ohms/sq cm was used for the characteristic longitudinal-wave impedance of uranium. It is to be noted that as a result of this high impedance the value of γ is never more than 12 degrees. Were this to be neglected in the present study, errors of only 0.05% in velocity would result. Although probably

[4] H. J. McSkimin, IRE Trans. on Ultrasonic Eng. **UE-5**, 25 (1957).

TABLE II. Summary of wave velocity-elastic modulus relations.

Velocity #	Crystal	Type Mode	Direction of particle motion	ρV^2	Limits of temperature, °C
1	*A*	long.	100	c_{11}	−196, +306
2	*A*	shear	010	c_{66}	−195, +23
3	*A*	shear	001	c_{55}	−195, +24
4	*B*	long.	010	c_{33}	−195, +281
5	*B*	shear	100	c_{66}	−195, +27
6	*B*	shear	001	c_{44}	−196, +31
7	*C*	long.	001	c_{33}	−195, +300
8	*C*	shear	100	c_{55}	−196, +32
9	*C*	shear	010	c_{44}	−140, +31
10	*D*	quasi-long.	hol[a]	$\frac{1}{2}\{c_{22}c^2+c_{11}s^2+c_{55}+[g(c_{12})]^2\}$	−196, +46
11	*D*	quasi-shear	$ho\bar{l}$[b]	$\frac{1}{2}\{c_{22}c^2+c_{11}s^2+c_{55}-[g(c_{12})]^2\}$	−127, +47
12	*D*	shear	010	$c_{66}c^2+c_{66}s^2$	−159, +28
13	*E*	quasi-long.	okl[a]	$\frac{1}{2}\{c_{33}c^2+c_{22}s^2+c_{44}+[g(c_{23})]^2\}$	−196, +53
14	*E'*	quasi-shear	$o\bar{k}l$[b]	$\frac{1}{2}\{c_{33}c^2+c_{22}s^2+c_{44}-[g(c_{23})]^2\}$	−176, +25
15	*E'*	shear	100	$c_{44}c^2+c_{66}s^2$	−181, +35
16	*F*	quasi-long.	$hk\sigma$[a]	$\frac{1}{2}\{c_{11}c^2+c_{22}s^2+c_{66}+[g(c_{12})]^2\}$	−196, +37
17	*F*	quasi-shear	$hk\bar{\sigma}$[b]	$\frac{1}{2}\{c_{11}c^2+c_{22}s^2+c_{66}-[g(c_{12})]^2\}$	−196, +33
18	*F*	shear	001	$c_{66}c^2+c_{44}s^2$	−196, +27

[a] Close to propagation direction given in Table I.
[b] 90° from that in quasi-long. mode.
$c=\cos\theta$, $s=\sin\theta$, where θ is the rotation angle for each crystal given in Table I plus $\Delta\theta$ from Eq.11.
$g(c_{12})=[c_{11}c^2-c_{66}c^2+c_{66}(c^2-s^2)]^2+4s^2c^2(c_{12}+c_{66})^2$
$g(c_{23})=[c_{22}s^2-c_{33}c^2+c_{44}(c^2-s^2)]^2+4s^2c^2(c_{23}+c_{44})^2$
$g(c_{13})=[c_{22}s^2-c_{11}c^2+c_{66}(c^2-s^2)]^2+4s^2c^2(c_{12}+c_{66})^2$.

negligible in view of the somewhat larger uncertainties encountered for shear waves, values of γ were obtained for all longitudinal-wave measurements except for temperatures above 150°C where the effect was negligible.

The characteristic impedance Z_0 for silicone oil, needed for the above calculations, is given in footnote reference 4. Figure 4 shows the variation of Z_0 for normal propanol as a function of temperature. This data was obtained by measurement of the absolute reflection coefficient between the fused-silica buffer and the alcohol.

For shear waves with transducer directly on the specimen the value of γ for use in Eq. (4) (n replaced with $n+\frac{1}{2}$ for phase opposition of echoes) cannot be determined readily since the seal thickness is not known. A second temperature run with two transducers instead of one can, of course, be used to provide direct measurement of γ; however, this is not entirely dependable because of difficulty in matching the seals. Calculations of γ at 25° and −195°C were then made using the formulas shown in Appendix C of footnote reference 4. Typical values of seal thickness and impedance for Nonaq were used. The effect on velocity of variations in γ over this temperature range was shown to be less than 0.1%, and was neglected in the computation of the moduli, but not in the estimation of maximum probable errors. (See Sec. 5.)

4. RESULTS

4.1 Basic Data

Values of r [Eq. (4)] as a function of temperature were obtained for all of the 18 wave modes listed in Table II. For each of the 3 longitudinal modes propagated in the principal directions the data consisted of at least 100 measurements over the range −195° to approximately 300°C. Data for the remaining modes were in the range of −195° to 35°C. Table II summarizes the temperature range for each set of measurements.

In most cases the propagated-wave frequencies were between 40 and 60 Mcps. This intermediate range of frequencies was used so as to circumvent possible lateral boundary and diffraction effects at low frequencies and the higher specimen losses which occur at higher frequencies. To determine whether r at any temperature was frequency dependent, the measurements for the longitudinal mode in crystal *C* were carried out using 3 different frequency bands, centered at 30 Mcps, 45 Mcps, and 90 Mcps. The results of this study showed no significant effects of frequency on the temperature dependence of wave velocity.

Most runs were successful to −195°C, but for certain shear modes seal failure occurred before the lowest temperature could be attained. These failures did not, however, prevent obtaining all the necessary data for determining the shear moduli and the cross-coupling moduli over the full low-temperature range since for both types of moduli one gets duplicate measurements from the specimen orientations available. For example, measurements on crystal *C* for the *YZ* shear c_{44} could not be made below −140°C, but crystal *B* yielded information for the same mode to −195°C. Similarly, shear-mode data from crystals *D* and *E'*, for computing c_{12} and c_{23}, respectively, could not be completed but the longitudinal modes provided data for the full range.

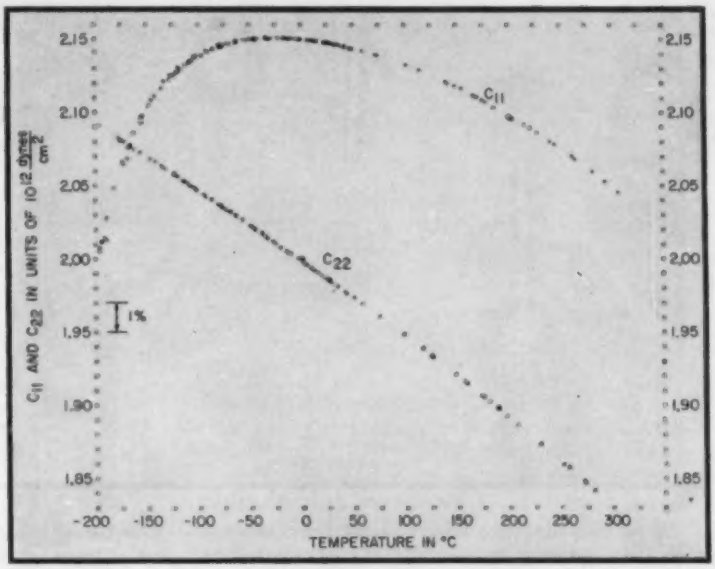

FIG. 5. Data points for c_{11} and c_{22}.

4.2 Thermal Expansion Corrections

The specimen thickness ratios, t/t_0 in Eq. (4), were evaluated from the third-order polynomials which best fit the lattice parameter determinations of Bridge *et al.*[2,5] covering the temperature range of $-253°$ to 640°C for b_T and c_T (unit cell dimensions along [010] and [001], respectively). The original data also gives the a_T parameter over the same temperature range; however, in view of the anomalous nature of the reported value at $-253°$C and the fact that this anomaly is supported by only one point, the polynomials used for evaluating the a_T parameter and the volume were based only on the data reported at and above $-210°$C. The polynomials used are as follows:

$$\begin{aligned} a_T &= 2.8517(1+23.528\times10^{-6}T+2.185\\ &\qquad \times10^{-9}T^2+27.806\times10^{-12}T^3)\\ b_T &= 5.8671(1+0.61\times10^{-6}T-2.32\\ &\qquad \times10^{-9}T^2-18.15\times10^{-12}T^3)\\ c_T &= 4.9542(1+19.36\times10^{-6}T+5.50\\ &\qquad \times10^{-9}T^2+23.60\times10^{-12}T^3), \end{aligned} \tag{5}$$

where the parameters are given in Angstrom units for a given T in °C.

For crystals A, B, or C the thickness ratios corresponded simply to a_T/a_0, b_T/b_0, or c_T/c_0. For crystals D, E, E', and F, the ratios t/t_0 were obtained from the approximated relations for homogeneous strain derived from transformation of second-order tensors. Since the strains due to thermal expansion are small, the following relations are sufficiently accurate:

$$\begin{aligned} (t/t_0)_D &= c_T/c_0\cdot\cos^2(\theta_0)_D+a_T/a_0\cdot\sin^2(\theta_0)_D\\ (t/t_0)_{E \text{ or } E'} &= c_T/c_0\cdot\cos^2(\theta_0)_E+b_T/b_0\cdot\sin^2(\theta_0)_E\\ (t/t_0)_F &= a_T/a_0\cdot\cos^2(\theta_0)_F+b_T/b_0\cdot\sin^2(\theta_0)_F, \end{aligned} \tag{6}$$

where θ_0 is the rotation angle noted in Table II and the lettered subscripts refer to the crystal involved.

4.3 Computation of Diagonal Moduli

The relations between the wave velocities and elastic-stiffness moduli for orthorhombic symmetry are derived in footnote reference 1 and are summarized in Table II. The 6 diagonal moduli are the stiffness factors, ρV^2, associated with the 9 modes propagated in principal directions which give c_{11}, c_{22}, and c_{33} and two separate determinations each of the shear moduli c_{44}, c_{55}, and c_{66}. The computation of these moduli at a given temperature simply involves the following relation:

$$\rho/\rho_0(V/V_0)^2\cdot(c_{ii})_0=c_{ii}, \tag{7}$$

where V/V_0 is obtained from Eq. (4), $(c_{ii})_0$ is the best value of the stiffness modulus at 25.0°C given in footnote reference 1 and the density ratio ρ/ρ_0 is computed from the unit cell volumes given by the data of footnote reference 2. The following polynomial was used for computing the unit cell volume at the temperature T in degrees centigrade:

$$\begin{aligned} (a_T)\cdot(b_T)\cdot(c_T) &= 82.8683(1+43.958\times10^{-6}T+9.379\\ &\qquad \times10^{-9}T^2+27.141\times10^{-12}T^3). \end{aligned} \tag{8}$$

Representative plots of the computed moduli vs temperature are given in Figs. 5 and 6; the former for

[5] Best-fit polynomials were obtained from data of footnote reference 2 by L. T. Lloyd, Argonne National Laboratory.

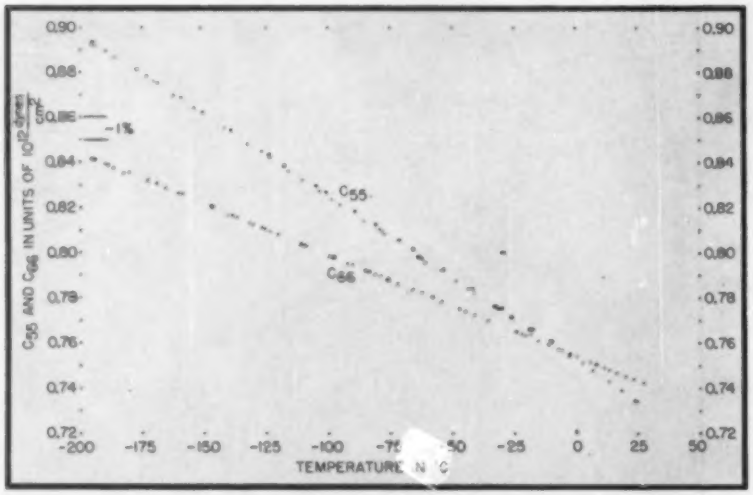

FIG. 6. Data points for c_{55} from crystals A and C, and c_{66} from crystals A and B.

c_{11} and c_{22}, and the latter plots showing the manner in which independently derived sets of shear moduli fit together. The points for c_{55} are from crystals A and C and the c_{66} points, from A and B. In neither case is there any systematic deviations between the different data.

Since the values of the diagonal moduli at a given temperature are involved in the computation of the cross-coupling moduli and also in subsequent computations of the compliance moduli all of the points obtained for each c_{ii} were fitted by least-mean-square analysis to polynomials up to the 7th order. The fitting was carried out by an IBM 704 computer program, the output of which gives the coefficients for each order from one through seven and the corresponding standard deviations of the residuals. The best-fit equation for each c_{ii} was then chosen as that which gave the smallest standard deviation. Table III gives the coefficients to be used for computing c_{ii} at any temperature in the range of the data. Figures 7–10 are the c_{ii} vs temperature curves obtained from the polynomials. With the exception of c_{11}, the diagonal moduli increase almost linearly with decreasing temperature. The slope of the curve for c_{11} is highly anomalous, however, being large and positive at low temperatures and gradually decreasing with increase in temperature to zero slope at -17.2°C.

4.4 Computation of Cross-Coupling Moduli

Once the diagonal moduli are obtained, each of the moduli c_{13}, c_{13}, and c_{23} can be computed from the wave velocities for either the quasi-longitudinal or quasi-shear modes in crystals F, D, and E or E', respectively, through the following relations:

$$(sc)^2(c_{12}+c_{66})^2 = (c_{11}c^2+c_{66}s^2-\rho V^2)(c_{22}s^2+c_{66}c^2-\rho V^2)$$

where $V=V_{16}$ or V_{17}, $s=\sin\theta_F$, $c=\cos\theta_F$,

$$(sc)^2(c_{12}+c_{66})^2 = (c_{22}c^2+c_{66}s^2-\rho V^2)(c_{11}s^2+c_{66}c^2-\rho V^2) \quad (9)$$

where $V=V_{10}$ or V_{11}, $s=\sin\theta_D$, $c=\cos\theta_D$,

$$(sc)^2(c_{23}+c_{44})^2 = (c_{33}c^2+c_{44}s^2-\rho V^2)(c_{22}s^2+c_{44}c^2-\rho V^2)$$

TABLE III. Best-fit polynomial coefficients for computing stiffness moduli of alpha uranium. Form of equation: $c_{ij}=a_0+a_1T+a_2T^2+\cdots+a^7T^7$. T is in °C.

Modulus and temp. range of data (lower limit is −195°C, upper limit indicated)	a_0	$a_1\times10^4$	$a_2\times10^7$	$a_3\times10^{10}$	$a_4\times10^{13}$	$a_5\times10^{15}$	$a_6\times10^{17}$	$a_7\times10^{19}$
c_{11}(+306)	2.1502	−0.5130	−14.63	+9.55	+3.63	+1.209	−81.19	+13.217
c_{22}(+281)	1.9982	−4.927	−1.207	−2.91	−2.36	+0.026	+3.61	−0.710
c_{33}(+300)	2.6962	−9.891	−3.98	+5.78	+2.22	−0.178	−6.06	+2.620
c_{44}(+31)	1.2621	−7.1423	−0.262	+80.94	+89.38	+2.580	...	...
c_{55}(+32)	0.7529	−7.3429	−5.054	−92.24	−59.93	−1.217	...	...
c_{66}(+27)	0.7544	−4.4696	−1.949	−29.64	−10.05	...	...	...
c_{13}(+37)	0.4584	+1.8706	+7.523	−157.08	−546.70	−43.272	−1068.09	...
c_{12}(+46)	0.2162	+0.3586	+11.968	+181.10	+112.86	+1.664	...	...
c_{23}(+52)	1.0784	−0.9019	−0.999	−139.15	−113.23	−2.347	...	...

where $V = V_{13}$ or V_{14}, $s = \sin\theta_{E,E'}$, $c = \cos\theta_{E,E'}$.

The appropriate ρV^2 was computed from the V/V_0 ratios through the following relation

$$\frac{\rho}{\rho_0}\left(\frac{V}{V_0}\right)^2 \cdot (\rho V^2)_0 = \rho V^2, \tag{10}$$

where $(\rho V^2)_0$ is the stiffness factor for the given direction of propagation at 25.0°C. The cross-coupling moduli were then computed from Eq. 9 using the best-fit polynomials given in Table III to evaluate the diagonal

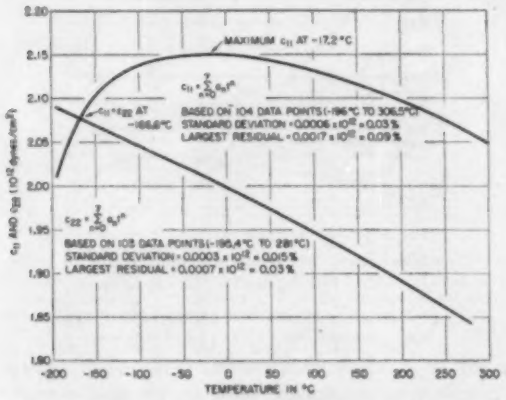
MAXIMUM c_{11} AT −17.2°C
$c_{11} = \sum_{n=0}^{7} a_n t^n$
BASED ON 104 DATA POINTS (−196°C TO 306.5°C)
STANDARD DEVIATION = 0.0006 × 10^{12} = 0.03%
LARGEST RESIDUAL = 0.0017 × 10^{12} = 0.09%
$c_{22} = \sum_{n=0}^{7} a_n t^n$
BASED ON 103 DATA POINTS (−196.4°C TO 28°C)
STANDARD DEVIATION = 0.0003 × 10^{12} = 0.015%
LARGEST RESIDUAL = 0.0007 × 10^{12} = 0.03%
c_{11} AND c_{22} (10^{12} dynes/cm²)
TEMPERATURE IN °C

FIG. 7. Plot of best-fit polynomial (Table III) for c_{11} and c_{22}.

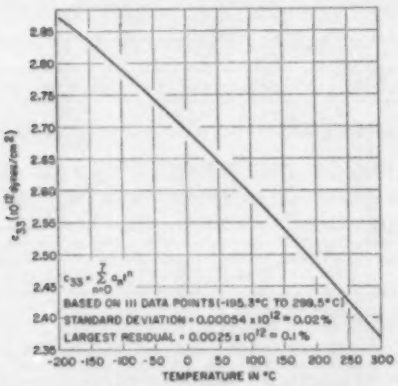
$c_{33} = \sum_{n=0}^{7} a_n t^n$
BASED ON 111 DATA POINTS (−195.3°C TO 299.5°C)
STANDARD DEVIATION = 0.00054 × 10^{12} = 0.02%
LARGEST RESIDUAL = 0.0025 × 10^{12} = 0.1%
c_{33} (10^{12} dynes/cm²)
TEMPERATURE IN °C

FIG. 8. Plot of best-fit polynomial (Table III) for c_{33}.

moduli at the temperature for which ρV^2 applied. The following approximation was used to evaluate the small change in rotation angles θ_D, θ_E, $\theta_{E'}$, and θ_F with temperature caused by anisotropic thermal expansion:

$$\Delta\theta = (\cos\theta \cdot \sin\theta)_0 K, \tag{11}$$

where

$$K = c_T/c_0 - a_T/a_0, \text{ for crystal } D$$
$$= c_T/c_0 - b_T/b_0, \text{ for crystals } E \text{ and } E'$$
$$= a_T/a_0 - b_T/b_0, \text{ for crystal } F.$$

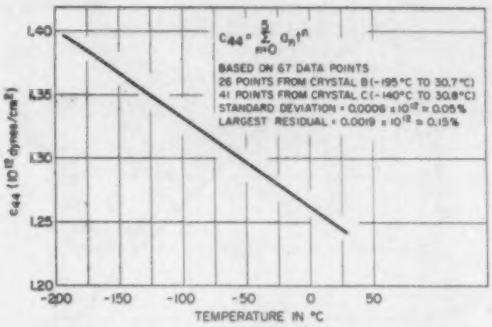
$c_{44} = \sum_{n=0}^{5} a_n t^n$
BASED ON 67 DATA POINTS
26 POINTS FROM CRYSTAL B (−195°C TO 30.7°C)
41 POINTS FROM CRYSTAL C (−140°C TO 30.8°C)
STANDARD DEVIATION = 0.0006 × 10^{12} = 0.05%
LARGEST RESIDUAL = 0.0019 × 10^{12} = 0.15%
c_{44} (10^{12} dynes/cm²)
TEMPERATURE IN °C

FIG. 9. Plot of best-fit polynomial (Table III) for c_{44}.

Figures 11–15 give the variation of the ρV^2 values with temperature for the coupled modes. The variation with temperature of c_{12}, c_{13}, and c_{23} derived from both sets of data for each crystal are given in Fig. 16. The open circles represent the moduli calculated from the quasi-shear mode data. The solid lines represent the polynomial best fitted to the moduli obtained using ρV_{QL}^2 (Table III). Since in all cases the 2 sets of moduli are generally within 1% of agreement, the latter polynomials serve adequately to describe all the computed data for the cross-coupling moduli.

4.5 Moduli-Temperature Coefficients

Some temperature coefficients $R = (1/c_{ij}) \cdot dc_{ij}/dT$ as calculated from the first derivatives of the best fit polynomials are shown in Table IV (p. 1635).

4.6 Cross-Checks

Since, basically, 18 relations were obtained involving only 9 moduli, numerous cross checks were afforded. The most direct is the comparison of the diagonal shear moduli, each derived from two independent measurements in 2 different crystals. These checks on c_{55} and c_{66} have been noted previously and are shown in Fig. 6.

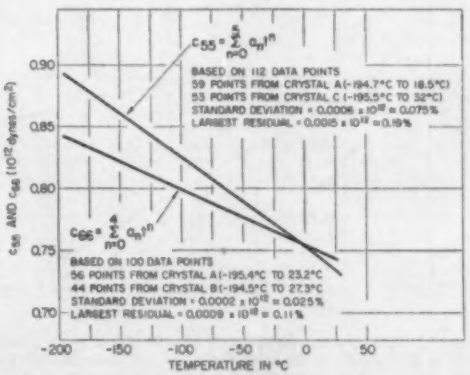
$c_{55} = \sum_{n=0}^{5} a_n t^n$
BASED ON 112 DATA POINTS
59 POINTS FROM CRYSTAL A (−194.7°C TO 18.5°C)
53 POINTS FROM CRYSTAL C (−195.5°C TO 32°C)
STANDARD DEVIATION = 0.0006 × 10^{12} = 0.075%
LARGEST RESIDUAL = 0.0015 × 10^{12} = 0.19%
$c_{66} = \sum_{n=0}^{4} a_n t^n$
BASED ON 100 DATA POINTS
56 POINTS FROM CRYSTAL A (−195.4°C TO 23.2°C
44 POINTS FROM CRYSTAL B (−194.5°C TO 27.3°C
STANDARD DEVIATION = 0.0002 × 10^{12} = 0.025%
LARGEST RESIDUAL = 0.0009 × 10^{12} = 0.11%
c_{55} AND c_{66} (10^{12} dynes/cm²)
TEMPERATURE IN °C

FIG. 10. Plot of best-fit polynomial (Table III) for c_{55} and c_{66}.

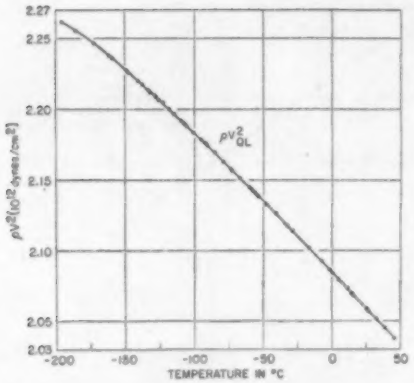

FIG. 11. Temperature dependence of quasi-longitudinal mode stiffness in crystal *D*.

For c_{44}, no direct comparison is shown here; however, the plot of the polynomial which best fits the 2 sets of data (Fig. 9) gives a very smooth and close to linear-temperature dependence with a maximum residual of 0.15%.

Further checks on the shear moduli are obtained from the pure shear mode data for the rotated orientations, i.e., velocities V_{12}, V_{15}, and V_{18} in Table II. The measured temperature dependence of these mode stiffnesses are plotted as solid circles in Figs. 12, 14, and 15 for V_{12}, V_{15}, and V_{18}, respectively. The open circles related to ρV_{12}^2 and ρV_{18}^2 are the corresponding stiffnesses computed using the directly determined shear moduli in the equations for ρV_s^2 given in Table II. In all cases the measured and observed values showed the same temperature dependence. The computed ρV_{15}^2 are not shown because they were not significantly different from the plotted measured points. The computed values for ρV_{18}^2 are however systematically lower than those observed due to the difference at the reference temperature, 25°C.

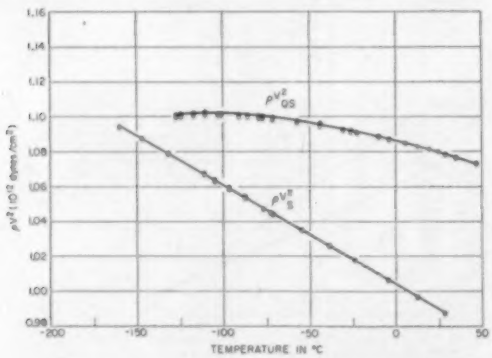

FIG. 12. Temperature dependence of pure shear mode stiffness (ρV_s^2) and quasi-shear mode stiffness (ρV_{QS}^2) in crystal *D*. Solid circles are measured; open circles were computed as described in Sec. 4.6.

The moduli c_{11}, c_{22}, and c_{33} can also be checked indirectly through the relations between the quasi-longitudinal and quasi-shear mode stiffnesses in the rotated orientations. From the equations for ρV^2 given in Table II one gets, for example, for crystal *D*,

$$\rho V_{QS}^2 = c_{33}\cos^2\theta_D + c_{11}\sin^2\theta_D + c_{55} - \rho V_{QL}^2. \quad (12)$$

Inserting the previously obtained values of c_{33}, c_{11}, and

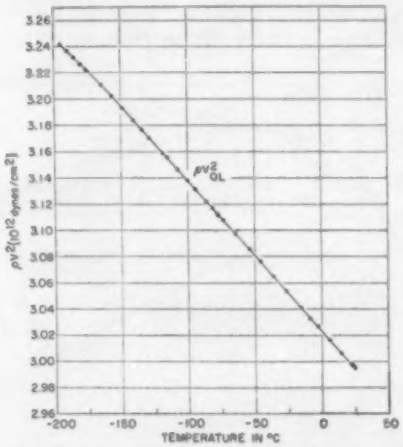

FIG. 13. Temperature dependence of quasi-longitudinal mode stiffness in crystal *E*.

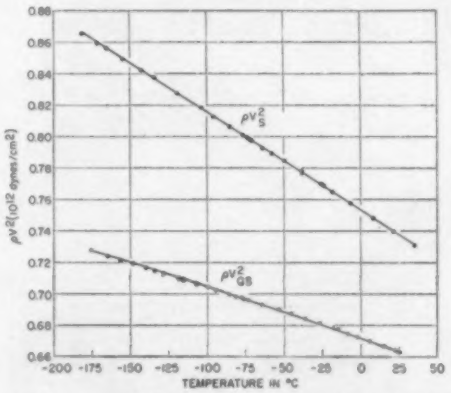

FIG. 14. Temperature dependence of pure shear mode stiffness (ρV_s^2) and quasi-shear mode stiffness (ρV_{QS}^2) in crystal *E*. Solid circles are measured; open circles were computed as described in Sec. 4.6.

c_{55} one can then compute ρV_{QS}^2 from the measured value of ρV_{QL}^2 and the appropriate θ_D. The computed ρV_{QS}^2 for each quasi-shear mode are given as the open circles in Figs. 12, 14, and 15. In all cases the agreement between measured and computed ρV_{QS}^2 is quite good considering the possibility of large deviations through the propagation of errors in the computed value. Of

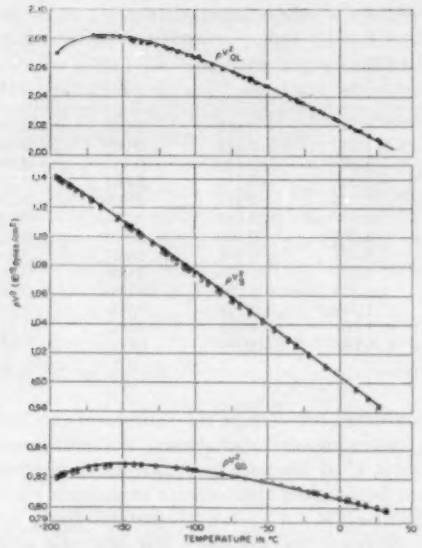

FIG. 15. Temperature dependence of quasi-longitudinal mode stiffness (ρV_{QL}^2), pure-shear mode stiffness (ρV_s^2) and quasi-shear mode stiffness (ρV_{QS}^2) in crystal F. Solid circles are measured; open circles were computed as described in Sec. 4.6.

special interest here are the pecularities in the curves obtained from crystals D and F which reflect the anomalous temperature dependence of c_{11}. Verification of this anomaly through independent measurements in 3 different crystals is indeed of interest. The explicit expressions for c_{11} from crystals D and F are as follows

$$c_{11}=[\rho(V_{QS}^2+V_{QL}^2)_D-(c_{55}+c_{33}\cos^2\theta_D)]/\sin^2\theta_D \quad (13)$$

$$c_{11}=[\rho(V_{QS}^2+V_{QL}^2)_F-(c_{66}+c_{22}\sin^2\theta_F)]/\cos^2\theta_F. \quad (14)$$

One can of course derive a complete set of diagonal moduli from the measurements on the rotated orienta-

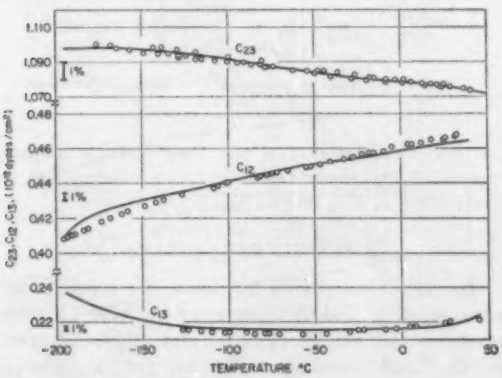

FIG. 16. Temperature dependence of cross-coupling moduli. Solid lines are polynomials (Table III) fitted to c_{ij} from quasi-longitudinal data. Open circles are c_{ij} computed from quasi-shear mode stiffnesses.

TABLE IV. Moduli-temperature coefficients derived from best-fit polynomials. $R=(1/c_{ij})(dc_{ij}/dT)$.

Modulus	Temperature °C	R in ppm/°C
c_{11}	−165	+812.9
···	−17.2	0
···	25	−56.9
···	200	−188.7
c_{22}	25	−250.8
c_{33}	25	−377.8
c_{44}	25	−557.9
c_{55}	25	−1063.5
c_{66}	25	−622.8
c_{12}	25	+326.9
c_{13}	−165	−1283.6
···	−50	0
···	25	+629.5
c_{23}	25	−123.2

tions by simultaneous solution of all the ρV^2 relations, as shown in footnote reference 1. In view of the normal behavior with temperature of the other diagonal moduli, however, it seems adequate to compute c_{11} by itself using previously measured values for the other variables. Table V gives a comparison of the c_{11} values at various temperatures as computed from ρV_1^2 and from Eqs. 13 and 14. All 3 sets of data indicate the same type of anomaly. The largest deviations, about 0.25%, occur in the temperature range of −180° to −160°C.

5. ESTIMATE OF PROBABLE ERRORS

The question of probable errors has been considered in some detail in footnote reference 1, where the uncertainties for the 25°C values of moduli are listed. These values have been used as the basis for the present measurements. To estimate the probable errors at other temperatures it would appear sufficient, then, to estimate uncertainties at the lowest temperature measured, i.e., −195°C.

For longitudinal waves, the maximum probable error

TABLE V. Comparison of c_{11} as computed from direct and indirect measurements.

Temperature °C	ρV_1^2 $\times 10^{-12}$ d/cm²	$(c_{11})_F$[a] $\times 10^{-12}$ d/cm²	$(c_{11})_D$[b] $\times 10^{-12}$ d/cm²
46.5	2.1448	···	2.1463
13.0	2.1493	···	2.1486
0.2	2.1502	2.1482	···
−9.5	2.1505	2.1496	2.1510
−15.6	2.1506	2.1502	···
−18.0	2.1506	2.1494	···
−22.0	2.1506	2.1499	2.1512
−25.0	2.1505	···	2.1506
−32.5	2.1503	2.1503	···
−52.2	2.1487	2.1492	···
−71.0	2.1459	···	2.1478
−127.0	2.1240	2.1261	2.1264
−168.6	2.0754	2.0800	···
−181.3	2.0486	2.0534	···
−195.8	2.0072	2.0092	···

[a] Obtained from Eq. (14).
[b] Obtained from Eq. (13).

TABLE VI. Compliance moduli for alpha uranium computed at various temperatures.

Temperature °C	Modulus in units of 10^{-12} cm²/d								
	s_{11}	s_{22}	s_{33}	s_{44}	s_{55}	s_{66}	s_{12}	s_{13}	s_{23}
25	0.491	0.673	0.479	0.804	1.362	1.346	−0.118	0.008	−0.261
20	0.490	0.671	0.478	0.801	1.355	1.342	−0.118	0.008	−0.260
0	0.489	0.666	0.473	0.792	1.328	1.326	−0.116	0.007	−0.257
−20	0.488	0.660	0.468	0.783	1.303	1.310	−0.114	0.007	−0.254
−40	0.488	0.655	0.464	0.775	1.279	1.295	−0.113	0.006	−0.250
−60	0.488	0.650	0.460	0.767	1.256	1.280	−0.111	0.006	−0.248
−80	0.489	0.646	0.456	0.759	1.233	1.266	−0.109	0.005	−0.245
−100	0.490	0.641	0.453	0.751	1.211	1.251	−0.108	0.004	−0.242
−120	0.491	0.637	0.449	0.743	1.190	1.237	−0.106	0.003	−0.240
−140	0.494	0.632	0.446	0.735	1.170	1.223	−0.105	0.002	−0.237
−160	0.500	0.627	0.442	0.728	1.151	1.210	−0.104	0.001	−0.234
−180	0.509	0.622	0.438	0.720	1.133	1.197	−0.102	−0.002	−0.231
−195	0.518	0.617	0.436	0.716	1.120	1.188	−0.099	−0.005	−0.228

in ratio r of Eq. (4) should be no more than 0.05% on the basis of the following considerations: (1) a possible 0.02% error in frequency measurements relative to the 25°C value, (2) a 0.02% error due to the approximate nature of the calculation for γ, and (3) a 0.04% error as a result of variable positioning of the specimen on the end of the buffer rod.

From Bridge's[3] data it would appear that the ratio l/l_0 might be in error by as much as 0.05%, allowing 10% uncertainty in the total variation of dimensions along either [100] or [001]. For [010], the expansitivity is quite small so that errors in l/l_0 for this direction would be less than 0.01%. Thus the maximum *probable* error in the quantity $r \cdot l/l_0$ is 0.07%. This figure should apply with sufficient accuracy to the rotated cuts also. Combining this with the previously calculated error for V_0 of 0.07% (see footnote reference 1), the final estimated probable error in V at −195°C is 0.1%. The probable error in density at −195°C (relative to 25° value) is given by $(0.05^2+0.05^2+0.01^2)^{\frac{1}{2}}=0.07\%$ so that the error in ρV^2 is only slightly over 0.2% for longitudinal waves. This is also the probable error for c_{11}, c_{22}, and c_{33}.

For shear waves, the effect of neglecting the phase shift for waves reflected at the transducer can be computed from a knowledge of the seal material properties (Appendix C of footnote reference 4). Unfortunately this can be only an approximate evaluation since the seal thickness is not known accurately. Using typical values, however, one obtains a possible error of 0.1% in r due to neglecting the change of phase shift with temperature, so that the error in ρV^2 is 0.3% (again considering other errors involved). This is also the value for the probable error in the diagonal shear moduli.

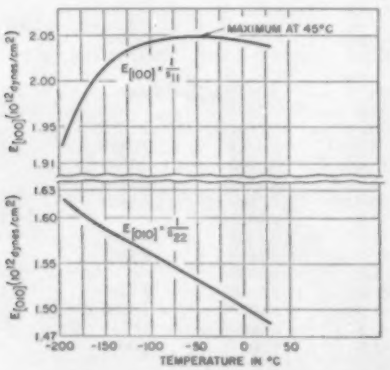

FIG. 17. Temperature dependence of Young's moduli in [100] and [010] directions.

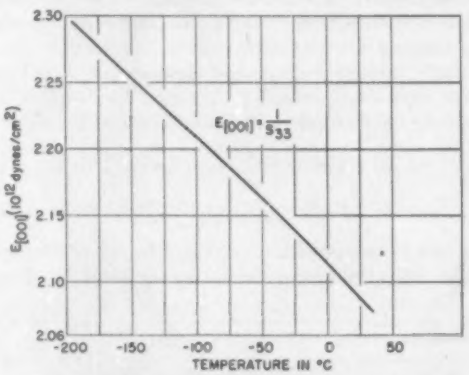

FIG. 18. Temperature dependence of Young's moduli in [001] direction.

Using the above results, and those listed in footnote reference 1, the uncertainties in c_{12}, c_{13}, and c_{23} are, respectively 1%, 3%, and 0.7%.

6. ELASTIC PARAMETERS

The elastic compliance moduli s_{ij} for temperatures between −195° and 35°C are given in Table VI. Computed Young's moduli E, linear and volume compressibilities, and Poisson's ratios for the 3 principal directions are plotted in Figs. 17–20. The temperature dependences of the Young's moduli are very similar to the corresponding stiffness moduli. The maximum in E_{100}

is however at a lower temperature (−45°C) than that of the maximum c_{11}. The anomalous behavior of elasticity in the [100] direction is further indicated in the linear compressibilities, which for [100] decreases significantly with increasing temperature. Although the compressibilities in [010] and [001] are normal in temperature dependence the anomaly in [100] predominates in the net sum to give an anomalous minimum volume compressibility at approximately −100°C.

The computed Poisson's ratios σ_{12}, σ_{21}, σ_{23}, and σ_{32} show normal temperature dependences. The [100]-[001] coupling is anomalous in that it decreases from −195°C and changes sign at approximately −160°C; however, the curvature of the plot indicates a normal temperature dependence above 35°C.

7. DISCUSSION

The abnormal features of the above results can be summarized as follows:

(a) dc_{11}/dT is both positive and negative in a temperature range for which no structural phase change occurs and is greatest in magnitude at the lowest temperature of measurement.

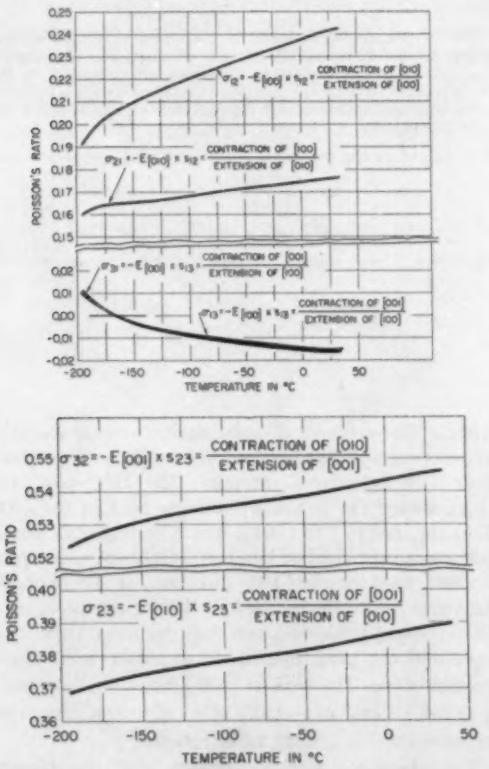
POISSON'S RATIO
TEMPERATURE IN °C
σ12 = -E[100] × S12 = CONTRACTION OF [010] / EXTENSION OF [100]
σ21 = -E[010] × S12 = CONTRACTION OF [100] / EXTENSION OF [010]
σ13 = -E[100] × S13 = CONTRACTION OF [001] / EXTENSION OF [100]
σ31 = -E[100] × S13 = CONTRACTION OF [001] / EXTENSION OF [100]
σ32 = -E[001] × S23 = CONTRACTION OF [010] / EXTENSION OF [001]
σ23 = -E[010] × S23 = CONTRACTION OF [001] / EXTENSION OF [010]

FIG. 19. Temperature dependence of Poisson's ratios pertaining to direction indicated. (σ_{ij} = contraction of j direction/extension of i direction, for tensile stress in i direction).

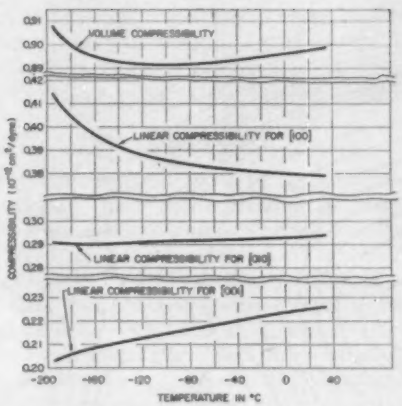

FIG. 20. Temperature dependence of adiabatic linear and volume compressibilities.

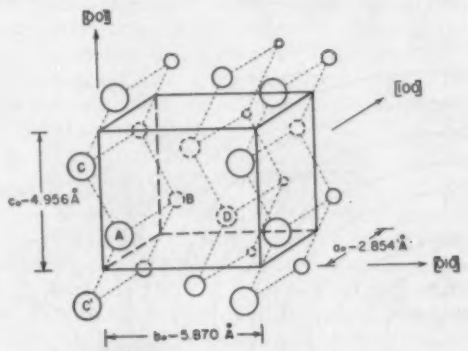

FIG. 21. Atomic arrangement in alpha-uranium crystal at 25°C. Orthorhombic unit cell indicated by solid lines.

(b) the computed Young's modulus E_{100} also goes through a maximum and the linear adiabatic compressibility for the [100] direction increases with decreasing temperature, below 35°C.

(c) the abnormal compressibility in the [100] direction causes an inversion in the temperature dependence of the bulk modulus at −100°C.

(d) Poisson ratios σ_{13} and σ_{31} are normal in algebraic sign at low temperatures but decrease with increasing temperature to negative values between −160° and +35°C.

There are two notable observations which can be made regarding the abnormalities: (1) the curvatures of the various plots indicate that the abnormalities in algebraic sign of the slopes are restricted to temperatures below +100°C, (2) all of the features mentioned above are related to the (010) crystallographic plane. The latter observation is apparently connected with the pecularities in the atom arrangement in the alpha-uranium structure shown in the schematic sketch in Fig. 21. Each atom (represented by the origin A) has

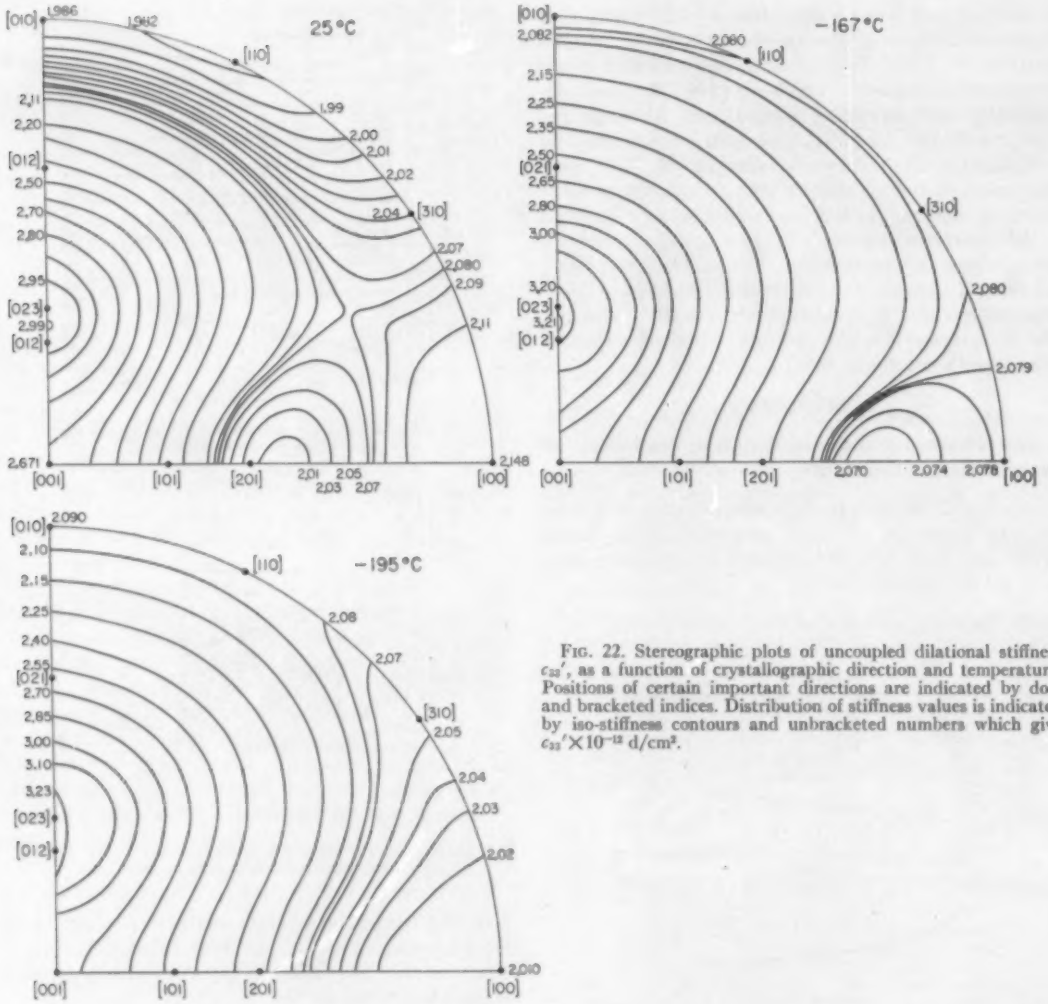

FIG. 22. Stereographic plots of uncoupled dilational stiffness c_{33}', as a function of crystallographic direction and temperature. Positions of certain important directions are indicated by dots and bracketed indices. Distribution of stiffness values is indicated by iso-stiffness contours and unbracketed numbers which give $c_{33}' \times 10^{-12}$ d/cm².

2 nearest neighbors, C and C' in directions 27° from [001] in the (100) plane at distances of 2.75 A. Two next nearest neighbors are along the [100] direction, represented by B in the figure, at slightly larger distances of 2.85 A. These 4 atoms form corrugated sheets spaced in the [010] direction with relatively wide separation, the third nearest neighbor D being 3.25 A away. Because of this loose-packing arrangement it is generally suggested that the 4 bonds of the AC and AB type are similar and of strongly directed covalent character.[6] This further suggests that the force constants associated with these 4 bonds would predominate in determining the anisotropy of the elastic stiffnesses. This appears to be indeed the case at intermediate temperatures as is shown, for example, from plotting the dilational stiffness c_{33}' (for a roving Z' axis) against crystal direction on a stereographic projection. Figure 22 contains 3 such plots with isostiffness contours. The 25°C plot, Fig. 22(a), shown the dominant stiffness peak in the (100) plane inclined 37° to [001], which corresponds closely to the nearest neighbor bond AC. Only one other peak is found, that for the [100] direction, or AB bond. As the temperature decreases to −195°C the position of the dominant peak does not vary by more than 1° in angle and the peak magnitude increases with almost constant slope. The peak at [100], however, disappears at −164°C, and at −195°C this direction represents the minimum c_{33}' among all directions.

The above correlation suggests that the binding energies involved in the AC and AB type bonds are not equivalent, at least in the range of temperatures below

[6] J. Freidel, J. Phys. Chem. Solids, **1**, 175 (1956).

25°C, and the difference in character of the binding-energy components increases with decreasing temperature. Since the interatomic distances A to C and A to B are so nearly alike the above conclusion implies that the elastic interactions in the crystal deviated widely from central forces at low temperatures but the deviation decreases with increasing temperature. Since neither specific heat[7] nor crystal-structure data[2] indicate well-defined transformations in the temperature range of the elasticity anomalies it would appear that the decrease in stiffness of the AB bond with temperature is associated with a broad transition in binding energies due to interactions between valence electrons spaced in the [100] direction. The present data added to the indicated low-temperature thermal expansion[2] anomaly in [100] would suggest that either the band structure is radically temperature dependent or that d electron-spin ordering occurs due to lattice contraction below 0°C. In this respect two papers have appeared which indicate that magnetic transitions may occur in the region of −100°C. Mallard observed a definite minimum at about −100°C in the magnetic susceptibility of a number of uranium specimens.[8] Bates and Leach show a relatively sharp and unusual increase in susceptibility on cooling below −75°C.[9] However, the authors of these works attribute the unusual data to a proposed dispersed UH_3 phase which is reported to be ferromagnetic below −100°C.[9] Consequently, a definite positive relation between the elastic and magnetic properties cannot be claimed at present. A careful study of the low-temperature magnetic properties in high-purity polycrystalline and single-crystal uranium is planned to resolve this question. Low-temperature thermal expansion data to verify the reported anomaly in the [100] direction would also be of interest in this respect.

[7] W. M. Jones, J. Gordon, and E. A. Long, J. Chem. Phys. **20**, 695 (1952).
[8] L. F. Bates and D. Hughes, Proc. Phys. Soc. (London) **B67**, 28 (1954).
[9] L. F. Bates and S. J. Leach, Proc. Phys. Soc. (London) **B69**, 997 (1956).

8. SUMMARY

The 9 elastic-stiffness moduli for alpha uranium have been computed over various temperature ranges from ultrasonic-wave velocity measurements. The data give c_{11}, c_{22}, and c_{33} over the range −195° to +300°C and the remaining moduli between −195° and +35°C. Extra data were obtained for cross checking all of the moduli between −195° and 35°C. The results show a marked weakening of the stiffness in the [100] direction as the temperature is decreased, which is attributed to abnormal changes in the second nearest-neighbor bond. The binding-force change is apparently related to a broad transition in valence electron energy states since specific-heat data show no anomalous peaks in the low-temperature range. Existing data on magnetic susceptibility indicates that a magnetic transition does exist at low temperatures; however, further magnetic measurements are necessary to establish the existence and nature of the transition.

9. ACKNOWLEDGMENTS

Part of this work was carried out under the auspices of the U. S. Atomic Energy Commission. The authors gratefully acknowledge the assistance of the following: T. B. Bateman (B. T. L.) for much of the data, C. Harrison (A. N. L.) for computer programming, R. E. Black (A. N. L.) for assistance in specimen preparation, Dr. D. O. Van Ostenburg (A. N. L.) for helpful discussions regarding interpretation, and L. T. Lloyd (A. N. L.) for criticism of the manuscript.

Photovoltaic Effect Derived from the Carnot Cycle

A. Rose
RCA Laboratories, Princeton, New Jersey
(Received January 25, 1960; and in final form June 10, 1960)

An expression for the maximum power derivable from any photovoltaic device is developed in terms of the incident light intensity measured in units of black body radiation. The expression shows the linear dependence of photovoltage on light intensity at low light levels, the logarithmic dependence at intermediate light levels and the saturation at high light levels. The analysis is used to resolve a paradox proposed by W. Shockley.

I. INTRODUCTION

THE following analysis was provoked in part by a paradox proposed by W. Shockley[1] and sketched in Fig. 1. A p-n junction has a forward bias of 0.1 v applied to it giving a forward current I. The forward current is a radiative recombination current such that the emitted photon stream of energy is $(h\nu/e)I$ where $h\nu$ is about 1.0 ev. The photon stream is allowed to fall on a photocathode of near-zero work function and gives rise to a photovoltaic effect such that the photocell can be considered as a battery capable of delivering a current I at a voltage close to 1.0 ev. The photovoltaic battery is then used to drive the p-n junction in the forward direction. The result is a perpetual motion device and a violation of the second law of thermodynamics. The first law (conservation of energy) is not violated since the difference in power between the one watt delivered by the photocell and the one-tenth watt supplied by the first battery is derived from the cooling of the junction. The second law is violated because heat is removed from the junction at or near room temperature to develop power in the photocell at or near room temperature.

The following analysis[2] resolves the paradox by showing that the photon stream radiated by the p-n junction can at most cause any photovoltaic device to deliver only as much power as is being delivered to the p-n junction, namely, a current of I at a potential of 0.1 v in the foregoing example.

II. ANALYSIS

Let radiation $L(\nu)$ be incident on a device uniformly from all directions. $L(\nu)$ is dimensionless and equal to the ratio of the incident light flux of frequency ν, per cm^2, per unit ν, to the corresponding blackbody radiation at the operating temperature T_1 of the device. One can then define a temperature T_2 characteristic of the added incident radiation by the relation

$$L(\nu)=f(T_2,\nu)/f(T_1,\nu), \tag{1}$$

where $f(T,\nu)=\text{const}/e^{(h\nu/kT)}-1$. The constant is $2\pi\nu^2/C^2$ and cancels out in the ratio.

The useful power that can be generated by the flux $L(\nu)$ is, by the Carnot-cycle argument,

$$P=\frac{Q}{t}\frac{T_2-T_1}{T_2}=[L(\nu)-1]f(T_1)h\nu\frac{T_2-T_1}{T_2}A\Delta\nu. \tag{2}$$

A is the useful area of the device, $\Delta\nu$ the frequency range of the incident radiation, and Q/t the net heat flux. If P is taken to be electrical power VI and *if the output current of electrons I/e is equal to the input stream of photons*, $[L(\nu)-1]f(T_1)A\Delta\nu$, then the maximum output photovoltage V is given from (2) by

$$eV=h\nu[(T_2-T_1)/T_2]. \tag{3}$$

From (1),

$$\frac{T_2-T_1}{T_2}=1-\frac{kT_1}{h\nu}[\ln(e^{h\nu/kT_1}-1+L(\nu))-\ln L(\nu)]$$

and (3) becomes

$$V=\frac{h\nu}{e}\left\{1-\frac{kT_1}{h\nu}[\ln(e^{h\nu/kT_1}-1+L(\nu))-\ln L(\nu)]\right\}. \tag{4}$$

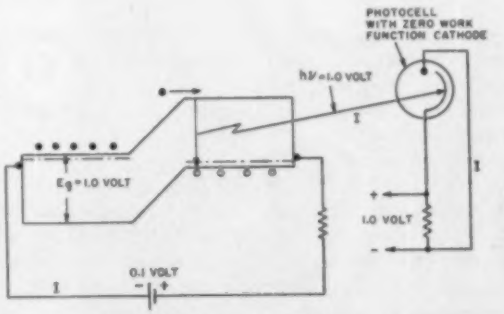

FIG. 1. Shockley paradox: A forward bias of 0.1 v on a p-n junction gives rise to a forward current I. A current I of 1.0-v photons is radiated by the p-n junction and falls on a photocell of near-zero work function giving rise to a current I of 1.0-v electrons. The photocell can be connected back into the p-n junction circuit to produce a self-sustaining source of light.

[1] A.A.A.S. meeting in Philadelphia, 1951.

[2] For a more restricted derivation of the photovoltaic effect from thermodynamic reasoning, see H. A. Müser, Z. Physik 148, 380 (1957). Müser assigns an elevated temperature to the excess carrier concentration rather than to the excess incident radiation.

III. DISCUSSION

Equation (4) gives the *maximum* photovoltage that can be obtained from any device for the light level $L(\nu)$, ambient temperature T_1 and the assumption that the output current of *electrons* is equal to the input current of *photons*. If one allows the output current of electrons to be θ times the input current of photons, then the output voltage becomes

$$V = V_1/\theta,$$

where V_1 is given by Eq. (4). In this way, the maximum output work called for by the Carnot cycle is maintained.

Low and Intermediate Light Range

For $1 \lesssim L(\nu) \ll e^{h\nu/kT_1}$, Eq. (4) reduces to the familiar form[2]

$$V = (kT_1/e)\ln L(\nu). \tag{5}$$

At low lights, namely, $1 \leq L(\nu) < 2$, Eq. (5) takes on the well-known linear form

$$V = (kT_1/e)[L(\nu) - 1]. \tag{6}$$

The virtue of Eqs. (5) and (6) is that the photovoltage is given in terms of an *absolute measure* of light intensity $L(\nu)$, that is, in units of blackbody radiation at T_1. Equation (5) gives the maximum photovoltage (subject to the assumption: output current of electrons equals input current of photons) that can be achieved by *any* device. The output voltage of an actual device like a *p-n* junction photovoltaic cell has the same form as Eqs. (5) and (6), but the light intensity required for a given voltage is shifted to higher light values (see Fig. 2). A *p-n* junction photocell would tend to match Eq. (5) if all of its recombinations across the forbidden zone were radiative, free-free recombinations and if the incident stream of photons within a range of kT of the forbidden gap were L times as large as the stream of blackbody (T_1) photons in the same range of energy.

High Light Range

For $L(\nu) \gg 2\exp(h\nu/kT_1)$, Eq. (4) reduces to

$$V = (h\nu/e) - (kT_1/e)[e^{h\nu/kT_1}/L(\nu)] \tag{7}$$

showing the approach to the saturation voltage $h\nu/e$. The minimum light intensity required for saturation according to Eq. (7) is given by

$$L(\nu) \approx e^{h\nu/kT_1}. \tag{8}$$

[2] Note that the incident (added) radiation is zero when $L(\nu) = 1$.

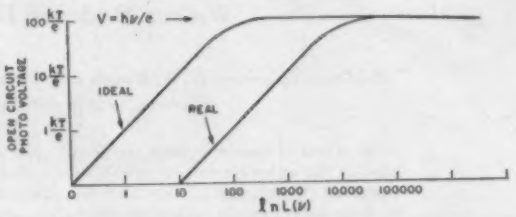

FIG. 2. Plot showing that a real photovoltaic device requires more light (by a constant factor) to produce a given voltage than the ideal device.

Numerical Example

What density of incident photons whose $h\nu$ is within kT of the forbidden gap of germanium is required to produce a photovoltage of kT/e at room temperature?

From Eq. (5), the photovoltage kT/e is achieved for $L(\nu) \approx 2$, that is, when the added density of photons is equal to the blackbody (T_1) density of photons.

The number of photons incident on a surface per square centimeter per second is

$$(2\pi\nu^2/c^2)(e^{h\nu/kT} - 1)^{-1}d\nu. \tag{9}$$

If $h\nu$ is taken equal to the forbidden gap of germanium, 0.7 v, and if $hd\nu = kT_1$, Eq. (9) gives

$$10^9 \text{ photons/cm}^2$$

or about 10^{-6} ft-c of 2600° incandescent light or about 10^{-5} ft-c of daylight. It is assumed in this computation that the photons of $h\nu > 0.7$ v have the same effect as those at 0.7 v.

Actual germanium photovoltaic cells require about 10^{13} photons/cm^2 for an output voltage of kT/e. This is to be compared with 10^9 photons/cm^2 for an ideal device.

Application to Shockley Paradox

The stream of photons emitted by the 0.1-v forward bias on the *p-n* junction in Fig. 1 can at most exceed the ambient radiation at $h\nu = 1.0$ v by the factor $\exp(e\Delta V/kT)$, where $\Delta V = 0.1$ v. Consequently, the intensity of radiation emitted is $L(\nu) = \exp(e\Delta V/kT)$. Insertion of this value of $L(\nu)$ into Eq. (5) gives

$$V = 0.1 \text{ v}.$$

The photocell, cannot, therefore, deliver a one volt current but only a 0.1-v current and no violation of the second law of thermodynamics is incurred.

ACKNOWLEDGMENT

I am grateful to D. O. North and E. G. Ramberg for a number of clarifying discussions on the subject of this paper.

Walker Modes in Large Ferrite Samples*

B. A. AULD
Microwave Laboratory, W. W. Hansen Laboratories of Physics, Stanford University, Stanford, California
(Received April 18, 1960; and in final form May 23, 1960)

The modes of resonance for a ferrite strip and a ferrite post resonator between conducting planes are found by taking appropriate combinations of uniform plane-wave solutions. It is shown that magnetostatic resonances (Walker modes) may exist even when the resonator dimensions are arbitrarily large, provided the mode indices satisfy certain restrictions.

I. INTRODUCTION

IT appears to be commonly believed that the size-independent resonances characteristic of Walker[1] modes may occur only in ferrite samples which are small compared with the free-space wavelength. This is not the case. In fact such resonances may exist in arbitrarily large samples. A convenient way of demonstrating this is by constructing the resonant modes from combinations of plane-wave solutions. This approach has the advantage of bringing out very graphically the interrelation between electromagnetic, magnetostatic, and exchange phenomena in ferrites.

II. PLANE WAVES IN AN UNBOUNDED REGION

The small-signal phenomenological theory of a lossless ferrite medium is based on Maxwell's equations,

$$\nabla\times\mathbf{h}-\epsilon(\partial/\partial t)\mathbf{e}=0 \quad \nabla\cdot(\mathbf{h}+\mathbf{m})=0$$
$$\nabla\times\mathbf{e}+\mu_0(\partial/\partial t)(\mathbf{h}+\mathbf{m})=0 \qquad \nabla\cdot\epsilon\mathbf{e}=0, \tag{1}$$

and the linearized equation of motion,

$$\partial\mathbf{m}/\partial t=\mathbf{z}\times(\omega_M\mathbf{h}-\omega_0\mathbf{m}+\omega_{ex}\ell^2\nabla^2\mathbf{m}), \tag{2}$$

where the dc bias field H_0 is in the positive z direction and

$$\omega_0=-\gamma\mu_0H_0,$$
$$\omega_M=-\gamma\mu_0M_s,$$

and

$$\omega_{ex}=-\gamma\mu_0H_{ex}.$$

If a plane-wave solution of the form $\epsilon^{j(\omega t-\mathbf{k}\cdot\mathbf{r})}$ is assumed, (2) is easily solved for $\mathbf{m}$ in terms of $\mathbf{h}$, leading to a "permeability tensor" for the medium,

$$\mathfrak{T}=\begin{bmatrix}\mu & j\kappa & 0\\ -j\kappa & \mu & 0\\ 0 & 0 & 1\end{bmatrix},$$

$$\mu=\mu_0+(\omega_M\omega_r/\omega_r^2-\omega^2), \tag{3}$$

$$\kappa=(\omega_M\omega/\omega_r^2-\omega^2),$$

where

$$\omega_r=\omega_0+\omega_{ex}\ell^2k^2. \tag{4}$$

This tensor is equivalent in form to Polder's permeability tensor,[2] but with ω_0 replaced by ω_r from (4). Maxwell's equations may now be written

$$\nabla\times\mathbf{h}-j\omega\epsilon\mathbf{e}=0 \quad \nabla\cdot(\mathfrak{T}\cdot\mathbf{h})=0$$
$$\nabla\times\mathbf{e}+j\omega\mu_0\mathfrak{T}\cdot\mathbf{h}=0 \qquad \nabla\cdot\epsilon\mathbf{e}=0. \tag{5}$$

Solutions to (5), neglecting exchange ($\omega_{ex}=0$), have been discussed by Polder[2] and Seidel.[3] For a wave propagating in the yz plane at an angle θ with the z axis, the dispersion relation is

$$\frac{k^2}{k_f^2}=\frac{(\mu^2-\mu-\kappa^2)\sin^2\theta+2\mu\pm\{(\mu^2-\mu-\kappa^2)^2\sin^4\theta+4\kappa^2\cos^2\theta\}^{\frac{1}{2}}}{2[(\mu-1)\sin^2\theta+1]}, \tag{6}$$

where $k_f=\omega(\mu_0\epsilon)^{\frac{1}{2}}$, and the corresponding electric and magnetic fields are

$$\mathbf{e}=-\left(\frac{k_f}{k}\right)\left(\frac{\mu_0}{\epsilon}\right)^{\frac{1}{2}}\begin{bmatrix}\dfrac{[\mu(k_f/k)^2-1]}{\kappa} & \dfrac{\cos\theta}{\sin^2\theta-(k_f/k)^2}\\ & \cos\theta\\ & -\sin\theta\end{bmatrix}\epsilon^{-j\mathbf{k}\cdot\mathbf{r}} \tag{7a}$$

* The research reported in this paper has been sponsored by the Electronics Research Directorate of the Air Force Cambridge Research Center, Air Research and Development Command, under contract to the U. S. Air Force.

[1] L. R. Walker, Phys. Rev. **105**, 390 (1957).
[2] D. Polder, Phil. Mag. **40**, 99 (1949).
[3] H. Seidel, Bell System Tech. J. **36**, 409 (1957).

and

$$\mathbf{h}=\begin{bmatrix} (k_f/k)^2 \\ (j/\kappa)[\mu(k_f/k)^2-1] \\ \dfrac{\mu(k_f/k)^2-1}{\kappa} \quad \dfrac{\cos\theta\sin\theta}{\sin^2\theta-(k_f/k)^2} \end{bmatrix} \epsilon^{-j\mathbf{k}\cdot\mathbf{r}}. \tag{7b}$$

According to (3) and (4), these results will apply when exchange torque is included, provided ω_0 is replaced by $\omega_0+\omega_{ex}\ell^2k^2$. Equation (6) then defines a manifold of dispersion curves bounded by the curves $\theta=0°$ and $\theta=90°$ shown in Fig. 1. At each value of θ the medium supports two types of wave, an ordinary wave for which $k/k_f\approx 1$ and an extraordinary wave for which k/k_f becomes very large at certain frequencies. As shown in the figure, the inclusion of exchange torque causes the lower branches of the extraordinary curves to bend upward for large values of k/k_f.

The lower branches of the extraordinary curves in Fig. 1 may conveniently be divided into three regions.

(a) $k/k_f\approx 1$. Here the electric and magnetic fields of (7) are of comparable magnitude. This may be termed the region of electromagnetic propagation.

(b) $1\ll k/k_f\ll\omega_0/(\omega_{ex}\ell^2k_f^2)$. From (7) the electric field is negligibly small in this region compared with the magnetic field

$$\mathbf{h}=\begin{bmatrix} 0 \\ -j/\kappa \\ -(j\cot\theta)/\kappa \end{bmatrix} \epsilon^{-j\mathbf{k}\cdot\mathbf{r}}, \tag{8}$$

where terms $(k_f/k)^2$ have been neglected. It is easily shown that the magnetic field (8) satisfies the magnetostatic equations,

$$\nabla\times\mathbf{h}=0 \quad \nabla\cdot(\mathfrak{T}\cdot\mathbf{h})=0. \tag{9}$$

This may, therefore, be termed the region of magnetic propagation. It corresponds to the very flat portions of the dispersion curves, where the frequency is

$$\omega^2=\omega_0(\omega_0+\omega_M\sin^2\theta). \tag{10}$$

These waves are therefore characterized by a low-phase velocity and a negligibly small group velocity. Magnetostatic plane waves may, of course, also be obtained directly from Walker's analysis. Such an approach would not, however, furnish information about the range of validity of the solutions.

(c) $\omega_0/(\omega_{ex}\ell^2k_f^2)\ll k/k_f$. Here the magnetic field is again given by (8). However, the exchange term now has a significant effect on the shape of the dispersion curves which bend upward into the familiar exchange spin-wave manifold,

$$\omega^2=(\omega_0+\omega_{ex}\ell^2k^2)(\omega_0+\omega_M\sin^2\theta+\omega_{ex}\ell^2k^2). \tag{11}$$

This may then be termed the region of exchange propagation.[4] These regions are, of course, not sharply defined, since the propagation characteristics vary continuously with k/k_f.

III. RESONANCES IN A STRIP BETWEEN CONDUCTING PLANES

Consider now the y-directed modes of propagation for a ferrite slab of thickness b between conducting planes, with the dc field normal to the slab. These may be developed by the well-known technique of taking combinations of uniform plane waves which satisfy the boundary conditions. In this case it is easily shown that the proper combinations are obtained by taking waves propagating at angles θ and $\pi-\theta$, where

$$k\cos\theta=m\pi/b \tag{12}$$

and m is any positive integer. The mode fields are then

$$\mathbf{e}=\left(\frac{\mu_0}{\epsilon}\right)^{\frac{1}{2}}\frac{k_f}{k}\begin{bmatrix} -\dfrac{[\mu(k_f/k)^2-1]}{\kappa}\dfrac{\cos\theta\sin(m\pi z/b)}{\sin^2\theta-(k_f/k)^2} \\ j\cos\theta\sin(m\pi z/b) \\ \pm\sin\theta\cos(m\pi z/b) \end{bmatrix} \epsilon^{\mp j(m\pi/b)y\tan\theta},$$

$$\mathbf{h}=\begin{bmatrix} (k_f/k)^2\cos(m\pi z/b) \\ j/\kappa[\mu(k_f/k)^2-1]\cos(m\pi z/b) \\ \pm\dfrac{[\mu(k_f/k)^2-1]}{\kappa}\dfrac{\cos\theta\sin\theta\sin(m\pi z/b)}{\sin^2\theta-(k_f/k)^2} \end{bmatrix} \epsilon^{\mp j(m\pi/b)y\tan\theta}, \tag{13}$$

[4] The merging of the electromagnetic wave and exchange spin-wave dispersion curves has also been described by J. Smit and H. P. J. Wijn, *Ferrites* (John Wiley & Sons, Inc., New York, 1959).

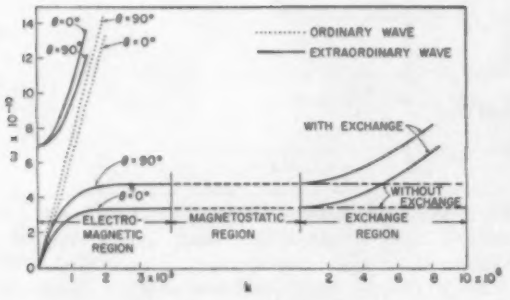

FIG. 1. Dispersion curves for uniform plane waves in an unbounded ferrite medium ($H_{dc}=1750$ oe, $4\pi M_s=1750$ oe). Note the change of scale on the horizontal axis (k in meters^{-1}).

where $0\leq\theta\leq\pi/2$. As in the case of uniform plane waves these modes may be categorized as ordinary or extraordinary according to the character of the plane wave constituents, with the extraordinary waves exhibiting regions of electromagnetic and magnetostatic propagation.[6] From the magnetostatic conditions

$$1\ll k/k_f\ll\omega_0/\omega_{ex}\ell^2k_f^2$$

and (12), the magnetostatic region of propagation is defined by

$$1\ll m\pi/k_fb\cos\theta\ll\omega_0/\omega_{ex}\ell^2k_f^2, \tag{14}$$

where θ is related to the frequency by (10). In this region the electric field in (13) is negligibly small compared with the magnetic field

$$\mathbf{h}=\begin{bmatrix}0\\ -j/\kappa[\cos(m\pi z/b)]\\ \mp(\cot\theta/\kappa)\sin(m\pi z/b)\end{bmatrix}\epsilon^{\mp j(m\pi/b)y\tan\theta}, \tag{15}$$

which satisfies the magnetostatic equations (9).

Propagation of the magnetostatic modes (15) occurs even for very small values of b, provided (14) is satisfied. This is, of course, the phenomenon of anomalous propagation described by Seidel.[6] The spacing b cannot, however, be arbitrarily small, since the analysis breaks down when the upper limit of (14) is exceeded, and exchange boundary conditions must then be considered. Magnetostatic modes of propagation for this structure have also been discussed by Damon and Eshbach,[7] following Walker's analysis, in the case of *thin* slabs. It has been shown here that these modes may exist even in slabs of arbitrary thickness, provided the mode index m is sufficiently large to satisfy (14).

The resonances of a ferrite strip between conducting planes (Fig. 2) may now be found, assuming a uniform dc field within the strip, by setting up the fields (13) inside the strip and matching to appropriate fields outside the strip. In the general case the algebraic details are somewhat complicated because the boundary conditions can be satisfied only by taking both ordinary and extraordinary waves inside the strip, and both *TE* and *TM* waves outside the strip. The discussion will therefore be confined to the case,

$$\cos\theta\ll m\pi/k_fb\ll\omega_0\cos\theta/\omega_{ex}\ell^2k_f^2. \tag{16}$$

This restriction guarantees that the extraordinary waves inside the strip are in the magnetostatic region (14), and that the regions outside the strip are far below cutoff. Under these conditions the boundary conditions may be satisfied with extraordinary waves inside the strip and TE_m modes outside the strip.

Since the structure has a twofold rotational symmetry about the z axis, the modes of resonance must be either even or odd with respect to this axis. For the even modes the magnetic field is

$$\mathbf{h}=\begin{bmatrix}0\\ 1/\kappa\{-\cos(m\pi z/b)\sin[(m\pi/b)y\tan\theta]\}\\ 1/\kappa\{-\cot\theta\sin(m\pi z/b)\cos[(m\pi/b)y\tan\theta]\}\end{bmatrix} \tag{17}$$

inside the strip and

$$\mathbf{h}=A\begin{bmatrix}0\\ \mp\cos(m\pi z/b)\\ -\sin(m\pi z/b)\end{bmatrix}\epsilon^{\mp(m\pi/b)y}, \tag{18}$$

outside, and [from (16)] the electric fields are everywhere negligibly small compared with the magnetic fields. Matching tangential $\mathbf{h}$ and normal $\mathbf{b}$ at the edges of the strip leads to the determinantal equation

$$\cot[(m\pi L/2b)\tan\theta]=\mu\tan\theta.$$

From (3), (4), and (10),

$$\mu=-\cot^2\theta \tag{19}$$

in the magnetostatic region, and the determinantal equation becomes

$$\cot[(m\pi L/2b)\tan\theta]=\cot\theta. \tag{20}$$

For each value of the mode index (18) has an infinity of roots θ_{mn}, each corresponding [from (10)] to a resonant frequency

$$\omega_{mn}^2=\omega_0(\omega_0+\omega_M\sin^2\theta_{mn}). \tag{21}$$

FIG. 2. Ferrite strip resonator between conducting planes.

[6] There would also be a region of exchange propagation if exchange boundary conditions were included. This has not been done here, and the analysis is not applicable to this region of propagation.

[6] H. Seidel, see footnote 3.

[7] R. W. Damon and J. R. Eshbach, Gen. Elec. Research Laboratory, Rept. No. 59-RL-2324 E, November, 1959.

These resonant frequencies depend only on the shape L/b of the strip and are independent of its size. Furthermore, it is easily shown that (17) and (18) satisfy magnetostatic equations. That is, these resonances exhibit the characteristics of Walker modes, and they will do so regardless of sample size, provided the mode index m is sufficiently large to satisfy (16).

Walker modes with $m=0$ may also be shown to occur in arbitrarily large samples. In this case $\theta=\pi/2$ [from (12)], and the fields within the strip are

$$\mathbf{e}=\left(\frac{\mu_0}{\epsilon}\right)^{\frac{1}{2}}\frac{k_f}{k}\begin{bmatrix}0\\0\\-\cos ky\end{bmatrix}$$

and (22)

$$\mathbf{h}=\begin{bmatrix}-j(k_f/k)^2\sin ky\\ 1/\kappa[\mu(k_f/k)^2-1]\sin ky\\ 0\end{bmatrix}$$

for the even modes. Outside the strip the fields are *TEM* modes,

$$\mathbf{e}=\left(\frac{\mu_0}{\epsilon_0}\right)^{\frac{1}{2}}\begin{bmatrix}0\\0\\-A\end{bmatrix}e^{\mp j\beta_0 z}$$

$$\mathbf{h}=\begin{bmatrix}\mp A\\0\\0\end{bmatrix}e^{\pm j\beta_0 z} \tag{23}$$

From the boundary conditions at the edges of the strip,

$$\cot(kL/2)=-j(k_f/k)(\epsilon/\epsilon_0)^{\frac{1}{2}},$$
$$A=j(k_f/k)^2\sin(kL/2)e^{j(k_0L/2)}.$$

In the magnetostatic region,

$$1\ll(k/k_f)\ll\omega_0/\omega_{cx}\ell^2k_f^2,$$
$$kL/2\to(n+\tfrac{1}{2})\pi, \tag{24}$$
$$A\to 0,$$

and

$$\omega_{0n}^2=\omega_0(\omega_0+\omega_M) \tag{25}$$

from (10). For these modes, therefore, the resonant frequencies are independent of the strip dimensions; and the electric field is again negligibly small compared with the magnetic field, which satisfies magnetostatic equations. This is true regardless of the strip dimensions, provided the mode index n is sufficiently large to satisfy the condition

$$1\ll[(2n+1)\pi/k_fL]\ll\omega_0/\omega_{cx}\ell^2k_f. \tag{26}$$

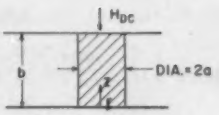

FIG. 3. Ferrite post resonator between conducting planes.

To summarize, it has been shown that, provided the mode indices are sufficiently large, certain resonances of a ferrite strip between conducting planes have the characteristics of Walker modes even when the dimensions of the strip are large compared with a free-space wavelength. That is, (a) the resonant frequencies depend on the shape of the strip but not on its size, (b) the magnetic field satisfies magnetostatic equations, and (c) the electric field is negligible. These remarks apply equally well, of course, to the modes of resonance with odd symmetry about the z axis.

IV. RESONANCES IN A POST BETWEEN CONDUCTING PLANES

By combining plane waves from (7) whose directions form a cone of aperture 2θ about the z axis and using Sommerfeld's integral representation of the cylinder functions, ingoing and outgoing radial wave solutions may be obtained. These may be classified as ordinary or extraordinary waves according to the nature of their plane-wave constituents. The ordinary waves exhibit no striking characteristics, but the extraordinary waves possess regions of electromagnetic, magnetostatic, and exchange propagation as in the case of plane waves.

The resonances of a ferrite post between conducting planes (Fig. 3) may now be found, assuming uniform dc field within the post, by setting up standing radial waves within the post and matching to appropriate fields outside the post. In the general case this is rather difficult because the boundary conditions can be satisfied only by taking both ordinary and extraordinary waves inside the post, and both E-type and H-type radial waves outside the post. The discussion will therefore be confined to the case (16). This restriction guarantees that the extraordinary waves within the post will be in the magnetostatic region and that the structure outside the post will be far below cutoff. The boundary conditions may then be satisfied by taking an extraordinary radial standing wave inside the post and an H-type radial wave outside the post. The magnetic field is therefore

$$\mathbf{h}=2\epsilon^{-jn\phi}\begin{bmatrix}+(1/\kappa)\cos(m\pi z/b)J_n'[(m\pi/b)r\tan\theta]\\ -j\dfrac{n}{(m\pi/b)r\tan\theta}\dfrac{\cos(m\pi z/b)}{\kappa}J_n\left[\left(\dfrac{m\pi}{b}\right)r\tan\theta\right]\\ -(1/\kappa)\cot\theta\sin(m\pi z/b)J_n[(m\pi/b)r\tan\theta]\end{bmatrix} \tag{27}$$

inside the post (see Appendix) and

$$\mathbf{h}=\epsilon^{-jn\phi}\begin{bmatrix}(m\pi/b)^2K_n'(m\pi r/b)\cos(m\pi z/b)\\ -j(n/r)(m\pi/b)K_n(m\pi r/b)\cos(m\pi z/b)\\ -(m\pi/b)^2K_n(m\pi r/b)\sin(m\pi z/b)\end{bmatrix} \quad (28)$$

outside the post, while the electric fields are everywhere negligibly small by comparison. Matching tangential $\mathbf{h}$ and normal $\mathbf{b}$ at the surface of the post and using (19), the resulting equation is

$$\frac{J_n[(m\pi a/b)\tan\theta]}{J_n'[(m\pi a/b)\tan\theta]}\times\frac{(K_n'(m\pi a/b)-[n\kappa/(m\pi a/b)]K_n(m\pi a/b))}{K_n(m\pi a/b)}=-\cot\theta. \quad (29)$$

For each value of the mode index, (29) has an infinite set of roots θ_{mn}; and from (10) the corresponding resonant frequencies are

$$\omega_{mn}^2=\omega_0(\omega_0+\omega_M\sin^2\theta_{mn}). \quad (30)$$

The resonant frequencies in (30) depend only on the shape of the post a/b and are independent of its size. Furthermore, the magnetic-field distributions satisfy the magnetostatic equations. These modes, therefore, exhibit all the characteristics of Walker modes, and this will be true even for arbitrarily large samples, provided only that the axial mode index m is sufficiently large to satisfy (16). As in the case of the strip resonator, Walker modes with $m=0$ may also be shown to exist in arbitrarily large samples, provided the radial-mode index satisfies a relation

$$1\ll p_{nm}/k_fa\ll\omega_0/\omega_M\ell^2k_f^2, \quad (31)$$

where p_{nm} is the mth root of $J_n(p)=0$.

V. SUMMARY

It has been demonstrated that, for a ferrite strip or a ferrite post resonator, modes possessing all the characteristics of Walker modes may exist in arbitrarily large resonators provided the mode indices satisfy relations (16) or (26) for the strip resonator and (16) or (31) for the post resonator. For a given mode, the *lower* limit of (16), (26), or (31) is eventually exceeded as the size of the resonator is increased. The mode then becomes electromagnetic in nature, having an electric field of appreciable strength and a resonant frequency which is size dependent. Resonances of this type in the post resonator have been studied by Steier and Coleman.[8] On the other hand, as the size of the resonator is reduced, the *upper* limit of (16), (26), or (31) is eventually exceeded for a given mode. Exchange effects then become important and the analysis presented here is not applicable, since exchange boundary conditions have not been considered.

APPENDIX

The magnetic-field distribution for a wave as in (15), propagating at an angle β to the x axis, is

$$\mathbf{h}_\beta(x,y,z)=\begin{bmatrix}-j\cos\dfrac{m\pi z}{b}\dfrac{\cos\beta}{\kappa}\\ -j\cos\dfrac{m\pi z}{b}\dfrac{\sin\beta}{\kappa}\\ -\dfrac{\cot\theta}{\kappa}\sin\dfrac{m\pi z}{b}\end{bmatrix}\epsilon^{-j(m\pi/b)\tan\theta(x\cos\beta+y\sin\beta)}.$$

The superposition of waves of this type, using a weighting function $g(\beta)$, gives a field distribution in cylindrical coordinates

$$\mathbf{h}(r,\phi,z)=\begin{bmatrix}-\dfrac{j}{\kappa}\cos\dfrac{m\pi z}{b}\displaystyle\int g(\beta)\cos(\phi-\beta)\epsilon^{-j\rho\cos(\phi-\beta)}d\beta\\ \dfrac{j}{\kappa}\cos\dfrac{m\pi z}{b}\displaystyle\int g(\beta)\sin(\phi-\beta)\epsilon^{-j\rho\cos(\phi-\beta)}d\beta\\ -\dfrac{\cot\theta}{\kappa}\sin\dfrac{m\pi z}{\beta}\displaystyle\int g(\beta)\epsilon^{-j\rho\cos(\phi-\beta)}d\beta\end{bmatrix},$$

where the elements of the column vector now represent r, ϕ, and z vector components and $\rho=(m\pi/b)(\tan\theta)r$. By assuming a weighting function $g(\beta)=(j^n/\pi)\epsilon^{-jn\beta}$, making the change of variable $\psi=\beta-\phi$, and integrating $-\pi$ to π, we have

$$\mathbf{h}(r,\phi,z)=\epsilon^{-jn\phi}\begin{bmatrix}+\dfrac{1}{\kappa}\cos\dfrac{m\pi z}{b}\dfrac{1}{2}\displaystyle\int_{-\pi}^{\pi}\left\{\frac{\epsilon^{-j(n-1)\psi}}{j^{-(n-1)}\pi}-\frac{\epsilon^{-j(n+1)\psi}}{j^{-(n+1)}\pi}\right\}\epsilon^{-j\rho\cos\psi}d\psi\\ +\dfrac{1}{j\kappa}\cos\dfrac{m\pi z}{b}\dfrac{1}{2}\displaystyle\int_{-\pi}^{\pi}\left\{\frac{\epsilon^{-j(n-1)\psi}}{j^{-(n-1)}\pi}+\frac{\epsilon^{-j(n+1)\psi}}{j^{-(n+1)}\pi}\right\}\epsilon^{-j\rho\cos\psi}d\psi\\ -\dfrac{\cot\theta}{\kappa}\sin\dfrac{m\pi z}{b}\displaystyle\int_{-\pi}^{\pi}\frac{\epsilon^{-jn\psi}}{j^{-n}\pi}\epsilon^{-j\rho\cos\psi}d\psi\end{bmatrix}.$$

[8] W. H. Steier and P. D. Coleman, J. Appl. Phys. **30**, 1454 (1959).

From Sommerfeld's integral representation of the cylinder functions, this becomes

$$\mathbf{h}(r,\phi,z)=\epsilon^{-jn\phi}\begin{bmatrix}\pm\frac{1}{\kappa}\cos\frac{m\pi z}{b}(J_{n-1}(\rho)-J_{n+1}(\rho))\\ -\frac{j}{\kappa}\cos\frac{m\pi z}{b}(J_{n-1}(\rho)+J_{n+1}(\rho))\\ -2\frac{\cot\theta}{\kappa}\sin\frac{m\pi z}{b}J_n(\rho)\end{bmatrix}.$$

Also, by using the following relations

$$(n/\rho)J_n(\rho)=[J_{n-1}(\rho)+J_{n+1}(\rho)]/2$$

and,

$$J_n'(\rho)=[J_{n-1}(\rho)-J_{n+1}(\rho)]/2,$$

this may be reduced finally to

$$\mathbf{h}(r,\phi,z)=2\epsilon^{-jn\phi}\begin{bmatrix}\pm\frac{1}{\kappa}\cos\frac{m\pi z}{b}J_n'(\rho)\\ -j\frac{n\cos(m\pi z/b)}{\rho\quad\kappa}J_n(\rho)\\ -\frac{\cot\theta}{\kappa}\sin\frac{m\pi z}{b}J_n(\rho)\end{bmatrix}.$$

JOURNAL OF APPLIED PHYSICS VOLUME 31, NUMBER 9 SEPTEMBER, 1960

Generation of Phonons in High-Power Ferromagnetic Resonance Experiments

ERNST SCHLÖMANN
Research Division, Raytheon Company, Waltham, Massachusetts
(Received May 19, 1960)

The magnetoelastic energy of ferromagnets leads to a coupling between spin waves and elastic vibrations. Because of this coupling the normal modes are not purely magnetic or purely elastic but contain admixtures of both kinds of excitation, the mixing being strongest when the unperturbed waves have the same frequency and wavelength. It is shown theoretically that under suitable conditions (of frequency, dc field, and sample shape) coupled magnetoelastic waves with wavelengths of the order of 1 μ or less can be generated in high-power ferromagnetic resonance experiments. The magnetoelastic interaction increases the threshold precession angle of the uniform mode, the fractional increase being proportional to the group velocity times the relaxation time for spin waves divided by the same quantity for transverse phonons.

1. INTRODUCTION

IT has been pointed out by Turov and Irkhin,[1] by Kittel,[2] and by Akhiezer and his collaborators[3] that the magnetoelastic energy of ferromagnets produces an interaction between spin waves and elastic vibrations. This interaction should be important primarily if the physical conditions are such that spin waves and elastic waves of the same wave number have the same frequency. If this condition is nearly satisfied, the normal modes of the system are no longer purely magnetic or purely elastic but mixtures of the two kinds of excitation. It has been suggested by Kittel[2] that this effect can be used for the generation of elastic waves with frequencies in the microwave range, and experiments by Bömmel and Dransfeld[4] have shown that this is indeed possible. In these experiments, thin films of nickel (approx. 1.8 μ thickness) and a disk of yttrium iron garnet (approx. 15-acoustic wavelengths thickness) were used; the frequency was 1 kMc. The interaction between spin waves and phonons can also lead to an increase in the acoustic absorption. This effect has been observed by Bömmel and Dransfeld[5] in single-crystal disks of yttrium iron garnet at 1 kMc.

Here we shall discuss the possibility of generating microwave phonons in samples of arbitrary size by means of the nonlinear saturation effects observed in ferromagnetic resonance at high-power levels. It has been known since the work of Suhl[6] that the saturation effects are caused by the excitation of spin waves. Under typical experimental conditions the wavelength of these spin waves should be of the same order of magnitude as that of elastic vibrations having the same frequency. So far it has not been possible to detect the spin waves directly, but a large amount of experimental evidence[7–11] lends considerable support to

[1] E. A. Turov and Yu. P. Irkhin, Phys. Metal Research **3**, 15 (1956).
[2] C. Kittel, Phys. Rev. **110**, 836 (1958).
[3] A. I. Akhiezer, V. G. Bar'iakhtar, and S. V. Peletminskii, J. Exptl. Theoret. Phys. (U.S.S.R.) **35**, 288 (1958), [English translation: Soviet Phys.—JETP **35**, 157 (1959)].
[4] H. Bömmel and K. Dransfeld, Phys. Rev. Letters **3**, 83 (1959).
[5] H. Bömmel and K. Dransfeld, Bull. Am. Phys. Soc., Ser. II **5**, 58 (1960).
[6] H. Suhl, J. Phys. Chem. Solids **1**, 209 (1957); Proc. I.R.E. **44**, 1270 (1956); J. Appl. Phys. **29**, 416 (1958).
[7] E. G. Spencer, R. C. LeCraw, and C. S. Porter, J. Appl. Phys. **29**, 429 (1958); R. C. LeCraw, E. G. Spencer, and C. S. Porter, *ibid.* **29**, 326 (1958).
[8] E. Schlömann and J. J. Green, Phys. Rev. Letters **3**, 129 (1959).
[9] E. Schlömann, J. H. Saunders, and M. H. Sirvetz, IRE Trans. on Microwave Theory Tech. **MTT-8**, 96 (1960); J. J.

Suhl's suggestion. The spin-wave phonon interaction should thus make it possible to generate microwave phonons by means of a uniform rf magnetic field of sufficiently large amplitude in samples which are very many wavelengths thick in all directions.

The discussion presented subsequently is based largely on Kittel's work.[2] Kittel's analysis has been extended in the following ways:

1. Phonon relaxation is taken into account.
2. Waves propagating in an arbitrary direction are considered. This problem has also been treated by Turov and Irkhin[1] and by Akhiezer and his collaborators,[3] whereas Kittel's analysis[2] is restricted to propagation in the direction of the dc magnetic field.
3. The nonlinear generation of phonons in a uniform microwave magnetic field of large amplitude is discussed.

In Sec. 2 the general properties of coupled magnetoelastic waves are described. Relaxation effects are taken into account in Sec. 3. In the following two sections the excitation of these waves by means of a nonuniform microwave magnetic field and by a uniform microwave magnetic field of large amplitude are discussed. The implications of these results are reviewed in the last section.

2. COUPLED MAGNETOELASTIC WAVES

The basic assumptions used in the present paper are essentially the same as those used by Kittel.[2] Thus we shall assume that the material is elastically isotropic and that the magnetoelastic energy has the form of Eq. (20) in footnote reference 2. According to Kittel[2] the equations of motion for small amplitudes are[12]

$$\dot{m}_x=-\gamma\left[(H-H_{ex}a^2\nabla^2)m_y+b\left(\frac{\partial R_y}{\partial z}+\frac{\partial R_z}{\partial y}\right)-Mh_y\right]$$

$$\dot{m}_y=\gamma\left[(H-H_{ex}a^2\nabla^2)m_x+b\left(\frac{\partial R_x}{\partial z}+\frac{\partial R_z}{\partial x}\right)-Mh_x\right]$$

$$\rho\ddot{R}_x=\alpha\nabla^2R_x+(\alpha+2\beta)\frac{\partial}{\partial x}(\nabla\cdot\mathbf{R})+\frac{b}{M}\frac{\partial m_x}{\partial z} \tag{1}$$

$$\rho\ddot{R}_y=\alpha\nabla^2R_y+(\alpha+2\beta)\frac{\partial}{\partial y}(\nabla\cdot\mathbf{R})+\frac{b}{M}\frac{\partial m_y}{\partial z}$$

$$\rho\ddot{R}_z=\alpha\nabla^2R_z+(\alpha+2\beta)\frac{\partial}{\partial z}(\nabla\cdot\mathbf{R})+\frac{b}{M}\left(\frac{\partial m_x}{\partial x}+\frac{\partial m_y}{\partial y}\right).$$

Here it is assumed that the dc magnetic field is applied in the z direction. m_x and m_y are the transverse components of the magnetic moment and M is the saturation magnetization. h_x and h_y are the transverse components of the magnetic field. They contain the externally applied microwave field as well as the dipolar field induced by uncompensated "magnetic charges" in the sample or at its surface. H is the internal (demagnetized) dc magnetic field, H_{ex} the "exchange field," and a the lattice constant. Contrary to the convention used by Kittel, the gyromagnetic ratio γ is assumed positive for electrons. Following Kittel's notation $\mathbf{R}$ is the displacement vector of a point in the solid from its original position in the unstrained solid, ρ is the mass density, α and β are the two elastic constants of the material (which is assumed elastically isotropic), and b is the magnetoelastic coupling coefficient (b_2 in Kittel's notation).

Consider first the propagation of waves in the direction of the dc field (i.e., no variation in the x and y directions). It is convenient to introduce complex variables

$$\begin{aligned} m&=m_x+im_y\\ R&=R_x+iR_y\\ h&=h_x+ih_y. \end{aligned} \tag{2}$$

No dipolar field is induced if the wavelength is much smaller than the sample size. The first four lines of Eq. (1) can thus be reduced to two simple complex equations,

$$\begin{aligned} \dot{m}&=i\gamma[(H-H_{ex}a^2\partial^2/\partial z^2)m+b(\partial/\partial z)R-Mh]\\ \rho\ddot{R}&=\alpha(\partial^2/\partial z^2)R+(b/M)(\partial/\partial z)m. \end{aligned} \tag{3}$$

The fifth equation is not coupled to the other four in the present case and describes longitudinal elastic vibrations.

We shall now temporarily omit the driving field h. Its influence will be discussed in Sec. 4. The equations of motion are satisfied by plane waves m, $R\sim e^{i(\omega t-kz)}$ where the coefficients satisfy a set of linear algebraic equations

$$\begin{aligned} (\omega-\omega_k)m+i\gamma bkR&=0\\ -i(bk/\rho M)m+(\omega^2-c_t^2k^2)R&=0. \end{aligned} \tag{4}$$

Here $\omega_k=\gamma(H+H_{ex}a^2k^2)$ is the spin-wave frequency and $c_t=(\alpha/\rho)^{\frac{1}{2}}$ is the velocity of transverse elastic waves. The two equations (4) are compatible if the secular determinant vanishes. Thus, we obtain the dispersion relation

$$(\omega-\omega_k)(\omega^2-c_t^2k^2)-\sigma c_t^2k^2=0, \tag{5}$$

where

$$\sigma=\gamma b^2/\alpha M. \tag{6}$$

For the subsequent discussion the important region is that in which the unperturbed modes cross. Let ω_{cr} be the frequency at which this happens. In the important region $\omega+c_tk\approx 2\omega_{cr}$ and Eq. (5) may be approximated by

$$(\omega-\omega_+)(\omega-c_tk)-s^2=0, \tag{7}$$

Green and E. Schlömann, IRE Trans. on Microwave Theory Tech. MTT-8, 100 (1960).

[10] E. Schlömann, J. J. Green, and U. Milano, J. Appl. Phys. 31, 386S (1960).

[11] E. Schlömann, Raytheon Tech. Rept. R-48 (1959).

[12] Equation (1) is slightly more general than Eqs. (28)–(31) of footnote reference 2 insofar as the direction of propagation is not restricted. Equation (1) follows from the Hamiltonian (25) of footnote reference 2, if the dipolar field is taken into account.

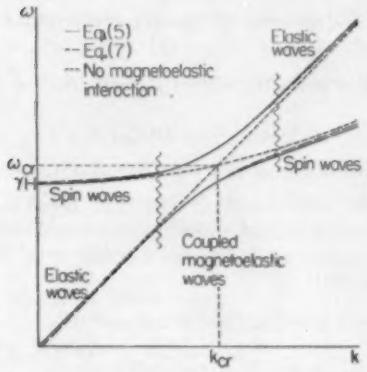

FIG. 1. Frequency vs wave number for coupled magnetoelastic waves. Away from the crossover region the waves are essentially purely magnetic or purely elastic. In the crossover region, however, they contain admixtures of both kinds of excitation. The third branch of the spectrum has been omitted. It corresponds to circularly-polarized transverse elastic waves with a sense of polarization opposite to that which excites ferromagnetic resonance.

where

$$s^2=\tfrac{1}{2}\sigma\omega_{cr}. \tag{8}$$

Figure 1 demonstrates the variation of the frequencies of the normal modes with wave number as given by Eqs. (5) and (7). In the region of the crossover the normal modes are mixtures of magnetic and elastic excitations. The minimum separation of the frequencies of the two branches is $2s$. A numerical estimate of σ and s for yttrium iron garnet can be derived from the known values of $c_t(=3.87\times10^5$ cm sec$^{-1})$,[13] $\rho(=5.2$ g cm$^{-3})$, $\alpha=\rho c_t^2(=7.8\times10^{11}$ d cm$^{-2})$, $M(=140$ oe), $\gamma(=1.76\times10^7$ oe^{-1} sec$^{-1})$, and an estimate of the magnetoelastic coupling constant $b\approx5\times10^6$ erg cm^{-3}.[13a] One obtains $\sigma\approx4\times10^6$ sec^{-1} and for a frequency of 10 kMc, $s\approx3.5\times10^8$ sec^{-1}. The fractional separation of the two branches is thus $s/\omega_{cr}\approx5\times10^{-3}$. The curves shown in Fig. 1 apply to the case in which $s/\omega_{cr}\approx10^{-1}$. It is seen that the approximate curves [given by Eq. (7)] are always very close to the exact curves [given by Eq. (5)]. For smaller values of s/ω_{cr} the deviations are even smaller. It thus appears that for most practical purposes the simplified dispersion relation (7) is a very good approximation.

Consider now the general case of waves propagating in an arbitrary direction. Thus, m_x, m_y, R_x, R_y, and R_z are proportional to $e^{i(\omega t-\mathbf{k}\cdot\mathbf{r})}$. The dipolar field is determined by the conditions $\nabla\times\mathbf{h}_{\rm dip}=0$, $\nabla\cdot\mathbf{h}_{\rm dip}=-4\pi\nabla\mathbf{M}$. Hence,

$$\mathbf{h}_{\rm dip}=-4\pi[\mathbf{k}(\mathbf{k}\cdot\mathbf{m})/k^2]. \tag{9}$$

Without loss of generality we may restrict the discussion to waves propagating in the xz plane, because all waves propagating under the same angle to the dc field must have the same frequency. It is convenient to introduce longitudinal and transverse components of the displacement vector $\mathbf{R}$. According to Fig. 2, R_z and R_x are related to the longitudinal component R_l and one of the transverse components R_t by

$$\begin{aligned}R_l&=R_z\cos\Theta+R_x\sin\Theta\\ R_t&=-R_z\sin\Theta+R_x\cos\Theta,\end{aligned} \tag{10}$$

where Θ is the angle between $\mathbf{k}$ and the z axis. R_y is necessarily transverse and will be designated by $R_{t'}$. One now obtains from Eqs. (1), (9), and (10)

$$\begin{aligned}&i\omega m_x+\gamma H_k m_y-i\gamma bk\cos\Theta R_{t'}=0\\ &(\gamma H_k+\omega_M\sin^2\Theta)m_x-i\omega m_y\\ &\qquad-i\gamma bk(\cos2\Theta R_t+\sin2\Theta R_l)=0\\ &(\omega^2-c_l^2k^2)R_t-i(bk/\rho M)\cos2\Theta m_x=0\\ &(\omega^2-c_t^2k^2)R_{t'}-i(bk/\rho M)\cos\Theta m_y=0\\ &(\omega^2-c_t^2k^2)R_l-i(bk/\rho M)\sin2\Theta m_x=0.\end{aligned} \tag{11}$$

Here

$$\begin{aligned}H_k&=H+H_{ex}a^2k^2\\ \omega_M&=\gamma4\pi M\end{aligned} \tag{12}$$

and

$$c_l=[2(\alpha+\beta)/\rho]^{\frac{1}{2}} \tag{13}$$

is the velocity of longitudinal elastic waves.

The secular determinant of the linear set of Eq. (11) is

$$\begin{aligned}D_k=&(\omega^2-c_t^2k^2)\{(\omega^2-c_t^2k^2)^2(\omega^2-\omega_k^2)-\sigma c_t^2k^2(\omega^2-c_t^2k^2)\\ &\times[(\gamma H_k+\omega_M\sin^2\Theta)\cos^2\Theta+\gamma H_k\cos^22\Theta]\\ &-\sigma^2c_t^4k^4\cos^2\Theta\cos^22\Theta\}-(\omega^2-c_t^2k^2)\sigma c_t^2k^2\sin^22\Theta\\ &\times[(\omega^2-c_t^2k^2)\gamma H_k+\sigma c_t^2k^2\cos^2\Theta].\end{aligned} \tag{14}$$

Here

$$\omega_k=[\gamma H_k(\gamma H_k+\omega_M\sin^2\Theta)]^{\frac{1}{2}} \tag{15}$$

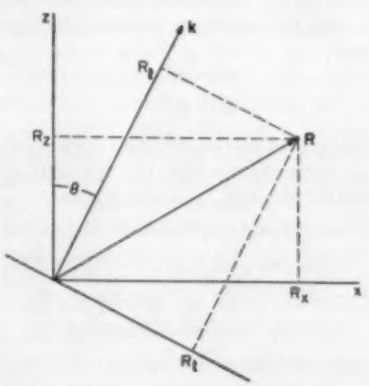

FIG. 2. Relationship between the z and x components and the longitudinal and transverse components of the displacement vector $\mathbf{R}$.

[13] D. T. Edmonds and R. G. Petersen, Phys. Rev. Letters 2, 499 (1959), quoting unpublished results of H. J. McSkimin.

[13a] This value is deduced from measurements of the magnetostrictive constants at room temperature. The author is greatly indebted to J. A. Osborn and his collaborators for making these results available prior to publication.

is the spin-wave frequency and σ is as given under Eq. (6).

The secular determinant D_k can be factorized for the cases in which $\Theta=0$ or $\Theta=\pi/2$. In the former case ($\Theta=0$)

$$D_k=(\omega^2-c_t^2k^2)[(\omega^2-c_t^2)(\omega+\omega_k)+\sigma c^2k^2] \times[(\omega^2-c_t^2k^2)(\omega-\omega_k)-\sigma c_t^2k^2]. \quad (16)$$

Here the last factor leads to the condition previously derived for this case [Eq. (5)]. The second factor leads to essentially the same condition because it becomes identical with the third if the sign of the frequency is reversed. For $\Theta=\pi/2$ the secular determinant (14) may be expressed as

$$D_k=(\omega^2-c_t^2k^2)(\omega^2-c_t^2k^2)[(\omega^2-c_t^2k^2)(\omega^2-\omega_k^2) -\gamma H_k\sigma c_t^2k^2]. \quad (17)$$

In this case the minimum separation of the coupled modes is smaller than in the previous case by the factor $2^{-\frac{1}{2}}H_k^{\frac{1}{2}}(H_k+4\pi M)^{-\frac{1}{2}}$.

In the later discussion it will be necessary to consider the interaction of non-z-directed spin waves and transverse phonons in some detail. We assume that the frequency is close to the crossover frequency for transverse waves of a given direction of propagation. Longitudinal waves of the same direction of propagation are then effectively decoupled because their crossover frequency is different. By way of approximation it is thus permissible to disregard the longitudinal vibrations altogether. For convenience the magnetic moment and the displacement vector may be expanded in Fourier series

$$\mathbf{m}(\mathbf{r},t)=\textstyle\sum_k \mathbf{m}^k e^{-i\mathbf{k}\cdot\mathbf{r}}$$
$$\mathbf{R}(\mathbf{r},t)=\textstyle\sum_k \mathbf{R}^k e^{-i\mathbf{k}\cdot\mathbf{r}}, \quad (18)$$

where $\mathbf{m}^k$ and $\mathbf{R}^k$ are time dependent. Here we have assumed periodic boundary conditions. The components of $\mathbf{k}$ are integer multiples of $2\pi/L$ where L is the length of the periodicity cube. Since $\mathbf{m}(\mathbf{r},t)$ and $\mathbf{R}(\mathbf{r},t)$ are real, the Fourier components satisfy the side conditions

$$\mathbf{m}^k=\mathbf{m}^{*-k}$$
$$\mathbf{R}^k=\mathbf{R}^{*-k}. \quad (19)$$

The equations of motion for the Fourier components can now be derived from Eqs. (1), (9), (10), and (18). One obtains for propagation in the xz plane

$$\begin{aligned}
&\dot{m}_x{}^k=-\gamma H_k m_y{}^k+i\gamma bk\cos\Theta R_{t'}{}^k\\
&\dot{m}_y{}^k=(\gamma H_k+\omega_M\sin^2\Theta)m_x{}^k-i\gamma bk\cos2\Theta R_t{}^k \quad (20)\\
&\ddot{R}_t{}^k+c_t^2k^2R_t{}^k+i(bk/\rho M)\cos2\Theta m_x{}^k=0\\
&\ddot{R}_{t'}{}^k+c_t^2k^2R_{t'}{}^k+i(bk/\rho M)\cos\Theta m_y{}^k=0.
\end{aligned}$$

We now introduce complex variables

$$m_k=\mu m_x{}^k+i\mu^{-1}m_y{}^k, \quad (21)$$

where

$$\mu=(\gamma H_k+\omega_M\sin^2\Theta)^{\frac{1}{2}}\omega_k^{-\frac{1}{2}}, \quad (22)$$

and ω_k is the spin-wave frequency as given by Eq. (15). Similarly,

$$R_k=\mu(\cos2\Theta)^{-1}R_t{}^k+i(\mu\cos\Theta)^{-1}R_{t'}{}^k \quad (23)$$

hence

$$\begin{aligned}
R_t{}^k&=(2\mu)^{-1}\cos2\Theta(R_k+R_{-k}{}^*)\\
R_{t'}{}^k&=(2i)^{-1}\mu\cos\Theta(R_k-R_{-k}{}^*),
\end{aligned} \quad (24)$$

where the side condition (19) has been used. By suitable multiplication and addition we now obtain two complex equations which are equivalent to the four equations (20)

$$\begin{aligned}
\dot{m}_k&=i\omega_k m_k+\tfrac{1}{2}\gamma bk[(\mu^{-2}\cos^2\!2\Theta+\mu^2\cos^2\Theta)R_k\\
&\quad+(\mu^{-2}\cos^2\!2\Theta-\mu^2\cos^2\Theta)R_{-k}{}^*] \quad (25)\\
\ddot{R}_k&+c_t^2k^2R_k+i(bk/\rho M)m_k=0.
\end{aligned}$$

The first line of Eq. (25) shows that in the absence of magnetoelastic coupling the spin-wave amplitudes m_k are proportional to $e^{i\omega_k t}$. According to the second line R_k is then also proportional to $e^{i\omega_k t}$. If this result is inserted into the first line it is seen that the term proportional to R_k leads to a resonant response in m_k, whereas the term proportional to $R_{-k}{}^*(\sim e^{-i\omega_k t})$ does not. By way of approximation it is, therefore, permissible to discard the latter term. The dispersion relation is then of the form of Eq. (5) previously derived for z-directed waves. The only difference is that the parameter σ, which characterizes the splitting, is replaced by $\sigma f(\Theta)$, where

$$f(\Theta)=\tfrac{1}{2}(\mu^{-2}\cos^2\!2\Theta+\mu^2\cos^2\Theta). \quad (26)$$

According to Eq. (8) the angular variation of the square of the splitting s of the coupled modes is also given by the function $f(\Theta)$. With the help of the definition of μ and ω_k [Eqs. (22) and (15)] $f(\Theta)$ may be expressed as

$$f(\Theta)=\tfrac{1}{2}[(2-5\sin^2\Theta+4\sin^4\Theta)(1+\tfrac{1}{4}\omega_M{}^2\omega^{-2}\sin^4\Theta)^{\frac{1}{2}} +\tfrac{1}{2}\omega_M\omega^{-1}\sin^4\Theta(3-4\sin^2\Theta)]. \quad (27)$$

In Fig. 3 this function is plotted for various values of the parameter ω_M/ω.

3. RELAXATION

In the further discussion, dissipation must be taken into account. Consider first the case of propagation in the direction of the dc field. In the complex notation used in Eqs. (2–4) the magnetic relaxation described by the Landau-Lifshitz equation can be taken into account by assigning an imaginary part to the gyromagnetic ratio. Thus γ is replaced by $\gamma+i\lambda$ and $\omega_k=\gamma H_k$ by

$$\Omega_k=\omega_k+i\tau_{sp}{}^{-1}, \quad (28)$$

where $\tau_{sp}=(\lambda H_k)^{-1}$ is the relaxation time of the unperturbed spin waves. Similar considerations apply in the case of non-z-directed waves.

In order to take the elastic relaxation into account, we replace $\ddot{R}$ in Eqs. (3) and (25) by $\ddot{R}+2\tau_{pk}{}^{-1}\dot{R}$, where

τ_{ph} is the relaxation time of the unperturbed phonons. Thus $\omega^2-c_t^2k^2$ in Eqs. (4) and (5) must be replaced by

$$\omega^2-2i\omega\tau_{ph}^{-1}-c_t^2k^2=(\omega-\pi_k)(\omega+\pi_k^*), \tag{29}$$

where

$$\pi_k=(c_t^2k^2-\tau_{ph}^{-2})^{\frac{1}{2}}+i\tau_{ph}^{-1}. \tag{30}$$

For practical purposes τ_{ph}^{-2} can be neglected as compared to $c_t^2k^2$. Relaxation is thus taken into account by assigning a positive imaginary part to the resonance frequencies ω_k and ck.

Instead of Eq. (4) we now obtain from Eq. (25), taking relaxation into account,

$$\begin{aligned}(\omega-\Omega_k)m_k+ip(\Theta)R_k&=0\\ -iqm_k+(\omega-\pi_k)R_k&=0.\end{aligned} \tag{31}$$

Here we have divided the second equation by $\omega+\pi_k^*$. The small imaginary contributions to the coupling terms

$$p(\Theta)=\gamma bkf(\Theta)\quad q=bk/2\omega_{cr}\rho M \tag{32}$$

have been neglected and the real part of $\omega+\pi_k^*$ has been approximated by $2\omega_{cr}$ as is permissible in the crossover region, which is of primary interest. The dispersion relation is, instead of Eq. (7),

$$(\omega-\Omega_k)(\omega-\pi_k)-s^2(\Theta)=0, \tag{33}$$

where $s^2(\Theta)=p(\Theta)q$. The eigenfrequencies are now complex. The imaginary part characterizes the relaxation rate of the normal modes. It can easily be shown from Eq. (33) that at the wave number, for which the unperturbed modes cross, the relaxation rates of the perturbed modes are equal to the algebraic mean of the relaxation rates of the unperturbed modes.

A numerical estimate of the spin-wave relaxation time τ_{sp} can be obtained from resonance measurements at high-power levels. For yttrium iron garnet the spin-wave linewidth ΔH_k is typically of the order of 3 oe (for z-directed spin waves measured at X band in spherical samples).[10] Thus, the spin-wave relaxation time is $\tau_{sp}=2/\gamma\Delta H_k\approx 4\times10^{-8}$ sec.

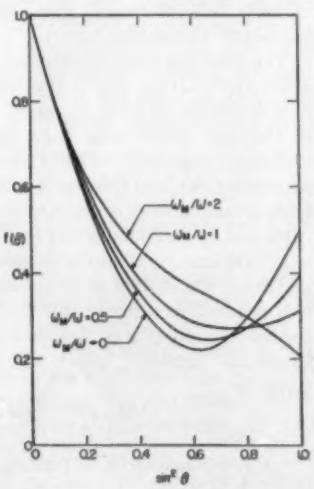

FIG. 3. Splitting of the magnetoelastic-mode spectrum as a function of the direction of propagation. The figure refers to the interaction of spin waves with transverse elastic waves.

The phonon-relaxation time τ_{ph} has been measured by Bömmel and Dransfeld[14] in quartz. At a frequency of 1 kMc and at temperatures greater than 60°K, the attenuation was found to be approximately 17 db/in. independent of temperature. Assuming that the attenuation is the same for yttrium iron garnet one finds that at this frequency the phonon-relaxation time is $\tau_{ph}\approx3\times10^{-6}$ sec. According to Bömmel and Dransfeld,[14] the attenuation increases with frequency, the dependence being between linear and quadratic. At 10 kMc one would thus expect a phonon-relaxation time of approximately 10^{-7} sec.

On using the previously derived estimate of the splitting $s(\approx3.5\times10^8\ \text{sec}^{-1})$ and the foregoing estimates for the relaxation times, one finds that $s^2\tau_{sp}\tau_{ph}\approx500$. It should be kept in mind that this estimate is very approximate. It appears very likely, however, that for some ferromagnetic materials such as yttrium iron garnet $s^2\tau_{sp}\tau_{ph}\gg1$, i.e., the splitting is large compared to the geometric mean of the widths of the two resonances. For many other materials (such as the rare earth iron garnets with short spin relaxation times) this relation is probably not valid. Nevertheless, we shall occasionally use it in the next two sections in order to simplify the discussion. The results so obtained have only limited validity. It will be seen later that the case of large splitting is physically more interesting than that of small splitting.

4. EXCITATION BY MEANS OF A NONUNIFORM MICROWAVE MAGNETIC FIELD

If the spatial variation of the applied microwave magnetic field is sufficiently rapid, spin waves of short wavelength can be excited directly. In nonconductors (such as ferrites and garnets) the microwave field does not vary appreciably over the distance of an acoustic wavelength (approx. $\frac{1}{2}\mu$), corresponding to a frequency of 10 kMc. The direct excitation of spin waves then requires a sample which is half a wavelength thick (or a low odd-multiple of a half-wavelength) and can occur only if the spins at the surface are subject to different anisotropy forces than those inside the material. It has been shown by Kittel[15] that the surface anisotropy need not be very large in order to effectively "pin down" the spins at the surface.

Bömmel and Dransfeld[4] have pointed out that the thickness of a magnetostrictive transducer bonded to a transmitting medium need not bear any relation to the acoustic wavelength. In this mode of operation the uniform spin precession is excited. This gives rise to a uniform magnetostrictive stress and generates elastic

[14] H. Bömmel and K. Dransfeld, Phys. Rev. Letters **2**, 298 (1959).
[15] C. Kittel, Phys. Rev. **110**, 1295 (1958), **112**, 2139 (1958).

waves at the surface of the adjacent transmitting medium.

In this section the direct excitation of spin waves with large elastic admixtures will be discussed. For the sake of simplicity it will be assumed that a driving field with a sufficiently rapid spatial variation is present. This situation cannot be realized experimentally but it is very similar to the situation of a very thin sample subject to a uniform driving field, when the surface spins are pinned down.

We shall restrict the discussion to z-directed waves and shall assume that the applied microwave field is circularly polarized. Thus,

$$h=h_x+ih_y=|h|e^{i(\omega t-kz)}. \tag{34}$$

If a linearly-polarized field is used, only one of the circular components excites the resonance, and only this component need be considered. The first line of Eqs. (4) and (31) must now be supplemented by the driving term $\gamma M|h|$ on the right-hand side. Here we have again neglected the small imaginary contribution to the gyromagnetic ratio present in a lossy material. After eliminating m_k from the two equations (31) one obtains

$$[(\omega-\Omega_k)(\omega-\pi_k)-s^2]R_k=iq\gamma M|h|. \tag{35}$$

We may now determine the physical conditions under which the elastic strain is largest for a given driving field $|h|$. Equation (35) shows that $|R_k|$ and hence the strain $k|R_k|$ is a maximum when the absolute value of the bracket on the left is a minimum. It is shown in Appendix 1 that this minimum is $2s(\tau_{sp}\tau_{ph})^{-\frac{1}{2}}$ provided that $s^2\geqslant(\tau_{sp}\tau_{ph})^{-1}$. The maximum strain is thus

$$k|R_k|_{\max}=|h|/h_0, \tag{36}$$

where

$$h_0=4\omega_{cr}\rho s/\gamma bk^2(\tau_{sp}\tau_{ph})^{\frac{1}{2}}=2(2\alpha/\gamma M\omega_{cr}\tau_{sp}\tau_{ph})^{\frac{1}{2}} \tag{37}$$

is a characteristic rf fieldstrength. It should be noticed that h_0 is not dependent on the magnetoelastic coupling coefficient. The validity of Eq. (37) is restricted, however, to the case in which the splitting of the coupled magnetoelastic modes is larger than the geometric mean of the two resonance widths. It was pointed out at the end of the last section that this condition is probably satisfied in many cases of practical interest. For yttrium iron garnet a numerical estimate of h_0 (using $\tau_{sp}=4\times10^{-8}$ sec, $\tau_{ph}=10^{-7}$ sec) yields $h_0\approx3\times10^3$ oe. Since rf magnetic fields of the order of 1 oe can be achieved without much trouble, it should be possible to obtain strain amplitudes of the order of 10^{-4}.

5. EXCITATION BY MEANS OF A UNIFORM MICROWAVE MAGNETIC FIELD OF LARGE AMPLITUDE

According to Suhl's theory[6] the nonlinear effects observed in ferromagnetic-resonance experiments are caused by the excitation of spin waves. Depending on the physical situation, the frequency of the potentially unstable modes equals the signal frequency or half the signal frequency. The half-frequency spin waves have an inherently lower threshold. Very often, however, the spin-wave spectrum does not extend into the region of half the signal frequency. Under these conditions the spin waves with frequencies equal to the signal frequency have the lowest threshold. It has been shown by Suhl[6] that for spheroidal samples at resonance this is the case if the signal frequency ω is larger than $2N_\perp\omega_M$, where $N_\perp$ is the transverse demagnetizing factor. The theory predicts that the threshold is lowest for z-directed spin waves. For this reason only transverse phonons can interact with the potentially unstable spin waves in this case.

Half-frequency spin waves are excited in the "subsidiary absorption" region below resonance and also at resonance if the signal frequency is low enough. According to the theory, the propagation vector of the potentially unstable modes includes an angle of approximately 45° with the direction of the dc magnetic field. For this reason interaction with longitudinal as well as transverse phonons can occur.

Half-frequency spin waves can also be excited by applying the rf magnetic field parallel to the dc field,[10,11] rather than perpendicular (as is usually done in magnetic resonance experiments). In this case the unstable spin waves propagate perpendicular to the direction of the dc field and hence interact only with transverse phonons.

In the following discussion we shall consider in detail the case in which the unstable spin waves are z directed (or very nearly so) and have the same frequency as the signal. However, the results can easily be extended to the case of xy-directed spin waves (as excited in a microwave magnetic field parallel to the dc field). Qualitatively similar considerations apply to the case of the half-frequency spin waves excited in the subsidiary absorption region.

The experimental conditions (of frequency, sample shape, etc.) under which the spin wave-phonon interaction should be most apparent, depend on curvature of the spin wave band (i.e., on the strength of the exchange coupling). For yttrium iron garnet this parameter has been inferred by Edmonds and Petersen[16] from measurements of the specific heat at low temperatures and by Schlömann and Green[8] from measurements of a "fine structure" in the decline of the ferromagnetic-resonance absorption with increasing power level. The two results agree reasonably well. According to Suhl,[6] the wave number k of the unstable spin waves is, for spheroidal samples, which are biased to resonance, given by

$$H_{cr}a^2k^2=4\pi MN_\perp, \tag{38}$$

[16] D. T. Edmonds and R. G. Petersen, Phys. Rev. Letters **2**, 499 (1959); **4**, 92 (1960).

where $N_\perp$ is the transverse demagnetizing factor. Edmonds and Petersen[16] have calculated that for spherical samples of yttrium iron garnet the wave-number of the unstable spin waves is

$$k_0 = 5.46 \times 10^5 \text{ cm}^{-1}. \tag{39}$$

For a given signal frequency ω the crossover condition is realized at resonance if the transverse demagnetizing factor is given by

$$N_\perp^0 = \tfrac{1}{2}(\omega/c_t k_0)^2. \tag{40}$$

At X band ($\omega/2\pi = 10^{10}$ sec^{-1}) the required value of $N_\perp$ is, according to Eqs. (39) and (40), approximately 0.03. This implies a ratio of diameter to thickness of more than 20:1.

In the foregoing discussion we have assumed that the sample is biased to resonance. Most of the previous experiments on high-power phenomena have in fact been carried out under these conditions, but similar effects can also be observed in the region above resonance. Here the nonlinearity leads to an increase of the absorption with increasing power level. On using the aforementioned numerical values one finds that at X band in spherical samples of yttrium iron garnet the crossover occurs approx 530 oe above resonance.

It was pointed out by Suhl[6] (see also footnote reference 11) that the important nonlinear terms in the equations of motion are those that describe a time-varying coupling between pairs of spin-wave amplitudes. This time-varying coupling can either be induced directly by the rf magnetic field ($\mathbf{h}_{rf}$ parallel $\mathbf{H}_{dc}$) or through the excitation of the uniform precessional mode ($\mathbf{h}_{rf}$ perpendicular $\mathbf{H}_{dc}$). In the latter case the equations of motion for the spin-wave amplitudes m_k become

$$\begin{aligned}(\omega-\Omega_k)m_k + ip(\Theta)R_k - g_k a_0^2 m_{-k}^* &= 0\\ -iqm_k + (\omega-\pi_k)R_k &= 0.\end{aligned} \tag{41}$$

Here $a_0 = (m_x^0 + im_y^0)/M$ is the amplitude of the uniform mode and g_k the coupling constant characterizing the nonlinear interaction between the spin-wave pair (m_k, m_{-k}^*) and the uniform mode. It is shown in footnote reference 11 that g_k is largest for z-directed spin waves ($\Theta=0$) and that its variation with Θ is approximately given by

$$g_k = \tfrac{1}{2}\omega_M(1-\tfrac{3}{2}\sin^2\Theta). \tag{42}$$

The magnetoelastic coupling constants $p(\Theta)$ and q are given by Eq. (32).

Equation (41) is valid only for ideal single crystals containing no inhomogeneities. In practice, such inhomogeneities are usually present and produce a scattering of energy from the uniform mode to the degenerate spin waves. It has been shown by H. Suhl[17] and the present author [9–11] that this scattering tends to smear out the sharp threshold expected for an ideal single crystal.

[17] H. Suhl, J. Appl. Phys. **30**, 1961 (1959).

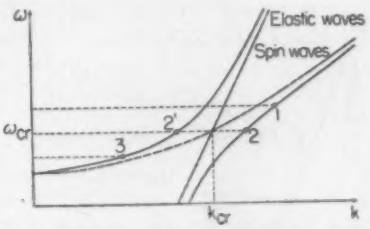

FIG. 4. Instability of coupled magnetoelastic waves at high power levels. If the signal frequency ω is sufficiently different from the crossover frequency ω_{cr} the unstable modes are essentially pure spin waves (points 1 and 3). If the signal frequency equals the crossover frequency the unstable modes have appreciable elastic admixtures. The two modes corresponding to points 2 and 2′ have the same instability threshold under those conditions.

In order to determine the threshold, we combine the two equations (41) with the "adjoint" pair of equations, obtained by replacing k by $-k$ and taking the complex conjugate. The secular determinant of the resultant system of linear equations is

$$D_k = |(\omega-\Omega_k)(\omega-\pi_k) - s^2(\Theta)|^2 - |\omega-\pi_k|^2 g_k^2 |a_0|^4. \tag{43}$$

For $|a_0|=0$ the solution ω of the secular equation $D_k=0$ has a positive imaginary part, and hence describes a decaying oscillation. As $|a_0|$ increases the imaginary part of ω decreases. The instability threshold is reached, when $D_k=0$ for real ω. At this point the oscillations are self-sustained. The threshold amplitude of the uniform mode is thus given by

$$|a_0|_{\text{th}}^4 = \min_k \left| \frac{(\omega-\Omega_k)(\omega-\pi_k) - s^2(\Theta)}{g_k(\omega-\pi_k)} \right|^2, \tag{44}$$

where ω is the (real) signal frequency. In the absence of magnetoelastic coupling the unstable spin waves are those for which $|\omega-\Omega_k|/g_k$ is largest. According to Eq. (42) this implies $\Theta=0$ (z-directed wave).

Consider now the threshold for z-directed waves when the signal frequency is close (but not necessarily equal) to the cross-over frequency. Figure 4 shows a plot of the frequency of the coupled magnetoelastic waves vs wave number. The real part of the numerator on the right of Eq. (44) vanishes along the two full lines indicated in Fig. 4. It may be expected that the minimum of the expression on the right of Eq. (44) occurs close to this line, if the relaxation times are sufficiently long. This expectation is confirmed by the detailed calculation presented in Appendix 2. The two branches of the mode spectrum shown in Fig. 4 give rise to two minima of the expression on the right of Eq. (44). It can readily be shown that the lowest minimum corresponds to those magnetoelastic waves with the smallest elastic admixture.

If the signal frequency is sufficiently different from the crossover frequency the unstable modes are essentially pure spin waves. The square of the threshold

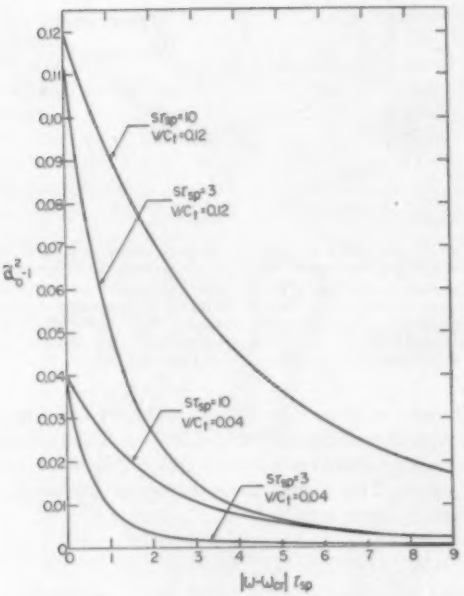

FIG. 5. Instability threshold of z-directed magnetoelastic waves as a function of the difference between signal frequency and crossover frequency. The calculated curves are based on the assumption that $\tau_{sp}/\tau_{ph}=1$.

precession angle is then

$$|\alpha_0|_{th}^2=\Delta H_k/4\pi M=2(\omega_m\tau_{sp})^{-1}, \tag{45}$$

where $\Delta H_k=2(\gamma\tau_{sp})^{-1}$ is a "linewidth" characteristic of the unstable spin waves. The threshold angle increases as the signal frequency approaches the crossover frequency. Details of this variation are calculated in Appendix 2. For convenience we define a reduced threshold amplitude $\tilde{\alpha}_0$ in such a way that it would equal unity in the absence of magnetoelastic coupling.

$$\tilde{\alpha}_0^2=\tfrac{1}{2}\omega_M\tau_{sp}|\alpha_0|_{th}^2. \tag{46}$$

In Fig. 5 the square of the reduced threshold amplitude is plotted vs $|\omega-\omega_{cr}|\tau_{sp}$ for two values of the splitting s and two values of the ratio of spin-wave velocity v and phonon velocity c_t. The two numerical values of v/c_t correspond roughly to the experimental situation in yttrium iron garnet at 10 kMc ($v/c_t=0.04$) and at 30 kMc ($v/c_t=0.12$). The largest increase in the threshold amplitude occurs when the signal frequency equals the crossover frequency. Under these conditions the square of the reduced threshold amplitude is to a good approximation

$$(\tilde{\alpha}_0^2)_{max}\approx 1+(v\tau_{sp}/c_t\tau_{ph}), \tag{47}$$

where v is the group velocity of spin waves at the crossover point. The quantity $\tilde{\alpha}_0^2-1$ approaches zero away from the crossover point. It is reduced to approximately half of its maximum value when the difference of signal frequency and crossover frequency is

$$|\omega-\omega_{cr}|_{\frac{1}{2}}\approx\tfrac{1}{2}s(v/c_t)^{\frac{1}{2}}. \tag{48}$$

The derivation of Eqs. (47) and (48), given in Appendix 2, assumes that the splitting is large compared to the geometric mean of the width of the two resonances. It was pointed out at the end of Sec. 3 that this condition is probably satisfied in many cases of interest.

In the preceding discussion it was assumed that z-directed waves have the lowest threshold even in the presence of magnetoelastic coupling. This assumption can be justified if the phonon relaxation time is sufficiently long so that according to Eq. (47) the magnetoelastic interaction does not lead to a large increase of the threshold. In general, however, this assumption is not justified. If the phonon relaxation time is sufficiently short the threshold of z-directed waves is raised sufficiently to permit instability of other waves propagating under a finite angle to the direction of the dc magnetic field. We shall restrict the discussion to the case in which the crossover condition is realized for z-directed waves. The detailed calculation presented in Appendix 2 shows that z-directed waves have the lowest threshold as long as

$$(v\tau_{sp}/c_t\tau_{ph})\leqslant\Delta/(2-\Delta), \tag{49}$$

where

$$\Delta=6(s/\omega_M)(v/c_t)^{\frac{1}{2}}. \tag{50}$$

If this condition is satisfied, Eq. (47) is applicable. If the condition is violated, the threshold is lower than implied by Eq. (47), because other magnetoelastic

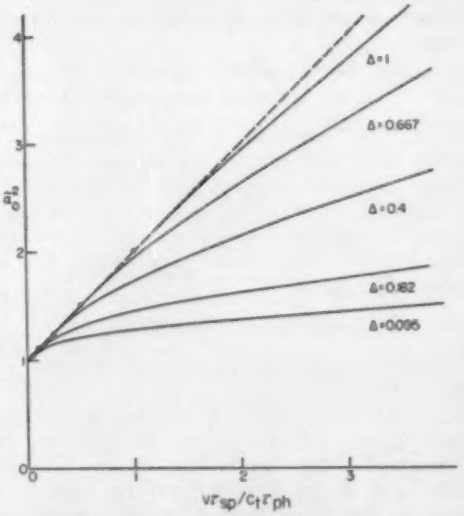

FIG. 6. Instability threshold of magnetoelastic waves as a function of the ratio of spin-wave and phonon-relaxation times. It is assumed that the signal frequency equals the crossover frequency of z-directed waves. The parameter Δ is defined by Eq. (50). The broken line characterizes the threshold of z-directed waves [Eq. (47)].

waves now go unstable before the z-directed waves do. In Fig. 6, the expected variation of $(\tilde{\alpha}_0^2)_{\max}$ with τ_{sp}/τ_{ph} is shown for several values of Δ. Using the previously derived estimates of s and v/c_t we find that for yttrium iron garnet at X band, $\Delta \approx 0.013$. The curves of Fig. 6 consist of two branches, which join with a continuous slope.

6. DISCUSSION

In the present section we shall briefly discuss the potential use of the spin wave phonon interaction for the study of fundamental properties of ferromagnetics and for possible applications.

The determination of the crossover point from high-power resonance experiments can be used to infer the curvature of the spin-wave band near $k=0$, hence the strength of the exchange coupling. The effect may also be useful in studying phonon-relaxation processes.

The nonlinear generation of magnetoelastic waves may be a useful research tool as a source of microwave phonons. The methods described in the literature either make use of a surface effect[18–20] or require very thin samples.[4] It is conceivable that the mechanism discussed in this paper being a bulk phenomenon may make it possible to generate larger amounts of microwave-phonon power.

Lastly, we point out that in principle the effect we have described lends itself to the construction of a phonon amplifier. Under suitable conditions, elastic vibrations transmitted through a ferromagnetic material exposed to a large rf magnetic field should increase in amplitude.

APPENDIX 1

The absolute square of the bracket on the left on Eq. (35) may be expressed as

$$\begin{aligned} F(A,B) &= |(A-ia)(B-ib)-s^2|^2 \\ &= (AB-s^2-ab)^2+(Ab+Ba)^2, \end{aligned} \tag{A1}$$

where

$$\begin{aligned} &A=\omega-\omega_b \quad a=\tau_{sp}^{-1} \\ &B=\omega-(c_t^2k^2-\tau_{ph}^{-2})^{\frac{1}{2}} \quad b=\tau_{ph}^{-1}. \end{aligned} \tag{A2}$$

Instead of minimizing the function F with respect to ω and k, we may minimize it with respect to A and B (keeping a, b, and s fixed). The conditions for an extremum

$$\begin{aligned} &(AB-s^2-ab)A+(Ab+Ba)a=0 \\ &(AB-s^2-ab)B+(Ab+Ba)b=0 \end{aligned} \tag{A3}$$

have two types of solutions. The first $A=B=0$ is associated with the crossover point of the unperturbed modes and corresponds to a value of F given by $F_1=(s^2+ab)^2=(s^2-ab)^2+4s^2ab$. The second solution is characterized by

$$\begin{aligned} &Ab=Ba \\ &AB-s^2+ab=0, \end{aligned} \tag{A4}$$

and corresponds to $F_2=4s^2ab$. Hence $F_2 \leqslant F_1$. Equation (A4) has real solutions (A,B) only if $s^2 \geqslant ab$. If this condition is satisfied, two solutions exist which correspond to the two branches of the magnetoelastic-mode spectrum (see Fig. 1). Both solutions lie in the vicinity of the crossover point of the unperturbed modes in an ω vs k representation. Their exact location depends on the ratio of the two relaxation times.

APPENDIX 2

In the vicinity of the crossover point the spin-wave frequencies are given by

$$\omega_k=\omega_{cr}+v(k-k_{cr}), \tag{A5}$$

where v is the group velocity of spin waves at the crossover point, ω_{cr} the crossover frequency, and k_{cr} the crossover wave number. It is convenient to use the following reduced notation

$$\begin{aligned} c_t(k-k_{cr})\tau_{sp}&=x \\ (\omega-\omega_{cr})\tau_{sp}&=y \\ s\tau_{sp}&=S \\ v/c_t&=\beta \\ \tau_{sp}/\tau_{ph}&=\xi. \end{aligned} \tag{A6}$$

The expression on the right-hand side of Eq. (44) is then for $\Theta=0$ proportional to

$$\begin{aligned} G(x,y) &= \left|\frac{(y-\beta x-i)(y-x-i\xi)-S^2}{y-x-i\xi}\right|^2 \\ &= \frac{[(y-\beta x)(y-x)-S^2-\xi]^2+[y-x+\xi(y-\beta x)]^2}{(y-x)^2+\xi^2}, \end{aligned} \tag{A7}$$

The minimum of $G(x,y)$ with respect to x is equal to the fourth power of the reduced threshold amplitude.

The minimum condition in general leads to a fifth-order equation, which cannot conveniently be solved. For $y=0$, however, the minimum condition reduces to a second-order equation in x^2 with the solution

$$x_{\min}^2=-\xi^2+S^2\beta^{-1}[1+2\xi S^{-2}(1+\beta\xi)]^{\frac{1}{2}}. \tag{A8}$$

The second solution must be discarded because x^2 would be negative, hence x imaginary. The reduced threshold amplitude is thus for $y=0$ from Eqs. (A7) and (A8) given by

$$\begin{aligned} G(x_{\min},0) &= (1+\beta\xi)^2[1-\beta\xi^2S^{-2}w^{-1}] \\ &\quad +\beta S^{-2}w^{-1}[S^2+\xi(1+\beta\xi)-S^2w]^2, \end{aligned} \tag{A9}$$

[18] K. N. Baranskii, Doklady Akad. Nauk. S.S.S.R. 114, 557 (1957) [English translation: Soviet Physics, Doklady 2, 237 (1957)].
[19] H. E. Bömmel and K. Dransfeld, Phys. Rev. Letters 1, 234 (1958).
[20] E. H. Jacobsen, Phys. Rev. Letters 2, 249 (1959).

where

$$w=[1+2\xi S^{-2}(1+\beta^2\xi)]^{\frac{1}{2}}. \tag{A10}$$

It was pointed out in Sec. 3 that in most cases of practical interest the splitting s is expected to be large compared to the geometric mean of the two linewidth $(\tau_{sp}\tau_{ph})^{-\frac{1}{2}}$. Thus $S^2\xi^{-1}\gg 1$. If $\beta\xi\lesssim 1$, as expected in most practical cases, Eq. (A9) reduces to

$$G(x_{\min},0)\approx(1+\beta\xi)^2, \tag{A11}$$

which is equivalent to Eq. (47).

For $y=0$ the extremum condition is also satisfied by $x=0$. The corresponding value of G is $G(0,0)=(S^2\xi^{-1}+1)^2$. If $S^2\xi^{-1}\gg 1$ as previously assumed $G(0,0)>G(x_{\min},0)$, so that $x=0$ corresponds to a maximum and $x_{\min}$ to a minimum as implied by our notation.

An approximate expression for the minimum of $G(x,y)$ with respect to x is obtained by imposing the condition that the first bracket in the numerator of Eq. (A7) vanishes. This approximate threshold is

$$\tilde{G}(y)=\frac{[(1-\beta\xi)y\pm(1+\beta\xi)(y^2+y_0^2)^{\frac{1}{2}}]^2}{[y\pm(y^2+y_0^2)^{\frac{1}{2}}]^2+\nu^2}, \tag{A12}$$

where

$$\begin{aligned} y_0&=2\beta^{\frac{1}{2}}(S^2+\xi)^{\frac{1}{2}}(1-\beta)^{-1}\\ \nu&=2\beta(1-\beta)^{-1}\xi. \end{aligned} \tag{A13}$$

It can be shown that for $y>0$ the upper sign in Eq. (A12) corresponds to the lowest threshold. It should be noticed that $(\nu/y_0)^2=\beta\xi/(S^2\xi^{-1}+1)\ll 1$ if the previously used assumptions $S^2\xi^{-1}\gg 1$, $\beta\xi\lesssim 1$ are valid. For $|y|\ll y_0$ and $\nu/y_0\ll 1$, the approximate threshold $\tilde{G}(y)$ is given by

$$\tilde{G}(y)=(1+\beta\xi)^2\left[1-\frac{4\beta\xi}{1+\beta\xi}\frac{|y|}{y_0}+\cdots\right]. \tag{A14}$$

Hence

$$\tilde{\alpha}_0^2-1=\tilde{G}^{\frac{1}{2}}-1=\beta\xi(1-2|y|/y_0+\cdots), \tag{A15}$$

i.e., y_0 is a measure of the frequency difference over which $\tilde{\alpha}_0^2-1$ falls to half its maximum value.

$$|\omega-\omega_{cr}|_{\frac{1}{2}}=\tfrac{1}{4}y_0\tau_{sp}^{-1}. \tag{A16}$$

If $\beta\ll 1$ and $S^2\xi^{-1}\gg 1$, Eq. (48) is obtained from Eq. (A16).

The approximate threshold $\tilde{G}(y)$ has been compared with the exact values $G(x_{\min},y)$. The latter values were obtained by numerical calculation on a digital computer. It was found that for $S^2\xi^{-1}>2$ the agreement between $\tilde{G}(y)$ and $G(x_{\min},y)$ is very good. The theoretical results, which are based on this approximate formula [Eqs. (A11), (A15), (A16), (47), and (48)], are therefore well justified, if $S^2\xi^{-1}\gg 1$ as expected.

Up until now we have considered the instability criterion only for waves traveling in the direction of the dc field. The justification for this procedure lies in the fact that in the absence of magnetoelastic coupling these waves have the lowest threshold. In the presence of such a coupling this is not necessarily true. We shall now reconsider the stability criterion without imposing the restriction that the unstable modes must propagate in the direction of the dc field. For simplicity, we shall confine the discussion to the case in which the angle Θ is rather small.

Using Eq. (42) the expression on the right-hand side of Eq. (44) can now be expressed as

$$G(x,y,z)=\left|\frac{(y-\beta x-\eta z-i)(y-x-i\xi)-S^2}{(1-\frac{1}{2}z)(y-x-i\xi)}\right|^2. \tag{A17}$$

Here $z=\sin^2\Theta$, $\eta=\frac{1}{2}\omega_M\tau_{sp}$, and we have used an approximate expression for the spin-wave frequency ω_k, which is valid if $\sin^2\Theta\ll H_k/4\pi M$. The function $G(x,y,z)$ minimized with respect to x and z equals the fourth power of the reduced threshold amplitude

$$\tilde{\alpha}_0^4=\min_{x,z}G(x,y,z). \tag{A18}$$

The problem of finding this minimum can in part be reduced to the problem already solved by the introduction of new variables x', y' such that

$$\begin{aligned} y'-x'&=y-x\\ y'-\beta x'&=y-\beta x-\eta z. \end{aligned} \tag{A19}$$

Hence

$$\begin{aligned} x'&=x-\eta z/(1-\beta)\\ y'&=y-\eta z/(1-\beta). \end{aligned} \tag{A20}$$

According to Eqs. (A7), (A17), and (A19),

$$G(x,y,z)=(1-\tfrac{1}{2}z)^{-2}G(x',y'). \tag{A21}$$

On using the fact that $G(x_{\min},y)$ agrees closely with $\tilde{G}(y)$, one obtains from Eqs. (A18), (A20), and (A21)

$$\tilde{\alpha}_0^4=\min_z(1-\tfrac{1}{2}z)^{-2}\tilde{G}[y-\eta z/(1-\beta)]. \tag{A22}$$

We now restrict the discussion to the crossover point (i.e., $y=0$) and make use of the approximations applicable if $S^2\xi^{-1}\gg 1$. It is then readily shown from Eqs. (A14) and (A22) that the minimum lies at $z=0$ if Eq. (49) is satisfied. If this condition is violated the minimum occurs at a finite positive value of z. The location of this minimum and the corresponding value of $\tilde{\alpha}_0^2$ have been determined by numerical calculations on a digital computer. The results are shown in Fig. 6.

Etch Pits in Pyrolytic Graphite*

ARAM TARPINIAN AND GEORGE E. GAZZA
Watertown Arsenal Laboratories, Watertown, Massachusetts
(Received March 31, 1960; and in final form May 2, 1960)

The observation of etch pits in pyrolytic graphite after ion-bombardment etching is described and their similarity to dislocation etch pits is speculated. Evidence of etch-pit multiplication in the form of slip-line segments and low-angle tilt boundaries is presented.

A NUMBER of electron microscope observations[1–4] have been made which are reported to be direct evidence of dislocations in graphite. Although there is no reason to believe that graphite is so perfect that it is free of dislocations, the concept of dislocations in graphite is received with some skepticism. The purpose of this note is to report some recent metallographic observations of etch pits in pyrolytic graphite which we feel may be direct evidence of dislocation sites.

Pyrolytic graphite is the term used to describe the graphitic deposit derived from the high temperature (above 2000°C) pyrolysis of organic vapors. The most common raw material in use today is methane gas. During pyrolysis, deposition of carbon on the hot substrate takes place, resulting in a buildup of layers having the graphitic structure. The orientation of the crystallites is such that the basal or (00.2) plane lies more or less parallel to the surface of the substrate. Owing to the peculiarities of the growth process, the basal planes are bowed with varying degrees of curvature, giving rise to a conical geometry to the grain structure.

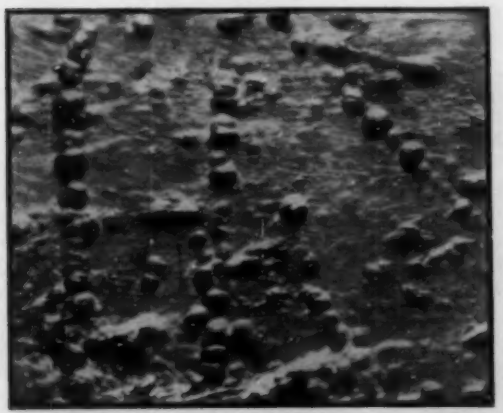

FIG. 1. Typical conical etch pits in pyrolytic graphite. Taken with oblique lighting. 750×

Specimens sectioned perpendicular to the basal plane were polished and etched. Etching was accomplished by cathode etching (ion bombardment) techniques using argon as the ionized gas. After etching for approximately 15 min, pits having a conical shape appear. The occurrence of single dislocations lining up to form subgrain boundaries and other features peculiar to etch pit arrays have been observed. Figures 1–4 show some of the etch pit patterns that are produced. All photographs are oriented such that the basal planes are generally vertical

FIG. 2. Etch pit pattern showing the multiplication of etch pits to form slip-line segments. Taken with oblique lighting. 750×

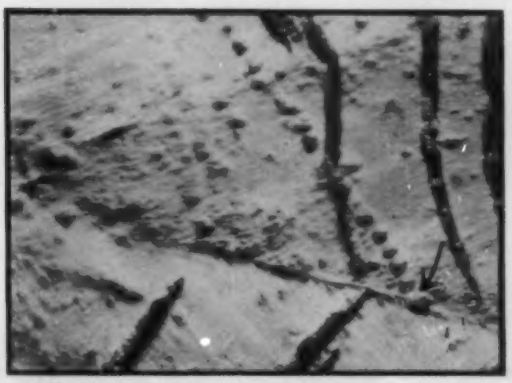

FIG. 3. Etch pit pattern showing the interruption of slip at a grain boundary. Taken with oblique lighting. 750×

* This work was supported by the Ordnance Corps, U. S. Army.
[1] T. Tsuzuku, Proceedings of the Conferences on Carbon, University of Buffalo, 1957, p. 433.
[2] T. Tsuzuku, Proceedings of the Fourth Biennial Conference on Carbon, University of Buffalo, 1959 (to be published).
[3] A. Grenall, Nature **182**, 448, (1958).
[4] I. M. Dawson and E. A. C. Follett, Proc. Roy. Soc. (London) **A253**, 390 (1959).

FIG. 4. Initiation of slip at the tip of a microcrack. Taken with oblique lighting. 750×

with the page. Figures 2 and 3 show the multiplication of etch pits in the form of slip line segments (indicated by arrows). Microcracks predominantly along the bowed basal planes are also seen. It is difficult to say for certain whether all of these are microcracks or actually some are closely spaced etch pits representing low-angle tilt boundaries. A few of these channels do appear to have etch pit structure within them. However, many of them are microcracks since they were observed prior to etching. The interruption of slip at a grain boundary is shown in Fig. 3. Figure 4 shows the initiation of slip at the tip of microcracks along the basal plane.

Whether or not mechanical polishing prior to etching is responsible for the observed structures has not been resolved at present. Although graphite does exhibit creep at room temperature, there is a question as to whether it does so by a plastic slip mechanism. It is our speculation that due to the anisotropic behavior of the graphite crystal lattice, thermal expansion in the *c* and *a* axes differs to such an extent as to create thermal stresses in the deposited layers (during high-temperature deposition and during cooling after deposition) which are high enough to initiate plastic flow and propagate microcracks.

Crystallographic Aspects of Extra Reflections in X-Ray Spectrochemical Analysis

N. Spielberg and J. Ladell
Philips Laboratories, Irvington-on-Hudson, New York
(Received May 11, 1960; and in final form June 2, 1960)

In x-ray spectrochemical analysis, a given crystal monochromator can give rise to higher-order reflections of the incident wavelength, which may be ascribed to the planes (*nh nk nl*), which are parallel to the principal planes (*hkl*). In addition to these, however, there may occur reflections due to other sets of planes which are slightly tilted with respect to (*hkl*). These reflections may lead to undesirable spectral interferences. The identification of these undesirable reflections and their dependence upon choice of various angular divergence parameters, on wavelength, and on the selection and orientation of the monochromators are discussed in terms of an instrumental figure of reflection and a detecting volume in reciprocal space. Topaz and quartz are used as specific examples of the problem.

I. INTRODUCTION

In apparatus for fluorescence x-ray spectrochemical analysis, it is desirable that the recorded spectra be as simple as possible, consistent with the complexity of the specimen being analyzed. Unfortunately, however, the dispersing crystals used inevitably contain numerous sets of crystallographic planes, and some of these may give rise to extra reflections. The most commonly recognized are the higher-order reflections arising from planes (*nh, nk, nl*) whose normals are collinear with the normal to the principal planes (*hkl*). In addition to these, however, there may be reflections from planes whose normals are slightly tilted with respect to the normal to the principal planes.

Figure 1(a) shows a chart from a conventional x-ray fluorescence analysis spectrograph with a pure tin specimen and a quartz analyzing crystal cut parallel to the $(10.\bar{2})$ planes and oriented so that the c axis of the crystal is in the plane containing the x-ray beam and the normal to the $(10.\bar{2})$ planes. In addition to the first and second order reflections of the SnK series lines, there are present also some very wide weak lines, marked *a b, c, d,* which at first glance would be attributed to radiation from some impurity in the specimen or some peculiar scattering phenomenon from the specimen. These lines, however, are due to reflections of Sn radiation from crystallographic planes whose normals are slightly tilted with respect to the normal to the $(10.\bar{2})$ planes. The line *b* in Fig. 1(a), for example, is due primarily to reflection of Sn$K\alpha$ radiation from the $(11.\bar{3})$ and $(2\bar{1}.\bar{3})$ planes of quartz. Aside from possible errors of interpretation the presence of the line *b* would interfere seriously with the measurement of small amounts of molybdenum, columbium, or zirconium in a tin matrix. It may also happen that some of these extra reflections appear superposed on the normal zero-level reflection; in that case their effect is primarily one of excessive broadening of line shape near the base of the line, thus interfering with the measurement of adjacent lines. This is shown in Fig. 2 for the case of Ba$K\alpha$ radiation with a quartz $(10.\bar{1})$ crystal.

In this paper the crystallography of these spurious effects will be discussed and techniques for their amelioration suggested. The discussion will be given in terms of the nonfocusing, flat crystal spectrograph, but applies equally well to focusing instruments.

II. ANGULAR DIVERGENCE PARAMETERS

The geometrical parameters of interest for the conventional nonfocusing spectrograph are shown in Fig. 3.

The central ray $\mathbf{s}_0$ from the specimen incident on the crystal at O is diffracted in a direction $\mathbf{s}$ making an angle T with $\mathbf{s}_0$, given by

$$\mathrm{T}=\cos^{-1}(\mathbf{s}\cdot\mathbf{s}_0), \tag{1}$$

T refers to the angle between the central ray from the

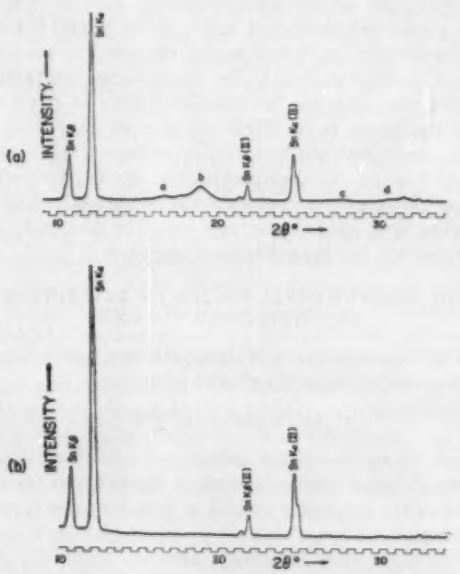

FIG. 1. Chart recording with Sn specimen and quartz analyzing crystal with surface parallel to $(10.\bar{2})$ planes and c axis of the crystal in the plane containing the x-ray beam and the normal to $(10.\bar{2})$ planes. (a) $\beta_1=13.2$, $\beta_2=16°$, permitting extra reflections marked *a, b, c, d*. (b) $\beta_1=3.6°$, $\beta_2=16°$, with suppression of extra reflections.

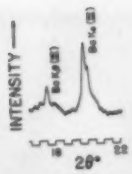

FIG. 2. Chart recording with Ba specimen and quartz analyzing crystal with surface parallel to (10.Ī) planes, and c axis in plane containing x-ray beam and normal to (10.Ī) planes. $\beta_1=13.2°$, $\beta_2=16°$, with extra reflections appearing underneath normal reflections.

specimen and the central ray into the detector, and must lie by definition in the equatorial plane. On the other hand, 2θ is the angle between any given ray from the specimen and the corresponding diffracted ray and need not lie in the equatorial plane. In most work in x-ray spectrochemical analysis, it is not necessary to distinguish between Υ and 2θ, and 2θ is conventionally used to designate the detector position. This convention has been followed in labelling the abscissas of Figs. 1 and 2. The direction of the axis of rotation of the crystal is specified by $\mathbf{t}_0$.

Because of the extended size of the source and crystal, the rays incident on the crystal can deviate from $\mathbf{s}_0$ up to a maximum amount $\pm\frac{1}{2}\alpha_1$ in the equatorial plane and up to a maximum amount $\pm\frac{1}{2}\beta_1$ in the lateral plane of incidence. Similarly because of the extended size of the crystal and detector, the rays scattered into the detector can deviate by a maximum amount $\pm\frac{1}{2}\alpha_2$ in the equatorial plane and $\pm\frac{1}{2}\beta_1$ in the lateral plane of diffraction. α_1, α_2, β_1, and β_2 are controlled by the limiting slits shown in Fig. 3. The shape, form, and position of the slits need not be considered here. In particular the arguments to be advanced here will apply to the case where multiple slits (Soller collimators) are used. In such a case the apertures α_1, etc., are determined by the collimator design or by the size of the source and the crystal, or by special apertures, etc. The design of these instruments has been discussed elsewhere.[1]

III. INSTRUMENTAL FIGURE OF REFLECTION AND DETECTING VOLUME

The reciprocal lattice of the crystal analyzer is defined as the totality of points $\mathbf{r}^*(hkl)$ given by

$$\mathbf{r}^*(hkl)=(h\mathbf{a}^*+k\mathbf{b}^*+l\mathbf{c}^*), \tag{2}$$

where hkl are the Miller indices and $\mathbf{a}^*$, $\mathbf{b}^*$, $\mathbf{c}^*$ the reciprocal lattice vectors related to the unit cell translations of the analyzing crystal $\mathbf{a}$, $\mathbf{b}$, $\mathbf{c}$ by definitions of the type

$$\mathbf{a}^*=\mathbf{b}\times\mathbf{c}/\mathbf{abc}. \tag{3}$$

If x rays of wavelength λ are incident upon the crystal along the direction $\mathbf{s}_0$, then the locus of points $\mathbf{r}^*(\xi,\eta,\zeta)$ in reciprocal space, satisfying the equation

$$1=[\lambda\mathbf{r}^*(\xi,\eta,\zeta)+\mathbf{s}_0]^2, \tag{4}$$

is designated the Ewald sphere of reflection. Diffraction from a given set of crystallographic planes (hkl) takes place in the direction $\mathbf{s}$ wherever the vector $\mathbf{r}^*(hkl)$ satisfies Eq. (4); the direction of diffraction is given by

$$\mathbf{s}=\lambda\mathbf{r}^*(hkl)+\mathbf{s}_0. \tag{5}$$

In the most commonly used arrangement for x-ray spectrochemical analysis, the detector rotates at twice the angular speed of the crystal. Ordinarily one thinks of the reciprocal lattice as being rigidly fixed to the crystal and rotating with it while $\mathbf{s}_0$ is stationary; however one can equally well consider that the reciprocal lattice is fixed and that $\mathbf{s}_0$ (and hence the sphere of reflection) rotates about the origin of the reciprocal lattice, and the terminus of $\mathbf{s}$ moves along a straight line which passes through the origin and at least one point of the reciprocal lattice.

The locus of points satisfying (4) is a sphere of radius $1/\lambda$. It is more convenient in considering conventional spectrographic instruments to have the "sphere of reflection" of unit radius, because such a sphere is applicable to all wavelengths emanating from the specimen, and can be considered as an integral part of the instrument. This can be accomplished by regarding the locus of points $\langle\mathbf{r}\rangle=\lambda\mathbf{r}^*$ satisfying the equation

$$1=(\langle\mathbf{r}\rangle+\mathbf{s}_0)^2, \tag{6}$$

as the unit sphere of reflection associated with the cen-

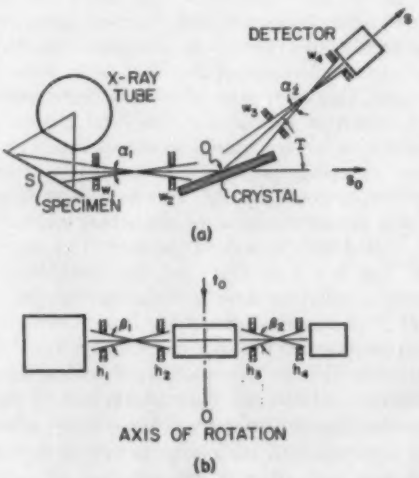

FIG. 3. Geometrical parameters for nonfocusing x-ray fluorescence spectrograph. (a) Equatorial plane, $\mathbf{s}_0$ and $\mathbf{s}$, indicate directions of incidence and reflection for central ray from specimen. Υ represents detector angle, and is measured in equatorial plane only. (b) Axial or lateral plane, which is perpendicular to equatorial plane. w_1, w_2, w_3, w_4, h_1, h_2, h_3, h_4 are the limiting slits or apertures which determine the angular divergence parameters α_1, α_2, β_1, β_2. $\mathbf{t}_0$, unit vector along axis of rotation of crystal.

[1] N. Spielberg, W. Parrish, and K. Lowitzsch, Spectrochim. Acta 13, 564–583 (1959).

tral ray $\mathbf{s}_0$. This is equivalent to multiplying the reciprocal lattice dimensions by a scale factor λ.

For each ray in the cone incident on the crystal there corresponds a unit sphere of reflection. The assemblage of these spheres, which have a common point at the origin of reciprocal space, generate a solid shell-like figure, the instrumental figure of reflection.

We shall designate this solid figure as the lunoid of reflection, since any plane section through it will generate a pair of lunes similar to those used in the indexing of oscillation photographs.[2,3] The center of the Ewald sphere associated with the central ray $\mathbf{s}_0$ shall be considered as the center of the lunoid, and any point within the shell can be described in terms of the values of α_1 and β_1 of the incident ray whose associated Ewald sphere passes through the point. Therefore, if a reciprocal lattice point lies within the lunoid of reflection, the Laue condition is satisfied for at least some rays in the incident beam and diffraction can take place in the direction $\mathbf{s}$ obtained by drawing a unit vector along the line joining the center of the appropriate Ewald sphere to the reciprocal lattice point. The diffracted rays will be recorded, however, only if they enter a detector. Because of the limiting apertures w_3, w_4, h_3, h_4 the detector can receive only those diffracted rays which have directions within $\pm\frac{1}{2}\alpha_2$ and $\pm\frac{1}{2}\beta_2$ of the unit vector $\mathbf{s}$ associated with the central ray $\mathbf{s}_0$. This is shown schematically in Fig. 4 in two dimensions. Only those reciprocal lattice points lying within the area $ABCD$ will be detected. In three dimensions the area $ABCD$ becomes a volume in reciprocal space, which shall be designated as the *detecting volume*. As the detector (linked 2:1 with the crystal) is rotated, the detecting volume then sweeps out a volume in reciprocal space, and all reciprocal lattice points lying within this volume will be recorded as reflections.

In general, the shape and position of the detecting volume depends in a complicated way upon the divergences α_1, α_2, β_1, β_2, the direction $\mathbf{s}_0$ of the central ray of the incident beam, and the angle Υ corresponding to the position of the detector. The concept of detecting volume is useful in ascertaining whether or not extra reflections can appear. The intensity of the extra reflections, however, also depends markedly upon the physical dimensions of the crystal, fluorescent source,

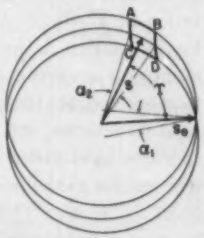

FIG. 4. Two-dimensional representation of instrumental figure of reflection. $\mathbf{s}_0$ and $\mathbf{s}$, directions of central incident and reflected rays; Υ, detector angle; $ABCD$, detecting volume; α_1, α_2 angular divergence parameters in equatorial plane.

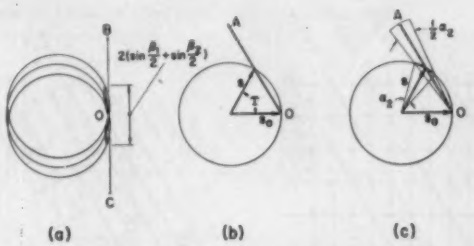

FIG. 5. (a) Lateral cross section through lunoid of reflection at $\Upsilon=0$ for the case α_1, α_2 negligible. Cross-hatched area is the section of the detecting volume. (b) Equatorial cross section through lunoid of reflection (α_1, α_2 negligible), showing locus OA, of end point of $\mathbf{s}$ (and hence midpoint of detecting volume) as 2:1 scanning proceeds. $\mathbf{s}_0$ and $\mathbf{s}$, directions of central incident and reflected rays; Υ, detector angle. (c) Equatorial view of 2:1 scanning scheme for case α_1, β_1, β_2 negligible, showing triangular-like figure swept out by arc of length α_2.

cross section of the detector and the linear separation of these elements.

To ascertain the information required to predict the possible occurrence of extra reflections in normal spectrochemical systems where moderate divergences and 2:1 scanning are employed,[1] two cases will be considered. In case *I*, the divergence is essentially restricted to the lateral plane of diffraction, and α_1 and α_2 are treated as negligible. This condition is usually realized in practice because of spectral resolution requirements. Figure 5(a) shows a cross section in the lateral plane of diffraction through the lunoid of reflection with $\Upsilon=0$. In this case the section of the detecting volume in the lateral plane of diffraction is a "bow tie" shaped figure. The total length of this figure projected on the line BOC is $2(\sin\frac{1}{2}\beta_1+\sin\frac{1}{2}\beta_2)$. As the detector scans, the center of the detecting volume (which corresponds to the end point of $\mathbf{s}$ in the equatorial plane) moves along the line OA in Fig. 5(b) as already described. The detecting volume, and in particular its projection onto the plane containing OA and BOC, will change shape somewhat as scanning proceeds; however, the length of the detecting volume parallel to BOC will not change. Therefore, the trace of the swept-out volume in the plane $OABC$ will be a rectangle of dimensions $2\times2(\sin\frac{1}{2}\beta_1+\sin\frac{1}{2}\beta_2)$, centered about the line OA.[4] All reciprocal lattice points that lie within this rectangle will be detected and recorded as reflections. Those points in the rectangle not lying on OA represent the tilted diffracting planes which give rise to the extra reflections. The intensity of diffraction for off line points decreases monotonically with distance from the line OA. This can be verified by comparing the beam width for zero divergence of the central ray (corresponding to points on OA) with the beam width for maximum divergence of the central ray (corresponding to points most remote from

[2] M. J. Buerger, *X-Ray Crystallography* (John Wiley & Sons, Inc., New York, 1942), pp. 193–198.

[3] J. D. Bernal, Proc. Roy. Soc. (London) **A113**, 117–160 (1926).

[4] Strictly speaking, the *projection* onto $OABC$ rather than the trace of the swept-out volume has the dimensions given. The relative difference between the trace and the projection depends upon α_1 and α_2.

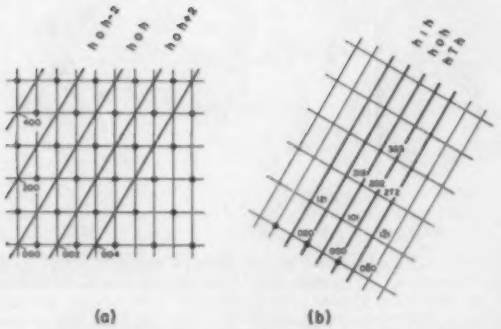

(a) (b)

FIG. 6. Reciprocal lattice nets of topaz crystal (a) ($h0l$) net, (b) (hkh) net. Points marked with circles represent planes of zero reflectivity owing to space group extinctions. The central heavy line represents the $h0h$ line in either case. The adjacent heavy lines represent lines of points which will be detected for sufficiently large values of $(\sin\frac{1}{2}\beta_1+\sin\frac{1}{2}\beta_2)$.

OA). From Fig. 3(b) it is clear that the beam width for zero divergence of the central ray has an aperture equal to the aperture of the smallest of h_1, h_2, h_3, or h_4, whereas the beam width for the maximum divergence of the central ray is zero.

If the spectrograph is designed so that all the required spectral resolution is achieved by a small value of α_1 and the detector is then placed very close to the crystal to increase intensity, we have case *II* in which α_1 is not negligibly small and we disregard the role of β_1 and β_2, which have already been considered under case *I*. The section in the equatorial plane of the detecting volume is then an infinitesimally thick arc of length α_2, as shown in Fig. 5(c). As the crystal rotates and the detector scans 2:1, the arc sweeps out an isosceles triangular area of apex angle $\frac{1}{2}\alpha_2$ with altitude equal to 2 reciprocal lattice units and parallel to the reciprocal lattice line being scanned. All reciprocal lattice points lying within the triangle will be detected and recorded as extra reflections.

IV. IDENTIFICATION AND INDEXING OF UPPER LEVEL REFLECTIONS

The principles used in the identification and indexing of the upper level reflections appearing on a given spectrometer chart are best described by considering an actual example.

The (303) planes of topaz are frequently used in x-ray spectrochemical analysis instruments because of their relatively high dispersion ($d=1.36$ A). The lattice parameters of topaz are $a=4.64$, $b=8.78$, and $c=8.38$ A[5]; hence $a^*=0.215$, $b^*=0.114$ and $c^*=0.119$ A^{-1}. The space group symmetry of the crystal establishes the following extinction rules[5]: Planes ($h0l$) reflect only if $(h+l)$ is even; planes ($0kl$) reflect only if k is even.

The most commonly used orientation, which we will designate as **A**, of the (303) planes is one in which $\mathbf{b}^*$ is perpendicular to the axis of rotation $\mathbf{t}$ of the crystal and $\mathbf{d}_{303}^*$ is perpendicular to $\mathbf{t}_0$. Because any other orientation of the crystal which maintains $\mathbf{d}_{303}^*$ perpendicular to $\mathbf{t}_0$ is permissible, we will also present data on an orientation designated as **B** in which $\mathbf{b}^*$ is turned 90° from its position in orientation **A**; that is, $\mathbf{b}^*$, is collinear with $\mathbf{t}_0$. Figure 6(a) shows the ($h0l$) net of topaz which is the net scanned in orientation **A**, and Fig. 6(b) shows the (hkh) net of topaz which is the net scanned in orientation **B**. Those reciprocal lattice points whose reflections are forbidden by space group symmetry are marked with open circles, and those lines of reciprocal lattice points parallel to the line of points $h0h$ have been drawn with heavy solid lines. It is clear that for scanning along the $h0h$ line of points without picking up extra reflections, Fig. 6(a) permits larger values of $(\sin\frac{1}{2}\beta_1+\sin\frac{1}{2}\beta_2)$ than Fig. 6(b).

Table I lists the approximate relative intensities of reflections observed for orientation **A** and **B** under various experimental conditions for Ba $K\alpha$, Sn $K\alpha$, and Mo $K\alpha$ radiations. For each set of experimental conditions the relative intensities were normalized such that the 606 or 6k6 reflections were taken as 100. The observed intensities demonstrated that the contributions from extra reflections increase with decreasing wavelength or increasing $2(\sin\frac{1}{2}\beta_1+\sin\frac{1}{2}\beta_2)$. While the relative trends of the numbers reported are correct, the actual values listed are peculiar to the experimental arrangements used.

Because the occurrence of extra reflections depends upon the incident wavelength, the spectrometer geometry, and the size and orientation of the reciprocal lattice cell of the monochromator crystal, the manifestation of extra reflections can be predicted when these factors are known. Let p^* be the distance from the line of reciprocal lattice points being scanned (OA, Fig. 5) to the closest point off the line. (The distance p^* is the reciprocal lattice repeat between zero and upper levels.) If $\bar{p}=\lambda p^*<(\sin\frac{1}{2}\beta_1+\sin\frac{1}{2}\beta_2)$, extra reflections will occur and the number of levels which may be observed will be equal to the integral number of times $\bar{p}$ is contained in $(\sin\frac{1}{2}\beta_1+\sin\frac{1}{2}\beta_2)$. The predicted number of levels of extra reflections (to one side of OA) for orientations **A** and **B** for the various experimental conditions are listed in Table I. In orientation **A**, $p^*=0.208$ A^{-1} and in orientation **B**, $p^*=0.114$ A^{-1}. It is clear from the data given for orientation **A** that in some instances the predicted number of levels of extra reflections is not observed. This happens because the geometrical arrangement of source, crystal, detector, etc., is such that the full intensity of the zero-level reflection is received by the detector, whereas for the upper-level only a fraction (dependent upon β_1, β_2, and $\bar{p}$) is received by the detector. This fraction may be small enough that a reciprocal lattice point of weak reflectivity will then be below the limit of detectability. This appears to be the case for the

[5] N. A. Alston and J. West, Z. Krist. **69**, 149–167 (1929).

TABLE I. Intensities of experimentally observed reflections for topaz (303) monochromator.

	Ba $K\alpha$ λ=0.387 A				Sn $K\alpha$ λ=0.492 A			Mo $K\alpha$ λ=0.71 A		
α_1^0	3.6	13.2	1.7	13.2	3.6	13.2	1.7	3.6	13.2	1.7
α_2^0	0.14	0.14	0.14	0.14	0.14	0.14	0.14	0.14	0.14	0.14
β_1^0	13.2	3.6	1.7	3.6	13.2	3.6	1.7	3.6	3.6	1.7
β_2^0	16.0	16.0	16.0	2.3	16.0	16.0	16.0	2.3	16.0	16.0
$2(\sin\frac{1}{2}\beta_1+\sin\frac{1}{2}\beta_2)$	0.500	0.341	0.309	0.103	0.500	0.341	0.309	0.103	0.341	0.309
Orientation A										
No. of upper levels predicted[a]	3	2	1	0	2	1	1	1	1	1
101	1	[b]	[b]	[b]	[b]	[b]	[b]	2	2	3
202	3	[b]	[b]	[b]	1	[b]	[b]	2	1	2
303	[c]	[c]	[c]	[c]	[c]	[c]	[c]	[c]	[c]	[c]
404	10	9	11	8	10	10	9	8	8	8
505	3	2	3	3	2	2	0	1	2	2
606	100	100	100	100	100	100	100	100	100	100
707	4	3	6	4	3	3	6	2	3	2
103 200[d]	15	[b]	0	0	8	[b]	[b]	2	0	0
204 301	9	7	0	0	4	2	0	2	0	0
305 402	12	4	0	0	5	0	0	3	0	0
406 503	24	12	0	0	14	3	0	6	0	0
507 604	0	0	0	0	0	0	0	0	0	0
608 705	8	0	0	0	0	0	0	0	0	0
709 806	11	8	0	0	8	0	0	1	0	0
Orientation B										
No. of upper levels predicted	5	3	3	1	4	3	2	3	2	1
1h1	91	[b]	[b]	[b]	[b]	[b]	[b]	108	15	2
2h2	39	24	19	[b]	29	19	10	27	9	2
3h3	[c]	[c]	[c]	[c]	[c]	[c]	[c]	[c]	[c]	[c]
4h4	63	50	47	12	66	42	26	49	9	8
5h5	9	6	6	3	8	5	4	4	3	2
6h6	100	100	100	100	100	100	100	100	100	100
7h7	9	8	5	6	8	6	4	4	3	2
8h8	7	2	2	[b]	[b]	[b]	[b]	1	2	2
919	5	2	3	[b]	[b]	[b]	[b]	5	3	2

[a] p^0=0.208 A^{-1}. Number of levels to one side of OA.
[b] No experimental data available.
[c] Off scale.
[d] These reflections and succeeding ones are for the first levels on either side of OA. Succeeding levels are not listed.
[e] p^0=0.114 A^{-1}. Number of levels to one side of OA.

experimental conditions listed for columns 4, 5, 8, 10, 11 of Table I, orientation **A**, for example.[6]

In orientation **B**, the extra (upper-level) reflections are superposed on the $h0h$ reflections of the zero level. The elimination of extra reflections is evidenced in columns 5 and 11 since the relative intensities for these columns, orientation **B**, are consistent with the relative intensities for orientation **A**. By comparing, for example, column 4 in orientations **A** and **B**, it is seen that more stringent reduction of lateral apertures is required to eliminate the extra reflections for orientation **B** where p^0 is much smaller than it is for orientation **A**.

It is worth noting that the reflectivities of the intermediate orders, e.g., 101, 202, 404, 505, etc., are not negligible for the topaz monochromator, and that these reflections cannot be suppressed.

Once the orientation of the reciprocal lattice has been determined, the indexing of extra reflections, when they occur, can be sufficiently accomplished graphically by projecting the upper level points upon the line of reciprocal lattice points in the plane of diffraction (the line OA in Fig. 5). The unequivocal identification of the extra reflections depends upon a detailed knowledge of structure factors and a more explicit intensity relationship than given in the preceding discussion. Extra reflections are easily identified because they are usually wider than the zero level reflections. The reason for this is apparent from Fig. 5(a). That part of the detecting volume which lies on the line containing $h0h$ is much narrower than the parts lying on adjacent lines; hence the detecting volume will pass through an $h0h$ reflection much more rapidly than the other reflections, and the observed $h0h$ profile will be narrow by comparison with other profiles. Alternatively one may consider that the reflecting planes of the extra reflections are tilted with respect to the limiting slits, so that the limiting slits seem wider, and hence the reflection profile is wider for the extra reflection.[1]

[6] It may be inferred from footnote 4 to Sec. III, that some of the missing reflections lie in the region between the boundary of the trace in the plane $OABC$ of the swept-out volume and the boundary of its projection onto $OABC$, and therefore should not be observed; but the simple theory given in this paper does not permit a more precise statement.

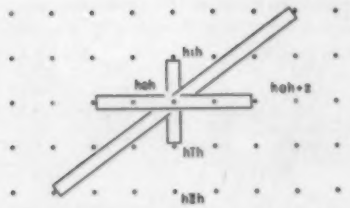

FIG. 7. Relative orientations of detecting volume for topaz reciprocal lattice net, looking down the $h0k$ line of points. Horizontal rectangle corresponds to orientation **A**, vertical rectangle to orientation **B** and oblique rectangle to an alternative orientation which would permit large values of $(\sin\frac{1}{2}\beta_1+\sin\frac{1}{2}\beta_2)$ without recording extra reflections.

V. DISCUSSION AND CONCLUSIONS

It is desirable that the dimension of the detecting volume in the lateral plane of diffraction $(\sin\frac{1}{2}\beta_1+\sin\frac{1}{2}\beta_2)$ be as large as possible, because this permits large values of β_1 and β_2, and these in turn control the intensity reflected by the principal planes of the monochromator crystal. For example, the conditions of the second column of Table I resulted in four times as much intensity for the topaz 303 reflection as the conditions of the fourth column.[1] On the other hand, if $(\sin\frac{1}{2}\beta_1+\sin\frac{1}{2}\beta_2)$ is too large, extra reflections will be detected. The limiting size of the detecting volume is therefore determined by its orientation relative to the reciprocal lattice. Thus, by judicious choice of orientation the detecting volume can be kept quite large and yet extra reflections can be avoided.

Three orientations of the detecting volume relative to the reciprocal lattice for the use of the (303) planes of topaz are shown in Fig. 7. The points shown represent a complete line of reciprocal lattice points perpendicular to the plane of the drawing. The rectangles shown represent the cross sections of detecting volumes for each of the three orientations. In each case the rectangle has been drawn with length such that the upper-level points (relative to $h0k$) are just excluded. The smallest rectangle (vertical) corresponding to orientation **B** represents the maximum size of the detecting volume which will exclude extra reflections for that orientation. Similarly, the intermediate (horizontal) rectangle shows the maximum detecting volume for orientation **A**. The largest rectangle represents an orientation for which the detecting volume is significantly larger than those for either **A** or **B**, yet extra reflections would still be avoided. Clearly, the thickness of the detecting volume (which is determined by α_1 and α_2) is also a factor in avoiding extra reflections. Thus if the thickness of the largest rectangle were doubled, points which are now avoided would be intercepted; accordingly, selective orientation is limited by all four-angular apertures.

In choosing a monochromator for x-ray fluorescence analysis applications where small wavelengths are to be encountered, those crystals with reciprocal lattices admitting large values of p^* are preferable. Where large values of p^* are impractical, i.e., sufficiently large crystals are unavailable for preferred cuts to be made, the reduction and/or elimination of extra reflections can be accomplished only by reducing the detecting volume. It is therefore desirable that instruments for spectrochemical analysis be provided with suitable means for varying β_1 and β_2.

Optical Observations Concerning the Polymorphic Transition in the Potassium Halides

S. WIEDERHORN AND H. G. DRICKAMER

(Received April 18, 1960; and in final form May 20, 1960)

At approximately 20 000 atm the potassium halides undergo a phase transition from the FCC (NaCl) structure to the SC (CsCl) structure. Using optical equipment developed in this laboratory various optical effects were observed including the rate of cutoff of the light and the wavelength dependence of the scattered light. The phase transition is apparently initiated by shear involving a large cutoff of light with little or no volume change. At the beginning and end of the transition the scattering is largely small particle scattering, with large particles dominating the middle region. Rb^+ impurity has little effect on the transition. Na^+ impurity apparently inhibits the nucleation strongly, and, to some extent, the growth.

From the absorption spectra of Pb^{++} ion impurity it is apparent the nuclei consist of hundreds of ions, rather than smaller units.

THE pressure induced, first order, phase transformation of the potassium halides has been studied by optical means. The potassium halides undergo a phase transformation at about 20 000 atm at room temperature,[1] and change from a sodium chloride to a cesium chloride type structure.[2,3] As these salts undergo transformation, they become opaque.[4] The opacity is due to light scattering, which is caused by the formation of some cesium chloride type phase within the sodium chloride phase. Information on the mechanism and kinetics of the transformation were obtained by making various optical measurements on the salt during the transformation.

Single crystals, obtained from the Harshaw Corporation, were used in all pure sample measurements. Impurity samples of NaCl and RbCl in KCl, and PbI_2 in KI were made in the laboratory from Fisher Certified ACS grade chemicals. The pressure equipment used has been described previously.[5] In order to obtain right-angle scattering measurements, a third window was added at right angles to the first two. All samples were one-eighth inch in thickness and except for the wavelength dependence readings, all light intensity measurements were made at 580 mμ. The wavelength dependence measurements were made at 50 mμ intervals from 450 to 650 mμ. The volume change of the sample as it proceeded through the transformation was obtained by measuring the displacement of the piston which, in turn, was obtained from the amount of oil used to displace it. The fraction of the sample transformed is calculated from these volume measurements.

The decrease in the intensity of the light being transmitted through a sample of potassium halide is due to light scattering, since the potassium halide does not absorb in the range studied, 450 to 650 mμ. The onset of darkening is an indication of the nucleation of the new phase. The intensity of the light coming through the bomb, at constant pressure, changes with time, as shown in Fig. 1. There is a continuous change in the shape of the curves as one passes from a low to a high pressure. In fact, if the individual curves are translated an appropriate distance along the time axis, they form part of a general curve. This leads one to believe that, except for the size of the time unit, the kinetics of the reaction are independent of the pressure. The transformation is therefore isokinetic, as defined by Avrami.[6–8]

The rate of darkening and the pressure at which darkening first occurs depends not only on the pressure used but also on the history of the sample. Table I shows how the pressure at which darkening first occurs varies with the number of times that the sample is transformed. For potassium chloride, the darkening occurs at the lowest pressure, 24 200 atm, the first time through the transition. The pressure at which darkening first occurs gradually approaches an upper limiting pressure, 25 900 atm, with succeeding times through

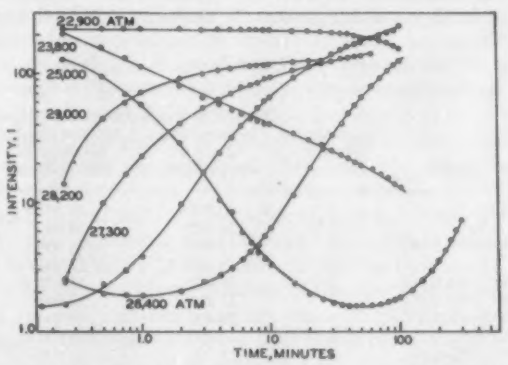

FIG. 1. Darkening curve KCl-single crystal-intensity vs time. Sample thickness 0.015 in.

[1] P. W. Bridgman, Z. Krist. **67**, 363 (1928).
[2] R. B. Jacobs, Phys. Rev. **54**, 468 (1938).
[3] J. C. Jamieson, J. Geol. **65**, 334 (1957).
[4] I. S. Jacobs, Phys. Rev. **93**, 993 (1954).
[5] R. A. Fitch, T. E. Slykhouse, and H. G. Drickamer, J. Opt. Soc. Am. **47**, 1015 (1957).
[6] M. Avrami, J. Chem. Phys. **7**, 1103 (1939).
[7] M. Avrami, J. Chem. Phys. **8**, 212 (1940).
[8] M. Avrami, J. Chem. Phys. **9**, 177 (1941).

TABLE I.

Sample	No. of times through the transformation	Pressure at which darkening first occurs—atmospheres
KCl	1	24 200
	2	25 500
	3	25 900
	4	25 900
	5	25 900
	10	25 900
KCl:Na 0.5%	1	25 100
	2	26 800
	4	27 700
	15	27 700
KCl:Rb 3.0%	1	23 800
	2	24 200
	3	25 100
	4	25 100
	5	25 500
	10	25 500

the transition. These results show that some sort of work hardening has occurred. It requires more energy to nucleate the new phase in a sample which has been transformed many times, than for one which has been transformed only once or twice. This energy increase is probably due to the breaking up of the sample from a single crystal into a polycrystalline mass, with large angle grain boundaries. X-ray diffraction patterns from samples which have been transformed more than ten times show that the samples are polycrystalline with very small crystals.

The transformation may proceed below the minimum darkening pressure. In order for this to happen, the pressure is first raised above the minimum darkening pressure and then quickly dropped to the pressure under consideration. The sample continues to darken and the transformation occurs at a pressure of only 100 atm above equilibrium. There is probably considerable reversibility once the nuclei have formed, and the continued darkening is probably due to growth rather than to new nucleation.

TABLE II.

Sample	No. of times through trans	Pressure at which volume first changes atmospheres	Pressure at which volume change is complete atmospheres
KCl	1	23 800	29 500
	10	26 400	30 800
KCl:Rb 3.0%	1	23 800	28 600
	10	26 800	29 900
KCl:Rb 0.1%	5	25 900	32 100
KCl:Rb 0.5%	5	27 200	32 100
KCl:Rb 3.0%	5	26 400	32 100
KCl:Na 0.1%	5	26 400	30 800
KCl:Na 1.0%	5	27 700	32 100
KCl:Na 3.7%	5	29 000	39 100
KCl:Na 10%	5	29 900	42 200
KCl:Na 0.5%	1	25 100	30 300
	2	26 800	33 800
	4	28 600	34 700
	15	28 200	33 000

The first time through the transition, the light intensity decreases quite suddenly, to a nearly constant final value, which depends on the pressure used. If the pressure is increased, the intensity again decreases quite suddenly. This is similar to the shattering that I. S. Jacobs[4] observed visually. The discrete decreases in intensity were observed visually. They appear to occur in times of the order of a second. The sample can also be heard to shatter as it proceeds through the transition the first time. No noise is heard in later transformations. The light intensity ceases to decrease in discrete jumps as the intensity approaches a minimum. After the first time through the transition, the light intensity changes in a continuous manner with pressure, as shown in Fig. 1.

Volume change measurements in Table II give results which are very similar to those obtained from intensity measurements. The first time through the transition, the pressure at which the transition starts

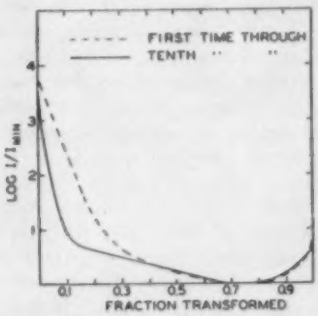

FIG. 2. Log I/I_{min} vs fraction transformed.

is 23 800 atm, 2600 atm lower than the tenth time through 26 400 atm. This is further proof that some sort of work hardening has occurred. The first time through the transformation, 15% of the sample is transformed at the pressure at which the volume initially starts to change discontinuously. If one attempts to increase the pressure, the volume merely decreases and the pressure stays constant. After the sample is about 15% transformed, it supports a higher pressure. In the original untransformed crystal, there are probably a great many points, of nearly equal activation energy, at which the transformation can start.

The intensity of light passing through the sample is calibrated with the fraction of the sample transformed into the new phase, by plotting the log I/I_{min} vs the fraction transformed, where I_{min} is the lowest intensity of light coming through the sample during the transformation. Figure 2 is a light intensity calibration curve for the first and tenth time through the transformation. The tenth time through the transformation, the light intensity changes by 4.3 orders of magnitude, and more

than 99.9% of the light has been cutoff before the sample is 10% transformed. The light intensity starts changing 400 atm before the initial change of volume. Thus many scattering centers are formed before any growth has occurred. If the nuclei of the new phase are equated with the scattering centers, this seems to indicate that the scattering centers are formed by some sort of shear mechanism.

The first time through the transformation, more growth occurs at the beginning of the transformation, than at the beginning of the transformation the tenth time through. The nuclei formed during the initial transformation grow to a larger size. The first time through the transformation, the light intensity changes 3.7 orders of magnitude and decreases to 99.9% of its initial value by the time the sample is 25% transformed.

The intensity of light coming through the sample, at any given fraction transformed, was found experimentally to have the following dependence on wavelength: $I/I_0 = a/\lambda^{\alpha}$; λ = wavelength; I = intensity of light coming through the sample at a given fraction transformed; I_0 = Intensity of light coming through the sample before any transformation has occurred; α = An experimentally determined constant, wavelength dependence; a = arbitrary constant.

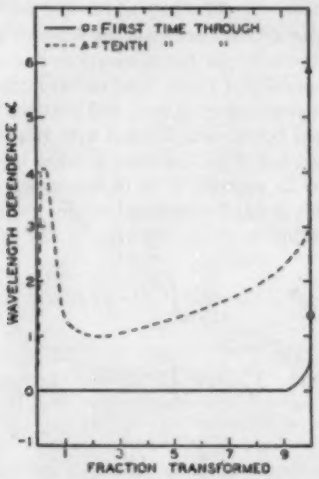

FIG. 3. Wavelength dependence α vs fraction transformed.

The approximate size of the regions being transformed were determined by measuring α for the light being transmitted at several different percentages transformed. Figure 3 is a plot of α vs the fraction transformed. The first time through the transformation, the value of α remains fairly constant throughout the transformation, rising to a value of 1.5 at the completion of the transformation. The results are quite different for a sample which has been transformed more than ten times. Then α rises to a value of 4 early in the transformation and then drops to a value of 1. It then increases to a value of about 6 at the end of the transformation. It is reasonable to assume that the large values of the wavelength dependence are caused by small particle scattering and the small values of α are caused by large particle scattering. The first time through the transformation, the scattering is probably caused by centers which are large in comparison to the wavelength of the light. The tenth time through the transformation, small particle scattering probably occurs at the beginning and at the end of the transformation. Scattering at the beginning of the transformation is caused by newly formed regions of the new phase. At the end of the transformation, the scattering is caused by residue of the old phase, which is still untransformed. It is possible that multiple scattering occurs in the middle of the transformation. The results of Chandrasekhar[9,10] show that forward scattering, from an atmosphere of Rayleigh-type particles, is negligible compared to the flux in the forward direction, up to an optical thickness of one. Therefore, the single particle scattering approximation should be valid up to an optical thickness of one and probably beyond. Between 80 and 90% of the wavelength dependence increase occurs when the optical density is less than 2.

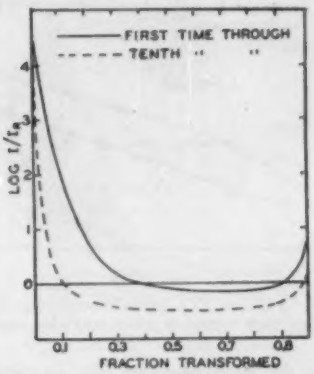

FIG. 4. Comparison of extinction with intensity of right angle scattering-KCl. Log I/I_R vs fraction transformed.

An indication that the particles are smaller the tenth time through the transition than they are the first comes from right angle scattering measurements. Figure 4 is a plot of log I/I_R vs the percent transformed, for the first and tenth time through the transformation. I is the intensity of the light coming directly through the bomb and I_R is the intensity of the light coming out of the bomb at right angles. Near the minimum intensity, a greater amount of light leaves the bomb at a right angle than at an angle of 180°. Since it is well known that small particles scatter more light at right

[9] S. Chandrasekhar and D. D. Elbert, Trans. Am. Phil. Soc. 44, 643 (1954).

[10] S. Chandrasekhar, *Radiative Transfer* (Clarendon Press, Oxford, England, 1950).

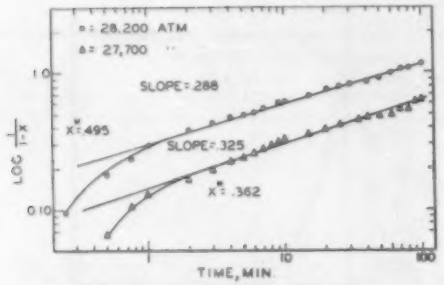

FIG. 5. Log1/1−x vs time-KCl. Tenth time through the transition. x^* = fraction transformed at which curve becomes linear.

angles than do large particles, the particles are apparently smaller the tenth time through the transition.

The fraction x of the potassium halide transformed to the new phase is a function of time and may be described by the equation,[7,11]

$$x=1-\exp(-bt^n),$$

where b and n are empirically determined constants. The slope of a plot of the log-log $(1/1-x)$ vs log$t$ is equal to n. For a single crystal of potassium chloride the first time through the transformation, the value of n is close to zero and the percent transformed remains nearly constant with time. The potassium chloride is transformed to its final value, approximately 18%, in less than 15 sec, which is the minimum time necessary to bring the equipment to a constant pressure. We may deduce from this observation that after 18% of the sample has been transformed, both the nucleation and growth of the new phase have ceased. For if either growth or nucleation continued, the sample would become completely transformed.

Figure 5 shows some typical kinetics curves for potassium chloride after it has been transformed more than ten times. The graphs show a great deal of curvature early in the transformation and approach straight lines for large times. The initial slope of the curves at 0.25 min is 1.25. Because of the large curvature, the slope of the curves are probably greater than this for times less than 0.25 min. When 40-60% of the sample has been transformed, the curves approach a straight line with a slope of about 0.3. The curve belonging to the sample which is transformed at the higher pressure, approaches a straight line at a higher percent of transformation. Qualitatively similar curves are obtained for potassium iodide.

Johnson and Mehl,[11] making the assumption that a domain could not grow across a grain boundary and that nucleation occurred, at a constant rate, only at grain boundaries, showed that n approached 1 at large times t. Cahn,[12] assuming that the rate of growth was constant and that the nucleation rate, $J=At^c$, showed that n could not be less than 1 at large times. Therefore, in order to explain the above data, it must be assumed that both the rate of nucleation and the rate of growth are time dependent and decrease with time. A derivation, using these assumptions, is given below.

Assume that both the rate of growth u and the rate of nucleation J, are functions of time. It is not known what these functions are. However, simple functions, which give a reasonable physical picture of what is happening, will be used. It is assumed that a domain will grow at a constant rate until a maximum size is attained, after which the growth stops. Since we know that growth will stop after a short time, in a crystal which is being transformed for the first time, the assumption that growth ceases is consistent with the experimental data. A second assumption is that the nucleation occurs at arbitrary points within the lattice and that $J=it^{-m}$, for $t>t_0$ where $0<m<1$. This is similar to the assumption made by Cahn.[12] In order to avoid a singularity in the nucleation rate at $t=0$, it will be assumed that there is an initial nucleation rate J_0, which is constant until $t=t_0$ and that the number of nuclei formed before $t=t_0$ is small with respect to those formed after. Let t^* be the time it takes for a nucleus to complete its growth. t^* is of the order of several seconds. This is small compared to the length of time it took to complete a run, 100 min

$$\text{for}\quad t<t^*\quad X_{ex}=gu^3\int_0^t(t-\tau)^3J\,d\tau \tag{1}$$

$$\text{for}\quad t>t^*\quad X_{ex}=gu^3\int_{t-t^*}^t(t-\tau)^3J\,d\tau+g(ut^*)^3\int_0^{t-t^*}J\,dt. \tag{2}$$

For $t\gg t^*$, the first term on the right of (2) becomes negligible

$$\begin{aligned}X_{ex}&=g(ut^*)^3\int_0^{t-t^*}J\,dt\\&=g(ut^*)^3J_0t_0+g(ut^*)^3i\left[\frac{t^{-m+1}}{-m+1}\right]_{t_0}^{t-t^*}\\&\simeq bt^{-m+1}.\end{aligned}$$

At large values of t,

$$n=1-m.$$

For $t\ll t^*$, Eq. (1) is used and the analysis by Cahn shows that the slope, $n=4-m$.

The experimental results obtained for potassium chloride fit the theory if $m=0.7$. The initial slope should be 3.3, however, it was not possible to measure

[11] W. A. Johnson and R. F. Mehl, Trans. Am. Inst. Mining and Met. Engrs. 135, 416 (1939).

[12] J. W. Cahn, Acta Met. 4, 449 (1956).

this slope with the equipment used. A similar analysis could be made for surface and edge nucleation.

The same type of experiments which were made on the pure potassium chloride, were made on impurity samples of rubidium chloride and sodium chloride in potassium chloride. Since rubidium chloride exists in the cesium chloride structure at 20 000 atm, it was thought that it would form nucleation centers for the phase transformation. This did not prove to be the case. In fact, rubidium chloride seemed to have little or no effect on the transformation. It was expected that sodium chloride would hinder the transformation. This was in fact observed.

The pressure at which darkening first occurs, vs the number of times through the transformation is given in Table I for KCl, KCl:Na 0.5%, and KCl:Rb 3%. It should be noticed that the first time through the transformation, the potassium chloride and the rubidium impurity samples start to darken at nearly the same pressure. The sodium impurity sample darkens at a slightly higher pressure. The pressure at which darken-

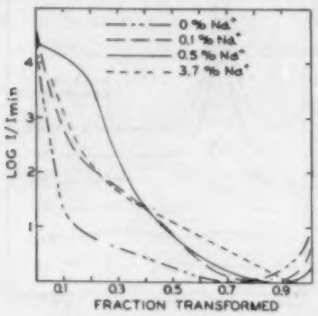

FIG. 6. Log I/I_{min} vs fraction transformed. Na^+ impurity in KCl. Tenth time through the transition.

ing first occurs increases with the number of times through the transition. An upper limiting pressure is finally reached. This final pressure is higher for samples with sodium impurity in them. The higher pressures obtained for sodium impurities are an indication that sodium impurities hinder the transition.

Table II is a summary of the pressure-volume data obtained for sodium and rubidium impurity samples. The similarity between the pure sample and the sample with rubidium impurities should be noted. The effect of the sodium impurity is noticeable in samples of high concentration.

Figures 6 and 7 are light intensity calibration curves for sodium and rubidium impurity samples. The curves, for the sodium impurities, show large deviations from the pure potassium chloride curve. Although the shapes of the sodium impurity curves are different, the samples are all about 40% transformed when 99.9% of the light has been cut off. This may be compared to the pure sample where 99.9% of the light is cut off before it is

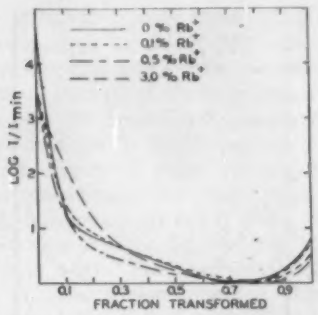

FIG. 7. Log I/I_{min} vs fraction transformed Rb^+ impurity in KCl. Tenth time through the transition.

7% transformed. At the beginning of the transformation, the 0.5% sodium impurity sample shows an especially large fraction transformed with little light intensity change. If the decrease in light intensity coming through the sample is associated with nuclei formation, the sodium impurity diagrams show that the nucleation rate is more strongly affected by the sodium impurity than is the rate of growth. In the pure sample, a great deal of nucleation occurs at the beginning of the transformation, without an accompanying volume change. This accounts for the large decrease in the light intensity with only a small amount of transformation. Less nucleation and more growth occurs at the beginning of the transformation in the sodium impurity samples. This accounts for the large amount of transformation accompanied by a relatively small change in the light intensity. The exact shape of each curve depends on the relative amounts of nucleation and growth occurring during the transformation. In general, a large slope of the light intensity calibration curve indicates that a great deal of nucleation is occurring.

The effects of rubidium on the transformation are quite small. In Fig. 7 the largest deviation from the

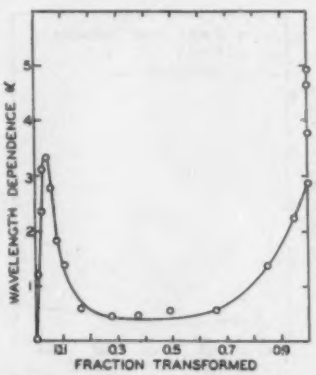

FIG. 8. Wavelength dependence curve KCl with 0.5% Rb. Fifth time through the transition.

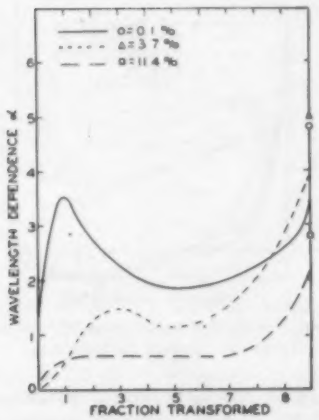

FIG. 9. Wavelength dependence curve. KCl:Na 0.1%; KCl:Na-3.7%; KCl:Na 11.4%; fifth time through the transition.

pure potassium chloride is for the 3.0% rubidium sample, for which the sample is about 23% transformed when 99.9% of the light intensity has been cut off. The 0.1 and 0.5% rubidium samples are 10 and 12% transformed when 99.9% of the light intensity has been cut off. The deviations are slight, showing that rubidium impurities have little effect on the phase transformation.

The wavelength dependence of the scattering was determined for the rubidium and sodium impurity samples. The results obtained for the rubidium are quite similar to those of the pure sample. Figure 8 is a plot of the wavelength dependence of a 0.5% rubidium impurity sample. The scattering results obtained for sodium impurity samples, Figs. 9 and 10, differ widely from the pure sample. As the sodium concentration increases, Fig. 9 the first scattering peak decreases in size and moves to a higher fraction transformed. The first peak always occurs at a percentage of transformation where the slope of the light intensity calibration curve is the greatest. This means that domains which

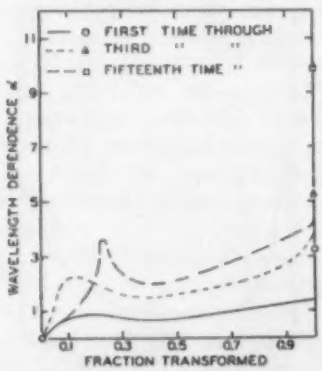

FIG. 10. Wavelength dependence curve; KCl:Na 0.5%; first, third, and fifteenth times through the transition.

are small when compared to a wavelength of visible light, occur at a point where the nucleation is the greatest. Small particle scattering occurs at the end of the transformation. Figure 10 shows how the wavelength dependence curves develop, for a 0.5% sodium impurity sample, as the sample is put through the transformation many times. The first time through, there is no peak at the beginning of the transformation and the scattering is caused mainly by large particles. As the sample is repeatedly put through the transformation, a peak, which is due to small particle scattering, appears at the beginning of the transformation. This is again proof that the sample breaks up into a polycrystalline mass after passing through a transformation many times. It is interesting that, after many times through the transformation, the 0.5% sodium impurity sample shows an extremely large wavelength dependence at the end of the transforma-

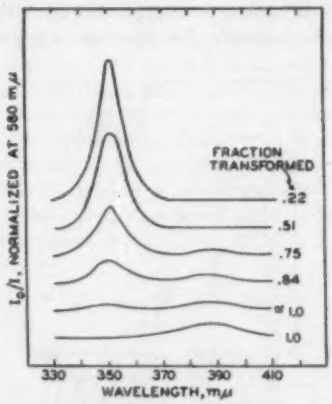

FIG. 11. Absorption spectra KI:Pb 0.5%; tenth time through the transition.

tion. Some other effect besides small particle scattering must also be involved.

The kinetics curves obtained for the impurity samples are similar in shape to those of pure potassium chloride, Fig. 5. The slope n of the rubidium impurity samples was about the same as the pure potassium chloride. The slope of the 0.5% sodium impurity sample is approximately equal to 0.08, which is about one-fourth of the value obtained for the pure sample. The low value of n is an indication that the nucleation rate of the sodium impurity sample is more strongly time dependent than that of the pure sample. From the theory described in the foregoing

$$J = i_0 t^{-0.92},$$

for the 0.5% sodium impurity sample. The curves of the impurity samples approach straight lines at between 30 and 60% transformed. The greater the pressure used for the transformation, the higher the

percent transformed at which the kinetics curves approach a straight line.

The absorption spectra of lead, thallium, and indium ions in a potassium iodide lattice were obtained as the potassium iodide proceeded through the transformation. The maximum absorption of the impurity peaks occurs at different wavelengths in the sodium chloride and the cesium chloride phases. The manner in which the peak shifts position as the potassium halide proceeds through the transformation gives some information on the size of the domains during the transformation. If the maximum size of the domains is small, 20–50 ions, then an impurity atom in a domain would feel the effect of neighboring domains and would not exist only in the field of its domain. The perturbation, of the neighboring domains, would be expected to effect the absorption spectra of the impurity ion and as the potassium halide proceeded through the transition, it might be expected that the absorption peak would gradually shift from a position characteristic of the sodium chloride phase, to one characteristic of the cesium chloride phase. On the other hand, if the maximum size of the domains is large, several hundred ions, then the perturbation of neighboring domains is negligible and two distinct peaks should exist during the transformation, one for those ions existing in the sodium chloride phase and one for those in the cesium chloride phase. Because of the large separation of the absorption peak in the different phases, the clearest results were obtained for lead impurities in potassium iodide lattice. Figure 11 shows the peak at various percentages transformed. The second peak appears at about 75% transformed. At nearly 100% transformed, the two peaks are of equal size. At 100% transformed, only one peak exists. The absorption peaks do not shift. One grows with respect to the other. The absorption peak of the sodium chloride phase is more intense than that of the cesium chloride phase, and probably hides the cesium chloride peak through most of the transformation. (The peak in the CsCl phase is very broad even at very high pressure.) It may be concluded that the domains contain at least several hundred ions during the transformation.

ACKNOWLEDGMENT

S. Wiederhorn would like to acknowledge financial assistance from a Monsanto Chemical Company Fellowship.

Production of Single-Crystal Copper Films at Low Temperatures

ARTHUR YELON AND R. W. HOFFMAN
Case Institute of Technology, Cleveland 6, Ohio

A method is described for the production of single-crystal films of copper at temperatures as low as −40°C. This method utilizes the epitaxy of copper on rocksalt. A thin layer of copper is evaporated on a single crystal of salt at 350°C. Then a thick layer is evaporated at the low temperature.

Films grown by this method have been examined using x-ray and etching techniques. It was found that some of these films had single-crystal regions of 1 mm diameter and larger. These crystallites had [100] directions within 1° to a normal to the film surface.

1. INTRODUCTION

IN 1936, Brück demonstrated that single-crystal copper films can be produced by epitaxy on rocksalt.[1] He found, however, that there is a minimum temperature, 300°C, below which epitaxy will not take place.

If one wishes to study the annealing of imperfections in copper films, they must be evaporated at 0°C or below, or else most of the interesting effects will be lost.[2,3] Therefore, a method has been devised by which single-crystal copper films can be produced at temperatures as low as −40°C.

The following is a description of this method, which consists of evaporating a thin layer of copper on a single crystal of rocksalt at 350°C, and then evaporating a thick layer at the desired temperature. Under the proper conditions, the thin layer forms a single crystal by epitaxy on the rocksalt, and the thick layer forms a single crystal by epitaxy on the thin layer.

2. EVAPORATION APPARATUS AND PROCEDURE

The evaporations in this experiment were performed in a vacuum system described previously by Story and Hoffman,[2] which had been modified to hold the freshly cleaved salt substrates.

A critical factor in the production of single-crystal films is the rate of evaporation. It has been shown[4–6] on both experimental and theoretical grounds that the probability of forming large aggregates in films on an amorphous backing is dependent upon the distance an atom can travel on the surface without colliding with other atoms. Thus, for low rates of evaporation and high temperatures, the probability of producing large aggregates is high. In order for epitaxy to take place on a crystalline substrate, an atom must be able to migrate to an appropriate site, dictated by the potential configuration of the substrate surface. Therefore, the same conditions which govern the formation of large aggregates on amorphous substrates will likewise govern the formation of single crystals on salt.

In the present experiment, successful results were achieved by evaporating the thin layer (about 120 A) at 350°C, at a rate of 6 to 8 A/sec. The substrate was then cooled to the desired temperature, and a thick film (about 1500 A) was evaporated. At 0°C, an evaporation rate of 20 A/sec and at −40°C, a rate of 12 A/sec were found to produce good films.

We were unable to produce single crystal films at −60°C with an evaporation rate of 9.6 A/sec.

The method of determining the thickness and rate of evaporation of the films has been discussed previously.[2]

At the start of evaporation the pressure was 1.5×10^{-6} to 4.0×10^{-6} mm Hg. During evaporation, the pressure did not exceed 10^{-5} mm Hg. At these pressures, evaporation rates much below those employed would have resulted in considerable contamination.

3. ANALYSIS OF THE FILMS

Three approaches were taken to determine that the films produced by the procedure previously described were in fact single crystals. X-ray pictures were taken in a powder camera and in a Laue camera, and portions of the films were examined under a microscope while they were being etched.

First, pictures were taken in the powder camera while the film was still on the salt. This served to give an over-all view of the nature of the undamaged film. Since the x-ray spot was 1 mm in diameter, and the beam made an angle of 81° to a normal to the film, a large section of the film was covered in each picture. A number of pictures of different parts of the film gave a general view of it.

For example, eight powder pictures of film X-Cu-36 were taken. Seven of these showed spots and no rings, and the eighth showed faint traces of rings along with the spots. This indicates that the film was almost entirely monocrystalline, but included one disordered region, which may have been due to the presence of a large step in the substrate.

Next, a piece of plexiglass was softened with chloroform and a portion of the salt was pressed, film side down, onto the plexiglass. This was allowed to dry and

[1] L. Brück, Ann. Physik **26**, 233 (1936).
[2] H. S. Story and R. W. Hoffman, Proc. Phys. Soc. (London) **B70**, 950 (1957).
[3] N. S. Rasor, ONR Tech. Rept. No. 14, Case Institute of Technology.
[4] H. Levenstein, J. Appl. Phys. **20**, 306 (1949).
[5] R. S. Sennett and G. D. Scott, J. Opt. Soc. Am. **40**, 203 (1950).
[6] Nancy J. Scott, U. S. Air Force Tech. Rept. No. 11, Cornell University.

harden, and then the salt was washed off with warm water. If the film and substrate were reasonably unstrained, the film remained undamaged in the process. If they were strained, there was a tendency for the film to peel. X-ray transmission pictures were then taken of the film on plexiglass in a Laue camera. These pictures were not, strictly speaking, Laue patterns. Since the film was thin (about 1600 A) only reflection of the K radiation from the molybdenum target of the x-ray tube from a given set of planes was intense enough to produce a detectable image. This made it possible to obtain information about the bending and misorientation of films which were nearly flat single crystals. For a perfect film, the [100] direction is normal to the surface of the film. For a beam parallel to this direction, one should, in principle, observe no spots. In practice, some of the (311) spots were found; and, on some of the films, all the (311) and some (420) spots were found. No other spots were ever observed. Usually, only four (311) spots were visible.

The appearance of any spots at all was due to a combination of three factors: the finite width of the x-ray beam, the bending of the film as a whole, and misorientation of crystals in the film. The effect of these is to permit a range of angles between a given plane and the beam. The significance of this can be understood by reference to Table I. For a given (hkl) the Bragg angle given is for MoK radiation, the tilt angle is the angle between the plane and the [100] direction, and the skew angle is the difference between

TABLE I. Skew angles for x-ray reflections.

hkl	Bragg angle	Tilt angle	Skew angle
111	9° 47′	35° 16′	25° 29′
200	11° 18′	0°	11° 18′
		90°	78° 42′
220	16° 8′	45°	28° 52′
		0°	16° 8′
222	20° 15′	35° 16′	15° 1′
311	18° 54′ (K_α)	64° 46′	54° 52′
		17° 33′	1° 21′
	17° 46′ (K_β)		13′
331	25° 43′	43° 33′	17° 50′
		13° 18′	12° 25′
333	30° 24′	35° 16′	4° 52′
400	23° 8′	0°	23° 8′
		90°	66° 52′
420	25° 59′ (K_α)	63° 26′	37° 27′
		26° 34′	35′
	24° 16′ (K_β)		2° 18′
422	28° 41′	54° 44′	26° 3′
		24° 6′	4° 35′

TABLE II. Analyses of representative films.

Film No.	T (°C)	Rate 1 (A/sec)	Rate 2 (A/sec)	Powder	Laue	Etch
X-Cu-11	0	27	29	Streaked spots, faint rings	Spots, no rings	
X-Cu-26	0	15	30	Strong spots, faint to strong rings	Spots, no rings	
X-Cu-36	0	6.8	20	Seven with no rings, one with faint rings	Eight with strong spots, one with double spots	
X-Cu-37	0	40	22			Line separation 0.8 mm and larger corresponds to thermal expansion cracks in the salt.
X-Cu-38	−20	32	18	Streaked spots, faint rings	Seven with nothing, one with many spots	Grains about 1 mm
X-Cu-39	−61	12	24	Rings with arcing, some spots	Nothing	Nonselective
X-Cu-40	−66	6.0	9.6	Streaked spots, some rings	Nothing	Large grains
X-Cu-41	−50	4.8	17	Streaked spots, some rings		
X-Cu-42	−41	6.0	12	One with spots, no rings; three with spots, faint rings	Spots no rings	

these; that is, the angle between the x-ray beam and the [100] direction which will result in a reflection.

For film X-Cu-36, two sets of (311) spots and one set of (420) spots appear. Consideration of Table I leads us to the conclusion that

$$1°21'<\Delta\theta<2°18',$$

where $\Delta\theta$ is the skew angle.

Purely geometrical considerations of the collimation of the beam, the first factor mentioned previously, yields a $\Delta\theta$ of 1° 24′. Thus, we can conclude that the film is flat and has its [100] direction parallel to the normal to the film surface to within 1°.

There can have been no rotations about this direction, or streaked spots or rings would have been observed.

Etching served to give further indication of sizes of single-crystal regions and of strains in the substrates. The films were etched with ammonia vapor and observed through a microscope. If there were fairly large single-crystal regions, ending in small-angle grain boundaries, or cracks in the substrate, the copper at the grain boundaries or cracks was etched preferentially. In some films, the grain size was determined by substrate cracks. When these were eliminated, the etch went nonpreferentially or indicated widely spaced boundaries.

4. RESULTS AND CONCLUSIONS

We were able, by the procedure previously described, to obtain single-crystal films at temperatures as low as −40°C. Below −50°C, this was no longer possible. However, a considerable degree of preferred orientation persisted to lower temperatures. The powder patterns showed considerable arcing at −60°C, with an evaporation rate of 9.6 A/sec. To obtain preferred orientation at much lower temperatures, it would seem that one would require a very slow rate.

Some of the analyses of the films which led to these conclusions are summarized in Table II. In this table, rate 1 is the rate of evaporation at 350°C, and rate 2 is the rate of evaporation at the low temperature.

The crystal axes of the copper films were not oriented with respect to the crystal axes of the salt in the manner which one would expect *a priori*. We found parallel orientation; that is, the (100) face of the copper is parallel to the (100) cleavage face of the rocksalt and the [001] direction of the copper is parallel to the [001] direction of the rocksalt. For the smallest possible misfit one expects the face diagonal direction of the copper to be parallel to the edge direction of the salt. These results are in agreement with the equally surprising results for silver on rocksalt.[7]

The method of low-temperature evaporation which has been described here should be applicable to any of the metals which can be grown by epitaxy on rocksalt: nickel, palladium, aluminum, gold, silver,[1] iron, and cobalt.[8]

ACKNOWLEDGMENTS

The authors wish to thank K. H. Rosette and Dr. T. G. Knorr for their assistance in the experimental work. This work was supported by the U. S. Atomic Energy Commission and by the National Carbon Company.

[7] D. W. Pashley, Advances in Phys. **5**, 173 (1956).
[8] L. E. Collins and O. S. Heavens, Proc. Phys. Soc. (London) **B70**, 265 (1957).

JOURNAL OF APPLIED PHYSICS VOLUME 31, NUMBER 9 SEPTEMBER, 1960

Effect of Li-B Ion Pairing on Li^+ Ion Drift in Si†

E. M. PELL
General Electric Research Laboratory, Schenectady, New York
(Received May 4, 1960; and in final form June 9, 1960)

When Li^+ and B^- ions are present simultaneously in Si, relatively immobile Li-B ion pairs are formed. Only those Li^+ ions which have not become paired with B^- are free to diffuse through the Si, and measurement of the effective diffusion rate of the Li^+ can thus be used to determine the fraction of Li^+ paired. Such measurements have been made in the range 2°–100°C using the method of ion drift in a *pn* junction. The results agree well with the Reiss model for ion pairing, yielding a distance of closest approach between Li^+ and B^- of 2.5–2.7 A. This value is larger than given by the sum of Li^+ and B^- radii; it is roughly equal to the distance from a lattice-atom site to the next-nearest interstitial site (2.72 A). The kinetics of the ion-pairing reaction have been investigated by the same technique. The resulting value for the capture radius of the B^- ion agrees satisfactorily with theory.

INTRODUCTION

A DETAILED model for ion-pairing in solids has been proposed by Reiss, Fuller, and Morin.[1] The model includes an evaluation of the equilibrium constant for the pairing reaction and an evaluation of the equilibrium separation of the ions. It also describes the kinetics of the pairing, such as would be observed after thermal dissociation and quench, and relates these kinetics to a "capture radius" descriptive of the immobile ion. This capture radius is to be distinguished from, and is much larger than, the equilibrium distance of approach.

The coulomb bond formed by ion pairing between a mobile donor ion such as Li^+ and a relatively immobile acceptor ion such as B^- would be expected to affect the net diffusion rate of the mobile ion, but at usual diffusion temperatures the effect cannot be seen because the combination of low binding energy and large entropy factor for dissociation results in complete thermal dissociation. At lower temperatures diffusion rates cannot easily be measured; however, in a different type of experiment based on the measurement of charged impurity scattering, in which the ions are required to move only the short distances necessary for association or dissociation, Reiss and his co-workers have been able to study a variety of such pairing reactions with Li in Ge and also the Li-Al pairing reaction in Si.[2]

The technique of ion drift in the field of a *pn* junction[3] permits a direct measurement of diffusion rates for diffusion constants down to 10^{-13} cm^2/sec, essentially because it permits the use of a large electric force to move the ions combined with a technique for measuring very small distances of motion. Since the diffusion rate of free Li^+ is accurately known in the same temperature range,[4] it appeared possible to measure directly the effect of ion pairing on the diffusion rate of the Li^+. Since this could easily be done as a function of temperature, the results would constitute a good check of the Reiss model, for the model predicts both the magnitude of ionic association and its temperature dependence once a single parameter, the distance of ionic separation, is fixed. The pairing of Li^+ and B^- in Si was of particular interest, for an anomalously large separation distance has been measured for this pair by the Reiss technique in Ge[1]; if this anomaly persisted in Si, it would increase the confidence in both techniques and underline the need for an explanation.

Such drift measurements should permit the determination of both the kinetics and the equilibria associated with pairing. Since an Li^+ ion is trapped when associated with B^- as an ion pair, and is then not free to diffuse, a comparison of the effective-diffusion constant with the free-Li^+ diffusion constant gives directly the fraction of the Li^+ ions which remain unpaired at any instant and temperature. After a quench from high temperature, this fraction decreases with time as pairing proceeds, and hence a measurement of diffusion rate vs time establishes the pairing kinetics. This leads, in turn, to a value for the capture cross section of the B^- ion for the Li^+ ion. The ultimate effective diffusion rate, compared with the diffusion rate of free Li^+, establishes the equilibrium dissociation constant.

II. EXPERIMENTAL PROCEDURES

In the present measurements, the diffusion constant is deduced from the rate at which the Li^+ ions drift in the field of a reverse-biased *np* junction. The *np* junction is prepared in a preliminary step by diffusing Li into the surface of a small bar of B-doped Si. The drift rate of the Li^+ ions, at a given temperature, is determined by measuring the rate of change of the capacitance of the junction. Complete details, with a full discussion of the experimental techniques, is given in footnote reference 3. Since the present samples were of low resistivity, surface problems were not serious, and the boron treatment

† The research reported in this paper has been sponsored by the Electronics Research Directorate of the Air Force Cambridge Research Center, Air Research and Development Command, under a U. S. Air Force contract.

[1] H. Reiss, C. S. Fuller, and F. J. Morin, Bell System Tech. J. **35**, 535 (1956); also H. Reiss, J. Chem. Phys. **25**, 400 (1956) and **25**, 408 (1956).

[2] J. P. Maita, J. Phys. Chem. Solids **4**, 68 (1958).

[3] E. M. Pell, J. Appl. Phys. **31**, 291 (1960).

[4] E. M. Pell, Phys. Rev. **119**, 1014 (1960).

described in footnote reference 3 was omitted. Gold plating of the surface and use of a dry oxygen ambient were retained. Sample dimensions were roughly 1 cm ×0.3 cm×0.3 cm, with the lithium diffused into one side. Junction areas were determined by electrical probing; they were nearly equal to the geometrical area of the sample face.

The Si used was B-doped single-crystal vacuum-grown floating-zone Si of either 0.15- or 1.05-ohm cm resistivity from Merck and Company. For reasons discussed in footnote reference 4, the oxygen content in this material (estimated as 10^{15} atoms/cm^3) is too low to make the Li-oxygen interaction significant. The boron concentration in the 0.15-ohm cm Si is, for reasons discussed in footnote reference 4 and also made clear in subsequent sections of this report, sufficiently high to ensure complete pairing in times short relative to the period of the observations. In the 1.05-ohm cm material, the time constant for pairing at 0°C is sufficiently longer that it can be experimentally measured to learn the trapping cross section of the B^- ion.

Ionic mobilities were determined from capacitance measurements by measuring the slopes of $1/C^2$ and $1/C^3$ vs time, using (1) the formula[2]

$$\mu=\frac{B(B-L/W)}{2V}\frac{d}{dt}(10^8/C)^2 \qquad (1)$$

for the region in which $1/C^2$ vs t gives a straight line, where C is the capacitance in $\mu\mu$f; and (2) the formula

$$\mu=\frac{B^3}{12VL}\frac{d}{dt}(10^8/C)^3 \qquad (2)$$

for the initial region in which $1/C^3$ vs t gives a straight line. In these formulas, μ is the mobility in cm^2/v sec, B is equal to the junction area in cm^2 multiplied by 1.06×10^{-8}, V is the reverse voltage applied to the junction during the ion drift, and W is the average junction width in units of $(10^8/C)$ in the region where the slope is measured. L is characteristic of the initial impurity gradient at the junction; in the present experiments it was calculated from the expression $L=(Dt)^{\frac{1}{2}}/K$, where D is the diffusion constant at the temperature of the preliminary Li indiffusion and K (defined as $d/[2(Dt)^{\frac{1}{2}}]$, where d is the distance from the surface to the junction) is a nondimensional distance parameter which may be found from the error function solution to the diffusion equation for the particular time t, the surface Li concentration, and the junction Li concentration characteristic of the preliminary Li indiffusion. From the mobility the effective diffusion constant was calculated using the Einstein relation, $D_{eff}=\mu kT/e$. Use of this relation involves the assumption that the Li is present as Li^+ and that the diffusion process is uncorrelated; the validity of these assumptions has been discussed previously.[5]

[5] E. M. Pell, Phys. Rev. **119**, 1222 (1960).

III. RESULTS AND DISCUSSION

Pairing Equilibria

Five samples prepared from the 0.15-ohm cm Si were used in the ion-drift experiments which measured the pairing equilibria. The drift rates were measured in each sample at room temperature, 50°, 75°, and 100°C. The initial data at room temperature were plotted as $1/C^3$ vs t, where C is the junction capacitance, and gave a straight line whose slope yielded a value for D in accordance with the model. Subsequent data at higher temperatures and also a final repeat run at room temperature were plotted as $1/C^2$ vs t and gave a straight line whose slope yielded D_{eff} in accordance with the model for later stages of ion drift.[3] These data were similar in all respects to data reproduced in the earlier works cited in footnotes (3, 4) and are therefore not repeated here. The initial and final runs at room temperature permitted a check for a change in D_{eff} with time which might be ascribable to incomplete pairing in the initial data. The value obtained in the final run was on the average about 20% higher than that obtained in the initial run, but the mean-probable errors overlapped. The discrepancy is therefore slight, if not meaningless, and it can be concluded that pairing was essentially complete in the initial data; nevertheless, to minimize the small possible error, the final room-temperature data were used in subsequent analysis in preference to the initial room-temperature data.

The five results at each temperature were averaged and mean-probable errors were calculated. The results are displayed in Fig. 1. The solid lines which are drawn through the data points represent that envelope of the data which is consistent with both the probable error

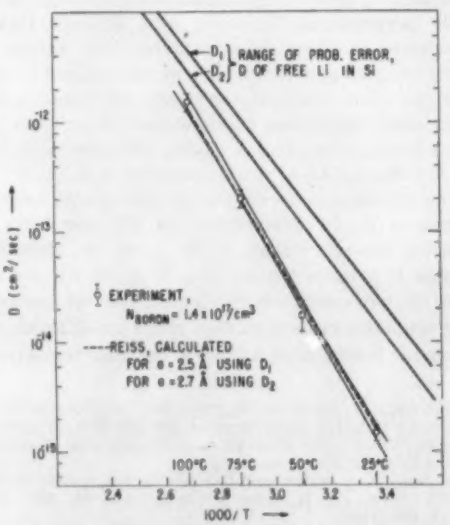

FIG. 1. Diffusion constant of Li^+ under conditions of ion pairing with B^-.

as determined from all samples at each temperature and the extreme range of measured slopes obtained for the individual samples. The other pair of solid lines represent previous results from free-Li^+ diffusion.[4] The dashed line represents the result of a calculation based on the Reiss model, using Table III and the equations in Sec. 9 of footnote reference 1 with the values for a noted in the figure.

Since the Reiss model specifies the dependence of the dissociation constant on the impurity concentration, the same experiment was repeated using 1.05 ohm cm Si. The results are given in Fig. 2, and it is seen that the normalization factor given by the Reiss model causes these data to fall within the experimental error of the other results. The good fit to the model is noteworthy since the choice of a single parameter determines both the slope and the magnitude of dissociation.

The resulting value for the distance of ionic separation between the Li^+ and the B^-, 2.5 to 2.7 A, is anomalously large, as it was also found to be in Ge (2.05–2.27 A in Ge[1]). It is to be compared with the sum of the ionic radius of Li^+ (0.60 A[6]) and the tetravalent radius of B (0.88 A[6]) which is 1.48 A. (The distance of separation has been found to be closely approximated by this sum in the case of larger acceptor impurities.[1,2]) This distance can be compared with the Si-Si distance of 2.35 A, which is also the distance from a Si atom to the nearest interstitial site, and with the distance from a Si atom to the next-nearest interstitial site, which is 2.72 A. The close correspondence with the next-nearest interstitial distance suggests that the Li^+ may indeed be located at this site in the lattice. No simple explanation for such a location is offered; local crystal distortions may be important. Any explanation must, of course, be consistent with the observation that the separation distance is smaller when the larger acceptors are involved.[1] It must also be consistent with the observation that the $Li^+ - B^-$ separation distance is smaller in Ge[1], in spite of the smaller attractive force arising from the greater polarizability of Ge.[7] It should be kept in mind that these separation distances are really derived from the activation energy for pair dissociation and assume a pure coulomb bond.

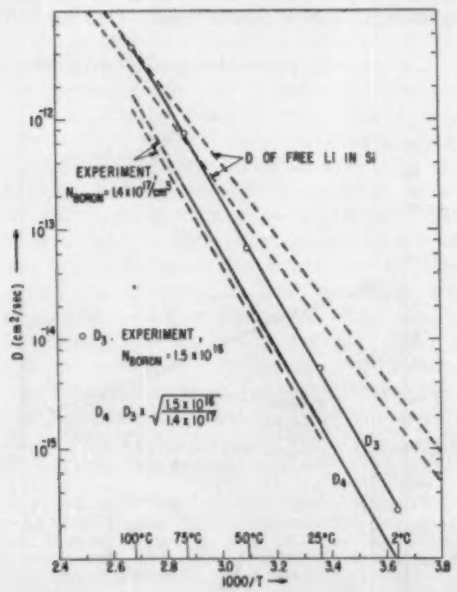

FIG. 2. Effect of variation of B^- concentration.

Kinetics

In the preceding experiments which measured the pairing equilibria, B^- concentrations and temperatures were chosen to give essentially complete pairing before the start of the measurements, and suitable checks were made to ensure that this was so. To measure the kinetics, on the other hand, it is necessary to start with minimum pairing and to arrange that the time constant for pairing will fall in a conveniently measurable range. Since the pairing process is similar in many respects to diffusion-limited precipitation, it would be expected that the time constant for pairing could be increased either by decreasing the diffusion constant through lowering the temperature or by decreasing the B^- concentration. In the kinetic measurements to be described, both methods were used. It was found that 1.05-ohm cm B-doped Si yielded samples with conveniently measurable time constants for pairing at 3°C. (This temperature, which varied between 2° and 3° from run to run, differed from the 0°C ice bath because the sample holder was outside the bath.) Since the initial ion-drift data are known to yield a straight line proportional to the effective ionic mobility, and hence to the unpaired Li^+ concentration, when the reciprocal of the cube of the junction capacitance $1/C^3$ is plotted vs time,[3] the pairing process will show up as a gradual decrease in slope on such a plot. (Eventually the slope will increase again when the transition region to constant $d(1/C^3)/dt$ is reached,[3] but the present experiments were not carried into this region). Such a decrease in slope is illustrated in Fig. 3. Had the time constant for pairing been much shorter, as in the previously described cases, the data would have fallen along the dashed line.

The rate at which the final slope is attained is a function of the effective "capture radius" of the B^- ions for the precipitating Li^+ ions. This radius r_0 (which is to be distinguished from the previously discussed equilibrium distance a) measures the probability/unit time that a diffusing Li^+ ion will be trapped by a B^- ion and its associated electric field, according to the formula $F = 4\pi r_0 DN$. Here N is the average number of unassoci-

[6] L. Pauling, *The Nature of the Chemical Bond* (Cornell University Press, Ithaca, 1960), 3rd ed., p. 514 and p. 246.

[7] Van Vleck, *The Theory of Electric and Magnetic Susceptibilities* (Oxford University Press, England, 1932).

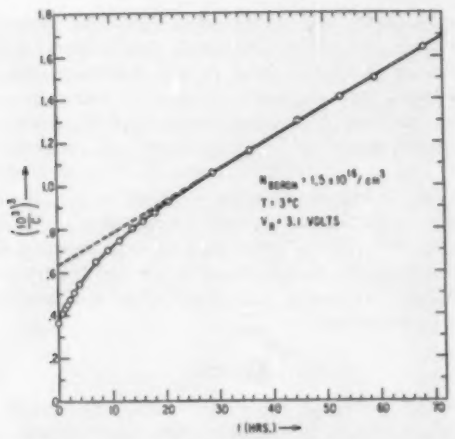

FIG. 3. Effect of ion pairing kinetics on ion drift in an np junction.

ated Li^+ ions/unit volume, D is the diffusion constant of free Li^+, and F is the probability that a B^- ion captures one Li^+ ion in unit time. The differential equation for the pairing kinetics follow from this definition of r_0. Thus, at any instant

$$-dN/dt = 4\pi r_0 D N N_B^- - N_p R, \quad (3)$$

where N_B^- is the average number of unassociated B^- ions per unit volume, N_p is the average number of Li-B pairs per unit volume, and R is the dissociation rate of such pairs. R can be evaluated from the requirement that $dN/dt=0$ at equilibrium. Denoting equilibrium concentrations with the superscript 0, and noting further that $N_B^- = N_B^{-0} + \Delta N_B^-$, $N = N^0 + \Delta N$, and $N_p = N_p^0 - \Delta N_B^-$, where the Δ's refer to departures from equilibrium, and also that $\Delta N = \Delta N_B^-$ and $N^0 = N_B^{-0}$ in the nearly perfectly compensated junction region, there is obtained

$$-dN/dt = 4\pi r_0 D \Delta N [N^0(2 + N^0/N_p^0) + \Delta N]. \quad (4)$$

This differential equation describes the pairing kinetics. It has for its solution,

$$\ln\{\Delta N/[N^0(2 + N^0/N_p^0) + \Delta N]\} = -4\pi r_0 D t N^0 (2 + N^0/N_p^0) + K, \quad (5)$$

where K is the value of the left-hand side of the equation at $t=0$.

It is next necessary to relate the experimentally measured time dependence of the diffusion constant to this solution. To do this, it is convenient to first modify and simplify Eq. (5). Note that if the ion pairs were entirely dissociated at equilibrium, one would measure the free-Li^+ diffusion constant D; however, if a smaller number N^0 are free, only these will contribute to the diffusion, so that an effective equilibrium diffusion constant, D_{eff}^0, given by $D_{eff}^0 = DN^0/N_{\text{total Li}}$, will be measured. Also, for small dissociation $N^0/N_{p0} \simeq N^0/N_{\text{total Li}}$, which in the present instance is about 0.1 and can therefore be neglected in Eq. (5). These two considerations make it possible to rewrite Eq. (5) as

$$\ln[\Delta N/(1 + \Delta N/2N^0)] - \ln 2N^0 = -8\pi r_0 D_{eff}^0 t N_{\text{total Li}} + K. \quad (6)$$

If one plots the left-hand side of Eq. (6) vs time, the results should fall along a straight line whose slope yields a time constant $1/\tau = 8\pi r_0 D_{eff}^0 N_{\text{total Li}}$.

The left-hand side of Eq. (6) can be related to the experiment by noting that the difference between the slope at time t and the final slope in Fig. 3 is proportional to ΔN, because the effective diffusion rate is proportional to the number of free Li^+ ions. It follows that $\Delta N/2N^0$ can be found from the ratios of this difference to the final slope. As an example, the left side of Eq. (6) has been plotted in Fig. 4 from the data of Fig. 3. The result yields a time constant of 9.4–11 hr. This time constant yields r_0 in accordance with the previous equation, provided that $N_{\text{total Li}}$ and D_{eff}^0 are known. $N_{\text{total Li}}$ is given by the sample resistivity and for this sample equals 1.5×10^{16} Li atoms/cm³. D_{eff}^0 is given by the final slope and in this case is 1.47×10^{-16} cm²/sec; however, since this value depends sensitively upon the junction area, it may be better to use a D_{eff}^0 based on more than one sample. From Figs. 1 and 2, this is judged to be $(2.0\text{–}2.8)\times10^{-16}$ cm²/sec for the present Li concentration. These considerations lead to a value for r_0 of 33–39 A.

It will be noted that the kinetics were measured with a relatively low junction bias of 3.1 v; ion-drift data in samples of this resistivity would normally be obtained using voltages over a decade higher. This low voltage

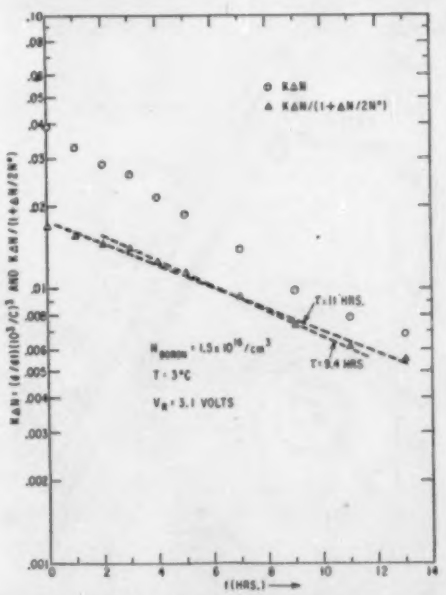

FIG. 4. Determination of the time constant for ion pairing.

was used in order to avoid field-dependent effects upon the capture radius. Two such effects can be visualized. The first results from the fact that the Li^+ ions are not undergoing a purely diffusive motion but have a net drift in the junction field superposed on their random motions. This drift can be fast enough relative to the diffusive motion so that the Li^+ ions are swept into the vicinity of the B^- traps at an appreciably greater rate than would be the case without the field. Such an increase in capture rate can be described as an increase in the effective capture radius. This effect has been calculated by F. S. Ham (see Appendix I); for a junction voltage of 46 v, corresponding to a junction field of 86 kv/cm, it should result in a 68% increase in the effective r_0. The second effect results from the fact that an Li^+ ion, which would in the absence of a field behave as though it were captured with certainty at the distance r_0 from a B^- ion, could in the presence of a sufficiently strong field be swept out again by the field even after approaching closer than r_0. To indicate that the previously mentioned field of 86 kv/cm is likely to be sufficiently strong, note that it will produce a potential drop in excess of 0.04 v in a distance corresponding to the theoretical B^- capture radius of 50 A; this is greater than kT/e, which in the theoretical model[1] is the coulomb binding energy at the distance r_0 in the absence of a field. An exact calculation of this second effect is difficult and has not been made. It will counteract the first effect; the net theoretical result upon $r_{0\,eff}$ is not known. Experimentally, the kinetics observed with a junction bias of 46 v resulted in values for r_0 which overlapped the range observed when 3.1 v was used,[8] which can be taken as evidence that the two effects are comparable for this value of bias.

The theoretical value for r_0 when the field can be neglected is given by e^2/kT[1] and is 50.5 A in Si; it is just the radius at which the coulomb binding energy is equal to kT/e. The present experimental value of 33–39 A is felt to be in reasonable agreement with the theoretical value, in view of the experimental errors inherent in using the slope of the original data. A slight further increase in the experimental r_0 may be justified by noting that the value for $D_{eff}{}^0$ was obtained from other samples drifted at higher junction fields (even though τ itself was obtained at negligible field), such that the potential drop in a distance equal to the jump distance for diffusion (equal to about 0.004 ev) was not entirely negligible; this could justify increasing r_0 by as much as 20% [equal to $\exp(0.004\ e/kT)$], yielding 40–47 A for the experimental value.

[8] This result is different from that reported at the 1960 New York American Physical Society Meeting. The previous result followed from an analysis based on $dN/dT=-4\pi Dr_0\Delta N\Delta N_{B^-}$, which neglects the contribution from the fraction of the pairs which are already dissociated at equilibrium.

It will be recognized that these kinetics can alternatively be used to obtain D_{eff} if one assumes the theoretical value for r_0, and it will be obvious that such a procedure would lead to a satisfactory value for D_{eff}. One cannot, however, obtain D without independent knowledge that the pairs are completely dissociated initially. In the present case, $D/D_{eff}\simeq 10$, whereas the ratio of initial to final slopes in Fig. 3 is only about 2.7, indicating that the pairs were far from completely dissociated. This lack of complete dissociation is not unreasonable in view of the length of time the samples spent at room temperature after the Li diffusion while they were being prepared for the drift measurements.

ACKNOWLEDGMENTS

The considerable advice and help of F. S. Ham is acknowledged with special gratitude. The author also wishes to acknowledge the advice of H. Ehrenreich and the critical reading of the manuscript by A. G. Tweet. He is indebted to D. J. Locke for the diligent and competent performance of the experiments.

APPENDIX I

F. S. Ham's result for the effect of the field in increasing the effective capture radius is outlined by him as follows:

"The steady state rate of flow F of diffusing material to a sphere of radius r_0 moving with velocity v is given by

$$F=(4\pi^2\rho_0 D^2/v)\sum_{l=0}^{\infty}(2l+1)(-1)^l \times[I_{l+\frac{1}{2}}(vr_0/2D)/K_{l+\frac{1}{2}}(vr_0/2D)].$$

Here ρ_0 is the density of the diffusing substance far from the sphere, and we have imposed the boundary condition that this density is zero on the sphere's surface. The functions $I_n(x)$ and $K_n(x)$ are modified Bessel functions of order n, of the first and second kind, respectively [as defined by G. N. Watson in "A treatise on the theory of Bessel functions" (Cambridge University Press, Cambridge, England, 1952), 2nd ed., p. 78]. Defining the effective capture radius r_{eff} by

$$F=4\pi r_{eff}D\rho_0,$$

we have therefore

$$r_{eff}/r_0=(\pi/2)(2D/vr_0)\sum_{l=0}^{\infty}(2l+1)(-1)^l [I_{l+\frac{1}{2}}(vr_0/2D)/K_{l+\frac{1}{2}}(vr_0/2D)].$$

The derivation of these results for spherical geometry is similar to that for a moving cylinder given by D. B. Concer [Quart. J. of Mech. and Appl. Math. **12**, 222 (1959)]."

JOURNAL OF APPLIED PHYSICS VOLUME 31, NUMBER 9 SEPTEMBER, 1960

Formation of Thin Polymer Films by Electron Bombardment*

ROBERT W. CHRISTY†
Space Technology Laboratories, Inc., Los Angeles 45, California
(Received April 4, 1960)

Thin insulating films, less than 100 A thick to a few thousand angstroms, were produced by bombarding a substrate with electrons in the presence of silicone oil vapor. The rate of deposition of the solid film was found to depend on the substrate temperature, electron beam current density, and oil vapor pressure. A theoretical expression for the rate is given which agrees satisfactorily with the experimental data. The films which were produced had excellent electrical insulating properties.

INTRODUCTION

IN electron optical systems, it is observed that surfaces which are struck by the electron beam become covered by a thin insulating film. This troublesome contamination has been studied,[1,2] and found to be due to interaction between the electron beam and organic vapor present in the vacuum system, arising from diffusion pump oil, vacuum grease, rubber, etc. It can be prevented by condensing the vapor on a cold trap, or by heating the bombarded surfaces.[2] The mechanism of the film formation[1] is the free radical polymerization of the organic molecules adsorbed on the surface, under the action of the bombarding electrons. The molecules are cross-linked by the electron beam to form a solid polymer film.

It has been suggested[3] that this effect could be usefully exploited where a thin insulating film is wanted. From this point of view, the organic silicon polymers[4] are particularly interesting, because of their excellent dielectric properties. We have therefore made a more detailed study of the factors affecting the film growth rate, using a silicone oil as raw material.

Considerable interest has already been shown in the cross linking of bulk polymers by high energy radiations.[5] The siloxanes, particularly polydimethylsiloxane, are among the polymers which have been examined.[6,7] The reaction rate theory has been considered in detail for the cross-linking of polyethylene.[8] The successive addition of polymer layers by radiation-induced cross linking of molecules on the surface cannot directly be described, however, from this information.

The present investigation concerns the rate of formation of solid films from a silicone oil vapor, DC 704 (Dow Corning Company, Midland, Michigan), under the influence of a low energy electron beam. The dependence of the growth rate on electron beam current and energy, oil pressure, and temperature will be discussed experimentally and theoretically. The resulting films, which are continuous at least down to thicknesses of the order of 50 A, have very interesting non-Ohmic electrical properties. These properties will be reported in detail later, however; the present article concerns principally the conditions under which the films are formed.

EXPERIMENTAL RESULTS

Our experiments were carried out in a bell-jar vacuum system, using DC 704 as diffusion pump oil. In order to avoid contamination from the pump oil, DC 704 was also chosen as the experimental silicone vapor, since in our system the pump oil could not be trapped without also trapping the experimental vapor. This precaution proved to be necessary. A separate source of DC 704 at room temperature, with a surface area of about 30 cm², was put in the system, but the presence of this source increased the rate of film formation by only about 20%. The total pressure in the vacuum system varied between 4×10^{-6} and 2×10^{-5} mm Hg. The rate of film formation was insensitive to the total pressure, but very sensitive to the partial pressure of the oil.

The polymer films were deposited onto a tin film about 1500 A thick, which had previously been evaporated on a flat glass substrate. The substrate was in thermal contact with a heat reservoir, so that its temperature could be controlled. Electrical connection was made to the tin film, through the thermocouple soldered to the substrate.

The electron source was an electron gun triode,[9] designed for the purpose. The gun was about 2 in. from the substrate. A circular aperture was about ¾ in. from the substrate. The electron beam was defocused, so that a spot of uniform current density about 2 mm in diameter was obtained on the substrate. The gun was operated with an accelerating voltage of 225v.

The measurement of electron current density at the substrate presented a problem because of secondary

* Supported in part by the Office of Naval Research. Paper presented at ONR Symposium on Superconductive Techniques for Computing Systems, May 18, 1960.
† Permanent address: Physics Department, Dartmouth College, Hanover, New Hampshire.
[1] K. M. Poole, Proc. Phys. Soc. (London) **B66**, 541 (1953).
[2] A. E. Ennos, Brit. J. Appl. Phys. **5**, 27 (1954).
[3] D. A. Buck and K. R. Shoulders (unpublished).
[4] E. G. Rochow, *Chemistry of the Silicones* (John Wiley & Sons, Inc., New York, 1946).
[5] F. A. Bovey, *Effects of Ionizing Radiation on Natural and Synthetic High Polymers* (Interscience Publishers, Inc., New York, 1958).
[6] A. Charlesby, Nature **173**, 679 (1954).
[7] A. Charlesby, Proc. Roy. Soc. (London) **A230**, 120 (1955).
[8] H. Okamoto and A. Isihara, J. Polymer Sci. **20**, 115 (1956).
[9] H. Moss, J. Brit. Inst. Radio Engrs. **6**, 99 (1946).

electron emission. The procedure adopted was to operate the gun with the anode at ground potential. The primary current to the film was measured by applying +90 v to the film, so as to collect nearly all the secondaries and eliminate their contribution to the net current. The film was then formed with the substrate at ground potential, so as to collect none of the secondaries, holding the emission constant by monitoring the total current to ground. The measured current density is probably accurate to about 10%.

The thickness of the resulting films was measured interferometrically,[10] after coating them with an opaque layer of silver. The uncertainty in this measurement was about ±70 A.

The solid film on the substrate grew linearly with time as a result of the electron bombardment. Some results for the deposition rate, in the presence of the vapor of DC 704, are shown in Fig. 1 as a function of electron current density at the substrate, for three different substrate temperatures. Each deposition was continued for 60 min, so that the uncertainty in the rate introduced by the thickness measurement was about 0.02 A/sec. The rate decreases with increasing temperature, as already found by Ennos.[2] It is not linear with beam current but appears to reach a saturation at high current densities.

It was not possible to increase the equilibrium vapor pressure of the oil in our vacuum system. The source of oil could be heated, but the large surface area at room temperature served as a sink, so that the only effect was to evaporate oil from the source onto the bell jar. The effective vapor pressure could be lowered, however, by cooling baffles in the system with liquid nitrogen. Under these circumstances the rate of film growth was decreased by an order of magnitude.

The films which are formed can be seen when they are thicker than about 200 A, and are slightly absorbing. Based on visual estimates of the absorption and interference colors, the real part of the index of refraction appears to be between 1.6 and 2.0, and the imaginary part (extinction coefficient) is probably not greater than 0.1. The electrical resistivity of the film material is greater than 10^{14} ohm-cm at low voltage. The current-voltage characteristic is approximately exponential over at least six orders of magnitude of current, for the thinner films, and changes very slightly between 300° and 4°K. The electrical breakdown strength is of the order of 10^7 v/cm.

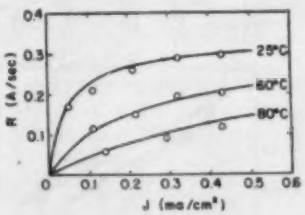

FIG. 1. Deposition rate R of solid polymer film as a function of electron beam current density J, at three different substrate temperatures. The lines are theoretical.

THEORY OF FILM GROWTH RATE

The rate of formation of solid polymer film on the substrate under the influence of electron bombardment can be calculated by a simple phenomenological theory. We assume there are N oil molecules per unit area adsorbed on the surface, with a mean time of stay τ. An electron hitting one of these molecules can tie it down permanently by forming a cross link, incorporating the molecule into the solid polymer film. Let P be the number of molecules per unit area which have been cross linked, so that dP/dt is the rate of growth of the film. Then, assuming a first-order rate process,

$$dP/dt=\sigma fN, \tag{1}$$

where σ is the cross section for the cross-linking collision and f is the number of electrons per unit area per unit time. Since every such cross-linking event removes an oil molecule from the number N on the surface,

$$dN/dt=F-N/\tau-dP/dt, \tag{2}$$

where F is the number of oil molecules which impinge on the surface from the vapor, per unit area per unit time.

On substituting Eq. (1) into (2) and integrating, we get

$$N=[F/(\sigma f+1/\tau)][1-Ke^{-(\sigma f+1/\tau)t}], \tag{3}$$

where K depends on the number of oil molecules initially on the surface. We now assume the surface is not completely covered with oil, so that $N<1/a$, where a is the area of an oil molecule. Then this assumption requires $F<(\sigma/a)f+1/a\tau$. The opposite case will be examined later.

On inserting Eq. (3) into (1) and integrating, we get

$$P=\frac{F}{1+(1/\sigma\tau f)}\left\{t+\frac{K}{\sigma f+1/\tau}[e^{-(\sigma f+1/\tau)t}-1]\right\}.$$

Unless both σf and $1/\tau$ are very small compared to unity (in which case P depends quadratically on t),

$$P\approx\{F/[1+(1/\sigma\tau f)]\}t. \tag{4}$$

The total thickness of the solid film is vP, where v is the volume of one molecule. Defining the rate of film formation by $R\equiv vP/t$, we have

$$R=vF/[1+(1/\sigma\tau f)] \quad \text{when} \quad F<(\sigma/a)f+(1/a\tau). \tag{5}$$

According to this result, at high current density or low temperatures, when $\sigma\tau f\gg 1$, the rate saturates at a value vF determined by the effective vapor pressure of the oil. At very low current density or high temperature, on the other hand, the rate is approximately

[10] S. Tolansky, *Multiple Beam Interferometry* (Oxford University Press, New York, 1948).

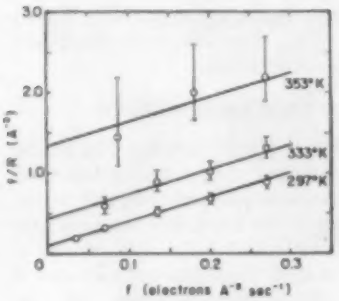

FIG. 2. Ratio of electron flux f to deposition rate R, vs electron flux, from the data of Fig. 1. Straight lines of the same slope are expected theoretically.

$\sigma\tau fvF$, depending also on current density and temperature.

In the case not yet considered, when the flux of oil molecules is so large that there is always a monolayer of oil, $N=1/a$ should be put into (1) so that

$$R=(\sigma/a)vf \quad \text{when} \quad F\geq(\sigma/a)f+(1/a\tau). \tag{6}$$

This result is independent of the oil pressure, since there is an oil molecule waiting to be hit by every electron. We have seen that in the opposite extreme when the electron flux is so high that every oil molecule is struck before it escapes from the surface, the rate is independent of electron current density.

The rate of film formation would not be expected to depend on the electron energy (unless σ is energy dependent), since not more than one collision on the surface is likely. The proportion of cross links may depend on electron energy, however, since more cross links may be formed in lower layers if the electrons are sufficiently energetic, provided the mean free path is shorter than the film thickness. If each electron produces one cross link, the number of cross links per unit area formed per unit time is f. On dividing by the rate of film formation calculated from Eq. (4), the number of cross links per molecule δ is

$$\delta=(1+\sigma\tau f)/\sigma\tau F. \tag{7}$$

When Eq. (6) applies, on the other hand, $\delta=1$. If the electrons are energetic enough to produce more than one cross link each, δ will be correspondingly greater. It will be seen below that δ is normally large.

In case the oil molecules impinge on the surface from an equilibrium vapor, F can be calculated from the vapor pressure p by[11]

$$F=\alpha p/(2\pi mkT)^{\frac{1}{2}}, \tag{8}$$

where m is the mass of the oil molecule, k is Boltzmann's constant, T is the absolute temperature, and the coefficient of evaporation α is the fraction of the impinging molecules which stick to the surface.

[11] E. H. Kennard, *Kinetic Theory of Gases* (McGraw-Hill Book Company, Inc., New York, 1938), pp. 63, 69.

COMPARISON OF RESULTS WITH THEORY

The theoretical case applicable to the present experimental situation will be seen to be that of low oil vapor pressure, in which the rate of film growth is given by Eq. (5). The flux of electrons is known from the electron beam current density J. The parameters vF and $\sigma\tau$ can most easily be determined by rewriting Eq. (5)

$$(f/R)=(1/vF)f+(1/\sigma\tau vF).$$

If (f/R) is plotted against f, straight lines should result, all with the same slope $(1/vF)$. The values of $\sigma\tau$ can be determined then from the intercepts at $f=0$.

The data of Fig. 1 are replotted in this way in Fig. 2. The errors indicated are calculated from the uncertainty in the film thickness measurement. Within this error, the data points lie on straight lines with the same slope, indicating that the effective oil vapor pressure determining F was constant. The slope of the lines drawn in Fig. 2 corresponds to

$$vF=0.33 \text{ A/sec}.$$

The values of $\sigma\tau$ determined from the intercepts in Fig. 2 are plotted logarithmically vs reciprocal absolute temperature in Fig. 3. Within the experimental errors, the points lie on a straight line, as would be expected if the cross section σ were independent of temperature and the mean time of stay τ of the molecules on the surface depended exponentially on reciprocal temperature. The equation of the line drawn in Fig. 3 is

$$\sigma\tau=1.7\times10^{-6}\exp(10\,000/RT) \text{ A}^2\text{sec},$$

where R is the gas constant in cal/mole-deg.

The curves drawn in Fig. 1 are calculated using this expression for $\sigma\tau$ and $vF=0.33$ A/sec, and give an adequate representation of the data. The rate of film growth should saturate at the value given by vF, namely, 0.33 A/sec at this oil vapor pressure, the saturation value being approached at lower current density the lower the substrate temperature. If the oil vapor pressure is reduced, the rate should be smaller, as observed. Although the energy of the bombarding electrons was not varied, the film formation has previously[1,2] been found to be independent of accelerating voltage.

In order to carry the analysis of the results any further, the properties of the oil molecule must be considered. The DC 704 fluid is stated to be an es-

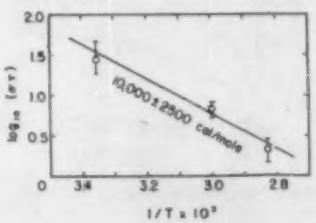

FIG. 3. Product of electron cross section σ for the cross linking event, with mean time of stay τ of the oil molecule on the substrate, vs reciprocal absolute temperature from Fig. 2.

sentially one-component methylphenylpolysiloxane. The molecule is similar to polydimethylsiloxane,

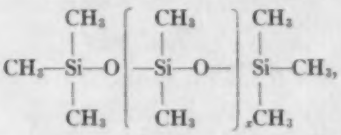

except that some of the CH_3 radicals are substituted by phenyl radicals C_6H_5. The phenyl/methyl ratio and the chain length x are proprietary secrets of the Dow-Corning Company. Some rough estimates, however, may be based on the published properties of polydimethylsiloxane.

A polydimethylsiloxane of the same viscosity as DC 704 would have a molecular weight of 3300 and a chain length $x=44$. We will therefore assume a molecular weight of about 4000 and chain length of about 40 units for the DC 704. Since the density is about one, the molecular volume v may be approximately 6000 A^3 and the area a about 1100 A^2.

With these assumptions, the rate at which oil molecules hit the surface is $F \approx 5\times10^{-5}$ A^{-2} sec^{-1}. From Eq. (8) one finds $\alpha p \approx 2\times10^{-9}$ mm Hg at room temperature. The equilibrium vapor pressure of DC 704 at 25°C is unknown, but if it is assumed that $\alpha \approx 1$ and the equilibrium pressure is about 2×10^{-9} mm at 25°C, then from the value[12] 2.3×10^{-6} mm Hg at 185°C an activation energy of about 12 kcal/mole is calculated for the vapor pressure. This value seems rather small, in comparison with the activation energy for polydimethylsiloxane of the assumed chain length.[13] It is possible, however, that the chain length of DC 704 assumed on the basis of the viscosity is a serious overestimate if the phenyl/methyl ratio is appreciable, since the substitution of phenyl groups would be expected to increase the viscosity.

The cross section σ for the cross-linking reaction cannot be determined from the present data. It would be expected to be less than the geometrical area of the molecule a, however, so that

$$\tau > 1.5\times10^{-9} \exp(10\,000/RT) \text{ sec.}$$

In a system constructed so that the flux of oil to the substrate could be increased until Eq. (6) applies, however, the ratio σ/a could be measured directly. If this ratio is not too small, deposition rates of hundreds of angstroms per second should be attainable at moderate beam current densities.

The number of cross links per molecule δ can be estimated from Eq. (7). At low current densities $\delta \approx 1/\sigma\tau F$, so that $\delta \approx 500$ at room temperature. At higher current densities, this figure will be greater. The figure will also be greater if each electron produces more than one cross link, as is possible since in bulk polymers about 10 ev electron energy per cross link is required.[14] Since only about 80 cross links per molecule are possible, it is concluded that under these circumstances the solid film will be completely cross linked.

CONCLUSION

From the theory and experiments described, it is concluded that the rate of formation of a solid polymer film by electron bombardment in the presence of a silicone oil vapor depends on the electron current density, the rate of impingement of oil molecules on the substrate, and the temperature of the substrate. The substrate temperature is effective in determining the probability that an oil molecule adsorbed on the substrate will spontaneously leave the surface before it is cross linked by an electron encounter. The lower the temperature the longer the molecule waits for such an encounter and the higher the deposition rate. The rate also depends on the flux of electrons, unless that is so large that an electron encounter occurs whenever an oil molecule lands on the surface, in which case the rate depends only on the flux of molecules to the surface. The rate is proportional to the flux of molecules unless, in the opposite extreme, that is so large that the surface is covered with oil molecules and an encounter occurs whenever an electron arrives, in which case the deposition rate depends only on the electron current density.

The solid films which are formed are probably completely cross linked. The nature of the cross links and the structure of the film have not been determined. The possible types of cross link are Si—Si, Si—CH_2—Si, and Si—CH_2—CH_2—Si, together with analogous C_6H_5 groups. In bulk material cross-linked by radiation, analysis of the evolved gas[7] indicates the presence of the last two types. The films may perhaps be regarded as similar to silicon monoxide with some organic substituents.

The films which were produced had excellent electrical insulating properties. In addition, the thinner films showed interesting non-Ohmic behavior, which is being studied further.

ACKNOWLEDGMENTS

The author wishes to thank Dr. Milton Clauser for permission to publish this material. The stimulation of discussions with Dr. F. W. Schmidlin and the technical assistance of Charles Marinoff are gratefully acknowledged.

[12] Information furnished by the Dow-Corning Company.
[13] D. F. Wilcock, J. Am. Chem. Soc. **68**, 692 (1946).
[14] A. M. Bueche, J. Polymer Sci. **19**, 297 (1956).

Influence of Crystallographic Orientation on the Charge Formation during Phase Changes in Solids*

S. MASCARENHAS AND L. G. FREITAS
Escola de Engenharia de San Carlos, Department of Physics, University of São Paulo, Brazil
(Received April 11, 1960; and in final form May 26, 1960)

The effect of charge separation during phase changes (Costa Ribeiro effect) is studied with naphthalene single crystals. By properly seeding the melt the authors showed that the effect is dependent on crystallographic orientation. Values of the trapped charge are 32×10^{-9} C/g for growth normal to cleavage plane, 2.5×10^{-9} C/g for growth along b axis, and 2.9×10^{-9} C/g for growth along a axis. If the effect is due to selective ionic trapping in the solid phase this observation may be important in zone refining techniques. If it is due to an electronic effect this points out to an orientation dependent double-layer at the solid-liquid interface.

I. GENERAL

THE formation of charge in solids during solidification (Costa Ribeiro or Thermodielectric effect) has been studied by several authors both experimentally[1–4] and theoretically,[5–9]; however, its basic mechanism is still not well understood. In a previous work[10] one of the authors has shown that the amount of charge that is trapped in an insulator upon solidification is different for a single crystal and a polycrystal. In particular, it was found that if a single crystal was used as a seed for the growth of $C_{10}H_{10}$ (naphthalene) and if the resulting solid deposit was also a single crystal then the charge per unit mass of the solid could be as much as 100 times larger than in a polycrystalline deposit. The present work is a study of the influence, if any, of the crystallographic orientation upon charge formation.

II. EXPERIMENTAL

Since the charging effect is best known in naphthalene, this material was used in the present investigation. The measuring system and procedures were, briefly, as follows (more details are given in footnote reference 10):

(a) A seed, previously oriented, was attached to a metallic electrode connected to an electrometer-capacitor system (Fig. 1). This electrode could be lowered so as to obtain a contact between the seed and the melt. The melted phase was supported by another metallic electrode which was heated. The system thus constituted a plane condenser having as a dielectric a solid and a liquid phase of naphthalene. The seed was placed in contact with the melt under such thermal conditions that a solid layer grew with the same crystallographic orientation as the seed.

(b) The capacity C in parallel with the electrometer was made high enough (~1000 $\mu\mu$f) so that variations in capacity in the growth cell could be considered negligible. The electrometer E was a string Wulf instrument in a heterostatic mounting and the whole system was contained inside a Faraday cage F. In this way the relation $Q/m=CV/m$, where Q is total charge, V is the final voltage in the electrometer, and m is the mass of the solified crystal could be obtained for each sample.

(c) The mass of the upper electrode and seed were measured before and after the growth so that the total deposited mass m could be determined.

(d) The seed single crystals were grown by two different techniques: one due to A. Dias Tavares[11] and the other due to M. Ferreira de Souza.[12] The orientation of the single crystals was determined using a polarization microscope and a technique described by Lipsett.[13] The check of the single-crystallinity of the solid deposit was made by the same technique.

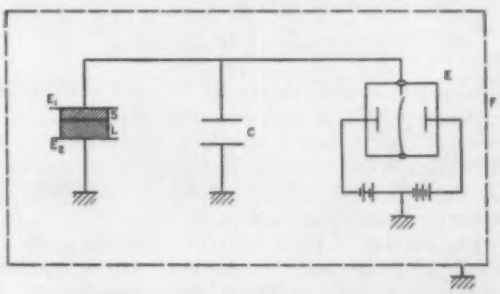

FIG. 1. E_1, upper insulated electrode with seed; E_2, lower heated electrode; S, solid phase; L, liquid phase; C, air condenser; E, Wulf electrometer; and F, Faraday cage.

* Work supported by the National Research Council of Brazil.
[1] J. Costa Ribeiro, Anais acad. brasil. cienc. **17**, 2 (1944); S. Mascarenhas, *ibid.* **26**, 345 (1954); E. Rodrigues, *ibid.* **26**, 381 (1954).
[2] E. J. Workman and S. E. Reynolds, Phys. Rev. **78**, 254 (1950).
[3] B. Krause and M. Renninger, Naturwissenschaften **40**, 52 (1953); Acta Cryst. **9**, 74 (1956).
[4] J. P. Lodge, M. L. Baker, and J. M. Pierrard, J. Chem. Phys. **24**, 716 (1956); see also R. Brill and H. Ender, Nature **176**, 925 (1955).
[5] B. Gross, Phys. Rev. **94**, 1545 (1952).
[6] A. Dias Tavares, Anais acad. brasil. cienc. **25**, 91 (1953).
[7] S. Mascarenhas, Anais acad. brasil. cienc. **26**, 336 (1954); see also footnote reference 10.
[8] E. W. B. Gill and G. F. Alfrey, Nature **169**, 203 (1952); E. W. B. Gill, Brit. J. Appl. Phys. Suppl. **2**, 516 (1953).
[9] P. Bonning, *Z.* angew. Phys. **8**, 516 (1956).
[10] S. Mascarenhas, thesis, University of São Paulo, 1958 (to be published in English in the Anais acad. brasil. cienc).
[11] A. Dias Tavares, Anais acad. brasil. cienc. **25**, 53 (1953).
[12] Ferreira de Souza (to be published).
[13] F. R. Lipsett, Can. J. Phys. **35**, 284 (1952).

(e) Three different orientations were used for the growth: (i) the cleavage plane (plane of axes a and b) parallel to the plane of the electrode [Fig. 2(a)] and growth normal to it; (ii) axis a in the plane of the electrode and growth in the direction of b; (iii) axis b in the plane of the electrode and growth along a.

(f) In all measurements the temperature of the melt was held at 90.0 ± 0.1°C and the purity of the material used was characterized by measuring its electrical conductivity at this temperature. This conductivity was 3×10^{-11} v cm^{-1} with an applied field of 0.6 kv/cm.[14]

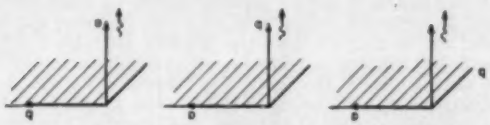

FIG. 2. Cross-hatched plane is a perspective view of the plane of the electrode. The curly arrow indicates direction of growth normal to the electrode, and a and b are the crystallographic axes.

(g) All voltage measurements were made after a waiting time which was long enough to eliminate possible transient hereditary effects (for details see footnote references 1 and 10). The mean crystallization rate was of the order of 0.5 mg/sec.

III. RESULTS

For each orientation a large number of measurements were made and probable errors calculated. Special care was taken to make each measurement with fresh material. In this way reproducible results were found with mean square relative errors less than 10%.

In Table I a general résumé is given for the three directions of growth. Here S is the mean square deviation, n the number of measurements, m the mass of the solid grown, and Q the product CV, where C is the capacity of the system.

IV. CONCLUSIONS

As can be seen from Table I the effect shows a strong dependence on crystallographic orientation. The value of the ratio Q/m can vary by a factor of 10 when the direction of growth changes from normal to parallel to the cleavage plane. A statistical analysis shows that the small difference between the values of Q/m in the a and b axes lies entirely within the limits of the experimental error. The main conclusions are as follows:

[14] Value related to residual current.

TABLE I. Influence of direction of crystal growth upon charge formation.

Growth direction	Q/m 10^{-9} C/g	S 10^{-9} C/g	n
Perpendicular to cleavage plane	32	2	37
Parallel to axis b	2.5	0.2	34
Parallel to axis a	2.9	0.2	29

(a) In previous work[10] it has been found experimentally that the rate of change of phase dm/dt does not affect the Q/m ratio as long as the deposit is a single crystal. Thus the influence or orientation cannot be simply ascribed to a change in the rate of growth of the crystal with orientation.

(b) If the effect is due to a preferential rejection or imprisonment of ionic impurities in the solid phase, as was suggested by Workman and Reynolds[18] for water solutions, our observations, in the case of C_6H_{10}, show that purification of the solid phase by crystallization methods from the melt, as in the zone-refining method, should depend on the orientation of the growth direction with respect to the crystallographic axis. A phenomenological interpretation of this result in terms of partition coefficients would lead to the conclusion that they depend on direction.

(c) In an attempt to explain the phenomenon in terms of an electronic effect we supposed[10] that as a result of an equalization of Fermi levels on the solid-liquid interface a double layer would be formed. This, coupled with the motion of the interface due to the phase change, would produce a space charge frozen in the highly insulating solid. Our results might in this case be an indication of the presence of an orientation-dependent double layer.

ACKNOWLEDGMENTS

We want to thank S. Sanches and S. Bastos Pereira for help during the measurements, and Professor H. Zocher, Professor G. Leal Ferreira, and Professor M. Tolentino for helpful discussions, and especially Professor R. Smoluchowski for his kindness in reading the manuscript.

Letters to the Editor

Chlorine and Iodine as Impurities in InAs and GaP

G. R. ANTELL
Research Department, Associated Electrical Industries (Manchester), Ltd., Trafford Park, Manchester 17, England
(Received May 19, 1960)

AS previously reported[1,2] the arsenides and phosphides of gallium and indium can be readily prepared in either powder or crystalline form by means of a reaction involving chlorine or iodine. Although it was known that indium arsenide could be melted under an atmosphere that contained either chlorine or iodine without materially altering the free-carrier concentration, it was not known whether this effect was due to the insolubility or to the electrical neutrality of the halogens in indium arsenide.

Samples taken from an ingot of indium arsenide which had been zone leveled under an atmosphere containing 1.2×10^{19} atoms of chlorine/cm³ have now been analyzed by the A.E.I. mass spectrometer for the analysis of solids (M.S. 7) and were found to contain about 10^{19} atoms of chlorine/cm³. The decrease in the Hall coefficient equivalent to the addition of about 8×10^{15} donors/cm³ was probably caused by the silicon and tin donor atoms[3] found present in small quantities in the chlorine-doped sample, but not in the original indium arsenide.

Crystals of gallium phosphide were grown from a vapor phase at 950°C in an atmosphere which contained 7×10^{15} atoms of iodine/cm³, but the iodine content of the material was found to be less than 10^{15} atoms/cm³.

The covalent radius of iodine[4] is 1.33 A, but since the radius of the largest impurity that would just fit interstitially in GaP is 1.26 A, the very low solubility of iodine in GaP is not unexpected. In the case of indium arsenide, the very high solubility of chlorine may be the result of the covalent radius of chlorine being only 0.99 A, while space is available to take interstitial impurities having radii up to 1.44 A.

The author would like to express his thanks to Dr. J. D. Waldron and R. Brown for carrying out the mass-spectrographic analysis and to Sir Willis Jackson, Director of Research and Education, Associated Electrical Industries (Manchester), Ltd., for permission to publish this note.

[1] G. R. Antell and D. Effer, J. Electrochem. Soc. **106**, 509 (1959).
[2] D. Effer and G. R. Antell, J. Electrochem. Soc. **107**, 252 (1960).
[3] E. Schillman, Z. Naturforsch. **11a**, 463 (1956).
[4] L. Pauling, *The Nature of the Chemical Bond* (Cornell University Press, Ithaca, New York, 1948).

Thermal Conversion in *n*-Type GaAs*

JOSEPH J. WYSOCKI
RCA Laboratories, Princeton, New Jersey
(Received June 15, 1960)

WHILE using *n*-type GaAs for device studies, it was found that material with a carrier concentration of 5×10^{16}/cc or less invariably converted to *p*-type when it was heated at temperatures of approximately 800°C for short times. This conversion occurred even though the wafers were generally heated in an ampule pumped down to at least 10^{-6} mm of Hg. Attempts to prevent conversion by etching the material and ampules in cp acids or by rinsing in a KCN solution before heat treatment were not successful. Similarly, thermal conversion was not prevented by allowing the GaAs to decompose during heating, or, conversely, by minimizing decomposition by maintaining an excess As pressure. The use of *n*-type impurities such as S and the use of C or Ga getters likewise did not prevent conversion. Experiments with thick wafers of GaAs definitely established that the conversion process proceeded from the surface inwards. It was also determined that the conversion was characterized by a diffusion constant of at least 10^{-8} cm²/sec at 850°C, and an activation energy less than 1 ev, suggesting an interstitial diffusion mechanism. The solid solubility of the impurity involved was certainly as great as the net concentration in the material investigated. Further experiments to determine if an impurity were involved consisted of duplicating the conversion behavior by the addition of an impurity, attempting to reconvert the material and devising means of preventing conversion.

It was possible to find one impurity, namely Cu, which duplicates the conversion process. As shown in this laboratory and by Fuller and Whelan,[1] Cu is a *p*-type impurity which has a sufficiently high solubility and diffusion rate to explain conversion of the material used in this study. The diffusion of Cu was also characterized by a low activation energy similar to that found in the conversion process. Furthermore, measurements of the hole concentration as a function of temperature in both Cu-diffused and thermally-converted samples by Meyerhofer[2] of these laboratories yielded the same impurity ionization energy. Finally, it was not possible to duplicate the conversion process with other impurities such as Zn, Cd, Au, Ni, S, etc., either because the diffusion rate was too low, the activation energy too high, or the impurity was a donor. The conversion could not be attributed to the vacancies produced by the loss of As since the presence or absence of an excess As atmosphere had little effect.

Since the data strongly suggested that Cu is responsible for thermal conversion, attempts were made to reconvert both Cu-diffused and converted wafers by heating with molten In or KCN. When In was used at 850°–950°C, the wafers remained *p*-type except in those regions where the GaAs had dissolved. Similarly, when the wafers were heated in molten KCN at 850°–950°C, it was possible to reconvert only one out of five Cu-diffused wafers and none of the converted wafers. The difficulty of removing Cu by leaching, except when the GaAs is molten, might be attributed to a strong Cu—As bond. Although Cu diffuses interstitially into the crystal, it becomes tightly bound in substitutional sites.[1]

The last phase of the experiments involved the attempt to prevent the occurrence of conversion by the removal of Cu contamination. One source of Cu was traced to the C.P. grade reagents used to clean and etch the GaAs. When the GaAs was etched in triple distilled reagents in which Cu was not present as determined by spectroscopic analysis, it was then possible to heat the GaAs without conversion taking place. For example, fourteen runs were made with *n*-type material with a carrier concentration of 8×10^{16}/cc. In six of these runs, commercial-grade acids were used in etching the wafers and all of the wafers converted. In the remaining eight runs, triple-distilled acids were used. Conversion occurred in only two of these runs illustrating not only the need for impurity-free reagents, but also the necessity for care and cleanliness in using them. It is noteworthy that studies by Theuerer *et al.*[3] on the heat treatment of Si indicated changes in the minority-carrier lifetime and resistivity which could also be attributed to impurities originating in the reagents used for cleaning and etching.

Acknowledgement is due to K. Weiser[4] and H. Nelson for contributions to these findings and to R. W. Pratt for his assistance in performing the experiments.

* The research reported here was sponsored in part by the U. S. Air Force, Air Force Cambridge Research Center, under contract.
[1] C. S. Fuller and M. J. Whelan, J. Phys. Chem. Solids **6**, 173 (1958).
[2] D. Meyerhofer (private communication).
[3] H. C. Theuerer, M. J. Whelan, H. E. Bridgers and E. Buehler, J. Electrochem. Soc. **104**, 721 (1957).
[4] K. Weiser, now at IBM, Poughkeepsie, New York.

Direct Observation of Antiphase Domain Boundaries in the $AuCu_3$ Superlattice

M. J. Marcinkowski and R. M. Fisher
Edgar C. Bain Laboratory for Fundamental Research, United States Steel Corporation Research Center, Monroeville, Pennsylvania
(Received June 2, 1960)

BAIN[1] in 1923 was the first to observe x-ray superlattice lines from the ordered $AuCu_3$ alloy. Since then interest in the order-disorder phenomena in general and in particular the $AuCu_3$ alloy has been very great, especially the manner in which the ordering transformation affects the physical and mechanical properties. In the past, all of the commonly used techniques of light and electron metallography have failed to reveal the size and configuration of the antiphase domains in ordered alloys so that most of the concepts concerning the domain microstructure have been deduced from indirect measurements such as x-ray and electron diffraction.

From these indirect measurements, it has been postulated that the ordered $AuCu_3$ alloy consists of a relatively stable "foam structure" of antiphase domains and that the domain boundaries between any two such domains lie on cube planes with the gold atoms on both sides of this boundary occupying different sublattices.

Recently, however, several investigations have achieved notable advances in studies of domain geometry by direct resolution of the antiphase domains by transmission electron microscopy of thin evaporated films. Ogawa[2] *et al.*, have obtained direct evidence of the antiphase domains in AuCu and Au-Cu-Zn alloys, and Pashley[3] and collaborators have also studied the microstructure of AuCu II as well as its transformation to AuCu I. This note describes the first observations by transmission electron microscopy of the domain boundaries in $AuCu_3$ and the first study where suitable specimens of an ordered alloy were prepared by electrothinning sheet samples. Thus, the structures observed are representative of those developed in bulk specimens eliminating the uncertainty that exists when evaporated films are used.

Figure 1 shows a transmission electron micrograph of a thin foil prepared by electrothinning a specimen of $AuCu_3$ heated to develop a high degree of order. The domain configuration is seen to consist of a network of rectangular blocks with an average size of about 750 A about as expected.

Diffraction analysis of this area showed that the domain boundaries which appear here as dark lines lie essentially on cube

FIG. 1. Antiphase domain configuration in the $AuCu_3$ superlattice.

FIG. 2. Extinction contours in fully ordered $AuCu_3$ showing antiphase domain boundary contrast along a pair of superlattice extinction contours.

planes which are perpendicular to the plane of the figure, whereas the larger dark areas represent (001) domain boundaries which lie in the plane of the foil. Traces of (100) and (010) planes are shown in the inset.

The origin of the contrast of the domain boundaries in electronmicrographs has been attributed to double diffraction or to interference effects, but neither of these explanations appear to apply to the present observations. In this case, it was observed that the essential condition for revealing the domain structure is that the crystal must be oriented for diffraction contrast using a strong superlattice reflection. This is illustrated in Fig. 2 where it may be seen that domain boundaries are visible only along the extinction contours.

It has been found that all the various types of domain contrast can be explained satisfactorily by the dynamical theory of electron diffraction as developed by Whelan and Hirsch[4] for the contrast in stacking faults in metal foils when the phase angle and extinction distances appropriate to ordered structures are introduced. The phase angle across an interface in a crystal is given by $\alpha = 2\pi \mathbf{g} \cdot \mathbf{R}$, where $\mathbf{g}$ is the reciprocal lattice vector of the reflection causing contrast and $\mathbf{R}$ is the displacement vector across the interface. In the case of stacking faults, this angle is 0 or $\frac{1}{2}\pi$, whereas for antiphase boundaries, it is 0 or π. In both of these cases, the contrast is 0 when the orientation is such that the phase angle is 0. For superlattice reflections, the extinction distances depend on the difference in electron scattering factor between Au and Cu and so are about four times longer than for the other reflections; thus unlike the case for stacking faults, multiple sets of fringes are not observed.

[1] E. C. Bain, Chem. & Met. Eng. **28**, 65 (1923).
[2] S. Ogawa, D. Watanabe, H. Watanabe, and T. Komoda, Phys. Soc. Japan **14**, 936 (1959).
[3] D. W. Pashley and A. E. B. Presland, J. Inst. Metals **87**, 419 (1959).
[4] M. J. Whelan and P. B. Hirsch, Phil. Mag. **2**, 1121, 1303 (1957).

High-Permeability Garnets

Elmer E. Anderson and J. Richard Cunningham, Jr.
U. S. Naval Ordnance Laboratory, White Oak, Maryland
(Received June 13, 1960)

WE have found that the substitution of indium for 10% of the iron in polycrystalline YIG (yttrium iron garnet) results in a 500% increase in the initial permeability. Although

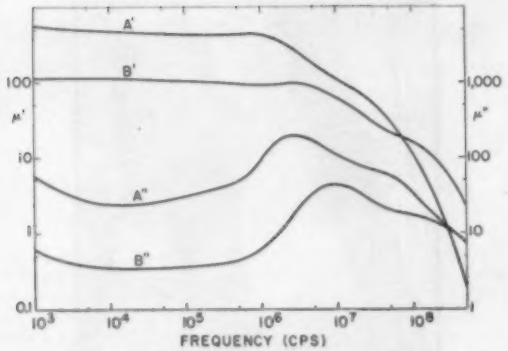

FIG. 1. Real and imaginary parts of the relative initial permeability vs frequency. The letters A and B refer, respectively, to the 10% indium sample and to YIG.

several other workers[1,2] have discussed indium substitutions in garnets, this letter is believed to be the first report of the large permeability which may be obtained in these materials. This increase is noteworthy since all other substituents which we have used to date have resulted in a decrease in the permeability of YIG.[3,4]

Figure 1 shows the dispersion of the initial relative permeability for samples of $3Y_2O_3 \cdot (4.5)Fe_2O_3 \cdot (0.5)In_2O_3$ and YIG for comparison. Note that the permeability of the indium sample begins to relax at about 1 Mc. However, below this frequency the permeability is $\sim$ 500 whereas that of YIG is $\sim$ 100. For a 6% replacement of iron by indium the permeability is $\sim$ 200 up to 4 Mc (not shown). A substitution of 14% indium was attempted but resulted in a mixture of garnet and perovskite phases. The upper limit on the amount of iron which can be replaced by indium is not precisely known, but the limit is somewhere between 5 and 20% according to Gilleo and Geller and Miyadai and his co-workers.

The materials were prepared by previously described[3] ceramic techniques with the exception that higher sintering temperatures were necessary to obtain high-density toroidal specimens. Powder samples were used for measurements of lattice constants, magnetic moments, and Curie temperatures. For the 10% indium sample shown in Fig. 1 the lattice constant is 12.436±0.005 A and the Curie point is in the vicinity of 450°K. These values are in good agreement with those previously reported by Gilleo and Geller.[1] A number of additional samples are currently being prepared in order to determine the upper limit to both the permeability and the allowable substitution of indium.

[1] M. A. Gilleo and S. Geller, Phys. Rev. **110**, 73 (1958).
[2] T. Miyadai, V. Shichijo, and I. Tsubokawa, J. Phys. Soc. Japan **14**, 853 (1959).
[3] E. E. Anderson, J. Appl. Phys. **30**, 299S (1959).
[4] G. F. McDuffie, Jr., J. R. Cunningham, Jr. and E. E. Anderson, J. Appl. Phys. **31**, 47S (1960).

Mechanism for the Production of *F* Centers in NaCl by Irradiation with Gamma Rays

J. H. CRAWFORD, JR., AND F. W. YOUNG, JR.
Solid State Division, Oak Ridge National Laboratory,[a] Oak Ridge, Tennessee
(Received June 6, 1960; and in final form June 13, 1960)

SEITZ[1] has suggested the following mechanism for the production of *F* centers by gamma-ray irradiation. Excitons created during irradiation of ionic crystals can recombine at crystalline imperfections such as dislocation jogs. Sufficient energy can thereby be deposited at the jogs to permit evaporation of cation-anion vacancy pairs from the dislocations, these evaporated vacancies becoming ionized subsequently to form color centers. Nowick[2] has observed that coloration in NaCl occurs in two stages: (a) a rapid, initial stage presumably due to the ionization of defects initially present, and (b) a slow stage attributed to generation of defects. The second stage appears to be dependent

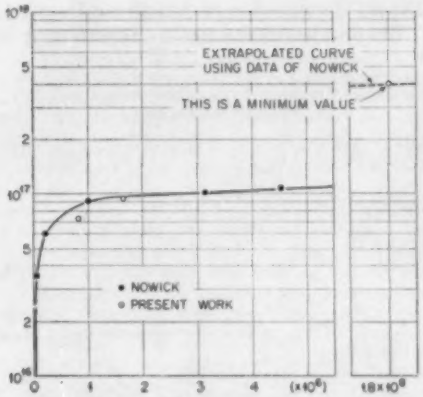

FIG. 1. *F* center concentration vs Co^{60} gamma-ray exposure (roentgens) for a NaCl crystal.

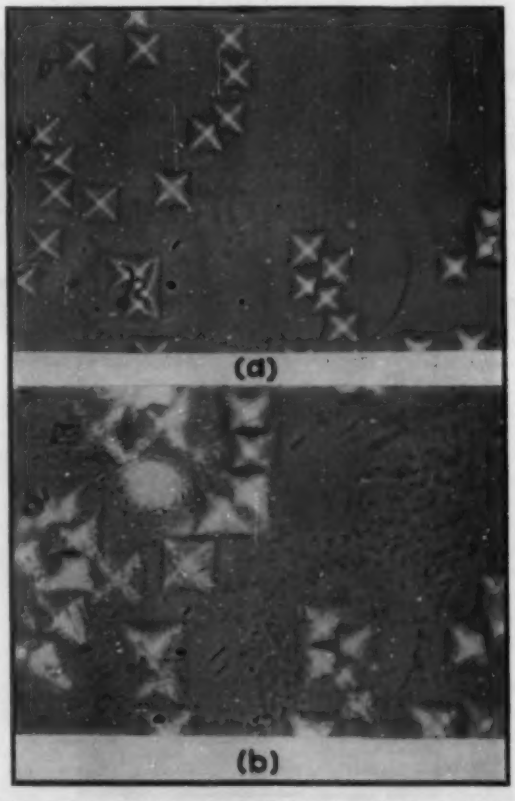

FIG. 2. Etch pits at dislocations in NaCl 1000×. (a) Before irradiation. (b) Same area after irradiation to generate 4×10^{17} *F* centers.

on dislocation density, thereby apparently substantiating the suggestion of Seitz.

However, if vacancies are evaporated from a dislocation, climb of the dislocation results. Consider an edge dislocation in the NaCl lattice. The Burgers vector lies in [110] and $b=4$ A.[3] There must be two half-planes for electrical neutrality and a pair (positive and negative ion) must be attached to or leave this dislocation at any time in order to preserve electrical neutrality. Thus one pair (which would subsequently correspond to one F center) evaporating from an edge dislocation would move the dislocation up 4 A and along its line 2.8 A. Thus, for 1 cm of line to climb 4 A along its length, 3.56×10^3 vacancy pairs would have to be evaporated. For a dislocation density of $5\times10^8/\text{cm}^2$ (from experimental count), assuming the total line length to be three times this number, $3\times5\times10^8\times3.56\times10^7=5.3\times10^{15}$ vacancies would have to be evaporated for each dislocation line in the crystal to climb 4 A. Thus, if 10^{17} F centers are generated by gamma-ray irradiation, each dislocation should climb 0.8 μ, while 4×10^{17} F centers would require a climb of 3 μ/dislocation.

The positions of the dislocations in NaCl can be detected as etch pits on (100) using as an etchant absolute ethyl alcohol containing 3 g of $HgCl_2$/liter (etching time 30 sec).[4] The exact position of the center of the pits can be located with the optical microscope to a precision of better than 0.5 μ. Thus, if the Seitz mechanism is responsible for the production of F centers, the resulting climb of the dislocations can be observed with the optical microscope.

A crystal of NaCl, obtained from Harshaw, was cleaved into thin plates with (100) on the flat sides. Pairs of these plates were etched to locate the dislocations, then irradiated with gamma rays from a Co^{60} source (flux $\sim10^4$r/hr, exposure temperature ~40°C), one of the plates used to measure the optical density for computing F-center concentration, and the other plate reetched to relocate the positions of the dislocations. The F-center concentrations are shown in Fig. 1 along with the data of Nowick.[2] The F center concentration of 4×10^{17} corresponds to the maximum adsorption coefficient detectable with the optical system and crystal thickness which were used. Thus, the actual value is greater than 4×10^{17} cm^{-3}. Photomicrographs of the etch pits on the same area before and after the irradiation which produced "the greater than" 4×10^{17} F centers/cm^3 are shown in Fig. 2. It is evident from Fig. 1 that most of these were produced during the slow stage process. Climb of 3 μ, which should have occurred here if the Seitz mechanism held, would require the center of the pit to be moved a distance of one-half its cross section after irradiation. Obviously, if any climb occurred, it was only a small fraction of that expected. New (clean) edge and screw, and grown-in dislocations were observed—none showed a measurable amount of climb. Thus, it appears that if any F centers were produced by evaporation of vacancies from the dislocations, they were not a significant fraction of the total number.

* Oak Ridge National Laboratory is operated by Union Carbide Corporation for the U. S. Atomic Energy Commission.

[1] F. Seitz, Revs. Modern Phys. **26**, 1 (1954).
[2] A. S. Nowick, Phys. Rev. 111, 16 (1958).
[3] S. Amelinckx, Nuovo cimento **7**, 569 (1958).
[4] P. R. Moran, J. Appl. Phys. **29**, 1768 (1958).

Germanium Crystals Grown from Hollow Cylindrical Seeds

R. C. FRANK
General Motors Research Laboratories, Warren, Michigan
AND
J. E. THOMAS, JR.†
Wayne State University, Detroit, Michigan

IN the process of preparing specimens for the study of the diffusion of gases in germanium it was found necessary to grow germanium crystals from hollow cylindrical seeds. The diffusion studies will be reported soon in another paper, but the crystals themselves have certain rather interesting characteristics which perhaps warrant special attention.

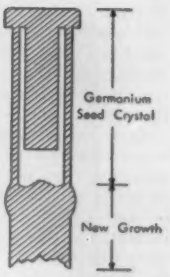

FIG. 1. Cross-sectional side view of the hollow-germanium seed crystal and new growth.

Large pieces of single-crystal and polycrystalline germanium were drilled with hollow, diamond tipped, coring drills of two different sizes. When the surplus material was gently broken away, this left a smooth thin-walled hollow cylinder. Each hollow cylinder was etched to remove the surface damage and then mounted on the pulling rod of the crystal grower and used as the seed for growing a new crystal. When the single-crystal seed was used the new growth was also single crystal. With this hollow cylindrical seed, the new crystal not only grew outward as is the usual case but it also grew inward and closed the cylinder at the center. The growth in the inward direction was extremely rapid and the hollow cylinder was closed almost immediately after the growing process started. A small hump formed in the center as shown in the diagram in Fig. 1. Since these cylinders were closed at the top, the hump may have been caused by reduction in gas pressure inside of the cylinder. Part of the hump may also have been produced as the germanium expanded on solidification. If one were to look down the hollow cylinder at the new growth one would see growth rings which are concentric about the center rotation. In the case of the single crystals, the growth rings are very circular and uniform. With each succeeding ring toward the center, the growth continues upward until finally a plateau is reached and there is no further growth upward until the very center is reached. As the crystal grows together an additional small step is formed.

There are also several interesting things about the polycrystalline growth. First of all, apparently there is no plateau formed and the growth continues steadily upward until the very center is reached. Also, although the contour lines have a tendency to be circular, they are warped considerably by the individual grains. This is interesting from another standpoint. Although grain boundaries are visible on both the inside and outside surfaces of the polycrystalline growth, the outside surface is as smooth and uniform as that of the single crystal; however, inside of the poly-

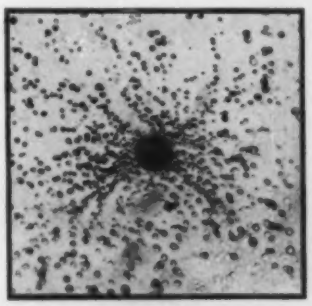

FIG. 2. Dislocation etch-pit pattern at the center of a single crystal grown from a hollow cylindrical seed. (137 X)

crystalline cylinder the surface is quite distorted. This suggests that inside of the cylinder the individual grains exercise a greater control over the direction of crystal growth and there is a slight tendency for dendritic growth. The crystal has a tendency to grow inward spontaneously but growth rings are also formed as the crystal rotates in the molten germanium.

Since the crystals grew inward from the hollow cylinder and met at the center it seemed likely that there might be poor epitaxy at the center which would result in an unusual array of dislocations. Therefore, one of the single-crystal specimens was polished with fine grinding compound and treated with CP-4 etchant. The dislocation pattern found is shown in Fig. 2. It is easily seen that at the very center where the growth came together the dislocation density is extremely high. The diameter of this region of high-dislocation density is about 45 μ. Outside of this region the density is somewhat lower and decreases further at greater distances from the center. From the over-all etch-pit pattern there appear to be traces of radial lineage. However, the lineage seems to have been quite randomly formed so it is difficult to identify any specific mechanisms involved in its production. The dislocations may have been formed as a result of the entrapment of molten germanium near the center which expanded on solidification.

* Supported in part by the U. S. Air Force.
† Present address: Semiconductor Division of Sylvania Electric, Woburn, Massachusetts.

Peltier Coefficient at a Solid-Liquid Interface

J. R. O'Connor
Electronic Material Sciences Laboratory, Air Force Cambridge Research Center, L. G. Hanscom Field, Bedford, Massachusetts
(Received May 16, 1960; and in final form June 15, 1960)

REISS[1] and more recently Bardeen and Chandrasekhar[2] have shown that the Peltier coefficient π is simply related to the velocity v of propagation of a dc biased solid-liquid interface. The relation is

$$\pi = jvH/2J, \tag{1}$$

where $j=4.184$ is the conversion factor from calories to joules, J is the current density in amp cm^{-2}, and H is the total heat of cal cm^{-3}. In the derivation of Eq. (1) Thomson heats have been neglected. However, the absolute Seebeck coefficient α has a strong temperature dependence at the melting point for most materials. As such, the Thomson coefficient τ computed from the second Kelvin relation is large, and Thomson voltages and heats can be appreciable.

Consider the solid-liquid interface as shown in Fig. 1. At thermal equilibrium the interface is held stationary at $x=0$ and the net heat flow across the interface is zero, that is,

$$k_sG_s - k_lG_l = 0, \tag{2}$$

where k is a thermal conductivity and G is a thermal gradient both evaluated at $x=0$. The subscripts s and l refer to the solid and liquid phases, respectively.

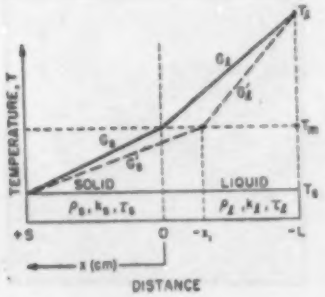

FIG. 1. Temperature distribution at a solid-liquid interface. At thermal equilibrium the interface is at $x=0$. For a current density $J>0$ the interface moves to $-x_1$.

When a current density $\mathbf{J}$ is passed through the interface, melting or solidification will occur depending on whether the polarity of the current produces net heating or cooling. In Fig. 1 it is assumed that solidification takes place and the interface comes to equilibrium at a position $-x_1$ where the gradients are now G_s' and G_l'. The temperature distribution in both the solid and liquid must now satisfy Domenicali's equation,[3]

$$\nabla\cdot k\nabla T + \rho|\mathbf{J}|^2 + \mathbf{J}\cdot\nabla\pi_i \pm \tau\mathbf{J}\cdot\nabla T = 0, \tag{3}$$

where ρ is the electrical resistivity in ohm-cm and the third term vanishes for a homogeneous material, a substance with zero internal Peltier coefficient. In addition to the usual boundary conditions the Peltier heat $\pm\pi\mathbf{J}$ which is either generated or absorbed at the interface must also be considered.

For $\mathbf{J}=0$, a solution of Eq. (3) is given by Eq. (2). This solution is exact for radiation; convection and fluid-flow effects are properly accounted for. For small values of $\mathbf{J}$, Burshtein's[4] solution of Eq. (3) will relate the G's and G's. The solution of Eq. (3) for the solid phase is

$$k_sG_s' = k_sG_s - \frac{|\mathbf{J}|^2 S\int_{T_s}^{T_m}\rho_s k_s dT\int_{T_s}^{T}k_s dT}{\left(\int_{T_s}^{T_m}k_s dT\right)^2} \pm \frac{|\mathbf{J}|\int_{T_s}^{T_m}\tau_s dT\int_{T_s}^{T}k_s dT}{\int_{T_s}^{T_m}k_s dT}. \tag{4}$$

Equation (4) assumes that $\mathbf{J}$ is sufficiently small so that the Thomson and Joule heats remain uncoupled. That is, terms such as the Thomson heat caused by the gradient produced by the Joule heat are negligibly small. For constant heat flow Eq. (4) can be rewritten

$$k_sG_s' = k_sG_s - N_J|\mathbf{J}|^2 S\langle\rho_s\rangle \pm N_T|\mathbf{J}|\langle\tau_s\rangle(T_m - T_s), \tag{5}$$

where N_J and N_T represent the fraction of Joule and Thomson heat returning to the interface and ρ, τ have been replaced by their average values over the temperature interval $(T_m - T_s)$. A similar equation can be written for the liquid phase.

The interface at equilibrium at position $-x_1$ must satisfy the condition $k_sG_s' - k_lG_l' = -|\mathbf{J}|\pi$. From Eq. (5) the distance x_1 is

$$|\mathbf{J}|[N_J(S+x_1)\langle\rho_s\rangle + \tfrac{1}{2}(L-x_1)\rho_l] = \pi \pm N_T\langle\tau_s\rangle(T_m - T_s). \tag{6}$$

In deriving Eq. (6) it has been assumed that (1) the properties of the liquid are metallic and (2) that over the small temperature interval $(T_l - T_m)$: $\rho_l \approx \langle\rho_l\rangle$, and $\tau_l = Td\alpha_l/dT \approx 0$. The magnitude of the resistive portion of Eq. (6) can be determined independent of Peltier and Thomson effects by replacing the dc current with its ac equivalent. For this condition the right side of Eq. (6) vanishes and the ratio $N_J\langle\rho_s\rangle/\rho_l$ can be determined.

With the interface at $-x_1$, a change in the polarity of $\mathbf{J}$ will cause the interface to move to the left. The initial velocity is given by

$$\pi \pm N_T\langle\tau_s\rangle(T_m - T_s) = jvH/2|\mathbf{J}| \tag{7}$$

and from Eq. (4).

$$1 - N_T = \int_{T_s}^{T_m}\tau_s dT dT \Big/ (T_m - T_s)\int_{T^*}^{T_m}\tau_s dT. \tag{8}$$

In deriving Eq. (7) the heat carried by the slowly moving interface is neglected. The Thomson voltage for most materials at the fusion point is of the same order of magnitude as the Peltier voltage. The sign of this voltage depends on the sign of the Thomson coefficient relative to that of the Peltier coefficient. For example, Pfann *et al.*[1] have shown that for Ge a velocity v of 0.003 cm sec^{-1} is obtained for a current density $|\mathbf{J}|$ of 20 amp cm^{-2}. Similar results have been obtained[5] by growing Ge ingots from the melt. With a value of $H=470$ cal cm^{-3} (which roughly accounts for

latent heat, changes in internal energies and volume expansion due to the phase change) the right hand side of Eq. (7) gives $\pi=0.147$ v. The Seebeck coefficient for intrinsic Ge has been derived by Johnson and Lark-Horowitz[6] as

$$\alpha_\tau=-k/e(2430/T-0.34)\ \mu\text{v/deg}.$$

This yields a positive Thomson coefficient of $86.3(2430)/T\ \mu$v/deg. Using this value of τ_s and a temperature difference of 400°K, Eq. (8) yields a value of $N_T=0.48$. The average value of τ_s over this same temperature range is approximately $210\ \mu$v/deg. These values lead to a positive Thomson voltage of ≈ 0.04 v. Equation (7) then gives a value of $\pi/T=90\ \mu$v/deg. This value is in agreement with that reported by Domenicali[7] ($\sim 70\ \mu$v/deg) who used a standard potentiometric method. In fact, if the Seebeck coefficient reported by Johnson and Lark-Horowitz is corrected by $18\ \mu$v/deg, as suggested by Domenicali, the two methods differ by less than $7\ \mu$v/deg.

Thomson effects in metals can also be appreciable. From Boydston's[8] data of α_s vs T for Bi an average τ_s (where $\tau_s<0$) can be found for a temperature interval near the melting point. These values lead to a Thomson voltage of ≈ 0.01 v. This value is added to $jvH/2J$ which has been reported[1,3] to be 0.014 v. This yields a value of $\pi\approx 0.024$ v which is in excellent agreement with Boydston.

For many materials neither the Seebeck nor Thomson coefficients are known at high temperatures. In these cases a combination of Eqs. (6) and (7) lead to an independent determination of both π and τ_s. For example, the data of Eq. (7) can be displayed as a plot of $v/|\mathbf{J}|$ vs (T_m-T_s). The intercept of this curve at $(T_m-T_s)=0$ yields a value for π and the slope of the curve at this point is equal to $\frac{1}{2}\tau_s$. To avoid errors associated with non-equilibrium effects (e.g., the finite time required for heat to diffuse a mean distance from the interface, etc.), the ratios $v/|\mathbf{J}|$ should be determined as $|\mathbf{J}|\to 0$. These results should then be consistent with the steady state values obtained from Eq. (6).

The writer acknowledges several helpful discussions with Dr. A. D. Johnson, Lt. F. Shepherd, and Dr. A. C. Yang.

[1] W. G. Pfann, K. E. Benson, and J. H. Wernick (with appendix by H. Reiss), J. Electronics **2**, 597 (1957).
[2] J. M. Bardeen and B. S. Chandrasekhar, J. Appl. Phys. **29**, 1372 (1958).
[3] C. A. Domenicali, J. Appl. Phys. **25**, 1310 (1954).
[4] A. I. Burshtein, Zhur. Tekh. Fiz. **27**, 1510 (1957).
[5] W. A. McLaughlin (private communication).
[6] V. A. Johnson and K. Lark-Horowitz, Phys. Rev. **92**, 226 (1953).
[7] C. A. Domenicali, J. Appl. Phys. **28**, 749 (1957).
[8] R. W. Boydston, Phys. Rev. **30**, 911 (1927).

Dislocation Ribbons and Stacking Faults in Graphite

P. DELAVIGNETTE AND S. AMELINCKX
Centre d'Etude de l'Energie Nucléaire, Mol-Donk (Belgium)
(Received May 2, 1960; and in final form June 6, 1960)

IN view of the peculiar structure of graphite, and as a consequence of the ease with which glide takes place between c layers, it was not *a priori* evident that dislocations with a Burgers vector in the basal plane would actually be required for glide. In a previous note[1] we reported the observation of dissociated-dislocation ribbons in the basal plane of graphite, by direct-transmission electron microscopy.[2] Dislocations intersecting the basal have been studied in synthetic graphite, by Dawson[3] using Moiré patterns. It is the purpose of this note to present further striking evidence for the dissociation of dislocations. We also determined the Burgers vectors of the partials and estimated the stacking-fault energy.

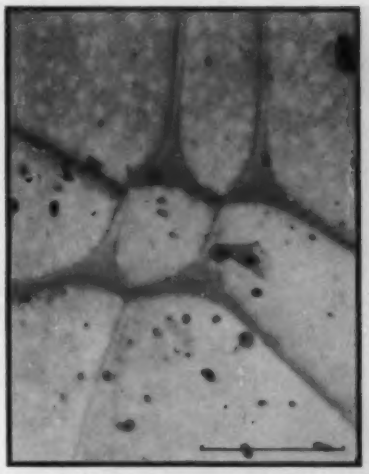

FIG. 2. Extended and contracted nodes and dislocation ribbons in graphite single-crystal flake. Note stacking-fault contrast inside extended nodes.

We first discuss briefly the geometry of the basal-plane dislocations in graphite. Figure 1 shows two successive layers of the normal variety of graphite. The shortest vectors that connect crystallographically equivalent carbon atoms are AA_1, AA_2, and AA_3. These are, therefore, the probable total glide vectors. However, it is clear that dissociation into two partials according to the scheme $A\alpha+\alpha A_1$ (1), or $A\beta+\beta A_1$ (2) would lower the elastic energy. If the stacking-fault energy is small, a visible dissociation into partials will result. There is indirect evidence that the stacking-fault energy should be small for the scheme (1), since some graphites have the "faulted" structure.[4] The dissociation (2) is less probable since it would lead to a stacking fault with higher energy.

That the stacking-fault energy is indeed very small is proved by the widely extended nodes and visibly dissociated ribbons shown in Fig. 2, a transmission electron micrograph of a cleavage flake of natural graphite. Neglecting the mutual interaction

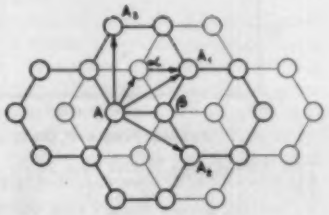

FIG. 1. The structure of graphite. The complete Burgers vectors are AA_1, AA_2, and AA_3, as well as their negatives. Dissociation into partials takes place according to the reaction $A\alpha+\alpha A_1$, or $A\beta+\beta A_1$. The first scheme gives rise to a small energy stacking fault.

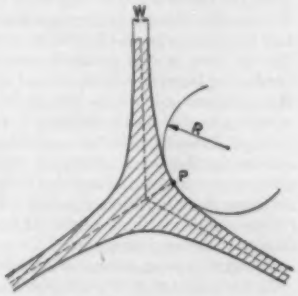

FIG. 3. Schematic view of extended node to illustrate significance of R and w.

FIG. 4. Contrast from the same area as Fig. 2, but for different orientations of the foil. Note the successive disappearance of each family of partials, allowing a determination of the Burgers vectors.

between partials and assuming elastic isotropy, one can estimate the order of magnitude of the stacking-fault energy E, from the radius of curvature R of the partial at a point P (Fig. 3), by using the relation[5]

$$E=\mu b^2/2R, \tag{3}$$

where b is the Burgers vector ($b=1.42\times10^{-8}$ cm) and μ the shear modulus. Taking the value $\mu=2.3\times10^{10}$ d/cm^2 determined by Bowman and Krumhansl[6] and since $R\simeq7.10^{-5}$ cm, we find $E\simeq3.5\times10^{-3}$ erg/cm^2.

The separation distance of two partials can also be used to derive a value for the stacking-fault energy.[7] If w is the width of the ribbon (see Fig. 3) we have, again assuming elastic isotropy,

$$E=\mu b^2(2-\nu)/8\pi w_0(1-\nu), \tag{4}$$

with

$$w_0=w\left(1-\frac{2\nu}{2-\nu}\cos2\alpha\right)^{-1}. \tag{5}$$

Here, ν is Poisson's ratio ($\nu=\frac{1}{3}$) and α is the angle between the ribbon and the total Burgers vector. With $w\simeq8.10^{-6}$ cm this formula leads to $E=5.10^{-3}$ ergs/cm^2. In view of the approximation used, the agreement is very good.

From the absence of contrast for certain dislocation segments and the knowledge of the indices of the reflection responsible for the contrast, in this particular orientation of the foil, one can deduce the Burgers vectors of these dislocation segments. We used the procedure outlined by Whelan.[8] Figure 4 shows a sequence of orientations for which different families of partials exhibit no contrast. From the selected area-diffraction patterns, the Burgers vectors are then easily deduced. In this case, one set of planes giving rise to absence of contrast for a given line is sufficient since we know that the Burgers vector is in the c plane. The Burgers vectors found are those suggested by the geometrical considerations of the second paragraph.

A more extensive account will be published elsewhere.

We are indebted to Mr. Goens, director of the C.E.N., MOL, for permission to publish this paper. We also wish to thank Mr. Nicasy for his skilfull preparation of specimens and Mr. Byens for careful photographic work.

[1] S. Amelinckx and P. Delavignette, Nature **185**, 603 (1960).
[2] W. Bollmann, Phys. Rev. **103**, 1588 (1956); P. B. Hirsch, R. W. Horne, and M. J. Whelan, Phil. Mag. **1**, 677 (1956); P. B. Hirsch, J. Silcox, R. E. Smallmann, and K. H. Westmacott, Phil. Mag. **3**, 897 (1958); A. Berghezan and A. Fourdeux, Compt. rend. **248**, 1333 (1959).
[3] I. M. Dawson and E. A. C. Follett, Proc. Roy. Soc. (London) **A253**, 390 (1959).
[4] H. Lipson, and A. R. Stokes, Proc. Roy. Soc. (London) **A181**, 101 (1942).
[5] M. J. Whelan, Proc. Roy. Soc. (London) **A249**, 114 (1959).
[6] J. C. Bowman and J. A. Krumhansl, J. Phys. Chem. Solids **6**, 367 (1958).
[7] W. T. Read, *Dislocations in Crystals*, (McGraw-Hill Book Company, Inc., New York, 1953), p. 131.
[8] M. J. Whelan, J. Inst. Metals **12**, 385 (1959).

Scattering of Radiation by a Plasma

FORREST I. BOLEY
Scott Laboratory of Physics, Wesleyan University, Middletown, Connecticut
(Received May 18, 1960)

THE purpose of this note is to describe a series of measurements on the scattering of microwave radiation by a plasma which are pertinent to recent work reported by Hershberger.[1] Hershberger has argued that the multiple resonances observed in the absorption and reflection spectrum of microwave radiation scattered by a positive column of a mercury discharge is accounted for by the dispersion relation given by Bohm and Gross[2] combined with a special supposition concerning the resonance conditions of plasma waves driven by the applied microwave field and confined by the cylindrical boundary conditions.

Since electron motions in the direction of the applied E field would be associated with such plasma wave resonances, all multiple resonances should give rise to dipole radiation patterns. This dipole character was found in measurements made by Boley.[3] However, additional results, to be reported here, seem to indicate the necessity for a more complete analysis of the problem to account for the detailed behavior of the multiple resonances.

Using the discharge tube described previously[3] in conjunction with an S-band waveguide system similar except in frequency to that used by Dattner,[4] the ratios of positive column currents for the primary and secondary resonances were determined as a function of the applied frequency. The resultant ratios which should by Hershberger's argument be independent of frequency are shown in Fig. 1.

These results would suggest that the agreement between theoretical and observed values of resonance current ratios as quoted by Hershberger may be fortuitous and that a modification and/or extension of previous theories may be required to account for their frequency dependence.

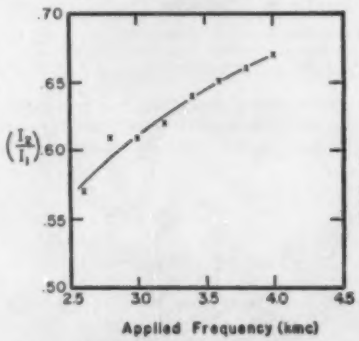

FIG. 1. Ratio of primary (I_1) to secondary (I_2) resonance currents as a function of the frequency of the applied radiation field.

[1] W. D. Hershberger, J. Appl. Phys. **31**, 417 (1960).
[2] D. Bohm and E. P. Gross, Phys. Rev. **75**, 1851 (1949).
[3] F. I. Boley, Nature **182**, 790 (1958).
[4] A. Dattner, Ericsson Technics No. 2, 309 (1957).

Drift Mobility in Neutron Irradiated *n*-Type Germanium

W. H. Closser
Sandia Corporation, Albuquerque, New Mexico
(Received May 18, 1960; and in final form June 20, 1960)

RECENTLY a model for neutron damage in germanium based on the theory of dipole diffusion of the minority carriers has been proposed by Gossick and Crawford.[1,2] For the case of *n*-type material the neutrons form small highly *p*-type regions in the *n*-type matrix. The *p* region is surrounded by a potential well, which arises because the position of the energy bands relative to the Fermi level differs within the region from that outside. The potential well blocks the passage of majority carriers, and at the same time greatly enhances the passage of the minority carriers, which in this case are holes.[1] The over-all representation of the damage site can be pictured as large void regions created in the matrix.

This model has had some previous support by other workers who have applied it to analyses of certain phases of neutron damage.[3,4] In addition to these particular phenomena which they have found explainable by this model, it also predicts a very large increase in the drift mobility of minority carriers for a low concentration of damage; for example, the model predicts an increase in the drift mobility of 40% when the concentration of the voids is sufficient to contain about 10% of the lattice volume.

Measurements of drift mobility in neutron irradiated *n*-type germanium indicate an initial increase in the drift mobility for low values of flux, prior to the decrease which normally occurs as the material approaches intrinsic, resulting from the radiation. This increase was not explainable by a charge center scattering analysis which is usually applied to neutron irradiated material.

The measurements were made on rectangular bars (0.2×0.1 ×2 cm) of germanium using a standard Haynes mobility measuring circuit[5] with a pulsed electric field to prevent overheating of the samples.

Neutrons were obtained from two sources: (a) a Van de Graaff accelerator using a deuterium on beryllium reaction yielding neutrons with a most probable energy of 4–5 Mev in the forward direction,[6] and (b) the Omega West reactor facility at Los Alamos which gave a normal fission spectrum that was slightly hardened by one foot of water, i.e., the thermal neutrons were removed. The most probable neutron energy was 1.34 Mev.[7]

The results of the Omega West irradiations are shown in Fig. 1, curve (a). The Van de Graaff results were similar, although the peak mobility was not quite as large, being about 10% greater than the intitial mobility value.

The experimental results show a maximum increase in the drift mobility of about 25% yielding an f of about 6% from the expression[8]

$$\mu=\mu_0[(1+2f)/(1-f)^2],$$

where μ and μ_0 are the measured mobility and initial mobility, respectively, and f is the fraction of the lattice volume contained in the voids. These results give the best support to date of the applicability of the Gossick model to neutron damage.

This model does not predict the decrease in mobility which follows, however, and the calculations on which it is based become invalid for an f larger than 0.2.

This author believes that in addition to the large void regions which are introduced by the neutrons, there are also point defects introduced outside of the void regions which act as scattering centers for the minority carriers. This assumption is based on data obtained from electron irradiated *n*-type germanium where it is known that the electrons produce point defects. Figure 1, curve (b) is a typical plot of drift mobility vs electron flux for an *n*-type germanium sample irradiated with 2 Mev electrons. The decrease in mobility is approximately proportional to the amount of

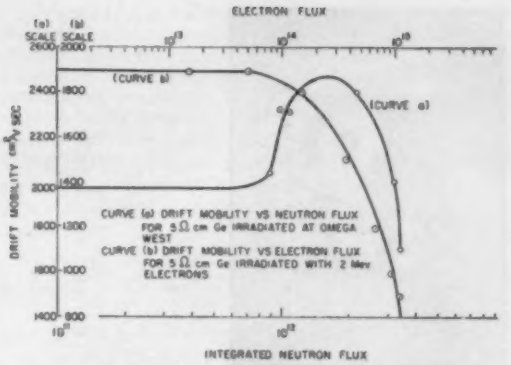

FIG. 1. Electron drift mobility vs (a) neutron irradiation, (b) electron irradiation.

irradiation received in the range where it varies with the flux. Of interest is the fact that no increase in mobility appears on the electron irradiation curve. Inasmuch as the same measuring procedure was used in both cases, this rules out the possibility that the increase observed in neutron irradiated material results from measuring techniques. Also it suggests that in the neutron case there is another factor, other than point defects, which influences the drift mobility. Thus, there are two competing processes determining the mobility, with the void regions determining the mobility at low fluxes and the point defects determining it at higher values of flux. This would explain why the increase in mobility which is observed experimentally is not as large as the increase predicted theoretically and would also explain the observed decrease which must occur as the sample goes intrinsic.

The author is indebted to Dr. Carol Zabel and his staff for use of the Omega West reactor, and to Dr. B. R. Gossick, Arizona State University, and H. J. Stein, Sandia Corporation, for their helpful discussions.

[1] B. R. Gossick, J. Appl. Phys. **30**, 1214 (1959).
[2] B. R. Gossick, J. Appl. Phys. **31**, 29 (1960).
[3] J. H. Crawford, Jr., and J. W. Cleland, J. Appl. Phys. **30**, 1204 (1959).
[4] H. J. Stein, Sandia Corporation (to be published).
[5] J. R. Haynes and W. Shockley, Phys. Rev. **81**, 835 (1951).
[6] A. I. Shpetnyi, J. Exptl. Theoret. Phys. (U.S.S.R.), **32**, 423 (1957).
[7] Work performed by G. Bouchard, Sandia Corporation (1960).
[8] B. R. Gossick, J. Appl. Phys. **31**, 745 (1960).

Growth Kinks in Copper Whiskers

S. Saimoto, V. Griffiths, and E. Teghtsoonian
Department of Mining and Metallurgy, University of British Columbia, Vancouver, British Columbia
(Received May 20, 1960)

DURING the preparation of copper whiskers for deformation studies, some whiskers were produced which contained sharp well-defined kinks. The purpose of this note is to report the results of orientation studies of such kinked whiskers.

The whiskers were produced by the method of hydrogen reduction of cupric chloride described by Brenner.[1] Using temperatures near 600°C, whiskers of about 10 μ-av diam and of lengths up to about 1 cm were grown. In addition to the straight untapered whiskers having a high degree of apparent perfection usually sought for plastic-flow studies, numerous examples of growth aberrations (including kinks, helices, surface pits, etc., as reported in the literature) were observed.[1]

Although kinked growth was not prevalent, a variety of values for the angle contained by the two arms at the kink has been observed. These angles include 60°, 90°, 120°, 135°, and 150°,

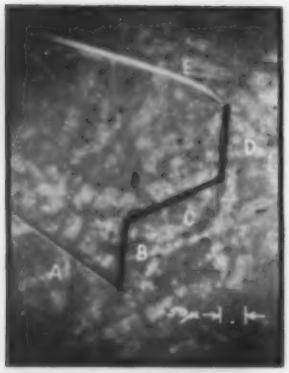

FIG. 1. Multikinked copper whisker.

with an accuracy of ±1°. No frequency distribution measurements were made.

The orientation relation across a kink has been the subject of both speculation and experimentation. Some[2] have argued that when the two arms of a kink have a common facet, there is probably no orientation change, the kinked whisker being a single crystal. Baker[3] has shown that this is indeed the case for Fe whiskers, even in the absence of common facets. In the present study, transmission x-ray Laue photographs have been used to show that Baker's conclusions also apply to Cu whiskers, although with notable exceptions discussed below.

One kinked whisker which has several interesting characteristics is shown in Fig. 1. This multibranched whisker has five segments labeled ABCDE in a counterclockwise direction. The fact that the segments are all coplanar greatly simplified measurement and manipulation. (It should be noted that the bend in the E branch is due to an accident during removal of the whisker from the boat). The interior angles at each of these kinks were measured as 60°, 120°, 120°, and 120°—again taken counterclockwise. Although it is not readily apparent in the photograph, branches B, C, and D have a common facet, while neither branch A nor branch E has a common facet with the central three.

From Laue x-ray transmission photographs it was established that branches B, C, and D are all one single crystal. Branches A and E are also single crystals, but of different orientation from the BCD section. In fact, branch A has the same spatial orientation as branch E, within experimental error. All segments have orientations such that a direction of the form ⟨110⟩ is parallel to the branch axis. The orientation difference between branch A and branch B is that produced by a rotation of approximately 73° about a direction ⟨110⟩. Thus, within the limits of experimental error, branches A and E can be shown to be in twinned orientation with respect to branches B, C, D.

These observations thus show two main features, (1) kinked growth with no change in orientation and (2) kinked growth with an orientation change resulting in a twinned relation. The first of these observations is in agreement with the mechanism suggested by Amelinckx[4] based on a dislocation minimizing its total length by forming in a direction normal to the growing face. It is not altogether clear as to what dislocation mechanism would give the second result. Qualitatively, it is a not unreasonable consequence of a combination of the above mentioned Amelinckx' mechanism, with a faulting in the stacking sequence on the {111} planes which is propagated by the continued growth. This would result in the observed, kinked twin.

A second whisker with interesting characteristics had a single kink with a contained angle of 150°. This whisker was helically twisted in one branch and straight in the other branch. Growth was from the helical branch to the straight branch, so that the transition from helical growth to straight growth occurred at the kink. Orientation determinations on this specimen showed that the helically twisted branch contained two orientations while the straight branch was a single crystal having the same orientation as one of the orientations in the helical portion. The occurrence of two orientations in the helical portion is contrary to the behavior to be expected on the basis of Amelinckx'[4] proposed mechanism.

This is part of a study financed by means of a grant from the Defence Research Board. Permission to publish this note is gratefully acknowledged.

[1] S. S. Brenner, Acta Met. **4**, 62 (1956).
[2] W. G. Courtney, J. Chem. Phys. **27**, 1349 (1957).
[3] G. S. Baker, J. Appl. Phys. **27**, 1561 (1956).
[4] S. Amelinckx, Phil. Mag. **3**, 425 (1958).

Effect of Pressure on the Dynamic Shear Behavior of Polyisobutylene*

A. W. NOLLE
University of Texas, Austin 12, Texas
(Received April 27, 1960)

THIS note reports limited data showing the effects of pressure on the shear viscoelastic properties of polyisobutylene. The quantities determined, for various pressures, are the velocity and absorption coefficient for transverse waves at a frequency of 2 Mc. The polyisobutylene, of viscosity average molecular weight 1.35×10^6, was from a batch used in a cooperative testing program sponsored by the National Bureau of Standards.[1] Pulsed-wave trains were generated and detected by separate Y-cut resonant quartz plates, each of 0.75-in. diam. Each was soldered to an individual cylinder of Y-cut quartz, 1.50 in. long. These cylinders replaced the glass blocks of an earlier experiment,[2] the change being made to reduce difficulties due to differential expansion at the crystal joints. The polyisobutylene sample, which was 0.071 cm thick at room temperature and atmospheric pressure, was bonded between the ends of the transmission cylinders at a temperature of approximately 130°C, while a force of several pounds was applied. No cement was required. A sleeve maintained coaxial alignment.

The assembly was placed in ethyl alcohol in the pressure apparatus used in previous work on longitudinal waves.[3] Absorption measurements were made as before,[2] on the basis of the difference between the average of the signal levels obtained by transmitting through the assembly in both directions, and the average of the signal levels obtained as echoes with the crystals successively connected for pulse-reflection operation. Consistent electrical impedances were used, and the crystal leads were separately shielded. Because the phase velocity and the absorption for the present

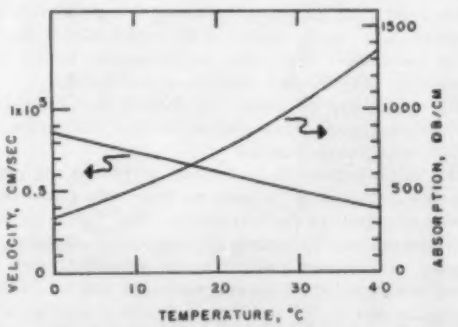

FIG. 1. Phase velocity and absorption coefficient computed from reduced shear data of Ferry, Grandine, and Fitzgerald.

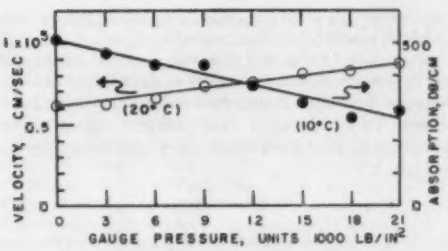

FIG. 2. Phase velocity and absorption coefficient variation with pressure, from present measurements.

material at atmospheric pressure can be calculated from the reduced-variables dynamic shear-modulus data of Ferry, Grandine, and Fitzgerald,[4] emphasis was placed on determining the changes of the quantities under pressure. In particular, the sample was too thin for accurate determination of the absolute value of the phase velocity. Thus, the change (with pressure) in the phase of the signal transmitted through the sample was observed, to approximately $\pm 3°$, the maximum change being about 200°.

Phase velocity and absorption coefficient values for atmospheric pressure, calculated from the FGF data,[4] are shown in Fig. 1. These values were used in computing amplitude corrections for the quartz-polymer interfaces, and the corresponding phase corrections. The latter were not used, as the effect in the phase velocity was less than 1%.

The method succeeds when the absorption is great enough to be measured readily with the given thickness of sample, but when the desired signals are still much stronger than those from other modes of propagation.[3] In the present case, absorption data were obtained at 10 ± 0.3°C, and phase velocity data at 20 ± 0.2°C, as shown in Fig. 2.

The results may be used to evaluate dT/dP for constant molecular jump rate. For present purposes, constant jump rate means constant dynamic modulus, or constant elastic wave propagation constants, for the corrections involving density ratios and absolute temperature ratios in the reduced variables scheme may be neglected without affecting the precision with which dT/dP can be found here. From the slopes in Figs. 1 and 2, we find $dT/dP = 0.010$ C°/atm from the absorption data, and $dT/dP = 0.015$ C°/atm from the velocity, giving a composite result of 0.013 C°/atm.

For comparison, a best-fit straight line for the data of footnote reference 3, where the shifts with temperature and pressure of the maximum in the bulk-wave absorption coefficient were investigated, gives 0.019 C°/atm. A calculated value in footnote reference 5, based on a theory by Bueche, gives 0.025 C°/atm which is not in disagreement with the preceding answer, in view of the uncertain knowledge of the values needed in the theory.

The present results, combined with those in footnote reference 3, are consistent with a suggestion made elsewhere,[6] that the same rate-determining mechanisms operate in both shear and volume processes. A better test would result from obtaining sufficient shear data under pressure to allow a reduced-variables treatment. Unfortunately, the program was interrupted because of electrolytic disintegration of the crystal solder joints under pressure, and an opportunity has not been found to resume the work. It has been shown recently[7] that a reduced variables presentation succeeds with the dynamic compressibility of rubber under various pressures.

A value of 0.023 C°/atm was found for dT/dP for constant hydrogen magnetic-resonance linewidth in polyisobutylene.[8] Constant jump rate evaluated from the dynamic compressibility rubber[7] gives $dT/dP = 0.024$ C°/atm.

The assistance of William J. Rowley in the experimental work is acknowledged.

Note added in proof. In the interpretation of the given data, the effect of pressure on the limiting low- and high-frequency compliances, and on the amplitude of the loss compliance function, is neglected, no data being available to estimate these effects. The corresponding temperature effects[4] are not serious for present purposes. In the dynamic compressibility of natural rubber,[7] the effects of both temperature and pressure on the high- and low-frequency compliances and on the amplitude of the loss function are significant in the dT/dP calculation, but the relaxing part of the compliance is relatively much less than for elastomers in shear.

* Assisted by the U. S. Office of Naval Research.

[1] R. S. Marvin, *Second International Congress of Rheology* (Butterworth Publications, London, 1954), p. 156.
[2] A. W. Nolle and P. W. Sieck, J. Appl. Phys. **23**, 888 (1952).
[3] H. Singh and A. W. Nolle, J. Appl. Phys. **30**, 337 (1959).
[4] J. D. Ferry, L. D. Grandine, and E. R. Fitzgerald, J. Appl. Phys. **24**, 911 (1953).
[5] F. Bueche, J. Chem. Phys. **21**, 1850 (1953).
[6] R. S. Marvin, R. Aldrich, and H. S. Sack, J. Appl. Phys. **25**, 1213 (1954).
[7] J. E. McKinney, H. V. Belcher, and R. S. Marvin, Trans. Soc. Rheol. **4** (1960). (To be published.)
[8] A. W. Nolle and J. J. Billings, J. Chem. Phys. **30**, 84 (1959).

Megavolt Electronics Cerenkov Coupler for the Production of Millimeter and Submillimeter Waves*

PAUL D. COLEMAN AND CHARLES ENDERBY
Ultramicrowave Group, University of Illinois
(Received May 18, 1960; and in final form June 17, 1960)

IT is sometimes assumed that the Cerenkov effect[1-3] is a weak interaction not capable of producing appreciable amounts of power. However, if a bunched, megavolt electron beam is used, then radiation at the watt level[4] can easily be produced with a simple, dielectric Cerenkov cone[5] which serves simultaneously as an energy converter and radiator.

A schematic diagram of the experimental arrangement for verifying the megavolt electronic Cerenkov coupler principle is shown in Fig. 1. A high-harmonic current, 1-Mev electron beam, obtained from an *S*-band Rebatron,[6] passes through a 4-mm diam hole in a large Teflon cone shaped as indicated in the drawing. The two cone angles ϕ and α have been chosen such that the coherent, harmonic, Cerenkov radiation, emerging at the characteristic angle $\vartheta = \cos^{-1}(v_p/v)$, is internally reflected at cone surface 1 striking cone surface 2 at the Brewster angle and exiting parallel to the cone axis. The phase velocity of light in the dielectric is v_p and the beam velocity is v.

Since the Cerenkov radiation, for the cone arrangement indicated, emerges in a TM mode-type pattern, it is most conveniently

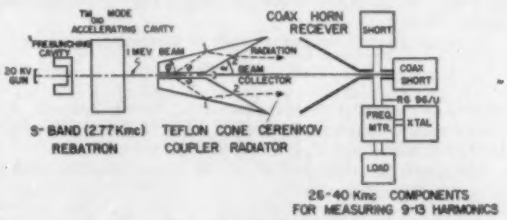

FIG. 1. Schematic diagram of Cerenkov coupler experiment using 9th to 13th beam-current harmonic from *S*-band Rebatron.

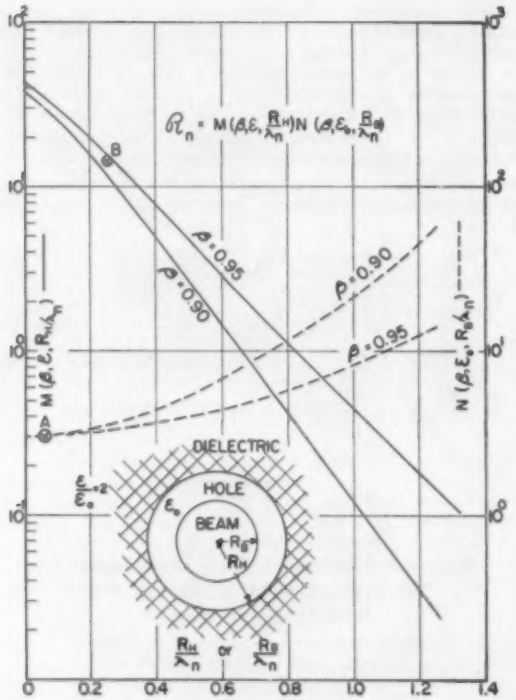

FIG. 2. Curves illustrating variation of interaction resistance with hole and beam radius.

detected in the 26- to 40-kMc range (9th to 13th S-band harmonic) by a coaxial horn. The center conductor of the horn can also be used to collect the beam electrons and return them to ground. The coax horn feeds into an RG 96/U waveguide system, through a 3-port frequency meter, to select a desired harmonic, and finally to a calibrated crystal detector where the power is measured.

Since conditions have been arranged to couple out all of the Cerenkov radiation produced, no reflected waves returning to the axis will be present. Hence, an accurate calculation of the power can be made by considering the simple problem of a beam passing through a hole in an infinite dielectric medium. For this case, it is only necessary to solve the scalar potential ϕ equation

$$\nabla^2\phi+k^2\phi=-\sum_n \frac{\rho_n}{\epsilon_0}e^{i(n\omega_0(t-z/v)} \tag{1}$$

appropriate to each region and evaluate the constants in the solutions by using the boundary conditions. The vector potential is given by $\bar{A}=\hat{l}_z\mu\epsilon_0\phi$. Here ρ_n is the charge density, assumed constant, for the nth harmonic, ω_0 is the base angular frequency of the Rebatron.

A computation of the power yields an expression of the form

$$\mathcal{P}_n=I_n^2L/\lambda_n\mathcal{R}_n, \tag{2}$$

where $I_n=\pi\mathcal{R}_B^2\rho_n$ is the beam current in the nth harmonic, L is the interaction length in the cone, λ_n is the harmonic wavelength in the free space, and $\mathcal{R}_n$ is the interaction resistance.

The interaction resistance $\mathcal{R}_n$ can be expressed as the product of two factors as follows:

$$\mathcal{R}_n=M(\beta,\epsilon,R_H/\lambda_n)N(\beta,\epsilon_0,R_B/\lambda_n), \tag{3}$$

where the function M describes the variation with respect to beam velocity $v=\beta c$, the dielectric constant ϵ, and dielectric hole size R_H, while N describes the variation with respect to beam velocity and beam radius R_B. Figure 2 gives curves of the functions M and N for the case $\epsilon=2\epsilon_0$ and two values of the velocity ratio β.

Using the data $R_H=2$ mm, $R_B=0.5$ mm, $\beta=0.93$, and $\lambda_n=8$ mm, then $N=3.1$ (point A) and $M=14.5$ (point B). An interaction length L of 5 cm yields the power expression for this experiment,

$$\mathcal{P}_n=280I_n^2. \tag{4}$$

Experimentally, a maximum of 0.3 w for $n=13$ were obtained with an average beam current I_0 of 0.028 amp. The harmonic current I_n must lie in the range $0\leq I_n\leq 2I_0$. Rebatron calculations for the 13th harmonic give $I_{13}\simeq 1.5I_0=0.042$ amp, hence, the theoretical power expected from Eq. (4) is 0.5 w.

While time has not permitted experimentally verifying the radiation pattern of the Cerenkov cone, the ray tracing technique must evidently be good since the receiving system was designed on this basis and gave excellent results.

The Cerenkov coupler technique described follows the megavolt electronics philosophy that it is easier to build characteristic frequencies into a beam than into the field structure coupling device. Nonresonant coupling structures can be physical optics type of devices, thereby avoiding all microwave problems. The fact that the device can be used simultaneously as an energy converter and radiator makes it doubly attractive. Increasing the interaction length L, the beam harmonic current I_n, and decreasing the hole size R_H, will make it possible to produce Cerenkov radiation in the range 1 or 5 w or greater in the submillimeter range.

* Work supported by WADD and U. S. Atomic Energy Commission under contract.

[1] M. Danos and H. Lashinsky, IRE Trans. **MTT-2**, 21 (1954).
[2] M. Danos, S. Geschwind, H. Lashinsky, and A. Van Trier, Phys. Rev. **92**, 828 (1953).
[3] H. Lashinsky, "Generation of microwaves by Cerenkov radiation," PIB, MRI, Symposium on Millimeter Waves (1959).
[4] I. E. Tamm, Am. Scientist **47**, 169 (1959).
[5] Ultramicrowave Group, Quart. Rept. No. 5 (1957).
[6] P. D. Coleman, J. Appl. Phys. **28**, 927 (1957).

Growth of GaAs Crystals in the ⟨111⟩ Polar Direction

P. L. MOODY, H. C. GATOS, AND M. C. LAVINE
Lincoln Laboratory, Massachusetts Institute of Technology, Lexington, Massachusetts*

(Received May 3, 1960; and in final form May 31, 1960)

IT was observed that the crystallographic polarity in the ⟨111⟩ direction has a pronounced effect on the perfection of GaAs crystals (zinc-blende structure) grown in that direction: Single crystals were consistently grown when the end of the ⟨111⟩ seed crystal terminating in As atoms (B{111} surface) is employed. By employing the opposite end of the seed, terminating with Ga atoms (A{111}surface), twinning or large-grain formation occurred rather than single-crystal growth. This effect is similar to that reported by the authors[1] in the case of InSb.

In the present study all of the GaAs crystals were pulled vertically in a syringe-type apparatus described elsewhere.[2] The seed was rotated at 10 rpm and pulled at 1 in./hr. Crystals of approximately constant diameter ($\frac{3}{4}$ in.) were pulled from an 1$\frac{1}{2}$-in. diam crucible with relatively small thermal gradients along the solid-liquid interface: the variation in dislocation density across the

diameter of single crystals grown under these conditions was less than 10%.

About 20 crystals were grown in the A⟨111⟩ direction by employing four different seeds. None of these A crystals was single. One A crystal from each seed, having a single-crystal core, was compared with the B single crystal obtained from the same seed. The dislocation density in the B crystal was found to be smaller than the dislocation density in the corresponding A crystal. relative dislocation densities were determined near the axis of the crystals by counting the number of dislocation etch pits[3] formed on the A surface perpendicular to the direction of growth. For each dislocation-density determination etch-pit counts were made on at least 16 areas totaling about 20 mm². The reproducibility was found to be within 10%. The ratios of the measured dislocation densities in the four pairs of crystals examined were 2.0, 1.6, 4.3, and 2.5. Furthermore, in the A crystals the dislocation density increased consistently with increasing distance from the seed. Typically an increase of approximately a factor of two was observed in a distance of ¼ in. No such trend was observed in the B crystals.

As in the case of InSb[1] here also, it is believed that the effect of the ⟨111⟩ crystallographic polarity on crystal growth is closely related to the bonding characteristics of the A and B surface atoms.[4] In particular, the strain associated with the deviation of the bonding of the surface A atoms from the tetrahedral configuration is believed to be responsible for the lesser degree of perfection of the crystals grown in the A⟨111⟩ direction.[1,4]

The present results answer the question[5] as to whether the perfection of GaAs crystals grown in the ⟨111⟩ direction depends on the polarity of the seed crystal. It is, of course, possible that for growth conditions other than those employed in this study the differences in perfection between the crystals grown in the A⟨111⟩ and the B⟨111⟩ directions can be accentuated or attenuated. In fact the effect of the ⟨111⟩ crystallographic polarity was not observed in GaAs crystals grown horizontally.[6] This difference between vertically pulled and horizontally grown GaAs crystals merits further investigation.

* Operated with support from the U. S. Army, Navy, and Air Force.
[1] H. C. Gatos, P. L. Moody, and M. C. Lavine, J. Appl. Phys. **31**, 212 (1960).
[2] P. L. Moody and C. Kolm, Rev. Sci. Instr. **29**, 1144 (1958).
[3] The etching solution employed was 1 (part by volume) conc HNO_3+1 conc HCl+1 H_2O.
[4] H. C. Gatos and M. C. Lavine, J. Electrochem. Soc. **107**, 427 (1960).
[5] S. G. Ellis, J. Appl. Phys. **30**, 947 (1959).
[6] J. L. Richards, J. Appl. Phys. **31**, 600 (1960).

Erratum: Depolarized Components of Light Scattered by Glasses. II. Influence of Nonannealable Strains on the Scattering

[J. Appl. Phys. **30**, 501–506 (1959)]

MARTIN GOLDSTEIN
*Mellon Institute, Pittsburgh, Pennsylvania**†

THERE are two errors in sign in the equations given on the bottom of the left-hand column of page 503, and in Eqs. (1) on the right-hand column of the same page, which are derived from them. The term in V_v having $\delta_{ab}a^3$ as a factor should appear with a plus sign, and the term in H_h having $\delta_{ab}a^3$ as a factor should appear with a minus sign.

* Pittsburg Plate Glass Company Fellowship.
† Present address: Scientific Laboratory, Ford Motor Company, Dearborn, Michigan.

Books Reviewed

Prompt, noncritical reviews appear in this column. Critical reviews of many of the books described here will appear in Physics Today, The Review of Scientific Instruments, *or* American Journal of Physics.

Progress in Semiconductors. A. F. GIBSON, F. A. KROGER, AND R. E. BURGESS, EDITORS. Pp. 285+vii. John Wiley & Sons, Inc., New York, 1960. Price $10.50.

At the present time, when hundreds of papers on semiconductors and allied subjects are published every year, it is difficult for any one specialist to read more than a small fraction if he is to leave any time for original work.

This annual series of volumes is planned to meet this difficulty. A limited number of topics taken from the whole field of semiconductors will be included each year. The articles generally will be critical reviews, giving an assessment of the present state of knowledge. Some, however, will contain significant amounts of original work. Each volume will be fully international.

Nuclear Fusion. WILLIAM P. ALLIS, EDITOR. Pp. 476. D. Van Nostrand Company, Inc., Princeton, New Jersey, 1960. Price $12.50.

Here in a carefully worked out presentation are the most significant ideas on fusion presented at the 1958 conference in Geneva. Contributors from some eleven nations presented papers and in this volume duplication has been removed, clarifications added where necessary and the subject matter indexed.

Following a general survey of world-wide controled thermonuclear research, plasma properties are discussed including diagnostics, waves, equilibrium and stability, and dynamics. Coverage of the types of thermonuclear machines, such as the pyrotron, the stellarator, injection machines, sustained and dynamic pinches, occupy over one-half of the book.

Radiation Pyrometry and its Underlying Principles of Radiant Heat Transfer. THOMAS R. HARRISON. Pp. 205+xxii. John Wiley & Sons, Inc., New York, 1960. Price $12.00.

Material in the first three chapters offers a unified discussion of the laws of emission, absorption, reflection, and transmission of thermal radiation, applicable to the field of radiant-heat transfer as well as radiation pyrometry. The remaining chapters include important descriptions and mathematical analyses of the physical and operating characteristics of radiation pyrometers and the application of emittance corrections. All necessary steps for mathematical deductions are given. The last chapter lists a number of valuable tables that show radiation pyrometer calibrations, optical characteristics of various substances, some radiation functions, and certain mathematical relationships that find application in radiation pyrometry.

Space Flight. Vol. 1. Environment and Celestial Mechanics. KRAFFT A. EHRICKE. Pp. 504. D. Van Nostrand Company, Inc., Princeton, New Jersey, 1960. Price $14.50.

Part one of the first volume covers the concept of space flight and the environment in which it will take place, to the extent that we know it at this time, with emphasis on the gaps in our present knowledge which require space research by means of rocket vehicles. The historical development of the space-flight concept is traced, and utility aspects showing the important correlation between utility and evolution of space flight discussed. For a more thorough understanding of the

environment in which space flight will take place, the author delves into our solar system from the viewpoint of the astronautical engineer, with emphasis on useful comprehensive tables of consistent data.

Through the use of many tables, graphs, and illustrations, as well as hand calculation and short-cut methods, this book will prove valuable in day-to-day research and development work, for preliminary design and systems analysis. Problems are given at the end of each celestial mechanics chapter.

Chemistry of Nuclear Power. J. K. Dawson and G. Long. Pp. 208. Philosophical Library, Inc., New York, 1959. Price $10.00.

This is a small but comprehensive book dealing with the role of the chemist in the development of nuclear energy. It does an excellent job of describing those phases of the nuclear science in which chemistry plays a vital part. The historical development used throughout makes it very interesting reading. It is certainly worthwhile reading for those schooled in chemistry but not necessarily the nuclear science. It would also fill a real gap in the knowledge of persons working in the branches of nuclear science other than chemistry.

Physics of the Atom. M. R. Wehr and James A. Richards, Jr. Pp. 356+liv. Addison-Wesley Publishing Company, Inc., Reading, Massachusetts, 1960. Price $8.50.

This book offers an introduction to modern physics suitable for any student with a background in college physics and mathematical competence at the level of calculus. It is designed to extend the introductory college physics course into the realm of atomic physics, and to give the student a proficiency in this field comparable to that which he has acquired in mechanics, heat, sound, electricity, and optics. It is intended for a one-term course in either a liberal arts or an engineering curriculum.

Optics of Thin Films. A. Vasicek. Pp. 385+x. North-Holland Publishing Company, Amsterdam. Interscience Publishers Inc., New York, 1960. Price $12.50.

This book does not aim at being a complete survey of all the papers published on films in optics, but it presents those problems which are important in optics and also problems solved during the last two decades by the author. The book deals with some prolems which have been completely solved and many which are still open.

The book contains many formulas and it is written in a clear, comprehensible way. It makes no great demands from the mathematical point of view and can, therefore, be read by anyone who is really interested in this young but important branch of physics.

Applications of Thermoelectricity. H. J. Goldsmid. Pp. 116. John Wiley & Sons, Inc., New York, 1960. Price $2.25.

This is the first short, introductory book on the subject by a specialist working in this field and will be useful to scientists and engineers entering the field for the first time while, at the same time, providing an elementary account of the applications of thermoelectricity to students and those whose main interests lie elsewhere.

Books Received

Solid State Physics in Electronics and Communications. Proceedings of an International Conference held in Brussels, June 2–7, 1958. Vol. 1: Semiconductors. Part 1. M. Desirant and J. L. Michiels, Editors. Pp. 638. Academic Press, Inc., New York, 1960. Price $18.00.

Medical Physics. Vol. 3. Otto Glasser, Editor-in-Chief. Pp. 721. The Year Book Publishers, Inc., Chicago, 1960. Price $25.00.

Progress in Solid Mechanics. Vol. 1. I. N. Sneddon and R. Hill, Editors. Pp. 439. Interscience Publishers, Inc., New York, 1960. Price $15.50.

Etudes De Pyrometrie Pratique. R. Alegre, M. Ancey, R. Kissil, R. Lacroix, G. Monnot, A. Moutet, M. Riviere, and G. Urbain. Pp. 187+xxxviii. Gauther-Villars, Paris, France, 1959.

Advances in Spectroscopy. Vol. 1. H. W. Thompson, Editor. Pp. 353. Interscience Publishers, Inc., New York, 1959. Price $12.50.

Trends in Atomic Physics (Essays dedicated to Lise Meitener, Otto Hahn, and Max von Laue). O. R. Frisch, F. A. Paneth, F. Laves, and P. Rosbaud, Editors. Pp. 285. Interscience Publishers, Inc., New York, 1959. Price $7.50.

Cryophysics. K. Mendelssohn. Pp. 170+xii. Interscience Publishers, Inc., New York, 1960. Price $4.50 (paperbound, $2.50).

Wave Propagation in a Random Medium. Lev. A. Chernov. Pp. 165. McGraw-Hill Book Company, Inc., New York, 1960. Price $7.50.

Announcements

New Editor, *Journal of Applied Physics*

On September 15, 1960, Dr. J. H. Crawford, Jr., became editor of the *Journal of Applied Physics*, replacing Dr. J. A. Krumhansl. Ethel C. McMillan will continue in the position of Assistant Editor. All comments and contributions should be addressed to the Journal's new office:

Dr. J. A. Crawford, Editor
Journal of Applied Physics
Solid State Division
Oak Ridge National Laboratory
Oak Ridge, Tennessee.

International Congress of Biophysics

An International Congress of Biophysics will be held in Stockholm from July 31 to August 4, 1961. The purpose of the meeting is to provide a forum for international communication in the field of biophysics. Participants may include members of national societies of biophysics, medical physics, and related fields; and other scientists interested in pure and applied biophysics. The meeting will be divided between a series of symposia devoted to special topics in biophysics and to presentations of a number of contributed papers in pure and applied biophysics submitted by the participants. Further information can be obtained from Dr. Bo Lindström at the Department of Medical Physics, Karolinska Institutet, Stockholm 60, Sweden.

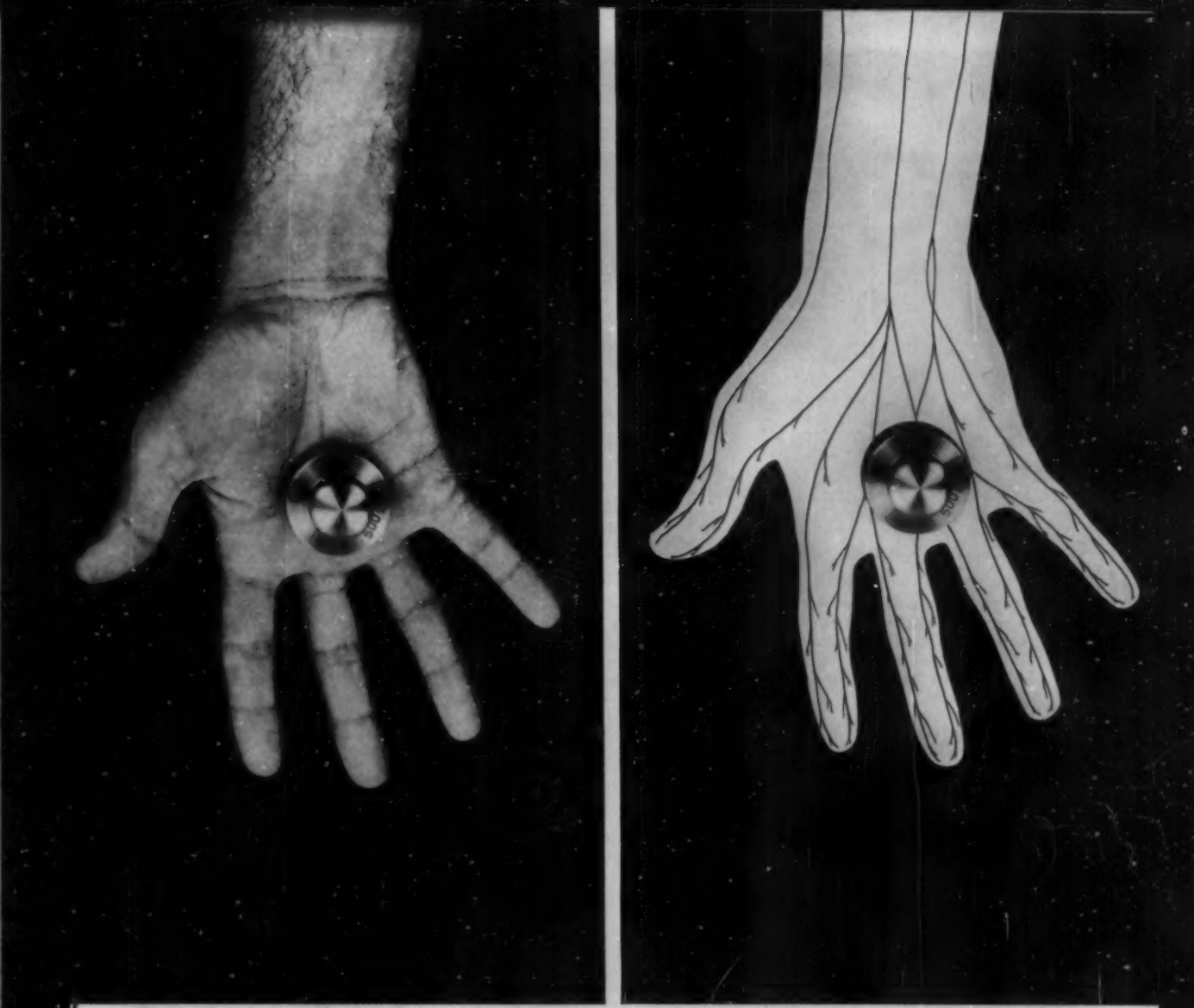

The relationship between subjective sensations (left) and the corresponding codes of the nervous system (right) are now under study at IBM.

Comparing human sensations and their related nerve signals

What is the relationship of a man judging the amount of pressure on his skin and a physiologist measuring the firing rate in animal nerves? The first is a subjective, or *psycho*physical measurement, while the second is *neuro*physiological. To find the relationship between these two kinds of measurements, they would have to be made on the same subject.

Recently developed techniques have now made this possible. At IBM Research, physiological psychologists measure nerve signals through simple contacts applied to human subjects. A stimulus is applied and the neural signals are recorded. Interfering responses are separated from test responses using a computer programmed to measure the systematic neural signals. Since the subjects can also describe the sensations produced, a direct comparison can be made.

In this way, IBM psychologists are learning more about the complex codes by which the neural network evokes the myriad sensations of human experience. Their eventual aim is to unravel the coding pattern from the stimulus input through the peripheral nerves to the brain and the sensations reported by the subjects.

This work is building a significant bridge between the separate fields of psychologists and physiologists. As a by-product, it is also shedding new light on the application of computers to biological and medical science.

IBM.RESEARCH

Investigate the many career opportunities available in exciting new fields at IBM.
International Business Machines Corporation, Dept. 579U, 590 Madison Avenue, New York 22, New York

THE 1960's WILL BE A DECADE OF TIME COMPRESSION . . .

More people will travel further in a shorter time—men will move in geocentric orbits at 18,000 mph—space probes will shrink our celestial environment. To accomplish these things, the time between research and application engineering will shrink dramatically.

Convair believes that the full potential of Technology in the Sixties will be realized through ideas originating in the minds of creative scientists and engineers. To implement this conviction, Convair-Fort Worth is pursuing an active research program in the engineering and physical sciences.

A position on the staff of the newly formed Applied Research Section offers opportunity rarely found for physicists and engineers at the doctorate level. Research programs in the fields of astrophysics, relativity, gravitation, physics of materials, and geophysics are in the formative stages of planning and activation. Active and mature programs in electronics, space mechanics, and thermodynamics are underway.

If you can qualify, a position within this section will offer unlimited growth potential. For further information, forward your personal resume to Dr. E. L. Secrest, Chief of Applied Research, Convair-Fort Worth, P. O. Box 748 J, Fort Worth, Texas.

CONVAIR/FORT WORTH
CONVAIR DIVISION OF
GENERAL DYNAMICS

FUNDAMENTAL RESEARCH OPPORTUNITIES

for

Physicists

Chemists

Metallurgists

Offered by Our

METALLURGICAL LABORATORIES

A multi-million-dollar facility, new and fully equipped, Affording Challenging Opportunities in

ALUMINUM, COPPER & BRASS, and NUCLEAR FUELS.

WELDING ENGINEERS

Welding or MET degree and at least 5 years' experience in welding research. Will be responsible for planning, supervising, and reporting research projects on metallurgical and physical phenomena in developing of improved welding methods for both aluminum and copper alloys.

PHYSICISTS OR METALLURGISTS

Ph.D's or equivalent, for fundamental studies of oxidation of aluminum and copper alloys. Good background in semi-conductor technology or metal physics required, together with good first-hand knowledge of the applicable experimental techniques. Some familiarity with aluminum or brass metallurgy is desirable. Previous industrial research experience is not mandatory.

SURFACE CHEMISTS

Fundamental surface chemical investigations involving application of electron-optics, ellipsometry, infra-red reflectance and other appropriate aids. Applicants should be interested in research rather than engineering approach.

A. Surface chemistry and physics of oxide films, including adsorption, electrochemical kinetics, electrical and optical structure and mechanism studies of metal finishing processes.

B. Chemistry of inter-action of metal and metal oxide surfaces with organic materials, molten salts and other metals. Approach is mechanistic and aimed at understanding of factors affecting surface interaction.

C. Investigation of chemical, electrochemical and metallurgical factors influencing kinetics of metal corrosion processes in various environments.

Send resume in confidence to:
E. R. PATTERSON, Salaried Employment Administrator

OLIN MATHIESON CHEMICAL CORP.

275 Winchester Ave., New Haven, Conn.

PHYSICISTS

SALARY: TO $16,000

Immediate high-level professional assignments are available in Hughes-Fullerton's new Computer Laboratory for Physicists qualified in the application of information theory to the solution of signal retrieval problems. These challenging positions involve advanced work in connection with the design and development of new large scale digital computers and digital systems.

These professional assignments involve such R & D areas as:

- **Solid state digital circuitry involving millimicrosecond logic**
- **Microwave carrier digital circuits**
- **Sub-microsecond core memory**
- **Thin film storage techniques**
- **Functional circuit concepts**
- **Micro-miniaturization concepts**
- **Tunnel diodes**
- **Microwave parametrons**
- **Circuit organization for maximal-speed computing**

Located in Southern California's Orange County (the nation's fastest growing electronics center), Hughes-Fullerton offers you: a stimulating working environment; private or semi-private offices; long-term stability.

CALL COLLECT TODAY!

For complete information on these challenging assignments, call us collect **today!** Ask for:

Mr. B. P. RAMSTACK at: TRojan 1-4080, ext. 3741.

Or, airmail resume to: HUGHES-FULLERTON R & D, P. O. Box 2097, Fullerton 1, California.

HUGHES

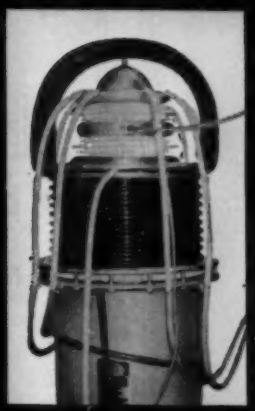

600,000 amperes help harness H-power

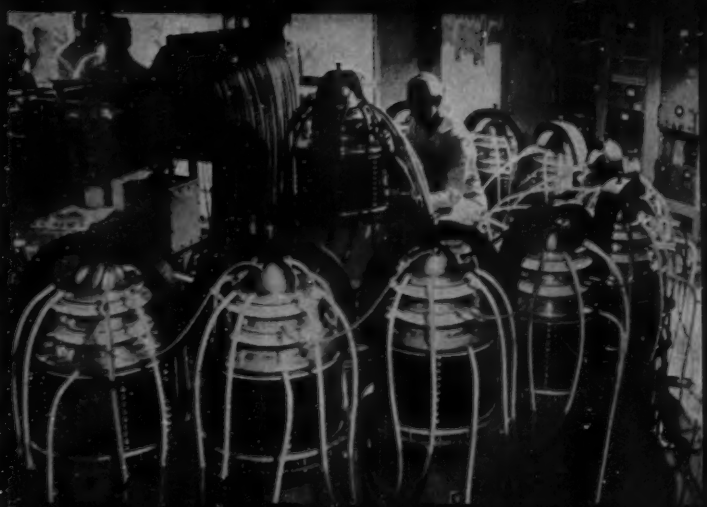

At the historic Geneva Atoms-For-Peace Conference, Los Alamos scientists unveiled **Scylla**—a fusion device used to heat a plasma of ionized heavy hydrogen particles millions of degrees by blasting it with a 600,000-ampere thunderbolt.

Surrounding the heart of this thermonuclear machine is a bank of low-inductance, energy-storage capacitors...each rated at 100,000 volts, each capable of a 20,000 megawatt peak surge.

This unique installation, like others of its type, is the result of long experience in capacitor specialization. If adherence to rigid specifications is a 'must' on your project—call us in to help with creative engineering. We invite inquiries for a single energy-storage capacitor or a complete energy-storage system including capacitors, racks, interconnecting lines, protective devices and charging power supply.

For further technical information, write for Bulletin No. 191 to Cornell-Dubilier Electric Corporation, New Bedford, Mass.

CDE **CORNELL-DUBILIER ELECTRONICS DIVISION**
FEDERAL PACIFIC ELECTRIC COMPANY

a vacuum pump as quiet as a . . .

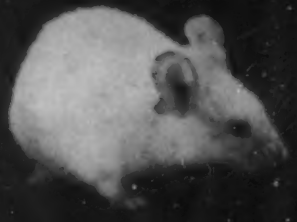

Steady and silent. That's the new Stokes Series H Microvac pump. Unique dynamic balancing provides hushed operation. And the compact Stokes pump saves up to 50% in valuable floor space.

Find out all the reasons why you get *more pumping performance per dollar* with Stokes Microvac pumps. Just write: Vacuum Equipment Division, F. J. STOKES CORPORATION, 5500 TABOR RD., PHILA. 20, PA.

STOKES

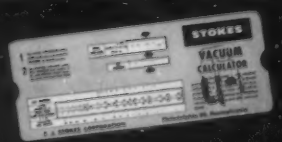

SEND TODAY
for your free
Vacuum Slide Calculator.

NUCLEAR PHYSICISTS

FOR MEDICAL AND SPACE RESEARCH

The Radiation Physics Department of the Nuclear Electronics Laboratory has several openings for Nuclear Physicists, preferably with Ph. D. Degrees and experience relating to the following areas:

SOLID STATE DETECTION DEVICES

Duties will involve design and participation in studies utilizing solid state detection devices and the conception of new applications for specialized radiation detectors. Primary duties will involve a space radiation measurement program.

DOSIMETRY

Preferred experience will include dosimetry, utilizing ionization chamber techniques, calorimetry, nuclear spectroscopy and film dosimetry. The responsibilities will be to design and operate radiological equipment in cooperative dosimetry programs. The programs are involved with medical and biological applications.

Please airmail your resume to:

MR. ROBERT A. MARTIN
Supervisor, Scientific Employment,
Hughes Engineering Personnel Dept.,
11940 W. Jefferson Blvd.,
Culver City 41, California

CREATING A NEW WORLD WITH ELECTRONICS

HUGHES

ENGINEERING DIVISION
AEROSPACE GROUP
HUGHES AIRCRAFT COMPANY

SOLID STATE PHYSICISTS ●

Expanding long-range programs require that Battelle add solid state physicists, physical chemists and electrical engineers to its professional staff.

The programs now under way cover a wide variety of interesting problems. Included are studies in thin films, "noise," transistors, rectifiers, thermoelectric energy conversion, semiconductor materials, and related topics.

The following openings are available:

- **Ph.D. in physics or physical electronics (preferably with 2 to 5 years experience) for theoretical solid state research.**
- **B.S. to Ph.D. level with experience in transistor materials and their applications to solid state devices.**
- **Recent graduate B.S. or M.S. with degree in physics or electrical engineering, to work with experienced scientists on application of solid state devices.**
- **M.S. or Ph.D. in physics or physical chemistry with an avid interest and experience in thin films and their applications to electronics.**

These positions offer unusual opportunities to work and study with outstanding scientists and technologists in an organization where initiative and creative enthusiasm is encouraged and appreciated.

For further details, application form and descriptive brochure, write to:

L. G. Hill

Battelle Memorial Institute
505 King Avenue Columbus 1, Ohio

YOUR POTENTIOMETRIC INSTRUMENTS

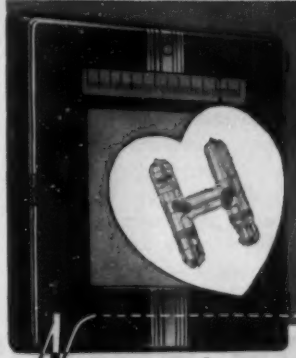

NO matter how perfect otherwise, the human organism isn't much good without a dependable heart. The same is true of your automatic temperature and pH control instruments. The "heart" of most such instruments for the past forty years has been the Eplab Standard Cell. It is a "yardstick" for translation of voltage to temperature or pH. The first American commercial cell of its type, constantly improved by research, it is "as standard as sterling". Get ACCURATE temperature or pH control with potentiometers and make sure the standard cells are EPLAB.

The Eppley Laboratory, Inc. 6 SHEFFIELD AVE. NEWPORT, R. I.

EPLAB *Standard* CELLS
FOR POTENTIOMETRIC INSTRUMENTS
"As Standard as Sterling"

483-9

A compact f/3.5 system yielding high **EFFICIENCY**

Designed to yield monochromatic illumination at wavelengths ranging between 220 and 2,800 millimicrons in the ultra-violet, visible and infrared regions. Compact and flexible, Monochromators are convenient to use with microscopes, colorimeters, photometers and similar instruments, and can be set up with auxiliary equipment for making transmission, absorption, emission, radiation, reflection, fluorescence and phosphorescence measurements or irradiation purposes.

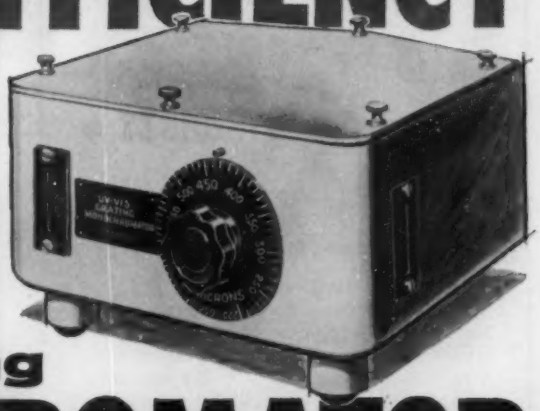

Farrand Grating

MONOCHROMATOR

Technical data available on request
Specify Bulletin No. 811AP

FARRAND OPTICAL CO., INC.
BRONX BLVD. AND EAST 238th STREET • NEW YORK 70, N. Y.
Engineering, Research, Development, Design and Manufacture of Precision Optical, Electronic and Scientific Instruments

SENIOR PHYSICIST

Magnetics department of our Research Division offers an unusual opportunity for a physicist or engineer (Ph.D. desirable) to participate in and lead experimental and theoretical studies in various aspects of magnetism and magnetic materials. Company sponsored projects are underway on thin films, fine particles, magneto-optics and allied areas. Job environment emphasizes individual achievement.

AMPEX CORPORATION

World Leader in Magnetic Recording

Send resumes to:

Donald F. Eldridge
Head, Magnetics Department
934 Charter Street
Redwood City, California

NOW!
PLOT and VISUALIZE ELECTRIC LINES OF FORCE

CENCO®
ELECTRIC FIELD MAPPING APPARATUS

A convenient teaching aid for college physics that graphically visualizes the equipotential lines of an electric field. Provides a dry method for plotting a variety of fields. May be used for electron lens calculations in more advanced work. Write for details.

No. 79587 Cenco Electric Field Mapping Apparatus.....$55.75

cenco®

CENTRAL SCIENTIFIC CO.
1718-A Irving Park Road • Chicago 13, Illinois
Branches and Warehouses—Mountainside, N. J. Boston • Birmingham • Santa Clara • Los Angeles • Tulsa Houston • Toronto • Montreal • Vancouver • Ottawa

USS TRITON'S HISTORIC VOYAGE

Nuclear Engineers and Scientists

When the Navy's first nuclear radar picket submarine surfaced after its pioneering underwater trip around the world, its engineroom log showed 41,500 trouble-free miles traversed in 84 days.

For KAPL engineers and scientists who designed and developed Triton's unique twin reactor propulsion system, this invisible voyage was a new triumph in nuclear engineering. The world's largest submarine is powered by a KAPL pressurized water cooled system fueled by enriched uranium. It features compact reactor cores and low weight-per-shaft horsepower.

NEW REACTOR MILESTONE LOGGED

BY THE KNOLLS ATOMIC POWER LABORATORY

Explorations currently underway at KAPL are aimed at achieving a new regime of simplification in reactor technology. Qualified Nuclear Engineers and Physicists are invited to inquire about current openings.

Appropriate scientific or engineering degree and U.S. citizenship required.

Address: Mr. A. J. Scipione, Dept. 37-MI

Knolls Atomic Power Laboratory

OPERATED FOR A E C BY

GENERAL ELECTRIC

Schenectady, New York

CENCO® HYVAC GAS BALLAST PUMPS

For vacuum applications plant and laboratory. Eliminates use of oil separators, centrifuges, refrigerated traps. Wide range of capacities.

For best possible results use Cenco pump oil. Write today for Bulletin 9C.

No. 91506-1 rated displacement, 70.0 liters per min.....$284.25

cenco®

CENTRAL SCIENTIFIC CO.

A Subsidiary of Cenco Instruments Corporation

1718-A Irving Park Road • Chicago 13, Illinois

Branches and Warehouses—Mountainside, N. J. Boston • Birmingham • Santa Clara • Los Angeles • Tulsa Houston • Toronto • Montreal • Vancouver • Ottawa

FERRITE DEPT. MANAGER to $25,000	RADAR PROJECTS MANAGER to $19,000	IR OPTICS DESIGN $10–15,000
COMMUNICATION SECTION CHIEF to $20,000	*Jobs All Fee Paid*	PROGRAMMERS 704, etc $9–16,000
DIGITAL DESIGN or LOGIC to $18,000	MICROWAVE APPLIED RESEARCH $13–18,000	COMPUTER PROJECT MANAGER to $18,500

STEVENS ASSOC.,

INC. AGCY.

CALL OR WRITE, D. L. GOLAN.....YU 6-0180

SUITE 410—ONE E. 42 ST, NY 17, NY

PETROLEUM PRODUCTION RESEARCH

Vacancies for men of initiative and imagination exist at the Gulf Research Center.

M.S. or Ph.D. Engineer or Physicist to study combustion phenomena as related to the recovery of crude oil. A solid background in mathematics is essential.

M.S. or Ph.D. Engineer or Physical Chemist to apply modern concepts in surface chemistry to the problems of oil recovery.

M.S. or Ph.D. Engineer or Physicist interested in a combination of experimental and theoretical work having as its object the design, construction and operation of scaled models of complex oil field processes.

M.S. or Ph.D. Engineer, Physicist or Applied Mathematician to work on long-range programs in the general fields of fluid flow and properties of porous media. The aim is to help build a body of information which may ultimately assist in the design of radically new schemes for oil recovery.

- *Modern facilities located near Pittsburgh.*
- *Liberal publication policy.* • *Salaries open.*

Reply to:

Gulf Research & Development Company
Attn: Employment Manager
P. O. Drawer 2038
Pittsburgh 30, Pennsylvania

High Performance ELECTROMAGNETS and Power Supplies

RUGGEDNESS
4" Electromagnet Type A
(4" pole diameter)
Fields up to 25,000 gauss.
Homogeneity of at least 1 part in 10^5 in ½ cc.

ROTATION
Rotating Base Type AE
360° scale.
Positive friction lock.

STABILITY
Current-Stabilized Power Supply Unit Type B.

Also available:—
1½" Electromagnet Type C—for Teaching purposes.
7" Electromagnet Type E—for Electron Resonance Work.
8" Electromagnet Type D—for Electron Resonance and Nuclear Magnetic Resonance work.
Direct Reading Magnetometer Type G.
Proton Resonance Magnetometer Type P.

NEWPORT INSTRUMENTS
(Scientific & Mobile) Ltd.
3 CRAWLEY ROAD, NEWPORT PAGNELL, BUCKS, ENGLAND
Telephone: NEWPORT PAGNELL 401/2

CAREERS IN PHYSICS

TABLE OF CONTENTS
Newly revised edition—1960
By Alpheus W. Smith & Winston L. Hole

Physicist (Poem by R. P. Lister)
Foreword (by Dr. Elmer Hutchisson, Director, American Institute of Physics)
Preface
I. Physics—A Way of Thinking
II. Physics as a Profession
III. Fields of Specialization in Fundamental and Applied Physics
IV. Interdisciplinary Fields of Specialization
V. Careers in Teaching and Research
VI. Physicists in Industry
VII. Careers in Federal Service
VIII. Careers in the Nuclear Sciences
IX. Careers in Research Institutes and Special-Purpose Laboratories
X. Physicists and the Future
Appendices
1. Nobel Laureates in Physics, 1901–1959
2. Partial List of Fundamental and Applied Physics Journals
3. Partial List of Research Laboratories Having Major Programs in Physics
4. Selected Sources and References
Index

310 Pages **50 Illustrations**

Price Prepaid $5.95

LONG'S COLLEGE BOOK CO. DEPT. JP
1836 N. High St. Columbus 1, Ohio

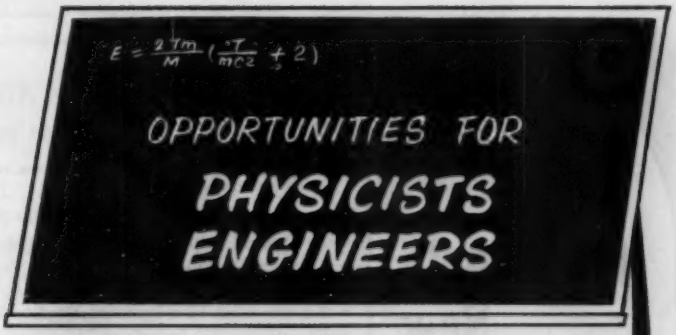

KEY POSITIONS ARE AVAILABLE AT VEECO'S NEW EXPANDED R & D LABORATORIES.

SOLID STATE PHYSICIST
Ph. D. With 5 years experience and a background with evaporation equipment and measurement of thin films, to plan and direct a program to develop techniques and equipment to produce thin films.

ELECTRONIC ENGINEER
Ph.D. or M.S. in physics or electrical engineering and 5 years experience in circuit design and development, with knowledge of transistors and miniature components. To direct expanded program in the development of such devices as D. C. amplifiers, electrometers and scintillation detectors, automatic control equipment for vacuum apparatus, equipment for measuring the properties of thin films.

Positions are also available in the R & D Department for Physicists and Engineers experienced in Ultrahigh Vacuum, Pumping, Leak Detection, Evaporation and Mass Spectrometry equipment and techniques.

For confidential consideration mail resume to:
WILLIAM LOCKOM
Personnel Director

Veeco

VACUUM-ELECTRONICS CORP.
TERMINAL DRIVE
PLAINVIEW, L. I., NEW YORK

SENIOR PHYSICIST

Advanced Memory Department of our Research Division offers an unusual opportunity for a physicist or engineer (Ph.D. desirable) to lead experimental and theoretical studies in new information storage media and techniques. Background in information storage or in solid state materials (ferroelectrics, scotophors, energy sensors, semiconductors or optical devices) essential. Company sponsored projects are underway in these areas and others may be initiated and directed by this man. Job environment emphasizes individual achievement.

AMPEX CORPORATION

World Leader in Magnetic Recording

Send resumes to:
Skipwith W. Athey
Director, Research Lab.
934 Charter Street
Redwood City, California

TADANAC BRAND
Special Research Grade
INDIUM

The purity of this specially refined indium is such that no individual impurity exceeds 0.1 ppm. It was developed primarily for use in the production of intermetallic compounds.

Other TADANAC Brand high purity metals or compounds include: Special Research Grade antimony and tin, High Purity Grade bismuth, cadmium, indium, lead, silver, tin, zinc and indium antimonide. Send for our brochure on TADANAC Brand High Purity Metals.

COMINCO

THE CONSOLIDATED MINING AND SMELTING COMPANY OF CANADA LIMITED
215 ST. JAMES ST. W., MONTREAL 1, QUEBEC, CANADA • PHONE AVenue 8-3103

C160

EE, ME, or Physics; BS, MS, Doctoral Degrees

A Unique Career Spot

Investigate New Positions

IN ADVANCED DEVELOPMENT AND PRODUCT ENGINEERING

- Thermoplastic Recording*
- Electronic Visual Amplifiers*

for Large Screen, High Brightness, High Resolution, Information Display Systems

- High Power AM, FM, Short Wave, TV (VHF-UHF) & Scatter Transmitters
- TV Studio Equipment — Mohochrome & Color
- TV & AM Station Audio Equipment
- UHF, VHF, & Microwave Antennas
- Transmission Line Systems, Studio TV Transmitter Link Equipment
- Educational TV, Industrial TV

GENERAL ELECTRIC'S TECHNICAL PRODUCTS OPERATION

... the "hatching place" of new commercial and military products in fields of

BROADCASTING • CLOSED CIRCUIT TV • SPECIAL VIDEO & DISPLAY

BS or Advanced degrees plus experience in one of the following areas

A. Geometric, Physical & Electron Optics
B. Circuit Design (Semiconductor & Tubed)
C. Mechanical design of products involving complex precision mechanisms, vacuum systems, optics, thermodynamics.

**Descriptive literature sent on request.*

Write in full confidence to: N. C. Murray, Engineering Sect. 37-M1
TECHNICAL PRODUCTS OPERATION
GENERAL ELECTRIC
Electronics Park, Room 215, Bldg. 7, Syracuse, New York

NEWS from the NRC Vacuum MICRONICLE*

REDHEAD MAGNETRON GAUGE READS VACUUM TO BELOW 10^{-12} mm Hg

Direct measurement of pressure from 10^{-4} to less than 10^{-12} mm Hg is easy with the new Model 552 Redhead Magnetron Ultra-High Vacuum Gauge and Model 752 UHV Gauge Control.

Cold cathode operation keeps the Model 552 elements from vaporizing and eliminates the need for outgassing circuit. S lf-regulated emission simplifies operation and maintains high signal to background ratio on all ranges. High sensitivity of 4.5 amp/mm Hg (air) permits use of standard electrometer amplifier. Response is virtually linear and almost instantaneous.

Partially transistorized Model 752 has only four operating controls: two switches, range selector, and zero set. Connections are provided for 0-10 mv recorder. Short time constant permits observation of pressure fluctuations. Gauge, magnet, and control now in stock at $195, $50, and $650.

RED-16

*Send for FREE periodical containing details on above plus other news about high vacuum.

NRC EQUIPMENT CORPORATION

A Subsidiary of National Research Corporation

Dept. P-9, 160 Charlemont Street, Newton 61, Mass.

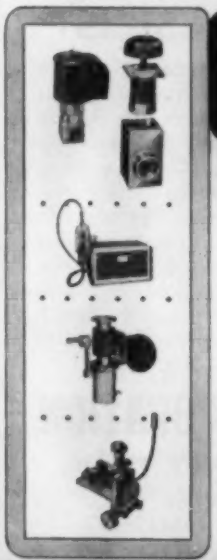

trouble-free
HIGH VACUUM COMPONENTS

VALVES...GAUGES...CONTROLS PUMPS...ACCESSORIES

VALVES: Bellow sealed, brass & stainless steel • Manual • Solenoid • Pneumatic

GAUGES & CONTROLS: Non-burnout ionization gauges, Bayard-Alpert type • Ultra-stable ionization gauge controls • Cold cathode discharge gauges and controls • Thermocouple gauges and controls

PUMPS: Diffusion pumps, air-cooled & water-cooled • Mechanical pumps, complete stock

ACCESSORIES: Standard and variable leaks • Quick couplings • Cold traps, Baffles • Electric degassing gun • "O"-ring sealed flanges • *Many others.*

FREE TECHNICAL BULLETINS
or complete CATALOG.
Write Department A-1437.

Veeco VEECO VACUUM CORP.
86-1 Denton Avenue, New Hyde Park
Long Island, New York
HIGH-VACUUM & LEAK DETECTION EQUIPMENT

HIGH IN RESOLVING POWER, EASIER TO MAINTAIN THAN ANY OTHER ELECTRON MICROSCOPE

BENDIX TRONSCOPE TRS-50 E1

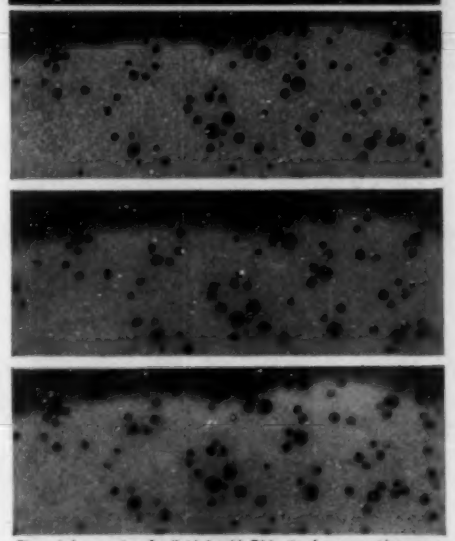

Through focus series of colloidal gold. Objective lens current increases from top to bottom.

BENDIX TRONSCOPE
demonstrates 20Å resolving power with no adjustments.

BENDIX TRONSCOPE
is first electron microscope with absolutely no decrease in resolving power from adjustments.

BENDIX TRONSCOPE
is the most trouble-free electron microscope in the world.

BENDIX TRONSCOPE,
including electron tubes, is *warranted unconditionally* for one year against defects in materials and workmanship. Service is available after warranty period on either a contract or a transportation, per diem, parts basis.

FULL DETAILS
can be obtained by writing Dept. EMSS.

Cincinnati Division
3310 Wasson Road • Cincinnati, Ohio

Bendix

Export Sales & Service:
Bendix International, 205 E. 42nd St., New York 17, N. Y.
Canada:
Computing Devices of Canada, Ltd., Box 508, Ottawa 4, Ont.

WHAT HAPPENS AT 1,200,000 FEET UP?

You can have the answer NOW . . . and leave theory and the educated guess to others. KINNEY offers fully developed working tools which provide pressures of better than 1 x 10^{-9} mm Hg . . . ready to work in areas heretofore closed to physicist and researcher.

Kinney®

TWO NEW DEVELOPMENTS IN ULTRA HIGH VACUUM

The KINNEY UH-9A Ultra High Vacuum System, (illustrated above) employing the principle of differential pumping, consistently produces Vacuum in the order of 1 x 10^{-9} mm Hg in the work chamber. KINNEY also offers a new Ionic High Vacuum System which develops pressures even lower than the $^{-9}$ scale. This system features the Ultek® Ion Pump for which KINNEY is exclusive distributor.

The facts about these significant developments in Vacuum technology are yours for the asking. **Write for KINNEY bulletins 4150, 4160 and 4450 today!**

KINNEY VACUUM DIVISION
THE NEW YORK AIR BRAKE COMPANY
3556J WASHINGTON STREET • BOSTON 30 • MASS.

Please send me copies of Bulletins 4150, 4160 and 4450 describing KINNEY Ultra High Vacuum Systems.

Name_____

Company_____

Address_____

City_____ Zone____ State_____

INDEX TO ADVERTISERS

Name	*Page*
AMPEX CORPORATION	xxx, xxxiii
ARNOLD ENGINEERING CO.	vii
AVCO EVERETT RESEARCH LAB.	xii
BATTELLE MEMORIAL INSTITUTE	xxix
BELL TELEPHONE LABORATORIES	v
BENDIX CORPORATION	xxxv
CENTRAL SCIENTIFIC CO. — Manufacturers of Cenco physical apparatus and instruments to meet all requirements of University, College and High School Physics Laboratories. Specializing in high vacuum pumps and development of instruments and apparatus for various sciences.	xxx, xxxi
CONSOLIDATED MINING & SMELTING CO.	xxxiii
CONVAIR/FORT WORTH Div. of General Dynamics	xxvi
CORNELL-DUBILIER ELECTRIC CORP. — Primarily interested in the design and manufacture of special type capacitors for thermonuclear work along the lines of the enclosed illustrations. These special fast discharge low inductance capacitors, operating in voltages up to 160 KV, have extensive use in the advanced study of high temperature and high current fields.	xxvii
CUSTOM SCIENTIFIC INSTRUMENTS, INC.	xviii
DELCO RADIO DIV. OF GENERAL MOTORS	vi
EASTMAN KODAK CO.	xi
EPPLEY LAB., INC.	xxix
FARRAND OPTICAL CO.	xxx
GENERAL ELECTRIC Knolls Atomic Power Lab.	xxxi
GENERAL ELECTRIC Technical Products Operation	xxxiv
GENERAL MAGNETICS, INC.	Insert at pages iii, iv
GENERAL RADIO CO. — Manufacturers of electronic measuring instruments; vacuum-tube voltmeters, amplifiers, and oscillators; wave analyzers, noise meters and analyzers, stroboscopes, laboratory standards of capacitance; inductance and frequency; impedance bridges, decade resistors and condensers, air condensers and variable inductors; rheostats, variacs, transformers; other laboratory accessories.	Cover 4
GULF RESEARCH & DEVELOPMENT CO.	xxxii
HARSHAW CHEMICAL CO.	Cover 2
HARVEY-WELLS ELECTRONICS, INC.	xxi
HUGHES AIRCRAFT CO.	xxvii, xxviii
IBM CORPORATION	xxv
INTERSCIENCE PUBLISHERS, INC.	xx
KEITHLEY INSTRUMENTS, INC. — Vacuum tube electrometers, microammeters, kilovoltmeters, static detectors, meg-megohm-meters, high gain dc amplifiers, dc vacuum tube voltmeters, high input impedance ac isolation amplifiers.	xiii
KINNEY VACUUM DIVISION, N. Y. AIR BRAKE CO.	xxxv
LONG'S COLLEGE BOOK CO	xxxii
LOS ALAMOS SCIENTIFIC LAB.	xix
McGRAW-HILL BOOK CO., INC.	xxxviii
MITRE CORPORATION	x
NRC EQUIPMENT CORP. — Manufacturers of standard and special high vacuum components, equipment, and systems including mechanical booster, and diffusion pumps; gauges; valves; seals; connectors; melting and heat-treating furnaces; coaters; impregnators; gas in metal analyzers; driers and freeze driers; altitude chambers; and leak detectors.	xxxiv
NEWPORT INSTRUMENTS LTD.	xxxii
OLIN MATHIESON CHEMICAL CORP.	xxvi
RADIO CORP. OF AMERICA	xv
SCHLUMBERGER WELL SURVEYING CORP.	xxiii
SPACE TECHNOLOGY LABORATORIES.	Cover 3
STEVENS ASSOCIATES, INC. AGENCY	xxxi
STOKES CORP., F. J. — Mechanical and oil vapor pumps; vacuum valves, gauges and other components; vacuum furnaces, metallizers, processing systems and other special high vacuum equipment.	xxviii
STROMBERG-CARLSON DIV. OF GENERAL DYNAMICS	xiv

INDEX—*Continued*

Name — *Page*

SYLVANIA ELECTRONIC PRODUCTS, INC. xvi

TEXAS INSTRUMENTS, INC. xvii

VARIAN ASSOCIATES
Instrument Div. ..... viii, ix
Vacuum Div. xxii

VEECO VACUUM CORP. ..... xxxiii, xxxiv

WELCH SCIENTIFIC CO., W. M. xxiv
Manufacturers of high-vacuum pumps, both mechanical and diffusion; vacuum gauges; electrical measuring instruments; physics equipment; and other items for the physical and chemical laboratories.

Position Open
for Person with Training and Experience in Semiconductors

to undertake research on materials for electronic components. Work will involve the preparation and study of thin films by various techniques. Background and experience in physics of solids and devices, or in thin films is desired. Company long established in production of component parts is initiating applied research activity in related areas. Challenging position for person wishing to work in a small vigorous group in new laboratory with responsibility for planning and executing projects.

Interested persons should send resumé to:

Supervisor of Electronics Research
Speer Carbon Research Laboratory
Packard Road and 47th Street
Niagara Falls, New York

- **STUDENT SECTION NEWSLETTER**
- **SPEAKERS For STUDENT SECTIONS**
- **MOVIES and FILM STRIPS For STUDENT SECTIONS**
- **GRADUATE SCHOOL INFORMATION**
- **PLACEMENT INFORMATION**
- **PHYSICS TODAY**

The above is some of the information sent systematically to all American Institute of Physics Student Sections. There are now 2300 student members in over 100 sections.

A booklet describing in detail the procedure for establishing Student Sections and the benefits which student organizations derive from membership will be sent upon request. Address all inquiries to:

Mrs. Ethel E. Snider, National Secretary
Student Sections
American Institute of Physics
335 East 45th Street
New York 17, N. Y.

An Opportunity to Use Your Scientific Knowledge

CHALLENGING! TIMELY! IMPORTANT!

If you are at home with the terminology of physics, mathematics, chemistry, electronics, astronomy, mechanical engineering, metallurgy, as related to aerospace technology, missiles, rocketry, etc., an intriguing and unusual job is waiting for you. The work will involve you with eminent U. S. scientists. You will identify and categorize abstracts from high level scientific articles. We will orient you for the screening of foreign scientific and technical literature in such areas of knowledge as missiles, aerospace technology, air defense, rocket propulsion, and aircraft.

Starting salary is excellent. The work is with one of the country's leading publishers, in New York City or Dayton, Ohio, depending on your qualification.

Please send us your resume as soon as you can.

Write Journal of Applied Physics, Box 960, 335 East 45th St., New York 17, N. Y.

Timely McGRAW-HILL Books

Beranek—NOISE REDUCTION. *Ready in September.*

Bharucha-Reid—ELEMENTS OF THE THEORY OF MARKOV PROCESSES AND THEIR APPLICATIONS. 469 pages. $11.50.

Beckenbach—MODERN MATHEMATICS FOR THE ENGINEER. Volume II. *Ready in January, 1961.*

Chernov—WAVE PROPAGATION IN A RANDOM MEDIUM. 176 pages. $7.50.

Collin—FIELD THEORY OF GUIDED WAVES. *Ready in October.*

Langmuir—ELECTROMAGNETIC FIELDS AND WAVES. *Ready in January, 1961.*

Middleton—AN INTRODUCTION TO STATISTICAL COMMUNICATION THEORY. 1140 pages. $25.00.

Oldenberg—INTRODUCTION TO ATOMIC AND NUCLEAR PHYSICS. New Third Edition. *Ready in January, 1961.*

Slater—QUANTUM THEORY OF ATOMIC STRUCTURE. Volumes I and II. Volume I—502 pages. $11.00. Volume II—*Ready in September.*

Williams and Young—ELECTRICAL ENGINEERING PROBLEMS. *Ready in September.*

Send for copies on approval

McGraw-Hill
BOOK COMPANY, INC.
330 West 42nd Street New York 36, N.Y.

When crews of SAC's 1st Missile Division successfully launched the USAF ICBM Atlas from Vandenberg Air Force Base, September 9, 1959, the world became aware that the United States had brought into being a formidable retaliatory power for peace. Within four months after the first operational launch, the Air Force doubly underlined this missile's capability. On a single day, January 26, 1960, the 16th and 17th consecutive successful Atlases were fired intercontinental ranges to predetermined targets from both Atlantic and Pacific bases.

After only five years of intensive development, including concurrent research, testing and fabrication under this nation's top military priority, Atlas is extremely versatile as well as powerful. It was the Project Score satellite vehicle and is scheduled for use in Project Mercury, the Man in Space Program, and in other space exploration missions. Thus, used as a booster for space projects, Atlas provides the nation with a key capability in scientific as well as military applications.

Space Technology Laboratories provides the systems engineering and technical direction for the Atlas as well as other portions of the Air Force Ballistic Missile Program. Much of what was learned in building Atlas has helped cut the lead-time in the development of such other Air Force Ballistic Missiles as Thor, Titan and Minuteman.

Among the industrial organizations which have worked in concert in developing Atlas are such major contractors as: Convair, Division of General Dynamics Corp. for airframe, assembly and test; General Electric Co. and Burroughs Corp. for radio guidance; Arma, Division of American Bosch and Arma Corp. for inertial guidance; Rocketdyne Division of North American Aviation, Inc., for propulsion; General Electric Co. for re-entry vehicle; Acoustica Associates for propellant utilization.

America's first intercontinental ballistic missile...is helping to bear the burden of today's power for peace

ATLAS

The continuing development of Atlas as well as other USAF missiles and related space probes, has created important positions on STL's technical staff for scientists and engineers with outstanding capabilities in: thermodynamics, aerodynamics, electronics, propulsion systems, structures, physics, computer technology, telemetry, and instrumentation. If you believe you can contribute in these or related fields and disciplines, you are invited to send your resume to:

SPACE TECHNOLOGY LABORATORIES, INC.

. . . for Tachometry and Slow-Motion Analysis of Machines and Electromechanical Devices

Intense, white light — 70 times brighter than previous model (4.2 million candlepower on low-speed range).

Short-duration light flash (1 to 6 μsec) "freezes" motion . . . practically eliminates blur . . . lets you clearly see details that are invisible with other commercial stroboscopes.

Long-throw beam reaches into machine innards — made possible by basic new flash tube developed exclusively for this instrument.

Measures speeds directly with ±1% accuracy up to 25,000 rpm . . . useful to at least 250,000 rpm.

Unique carrying case provides full enclosure for protection against damage and doubles as an adjustable stand for convenient bench use.

Pivoting lamp rotates 360° horizontally and 180° vertically.

One simplified dial and range control adjusts rate of flash — eliminates errors accidentally caused by reading wrong scale.

Type 1531-A STROBOTAC $260. ***Write for complete information.***

GENERAL RADIO COMPANY
WEST CONCORD, MASSACHUSETTS